

Magnetospheric Multiscale (MMS) Project

# Calibration and Measurement Algorithms Document (CMAD)

V2.0

Submitted: 22 November 2022



---

**Goddard Space Flight Center  
Greenbelt, Maryland**

**National Aeronautics and  
Space Administration**

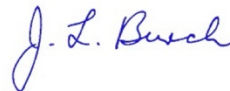
**MAGNETOSPHERIC MULTISCALE (MMS)  
Calibration and Measurement Algorithms Document (CMAD)**


---

Dr. Barbara Giles, GSFC MMS Project Scientist

14 November 2022  
Date


---

Dr. James Burch, SwRI MMS Science PI

21 November 2022  
Date

By signing this document, signatories are certifying that the content herein is acceptable direction for managing the project’s data and that they will ensure its implementation by those over whom they have authority.

Copy to: HQ Program Scientist

**REVISION HISTORY**

Revision Level	DESCRIPTION	EFFECTIVE DATE
Rev 0	Outline submitted to FY2020 Senior Review	2 June 2020
Rev 1	Full Draft, released for review and validation by MMS ITF Team	15 Feb 2022
Rev 2	V2.0 Public Release	22 Nov 2022

**TABLE OF CONTENTS**

<b>1.0</b>	<b>INTRODUCTION .....</b>	<b>8</b>
1.1	GENERAL INFORMATION .....	8
1.2	PURPOSE.....	8
1.3	CONTENTS .....	8
1.4	MISSION OVERVIEW STATUS .....	9
1.5	REFERENCES.....	10
<b>2.0</b>	<b>ACTIVE SPACECRAFT POTENTIAL CONTROL (ASPOC) .....</b>	<b>11</b>
2.1	ASPOC OVERVIEW .....	11
2.1.1	<i>Status of ASPOC Instruments</i> .....	12
2.2	ASPOC MEASUREMENT STANDARDS, VOLUME, AND TIMING .....	13
2.2.1	<i>Accuracy of ASPOC Time Tags in L1b/SITL Data</i> .....	13
2.2.2	<i>Accuracy of ASPOC Time Tags in L2 Data</i> .....	13
2.2.3	<i>Relative Telemetry Allocations and Data Volume</i> .....	13
2.3	ASPOC CALIBRATION AND VALIDATION .....	14
2.3.1	<i>Pre-Flight / On-Ground Calibration</i> .....	14
2.3.2	<i>In-Flight Calibration</i> .....	15
2.3.3	<i>Validation</i> .....	16
2.4	MEASUREMENT ALGORITHM DESCRIPTIONS.....	16
2.4.1	<i>Theoretical Basis (Operating Modes)</i> .....	16
2.4.2	<i>Conversion of Instrument Signals</i> .....	18
2.4.3	<i>Error Analysis and Known Features in the Dataset</i> .....	19
2.4.4	<i>ASPOC Data Quality Flags</i> .....	29
2.5	DATA PRODUCTION ALGORITHM DESCRIPTIONS.....	30
2.5.1	<i>ASPOC L1b/SITL Data Products</i> .....	30
2.5.2	<i>ASPOC L2 Data Products</i> .....	30
2.5.3	<i>Quicklook Data Products</i> .....	30
2.6	APPENDIX A- ASPOC REFERENCES .....	33
<b>3.0</b>	<b>MAGNETIC EPHEMERIS COORDINATES (MEC) .....</b>	<b>34</b>
3.1	MEC OVERVIEW.....	34
3.2	COORDINATE SYSTEMS.....	34
3.2.1	<i>Spinning, Spacecraft-fixed Systems</i> .....	34
3.2.2	<i>De-spun Systems</i> .....	34
3.2.3	<i>Geophysical Systems</i> .....	34
3.2.4	<i>JPL DE421 Ephemerides</i> .....	35
3.2.5	<i>Relationship Between Celestial and Magnetospheric Coordinate Systems</i> .....	36
3.3	IMPLEMENTATIONS AND SOFTWARE LIBRARIES USED .....	36
3.4	IMPLEMENTATION DETAILS FOR TRANSFORMATIONS REQUIRING ATTITUDE DATA .....	37
3.4.1	<i>FDOA Attitude Inputs</i> .....	37
3.4.2	<i>Calculation of ECI_to_DBCS and ECI-to_BCS Coordinate Systems</i> .....	38
3.4.3	<i>Attitude Interpolation</i> .....	38
3.4.4	<i>Quaternion Definitions and Usage</i> .....	38
3.4.5	<i>Transformations Between Spinning and De-spun Coordinate Systems</i> .....	39
3.5	IMPLEMENTATION DETAILS FOR TRANSFORMATIONS REQUIRING EPHEMERIS DATA .....	39
3.5.1	<i>FDOA Ephemeris Inputs</i> .....	39
3.5.2	<i>Ephemeris Interpolation</i> .....	40
3.5.3	<i>Transformations Between Systems</i> .....	40
3.6	LEVEL 2 ATTITUDE AND EPHEMERIS FILE CONTENTS.....	40
3.6.1	<i>Ancillary Data</i> .....	40

3.6.2	<i>Attitude</i> .....	41
3.6.3	<i>Coordinate Transformations</i> .....	41
3.6.4	<i>Position and Velocity</i> .....	41
3.6.5	<i>Magnetic Field Model Dependent Quantities</i> .....	42
3.6.6	<i>Version Numbering</i> .....	42
3.7	MEC APPENDICES.....	43
3.7.1	<i>Appendix A- References</i> .....	43
<b>4.0</b>	<b>FAST PLASMA INVESTIGATION (FPI)</b> .....	<b>45</b>
4.1	FPI OVERVIEW .....	45
4.1.1	<i>Status of FPI Spectrometers</i> .....	45
4.1.2	<i>Status of FPI Science Data</i> .....	46
4.2	FPI DATA USAGE SUMMARY CHECKLIST .....	47
4.3	FPI MEASUREMENT STANDARDS AND VOLUME.....	48
4.3.1	<i>FPI Measurement Timing</i> .....	48
4.3.1.1	Overview .....	48
4.3.1.2	Burst Data Product Timing .....	49
4.3.1.2.1	Microsecond Level Precision .....	49
4.3.1.3	Fast Survey Data Product Timing .....	49
4.3.1.4	Slow Survey Data Product Timing .....	50
4.3.2	<i>Relative Telemetry Allocations and Data Volume</i> .....	50
4.4	FPI CALIBRATION AND VALIDATION .....	51
4.4.1	<i>Calibration Overview</i> .....	51
4.4.2	<i>Pre-Flight / On-Ground Calibration</i> .....	52
4.4.3	<i>In-Flight Calibration</i> .....	52
4.4.3.1	Operating Point Calibration .....	53
4.4.3.2	Burst Calibration .....	54
4.4.4	<i>Compression Pipeline</i> .....	55
4.4.5	<i>Science Data Validation</i> .....	56
4.5	MEASUREMENT ALGORITHM DESCRIPTIONS.....	57
4.5.1	<i>Theoretical Basis</i> .....	57
4.5.2	<i>Conversion of Instrument Signals to Phase Space Density</i> .....	57
4.5.3	<i>Instrument Thresholds vs Ambient Plasma Distribution</i> .....	58
4.5.4	<i>Counting Statistics and Establishing the 1-Count Level</i> .....	58
4.5.5	<i>Quasi-Neutrality Check</i> .....	58
4.5.6	<i>FPI in the Solar Wind</i> .....	59
4.5.7	<i>Error Analysis and Known Features in the Dataset</i> .....	59
4.5.7.1	Correction for Spacecraft Potential .....	59
4.5.7.2	Correction for DES Photoelectrons .....	60
4.5.7.3	Correction for Compression Artifacts .....	61
4.5.7.4	Correction for Pointing Error .....	62
4.5.7.5	Correction for Penetrating Radiation.....	62
4.5.7.6	Correction for Spintones.....	63
4.5.8	<i>DES/DIS Quality Flags</i> .....	64
4.5.8.1	Distribution File Flags.....	64
4.5.8.2	Moments File Flags .....	64
4.6	DATA PRODUCTION ALGORITHM DESCRIPTIONS.....	65
4.6.1	<i>File Structure L2 3D DES/DIS Distributions (skymaps)</i> .....	65
4.6.2	<i>File Structure L2 DES Distribution Aux</i> .....	65
4.6.3	<i>File Structure L2 DES/DIS Moments</i> .....	65
4.6.4	<i>File Structure L2 DES/DIS Moments Aux</i> .....	67
4.6.5	<i>Calculation of L2 DES/DIS Plasma Moments</i> .....	69
4.6.6	<i>Calculation of L3 DES/DIS Pseudo Moments</i> .....	75
4.7	FPI APPENDICES .....	75



4.7.1	Appendix A- Voltages Over Time / Voltage Operations .....	75
4.7.2	Appendix B- Stepping Tables Over Time .....	82
4.7.3	Appendix C- Energy Profiles by Mission Phase.....	84
4.7.4	Appendix D- FPI References .....	86
<b>5.0</b>	<b>HOT PLASMA COMPOSITION ANALYZER (HPCA) .....</b>	<b>89</b>
5.1	HPCA OVERVIEW .....	89
5.1.1	Status of the HPCA Instruments.....	89
5.2	HPCA MEASUREMENT STANDARDS, VOLUME, TIMING, AND COORDINATES .....	90
5.2.1	Accuracy of HPCA Time Tags in L2 Data .....	90
5.3	RELATIVE TELEMETRY ALLOCATIONS AND DATA VOLUME.....	90
5.3.1	Basic Instrument Information for Algorithm Development .....	91
5.3.1.1	ESA .....	91
5.3.1.2	TOF.....	92
5.3.1.3	Determining Doubly Charged Oxygen Counts .....	94
5.3.2	Coordinates / Phase Space Scanning Dimensions.....	95
5.3.2.1	ESA Voltages – Energy.....	95
5.3.2.2	Start Anodes – Elevation.....	96
5.3.2.3	Spacecraft Rotation – Azimuth .....	99
5.3.3	Geometric Factor .....	102
5.3.3.1	Effective Area.....	102
5.3.3.2	Integrated Energy-Azimuth Response, $\langle \Delta E/E \Delta \alpha \rangle$ .....	104
5.3.3.3	Geometric Factor for HPCA.....	104
5.4	HPCA CALIBRATION AND VALIDATION .....	104
5.4.1	Pre-Flight / On-Ground Calibration.....	104
5.4.2	In-Flight Calibration .....	105
5.4.3	Compression Pipeline and Lossy Compression.....	105
5.4.4	Validation .....	105
5.5	MEASUREMENT ALGORITHM DESCRIPTIONS.....	106
5.5.1	Theoretical Basis.....	106
5.5.2	Error Analysis and Known Features .....	107
5.6	DATA PRODUCTION ALGORITHM DESCRIPTIONS.....	107
5.6.1	Level 0 - Counts.....	107
5.6.2	Level 1a - Flux .....	107
5.6.3	Level 1b - $f_s(v)$ .....	108
5.6.4	Plasma Distribution Moments .....	109
5.6.4.1	Ion Number Density ( $n_s$ ).....	110
5.6.4.2	Ion Bulk Velocity ( $u_s$ ).....	110
5.6.4.3	Scalar Ion Temperature.....	111
5.6.4.4	Ion Temperature Tensor .....	112
5.6.5	Data Products with RF .....	115
5.6.6	Level 2 Data Products: In the Magnetic Field Reference Frame .....	115
5.6.6.1	Bulk Velocity in the Magnetic Field Frame.....	115
5.6.6.2	F(v) in Field Aligned Coordinates .....	116
5.6.7	HPCA Quality Flags .....	118
5.6.8	File Structure L2 Ion CDF File.....	118
5.6.9	File Structure L2 Moments CDF File .....	120
5.6.10	File Structure L2 TOF Counts CDF File .....	123
5.7	APPENDIX A- HPCA REFERENCES .....	124
<b>6.0</b>	<b>ENERGETIC PARTICLE DETECTOR (EPD) .....</b>	<b>125</b>
6.1	EPD OVERVIEW.....	125
6.1.1	Energetic Ion Spectrometer (EIS) .....	126
6.1.2	Fly's Eye Energetic Particle Sensor (FEEPS) .....	127

6.1.3	<i>Status of EPD Sensors</i> .....	129
6.2	EPD MEASUREMENTS STANDARDS, VOLUME, AND TIMING .....	129
6.2.1	<i>EIS Viewing</i> .....	129
6.2.2	<i>FEEPS Viewing</i> .....	130
6.2.3	<i>EPD Ephemeris and Magnetic Field Information Requirements</i> .....	131
6.2.4	<i>EIS File Versioning</i> .....	131
6.3	EPD CALIBRATION AND VALIDATION .....	133
6.3.1	<i>EIS Pre-Flight / On-Ground Calibration</i> .....	133
6.3.2	<i>EIS In-Flight Calibration</i> .....	133
6.3.3	<i>FEEPS Pre-Flight / On-Ground Calibration</i> .....	135
6.3.3.1	FEEPS Lowest-Energy Channels .....	136
6.3.3.2	FEEPS Flat Field .....	137
6.3.4	<i>FEEPS In-Flight Calibration</i> .....	137
6.3.5	<i>Data Processing Pipeline</i> .....	139
6.3.6	<i>Validation</i> .....	141
6.4	EPD ALGORITHM DESCRIPTIONS.....	141
6.4.1	<i>Conversion from Counts/sec to Flux (L1-&gt;L2)</i> .....	141
6.4.2	<i>FEEPS Conversion from Counts to Flux (L1-&gt;L2)</i> .....	142
6.4.3	<i>FEEPS Data Quality Flags</i> .....	143
6.4.4	<i>EIS Calibration Matrix Overview</i> .....	146
6.4.5	<i>Known Features in the Dataset (Data Caveats)</i> .....	148
6.4.5.1	EIS .....	148
6.4.5.2	FEEPS.....	150
6.5	DATA PRODUCTS .....	152
6.5.1	<i>Data Products Overview</i> .....	152
6.5.2	<i>File Structure L2 FEEPS Electron</i> .....	154
6.5.3	<i>File Structure L2 FEEPS Ion</i> .....	156
6.5.4	<i>File Structure EIS Electronenergy</i> .....	158
6.5.5	<i>File Structure L2 EIS ExTOF and PHxTOF</i> .....	158
6.5.6	<i>File Structure L2 EIS PHxTOF</i> .....	160
6.5.7	<i>Level 3 EPD Products</i> .....	164
6.6	APPENDIX A- EIS REFERENCES.....	166
6.7	APPENDIX A- FEEPS REFERENCES.....	167
<b>7.0</b>	<b>FIELDS</b> .....	<b>169</b>
7.1	OVERVIEW.....	169
7.2	FIELDS TIMING.....	169
7.3	APPENDIX A- FIELDS REFERENCES.....	170
<b>8.0</b>	<b>FLUX GATE MAGNETOMETER (FGM)</b> .....	<b>171</b>
8.1	FGM OVERVIEW .....	171
8.1.1	<i>Status of FGM Magnetometers</i> .....	172
8.2	FGM MEASUREMENT STANDARDS, VOLUME, AND TIMING.....	174
8.2.1	<i>FGM Requirements</i> .....	174
8.2.2	<i>FGM Coordinate Systems</i> .....	174
8.2.3	<i>Accuracy of FGM Time Tags in L2 Data</i> .....	175
8.2.4	<i>Data Volume</i> .....	177
8.3	MAGNETOMETER MEASUREMENT ALGORITHM AND UNCERTAINTY ESTIMATION.....	178
8.3.1	<i>Measurement Algorithm</i> .....	178
8.3.2	<i>Net Uncertainty Estimation</i> .....	179
8.4	FGM CALIBRATION AND VALIDATION .....	180
8.4.1	<i>Pre-Flight Calibration / On-Ground Calibration</i> .....	180

8.4.2	<i>In-Flight Calibration</i> .....	181
8.4.3	<i>Science Data Assessment (Validation)</i> .....	185
8.4.4	<i>Known Issues</i> .....	187
8.5	FGM DATA PRODUCTION ALGORITHM DESCRIPTIONS .....	193
8.5.1	<i>Description of Data Products</i> .....	193
8.5.2	<i>Data Production Algorithms</i> .....	193
8.5.3	<i>L2 File Structure</i> .....	194
8.5.3.1	Survey File Conventions .....	195
8.5.3.2	Burst File Conventions .....	195
8.5.3.3	File Name Conventions .....	195
8.5.3.4	Version Numbering Conventions .....	195
8.5.3.5	L2 File Content .....	196
8.5.3.6	Data Flag Definitions .....	198
8.5.3.7	Error Estimation Metadata in CDF Files .....	199
8.6	APPENDIX A- FGM REFERENCES .....	199
<b>9.0</b>	<b>SEARCH COIL MAGNETOMETER (SCM)</b> .....	<b>203</b>
9.1	SCM OVERVIEW .....	203
9.2	AC MAGNETIC FIELD WAVEFORMS (ACB) .....	204
9.2.1	<i>Overview</i> .....	204
9.2.1.1	Heritage .....	204
9.2.1.2	Product Description .....	204
9.2.2	<i>Theoretical Description</i> .....	205
9.2.3	<i>Calibration and Validation</i> .....	211
9.2.3.1	Calibration .....	211
9.2.3.1.1	Pre-Flight / On-Ground Calibration .....	212
9.2.3.1.2	In-Flight Calibration .....	212
9.2.3.2	Confidence in Measurements .....	213
9.2.3.3	Comparison of Other Measurements .....	213
9.2.3.4	Quality Control and Diagnostics .....	213
9.3	AC MAGNETIC FIELD POWER SPECTRAL DENSITY (BPSD) .....	214
9.3.1	<i>Overview</i> .....	214
9.3.1.1	Heritage .....	214
9.3.2	<i>Product Description</i> .....	214
9.3.3	<i>Theoretical Description</i> .....	215
9.3.4	<i>Calibration and Validation</i> .....	215
9.4	APPENDIX A- SCM REFERENCES .....	216
<b>10.0</b>	<b>ELECTRON DRIFT INSTRUMENT (EDI)</b> .....	<b>218</b>
10.1	EDI OVERVIEW .....	218
10.1.1	<i>Status of EDI</i> .....	219
10.1.2	<i>Mode Scheduling</i> .....	220
10.2	EDI DATA VOLUME AND TIMING .....	221
10.2.1	<i>Electric Field Mode Time Tags</i> .....	221
10.2.2	<i>Ambient Electron Mode Time Tags</i> .....	222
10.2.3	<i>EDI Data Volume</i> .....	222
10.3	EDI CALIBRATION AND VALIDATION .....	222
10.3.1	<i>Pre-Flight / On-Ground Calibration</i> .....	222
10.3.1.1	Electron Guns .....	223
10.3.1.2	Detectors .....	225
10.3.1.2.1	Sensor Tests .....	225
10.3.1.2.2	Optics Modeling .....	227
10.3.1.2.3	Detector Characterization .....	227
10.3.2	<i>In-Flight Calibration</i> .....	230

10.3.2.1	Electric Field Mode .....	230
10.3.2.2	Ambient Electron Mode.....	230
10.3.3	<i>Validation</i> .....	232
10.4	EDI ELECTRIC FIELD MEASUREMENT ALGORITHM DESCRIPTIONS.....	233
10.4.1	<i>Theoretical Basis</i> .....	233
10.4.2	<i>Error Analysis and Known Features in the Dataset</i> .....	233
10.4.3	<i>EDI Quality Flags</i> .....	233
10.5	EDI AMBIENT ELECTRON MEASUREMENT ALGORITHM DESCRIPTIONS.....	234
10.5.1	<i>Theoretical Basis</i> .....	234
10.5.1.1	Ambient Mode Raw Telemetry.....	234
10.5.1.1.1	Survey Telemetry .....	234
10.5.1.1.2	Burst Telemetry.....	234
10.5.1.1.3	Flip Flags .....	235
10.5.1.1.4	Anode Selection / Placemat .....	235
10.5.1.2	L1A Variable Relation to L2 Data Product Names .....	235
10.5.1.3	Anode Placement Details.....	237
10.5.1.4	Calculation of Azimuth Angles for Data Channels.....	237
10.5.1.5	Flip Flag Summary.....	238
10.5.2	<i>Error Analysis and Known features in the Dataset</i> .....	238
10.5.2.1	Dead Time Correction .....	238
10.5.2.2	Calculation of Ambient Electron Flux Errors .....	239
10.5.3	<i>EDI Quality Flags</i> .....	239
10.6	EDI DATA PRODUCTION ALGORITHM DESCRIPTIONS.....	239
10.6.1	<i>E-Field Data Processing</i> .....	240
10.6.1.1	Triangulation Analysis .....	241
10.6.1.2	Time-of-Flight Analysis.....	241
10.6.1.3	Filtering of L2 Pre Data.....	242
10.6.1.4	File Structure L2 EFIELD Data .....	242
10.6.2	<i>Quality-Zero Data</i> .....	243
10.6.2.1	File Structure L2 Quality-Zero Data.....	244
10.6.3	<i>Ambient Mode Data</i> .....	245
10.6.3.1	File Structure L2 AMBIENT Field Aligned Mode Data .....	247
10.6.3.1.1	Survey.....	247
10.6.3.1.2	Burst .....	248
10.6.3.2	File Structure L2 AMBIENT Alternating Pitch Angle Mode Data .....	249
10.6.3.2.1	Survey.....	249
10.6.3.2.2	Burst.....	251
10.6.3.3	File Structure L2 AMBIENT Perpendicular Mode Data.....	253
10.6.3.3.1	Survey.....	253
10.6.3.3.2	Burst .....	254
10.7	APPENDIX A- EDI REFERENCES .....	255
<b>11.0</b>	<b>ELECTRIC DOUBLE PROBES (EDP) .....</b>	<b>256</b>
11.1	EDP OVERVIEW .....	256
11.1.1	<i>Status of EDP Probes</i> .....	258
11.2	EDP MEASUREMENTS AND TIMING .....	259
11.2.1	<i>Pre-Flight / On-Ground Calibration</i> .....	260
11.3	EDP CALIBRATION AND VALIDATION .....	260
11.4	EDP ALGORITHM DESCRIPTIONS.....	261
11.4.1	<i>Theoretical Basics</i> .....	261
11.4.2	<i>SDP Algorithm</i> .....	261
11.4.3	<i>ADP Algorithm</i> .....	262
11.4.4	<i>EPSD Algorithm</i> .....	264
11.5	DATA PRODUCTS .....	265
11.5.1	<i>L2 Data Products</i> .....	267

11.5.2	<i>Bitmasks and Quality Flags</i> .....	267
11.5.3	<i>Level 1 Data Products</i> .....	268
11.5.4	<i>Level 2 Data Products</i> .....	268
11.6	APPENDIX A- EDP REFERENCES .....	270
<b>12.0</b>	<b>FLUXGATE-SEARCHCOIL-MERGED MAGNETIC FIELD (FSM)</b> .....	<b>271</b>
12.1	FSM OVERVIEW .....	271
12.2	INPUT DATA .....	271
12.2.1	<i>FGM</i> .....	271
12.2.2	<i>SCM</i> .....	272
12.3	MERGING METHODOLOGY.....	272
12.3.1	<i>In-Flight Noise Floor</i> .....	272
12.3.2	<i>Cross-Over Frequency</i> .....	275
12.3.3	<i>Cross-Calibration</i> .....	275
12.3.4	<i>FIR Filters</i> .....	276
12.3.5	<i>Improved Noise Floors</i> .....	277
12.3.6	<i>Validation</i> .....	278
12.4	DATA PRODUCT ALGORITHM DESCRIPTIONS.....	279
12.5	FILE STRUCTURE .....	279
12.5.1	<i>L3 FSM 8kHz</i> .....	279
12.5.1.1	Variables .....	279
12.5.1.2	File Versions.....	280
12.6	APPENDIX A- FSM REFERENCES .....	280
<b>13.0</b>	<b>APPENDIXES</b> .....	<b>282</b>
13.1	ABBREVIATIONS AND ACRONYMS .....	282
13.2	UNITS AND MEASUREMENT .....	287
13.3	LIST OF FIGURES .....	289
13.4	LIST OF TABLES .....	292

## 1.0 INTRODUCTION

### 1.1 GENERAL INFORMATION

The Magnetospheric Multiscale (MMS) mission is the fourth mission of the Solar Terrestrial Probe (STP) program of the National Aeronautics and Space Administration (NASA). The MMS mission utilizes four identically instrumented observatories to perform the first definitive study of magnetic reconnection in space and tests critical hypotheses about reconnection. Magnetic reconnection is the primary process by which energy is transferred from the solar wind to the Earth's magnetosphere and is also fundamental to the explosive release of energy during substorms and solar flares.

The MMS mission studies magnetic reconnection in the Earth's magnetosphere, magnetosheath, bowshock, and heliosphere within 29R<sub>E</sub>. The four MMS observatories primarily fly in a tetrahedral formation to unambiguously determine the orientation of the magnetic reconnection layer.

### 1.2 PURPOSE

The MMS Calibration and Measurement Algorithm Document (CMAD) describes the overall concept for calibrating the many instruments onboard Magnetospheric Multiscale (MMS), including pre-flight and in-flight calibrations, and details the algorithms for converting instrument signals to physical quantities, including signal estimates, error analyses, and error budgets.

This document is not designed to be the only reference for these aspects of the MMS instrumentation. Other, more detailed documents and publications are referenced that describe the instrumentation designs, operations, ground systems, and data products. For example, a close companion to this document is the MMS Data Product Management Plan (PDMP) and this document does not repeat the materials therein.

### 1.3 CONTENTS

All plans and algorithms are described as they were known during the applicable extended mission period. Future changes in instrument operations and/or understanding of calibrations and algorithms may require modifications to this document. The document is organized as follows:

**Table 1-1 Contents: Sections and Instrumentation**

Section and Associated Instrumentation: Particles / Other					
Section	2	3	4	5	6
Instrument	ASPOC	MEC	FPI	HPCA	EPD
Subsystem			DES		FEEPS
			DIS		EIS

Section and Associated Instrumentation: Fields						
Section	7	8	9	10	11	12
Instrument	FIELDS	FIELDS: FGM	FIELDS: SCM	FIELDS: EDI	FIELDS: EDP	FIELDS: FSM
Subsystem	Overview	AFG		E-Field	ADP	
	Fields Timing	DFG		Electrons	SDP	

**Acronyms Defined in Table of Contents and in Acronym List**

### 1.4 MISSION OVERVIEW STATUS

The status of the instruments throughout this mission can be broken down between the respective instrument groups as illustrated throughout this document; meanwhile, the below table represents the status of instruments collectively in relation to one another within each spacecraft. All instruments are operating nominally with, remarkably, few exceptions. For greater descriptions of the statuses of each instrument and the work of their corresponding groups, see sections 2.0 through 12.0 of this document. It is important to note that the information in the following table is subject to change over the mission lifespan.

MMS1								MMS2												
Central Data Processor				DFG		AFG		SCM		Central Data Processor				DFG		AFG		SCM		BField
SDP1	SDP2	SDP3	SDP4	ADP1	ADP2	EDI1	EDI2	SDP1	SDP2	SDP3	SDP4	ADP1	ADP2	EDI1	EDI2	EField				
DIS0	DIS1	DIS2	DIS3	DES0	DES1	DES2	DES3	DIS0	DIS1	DIS2	DIS3	DES0	DES1	DES2	DES3	Fast Electrons/Ions				
FEEPS1				FEEPS2				FEEPS1				FEEPS2				Electrons				
EIS (SSD OFF)				HPCA				EIS				HPCA				Ions/Comp				
A1E1	A1E2	A1E3	A1E4	A2E1	A2E2	A2E3	A2E4	A1E1	A1E2	A1E3	A1E4	A2E1	A2E2	A2E3	A2E4	ASPOC				
MMS3								MMS4												
Central Data Processor				DFG		AFG		SCM		Central Data Processor				DFG		AFG		SCM		BField
SDP1	SDP2	SDP3	SDP4	ADP1	ADP2	EDI1	EDI2	SDP1	SDP2	SDP3	SDP4	ADP1	ADP2	EDI1	EDI2	EField				
DIS0	DIS1	DIS2	DIS3	DES0	DES1	DES2	DES3	DIS0	DIS1	DIS2	DIS3	DES0	DES1	DES2	DES3	Fast Electrons/Ions				
FEEPS1				FEEPS2				FEEPS1				FEEPS2				Electrons				
EIS				HPCA				EIS				HPCA				Ions/Comp				
A1E1	A1E2	A1E3	A1E4	A2E1	A2E2	A2E3	A2E4	A1E1	A1E2	A1E3	A1E4	A2E1	A2E2	A2E3	A2E4	ASPOC				

Green = nominal ops  
Yellow = partial ops

**Table 4b.2 Instrument Status**

Grey = on hold as backup  
White = non-operational

**Table 1-2 Instrument Status Table**

Throughout the lifespan of the mission, the spacecrafts have gone through, and continue to go through, the course of mission phases with each passing calendar year. Each mission phase determines varying science data collections and scheduled operations applicable to each individual instrument team. Within these phases, the mission orbits must satisfy certain engineering requirements with respect to and regard for the duration and depth of Earth’s shadow that the spacecrafts are able to experience without restraint to their normal operations as well as with regard to the spacecraft’s fuel usage, amongst other orbit constraints.

The mission phases based on particular start and end dates and differing descriptors and orbit ranges are demonstrated in the following table.

Mission Phase	Start	End	Phase Description	Orbit Range
<b>Launch</b>	n/a	March 15, 2015	n/a	n/a
<b>Commissioning</b>	March 15, 2015	Sept 1, 2015	Nightside -> Dusk Flank	1 – 173
<b>Phase 1a</b>	Sept 1, 2015	March 8, 2016	12R <sub>E</sub> Dayside	173 – 363

<b>Phase 1x</b>	March 8, 2016	Sept 12, 2016	12R <sub>E</sub> Dayside, Nightside, Dusk	363 – 552
<b>Phase 1b</b>	Sept 12, 2016	Jan 31, 2017	12R <sub>E</sub> Dayside	552 – 694
<b>Phase 2a</b>	Jan 31, 2016	May 1, 2017	Apogee Raise, Dawn	694 – 748
<b>Phase 2b</b>	May 1, 2017	Sept 1, 2017	25R <sub>E</sub> Nightside	748 – 792
<b>Phase 3a</b>	Sept 1, 2017	Nov 14, 2017	25R <sub>E</sub> Dusk Flank	792 – 818
<b>Phase 3b</b>	Nov 14, 2017	March 13, 2018	25R <sub>E</sub> Dayside	818 – 860
<b>Phase 3c</b>	March 13, 2018	May 25, 2018	25R <sub>E</sub> Dawn Flank	860 – 886
<b>Phase 3d</b>	May 25, 2018	Sept 28, 2018	25R <sub>E</sub> Nightside	886 – 930
<b>Phase 4a</b>	Sept 28, 2018	Nov 29, 2018	25R <sub>E</sub> Dusk Flank	930 – 953
<b>Phase 4b</b>	Nov 29, 2018	April 16, 2019	25R <sub>E</sub> Dayside	953 – 997
<b>Phase 4c</b>	April 16, 2019	June 29, 2019	29R <sub>E</sub> Dawn Flank	997 – 1018
<b>Phase 4d</b>	June 29, 2019	Sept 30, 2019	29R <sub>E</sub> Nightside	1018 – 1044
<b>Phase 5a</b>	Sept 30, 2019	Nov 24, 2019	29R <sub>E</sub> Dusk Flank	1044 – 1060
<b>Phase 5b</b>	Nov 24, 2019	April 23, 2020	29R <sub>E</sub> Dayside	1060 - 1103
<b>Phase 5c</b>	April 23, 2020	June 22, 2020	29R <sub>E</sub> Dawn Flank	1103 – 1121
<b>Phase 5d</b>	June 22, 2020	Oct 6, 2020	29R <sub>E</sub> Nightside	1121 – 1150
<b>Phase 6a</b>	Oct 6, 2020	Nov 24, 2020	29R <sub>E</sub> Dusk Flank	1150 – 1165
<b>Phase 6b</b>	Nov 24, 2020	April 27, 2021	29R <sub>E</sub> Dayside	1165 – 1208
<b>Phase 6c</b>	April 27, 2021	June 24, 2021	29R <sub>E</sub> Dawn Flank	1208 – 1224
<b>Phase 6d</b>	June 24, 2021	Oct 6, 2021	29R <sub>E</sub> Nightside	1224 – 1255
<b>Phase 7a</b>	Oct 6, 2021	Nov 28, 2021	29R <sub>E</sub> Dusk Flank	1255 – 1268
<b>Phase 7b</b>	Nov 28, 2021	April 28, 2022	29R <sub>E</sub> Dayside	1268 – 1313
<b>Phase 7c</b>	April 28, 2022	June 9, 2022	29R <sub>E</sub> Dawn Flank	1313 – 1325
<b>Phase 7d</b>	June 9, 2022	Oct 17, 2022	29R <sub>E</sub> Nightside	1325 – 1362
<b>Phase 8a</b>	Oct 17, 2022		29R <sub>E</sub> Dusk Flank	1362 -

**Table 1-3 MMS Mission Phases**

## 1.5 REFERENCES

The following documents and drawings in effect on the day this specification was signed **shall** apply to the extent specified herein. In the event of conflict between this document and any referenced document, the document with latest publication date will govern.

The following is a list of applicable references and publications.

<b>Section</b>	<b>Document Number</b>	<b>Title</b>	<b>Revision/Date</b>
Many	461-PROJ-PLAN-0139	MMS Project Data Management Plan	Rev 1 / tbd FY2021



## Table 1-4 MMS Project Applicable Documents

### 2.0 ACTIVE SPACECRAFT POTENTIAL CONTROL (ASPOC)

#### 2.1 ASPOC OVERVIEW

The ASPOC instrument emits a beam of positive indium ions at energies of order 4 to 12 keV and currents of up to  $\sim 70 \mu\text{A}$  in order to control the electrical potential of the spacecraft. The emission of positive charges from the spacecraft balances the excess of charge accumulating on the vehicle from interactions with the environment. For the case of primary concern here, where photoemission of electrons drives the spacecraft potential positive relative to the plasma potential, it is necessary to emit positive ions.

By adjusting the positive emission current, the spacecraft potential can thus be adjusted to near zero value. Hence, the output of the instrument is an energetic ion beam with known energy and controlled current. By applying currents of several 10's of  $\mu\text{A}$  on the MMS spacecraft, the equilibrium potential will in any environment be driven into a regime which is independent of the ambient plasma density, and mainly be governed by the active ion beam current and the properties (mainly current and energy distribution) of the photo-electrons from the spacecraft surface, both of them are constant.

As a result, the spacecraft potential will be clamped to a value at which the current of the photoelectrons overcoming the potential barrier around the spacecraft equals the ion beam current. This equilibrium is established at potentials of a few Volts positive, as an inverse function of the ion beam current.

Two ASPOC instruments are installed on each of the four spacecraft and emit ion beams in antiparallel direction for symmetry reasons. Each instrument contains four individual emitters which are operated one at a time, for redundancy reasons and in order to ensure the required lifetime. Two individual ion emitters are contained in one ion emitter "module" and have a common high voltage supply. The indium reservoir and the capillary sitting on top are kept at high voltage. The ion sources are individually and indirectly heated from below by a resistor embedded into a ceramic insulator tube. This scheme enables the source to be heated from a grounded power supply and the tip itself still being kept at high voltage. The selection of the active emitter is made by switching high voltage to one of the emitter modules, and secondly by heating the active emitter.

A full description of the instrument design can be found in the ASPOC User Manual. First results from space, showing the spacecraft control capabilities of ASPOC can be found in the publication:

Nakamura, R., K. Torkar, M. Andriopoulou, H. Jeszenszky, C. P. Escoubet, F. Cipriani, P. A. Lindqvist, S. A. Fuselier, C. J. Pollock, B. L. Giles, Y. Khotyaintsev (2017), Initial Results From the Active Spacecraft Potential Control Onboard Magnetospheric Multiscale Mission, IEEE Transactions on Plasma Science, 45 (8), 1847-1852.

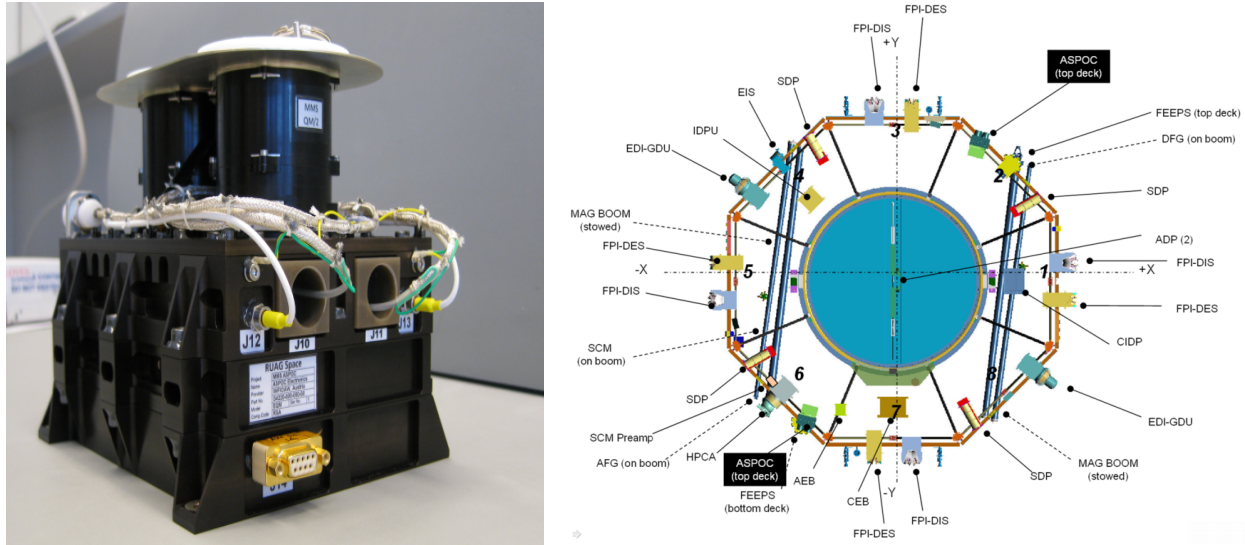


**Figure 2-1 ASPOC Instrument Picture and Spacecraft Accommodation**

The two ASPOC instruments are mounted at opposite sides of the instrument deck by means of brackets as shown in Figure 2-1. The ion beams of the two ASPOC instruments point in antiparallel directions such that the center axis of the ion beam is equidistant to the SDP probes. The only surfaces exposed to space shall be the top plates of the emitter modules. The rest of the instrument is inside the spacecraft envelope or covered by the Multi-Layer Insulation (MLI) of the spacecraft.

### 2.1.1 Status of ASPOC Instruments

The ASPOC instrument status as of September 30<sup>th</sup>, 2022 is shown in the following table:

Parameters (status as of 09/30/2022)	MMS1		MMS2		MMS3		MMS4	
	Unit A (FM9)	Unit B (FM2)	Unit A (FM3)	Unit B (FM5)	Unit A (FM7)	Unit B (FM8)	Unit A (FM4)	Unit B (FM6)
Emitter selection for phase 1-6	E2	E1	E3 <sup>1)</sup>	E2	E3	E3	E3	E2
Filament impedance [Ohm]	204	220	209	208	220	207	212	220
Filament power [W]	0.83	0.62 <sup>2)</sup>	0.83	0.83	0.70 <sup>1)</sup>	0.83	0.83	0.66 <sup>2)</sup>
Nominal operating current [ $\mu$ A]	10.0	10.0	10.0	10.0	10.0	10.0	10.0	10.0
Nominal beam energy [kV]	5.6	6.1	6.3	6.0	5.6	6.3	6.2	5.7
Cleaning cycles performed	4	0	0	0	0	0	0	4
Operating hours (total)	61363	61172	59331	60626	60799	60609	60691	60282
Operating hours (active)	20938	20937	19120	20617	20818	20824	20647	20648
Indium usage [%]	92.1	91.4	5.0 <sup>1)</sup>	91.0	91.6	92.1	91.3	91.1
Rest @ 20 $\mu$ A operation [h]	644	701	7740 <sup>1)</sup>	732	687	647	708	726
Rest @ 10 $\mu$ A operation [h]	1797	1956	21601 <sup>1)</sup>	2043	1918	1807	1981	2027

<sup>1)</sup> Emitter changed 09/2021    <sup>2)</sup> Power reduced due to active filament temperature (impedance) control

**Table 2-1 Status of ASPOC Instruments Table**

**2.2 ASPOC MEASUREMENT STANDARDS, VOLUME, AND TIMING**

**2.2.1 Accuracy of ASPOC Time Tags in L1b/SITL Data**

ASPOC Level-1b and Scientist In The Loop (SITL) data products are containing calibrated raw data having a resolution that corresponds to the data acquisition cycle on-board. The following data products are available (given resolutions are typical values):

- Ion beam current, energy, ~ 1s resolution
- Total emitter current, ~ 1 s resolution
- Status and housekeeping, ~ 40 s resolution
- Spacecraft potential as used for control loop, ~1 s resolution
- Emitter heater current and voltage, ~ 20 s resolution
- Status flags and parameters, ~ 40 s resolution
- Secondary voltages, ~ 60 s resolution
- Internal temperatures, ~ 40 s

**2.2.2 Accuracy of ASPOC Time Tags in L2 Data**

ASPOC Level-2 products are daily files containing interpolated data at a resolution of 1 second (86400 records per file). For science analysis, ASPOC provides the following data:

- Ion beam current
  - individual ASPOC 1 and ASPOC 2 currents
  - and the sum
- Ion beam energies of individual ASPOCs
- Data quality information
- Individual ASPOC 1 and ASPOC 2 modes
- ASPOC ON/OFF status (ON indicates that at least one ASPOC is emitting ions)

**2.2.3 Relative Telemetry Allocations and Data Volume**

The nominal allocated downlink bit rate for one ASPOC unit is 150 Bits Per Second (BPS), which is composed as follows:

TELEMETRY PACKET		SIZE	REGULAR ?	PERIOD	RATE
NAME	DESCRIPTION	[BYTES]	[YES/NO]	[SECS]	[BPS]
ASxHNORM	Normal housekeeping data	96	Yes	40	19,20
ASxHEXTD	Extended housekeeping data	196	Yes	20	78,40
ASxHSTAT	Bent-pipe status message	20	Yes	4 <sup>(*)</sup>	40,00
ASxHKRNL	Kernel status information	40	Yes	60	5,33
ASxHDUMP	Memory dump data	276	No	600	3,68
<b>Total</b>					<b>146,61</b>

**Table 2-2 ASPOC Telemetry Allocation**

(\*) The ASPOC status message is generated once per second. During nominal operation, the Central Instrument Data Processor (CIDP) skips 3 out of 4 packets, resulting in a data period of 4 seconds.

Without memory dump packets, which are just downlinked on demand, the typical downlink data volume for one ASPOC unit is 1.51 Mbytes per day.

### 2.3 ASPOC CALIBRATION AND VALIDATION

#### 2.3.1 Pre-Flight / On-Ground Calibration

The ASPOC instruments were switched ON, starting from March 28, 2015, during the commissioning phase. The commissioning activities consisted of different types of tests: low-voltage checkout, high-voltage checkout and single-emitter verification, simultaneous operation of two emitters, test of feedback loop using spacecraft potential information obtained from the spin-plane double probe (SDP) measurements, validation of effects on spacecraft potential control when the electron drift instrument (EDI) is emitting electron beams, long-term stability test, and interference test with other instruments.

It has already been shown in the early commissioning phase that ASPOC successfully controlled the spacecraft potential to be kept at values below 4 V, fulfilling the science requirement of MMS. As an example of commissioning-phase operations, Figure 2-2 shows the results from the extended dual-beam test of MMS4 performed on July 19, 2015. The spacecraft potential data transferred onboard ASPOC from SDP, ion currents emitted from ASPOC 1 and ASPOC 2, and the sum of the two emitters' currents are shown in Figure 2-2.

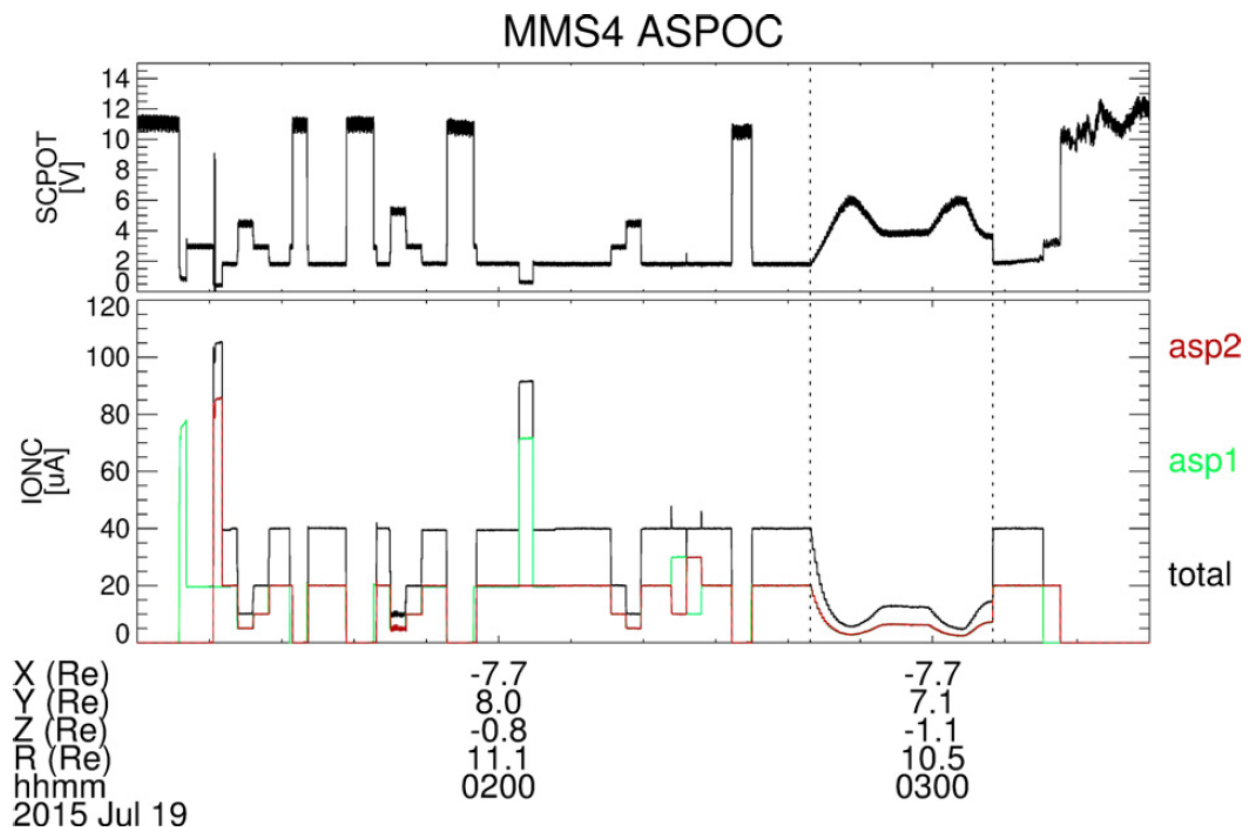


### Figure 2-2 ASPOC Results from the Extended Dual-Beam Test on MMS4

During the extended tests, different current levels and different operation modes were tested. The nominal operation of ASPOC is to emit the ion beams by setting a constant current level for each of the ASPOC units. ASPOC, however, can also be operated in a way that a target spacecraft potential level is set and the ASPOC current level is automatically modified by referring to the spacecraft potential level onboard. This mode is called the feedback mode and was successfully tested during the time interval shown in Figure 2-2 (between the times indicated by the two vertical dotted lines). This mode also requires master–slave mode of two ASPOCs, for which the slave ASPOC duplicates the beam current of the master. The feedback mode not only allows keeping the spacecraft potential level close to the target value, but also enables avoiding unnecessary indium consumptions by emitting very strong ASPOC current. During this interval, the target spacecraft potential value was set to 4 V.

At the beginning of this test, the spacecraft potential was below 2 V and hence the total current level decreased. After a temporary overshoot to 6 V, the potential eventually settled at a correct constant level of 4 V after about 10 min. This procedure was repeated with a different master–slave configuration. By varying control loop parameters and the average time interval of SDP data, it is possible to tune the response time in order to minimize the overshoot level.

ASPOC started routine operations in a pseudo nominal configuration at the end of July 2015 after the completion of all the planned tests and the selection of the optimal emitter pairs for the operational phase. The nominal operation mode during the science phase is the constant current mode where a constant beam current level of 10  $\mu\text{A}$  is set for both emitters. ASPOC has always been operating in this nominal mode during the following science phases. All the ASPOC level 2 science data products are publicly available from the Science Data Center (SDC) (<https://lasp.colorado.edu/mms/sdc/public/>).

First results from space showing the spacecraft control capabilities of ASPOC and calibration considerations, in particular

- Effects of ASPOC on Plasma Measurements,
- Plasma Density Derivation using ASPOC current and spacecraft potential, and Effects of ASPOC on Electric Field Measurements

A full description of ASPOC and its calibration results relative to this section can be found in the publication:

Nakamura, R., K. Torkar, M. Andriopoulou, H. Jeszenszky, C. P. Escoubet, F. Cipriani, P. A. Lindqvist, S. A. Fuselier, C. J. Pollock, B. L. Giles, Y. Khotyaintsev (2017), Initial Results From the Active Spacecraft Potential Control Onboard Magnetospheric Multiscale Mission, *IEEE Transactions on Plasma Science*, 45 (8), 1847-1852.

#### 2.3.2 In-Flight Calibration

Given the nature and the comparatively easy design of the ASPOC instrument, no dedicated in-flight calibration activities are necessary.

Nevertheless, in order to characterize the relationship between the ion emission current and the Spacecraft (S/C) potential measured by the Spin-Plane Double Probe Instrument (SDP), ASPOC performs beam current sweeps on a regular basis. The sweeps cover a current range between 5  $\mu\text{A}$  and 50  $\mu\text{A}$  with steps of 5  $\mu\text{A}$ .

Typically, but not always, the current sweeps will be scheduled in co-ordination with the overall planning at the entry into or at the exit from the region of interest, in intervals of one or more orbits.

### 2.3.3 Validation

Data validation and quality control includes visual inspection of plots produced from all data products and spot-checks of the data products proper. There is software in place to visualize the data products in combined displays, which facilitates the detection of inconsistencies and anomalies.

The consistency between data products will be checked in many aspects, including:

- Correlation between ion current and spacecraft potential,
- Correlation between ion current and total current flowing into the emitter,
- Correlation between currents in the emitter system and the derived quality flag,
- Correlation between ion current data products at different time resolutions,
- Correlation between instrument status and ion emission. This includes several checks, such as ion emission cannot occur with cold heater, in some instrument modes, without voltage applied to emitter.

Some of these checks can be carried out by the production software and raise warning messages. The other checks will be carried out manually/visually.

If an anomaly is found, which is related to the processing software, the production will be stopped, and new versions of data products will be generated after correction. If an identified anomaly can be attributed to the instrument performance or status, a new entry into the caveats file will be generated.

The dedicated display software also supports manual entries into the caveats file. In order to check the quality of the data products, not only the dedicated software will be used, but also the Common Data Format (CDF) validation tools will be used to check the syntax of the products.

## 2.4 MEASUREMENT ALGORITHM DESCRIPTIONS

### 2.4.1 Theoretical Basis (Operating Modes)

There are several state machines in the flight software (FSW) with a small number of operational modes in each.

In standby mode (STDB) both the emitters and their heaters are turned off. The standby mode is also the safe mode of the instrument, to which it returns autonomously under certain error conditions. The transition into standby mode also clears all error flags and the emitter selection, and disables high voltage and the heaters.

Start-up (STUP) is a state of the instrument at the beginning of an active mode when the emitter is being warmed up and ion emission has not yet started. Depending on ambient temperature and emitter condition it takes about 30 to 35 minutes to reach a temperature inside the emitters which is sufficient to ignite the ion beam. The start-up mode duration is commandable and shall exceed the actual warm-up time; the nominal value is 35 minutes. Within this period the "instrument mode" reported in telemetry will be already the commanded target mode, although there is no ion emission yet.

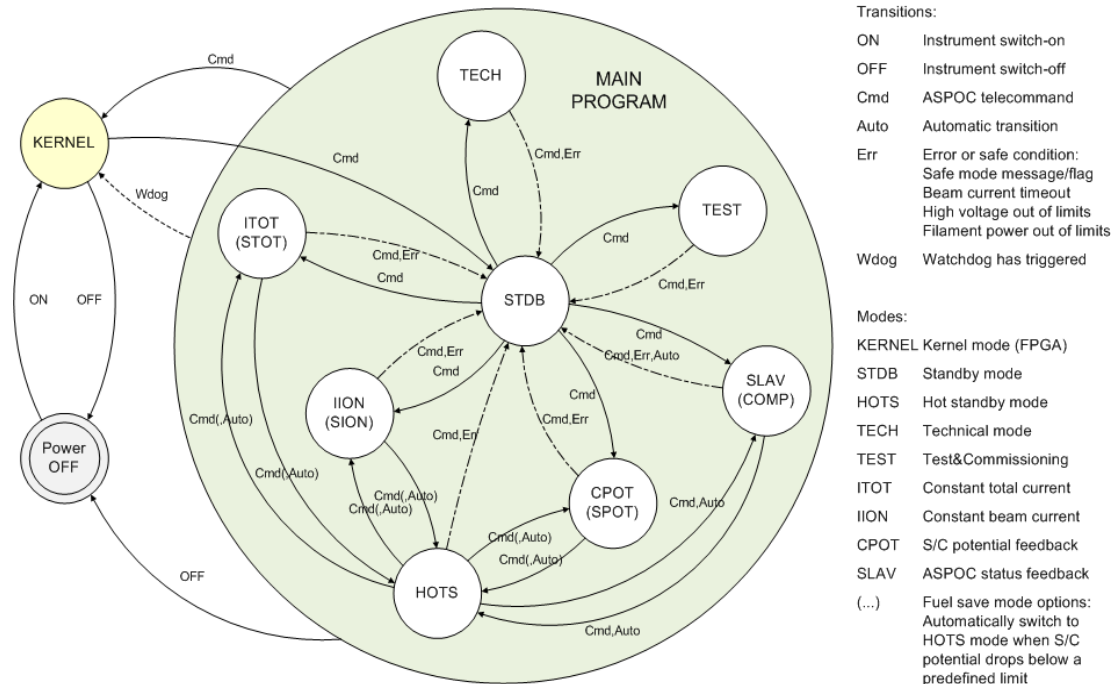


**Figure 2-3 ASPOC Operating Modes**

In order to reduce the time before emission starts, a “hot standby” mode (HOTS) keeps the indium in a liquid state. This mode can be used to interrupt the ion emission by command, without change of modes or emitters before and after the break. The re-ignition time is reduced to the time required to sweep the high voltage (less than a minute).

The most widely used active mode of the instrument will be the "constant total current mode" (ITOT). It sets a constant output current of the high voltage unit, which includes any losses inside the lens system. Experience has shown that the resulting emission of an almost constant ion current fulfils all requirements for spacecraft potential control in the magnetosphere and the solar wind even without on-board feedback from measurements of the spacecraft potential. When the fuel save mode option (STOT) is activated, the instrument also listens to the S/C potential message. If the beam is on, and the potential remains below the off-trigger value for more than the trigger delay time, then the instrument switches into hot standby mode. If the beam is off, and the potential remains above the on-trigger value for more than the trigger delay time, then the instrument performs in the same way as in the standard total current mode.

In "constant ion current mode" (IION) the processor of the instrument reads the monitor of the outgoing beam current and adjusts the output current of the high voltage supply to compensate for any losses in the system. When the fuel save mode option (SION) is activated, the instrument also listens to the S/C potential message. If the beam is on, and the potential remains below the off-trigger value for more than the trigger delay time, then the instrument switches into hot standby mode. If the beam is off, and the potential remains above the on-trigger value for more than the trigger delay time, then the instrument performs in the same way as in the standard ion current mode.

In the so-called feedback mode (CPOT), a measurement of the spacecraft potential is supplied to ASPOC by the SDP Instrument and this information is then used to adjust the beam current in order to maintain a constant value of the potential in a closed-loop scheme. The measurements of the spacecraft potential are updated once every second and sent to ASPOC via dedicated messages (CIDP Bent-Pipe Telemetry).

When the fuel save mode option (SPOT) is activated, the beam is on, and the potential remains below the off-trigger value for more than the trigger delay time, then the instrument switches into hot standby mode. If the beam is off, and the potential remains above the on-trigger value for more than the trigger delay time, then the instrument performs in the same way as in the standard feedback mode.

In slave mode (SLAV), the instrument performs a startup as in constant ion current mode. As soon as normal operational status is reached (startup completed), the instrument listens to the beam current and mode information received through the ASPOC status message from the other (master) unit (CIDP Bent-Pipe Telemetry) and follows the master. When the compensating mode option (COMP) is activated and the beam current of the master is non-zero, the instrument uses a set value for its own control loop twice the set value of the beam current minus the beam current of the master. In this way the sum of both ion beam currents stays at 2 times the value of the beam current commanded to the compensating slave.

The “test and commissioning” mode (TEST) will be used occasionally for low level software and interface tests and to measure the effective filament temperature when the instrument is active. Finally, a technical mode (TECH) is available for low-level commanding during commissioning and re-commissioning of emitters and to adjust operational parameters.

#### 2.4.2 Conversion of Instrument Signals

The transformation of analogue parameters from raw values (R) into physical values (P) can be performed by means of a linear relation:

$$P = C0 + C1 * R + C2 * R^2$$

Table 2-3 lists values of C0, C1 and C2, and the values of P for different raw data values R.

#	C0	C1	C2	R	P(R)	UNIT	DESCRIPTION
1	-273.0	0.1221	0.0	0 4095	-273.0 227.0	°C	Temperature sensors
2	0.0	0.001221	0.0	0 4095	0.00 5.00	V	+3.3 V voltage monitor
3	0.0	0.001589	0.0	0 4095	0.00 6.51	V	+5 V voltage monitor
4	0.0	0.003391	0.0	0 4095	0.00 13.89	V	+12 V voltage monitor
5	0.0	-0.004223	0.0	0 4095	0.00 -17.29	V	-12 V voltage monitor
6	0.0	0.030525	0.0	0 4095	0.0 125.0	μA	Emitter currents
7	0.0	0.0030525	0.0	0 4095	0.00 12.50	kV	High voltage values
8	0.0	0.004884	0.0	0 4095	0.00 20.00	V	Filament voltage monitor
9	0.0	0.030525	0.0	0 4095	0.0 125.0	mA	Filament current monitor



10	0.0	0.001221	0.0	0 4095	0.00 5.00	V	Filament and HV converter output
11	0.0	0.004	0.0	0 4095	0.00 16.38	V	Spacecraft potential
12	0.0	0.0006105	0.0	0 4095	0.00 2.50	W	Filament power
13	0.0	0.078144	0.0	0 4095	0.0 320.0	Ohm	Filament impedance
14	-241.549	0.17775586	8.004346e-6	236 1280 4095	-199.0 -0.9 620.6	°C	Filament temperature(*)

**Table 2-3 ASPOC Calibration Table**

(\*) The calibration curve for the filament temperature is an approximation (maximum deviation is +/- 1 °C for the given range).

### 2.4.3 Error Analysis and Known Features in the Dataset

This chapter identifies known issues in the ASPOC data products, whereby data quality aspects as described in section 2.4.4 were taken into account. The information is provided in tabular format, containing the spacecraft, the affected time range, the number of records with an emission quality less than 2 (moderate to poor), and a severity rating (0=low, 1=high) for each anomaly.

S/C	Start Date	End Date	#Records	Severity
MMS1	2015-07-07T18:46:47Z	2015-07-07T19:02:34Z	948	1.000
MMS1	2015-07-10T18:11:40Z	2015-07-10T18:12:18Z	39	1.000
MMS1	2015-07-15T15:35:07Z	2015-07-15T15:35:43Z	37	1.000
MMS1	2015-07-18T17:58:23Z	2015-07-18T17:59:00Z	38	1.000
MMS1	2015-08-04T21:15:00Z	2015-08-04T21:50:39Z	46	0.021
MMS1	2015-08-11T13:44:26Z	2015-08-11T23:59:46Z	1632	0.044
MMS1	2015-08-12T00:00:14Z	2015-08-12T17:44:52Z	659	0.010
MMS1	2015-08-13T16:02:32Z	2015-08-13T23:59:43Z	6371	0.223
MMS1	2015-08-14T00:00:11Z	2015-08-14T23:59:58Z	23506	0.272
MMS1	2015-08-15T00:00:00Z	2015-08-15T23:59:58Z	16012	0.185
MMS1	2015-08-16T00:00:00Z	2015-08-16T23:59:58Z	35343	0.409
MMS1	2015-08-17T00:00:00Z	2015-08-17T15:30:44Z	12769	0.229
MMS1	2015-09-16T17:53:19Z	2015-09-16T19:00:17Z	1476	0.367
MMS1	2015-10-06T07:30:45Z	2015-10-06T08:16:25Z	40	0.015
MMS1	2015-11-07T13:25:46Z	2015-11-07T14:27:03Z	124	0.034
MMS1	2016-01-12T08:46:09Z	2016-01-12T09:26:14Z	1546	0.643
MMS1	2016-01-13T06:04:20Z	2016-01-13T06:27:28Z	364	0.262
MMS1	2016-04-24T00:35:17Z	2016-04-24T00:37:06Z	37	0.336
MMS1	2016-05-02T21:33:39Z	2016-05-02T23:35:34Z	248	0.034
MMS1	2016-11-14T19:51:19Z	2016-11-14T20:54:48Z	2509	0.659
MMS1	2017-02-22T21:19:53Z	2017-02-22T22:42:16Z	169	0.034
MMS1	2017-02-24T03:25:56Z	2017-02-24T06:35:54Z	393	0.034
MMS1	2017-02-25T11:36:22Z	2017-02-25T14:28:34Z	1987	0.192
MMS1	2017-02-26T19:17:33Z	2017-02-26T22:32:14Z	6265	0.536
MMS1	2017-02-28T03:13:56Z	2017-02-28T06:28:37Z	8950	0.766
MMS1	2017-03-01T11:09:48Z	2017-03-01T14:24:29Z	6975	0.597

S/C	Start Date	End Date	#Records	Severity
MMS1	2017-03-02T20:47:02Z	2017-03-02T23:59:58Z	11562	0.999
MMS1	2017-03-03T00:00:00Z	2017-03-03T00:01:45Z	106	1.000
MMS1	2017-03-04T08:05:47Z	2017-03-04T10:51:23Z	5895	0.593
MMS1	2017-03-07T06:48:59Z	2017-03-07T06:49:59Z	61	1.000
MMS1	2017-03-17T05:52:40Z	2017-03-17T05:53:44Z	65	1.000
MMS1	2017-08-15T00:58:47Z	2017-08-15T19:20:37Z	1678	0.025
MMS1	2017-12-15T02:05:01Z	2017-12-15T05:29:07Z	288	0.024
MMS1	2017-12-17T06:26:22Z	2017-12-17T09:02:26Z	3879	0.414
MMS1	2018-06-04T07:52:35Z	2018-06-04T11:56:00Z	1480	0.101
MMS1	2018-06-23T04:47:22Z	2018-06-23T05:26:36Z	2350	0.998
MMS1	2018-07-12T16:39:57Z	2018-07-12T23:59:58Z	561	0.021
MMS1	2018-07-13T00:00:00Z	2018-07-13T00:01:48Z	33	0.303
MMS1	2018-07-18T13:52:10Z	2018-07-18T13:56:30Z	38	0.146
MMS1	2018-08-10T21:53:40Z	2018-08-10T21:59:48Z	250	0.678
MMS1	2018-08-14T23:22:08Z	2018-08-14T23:30:12Z	187	0.386
MMS1	2018-09-06T21:29:53Z	2018-09-06T21:31:27Z	71	0.747
MMS1	2018-09-07T00:55:08Z	2018-09-07T01:34:47Z	49	0.021
MMS1	2018-11-05T11:07:57Z	2018-11-05T11:09:56Z	43	0.358
MMS1	2018-11-06T07:02:07Z	2018-11-06T07:07:10Z	24	0.079
MMS1	2018-12-22T07:17:40Z	2018-12-22T07:18:21Z	25	0.595
MMS1	2018-12-25T18:02:09Z	2018-12-25T23:13:13Z	395	0.021
MMS1	2018-12-30T18:54:32Z	2018-12-30T20:17:25Z	167	0.034
MMS1	2019-01-03T00:01:59Z	2019-01-03T00:04:25Z	57	0.388
MMS1	2019-01-09T10:03:49Z	2019-01-09T23:54:22Z	534	0.011
MMS1	2019-01-10T04:13:47Z	2019-01-10T04:49:01Z	40	0.019
MMS1	2019-01-11T04:21:45Z	2019-01-11T09:10:18Z	13522	0.781
MMS1	2019-02-17T18:44:35Z	2019-02-17T18:45:57Z	83	1.000
MMS1	2019-02-20T19:34:34Z	2019-02-20T19:41:15Z	210	0.522
MMS1	2019-09-16T15:51:11Z	2019-09-16T15:52:21Z	23	0.324
MMS1	2019-12-24T17:39:21Z	2019-12-24T20:10:44Z	98	0.011
MMS1	2019-12-27T15:14:57Z	2019-12-27T15:16:29Z	57	0.613
MMS1	2020-08-28T11:01:49Z	2020-08-28T11:03:14Z	58	0.674
MMS1	2020-08-30T20:45:31Z	2020-08-30T20:46:31Z	45	0.738
MMS1	2020-09-25T00:58:32Z	2020-09-25T01:00:51Z	37	0.264
MMS1	2020-11-03T18:04:46Z	2020-11-03T18:08:11Z	45	0.218
MMS1	2020-11-14T09:13:32Z	2020-11-14T09:41:26Z	1675	1.000
MMS1	2020-11-16T20:24:42Z	2020-11-16T20:37:39Z	778	1.000
MMS1	2020-11-28T06:52:41Z	2020-11-28T07:21:25Z	284	0.165
MMS1	2020-12-01T00:52:30Z	2020-12-01T01:02:54Z	187	0.299
MMS1	2021-09-17T00:44:49Z	2021-09-17T04:04:08Z	5663	0.473
MMS1	2021-10-04T16:45:44Z	2021-10-04T16:56:49Z	412	0.619
MMS1	2021-10-11T21:35:57Z	2021-10-11T21:52:19Z	111	0.113
MMS1	2021-12-25T14:50:21Z	2021-12-25T18:59:24Z	5894	0.394
MMS1	2021-12-26T03:24:22Z	2021-12-26T06:59:35Z	3813	0.295
MMS1	2021-12-29T16:17:46Z	2021-12-29T16:19:55Z	23	0.177
MMS1	2022-01-05T08:36:04Z	2022-01-05T21:36:58Z	664	0.014
MMS1	2022-01-08T17:14:59Z	2022-01-08T22:14:05Z	1404	0.078
MMS1	2022-01-12T18:17:52Z	2022-01-12T18:19:04Z	71	0.973
MMS1	2022-01-15T18:29:04Z	2022-01-15T18:30:04Z	61	1.000
MMS1	2022-01-19T09:43:08Z	2022-01-19T20:57:53Z	1605	0.040
MMS1	2022-01-22T19:52:51Z	2022-01-22T22:44:34Z	622	0.060
MMS1	2022-01-23T00:23:12Z	2022-01-23T12:18:29Z	8098	0.189

S/C	Start Date	End Date	#Records	Severity
MMS1	2022-01-26T08:34:23Z	2022-01-26T23:44:03Z	1779	0.033
MMS1	2022-01-29T20:59:25Z	2022-01-29T23:52:11Z	472	0.046
MMS1	2022-01-30T00:02:58Z	2022-01-30T09:50:17Z	561	0.016
MMS1	2022-02-05T23:16:25Z	2022-02-05T23:44:31Z	44	0.026
MMS1	2022-02-06T00:36:49Z	2022-02-06T10:04:28Z	769	0.023
MMS1	2022-02-09T11:52:01Z	2022-02-09T13:32:11Z	1722	0.286
MMS1	2022-02-12T23:16:55Z	2022-02-12T23:48:10Z	385	0.205
MMS1	2022-02-13T00:10:30Z	2022-02-13T10:58:27Z	1254	0.032
MMS1	2022-02-16T15:00:44Z	2022-02-16T15:03:50Z	179	0.957
MMS1	2022-02-20T00:20:38Z	2022-02-20T16:17:41Z	2058	0.036
MMS1	2022-03-02T14:37:26Z	2022-03-02T15:12:50Z	270	0.127
MMS1	2022-03-03T01:41:26Z	2022-03-03T03:42:54Z	111	0.015
MMS1	2022-03-06T05:55:12Z	2022-03-06T19:16:07Z	4919	0.102
MMS1	2022-03-09T14:54:29Z	2022-03-09T18:25:20Z	428	0.034
MMS1	2022-03-10T06:30:32Z	2022-03-10T07:19:04Z	31	0.011
MMS1	2022-03-13T03:19:30Z	2022-03-13T06:16:35Z	5947	0.560
MMS1	2022-03-17T04:25:03Z	2022-03-17T09:00:42Z	978	0.059
MMS1	2022-03-20T04:20:11Z	2022-03-20T20:32:51Z	6916	0.119
MMS1	2022-03-23T16:39:29Z	2022-03-23T21:17:19Z	6706	0.402
MMS1	2022-03-27T05:04:28Z	2022-03-27T19:36:15Z	11948	0.228
MMS1	2022-03-30T18:03:35Z	2022-03-30T22:54:10Z	751	0.043
MMS1	2022-03-31T06:16:43Z	2022-03-31T08:18:10Z	1328	0.182
MMS1	2022-04-03T06:14:17Z	2022-04-03T23:54:49Z	736	0.012
MMS1	2022-04-06T21:34:55Z	2022-04-06T22:26:26Z	62	0.020
MMS1	2022-04-10T07:07:07Z	2022-04-10T11:06:19Z	1103	0.077
MMS1	2022-04-13T19:35:41Z	2022-04-13T23:59:58Z	10749	0.678
MMS1	2022-04-14T00:00:00Z	2022-04-14T13:56:13Z	9541	0.190
MMS1	2022-04-17T07:59:17Z	2022-04-17T23:55:28Z	7439	0.130
MMS1	2022-04-18T00:05:54Z	2022-04-18T02:36:51Z	223	0.025
MMS1	2022-04-20T20:23:19Z	2022-04-20T21:09:03Z	87	0.032
MMS1	2022-04-24T08:51:15Z	2022-04-24T23:53:43Z	1523	0.028
MMS1	2022-04-25T00:01:08Z	2022-04-25T04:16:45Z	771	0.050
MMS1	2022-04-27T21:25:58Z	2022-04-27T22:30:16Z	156	0.040
MMS1	2022-04-28T01:57:30Z	2022-04-28T16:26:45Z	5628	0.108
MMS1	2022-05-01T11:09:04Z	2022-05-01T11:59:28Z	1201	0.397
MMS1	2022-05-05T01:27:11Z	2022-05-05T18:56:46Z	1973	0.031
MMS1	2022-05-22T11:55:10Z	2022-05-22T12:08:44Z	815	1.000
MMS1	2022-05-23T06:53:56Z	2022-05-23T11:35:43Z	1783	0.105
MMS1	2022-05-29T14:00:02Z	2022-05-29T14:03:17Z	196	1.000
MMS1	2022-06-02T04:03:33Z	2022-06-02T19:05:08Z	863	0.016
MMS1	2022-06-05T13:53:53Z	2022-06-05T16:10:53Z	160	0.019
MMS1	2022-06-06T02:16:04Z	2022-06-06T06:58:59Z	3283	0.193
MMS1	2022-06-17T06:45:25Z	2022-06-17T06:56:42Z	319	0.471
MMS1	2022-06-20T20:11:03Z	2022-06-20T23:37:01Z	2361	0.191
MMS1	2022-06-23T01:18:54Z	2022-06-23T03:22:52Z	832	0.112
MMS1	2022-06-24T07:57:12Z	2022-06-24T11:02:32Z	936	0.084
MMS1	2022-06-26T14:23:06Z	2022-06-26T17:56:22Z	318	0.025
MMS1	2022-06-29T21:33:41Z	2022-06-29T21:57:36Z	288	0.201
MMS1	2022-06-30T00:28:45Z	2022-06-30T00:29:20Z	36	1.000
MMS1	2022-07-01T04:06:19Z	2022-07-01T04:08:36Z	47	0.341
MMS1	2022-07-03T06:24:01Z	2022-07-03T06:25:35Z	62	0.653
MMS1	2022-07-06T17:47:46Z	2022-07-06T18:29:27Z	325	0.130

S/C	Start Date	End Date	#Records	Severity
MMS1	2022-07-07T01:41:02Z	2022-07-07T19:07:48Z	853	0.014
MMS1	2022-07-15T04:33:10Z	2022-07-15T04:39:42Z	338	0.860
MMS1	2022-07-16T07:38:39Z	2022-07-16T11:48:49Z	1187	0.079
MMS1	2022-07-23T03:37:56Z	2022-07-23T12:36:57Z	721	0.022
MMS1	2022-07-24T07:00:56Z	2022-07-24T20:59:02Z	1489	0.030
MMS1	2022-07-25T07:21:19Z	2022-07-25T19:53:25Z	568	0.013
MMS1	2022-08-12T16:05:33Z	2022-08-12T23:59:58Z	9668	0.340
MMS1	2022-08-13T00:00:00Z	2022-08-13T23:59:58Z	37407	0.433
MMS1	2022-08-14T00:00:00Z	2022-08-14T23:59:56Z	63803	0.738
MMS1	2022-08-15T00:04:44Z	2022-08-15T00:41:14Z	1018	0.465
MMS1	2022-08-16T16:19:34Z	2022-08-16T17:04:25Z	387	0.144
MMS1	2022-08-24T03:09:57Z	2022-08-24T23:42:09Z	1507	0.020
MMS1	2022-08-25T00:00:36Z	2022-08-25T02:41:33Z	1275	0.132
MMS1	2022-09-01T10:03:17Z	2022-09-01T12:03:59Z	500	0.069
MMS1	2022-09-05T16:21:09Z	2022-09-05T22:15:03Z	4996	0.235
MMS1	2022-09-09T20:43:35Z	2022-09-09T23:40:04Z	1588	0.150
MMS1	2022-09-16T14:16:27Z	2022-09-16T15:02:54Z	46	0.016
MMS1	2022-09-21T04:20:07Z	2022-09-21T21:16:55Z	52044	0.853
MMS2	2015-07-01T02:08:37Z	2015-07-01T04:03:03Z	82	0.012
MMS2	2015-07-20T15:20:27Z	2015-07-20T15:22:07Z	101	1.000
MMS2	2015-07-23T01:08:08Z	2015-07-23T01:09:03Z	56	1.000
MMS2	2015-08-20T22:22:52Z	2015-08-20T23:59:12Z	74	0.013
MMS2	2015-08-30T10:00:11Z	2015-08-30T22:10:55Z	1233	0.028
MMS2	2015-09-21T06:11:32Z	2015-09-21T14:00:50Z	685	0.024
MMS2	2015-12-31T09:37:54Z	2015-12-31T10:17:10Z	161	0.068
MMS2	2017-02-17T23:17:56Z	2017-02-17T23:19:56Z	114	0.942
MMS2	2017-03-07T06:38:32Z	2017-03-07T06:39:31Z	60	1.000
MMS2	2017-03-17T05:43:26Z	2017-03-17T05:44:30Z	64	0.985
MMS2	2017-08-12T03:34:36Z	2017-08-12T03:35:07Z	30	0.938
MMS2	2017-08-13T02:15:47Z	2017-08-13T02:17:28Z	87	0.853
MMS2	2017-08-27T00:42:06Z	2017-08-27T00:42:31Z	25	0.962
MMS2	2017-09-19T23:20:43Z	2017-09-19T23:21:15Z	30	0.909
MMS2	2017-09-20T13:48:24Z	2017-09-20T13:49:27Z	56	0.875
MMS2	2017-09-23T05:59:40Z	2017-09-23T06:00:34Z	53	0.964
MMS2	2017-10-12T15:49:08Z	2017-10-12T15:49:55Z	42	0.875
MMS2	2017-11-06T23:11:06Z	2017-11-06T23:24:04Z	302	0.388
MMS2	2017-11-08T01:38:57Z	2017-11-08T13:31:58Z	567	0.013
MMS2	2017-11-09T15:52:20Z	2017-11-09T23:33:41Z	1595	0.058
MMS2	2017-11-10T03:20:13Z	2017-11-10T17:39:37Z	1243	0.024
MMS2	2017-11-13T02:31:27Z	2017-11-13T18:46:47Z	8148	0.139
MMS2	2018-01-03T16:59:58Z	2018-01-03T17:00:22Z	22	0.880
MMS2	2018-02-09T00:06:05Z	2018-02-09T11:24:32Z	2448	0.060
MMS2	2018-04-29T04:28:37Z	2018-04-29T04:29:52Z	70	0.921
MMS2	2018-05-04T13:42:14Z	2018-05-04T13:42:45Z	28	0.875
MMS2	2018-05-21T13:23:57Z	2018-05-21T13:24:33Z	35	0.946
MMS2	2018-05-26T13:52:54Z	2018-05-26T13:53:23Z	28	0.933
MMS2	2018-05-27T11:22:41Z	2018-05-27T11:23:11Z	30	0.968
MMS2	2018-06-06T05:38:04Z	2018-06-06T05:38:48Z	44	0.978
MMS2	2018-06-15T22:55:00Z	2018-06-15T22:55:25Z	25	0.962
MMS2	2018-06-27T00:33:52Z	2018-06-27T00:34:35Z	37	0.841
MMS2	2018-07-01T02:34:06Z	2018-07-01T02:34:57Z	48	0.923
MMS2	2018-07-04T07:03:42Z	2018-07-04T07:04:24Z	42	0.977

S/C	Start Date	End Date	#Records	Severity
MMS2	2018-07-08T10:01:42Z	2018-07-08T10:02:05Z	24	1.000
MMS2	2018-07-22T02:20:09Z	2018-07-22T11:23:32Z	759	0.023
MMS2	2018-07-26T18:22:27Z	2018-07-26T18:23:28Z	54	0.871
MMS2	2018-08-16T11:06:25Z	2018-08-16T11:06:50Z	25	0.962
MMS2	2018-08-19T19:40:07Z	2018-08-19T19:50:33Z	61	0.097
MMS2	2018-08-27T14:57:58Z	2018-08-27T14:58:33Z	33	0.917
MMS2	2018-09-07T11:27:25Z	2018-09-07T11:27:51Z	25	0.926
MMS2	2018-09-10T01:56:43Z	2018-09-10T01:57:13Z	28	0.903
MMS2	2018-09-11T09:23:22Z	2018-09-11T09:24:03Z	37	0.881
MMS2	2018-09-22T01:39:38Z	2018-09-22T01:40:03Z	24	0.923
MMS2	2018-09-29T11:53:27Z	2018-09-29T11:53:53Z	24	0.889
MMS2	2018-10-17T11:50:35Z	2018-10-17T11:51:11Z	37	1.000
MMS2	2018-10-26T08:58:08Z	2018-10-26T08:58:29Z	21	0.955
MMS2	2018-11-14T15:53:55Z	2018-11-14T23:52:31Z	363	0.013
MMS2	2018-11-15T00:20:55Z	2018-11-15T23:56:57Z	1220	0.014
MMS2	2018-11-16T00:04:02Z	2018-11-16T23:38:26Z	6303	0.074
MMS2	2018-11-17T01:47:02Z	2018-11-17T22:51:10Z	1432	0.019
MMS2	2018-11-18T12:49:28Z	2018-11-18T22:35:57Z	1409	0.040
MMS2	2019-02-21T10:44:55Z	2019-02-21T18:33:59Z	1976	0.070
MMS2	2019-02-22T00:24:33Z	2019-02-22T16:00:32Z	1009	0.018
MMS2	2019-09-13T21:36:53Z	2019-09-13T21:37:23Z	31	1.000
MMS2	2019-09-17T18:13:49Z	2019-09-17T23:16:47Z	914	0.050
MMS2	2019-09-23T06:49:53Z	2019-09-23T06:50:16Z	22	0.917
MMS2	2019-09-28T11:19:17Z	2019-09-28T11:19:39Z	22	0.957
MMS2	2019-10-03T15:47:06Z	2019-10-03T15:47:29Z	23	0.958
MMS2	2019-10-05T23:39:08Z	2019-10-05T23:39:43Z	34	0.944
MMS2	2020-07-07T21:49:47Z	2020-07-07T22:50:06Z	90	0.025
MMS2	2020-10-31T03:42:22Z	2020-10-31T06:41:30Z	957	0.089
MMS2	2020-12-01T00:52:00Z	2020-12-01T02:04:48Z	1390	0.318
MMS2	2020-12-12T09:06:53Z	2020-12-12T09:31:21Z	1386	0.943
MMS2	2020-12-15T01:34:26Z	2020-12-15T20:57:31Z	8031	0.115
MMS2	2021-09-06T12:54:04Z	2021-09-06T16:25:57Z	191	0.015
MMS2	2021-09-07T00:11:49Z	2021-09-07T02:51:37Z	2868	0.299
MMS2	2021-09-16T20:33:05Z	2021-09-16T20:35:16Z	132	1.000
MMS2	2021-09-23T13:21:37Z	2021-09-23T14:28:34Z	266	0.066
MMS2	2021-11-02T16:29:53Z	2021-11-02T20:27:30Z	1268	0.089
MMS2	2022-02-13T00:48:14Z	2022-02-13T00:49:26Z	73	1.000
MMS2	2022-03-17T05:25:39Z	2022-03-17T08:35:41Z	232	0.020
MMS2	2022-07-07T20:07:21Z	2022-07-07T22:37:16Z	4686	0.521
MMS3	2015-07-15T22:16:31Z	2015-07-15T22:49:35Z	162	0.082
MMS3	2015-07-18T15:34:28Z	2015-07-18T15:35:41Z	74	1.000
MMS3	2015-07-19T17:59:37Z	2015-07-19T18:00:25Z	49	1.000
MMS3	2017-01-04T14:48:46Z	2017-01-04T15:04:35Z	25	0.026
MMS3	2017-01-19T11:56:06Z	2017-01-19T13:57:51Z	244	0.033
MMS3	2017-03-17T13:40:44Z	2017-03-17T13:41:48Z	65	1.000
MMS3	2017-11-22T14:11:54Z	2017-11-22T14:50:17Z	257	0.112
MMS3	2018-01-12T01:51:12Z	2018-01-12T01:52:10Z	56	0.949
MMS3	2018-01-26T07:40:21Z	2018-01-26T08:03:43Z	71	0.051
MMS3	2018-04-23T18:35:05Z	2018-04-23T19:04:13Z	1120	0.640
MMS3	2018-07-12T15:15:46Z	2018-07-12T20:57:03Z	5177	0.253
MMS3	2018-08-06T06:46:05Z	2018-08-06T08:08:36Z	131	0.026
MMS3	2018-08-12T06:08:03Z	2018-08-12T06:11:29Z	39	0.188

S/C	Start Date	End Date	#Records	Severity
MMS3	2018-09-20T10:35:57Z	2018-09-20T11:37:44Z	45	0.012
MMS3	2018-10-20T11:17:39Z	2018-10-20T11:39:36Z	257	0.195
MMS3	2018-10-27T17:17:49Z	2018-10-27T19:03:30Z	117	0.018
MMS3	2018-11-04T12:44:50Z	2018-11-04T14:04:44Z	55	0.011
MMS3	2018-11-10T13:42:43Z	2018-11-10T17:18:16Z	10671	0.825
MMS3	2018-11-16T03:40:40Z	2018-11-16T03:57:44Z	56	0.055
MMS3	2018-12-15T23:31:59Z	2018-12-15T23:34:25Z	147	1.000
MMS3	2018-12-17T18:21:42Z	2018-12-17T18:22:08Z	21	0.778
MMS3	2018-12-31T05:59:49Z	2018-12-31T06:00:16Z	25	0.893
MMS3	2019-01-01T04:27:48Z	2019-01-01T06:01:02Z	312	0.056
MMS3	2019-01-05T08:33:39Z	2019-01-05T20:43:44Z	1082	0.025
MMS3	2019-01-06T15:16:09Z	2019-01-06T23:13:25Z	1354	0.047
MMS3	2019-01-17T22:39:40Z	2019-01-17T23:04:44Z	43	0.029
MMS3	2019-01-31T05:48:16Z	2019-01-31T05:49:29Z	74	1.000
MMS3	2019-02-13T05:16:52Z	2019-02-13T23:15:18Z	1431	0.022
MMS3	2019-02-14T04:56:13Z	2019-02-14T23:59:04Z	2900	0.042
MMS3	2019-02-15T00:00:29Z	2019-02-15T23:59:58Z	34052	0.394
MMS3	2019-02-16T00:00:00Z	2019-02-16T23:59:58Z	38793	0.449
MMS3	2019-02-17T00:00:00Z	2019-02-17T23:57:38Z	30267	0.351
MMS3	2019-02-18T00:02:23Z	2019-02-18T18:25:02Z	38738	0.586
MMS3	2019-02-19T01:42:26Z	2019-02-19T23:58:42Z	41753	0.521
MMS3	2019-02-20T00:01:23Z	2019-02-20T23:59:58Z	78460	0.909
MMS3	2019-02-21T00:00:00Z	2019-02-21T23:58:16Z	28922	0.335
MMS3	2019-02-22T00:00:58Z	2019-02-22T16:54:17Z	21643	0.356
MMS3	2019-02-23T00:18:03Z	2019-02-23T21:55:49Z	4281	0.055
MMS3	2019-02-24T00:59:36Z	2019-02-24T23:12:32Z	5232	0.065
MMS3	2019-04-05T13:27:19Z	2019-04-05T13:44:49Z	634	0.603
MMS3	2019-04-16T15:24:59Z	2019-04-16T15:26:59Z	21	0.174
MMS3	2019-06-07T11:02:02Z	2019-06-07T11:57:33Z	87	0.026
MMS3	2019-08-07T08:46:34Z	2019-08-07T08:47:16Z	35	0.814
MMS3	2019-09-09T04:50:38Z	2019-09-09T21:29:39Z	1163	0.019
MMS3	2019-09-13T03:01:36Z	2019-09-13T03:15:51Z	575	0.672
MMS3	2019-09-26T03:02:21Z	2019-09-26T16:15:54Z	533	0.011
MMS3	2019-12-27T17:05:04Z	2019-12-27T17:29:23Z	23	0.016
MMS3	2020-07-22T07:47:19Z	2020-07-22T11:15:30Z	150	0.012
MMS3	2020-07-26T00:43:42Z	2020-07-26T01:46:15Z	2532	0.674
MMS3	2020-07-27T14:44:47Z	2020-07-27T14:47:11Z	115	0.793
MMS3	2020-07-29T19:04:45Z	2020-07-29T23:54:39Z	800	0.046
MMS3	2020-08-01T06:57:06Z	2020-08-01T10:21:25Z	2092	0.171
MMS3	2020-08-02T00:19:42Z	2020-08-02T21:42:13Z	33317	0.433
MMS3	2020-08-03T01:18:22Z	2020-08-03T15:40:15Z	6925	0.134
MMS3	2020-08-04T22:20:18Z	2020-08-04T22:21:20Z	63	1.000
MMS3	2020-08-05T00:44:15Z	2020-08-05T05:36:58Z	2047	0.117
MMS3	2020-08-26T13:31:23Z	2020-08-26T18:12:52Z	7530	0.446
MMS3	2020-08-27T02:21:47Z	2020-08-27T14:49:58Z	1590	0.035
MMS3	2020-08-31T10:59:48Z	2020-08-31T22:25:41Z	2285	0.056
MMS3	2020-09-02T01:30:05Z	2020-09-02T21:13:36Z	3209	0.045
MMS3	2020-09-03T00:10:59Z	2020-09-03T10:25:57Z	1431	0.039
MMS3	2020-09-04T11:02:57Z	2020-09-04T11:07:53Z	249	0.838
MMS3	2020-09-05T12:27:26Z	2020-09-05T22:12:09Z	411	0.012
MMS3	2020-09-12T08:22:16Z	2020-09-12T17:57:43Z	2911	0.084
MMS3	2020-09-14T04:42:26Z	2020-09-14T04:51:42Z	37	0.066

S/C	Start Date	End Date	#Records	Severity
MMS3	2020-09-15T21:21:23Z	2020-09-15T23:53:20Z	492	0.054
MMS3	2020-09-16T14:32:45Z	2020-09-16T17:09:14Z	161	0.017
MMS3	2020-09-17T23:37:30Z	2020-09-17T23:53:53Z	870	0.884
MMS3	2020-09-18T00:13:47Z	2020-09-18T14:34:18Z	44765	0.867
MMS3	2020-09-19T07:41:45Z	2020-09-19T23:59:58Z	58694	1.000
MMS3	2020-09-20T00:00:00Z	2020-09-20T23:59:58Z	86399	1.000
MMS3	2020-09-21T00:00:00Z	2020-09-21T23:59:58Z	86371	1.000
MMS3	2020-09-22T00:00:00Z	2020-09-22T23:59:58Z	29433	0.341
MMS3	2020-09-23T00:00:00Z	2020-09-23T23:59:58Z	84898	0.983
MMS3	2020-09-24T00:00:00Z	2020-09-24T15:30:24Z	54942	0.984
MMS3	2020-10-03T12:30:45Z	2020-10-03T12:34:27Z	134	0.601
MMS3	2020-10-10T07:48:19Z	2020-10-10T08:18:38Z	170	0.093
MMS3	2020-10-13T02:34:27Z	2020-10-13T05:29:16Z	4210	0.401
MMS3	2020-10-23T05:17:23Z	2020-10-23T07:10:22Z	420	0.062
MMS3	2020-10-26T21:55:44Z	2020-10-26T23:27:51Z	683	0.124
MMS3	2020-10-30T11:12:51Z	2020-10-30T12:49:40Z	118	0.020
MMS3	2020-11-03T02:19:03Z	2020-11-03T02:19:47Z	21	0.467
MMS3	2020-11-13T10:01:28Z	2020-11-13T13:05:54Z	304	0.027
MMS3	2020-11-14T05:38:51Z	2020-11-14T09:37:16Z	10023	0.701
MMS3	2020-11-16T20:24:30Z	2020-11-16T21:17:17Z	141	0.045
MMS3	2020-11-21T04:15:41Z	2020-11-21T04:19:15Z	79	0.367
MMS3	2020-11-24T00:53:20Z	2020-11-24T17:01:23Z	872	0.015
MMS3	2020-11-27T10:49:29Z	2020-11-27T12:58:17Z	313	0.040
MMS3	2020-11-28T04:11:34Z	2020-11-28T09:10:07Z	336	0.019
MMS3	2020-12-12T05:40:46Z	2020-12-12T05:44:13Z	158	0.760
MMS3	2020-12-18T14:42:48Z	2020-12-18T17:41:41Z	753	0.070
MMS3	2020-12-19T05:39:32Z	2020-12-19T09:25:01Z	1210	0.089
MMS3	2020-12-22T04:40:58Z	2020-12-22T21:35:43Z	7241	0.119
MMS3	2020-12-29T05:40:59Z	2020-12-29T21:06:20Z	668	0.012
MMS3	2021-01-05T19:07:25Z	2021-01-05T19:49:56Z	159	0.062
MMS3	2021-01-16T06:46:43Z	2021-01-16T07:35:36Z	144	0.049
MMS3	2021-01-19T06:53:06Z	2021-01-19T07:00:35Z	292	0.649
MMS3	2021-01-22T18:28:42Z	2021-01-22T20:06:03Z	1201	0.206
MMS3	2021-01-26T20:56:27Z	2021-01-26T20:58:38Z	132	1.000
MMS3	2021-01-29T18:42:22Z	2021-01-29T19:04:46Z	652	0.485
MMS3	2021-01-30T09:45:50Z	2021-01-30T10:42:10Z	42	0.012
MMS3	2021-02-06T06:31:07Z	2021-02-06T11:30:45Z	10979	0.611
MMS3	2021-05-18T13:32:08Z	2021-05-18T13:35:57Z	120	0.522
MMS3	2021-10-12T23:02:01Z	2021-10-12T23:08:10Z	84	0.227
MMS3	2022-07-04T05:33:07Z	2022-07-04T05:33:29Z	23	1.000
MMS3	2022-07-08T01:08:18Z	2022-07-08T23:51:01Z	5641	0.069
MMS4	2015-07-19T01:20:32Z	2015-07-19T02:35:03Z	190	0.042
MMS4	2015-07-22T15:22:54Z	2015-07-22T15:23:56Z	61	0.968
MMS4	2015-07-28T16:09:46Z	2015-07-28T16:11:09Z	84	1.000
MMS4	2015-08-05T03:37:33Z	2015-08-05T12:50:51Z	900	0.027
MMS4	2015-08-06T12:43:59Z	2015-08-06T23:04:48Z	511	0.014
MMS4	2015-08-14T11:49:59Z	2015-08-14T17:12:46Z	455	0.023
MMS4	2015-08-17T11:29:10Z	2015-08-17T13:29:38Z	179	0.025
MMS4	2015-12-13T10:05:36Z	2015-12-13T12:10:30Z	158	0.021
MMS4	2016-02-28T02:42:54Z	2016-02-28T02:43:21Z	28	1.000
MMS4	2016-08-12T08:02:14Z	2016-08-12T08:59:58Z	1240	0.358
MMS4	2016-08-13T07:55:48Z	2016-08-13T08:54:59Z	3409	0.960

S/C	Start Date	End Date	#Records	Severity
MMS4	2016-08-14T07:51:01Z	2016-08-14T08:49:58Z	3495	0.988
MMS4	2016-08-15T07:40:20Z	2016-08-15T08:39:58Z	3528	0.986
MMS4	2016-08-16T07:00:47Z	2016-08-16T07:15:22Z	66	0.075
MMS4	2016-08-17T07:58:05Z	2016-08-17T07:59:10Z	66	1.000
MMS4	2017-02-05T08:58:26Z	2017-02-05T10:10:04Z	128	0.030
MMS4	2017-02-07T10:39:11Z	2017-02-07T10:53:48Z	145	0.165
MMS4	2017-02-13T08:03:45Z	2017-02-13T11:18:07Z	11521	0.988
MMS4	2017-02-14T10:22:18Z	2017-02-14T13:27:00Z	10622	0.958
MMS4	2017-02-15T13:58:50Z	2017-02-15T17:01:49Z	728	0.066
MMS4	2017-02-16T18:54:54Z	2017-02-16T20:01:35Z	88	0.022
MMS4	2017-02-21T14:22:58Z	2017-02-21T16:50:16Z	4383	0.496
MMS4	2017-02-22T22:19:08Z	2017-02-22T23:50:30Z	195	0.036
MMS4	2017-03-04T07:34:26Z	2017-03-04T07:40:28Z	26	0.072
MMS4	2017-03-17T08:03:10Z	2017-03-17T08:04:15Z	66	1.000
MMS4	2017-05-06T10:32:37Z	2017-05-06T13:23:31Z	899	0.088
MMS4	2017-06-23T00:37:26Z	2017-06-23T03:38:10Z	805	0.074
MMS4	2017-07-04T01:19:11Z	2017-07-04T01:23:21Z	28	0.112
MMS4	2017-07-06T21:05:32Z	2017-07-06T21:26:04Z	77	0.062
MMS4	2017-07-13T05:55:08Z	2017-07-13T08:07:25Z	532	0.067
MMS4	2017-07-19T00:04:15Z	2017-07-19T00:08:44Z	32	0.119
MMS4	2017-07-20T01:41:48Z	2017-07-20T13:09:01Z	1122	0.027
MMS4	2017-08-06T10:58:00Z	2017-08-06T13:56:28Z	1073	0.100
MMS4	2017-08-08T21:18:21Z	2017-08-08T21:21:58Z	148	0.679
MMS4	2017-08-09T01:58:48Z	2017-08-09T18:34:37Z	3655	0.061
MMS4	2017-09-01T06:31:04Z	2017-09-01T18:55:38Z	523	0.012
MMS4	2017-10-18T00:02:54Z	2017-10-18T00:03:28Z	35	1.000
MMS4	2017-11-14T00:16:04Z	2017-11-14T02:16:16Z	435	0.060
MMS4	2017-11-25T09:30:34Z	2017-11-25T09:32:04Z	26	0.286
MMS4	2018-02-06T01:12:48Z	2018-02-06T03:50:50Z	455	0.048
MMS4	2018-02-11T16:20:20Z	2018-02-11T23:22:19Z	541	0.021
MMS4	2018-02-12T00:00:03Z	2018-02-12T00:01:14Z	72	1.000
MMS4	2018-03-01T05:58:37Z	2018-03-01T07:00:53Z	129	0.035
MMS4	2018-03-12T09:09:17Z	2018-03-12T13:16:04Z	2785	0.188
MMS4	2018-03-17T11:49:04Z	2018-03-17T21:10:20Z	1286	0.038
MMS4	2018-03-21T00:14:34Z	2018-03-21T00:15:15Z	42	1.000
MMS4	2018-03-23T00:28:56Z	2018-03-23T15:46:33Z	1359	0.025
MMS4	2018-03-26T02:43:06Z	2018-03-26T16:01:59Z	13561	0.283
MMS4	2018-03-31T11:56:45Z	2018-03-31T23:58:29Z	1273	0.029
MMS4	2018-04-01T02:41:23Z	2018-04-01T07:10:37Z	14625	0.905
MMS4	2018-04-03T06:46:21Z	2018-04-03T06:47:20Z	60	1.000
MMS4	2018-04-06T02:23:55Z	2018-04-06T20:52:23Z	11071	0.166
MMS4	2018-04-08T21:59:12Z	2018-04-08T22:28:06Z	102	0.059
MMS4	2018-04-09T04:58:52Z	2018-04-09T17:47:53Z	2589	0.056
MMS4	2018-04-11T17:33:09Z	2018-04-11T22:32:41Z	3947	0.220
MMS4	2018-04-12T01:03:54Z	2018-04-12T13:32:24Z	4854	0.108
MMS4	2018-04-14T13:03:17Z	2018-04-14T23:59:58Z	39391	1.000
MMS4	2018-04-15T00:00:00Z	2018-04-15T07:36:41Z	24306	0.887
MMS4	2018-04-20T08:47:35Z	2018-04-20T23:24:52Z	8386	0.159
MMS4	2018-04-22T23:48:05Z	2018-04-22T23:58:28Z	351	0.562
MMS4	2018-04-23T00:01:05Z	2018-04-23T16:16:57Z	14235	0.243
MMS4	2018-04-25T21:34:42Z	2018-04-25T22:54:34Z	546	0.114
MMS4	2018-04-26T01:16:33Z	2018-04-26T09:33:55Z	5773	0.193



S/C	Start Date	End Date	#Records	Severity
MMS4	2018-04-28T14:58:32Z	2018-04-28T23:59:57Z	9740	0.300
MMS4	2018-04-29T00:00:01Z	2018-04-29T10:13:59Z	10440	0.283
MMS4	2018-05-01T10:26:03Z	2018-05-01T14:58:03Z	1885	0.115
MMS4	2018-05-02T02:29:08Z	2018-05-02T03:58:27Z	1005	0.187
MMS4	2018-05-04T06:53:11Z	2018-05-04T22:14:10Z	1530	0.028
MMS4	2018-05-07T01:43:37Z	2018-05-07T18:06:02Z	37522	0.637
MMS4	2018-05-09T21:25:43Z	2018-05-09T22:36:06Z	407	0.096
MMS4	2018-05-10T08:19:13Z	2018-05-10T08:42:37Z	609	0.433
MMS4	2018-05-12T21:33:54Z	2018-05-12T21:34:21Z	28	1.000
MMS4	2018-05-15T15:16:31Z	2018-05-15T15:34:48Z	480	0.437
MMS4	2018-05-18T08:14:03Z	2018-05-18T23:25:39Z	1639	0.030
MMS4	2018-05-25T06:47:40Z	2018-05-25T07:56:39Z	52	0.013
MMS4	2018-05-28T03:04:51Z	2018-05-28T19:47:00Z	2536	0.042
MMS4	2018-06-06T11:37:42Z	2018-06-06T12:22:32Z	264	0.098
MMS4	2018-06-07T02:36:03Z	2018-06-07T02:56:22Z	55	0.045
MMS4	2018-06-09T13:00:38Z	2018-06-09T13:02:00Z	26	0.313
MMS4	2018-06-11T04:27:23Z	2018-06-11T05:38:18Z	2704	0.635
MMS4	2018-06-12T01:29:37Z	2018-06-12T23:45:46Z	8791	0.110
MMS4	2018-06-15T04:54:29Z	2018-06-15T10:12:22Z	511	0.027
MMS4	2018-06-19T00:02:00Z	2018-06-19T20:57:56Z	2087	0.028
MMS4	2018-06-22T12:15:17Z	2018-06-22T22:37:50Z	1080	0.029
MMS4	2018-06-23T00:13:48Z	2018-06-23T22:34:31Z	6525	0.081
MMS4	2018-06-24T08:05:28Z	2018-06-24T08:44:36Z	1575	0.670
MMS4	2018-07-03T18:07:48Z	2018-07-03T19:19:48Z	68	0.016
MMS4	2018-07-12T03:54:56Z	2018-07-12T23:02:40Z	3411	0.050
MMS4	2018-07-13T01:26:18Z	2018-07-13T22:20:59Z	2524	0.034
MMS4	2018-07-14T23:52:08Z	2018-07-14T23:59:01Z	25	0.060
MMS4	2018-07-15T00:00:28Z	2018-07-15T00:01:06Z	30	0.769
MMS4	2018-07-16T17:32:12Z	2018-07-16T17:33:08Z	34	0.596
MMS4	2018-07-23T12:48:29Z	2018-07-23T14:30:18Z	511	0.084
MMS4	2018-07-28T10:55:10Z	2018-07-28T10:58:51Z	202	0.910
MMS4	2018-07-30T01:13:06Z	2018-07-30T23:00:15Z	21825	0.278
MMS4	2018-07-31T22:07:38Z	2018-07-31T22:14:45Z	125	0.292
MMS4	2018-08-01T04:41:08Z	2018-08-01T21:20:23Z	2713	0.045
MMS4	2018-08-03T04:50:48Z	2018-08-03T18:18:50Z	519	0.011
MMS4	2018-08-04T00:58:22Z	2018-08-04T15:41:21Z	1071	0.020
MMS4	2018-08-07T21:42:36Z	2018-08-07T23:14:30Z	2967	0.538
MMS4	2018-08-08T02:33:11Z	2018-08-08T03:08:24Z	1489	0.704
MMS4	2018-08-09T02:40:38Z	2018-08-09T21:42:25Z	1774	0.026
MMS4	2018-08-11T05:45:21Z	2018-08-11T07:45:31Z	4727	0.656
MMS4	2018-08-12T03:38:01Z	2018-08-12T23:57:50Z	19666	0.269
MMS4	2018-08-13T00:01:00Z	2018-08-13T03:08:50Z	8166	0.725
MMS4	2018-08-16T08:59:35Z	2018-08-16T09:01:11Z	97	1.000
MMS4	2018-08-25T11:48:52Z	2018-08-25T12:01:50Z	639	0.820
MMS4	2018-08-26T03:03:55Z	2018-08-26T03:07:29Z	181	0.842
MMS4	2018-08-30T14:42:58Z	2018-08-30T14:56:09Z	24	0.030
MMS4	2018-09-02T05:06:39Z	2018-09-02T05:07:34Z	55	0.982
MMS4	2018-09-14T05:12:42Z	2018-09-14T05:15:30Z	168	0.994
MMS4	2018-09-20T21:48:11Z	2018-09-20T23:38:23Z	217	0.033
MMS4	2018-09-23T14:58:02Z	2018-09-23T15:11:40Z	628	0.767
MMS4	2018-09-28T21:04:15Z	2018-09-28T21:15:25Z	32	0.048
MMS4	2018-10-05T07:35:13Z	2018-10-05T08:54:37Z	100	0.021

S/C	Start Date	End Date	#Records	Severity
MMS4	2018-10-12T07:28:53Z	2018-10-12T07:35:30Z	84	0.211
MMS4	2018-10-29T00:22:56Z	2018-10-29T00:28:35Z	340	1.000
MMS4	2018-11-08T08:57:21Z	2018-11-08T08:58:08Z	48	1.000
MMS4	2018-11-14T20:14:42Z	2018-11-14T20:18:32Z	231	1.000
MMS4	2018-11-25T08:40:10Z	2018-11-25T08:52:30Z	284	0.383
MMS4	2018-12-05T23:26:54Z	2018-12-05T23:59:58Z	565	0.285
MMS4	2018-12-06T00:00:00Z	2018-12-06T00:04:34Z	239	0.869
MMS4	2018-12-19T15:59:49Z	2018-12-19T16:26:27Z	30	0.019
MMS4	2018-12-20T12:02:51Z	2018-12-20T12:09:46Z	94	0.226
MMS4	2018-12-26T22:03:00Z	2018-12-26T23:00:28Z	74	0.021
MMS4	2018-12-27T00:21:54Z	2018-12-27T01:27:26Z	336	0.085
MMS4	2019-01-01T02:45:05Z	2019-01-01T04:30:09Z	83	0.013
MMS4	2019-01-16T04:58:42Z	2019-01-16T06:39:26Z	445	0.074
MMS4	2019-01-23T08:43:37Z	2019-01-23T10:43:37Z	89	0.012
MMS4	2019-01-28T06:23:46Z	2019-01-28T16:09:53Z	390	0.011
MMS4	2019-02-08T13:24:51Z	2019-02-08T13:29:08Z	22	0.085
MMS4	2019-02-16T01:44:53Z	2019-02-16T02:23:06Z	39	0.017
MMS4	2019-02-22T06:04:35Z	2019-02-22T07:57:03Z	1901	0.282
MMS4	2019-02-23T17:53:13Z	2019-02-23T19:37:41Z	317	0.051
MMS4	2019-04-02T05:46:54Z	2019-04-02T16:04:35Z	423	0.011
MMS4	2019-04-23T19:51:27Z	2019-04-23T20:36:33Z	81	0.030
MMS4	2019-06-08T03:37:57Z	2019-06-08T03:40:44Z	124	0.738
MMS4	2019-06-28T12:40:13Z	2019-06-28T12:42:55Z	43	0.264
MMS4	2019-07-02T04:07:24Z	2019-07-02T12:33:59Z	956	0.031
MMS4	2019-07-05T12:32:24Z	2019-07-05T13:39:48Z	3357	0.830
MMS4	2019-07-06T00:00:51Z	2019-07-06T02:35:36Z	156	0.017
MMS4	2019-07-09T00:36:02Z	2019-07-09T01:18:06Z	174	0.069
MMS4	2019-07-12T12:38:46Z	2019-07-12T16:32:20Z	2213	0.158
MMS4	2019-07-19T13:01:18Z	2019-07-19T16:16:18Z	290	0.025
MMS4	2019-07-20T00:20:41Z	2019-07-20T04:20:49Z	4644	0.322
MMS4	2019-07-23T02:27:18Z	2019-07-23T02:45:05Z	1048	0.981
MMS4	2019-08-16T01:07:09Z	2019-08-16T13:45:54Z	1107	0.024
MMS4	2019-09-08T10:21:52Z	2019-09-08T15:52:22Z	224	0.011
MMS4	2019-10-04T10:28:28Z	2019-10-04T11:18:53Z	2386	0.788
MMS4	2019-10-12T09:54:04Z	2019-10-12T09:55:28Z	75	0.882
MMS4	2019-10-14T03:30:08Z	2019-10-14T03:31:28Z	32	0.395
MMS4	2019-12-03T17:48:25Z	2019-12-03T20:36:39Z	377	0.037
MMS4	2019-12-07T04:19:38Z	2019-12-07T09:16:02Z	1045	0.059
MMS4	2019-12-17T04:18:59Z	2019-12-17T06:19:48Z	135	0.019
MMS4	2020-01-04T05:11:47Z	2020-01-04T05:25:59Z	84	0.098
MMS4	2020-01-21T04:54:25Z	2020-01-21T17:51:55Z	696	0.015
MMS4	2020-01-28T09:14:36Z	2020-01-28T09:48:43Z	194	0.095
MMS4	2020-02-11T10:29:19Z	2020-02-11T10:38:11Z	60	0.113
MMS4	2020-02-15T09:07:43Z	2020-02-15T11:16:30Z	222	0.029
MMS4	2020-02-18T07:53:01Z	2020-02-18T12:14:06Z	438	0.028
MMS4	2020-02-22T08:42:25Z	2020-02-22T12:51:54Z	280	0.019
MMS4	2020-02-28T20:10:46Z	2020-02-28T21:54:46Z	299	0.048
MMS4	2020-02-29T08:48:06Z	2020-02-29T09:50:30Z	3142	0.839
MMS4	2020-03-06T22:09:06Z	2020-03-06T23:52:19Z	313	0.051
MMS4	2020-03-10T09:31:57Z	2020-03-10T12:52:08Z	3602	0.300
MMS4	2020-03-24T09:28:39Z	2020-03-24T13:48:20Z	3198	0.205
MMS4	2020-03-31T09:09:41Z	2020-03-31T13:54:13Z	7077	0.415

S/C	Start Date	End Date	#Records	Severity
MMS4	2020-04-03T21:20:41Z	2020-04-03T23:59:47Z	1312	0.137
MMS4	2020-04-04T00:01:22Z	2020-04-04T09:58:17Z	655	0.018
MMS4	2020-04-21T10:56:25Z	2020-04-21T14:22:52Z	222	0.018
MMS4	2020-05-05T10:07:17Z	2020-05-05T13:24:39Z	254	0.021
MMS4	2020-05-15T23:12:19Z	2020-05-15T23:54:34Z	514	0.203
MMS4	2020-05-16T17:44:53Z	2020-05-16T20:36:42Z	1943	0.188
MMS4	2020-06-29T03:49:47Z	2020-06-29T03:50:33Z	47	1.000
MMS4	2020-07-24T09:01:11Z	2020-07-24T09:40:20Z	65	0.028
MMS4	2020-08-06T20:13:06Z	2020-08-06T20:15:44Z	29	0.182
MMS4	2020-09-19T20:07:14Z	2020-09-19T20:09:03Z	27	0.245
MMS4	2020-09-22T02:27:57Z	2020-09-22T02:49:49Z	1129	0.860
MMS4	2020-10-27T15:45:00Z	2020-10-27T15:58:48Z	55	0.066
MMS4	2021-01-22T20:43:35Z	2021-01-22T20:45:57Z	35	0.245
MMS4	2021-02-09T09:46:04Z	2021-02-09T09:50:28Z	54	0.204
MMS4	2021-03-19T21:58:39Z	2021-03-19T22:01:53Z	27	0.138
MMS4	2021-03-30T12:21:23Z	2021-03-30T12:24:50Z	34	0.163
MMS4	2021-04-06T10:56:46Z	2021-04-06T10:59:43Z	22	0.124
MMS4	2021-04-23T23:12:33Z	2021-04-23T23:15:55Z	176	0.867
MMS4	2021-05-22T18:31:35Z	2021-05-22T18:35:26Z	29	0.125
MMS4	2021-05-25T14:57:14Z	2021-05-25T14:59:39Z	26	0.178
MMS4	2021-05-26T03:31:24Z	2021-05-26T03:35:28Z	50	0.204
MMS4	2021-06-05T21:25:07Z	2021-06-05T21:33:35Z	38	0.075
MMS4	2021-06-08T13:21:22Z	2021-06-08T13:26:55Z	33	0.099
MMS4	2021-06-22T06:45:20Z	2021-06-22T06:49:30Z	37	0.147
MMS4	2021-06-25T11:21:29Z	2021-06-25T11:47:58Z	213	0.134
MMS4	2021-07-08T13:29:07Z	2021-07-08T13:33:13Z	68	0.275
MMS4	2021-07-13T14:41:34Z	2021-07-13T14:46:56Z	59	0.183
MMS4	2021-08-21T14:31:32Z	2021-08-21T14:59:13Z	481	0.289
MMS4	2021-09-03T05:48:06Z	2021-09-03T05:53:32Z	32	0.098
MMS4	2021-09-30T11:29:00Z	2021-09-30T11:35:49Z	152	0.371
MMS4	2021-10-20T10:22:50Z	2021-10-20T10:49:53Z	121	0.075
MMS4	2021-11-27T06:33:05Z	2021-11-27T10:50:46Z	3792	0.245
MMS4	2021-11-28T00:07:13Z	2021-11-28T00:55:37Z	318	0.109
MMS4	2022-01-08T20:04:17Z	2022-01-08T20:32:23Z	99	0.059
MMS4	2022-01-15T18:29:00Z	2022-01-15T18:30:00Z	61	1.000
MMS4	2022-02-05T22:56:59Z	2022-02-05T22:57:43Z	25	0.556
MMS4	2022-08-27T14:27:19Z	2022-08-27T14:28:30Z	72	1.000

**Table 2-4 ASPOC Data Product Issues as of 09/30/2022**

#### 2.4.4 ASPOC Data Quality Flags

All ASPOC science data products do contain beam current quality flags in a dedicated status byte. The ion emission quality bytes are encoded as follows:

- 0 no emission, both ASPOC units are off
- 1 emission; I\_BEAM/I\_TOTAL > 0.97(excellent)
- 2 emission; I\_BEAM/I\_TOTAL > 0.92 (good)
- 3 emission; I\_BEAM/I\_TOTAL > 0.75 (moderate)
- 4 emission; I\_BEAM/I\_TOTAL > 0.3 (weak)
- 5 emission; I\_BEAM/I\_TOTAL > 0.0 (poor)
- 6 at least one unit in cleaning mode

7           at least one unit in startup mode  
255         fill value (no data)

## 2.5 DATA PRODUCTION ALGORITHM DESCRIPTIONS

ASPOC generates Quicklook, L1b/SITL, and L2 science data products. L1b/SITL and L2 data products are provided in CDF files, while Quicklook products are represented by data plots saved in PNG file format. The CDF files are formatted in accordance with the MMS CDF File Format Guide. The MMS file name convention is applied to all files.

### 2.5.1 ASPOC L1b/SITL Data Products

ASPOC Level-1b and SITL data products are containing calibrated raw data having a resolution that corresponds to the data acquisition cycle on-board. The following data products are available (given resolutions are typical values):

- Ion beam current, energy, ~ 1s resolution
- Total emitter current, ~ 1 s resolution
- Status and housekeeping, ~ 40 s resolution
- Spacecraft potential as used for control loop, ~1 s resolution
- Emitter heater current and voltage, ~ 20 s resolution
- Status flags and parameters, ~ 40 s resolution
- Secondary voltages, ~ 60 s resolution
- Internal temperatures, ~ 40 s resolution

### 2.5.2 ASPOC L2 Data Products

ASPOC Level-2 products are daily files containing interpolated data at a resolution of 1 second (86400 records per file). For science analysis ASPOC will provide the following data:

- Ion beam current
  - individual ASPOC 1 and ASPOC 2 currents
  - and the sum
- Ion beam energies of individual ASPOCs
- Data quality information
- Individual ASPOC 1 and ASPOC 2 modes
- ASPOC ON/OFF status (ON indicates that at least one ASPOC is emitting ions)

### 2.5.3 Quicklook Data Products

ASPOC Quicklook data products are PNG graphic files containing daily plots of key parameters, which reflect the status of the instrument. The following parameters are shown:

- Spacecraft potential
- Ion beam current
- Total emitter current
- Beam energy
- Filament power
- Filament impedance

The graphic on the next page shows a sample plot of ASPOC data from the MMS1 spacecraft. The bar at the bottom of the plot indicates the quality of the ion emission:

- OFF = instrument not active
- Q1-Q5 = emission quality (1=good, 5=bad)
- CLN = cleaning active
- NOE = no emission (startup active)

In addition, the background color of the plot shows if ASPOC is active and emits a significant number of ions.

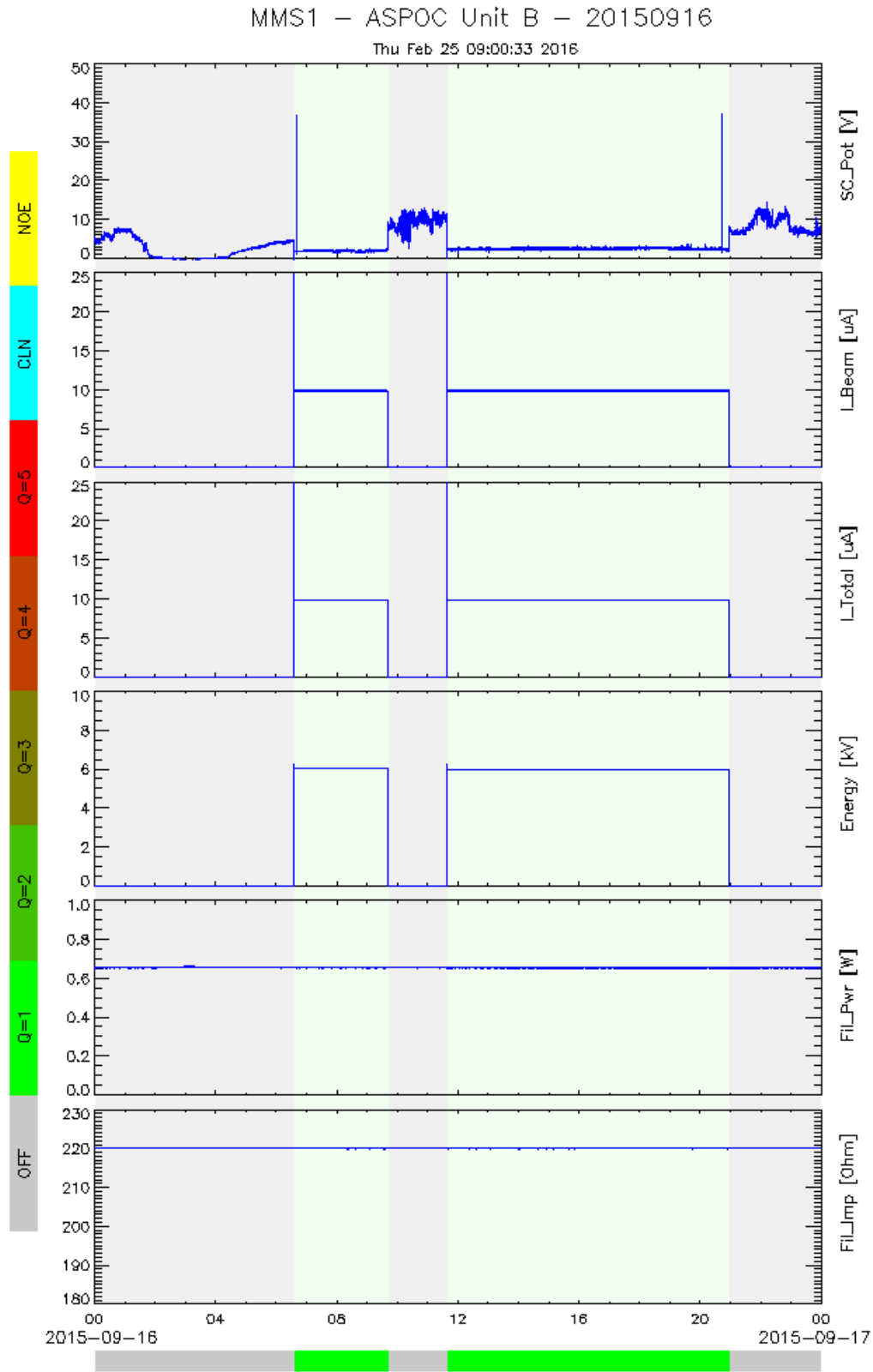


**Table 2-5 ASPOC Quicklook Data Plot**

**2.6 APPENDIX A- ASPOC REFERENCES**

The following documents and drawings in effect on the day this specification was signed **shall** apply to the extent specified herein. In the event of conflict between this document and any referenced document, the document with latest publication date will govern.

The following is a list of applicable references and publications.

<b>Section</b>	<b>Document Number</b>	<b>Title</b>	<b>Revision/Date</b>
	MMS-ASP-IWF-TN-0042	MMS ASPOC Science Data Products Guide	2.0, 02/25/2016
	MMS-ASP-IWF-UM-0001	MMS ASPOC User Manual	1.0, 09/01/2015
	<a href="http://doi.org/10.1109/TPS.2017.2694223">http://doi.org/10.1109/TPS.2017.2694223</a>	Nakamura, R., K. Torkar, M. Andriopoulou, H. Jeszenszky, C. P. Escoubet, F. Cipriani, P. A. Lindqvist, S. A. Fuselier, C. J. Pollock, B. L. Giles, Y. Khotyaintsev (2017), Initial Results From the Active Spacecraft Potential Control Onboard Magnetospheric Multiscale Mission, IEEE Transactions on Plasma Science, 45 (8), 1847-1852.	

**Table 2-6 ASPOC Applicable Documents**

### 3.0 MAGNETIC EPHEMERIS COORDINATES (MEC)

#### 3.1 MEC OVERVIEW

The Magnetic Ephemeris and Coordinates (MEC) products provide information about the location and attitude, and magnetic connectivity of the four satellites comprising the Magnetospheric Multiscale (MMS) mission.

The MEC products are provided in files named after the magnetic field model used for the field-dependent quantities within the data files. These models are: T89D – the Kp-parameterized Tsyganenko 1989 model; T89Q – the Tsyganenko 1989 model with Kp=2; TS04D – the solar wind-parameterized Tsyganenko & Sitnov 2005 model. It is important to note that the key products such as position, velocity, and coordinate transformations do not depend on the magnetic field model and therefore are identical in each model product.

From a user perspective, this means that all position vectors, velocity vectors, quaternions for coordinate transformation, and attitude information can be taken from any file for the desired time period. As the T89Q product does not rely on ancillary data it will be available in final form at the lowest latency and is therefore recommended for any products not depending on the magnetic field model. For clarity, we note that the Geocentric Solar Magnetospheric (GSM) and Solar Magnetic (SM) coordinate systems (see section 3.2) are not magnetic field model dependent in this context; these coordinate systems rely on the orientation of the dipole axis and Earth's magnetic moment, both of which are derived from the International Geomagnetic Reference Field (IGRF – a representation of Earth's internal field).

#### 3.2 COORDINATE SYSTEMS

The MEC products provide information related to the coordinate systems listed below. These can be broken down into coordinate systems based on the satellite (sections 3.2.1 and 3.2.2) and geophysical coordinate systems (section 3.2.3). To convert between these systems the MEC data products provide quaternions, see section 3.4.3 for definitions and usage details. The satellite-based coordinate systems are defined in the Alignment and Coordinate System Document listed in Table 3-6.

##### 3.2.1 Spinning, Spacecraft-fixed Systems

- BCS – Body Coordinate System (Spinning Spacecraft Body)
- SSL – Spinning Spacecraft, Angular Momentum Vector (L) Aligned
- SMPA – Spinning Major Principal Axis (MPA)-Aligned Coordinates

##### 3.2.2 De-spun Systems

- DBCS – De-spun Body Coordinate System (despin around BCS Z-axis).
- DSL – De-spun Spacecraft L-Vector Coordinate System (Despin around L). Non-spinning frame, in which the Z-axis is fixed in inertial space, but the transformation to DBCS is time-dependent (as well as phase-dependent).
- DMPA – De-spun Major Principal Axis (despin around Major Principal Axis). A non-spinning frame that has a fixed orientation relative to DBCS, but whose axes orientations wobble with respect to inertial space at the nutation rate.

##### 3.2.3 Geophysical Systems

- ECI (GEI/J2000) – Earth-Centered Inertial (ECI). To fully specify the system the equinox must be defined. This system uses the mean equinox at the J2000 epoch. The z-axis is aligned with the mean celestial pole at J2000; the x-axis is aligned with the mean equinox at J2000; the y-axis



completes and lies in the plane of the celestial equator. Other Earth-Centered Inertial systems are used, as shown in Figure 3-1, the most important of which is Mean of Date (MOD).

- MOD – Mean of Date (MOD) accounts for precession of the mean equinox between the J2000 epoch and the date of interest. The definition follows that of ECI, but uses the mean equinox and mean equator of the date of interest. The coordinate system is thus time-dependent.
- GSE – Geocentric Solar Ecliptic (GSE) is not an inertial system. It is Earth-centered with the x-axis pointing towards the Sun. The y-axis lies in the mean ecliptic plane of date, pointing in the anti-orbit direction. The z-axis is parallel to the mean ecliptic pole of date.
- GSE2000 – This system is defined similarly to GSE, but uses the J2000 epoch instead of the date of interest.
- GSM – Geocentric Solar Magnetospheric (GSM) is similar to GSE, but is defined such that the centered dipole axis lies in the x-z plane. As in all of these systems, z is positive northward. The y-axis is then perpendicular to both the Sun-Earth line and the centered dipole axis. The centered dipole axis is defined for the date of interest using the first three coefficients of the IGRF. GSM is therefore a rotation about the x-axis from GSE.
- SM – Solar Magnetic (SM) is defined such that the z-axis is aligned with the dipole axis of date and the y-axis is perpendicular to both the Sun-Earth line and the dipole axis. As with GSE and GSM y is positive in the anti-orbit direction. The x-axis is therefore not aligned with the Sun vector. SM is a rotation about the y-axis from the GSM system.
- GEO – Geocentric Geographic (GEO) is an Earth-centered, Earth-fixed (ECEF) coordinate system. In this system a point on the surface of the Earth has fixed coordinates as Earth rotates. The x-axis lies in the Earth's equatorial plane (zero degrees latitude) and intersects the Prime Meridian (zero degrees longitude; the meridian of Greenwich, UK). The z-axis points to *true North*, which is roughly aligned with the instantaneous rotation axis of Earth. For low- or zero-altitude applications this system is often given in a spherical representation, however for astrophysical purposes it is usually represented as a Cartesian system (including here). This system is equivalent to the International Terrestrial Reference Frame (ITRF).

### 3.2.4 JPL DE421 Ephemerides

As will be detailed in section 3.2.5, one of the fundamental quantities on which coordinate system definitions and transformations are based is the Sun vector. While numerous analytic expressions have been put forward to approximate this (see, e.g., [1, 2, 3]), they all have differing accuracy at different times. The LANLGeoMag software library [4, 5], in addition to two analytic expressions, allows use of the Jet Propulsion Laboratory (JPL) Development Ephemeris (DE). The MMS mission has adopted use of DE421 [6] as the standard description of orbits of solar system bodies. DE421 is intended for use between the years 1900 and 2050, encapsulating the expected span of the MMS mission, and providing sub-kilometer accuracy for the position of the Earth [6] with the solar position and velocity derived to maintain the solar system barycenter at the origin of the International Celestial Reference Frame (ICRF). For the MMS mission, and the MEC products, the Sun vector is defined as the vector from the DE421 Earth position to the DE421 Sun position, where the Earth position defines the origin of all Earth-centered coordinate systems (such as the ITRF).

### 3.2.5 Relationship Between Celestial and Magnetospheric Coordinate Systems

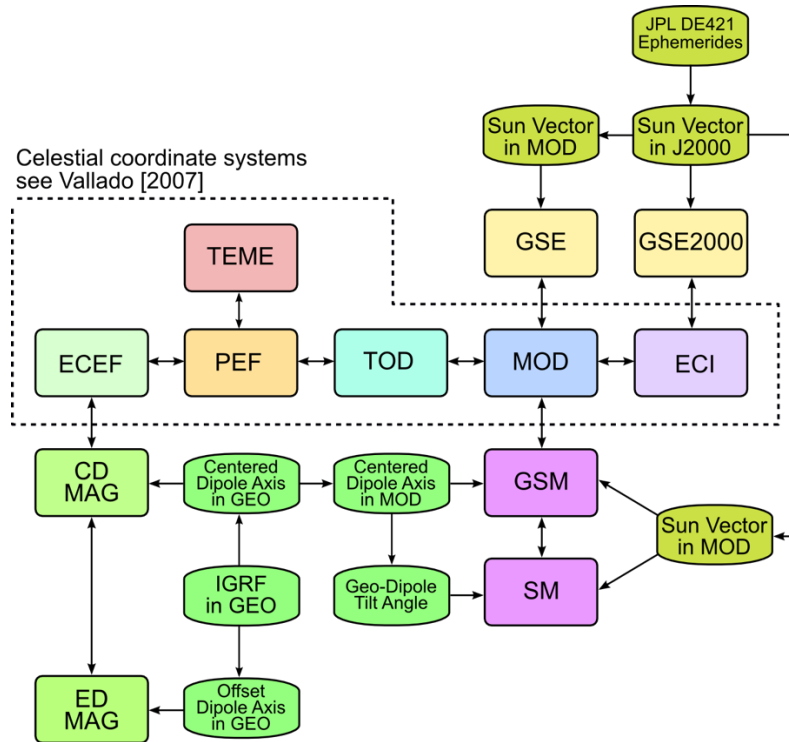


**Figure 3-1 Relationship Between Astrophysical and Magnetospheric Coordinate Systems. (Coordinate systems and transformations in the dashed box are described in detail by Vallado [2007]. (Adapted from LANLGeoMag documentation.))**

Figure 3-1 illustrates how the various celestial coordinate systems described by [1] (see section 3.7) are related to the magnetospheric coordinate systems described here. The coordinate systems and transformations in the dashed box are the standard celestial systems described in detail by [1]. ECEF (more commonly referred to as GEO or ITRF), ECI, and Mean-Of-Date (MOD) are described above, and the other intermediate coordinate systems are True-Of-Date (TOD), and Pseudo Earth Fixed (PEF). Transformation of ECI to MOD accounts for precession of the ecliptic, while the MOD to TOD transformations account for smaller amplitude nutation effects. The TOD to PEF transformation corrects for very small effects of *polar motion* (see section 3.7.3 of [1].) The TEME (True Equator, Mean Equinox) coordinate system is the inertial system used by the SGP4 orbit propagation code (using the so-called *Two Line Elements* or *Keplerian Elements*), and it is most closely tied to the PEF system.

The geomagnetic coordinate systems are shown in the lower left part of the figure, while the solar based GSE systems are shown in the upper right. The vertical column of boxes containing GSE, MOD, GSM, and SM are the standard system of coordinates traditionally used in magnetospheric physics [2, 3]. For comparison with other implementations used in the space physics community, see the next section.

### 3.3 IMPLEMENTATIONS AND SOFTWARE LIBRARIES USED

The implemented astrophysical coordinate systems and transformations are consistent with the International Astronomical Union (IAU) Fifth Fundamental Catalogue (FK5). The ICRF used by DE421 supersedes the FK5 system used here, but the ICRF celestial pole is consistent with FK5 to within the uncertainty of the FK5 celestial pole ( $\pm 50$  milliarcseconds), with an offset between the ICRF pole and the FK5 pole of about 23 milliarcseconds, and is considered of sufficient accuracy for MMS science. The

astrophysical and geophysical coordinate systems used by MEC all use the software implementations from the LANLGeoMag library [4, 5]. Following [1] LANLGeoMag uses the FK5 system. While some references for geophysical coordinate systems use truncated series for key calculations (e.g., [2], but see the discussion in [3] for comments on the implied error) such as Greenwich Mean Sidereal Time, LANLGeoMag uses the full series to maintain precision and accuracy. The IAU 1976 precession model and the IAU 1980 theory of nutation are used to describe the changes in the equinox and pole. Full details can be found in [1].

One consequence of the explicit integration of the geophysical systems with astrophysical systems as defined in Figure 3-1 is that all geophysical systems are explicitly derived from an inertial system with an explicit reference epoch. Earlier work [2, 7] implicitly referenced the geophysical coordinate systems to “epoch-of-date”. Depending on whether only precession is accounted for, or also the effects of nutation, this would correspond to MOD or TOD. However, [3] explicitly define geophysical systems using TOD and small differences in transformations would result from changing reference inertial system. The difference between using MOD or TOD was reported by [8] as being insignificant relative to the errors in determining spacecraft position. For the purposes of this document we note that the MEC transformations follow the implementation in LANLGeoMag, as used for the earlier Van Allen Probes mission. When comparing to (or combining with) transformations from other software libraries, it is important to verify the reference inertial coordinate system, the derivation of the Sun vector, and the accuracy of the equations used to calculate the necessary astrophysical quantities; most widely used coordinate transformation routines in space physics are based on [2, 7] and do not explicitly define the inertial system as either TOD or MOD. To maintain accuracy, it is recommended to follow the coordinate system definitions given here and the Earth and Sun positions from DE 421.

### 3.4 IMPLEMENTATION DETAILS FOR TRANSFORMATIONS REQUIRING ATTITUDE DATA

#### 3.4.1 FDOA Attitude Inputs

The Level-2 Ephemeris data is computed from inputs produced by the Flight Dynamics Operations Area (FDOA).

The attitude inputs provided from FDOA are:

- ISO Time,
- TAI (number of SI seconds since 1958-001T00:00:00 UTC),
- ECI-to-BCS quaternion (for frame rotation),
- the X, Y, Z rotation rate components (deg/s) (instantaneous spin axis in body frame),
- w-phase (Sun-to-body-X dihedral angle about rotation rate vector) (deg),
- right ascension (deg) and declination (deg) of body Z-axis,
- Z-phase (Sun-to-body-X dihedral angle about body Z-axis) (deg),
- right ascension (deg) and declination (deg) of angular momentum (L),
- L-phase (Sun-to-body-X dihedral angle about angular momentum vector L) (deg),
- right ascension (deg) and declination (deg) of major principal axis (P),
- P-phase (Sun-to-body-X dihedral angle about major principal axis P) (deg),
- nutation angle (deg),
- Quality flag:
  - EKF=good extended Kalman filter solution with star tracker data
  - CNV=filter not yet converged
  - SUN=no tracker data; spin phase obtained from Sun sensor data

INT=no tracker or Sun sensor data; phase interpolated from neighboring tracker data  
BAD=no tracker or Sun sensor data for a time span too large for interpolation

These quantities are computed and reported (by FDOA) at irregular intervals on a time cadence of approximately 0.5 to 1.0 s.

### 3.4.2 Calculation of ECI\_to\_DBCS and ECI-to\_BCS Coordinate Systems

Conversion of coordinates between the Earth Centered Inertial J2000 (ECI) frame and the Body Centered System (BCS) frame can be accomplished by either using the FDOA-provided ECI-to-BCS quaternions or by constructing the transformation matrices and associated quaternions from the other FDOA-provided quantities. In the present implementation of the Level-2 Ephemeris products, the latter approach is used for two reasons: 1) The ECI-to-BCS quaternions in the raw FDOA attitude files are transformations of the frames rather than vectors (which are inverses of one another), and 2) the provided quaternions do not have very high numerical precision. In order to produce higher-precision ECI-to-BCS quaternions that rotate vectors instead of coordinate frames, we first compute the ECI-to-DBCS transformation matrix. For the DBCS system, Z-axis is along the Body Z axis (provided in ECI frame by FDOA), the Y-axis is normal to the plane defined by the Z-axis and the sun vector, S (where  $S = \text{Sun\_DE421} - \text{Position\_SC}$ ), and the X-axis completes a right-hand Cartesian system.

The DBCS-to-BCS transformation matrix is just a rotation around the Z-axis by  $-Z\_Phase$  radians (also provided by FDOA). The overall transformation from ECI to BCS is then computed as the product of the two rotation matrices. The composite rotation matrix is then transformed to a unit quaternion (using routines in LANLGeoMag).

### 3.4.3 Attitude Interpolation

In order to provide attitude information on a regular time grid for the survey (30s cadence) and burst mode (30 ms cadence) files, the quantities provided by FDOA are interpolated in time. This is accomplished by interpolating the unit quaternions using Spherical Linear Interpolation (often referred to as SLERP) and by using linear interpolation of the other scalar quantities provided by FDOA (specifically, the Right Ascension and Declination of the Body Z-axis and the Z-phase angle). Although new (vector-rotating) ECI-to-BCS quaternions are computed from the interpolated scalar quantities, the SLERP-interpolated (frame-rotating) FDOA quaternions are used to provide a check on the calculations.

### 3.4.4 Quaternion Definitions and Usage

Quaternions are a number system that extends the complex numbers and are widely used in calculations of rotations. Quaternions provide a more compact and efficient representation of a rotation than a standard rotation matrix. The MEC files include a “quaternion\_representation” variable that gives the order of the quaternion components. In version 2.y.z of the MEC data this is given as [qx, qy, qz, qw]. This representation means that the first three elements of the quaternion variables give the three *vector parts* of the quaternion and the last element gives the *scalar part*. All quaternions are provided as a rotation from ECI to a target system. To illustrate the use, assume we aim to transform the GSE position vector (‘mms1\_mec\_r\_gse’) to the GSM coordinate system. For this we:

- Take the conjugate of the ECI→GSE quaternion (‘mms1\_mec\_quat\_eci\_to\_gse’)
- Multiply the ECI→GSM quaternion by the GSE→ECI quaternion. Note that quaternion multiplication is not commutative.
- Use the resultant quaternion to convert GSE→GSM in a vector rotation operation.

Reference implementations for quaternion operations are given in the LANLGeoMag software [4, 5] and Python versions are provided in SpacePy [9, 10]. Other implementations are available for most popular programming languages.

In order to interpolate quaternions to a desired time, the end user should use SLERP (Spherical Linear Interpolation). If  $q_1$  and  $q_2$  are unit quaternion rotations (i.e. they represent transformations from one system to another) defined at times  $t_1$  and  $t_2$  respectively, and we wish to obtain the quaternion at time  $t$  (such that  $t_1 \leq t \leq t_2$ , then SLERP for quaternions can be expressed with the very simple formula;

$$q(t) = q_0(q_0^{-1}q_1)^u$$

Where  $u = (t - t_1)/(t_2 - t_1)$  (i.e.  $u = 0$  when  $t = t_1$  and  $u = 1$  when  $t = t_2$ ). The routines to accomplish the quaternion operations can be found in LANLGeoMag and SpacePy libraries.

### 3.4.5 Transformations Between Spinning and De-spun Coordinate Systems

Quaternions are provided for transforming vectors from the ECI system to the following systems:

- BCS
- DBCS
- DMPA
- DSL
- GEO
- GSE
- GSE2000
- GSM
- SM
- SMPA
- SSL

For details on how these coordinate frames are defined, refer to the in “Magnetospheric Multiscale (MMS) Project Alignment and Coordinate System Document” [12].

## 3.5 IMPLEMENTATION DETAILS FOR TRANSFORMATIONS REQUIRING EPHEMERIS DATA

### 3.5.1 FDOA Ephemeris Inputs

The inputs obtained from the FDOA for ephemeris include the following quantities:

- Epoch (UTC)
- Epoch in TAI
- X, Y, Z position components in the Mean of J2000 system (units in km)
- VX, VY, VZ velocity components in the Mean of J2000 system (units in km/s)
- Mass in kg

These quantities are reported approximately every 30s.

### 3.5.2 Ephemeris Interpolation

In order to interpolate to a regular grid at arbitrary time resolution, we use Hermite interpolation. Hermite interpolation interpolates data points as a polynomial function of order  $q$ , and ensures that the solution matches both position and velocity points simultaneously. For the L2-ephemeris, we use the Gnu Scientific Library (GSL) routines for Hermite interpolation.

### 3.5.3 Transformations Between Systems

In order to transform between coordinate systems using the quaternions, the general prescription is as follows. If  $r_{eci}$  is a position vector in ECI coordinates and we wish to compute the position vector in GSM coordinates,  $r_{gsm}$ , then we would need a ECI-to-GSM quaternion,  $q_{eci\_to\_gsm}$  and perform the following quaternion operation;

$$r_{gsm} = q_{eci\_to\_gsm} r_{eci} q_{eci\_to\_gsm}^{-1}$$

Where  $q^{-1}$  is the inverse of  $q$ . Note that as with rotation matrices, quaternions can be chained together to produce composite rotations. As with matrix multiplication, careful attention must be paid to the order of quaternion multiplication. For example, if one has a custom quaternion that transforms from “my\_frame” to ECI, then,

$$r_{eci} = q_{my\_frame\_to\_eci} r_{my\_frame} q_{my\_frame\_to\_eci}^{-1}$$

And one can obtain a new quaternion to go from “my\_frame” to GSM as follows;

$$r_{gsm} = q_{eci\_to\_gsm} \{q_{my\_frame\_to\_eci} r_{my\_frame} q_{my\_frame\_to\_eci}^{-1}\} q_{eci\_to\_gsm}^{-1}$$

$$r_{gsm} = q_{eci\_to\_gsm} q_{my\_frame\_to\_eci} r_{my\_frame} (q_{eci\_to\_gsm} q_{my\_frame\_to\_eci})^{-1}$$

where the later results because  $(pq)^{-1} = q^{-1}p^{-1}$ . Thus, a new quaternion to go from “my\_frame” to GSM can be computed as;

$$q_{my\_frame\_to\_gsm} = q_{eci\_to\_gsm} q_{my\_frame\_to\_eci}$$

Also note that if one has a quaternion to go from one system to another, the quaternion for the reverse transformation is just its inverse.

## 3.6 LEVEL 2 ATTITUDE AND EPHERMERIS FILE CONTENTS

The variables contained within the MEC level 2 ephemeris and attitude files are consistent between the survey mode and burst mode files. The difference between these two data modes is that the survey files are provided at a 30-second cadence, while the burst mode files are provided at a resolution of 30 milliseconds.

Most variables follow the MMS variable naming convention and are of the form  $[sat]_{[instr]}[quant]$ , where  $sat$  represents the satellite (e.g.,  $mms2$ ),  $instr$  represents the instrument (here this is  $mec$ ). The variable column in the tables below list  $[quant]$ . Where units are left blank they are either not applicable or the quantity is dimensionless. Additional metadata is provided in the data files following the mission guidelines.

### 3.6.1 Ancillary Data

Variable	Units	Type	Description
Epoch	ns	CDF TIME TT2000	Nanoseconds from J2000

dipole tilt	degrees	CDF DOUBLE	Dipole tilt angle
dst	nT	CDF DOUBLE	Dst index from QinDenton files
earth eclipse flag		CDF INT4	Earth eclipse flag
ext_model		CDF CHAR	External Magnetic Field Model
gmst	degrees	CDF DOUBLE	Greenwich Mean Sidereal Time
int_model		CDF CHAR	Internal field model
kp		CDF DOUBLE	Kp index from QinDenton files
l dipole		CDF DOUBLE	Dipole L-shell value
moon eclipse flag		CDF INT4	Moon eclipse flag

**Table 3-1 Ancillary Data**

The eclipse flags are defined such that zero is no eclipse, one indicates penumbral eclipse, two denotes umbral eclipse.

### 3.6.2 Attitude

Variable	Units	Type	Description
L_phase	degrees	CDF_DOUBLE	Sun to body-X dihedral angle about angular momentum vector
L_vec	degrees	CDF_DOUBLE	Right ascension and declination of angular momentum vector
P_phase	degrees	CDF_DOUBLE	Sun to body-X dihedral angle about major principal axis
P_vec	degrees	CDF_DOUBLE	Right ascension and declination of major principal axis
Z_phase	degrees	CDF DOUBLE	Sun to body-X dihedral angle about body Z-axis
Z_vec	degrees	CDF DOUBLE	Right ascension and declination of body Z-axis

**Table 3-2 Attitude Data**

### 3.6.3 Coordinate Transformations

Variable	Units	Type	Description
quat eci to bcs		CDF DOUBLE	Quaternion rotation from ECI to BCS
quat eci to dbcs		CDF DOUBLE	Quaternion rotation from ECI to DBCS
quat eci to dmpa		CDF DOUBLE	Quaternion rotation from ECI to DMPA
quat eci to dsl		CDF DOUBLE	Quaternion rotation from ECI to DSL
quat eci to geo		CDF DOUBLE	Quaternion rotation from ECI to GEO
quat eci to gse		CDF DOUBLE	Quaternion rotation from ECI to GSE
quat eci to gse2000		CDF DOUBLE	Quaternion rotation from ECI to GSE2000
quat eci to gsm		CDF DOUBLE	Quaternion rotation from ECI to GSM
quat eci to sm		CDF DOUBLE	Quaternion rotation from ECI to SM
quat eci to smpa		CDF DOUBLE	Quaternion rotation from ECI to SMPA
quat eci to ssl		CDF DOUBLE	Quaternion rotation from ECI to SSL

**Table 3-3 Coordinate Transformation Data**

### 3.6.4 Position and Velocity

Variable	Units	Type	Description
r_e ci	km	CDF DOUBLE	Position vector in ECI/J2000
r_geo	km	CDF DOUBLE	Position vector in GEO
r_gse	km	CDF DOUBLE	Position vector in GSE
r_gse2000	km	CDF DOUBLE	Position vector in GSE2000
r_gsm	km	CDF DOUBLE	Position vector in GSM
r_sm	km	CDF DOUBLE	Position vector in SM

r_moon_de421_eci	km	CDF_DOUBLE	Geocentric position vector of the Moon in ECI
r_sun_de421_eci	km	CDF_DOUBLE	Geocentric position vector of the Sun in ECI
v_eci	km/s	CDF_DOUBLE	Velocity in ECI/J2000
v_geo	km/s	CDF_DOUBLE	Velocity in GEO
v_gse	km/s	CDF_DOUBLE	Velocity in GSE
v_gse2000	km/s	CDF_DOUBLE	Velocity in GSE2000
v_gsm	km/s	CDF_DOUBLE	Velocity in GSM
v_sm	km/s	CDF_DOUBLE	Velocity in SM
geod_height	km	CDF_DOUBLE	Geodetic height
geod_lat	degrees	CDF_DOUBLE	Geodetic latitude
geod_lon	degrees	CDF_DOUBLE	Geodetic longitude
mlat	degrees	CDF_DOUBLE	Magnetic latitude
mlt	hours	CDF_DOUBLE	Magnetic local time

**Table 3-4 Position and Velocity Data**

### 3.6.5 Magnetic Field Model Dependent Quantities

Variable	Units	Type	Description
bfn_gsm	nT	CDF_DOUBLE	Magnetic field (in GSM) at northern footpoint
bfs_gsm	nT	CDF_DOUBLE	Magnetic field (in GSM) at southern footpoint
bmin_gsm	nT	CDF_DOUBLE	Magnetic field (in GSM) at minimum-B point
bsc_gsm	nT	CDF_DOUBLE	Magnetic field (in GSM) at spacecraft
pfn_geod_latlon	degrees	CDF_DOUBLE	Geodetic latitude & longitude of northern footpoint
pfn_gsm	km	CDF_DOUBLE	GSM position of northern footpoint
pfs_geod_latlon	degrees	CDF_DOUBLE	Geodetic latitude & longitude of southern footpoint
pfs_gsm	km	CDF_DOUBLE	GSM position of southern footpoint
pmin_gsm	km	CDF_DOUBLE	GSM position of minimum-B point
loss_cone_angle_n	degrees	CDF_DOUBLE	Northern loss cone angle
loss_cone_angle_s	degrees	CDF_DOUBLE	Southern loss cone angle
fieldline_type		CDF_INT4	Fieldline type

**Table 3-5 Magnetic Field Mode Dependent Quantities Data**

Footpoints of field lines are defined to be at 100km geodetic altitude, using the WGS84 geoid. The field line type can take the following valid values: 0 = Interplanetary magnetic field (IMF); 1 = Closed; 2 = Open Northern Lobe; 3 = Open Southern Lobe. Error values are: -1 = Inside Earth; -2 = Target Height Unreachable; -3 = Bad Trace.

### 3.6.6 Version Numbering

The version numbers for MEC data files use a *major.minor.micro* (x.y.z) scheme.

- Changes to the major version number indicate a change in data product contents or definitions that would break existing processing that uses the products.
- Changes to the minor version number are used to indicate the data quality for the magnetic field model. If required input data is missing, default values are used for a nominal quiet time and the minor version number is 0. If provisional input data is used (such as real-time values of the Kp index) the version number is 1. If definitive input data is used the version number is 2.
- The micro version number is incremented every time a file is reprocessed with the same major and minor version numbers. A common cause of incremented micro version numbers is a reprocessing due to an update in the raw position and attitude data received from NASA's Flight Dynamics Operations Area.



At the time of writing the major version number is 2. The major change that required an increment of the major version number was a change of definition of quaternions. In version 1.y.z the quaternions defined a frame rotation, and in version 2.y.z the quaternions define a vector rotation.

### 3.7 MEC APPENDIXES

#### 3.7.1 Appendix A- References

Section	Document Number	Title	Revision/Date
tbd	461-SYS-SPEC-0115X	Alignment and Coordinate System Document	Rev X/ July 22, 2014
		Code available from <a href="https://github.com/drsteve/LANLGeoMag">github.com/drsteve/LANLGeoMag</a> .	
		Code available from <a href="https://github.com/spacepy/spacepy">github.com/spacepy/spacepy</a> , or via the Python Package Index (PyPI) using 'pip'.	
	<a href="https://ipnpr.jpl.nasa.gov/progress_report/42-178/178C.pdf">https://ipnpr.jpl.nasa.gov/progress_report/42-178/178C.pdf</a>	Folkner, W. M., Williams, J. G., & Boggs, D. H. (2009). The planetary and lunar ephemeris DE 421. IPN progress report, 42(178), 1-34.	
	<a href="https://doi.org/10.1016/S0032-0633(01)00119-2">https://doi.org/10.1016/S0032-0633(01)00119-2</a>	Fränz, M., & Harper, D. (2002). Heliospheric Coordinate Systems. <i>Planetary and Space Science</i> , 50(2), 217-233.	
	<a href="https://doi.org/10.1007/s00585-995-0713-8">https://doi.org/10.1007/s00585-995-0713-8</a>	Hapgood, M. A. (1995, July). Space physics coordinate transformations: the role of precession. In <i>Annales Geophysicae</i> (Vol. 13, No. 7, pp. 713-716). Copernicus GmbH.	
	<a href="https://doi.org/10.5281/zenodo.1195041">https://doi.org/10.5281/zenodo.1195041</a>	Henderson, M. G., S. K. Morley, J. Niehof, and B. A. Larsen, <i>LANLGeoMag v1.5.16</i> , Zenodo	
	<a href="https://doi.org/10.5281/zenodo.4472086">https://doi.org/10.5281/zenodo.4472086</a>	Morley, S. K., J. T. Niehof, D. T. Welling, B. A. Larsen, J. Haiducek, A. Merrill, P. Killick, A. Reimer, M. Engel, A. Stricklan, A. Hendry, M. G. Henderson, <i>SpacePy 0.2.2</i> , Zenodo	
		Russell, C. T. (1971). Geophysical coordinate transformations. <i>Cosmic Electrodynamics</i> , 2(2), 184-196.	

		Vallado, D. A. and McClain, W.D., <i>Fundamentals of Astrodynamics and Applications</i> , 3rd ed., Microcosm Press, El Segundo, CA, 2007, Sec. 3.7.3 (see equation 3-78.)	
--	--	---	--

**Table 3-6 MEC Applicable Documents**

## 4.0 FAST PLASMA INVESTIGATION (FPI)

### 4.1 FPI OVERVIEW

The Fast Plasma Investigation (FPI) measures the differential directional flux of magnetospheric electrons and ions on the Magnetospheric Multiscale Mission (MMS) with unprecedented time resolution to resolve kinetic-scale plasma dynamics. Utilizing four dual 180-degree top hat spectrometers for electrons (DES) and four dual 180-degree top hat spectrometers for ions (DIS) around the periphery of each of the four MMS spacecraft, the spectrometers use electrostatic field-of-view deflection to provide  $4\pi$ -sr field-of-view with, at worst, 11.25-degree sample spacing. Energy/charge sampling is provided by swept electrostatic energy/charge selection over the range from a few eV/q to 30000 eV/q.

FPI performs rapid collection of electrons and positive ions in phase space densities within and near sites in the Earth's magnetosphere where reconnection (or the interconnection of magnetic field lines and astrophysical plasmas) takes place for the purpose of determining the kinetic processes occurring in the electron diffusion region that are responsible for collisionless magnetic reconnection, especially in regard to how reconnection is initiated.

A full description of the design of FPI, its ground calibration results, its in-flight calibration plan, its operational concept, and an overview of its data products can be found in the publication:

Pollock, C., Moore, T., Jacques, A., Burch, J., Gliese, U., Saito, Y., ... & Zeuch, M. (2016). Fast plasma investigation for magnetospheric multiscale. *Space Science Reviews*, 199(1), 331-406.

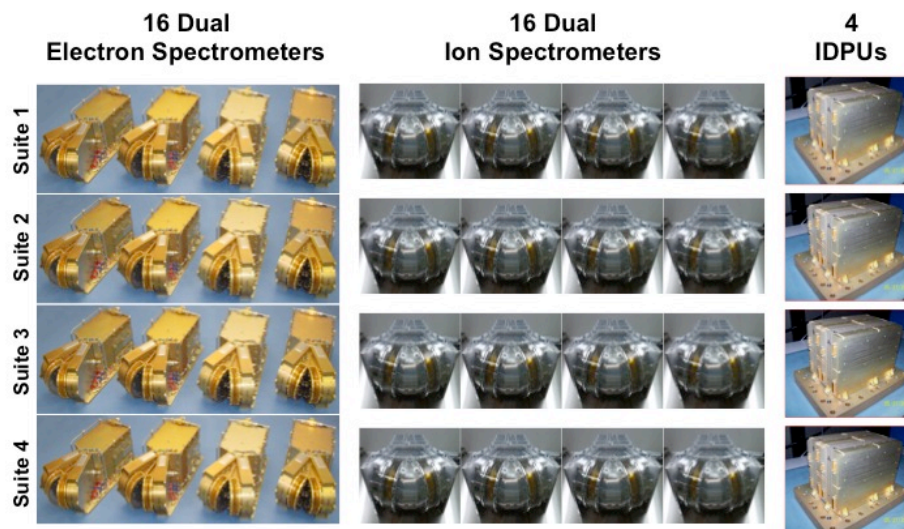


**Figure 4-1 The 64 FPI Spectrometers and 4 IDPU**

#### 4.1.1 Status of FPI Spectrometers

FPI consists of eight high-speed sensors for each species, packaged in pairs as dual spectrometers, spaced around each spacecraft perimeter. This design was implemented in order to ensure that full azimuthal sampling need not depend on the spin of the spacecraft while allowing for measurement of ion and electron phase space densities at extremely high speeds. Measurements are taken at 32 different energies in 512 different directions with uniform coverage of the sky. The statistical and systematic uncertainties

of FPI data have been quantified, and Level-2 (L2) FPI data products regularly provide high-fidelity estimates of current densities using data from only a single spacecraft, enabling unprecedented studies of kinetic-scale physics. In November 2017, FPI introduced a refined energy sweep table for solar wind observations (ions: 197 eV-9222 eV; electrons: 4 eV-940 eV).

All FPI electron and ion spectrometers are functioning nominally with the exception of the following:

- MMS3 DIS008: On 6 February 2018 22:08 UTC (orbit 700), one of the two ion spectrometers in quadrant 0 began erroneously measuring anomalous counts in the highest energy ranges. Cause of the anomaly remains unknown. As a result of the anomaly, the configuration of this spectrometer pair was modified to prevent the taking of measurements above 11 keV. During sampling by other MMS3 ion spectrometer pairs above 11 keV, DIS008 repeats its highest allowed operational energy setting.
- MMS4 DES210: On 7 June 2018 12:43 UTC, the electron spectrometer pair in quadrant 1 suffered a high voltage failure and was subsequently shut down.
- MMS4 DES215: On 15 July 2018 00:47 UTC, the electron spectrometer pair in quadrant 0 suffered a high voltage failure and was subsequently shut down.

The following is a table of the anomalies that have occurred in regards to the FPI spectrometers since the start of the mission, as discussed in detail above.

Date	Time (UTC)	FPI Unit	Flight Module	Apparent Failure (Determined Via Diagnostic Testing and Analysis)
2/6/2017	22:08	DIS0	DIS008	Erroneous high counts in approx. x5 pixels at the highest energy steps
6/5/2018	12:43	DES1	DES210	HV801 on ESA high range stepper circuit
7/15/2018	00:49	DES0	DES215	HV801 on Deflector0 high range stepper circuit

**Table 4-1 FPI Off-Nominal Spectrometer Status**

#### 4.1.2 Status of FPI Science Data

FPI L2 publication quality distributions and moments are generally available for all designated science regions of interest. In addition, FPI burst resolution L2 distributions and moments are generally available for all time segments selected by the SITL and successfully downlinked. The following accommodations were made in order to mitigate the FPI anomalies cited above:

- MMS3 DIS data: For MMS3 ion spectrometer energy steps higher than 11 keV from areas of the sky in which DIS008 does not contribute, an average phase space density ratio is obtained between that energy and 11 keV. DIS008 distribution data is then scaled by that ratio under the assumption that the angular structure at the highest DIS008 sampled energy is similar to any higher energy sampled by the other spectrometers. This is repeated for all energy steps that would, under nominal conditions, be above the highest DIS008 sampled energy. During data validation, any MMS3 ion measurements exhibiting high spintone counts relative to the other MMS observatories are flagged, as they are most likely an indication of differing angular structure at high energies.

- MMS4 DES data: Post-anomaly MMS4 electron Fast Survey distributions contain fill values (-1e31) to indicate look directions where DES210 and DES215 combined observations contribute greater than 75% of the time accumulation. MMS4 electron burst distributions contain fill values (-1e31) to indicate look directions corresponding to DES210 and DES215 observations. MMS4 moments files are not generated.

The FPI ground system processes all available downlinked Fast Survey and burst data, including partial segments and those that were not downlinked for all MMS observatories. That said, there are a small number of Fast Survey and burst intervals in which data is not completely available for FPI. The reasons for the incomplete record of FPI data include the following:

- No FPI data is available
  - Maneuvers: FPI is placed into safe mode (i.e., does not operate) during a window beginning thirty minutes prior to and extending to thirty minutes after the conclusion of any spacecraft maneuver.
  - Spacecraft anomalies: No FPI data collected when an observatory is in emergency safe mode.
  - Scheduled downtime: FPI did not collect science data during specific mission phases, including the majority of Phase 1X (with the exception of Bursty Bulk Flow (BBF) testing), for almost two months prior to the first tail pass, and during the long shadows of the summer of 2019.
  - Unscheduled downtime: FPI was placed in safe mode during analysis and mitigation activities of the DIS008 (MMS3) and DES210/DES215 anomalies (MMS4).
  - BDM artifacts/anomalies: There are a number of burst segments, many of them with SITL messages like "orphan burst buffer sweep," where there is no associated data.
- FPI data not publicly released
  - Tests: The FPI operations team conducts occasional tests during which no scientifically usable data is collected. This includes FPI data collected during much of Phase 1X and the FPI noise test.
  - Spacecraft anomalies: FPI data that is determined to be scientifically unusable due to spacecraft anomalies. Examples include the MMS3 timing issue in January 2017.
  - FPI anomalies: FPI data that is determined to be scientifically unusable due to an instrument anomaly, such as during sensor anomalies or faulty configuration.
- FPI distributions released, but no moments
  - FPI MMS4 DES data beginning with June 2018 due to the DES210/DES215 anomalies discussed above.
  - Data collected during moon shadows, including two short periods on 2017-11-19 and 2019-12-27.
  - Segments where there is no available magnetic field or spacecraft potential data.

## 4.2 FPI DATA USAGE SUMMARY CHECKLIST

When it comes to analyzing the FPI data on the MMS mission, there are important items that have been considered over the lifetime and continue to be considered as the mission continues:

FPI in the Solar Wind	4.1.1 & 4.5.6
Burst Segments	4.3.1.2 & 4.4.3.2
Instrument Thresholds vs Ambient Plasma Distribution	4.5.3

Counting Statistics and Establishing the 1-Count Level	4.5.4
Quasi-Neutrality Check	4.5.5
FPI Moment Error Calculations	4.5.7
Photoelectron Contributions	4.5.7.2
Compression Artifacts	4.5.7.3
Background Radiation	4.5.7.5
Quality Flags	4.5.8

**Table 4-2 Data Usage Summary Checklist**

Overall, the checklist provides a guide of the known data features and recommendations for mitigation. However, it is up to the data user to review the data and carefully consider what the measured signals indicate about the natural plasma environment versus what is indicated about any spacecraft induced plasma environment. Meanwhile, the FPI team continues to work diligently to remove as many induced effects as is possible from the FPI moment values within the data processing pipeline. Information of the components of this checklist can be found throughout the rest of the FPI section of this document as referenced above.

### **4.3 FPI MEASUREMENT STANDARDS AND VOLUME**

#### **4.3.1 FPI Measurement Timing**

##### **4.3.1.1 Overview**

**The time variable in all FPI data products mark the beginning of the data collection interval.** FPI commands stepping durations within a Stepping Table on the order of 0.5  $\mu$ s for 128 steps in a cycle, totaling 30 ms for DES and 150 ms for DIS. The count integration times for each species are the same for every step in the sequence: 195  $\mu$ s for DES and 1000  $\mu$ s for DIS. The settling times are apportioned across the sweeps based on detailed characterization of the dynamic behavior of each high voltage stepper supply. At the end of a stepping cycle, a 16-by-32 pixel resolution skymap is generated for each of 32 targeted energy levels.

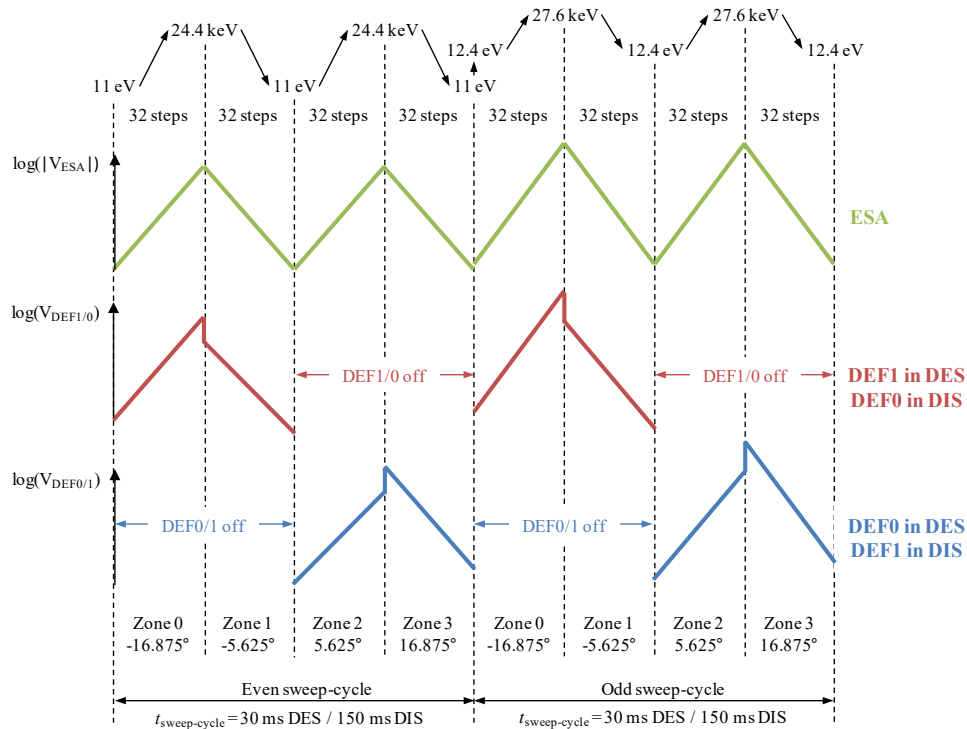


**Figure 4-2 Measurements of the ESA and Deflector Plates in the DxS**

#### 4.3.1.2 Burst Data Product Timing

The Burst Data Product applies a single timestamp to all 32 skymaps generated within a stepping cycle. In this mode, complete sets of 8192 measurements are acquired every 30ms for DES and every 150 ms for DIS. As depicted in Figure 4-2, the ESA and Deflector step up and down together in a cycle. The skymap for each energy level is filled throughout the stepping cycle and is not complete until Zone 3. Therefore, the decision was made to utilize the cycle start time as the timestamp for all skymaps. A Burst Data Product may be compressed if the counts measured exceeds [limit] and is flagged within the data product.

##### 4.3.1.2.1 Microsecond Level Precision

Each measurement in the 128-step cycle captures counts in 16 azimuth angles from both heads for each of the 4 units, totaling 128 measurements per step. While the average time allocated between stepper transitions is  $234 \mu\text{s}$  ( $30 \text{ ms}/128 \text{ steps}$ ) for DES and  $1172 \mu\text{s}$  ( $150 \text{ ms}/128 \text{ steps}$ ) for DIS, the actual time allocated per-step will differ from the average calculation up to  $250 \mu\text{s}$ . To enable microsecond-level precision of FPI data products, the FPI team produces offsets for each step within a cycle for each of the 61 (and counting) unique Stepping Tables that have been utilized in operations. The correct microsecond offset table is included in every Burst Data Product for users to apply to each skymap.

##### 4.3.1.3 Fast Survey Data Product Timing

The Fast Survey Data Product accumulates each of the 32 energy skymaps for 4.5 seconds, with a net result of 150 DES ( $4.5 \text{ s}/30 \text{ ms}$ ) or 30 DIS ( $4.5 \text{ s}/150 \text{ ms}$ ) Burst Data Products per accumulation cycle. This accumulation results with a “smeared” effect as the spacecraft rotates for the duration. The accumulation start time is used as the timestamp for each set of skymaps. A Fast Survey Data Product may be

compressed if the counts measured exceeds [limit] and is flagged within the data product. Additionally, the Fast Survey Mode is the nominal data collection mode for the Instrument Suite (IS), producing full Survey and Burst Data Telemetry continuously.

**4.3.1.4 Slow Survey Data Product Timing**

The Slow Survey Data Product accumulates each of the 32 energy skymaps for a duration of 3 spins, as provided by a Delphi pulse count. This results in a variable duration utilized per accumulation cycle. The Slow Survey mode utilizes different stepping tables than the Burst and Fast Survey Data Products. Slow Survey mode also utilizes a single quadrant (one DES and one DIS unit) while active; the selected quadrant is specified upon entering the Slow Survey mode. The accumulation start time is used as the timestamp for each set of skymaps. A Slow Survey Data Product may be compressed if the counts measured exceeds [limit] and is flagged within the data product. The Slow Survey Mode is a low data rate mode used when the Spacecraft is not in or near a targeted ROI. In this mode, a reduced set of Survey Data Telemetry is produced while Burst Data Telemetry is not.

**4.3.2 Relative Telemetry Allocations and Data Volume**

The FPI compression routines ensure a maximum data volume for science data products. Due to the level of compression, the Slow Survey and Fast Survey are essentially always lossy and occupy the full allocation. The burst data, by contrast, are generally compressed losslessly to a smaller volume than the maximum allocation. Because of this, the actual data usage for FPI burst data is highly variable based on environment, thus a peak and an average are both provided, along with other telemetry usage rates, in Table 4-3. FPI also collects, and downlinks, trigger data, however these data are included in the Fast Survey packet.

<b>Slow Survey</b>	<b>Fast Survey</b>	<b>Burst</b>	
1.28	10.24	1A	1B ->
		<b>Peak</b>	
		1560.00	1966.08
		<b>Average</b>	
		1343.00	1427.00

**Table 4-3 Telemetry Use Rates for FPI (kbit/s)**

The FPI burst telemetry usage was updated after MMS Phase 1A to mitigate compression related error in the DES burst data. It is also noteworthy that as two DES analyzers on MMS4 were powered off, the telemetry usage by FPI on MMS4 has lessened correspondingly. Distributions of the DES compressed image size for the four observatories are shown in Figure 4-3.



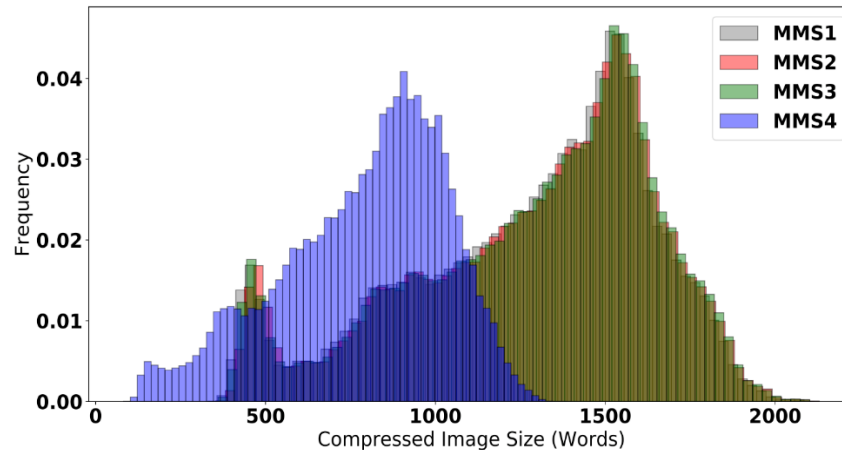


**Figure 4-3 Distribution of DES Image Sizes for the Four Observatories After Two DES Were Powered Off**

#### 4.4 FPI CALIBRATION AND VALIDATION

A full description of the design of FPI and its calibration results relative to this 4.4 section can be found in the publication:

Pollock, C., Moore, T., Jacques, A., Burch, J., Gliese, U., Saito, Y., ... & Zeuch, M. (2016). Fast plasma investigation for magnetospheric multiscale. *Space Science Reviews*, 199(1), 331-406.

##### 4.4.1 Calibration Overview

Most importantly in the full calibration program, certain mathematical functions and calibration measures can only be performed on the ground, meaning on-orbit activities rely heavily on the precise framework laid out prior to flight. Within this concept, not only does calibration depend on on-ground versus in-flight, but it depends heavily on the types of particle instruments as well. The most common instrument for low-level plasmas consists of a top-hat electrostatic analyzer (ESA) geometry coupled with a microchannel-plate-based (MCP-based) detection system. Each of the four spacecraft carries eight FPI electron spectrometers (DES) and eight FPI ion spectrometers (DIS). These are packaged in pairs in back-to-back configuration, as dual spectrometers for each species: DES and DIS. Four dual spectrometers for each species are placed around the MMS instrument deck perimeter at 90° intervals. For each dual spectrometer, the two (undeflected) 180° field of view (FOV) fans are separated by 45° in azimuth. This FPI measurement approach means that the 3D velocity distribution functions for electrons and ions will each be assembled using eight different spectrometers, four different ESA high voltage (HV) stepping supplies, and eight different deflection HV stepping supplies. While common sets of energies and angles are targeted, the spectrometers and their HV stepping supplies all have slightly different properties that, in the case of the supplies, will evolve differently through mission life. To compensate, the effects of the voltage commands used in targeting these energy and angle sets will be monitored closely and individual HV offsets will be applied over time for each of the spectrometers. The samples in velocity space have not only absolute, but also relative uncertainties within a single 3D distribution. For this reason, separate sweep table constants are maintained for each dual spectrometer tailored to the individual HV supplies; these will be maintained and updated as necessary. The appropriate voltages are initially based on careful laboratory calibrations and have been and will continue to be updated throughout the life of the mission as determined necessary by in-flight calibration activities.

#### 4.4.2 Pre-Flight / On-Ground Calibration

The DIS and DES flight units were calibrated in different locations in order to fulfill the timeline of this mission due to the fact that the magnitude of the FPI development and deployment required a distributed effort and the full expertise and support of numerous institutions. The timeline in this case in which the development of the instruments and spacecrafts took place occurred from 2008 to 2013, with integration and testing then having been performed from 2013 to 2014 prior to the launch and commissioning in October 2014 - January 2015. Goddard Space Flight Center (GSFC) provided development and delivery of the DES instruments and the Instrument Data Processing Units (IDPU), as well as operation and calibration procedures and associated flight software in the form of Central Instrument Data Processor (CIDP) macros. The DIS instruments were developed by the Japanese Meisei Electric Co., Ltd. under contract to Southwest Research Institute (SwRI) and with the guidance and direction both from co-Investigators at the Japanese Institute for Aeronautics and Astronautics (ISAS) and from GSFC. The Low Voltage Power Converters (LVPC) in the DES, DIS and IDPU were developed by the U.S. Space Power Electronics, Inc. The Southwest Research Institute developed the DES and DIS High Voltage Power Supplies (HVPS). GSFC procured the DES MCPs from Photonis USA and performed the preconditioning and testing for flight. The DIS MCPs were procured from Photonis France S.A.S. by the French Institut de Recherche en Astrophysique et Planetologie (IRAP). IRAP also conditioned, tested and mounted the DIS MCPs on anode boards provided by Meisei. These MCP/anodes were then re-tested by IRAP before re-delivery to Meisei for integration into the DIS sensors. The thirty-two DES and four IDPUs were functionally and environmentally tested and calibrated at GSFC. The thirty-two DIS' were environmentally tested at Meisei and ISAS (including pre- and post- environmental beam testing) and were calibrated at NASA's Marshall Space Flight Center (MSFC) Low Energy Electron and Ion Facility (LEEIF). Additional testing was performed by the GSFC FPI team after the initial deliveries, including live high voltage testing with particle sources late in the MMS observatory-level thermal vacuum sequence and an extended (1500 hours) thermal vacuum testing of all DIS and DES units designed to purge potentially thermally compromised HV801 opto-couplers. GSFC has lead responsibility for FPI Phase E mission activities in close collaboration with the development partner institutions. While all DES are nominally identical, as are all DIS, individual performance varies due to the variations in part, detectors, surface machining/finishing, and assembly; some variations in parts can change throughout the mission life. Within the specific case of FPI, the DES utilizes hemispheric geometry while the DIS incorporates toroidal geometry.

The full calibration program included determination of the operating point (MCP gain and voltage, and discriminator threshold), characterization of signal loss due to MCP gain variation, relative pixel to pixel MCP efficiency variation, cross talk, noise, coupled energy/azimuth-angle band pass locations, shapes and amplitudes and their dependence on high voltage stepper supply states, and the locations and shapes of the polar angle band passes and any dependence they have on high voltage stepper supply state. The ground calibration also characterized system dead time and the effectiveness of UV rejection. The general ground-based calibration procedure was (1) illuminate sensor with a beam sufficiently broad to fill the entrance aperture and sufficiently narrow in both energy and 2D angle to approximate an impulse stimuli; (2) execute  $V_{ESA}$  and  $V_{DEF}$  sweeps centered at voltages to pass the beam particles and wide enough to capture the  $V_{ESA}/V_{DEF}$  band pass; and (3) mechanically articulate the sensor to measure beam incidence over the complete angular range of pixel response. The zero deflection state—used in Slow Survey mode and in the case of an anomaly—was also calibrated.

#### 4.4.3 In-Flight Calibration

To ensure the data from each set of eight spectrometers can be corrected to yield an accurate output for a given input, an extensive laboratory and in-flight calibration regimen was developed to appropriately balance operating parameters and to identify and correct for instrument variability and noise. The

extensive program of in-flight calibration is additionally executed for the purpose of maintaining a high standard of instrument calibration for all units. Quantities of interest in this calibration program include the detector systems' operating points, detection efficiencies, and HV stepping supply performance. FPI in-flight operational sequences are implemented in the form of Absolute Time Sequence (ATS) commands, which designate when planned activities are to be executed in the context of each spacecraft's activities. In this case, all activities are performed in accordance with the FPI mode-switching diagram shown in Figure 4-4. Individual commands, Relative Time Sequences (RTS) or Macros, represent individual commands that may take form in elements in the ATS. The use of these individual commands allows FPI to execute the vast array of command sequences necessary to maintain stable for orbit. An extensive program of in-flight calibration is executed for the purpose of maintaining a high standard of instrument calibration for all units. While in-flight options are limited to many instrument parameters that have been stored in up-loaded tables and/or in comment registers, they are able to be adjusted based on experience and the results of on-orbit calibration sequences.

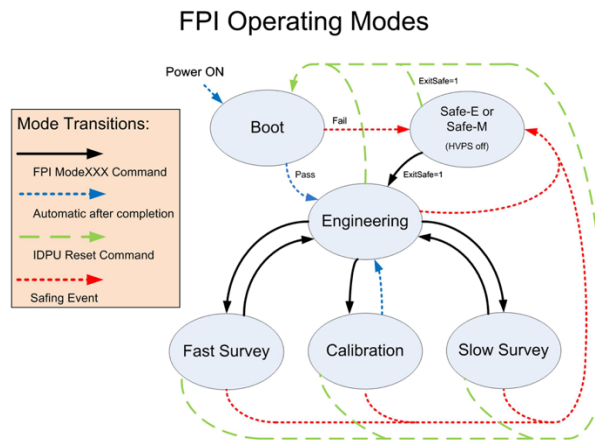
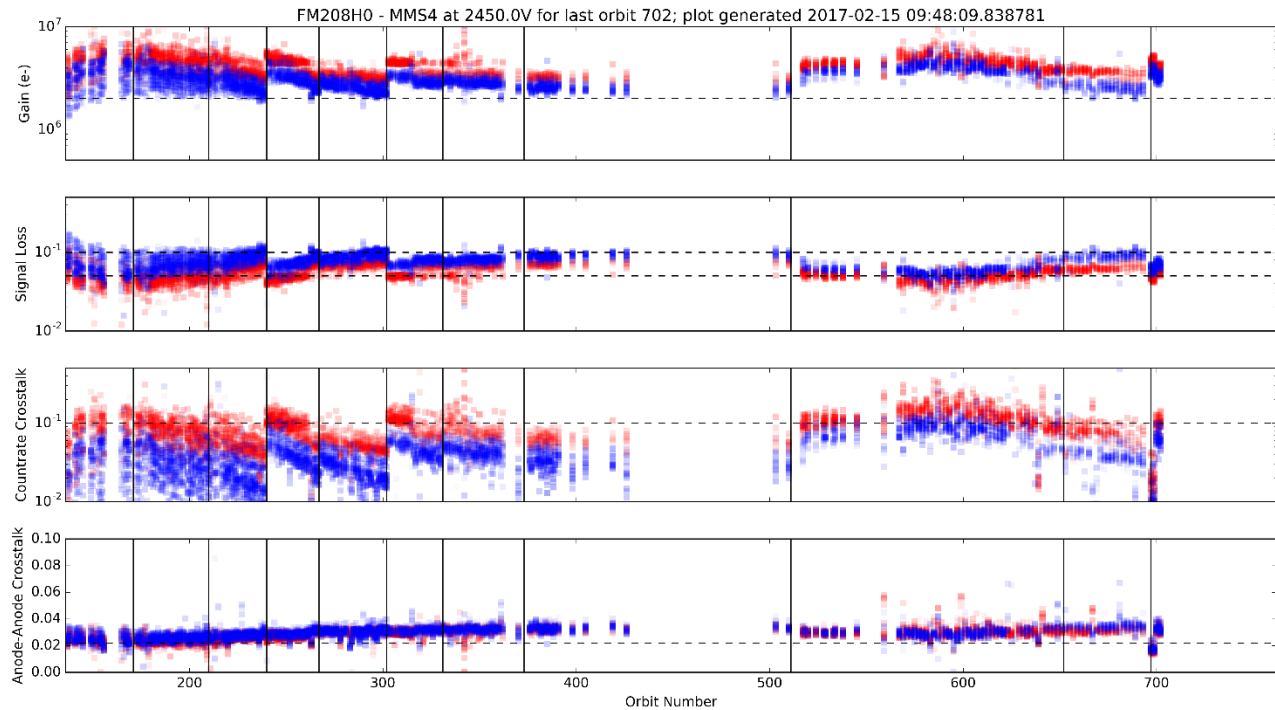


Figure 4-4 FPI IDPU State Diagram of Modes of Operations

#### 4.4.3.1 Operating Point Calibration

The Operating Point Calibration is a method to balance the signal loss and crosstalk of the detection system, minimizing both, and ensuring that all spectrometers are at a similar operating point (crosstalk / signal loss balance). The discriminator threshold is swept through its applicable operating range at the current MCP operating voltage, and a value 50V higher. The resulting data are evaluated to determine the best MCP voltage to maintain the desired operating point. If needed, the MCP voltage is increased during periodic macro loads; the operating discriminator threshold is held constant.

The gain is nonuniform around the MCP due to the relative angle of the pore entrance to the incoming particle trajectory. Because a single MCP voltage is applied, and a single discriminator voltage is applied to all preamplifiers, a spread in operating point is typically present over the 16 pixels of a given head. As shown by the blue points (current MCP voltage) in Table 4-5, operating points are typically chosen such that the count rate crosstalk is below 10% for all DES pixels, or below 5% for all DIS pixels. Allowing the crosstalk to float up to these values will minimize the corresponding signal loss.



**Figure 4-5 Sample Operating Point Calibration Plot (for all pixels at current voltage (blue) and an increase of 50V (red). Vertical black lines represent opportunities for a voltage increase (macro loads)).**

In flight, the operating point calibration is run close to L7 on both the inbound and outbound leg of the orbit, when time permits. On the ground, the DIS flight units were calibrated at the NASA MSFC Low Energy Electron and Ion Facility, and the DES were calibrated at NASA GSFC Space Plasma Instrumentation Facility.

#### 4.4.3.2 Burst Calibration

The burst calibration process consists of the combination of algorithmic development and human oversight that is required in order to translate the low-level instrument telemetry into science-quality datasets that have been reviewed and are suitable for public release. The collection of count-values (32 azimuth-angles x 32 energies x 16 zenith-angles, characterizing all of this phase space) which results from each iteration is called “burst”, a “burst sky-map”, or a “burst-map”. There is an on-board evaluation of each burst which selects a subset of burst for ground segment processing. Burst data calibration is performed by acquiring burst resolution data for a period of up to three spins (60 s) at a selected point within the ROI of each orbit. This data is used to perform statistical analyses and flat-fielding of the FPI look directions. The errors are then corrected during ground processing. The particular data to be used are selected by the FPI team and marked for download through a similar interface to that used by the Scientist in the Loop.

Full description of the flat-fielding algorithm can be found in the publication:

Gershman, D. J., Dorelli, J. C., Avanov, L. A., Gliese, U., Barrie, A., Schiff, C., et al. (2019). Systematic uncertainties in plasma parameters reported by the fast plasma

investigation on NASA's magnetospheric multiscale mission. *Journal of Geophysical Research: Space Physics*, 124, 10345– 10359. <https://doi.org/10.1029/2019JA026980>.

Beyond burst data calibration, burst voltage calibration used may be used in conjunction with ensemble calibration to provide relative calibration of the stepper voltages. Several spins of burst data are collected and the relative position of sharp gradients and features are compared from spectrometer to spectrometer in velocity space. These measurements are then compared to pull out corrective voltages to the high voltage steppers.

Full description of the high-voltage offsets can be found in the publication:

Barrie, A. C., Schiff, C., Gershman, D. J., Giles, B. L., & Rand, D. (2021). Calibrating electrostatic deflection of charged particle sensors using ambient plasma measurements. *Journal of Geophysical Research: Space Physics*, 126, e2021JA029149. <https://doi.org/10.1029/2021JA029149>

#### 4.4.4 Compression Pipeline

The spectrometers on the MMS spacecraft are dual half top analyzers that measure the 3-D plasma environment, and the IDPU processes the data, including performing data compression. FPI produces a full-sky count image (sky map) every 30 ms for electrons (DES) and every 150 ms for ions (DIS). The compression routine is evaluated by determining how small can a sky map be compressed while maintaining lossless compression as well as when truncation of DWT coefficients becomes necessary in lossy compression mode and what are the characteristics of the introduced compression error. Methods of compression can further be broken down into data modes- Fast Survey (FS) and Slow Survey (SS), each with their own parameters and effects.

FPI DES and DIS data are compressed within the instrument data processor using an algorithm designed for image compression.

- (1) 3D data are arranged into 2D arrays
- (2) A wavelet transform acts as a low pass/high pass filter
- (3) Low pass/high pass component arrays are created
- (4) Bit-plane encoding is applied to the arrays
- (5) Starting with the high-frequency components, bits of lesser significance are discarded until size is reduced to a pre-set limit
- (6) An inverse process on the ground reconstructs the data array (image)

FPI captures data over 100 times faster than previous plasma instruments, such as the CLUSTER (Geach et al., 2005) mission, requiring a higher compression ratio to fit within the telemetry allocation. These faster time resolution measurements enable scientists to observe phenomena that are spatially narrow or short in time duration, such as the electron diffusion region of a reconnecting magnetic field (Burch, Torbert, et al., 2016). This increased data rate, however, leads to proportionally increasing data volumes that must be addressed by more advanced data compression algorithms. FPI uses a Discrete Wavelet Transform and Bit Plane Encoder (DWT/BPE) (Winterrowd et al., 2010) for data compression. This is the first plasma instrument to use this method of compression, and thus serves as a benchmark for future plasma spectrometers. The DWT/BPE wavelet compression is able to compress > 99% of the FPI burst data in a lossless manner, with a compression ratio of about 5:1. The remaining 1% of data have some amount of compression error introduced, but this is considered negligible from a science perspective (Barrie et al., 2017, 2018). When the wavelet-transform data exceed the pre-set buffer limit compression

loss occurs. The compression error typically has a small effect on plasma moments. Fast Survey data is compressed more, at a rate of near 17:1. These data suffer from a greater induced error, however new efforts by the FPI team are underway to correct for these compression artifacts (da Silva et al., 2020). When applied to images, the process progressively degrades fine-scale features, but typically produces reconstructed images that are recognizable. When applied to plasma measurements, the process has the potential to alter features in a way that could affect interpretation of the data.

The majority of DIS burst sky maps are compressed in a lossless fashion, with no error introduced during compression. While approximately half of DES maps had some level of loss, it was found that there is little effect on the plasma moments and that errors present in individual sky maps are typically minor. However, this still is not to say that any compression loss cannot or will not affect the accuracy of plasma parameters. Despite the suggested tweaks, it was found that wavelet-based compression, and a DWT/BPE algorithm in particular, is highly suitable to data compression for plasma measurement instruments and can be recommended for future missions.

Full description of compression pipeline data can be found in the publication:

Barrie, A. C., Smith, S. E., Dorelli, J. C., Gershman, D. J., Yeh, P., Schiff, C., and Avakov, L. A. (2017), **Performance of a space-based wavelet compressor for plasma count data on the MMS Fast Plasma Investigation**, *J. Geophys. Res. Space Physics*, 122, 765–779, doi:10.1002/2016JA022645.

#### 4.4.5 Science Data Validation

Over the mission lifespan, validation has been applied over each segment in their own relevant parameters. Prior to launch, validation took place through the hundreds of tests on the instruments and their purposes. Through the launched-mission's lifecycle, validation has transformed into ongoing reviews of the data as well as corrections to the instruments as needed as the data continues to progress.

The FPI team manages the operating point of each spectrometer by capturing a small amount of calibration data each orbit. This data is then processed and trended to create a picture of the balance between gain, signal loss, and cross talk for each of the 64 individual sensor heads. The FPI team assesses this data weekly for short term trends or behaviors and over the longer term for the trends evident in the data. The trends in the data inform if and when each sensor head may need a small adjustment to the applied MCP voltage. Using this approach throughout the mission the FPI team has been able to manage the spectrometer operating points to maintain a consistently optimal balance and performance of each sensor.

To validate FPI science data, each corrected FPI fast survey file is examined to ensure that:

- (1) Spintone amplitudes are less than 50km/s in the magnetosheath
- (2) Density counts are in agreement across all four observatories in a variety of environments
- (3) Any systematic offsets in the bulk velocity's z-component do not exceed a few km/s in the magnetosheath

Full description of the spin tones and offsets in FPI data can be found in the publication:

Gershman, D. J., Dorelli, J. C., Avakov, L. A., Gliese, U., Barrie, A., Schiff, C., et al. (2019). Systematic uncertainties in plasma parameters reported by the fast plasma

investigation on NASA's magnetospheric multiscale mission. *Journal of Geophysical Research: Space Physics*, 124, 10345– 10359. <https://doi.org/10.1029/2019JA026980>.

Because FPI burst and fast survey science data use the same underlying correction tables, the quality of the data between the two modes is equivalent. Therefore, validation of the fast survey data is sufficient to ensure the validity of the burst data.

In addition, the FPI team confirms that any missing science data correlates with expected routine or anomalous outages.

## 4.5 MEASUREMENT ALGORITHM DESCRIPTIONS

### 4.5.1 Theoretical Basis

The “spacecraft coordinate system” (‘S/C’ designation) for a given platform rotates and translates with that spacecraft, and defines the original frame for portraying the FPI data. The several different data sets produced on the ground share common elements of methodology. The fundamental scientific data product is the velocity distribution function,  $(x,v,t)$ , which is directly related to the measured skymaps. It is a probability density or phase space density such that  $(\mathbf{x},\mathbf{v},t)d\mathbf{x}d\mathbf{v}$  is the number of particles in phase space volume element  $d\mathbf{x}d\mathbf{v}$  at time  $t$ .

### 4.5.2 Conversion of Instrument Signals to Phase Space Density

The FPI is dedicated to the rapid measurement of the phase space densities of electrons and positive ions within and near sites in Earth’s magnetosphere where reconnection occurs. The basic scientific quantities are the phase space densities and the plasma moments. This high temporal resolution in 3D phase space measurements is unprecedented in the history of scientific space flight and by far the single biggest driver on the design and implementation of the experiment. The deployment strategy allows measurement of the 3D ion and electron phase space densities at speeds limited primarily by the stepper speeds of the high voltage power supplies and the counting statistics possible within the very short accumulation intervals imposed. The fundamental scientific data product is the velocity distribution function,  $f(\mathbf{x},\mathbf{v},t)$ , which is directly related to the measured skymaps. It is a probability density or phase space density such that  $f(\mathbf{x},\mathbf{v},t)d\mathbf{x}d\mathbf{v}$  is the number of particles in phase space volume element  $d\mathbf{x}d\mathbf{v}$  at time  $t$ .

In deriving the relationship between the velocity distribution function and the skymaps, it is assumed that all of the entrance apertures of a DxS analyzer are illuminated by particles drawn from the same velocity distribution. Phase-space is sampled repeatedly and seamlessly (no “gaps” in time) with a rapid (species-dependent) cadence. The velocity distribution function contains considerable information regarding the physical state of the plasma. Plasma fluid parameters are computed as moments of the particle velocity distributions. The technique integrates  $f(\mathbf{v})$ , weighted by powers of  $\mathbf{v}$ , over the 3-dimensional velocity space. For the FPI data products, the integrals are evaluated numerically. This method has the advantage that it does not depend on a-priori assumptions about the form of the distribution functions. Corrections to the energies, and hence the velocities, due to a non-zero spacecraft surface potential are made prior to the integration.

More specific phase space density equations can be found in the publication:

Pollock, C., Moore, T., Jacques, A., Burch, J., Gliese, U., Saito, Y., ... & Zeuch, M. (2016). Fast plasma investigation for magnetospheric multiscale. *Space Science Reviews*, 199(1), 331-406.

The unprecedented spatiotemporal resolution and exceptional data quality of the phase space densities provided by the FPI spectrometers from all four spacecraft have enabled the successful determination of phase space density gradient measurements. One immediate scientific application of this capability is the direct measurement of the velocity-space structure of terms in the Vlasov equation [Shuster *et al.*, 2021]. For DES, temporal derivatives  $\partial f_e / \partial t$  computed in the frame of an individual spacecraft can be determined at a cadence of 30 ms. The vector spatial gradient term  $\nabla f_e$  can be approximated using four spacecraft data and making use of the usual linear gradient assumption, which in turn can be used to determine the full  $v \cdot \nabla f_e$  term [Shuster *et al.*, 2019]. The resolution of these spatial derivatives is limited by the inter-spacecraft separation, which at the dayside region of interest is commonly on the order of 10 km. In principle, the velocity-space gradient term  $\nabla f_e$  can also be measured on each spacecraft and is limited by the energy spacing, which for a typical thermal electron is on the order of 10 eV.

More detailed discussion and presentation of the science applications and techniques implemented to obtain phase space density gradient measurements using DES data may be found in the publications:

Shuster, J., Gershman, D., L.-J. Chen, et al. (2019), MMS Measurements of the Vlasov Equation: Probing the Electron Pressure Divergence Within Thin Current Sheets, *Geophys. Res. Lett.*, 46, <https://doi.org/10.1029/2019GL083549>.

Shuster, J., Gershman, D., Dorelli, J., Giles, B., et al. (2021), Structures in Terms of the Vlasov Equation Observed at Earth's Magnetopause, *Nature Physics*, <https://doi.org/10.1038/s41567-021-01280-6>.

#### 4.5.3 Instrument Thresholds vs Ambient Plasma Distribution

The FPI L2 data products reflect the full range of plasma populations in proximity to the spectrometers. This includes the ambient plasma environment within that energy range and – on occasion – spurious plasma populations induced in the vicinity of the spacecraft. All the while, the FPI team tags its data with a variety of quality flags to indicate intervals that need warrant consideration -- and perhaps correction -- when using the data for event analysis. Within this, the FPI quality flag definitions are identical for Quicklook and L2 data products.

#### 4.5.4 Counting Statistics and Establishing the 1-Count Level

In knowing and using the statistical error information provided in the CDF files, the error associated with the inherent spectrometer counting statistics is provided in those CDF files for both the moments and for the distributions while the actual counts can still be recovered.

More specific descriptions of how statistical errors are calculated for FPI moments can be found in the publication:

Gershman, D. J., Dorelli, J. C., F.-Viñas, A., and Pollock, C. J. (2015), The calculation of moment uncertainties from velocity distribution functions with random errors, *J. Geophys. Res. Space Physics*, 120, 6633–6645. <https://doi.org/10.1002/2014JA020775>.

#### 4.5.5 Quasi-Neutrality Check

For L2 data, FPI densities were initially scaled by an overall factor to match those of plasma waves. The overall sensitivity of DES and DIS can be subject to change with each FPI macro load in which the voltages applied to the MCP detector stack for each sensor are adjusted. In Phase 1a, the relative



sensitivity of DIS across spacecraft has not been observed to change. The sensitivity of DES with respect to DIS has changed by ~10-20% over the course of commissioning and Phase 1a. A correction factor for DES densities is derived from observations of DES and DIS in the magnetosheath. The minimum time-scale for which a correction factor can be applied is an entire orbit, though in practice the same correction factor is typically used for all orbits in a given correction cycle (~30 days). Periods where changes in DES and DIS densities are correlated and have the same ratio as in adjacent quiet magnetosheath intervals suggest that the entire relevant ion and electron distribution functions are being sampled.

#### 4.5.6 FPI in the Solar Wind

Onboard summing of burst counts to form Fast Survey data products leads to increased numbers of counts/bin in Fast Survey skymaps. In the solar wind, the maximum number of allowable counts in each bin is exceeded leading to clipping and resulting in a distortion of the plasma moments. FPI's field-of-view is binned with 11.25x11.25 deg resolution. In the polar angle direction (+Z to -Z for each sensor), angular space is continually sampled. However, the angular response in the azimuthal direction (X-Y plane) is <10deg. Therefore, as deflection states sweep out the azimuthal plane, there are gaps in the angular sampling of ambient plasma. Sharp angular structure in both DIS and DES can lead to apparent 'spikes' in the plasma moments that are spin-phase dependent. Such a phenomenon occurs often in high Mach number plasmas, such as the solar wind.

A detailed study of FPI's response in the solar wind can be found in the publication:

Roberts, O. W., Nakamura, R., Coffey, V. N., Gershman, D. J., Volwerk, M., Varsani, A., et al. (2021). A study of the solar wind ion and electron measurements from the magnetospheric multiscale mission's fast plasma investigation. *Journal of Geophysical Research: Space Physics*, 126, e2021JA029784. <https://doi.org/10.1029/2021JA029784>

#### 4.5.7 Error Analysis and Known Features in the Dataset

The goal of error analysis is to specify what uncertainties attend the azimuth, energy, zenith-angle, count, and phase-space density measurements reported in the data products. The FPI L2 data products reflect the full range of ~few eV to ~30 keV plasma populations in proximity to the spectrometers. This includes the ambient plasma environment within that energy range and – on occasion – spurious plasma populations induced in the vicinity of the spacecraft. For example, when the MMS EDI instrument is emitting 500 eV electrons, one or more FPI spectrometers often registers the signal in DES energy bin 16.

The FPI team has attempted to remove as many induced effects as is possible from the moment values (des-moms and dis-moms files) within the data processing pipeline. That said, the FPI full plasma distributions (des-dist and dis-dist files) are provided without correction so that analysis work can be performed appropriate to the specific hypothesis under study.

##### 4.5.7.1 Correction for Spacecraft Potential

The sampled energies (E, units eV) reported in the FPI L2 CDFs must be corrected for spacecraft charging effects (see Gershman et al. [2017]). Adjusted energies are calculated as:

$$E' = E \pm \Phi_{\text{avg}} \quad (2)$$

where the '+' and '-' apply for ions and electrons, respectively, and  $\Phi_{\text{avg}}$  is the average L2 spacecraft potential over each measurement interval. The specific file used for a particular L2 FPI moments CDF is listed in the meta data under global attribute 'Spacecraft\_potential\_filenames.'

For electrons, measurements from energies below  $\Phi_{\max}$ , the peak spacecraft potential over a measurement interval, are excluded from the moments integrations to ensure no contribution from spacecraft photoelectrons.

In addition to an adjustment of energy, the directional component of particle velocity is also affected by spacecraft charging because the plasma sheath is not a perfect sphere. While not performed routinely, in areas of particular interest, a calculation can be performed to reassign particles based on traces of their path through the spacecraft plasma sheath.

More information can be found in the publications:

Barrie, A. C., et al. "Characterizing spacecraft potential effects on measured particle trajectories." *Physics of Plasmas* 26.10 (2019): 103504.

Gershman, D. J., Avakov, L. A., Boardsen, S. A., Dorelli, J. C., Gliese, U., Barrie, A. C., ... Pollock, C. J. (2017). Spacecraft and instrument photoelectrons measured by the dual electron spectrometers on MMS. *Journal of Geophysical Research: Space Physics*, 122, 11,548– 11,558. <https://doi.org/10.1002/2017JA024518>

#### 4.5.7.2 Correction for DES Photoelectrons

Burst data obtained during commissioning in the hot plasma sheet in the absence of a significant field-aligned electron population were used to characterize the internally generated photoelectrons as a function of energy, deflection state, polar angle, and spinphase. This model is available as a CDF for users interested in estimating the impact of internally generated photoelectrons on their analyses. Photoelectron skymaps [32x16x32] in units of phase space density, denoted as  $f_{\text{photo}}$ , are provided as a function of energy table and spacecraft spin phase. There are subtle changes in the photoelectron fluxes as a function of spacecraft spinphase because the EUV from the Sun has different incident angles to each analyzer. All observatories exhibit similar behavior such that the same angular structure of the photoelectron model is used for all spacecraft. There is a single tuning factor for each that controls the effective density of the photoelectrons. This tuning factor varies both with time and with spacecraft. The tuning factor was selected for each observatory as a function of time to give  $V_{i,x} \sim V_{e,x}$  inside the magnetosphere. The tuning factors range from  $\sim 0.5$ -1 and are likely accurate to  $\pm 0.1$ . These factors are included as global attributes in DES moment CDF files as 'photo\_scale\_factor.'

Internally generated photoelectrons, unaffected by the spacecraft potential in the sun direction produce an effective cold electron component with density  $\sim 0.5$ -1  $\text{cm}^{-3}$  and bulk velocity  $\sim 750$  km/second the anti-sunward direction. This component varies with spacecraft spin phase. A model for this signal has been developed and the signal removed for the moment calculations as of software release v2.0. It is important to note, that, these photoelectrons (internal and spacecraft) are not removed from the skymap data product as users need to be aware of this signal for their specific data interval and how its removal might affect analysis and interpretations.

CDFs that contain the unscaled DES instrument photoelectron model are available on the MMS SDC at [/mms/sdc/public/data/models/fpi](https://mms.sdc/public/data/models/fpi). Different model CDFs are needed for burst (brst) and fast survey (fast) modes and for each FPI energy-stepper table ('pX-Y'). The relevant photoelectron model is included as a global attribute in the meta data for each FPI moms CDF as field 'Photoelectron\_model\_filenames'.

To obtain the relevant instrument photoelectron model distribution for a given record:

1. Determine the value of *startdelphi\_count\_fast* or *startdelphi\_count\_burst* for the skymap of interest (record varying). This will be a number between 0 and 5759 and is a measure of spacecraft spin-phase (1/16° bins).
2. Find the index I in the *startdelphi\_counts\_burst* or *startdelphi\_counts\_fast* array [360 possibilities] whose corresponding value is closest to the measured *startdelphi\_count\_burst* or *startdelphi\_count\_fast* for the skymap of interest.
3. The closest index can be approximated by  $I = \text{floor}(\text{startdelphi\_count\_burst}/16)$  or  $I = \text{floor}(\text{startdelphi\_count\_fast}/16)$
4. For burst mode data, determine the value of *steptable\_parity* for the skymap of interest (record varying). This will be either 0 or 1.

In the appropriate photoelectron model CDF:

- (1) For burst data, take  $f_{\text{photo}} = \text{bgdist\_p0\_burst}$  or  $f_{\text{photo}} = \text{bgdist\_p1\_burst}$  entry with index I for parity 0 and parity 1 data respectively.
- (2) For fast survey data, take  $f_{\text{photo}} = \text{bgdist\_fast}$  with index I.

$f_{\text{photo}}$  can now be scaled by  $n_{\text{photo}}$  in order to obtain the estimated contribution of photoelectrons to a given skymap. These phase space densities are independent of spacecraft potential. Corrected phase space densities are calculated as:

$$f = f_{L2} - n_{\text{photo}} f_{\text{photo}}. \quad (1)$$

Negative phase space densities are permitted in the numerical integration. There is uncertainty in  $n_{\text{photo}}$  and in the model itself. Adjustment of  $n_{\text{photo}}$  to achieve  $V_{ix} \sim V_{ex}$  can result in improved performance.

More information about internally generated photoelectrons can be found in the publication:

Gershman, D. J., Avanyov, L. A., Boardsen, S. A., Dorelli, J. C., Gliese, U., Barrie, A. C., ... Pollock, C. J. (2017). Spacecraft and instrument photoelectrons measured by the dual electron spectrometers on MMS. *Journal of Geophysical Research: Space Physics*, 122, 11,548– 11,558. <https://doi.org/10.1002/2017JA024518>

#### 4.5.7.3 Correction for Compression Artifacts

In Phase 1A of the mission, the DES compression was set to a level which, for high density/temperature plasmas, occasionally produced artifacts in the data. While not routinely performed, a neural network based correction can be used to remove these artifacts in areas of particular scientific interest.

With regard to spin-periodicities / velocity offsets, compression artifacts can be different for Survey and Burst data products. Imperfect spectrometer response correction tables (e.g., for signals dominating the very lowest or very highest energy channels; for data intervals very near a FPI macro change; and for data intervals for which sufficient burst calibration data was not readily available). Some of these can be addressed with time. Imperfect spacecraft potential or photoelectron signal correction. For some data intervals, data users will necessarily need to apply custom corrections. In some cases, even when the in-flight calibration tables have reduced the spin-period electron bulk velocity signal amplitude to below 50 km/s, there may appear more significant 20 s oscillations in the current density  $n \cdot e \cdot (V_i - V_e)$  (comparable to real current densities at the magnetopause). This is a known issue and is currently beyond the scope of our current L2 processing. If such current density oscillations are noticed, please contact the FPI team,

and we will address these on a case-by-case basis until we are able to incorporate a correction into our routine L2 processing.

More information can be found in the publication:

da Silva, D., Barrie, A., Gershman, D., Elkington, S., Dorelli, J., Giles, B., & Paterson, W. (2020). Neural network repair of Lossy compression Artifacts in the September 2015 to March 2016 duration of the MMS/FPI data set. *Journal of Geophysical Research: Space Physics*, 125, e2019JA027181. <https://doi.org/10.1029/2019JA027181>

#### 4.5.7.4 Correction for Pointing Error

The cross wiring of the FPI power supplies (see Pollock [2016]) leads to an inherent look direction bias, which is of opposite polarity between the two sensor heads. This leads to an average pointing error of  $\sim 1$  degree. This pointing error also drifts with time as the system ages. A trending analysis is used to monitor this pointing error over time to confirm that the pointing offset error is small relative to the angular resolution. While not performed routinely, if desired for a case of particular scientific interest, customized moments can be calculated using corrected pointing unit vectors.

More information can be found in the publications:

Barrie, A. C., Schiff, C., Gershman, D. J., Giles, B. L., & Rand, D. (2021). Calibrating electrostatic deflection of charged particle sensors using ambient plasma measurements. *Journal of Geophysical Research: Space Physics*, 126, e2021JA029149. <https://doi.org/10.1029/2021JA029149>

Pollock, C., Moore, T., Jacques, A., Burch, J., Gliese, U., Saito, Y., ... & Zeuch, M. (2016). Fast plasma investigation for magnetospheric multiscale. *Space Science Reviews*, 199(1), 331-406.

#### 4.5.7.5 Correction for Penetrating Radiation

Penetrating radiation can result in an apparent stationary, isotropic population of plasma in MMS/FPI data [see Gershman et al. 2019]. Penetrating radiation can affect both DES and DIS, but tends to impact DIS data more so in the magnetotail, where ambient count rates are low.

The DIS moments CDF provides fields ‘numberdensity\_bg’, ‘pres\_bg’, and ‘spectr\_bg’, which represent the estimated number density, scalar pressure, and differential energy flux associated with penetrating radiation.

These quantities are calculated as follows:

1. The 5 lowest values (not energies) of the omni-directional spectrogram are averaged to provide ‘spectr\_bg’
2. Spectr\_bg is used to generate an isotropic phase space density distribution using  $f\_bg = \text{spectr\_bg} * 2 / v^4$ .
3. F\_bg is integrated through an identical moments calculation (extrapolation, energy range, etc....) as the corresponding L2 moments record.

4. Numberdensity\_bg is the density from f\_bg
5. Pres\_bg is the scalar pressure from f\_bg, i.e., (Pres\_xx + Pres\_yy + Pres\_zz)/3.

Assuming that off-diagonal components of the pressure tensor and bulk velocity components of the background population are zero, n\_bg and p\_bg can be used to correct L2 moments for the effects of penetrating radiation (see Gershman et al. 2019)

$$\begin{aligned}
 n^* &= n_{FPI} - n_b, \\
 V_i^* &= \frac{n_{FPI} V_{FPI,i}}{n^*}, \\
 P_{ij}^* &= (P_{FPI,ij} + mn_{FPI} V_{FPI,i} V_{FPI,j}) - P_{b,ij} - mn^* V_i^* V_j^*,
 \end{aligned}$$

and

$$T_{ij}^* \equiv \frac{P_{ij}^*}{n^* k_B}.$$

Note that n\_bg and pres\_bg will scale proportionally to spectr\_bg, so a more careful estimate of background can be obtained and used to scale all three numbers simultaneously.

More information about correcting for penetrating radiation can be found in the publication:

Gershman, D. J., Dorelli, J. C., Avakov, L. A., Gliese, U., Barrie, A., Schiff, C., et al. (2019). Systematic uncertainties in plasma parameters reported by the fast plasma investigation on NASA's magnetospheric multiscale mission. *Journal of Geophysical Research: Space Physics*, 124, 10345– 10359. <https://doi.org/10.1029/2019JA026980>.

#### 4.5.7.6 Correction for Spintones

Imperfect flat-fielding (~1% residual errors) can result in significant (>10 km/s) spin-tones in DES bulk velocities [Gershman et al. 2019]. Because these systematic uncertainties are superimposed on the true velocity, an estimated spin-tone can in many cases be directly subtracted from DES data. Spin-tones are calculated in DBCS for Vxe and Vye only, though this technique can be extended to any quantify of interest (e.g., heat flux).

To calculate spin tone amplitudes, we apply a Butterworth IIR bandpass filter with coefficients:

Order	Numerator	Denominator
0	5.97957804e-05	1.0
1	0	-1.42301183
2	-2.98978902e-04	4.79664124
3	0	-4.79501766
4	5.97957804e-04	8.43180163
5	0	-5.93211177
6	-5.97957804e-04	6.88161394
7	0	-3.18997794
8	2.98978902e-04	2.60446833
9	0	-0.62795853
10	-5.97957804e-05	0.35992825

**Table 4-4 Spintone Amplitudes**

To obtain spin-tone estimates,

1. Load record-varying fast survey data from a 1D data product of interest (e.g., Vxe\_dbcs, Vye\_dbcs), a science region of interest is loaded
2. Apply Butterworth filter to data (using sample number instead of time)
3. Reverse filtered dataset
4. Apply Butterworth filter to reverse filtered dataset
5. Reverse newly filtered dataset

The forward-reverse filtering above is done to obtain zero phase distortion of the data. Spin-tones are then interpolated to burst cadence to provide high-resolution spin-tone estimates, and converted to GSE. Note that any real signal frequency content within the filter's bandpass will contribute to the spin-tone amplitude. The spin-tone field therefore provides an upper bound estimate to the systematic uncertainty associated with imperfect flat-fielding.

#### 4.5.8 DES/DIS Quality Flags

FPI tags its data with a variety of quality flags to indicate intervals that need warrant consideration -- and perhaps correction -- when using the data for event analysis. It is important to check these and address any noted features.

##### 4.5.8.1 Distribution File Flags

Bit	Description
0	Manually flagged interval
1	Overcounting/saturation effects likely present in skymap
2	Compression pipeline error

##### 4.5.8.2 Moments File Flags

Bit	Description
0	Manually flagged interval
1	Overcounting/saturation effects likely present in skymap
2	Reported spacecraft potential above 20V
3	Invalid/unavailable spacecraft potential
4	Significant (>25%) cold plasma (<10eV) component
5	Significant (>25%) hot plasma (>30keV) component
6	High sonic Mach number ( $v/v_{th} > 2.5$ )c
7	Low calculated density ( $n < 0.05 \text{ cm}^{-3}$ )
8	BentPipe magnetic field used instead of brst l2pre magnetic field
9	Survey l2pre magnetic field used instead of brst l2pre magnetic field (burst only)
10	No internally generated photoelectron correction applied (DES only)
11	Compression pipeline error

- 12 spintone calculation error (DBCS only)
- 13 significant ( $\geq 20\%$ ) penetrating radiation (DIS only)

Note that in MMS3 DIS moments files, the Bit 0 flag is set for data that has unusually large spintone due to the DIS008 anomaly, as discussed in section 4.1.2.

#### 4.6 DATA PRODUCTION ALGORITHM DESCRIPTIONS

##### 4.6.1 File Structure L2 3D DES/DIS Distributions (skymaps)

Variable	Units	Type	Dim	Description
Epoch	ns	CDF_TIME_TT2000	1	Observation start time derived from packet time
errorflags	32-bit error flags	CDF_UINT4	1	Vector of data-quality indicators at epoch
compressionloss	0, 1	CDF_UINT1	1	Compression lossless/lossy indicator at epoch
steptable_parity	0, 1	CDF_UINT1	1	Step table parity
startdelphi_count	del-phi counts	CDF_UINT2	1	Del-Phi (obs spin-phase) count at epoch
startdelphi_angle	deg	CDF_REAL4	1	Del-Phi (obs spin-phase) angle at epoch
phi	deg	CDF_REAL4	32	Sky-map instrument azimuthal angles
dist	$s^3/cm^6$	CDF_REAL4	32 x 16 x 32	Sky-map instrument distribution
disterr	$s^3/cm^6$	CDF_REAL4	32 x 16 x 32	Sky-map instrument distribution 1-sigma error
avgflcounts	$s^3/cm^6$	CDF_REAL4	32	Avg fl-count level as a function of energy
steptimeoffsets	us	CDF_REAL4	32 x 16 x 32	Sky-map microsecond offsets from epoch
sector_despinp	00-32	CDF_UINT1	1	Sector de-Spin P value
energy	eV	CDF_REAL4	32	Sky-map energy bin centers
energy_delta	eV	CDF_REAL4	32	Sky-map delta energies

Table 4-5 L2 3D DES/DIS Skymaps

##### 4.6.2 File Structure L2 DES Distribution Aux

Variable	Units	Type	Dim	Description
Epoch	ns	CDF_TIME_TT2000	1	Observation start time derived from packet time
errorflags	32-bit error flags	CDF_UINT4	1	Vector of data-quality indicators at epoch
disterr_photo	$s^3/cm^6$	CDF_REAL4	32 x 16 x 32	DES modeled photoelectron distribution
energy	eV	CDF_REAL4	32	Sky-map energy bin centers
energy_delta	eV	CDF_REAL4	32	Sky-map delta energies

Table 4-6 L2 DES Distribution Aux

##### 4.6.3 File Structure L2 DES/DIS Moments

Variable	Units	Type	Dim	Description
Epoch	ns	CDF_TIME_TT2000	1	Observation start time derived from packet time

errorflags	32-bit error flags	CDF_UINT4	1	Vector of data-quality indicators at epoch
compressionloss	0, 1	CDF_UINT1	1	Compression lossless/lossy indicator at epoch
steptable_parity (burst only)	0, 1	CDF_UINT1	1	Step table parity
startdelphi_count	del-phi counts	CDF_UINT2	1	Del-Phi (obs spin-phase) count at epoch
startdelphi_angle (burst only)	deg	CDF_REAL4	1	Del-Phi (obs spin-phase) angle at epoch
sector_despinp (burst only)	00-32	CDF_UINT1	1	Sector de-Spin P value
pitchangdist_lowen (DES only)	keV/(cm <sup>2</sup> s sr keV)	CDF_REAL4	30	Electron pitch-angle distribution for "low" energies
pitchangdist_miden (DES only)	keV/(cm <sup>2</sup> s sr keV)	CDF_REAL4	30	Electron pitch-angle distribution for "mid" energies
pitchangdist_highen (DES only)	keV/(cm <sup>2</sup> s sr keV)	CDF_REAL4	30	Electron pitch-angle distribution for "high" energies
energyspectr_px	keV/(cm <sup>2</sup> s sr keV)	CDF_REAL4	32	Electron/Ion energy spectrum "near" +X in DBCS
energyspectr_mx	keV/(cm <sup>2</sup> s sr keV)	CDF_REAL4	32	Electron/Ion energy spectrum "near" -X in DBCS
energyspectr_py	keV/(cm <sup>2</sup> s sr keV)	CDF_REAL4	32	Electron/Ion energy spectrum "near" +Y in DBCS
energyspectr_my	keV/(cm <sup>2</sup> s sr keV)	CDF_REAL4	32	Electron/Ion energy spectrum "near" -Y in DBCS
energyspectr_pz	keV/(cm <sup>2</sup> s sr keV)	CDF_REAL4	32	Electron/Ion energy spectrum "near" +Z in DBCS
energyspectr_mz	keV/(cm <sup>2</sup> s sr keV)	CDF_REAL4	32	Electron/Ion energy spectrum "near" -Z in DBCS
energyspectr_par (DES only)	keV/(cm <sup>2</sup> s sr keV)	CDF_REAL4	32	Electron energy parallel to the magnetic field direction
energyspectr_anti (DES only)	keV/(cm <sup>2</sup> s sr keV)	CDF_REAL4	32	Electron energy anti-parallel to the magnetic field direction
energyspectr_perp (DES only)	keV/(cm <sup>2</sup> s sr keV)	CDF_REAL4	32	Electron energy perpendicular to the magnetic field direction
energyspectr_omni	keV/(cm <sup>2</sup> s sr keV)	CDF_REAL4	32	Omni-directional electron/ion energy spectrum
numberdensity	cm <sup>-3</sup>	CDF_REAL4	1	Number density
numberdensity_err	cm <sup>-3</sup>	CDF_REAL4	1	Number density error
densityextrapolation_low	cm <sup>-3</sup>	CDF_REAL4	1	Estimated (via extrapolation to 0) contribution to density integral below 10eV
densityextrapolation_high	cm <sup>-3</sup>	CDF_REAL4	1	Estimated (via extrapolation to infinity) contribution to density integral above 30keV
bulkv_dbcs	km/s	CDF_REAL4	3	Bulk-velocity vector in DBCS



bulkv_spin_dbcs (fast/burst only)	km/s	CDF_REAL4	3	Bulk-velocity spintone vector in DBCS
bulkv_gse	km/s	CDF_REAL4	3	Bulk-velocity vector in GSE
bulkv_spin_gse (fast/burst only)	km/s	CDF_REAL4	3	Bulk-velocity spintone vector in GSE
bulkv_err	km/s	CDF_REAL4	3	Bulk-velocity error vector
prestensor_dbcs	nPa	CDF_REAL4	3 x 3	Pressure tensor in DBCS
prestensor_gse	nPa	CDF_REAL4	3 x 3	Pressure tensor in GSE
prestensor_err	nPa	CDF_REAL4	3 x 3	Pressure tensor error
temptensor_dbcs	eV	CDF_REAL4	3 x 3	Temperature tensor in DBCS
temptensor_gse	eV	CDF_REAL4	3 x 3	Temperature tensor in GSE
temptensor_err	eV	CDF_REAL4	3 x 3	Temperature tensor error
heatq_dbcs	mW/m <sup>2</sup>	CDF_REAL4	3	Heat-flux vector in DBCS
heatq_gse	mW/m <sup>2</sup>	CDF_REAL4	3	Heat-flux vector in GSE
heatq_err	mW/m <sup>2</sup>	CDF_REAL4	3	Heat-flux error vector
temppara	eV	CDF_REAL4	1	Parallel temperature
tempperp	eV	CDF_REAL4	1	Perpendicular temperature
energy	eV	CDF_REAL4	32	Sky-map energy bin centers
energy_delta	eV	CDF_REAL4	32	Sky-map delta energies

**Table 4-7 L2 DES/DIS Moments**

#### 4.6.4 File Structure L2 DES/DIS Moments Aux

Variable	Units	Type	Dim	Description
Epoch	ns	CDF_TIME_TT2000	1	Observation start time derived from packet time
errorflags	32-bit error flags	CDF_UINT4	1	Vector of data-quality indicators at epoch
compressionloss	0, 1	CDF_UINT1	1	Compression lossless/lossy indicator at epoch
steptable_parity (burst only)	0, 1	CDF_UINT1	1	Step table parity
startdelphi_count	del-phi counts	CDF_UINT2	1	Del-Phi (obs spin-phase) count at epoch
startdelphi_angle (burst only)	deg	CDF_REAL4	1	Del-Phi (obs spin-phase) angle at epoch
sector_despinp (burst only)	00-32	CDF_UINT1	1	Sector de-Spin P value
pitchangdist_lowen (DES only)	keV/(cm <sup>2</sup> s sr keV)	CDF_REAL4	30	Electron pitch-angle distribution for "low" energies
pitchangdist_miden (DES only)	keV/(cm <sup>2</sup> s sr keV)	CDF_REAL4	30	Electron pitch-angle distribution for "mid" energies
pitchangdist_highen (DES only)	keV/(cm <sup>2</sup> s sr keV)	CDF_REAL4	30	Electron pitch-angle distribution for "high" energies
energyspectr_px	keV/(cm <sup>2</sup> s sr keV)	CDF_REAL4	32	Electron/Ion energy spectrum "near" +X in DBCS
energyspectr_mx	keV/(cm <sup>2</sup> s sr keV)	CDF_REAL4	32	Electron/Ion energy spectrum "near" -X in DBCS

energyspectr_py	keV/(cm <sup>2</sup> s sr keV)	CDF_REAL4	32	Electron/Ion energy spectrum "near" +Y in DBCS
energyspectr_my	keV/(cm <sup>2</sup> s sr keV)	CDF_REAL4	32	Electron/Ion energy spectrum "near" -Y in DBCS
energyspectr_pz	keV/(cm <sup>2</sup> s sr keV)	CDF_REAL4	32	Electron/Ion energy spectrum "near" +Z in DBCS
energyspectr_mz	keV/(cm <sup>2</sup> s sr keV)	CDF_REAL4	32	Electron/Ion energy spectrum "near" -Z in DBCS
energyspectr_par (DES only)	keV/(cm <sup>2</sup> s sr keV)	CDF_REAL4	32	Electron energy parallel to the magnetic field direction
energyspectr_anti (DES only)	keV/(cm <sup>2</sup> s sr keV)	CDF_REAL4	32	Electron energy anti-parallel to the magnetic field direction
energyspectr_perp (DES only)	keV/(cm <sup>2</sup> s sr keV)	CDF_REAL4	32	Electron energy perpendicular to the magnetic field direction
energyspectr_omni	keV/(cm <sup>2</sup> s sr keV)	CDF_REAL4	32	Omni-directional electron/ion energy spectrum
numberdensity	cm <sup>-3</sup>	CDF_REAL4	1	Number density
numberdensity_err	cm <sup>-3</sup>	CDF_REAL4	1	Number density error
densityextrapolation_low	cm <sup>-3</sup>	CDF_REAL4	1	Estimated (via extrapolation to 0) contribution to density integral below 10eV
densityextrapolation_high	cm <sup>-3</sup>	CDF_REAL4	1	Estimated (via extrapolation to infinity) contribution to density integral above 30keV
bulkv_dbcs	km/s	CDF_REAL4	3	Bulk-velocity vector in DBCS
bulkv_spin_dbcs (fast/burst only)	km/s	CDF_REAL4	3	Bulk-velocity spintone vector in DBCS
bulkv_gse	km/s	CDF_REAL4	3	Bulk-velocity vector in GSE
bulkv_spin_gse (fast/burst only)	km/s	CDF_REAL4	3	Bulk-velocity spintone vector in GSE
bulkv_err	km/s	CDF_REAL4	3	Bulk-velocity error vector
prestensor_dbcs	nPa	CDF_REAL4	3 x 3	Pressure tensor in DBCS
prestensor_gse	nPa	CDF_REAL4	3 x 3	Pressure tensor in GSE
prestensor_err	nPa	CDF_REAL4	3 x 3	Pressure tensor error
temptensor_dbcs	eV	CDF_REAL4	3 x 3	Temperature tensor in DBCS
temptensor_gse	eV	CDF_REAL4	3 x 3	Temperature tensor in GSE
temptensor_err	eV	CDF_REAL4	3 x 3	Temperature tensor error
heatq_dbcs	mW/m <sup>2</sup>	CDF_REAL4	3	Heat-flux vector in DBCS
heatq_gse	mW/m <sup>2</sup>	CDF_REAL4	3	Heat-flux vector in GSE
heatq_err	mW/m <sup>2</sup>	CDF_REAL4	3	Heat-flux error vector
temppara	eV	CDF_REAL4	1	Parallel temperature
tempperp	eV	CDF_REAL4	1	Perpendicular temperature
energy	eV	CDF_REAL4	32	Sky-map energy bin centers
energy_delta	eV	CDF_REAL4	32	Sky-map delta energies

numberdensity_part	cm <sup>-3</sup>	CDF_REAL4	32	Number density for each starting energy
bulkv_part_dbcs	km/s	CDF_REAL4	32 x (3 x 1)	Bulk-velocity vector in DBCS for each starting energy
bulkv_part_gse	km/s	CDF_REAL4	32 x (3 x 1)	Bulk-velocity vector in GSE for each starting energy
prestensor_part_dbcs	nPa	CDF_REAL4	32 x (3 x 3)	Pressure tensor in DBCS for each starting energy
prestensor_part_gse	nPa	CDF_REAL4	32 x (3 x 3)	Pressure tensor in GSE for each starting energy
temptensor_part_dbcs	eV	CDF_REAL4	32 x (3 x 3)	Temperature tensor in DBCS for each starting energy
temptensor_part_gse	eV	CDF_REAL4	32 x (3 x 3)	Temperature tensor in GSE for each starting energy
temppara_part	eV	CDF_REAL4	32	Parallel temperature for each starting energy
tempperp_part	eV	CDF_REAL4	32	Perpendicular temperature for each starting energy
part_index	0-31	CDF_UINT2	1	Recommended energy index for this epoch
scpmean	V	CDF_REAL4	1	Mean spacecraft potential derived from MMS Electric field Double Probe
bhat_dbcs	nT	CDF_REAL8	3	Unit vector magnetic field direction derived from MMS Fluxgate Magnetometers
gse_xform	N/A	CDF_REAL4	3 x 3	Matrix used to transform dbcs to gse

**Table 4-8 L2 DES/DIS Moments Aux**

#### 4.6.5 Calculation of L2 DES/DIS Plasma Moments

FPI uses the typically defined set of plasma moments (e.g., *Paschmann et al.* [1998]). Moments calculations are carried out the DBCS coordinate system using Level 2 phase space density distributions and their associated energy-angle bins as described below.

Plasma Parameter	Moment Calculation	Units
Number Density	$n \equiv \iiint d^3\mathbf{v} f(\mathbf{v}, \theta, \varphi)$	cm <sup>-3</sup>
Bulk Velocity	$\mathbf{V} \equiv \frac{\iiint d^3\mathbf{v} \mathbf{v} f(\mathbf{v}, \theta, \varphi)}{n}$	km/s
Temperature Tensor	$\bar{\mathbf{T}} \equiv \frac{m \iiint d^3\mathbf{v} (\mathbf{v} - \mathbf{V})(\mathbf{v} - \mathbf{V}) f(\mathbf{v}, \theta, \varphi)}{nk_B}$	eV
Pressure Tensor	$\bar{\mathbf{P}} \equiv nk_B \bar{\mathbf{T}}$	nPa

Heat Flux Vector	$\mathbf{q} \equiv \frac{m \iiint d^3\mathbf{v} v^2 f(v, \theta, \varphi)}{2} - \frac{nmV^2\mathbf{V}}{2} - \left( \left( \frac{\text{Tr}\bar{\mathbf{P}}}{2} \right) \bar{\mathbf{I}} + \bar{\mathbf{P}} \right) \cdot \mathbf{V}$	mW/m <sup>2</sup>
------------------	---	-------------------

**Table 4-9 Definition and Units of MMS/FPI Plasma Moments**

The following constants are adopted to ensure proper unit conversion:

Symbol	Description	Value
m <sub>i</sub>	Mass of ion (assuming H <sup>+</sup> )	1.6726 x 10 <sup>-24</sup> g
m <sub>e</sub>	Mass of electron	9.1094 x 10 <sup>-28</sup> g
E <sub>1eV</sub>	Energy of 1eV particle	1.6022 x 10 <sup>-12</sup> erg
T <sub>1eV</sub>	Temperature of 1eV plasma	11604 K
k <sub>B</sub>	Boltzmann's Constant	1.3807 x 10 <sup>-16</sup> erg/K

**Table 4-10 Constants Used in the Calculation in MMS/FPI Plasma Moments**

### Distribution Function Pre-Conditioning:

Specific energy and angle targets for a particular skymap are included as record varying entries in FPI distribution function CDFs (DBCS coordinates). FPI uses a trapezoidal triple integration scheme for its calculation of plasma moments, i.e., implicitly linearly interpolates between adjacent phase space values. Before being sent to the integration routine, skymaps are preprocessed as described below. Because FPI has a finite energy range, we remap calculated energies using the relation:

$$U \equiv \frac{E'}{E_0 + E'} \quad (3)$$

Here, E<sub>0</sub> is a constant (nominally 100 eV) that is used to remap energies from E' → (0, ∞) to U → (0,1). The final integral is not a strong function of E<sub>0</sub>. The default E<sub>0</sub> = 100 eV was chosen as typical plasmas sampled by MMS have significant phase space density at that energy. The value of E<sub>0</sub> (units eV) used in this remapping are found in the meta data of a given L2 FPI moments CDF as global attribute 'Energy\_e0'

The low energy bound and upper energy bounds starting for the integration is listed in the CDF meta data as global attributes 'Lower\_energy\_integration\_limit' and 'Upper\_energy\_integration\_limit', respectively. Nominally the lower limit is 10eV (even when lower energies are sampled) and the highest available energy. Exceptions to this is interval used for the *Torbert et al.* [2018] interval where the Level-2 integration was started at 100eV, and in the solar wind stepping table for DES where all energies are included.

Boundary points  $f(U, \theta, \varphi = \varphi_{\min} + 360^\circ) = f(U, \theta, \varphi = \varphi_{\min})$  are added to ensure that the periodic boundary condition is incorporated into the azimuthal integration.

Boundary points  $f(U, \theta = 0^\circ, \varphi) = 0$  and  $f(U, \theta = 180^\circ, \varphi) = 0$  are added to ensure that the polar integration ranges from 0 to 180. The sin(theta) dependence of the polar integration force the integrand at theta = 0 and 180 to zero regardless of the value of the phase space density.

Boundary points  $f(U=0, \theta, \varphi) = 0$  and  $f(U=1, \theta, \varphi) = 0$  are added to ensure the integration goes from  $E' = 0$  to  $\infty$ . The scaling of the integrand by  $v^2$  forces it to zero regardless of the ambient phase space density, and there is the assumption that at  $E' \rightarrow \infty$ , the phase space density of thermal plasmas approaches zero.

### Low-Energy and High-Energy Extrapolation:

Low-energy and high-energy extrapolation of moments integrals are achieved by default through the inclusion of the  $U = 0$  and  $U = 1$  data points in the numerical integration. The use of extrapolation for a given interval is listed in CDF meta data as fields '*Low\_energy\_extrapolation*' and '*High\_energy\_extrapolation*'. If disabled, the corresponding  $U = 0$  or  $U = 1$  points are excluded from the integration. By default, in Level-2 data, DES has both low-energy and high-energy extrapolation enabled, since there is often finite phase space density near  $U = 0$ . DIS has only high-energy extrapolation enabled since there is often no significant ambient phase space density near  $U = 0$ .

The contribution of the low-energy and high-energy extrapolations to the number density (i.e., the first and last terms in the trapezoidal integration) are included as record varying fields *densityextrapolation\_low* and *densityextrapolation\_high*, respectively.

### FPI Moments Integrals:

After remapping and applying extrapolations, FPI moments are then computed using the following integrals (assuming phase space densities in units  $s^3 cm^{-6}$ ).

#### Number Density:

$$n \equiv \frac{\sqrt{2}}{m^2} (E_0 E_{1eV})^{\frac{3}{2}} \int_0^1 dU \frac{\sqrt{U}}{(1-U)^2} \int_0^\pi d\theta \sin \theta \int_0^{2\pi} d\varphi f(U, \theta, \varphi) \quad (4)$$

#### Bulk Velocity:

$$V_x \equiv -\frac{2 \times 10^{-5}}{nm^2} (E_0 E_{1eV})^2 \int_0^1 dU \frac{U}{(1-U)^3} \int_0^\pi d\theta \sin^2 \theta \int_0^{2\pi} d\varphi \cos \varphi f(U, \theta, \varphi) \quad (5)$$

$$V_y \equiv -\frac{2 \times 10^{-5}}{nm^2} (E_0 E_{1eV})^2 \int_0^1 dU \frac{U}{(1-U)^3} \int_0^\pi d\theta \sin^2 \theta \int_0^{2\pi} d\varphi \sin \varphi f(U, \theta, \varphi) \quad (6)$$

$$V_z \equiv -\frac{2 \times 10^{-5}}{nm^2} (E_0 E_{1eV})^2 \int_0^1 dU \frac{U}{(1-U)^3} \int_0^\pi d\theta \sin \theta \cos \theta \int_0^{2\pi} d\varphi f(U, \theta, \varphi) \quad (7)$$

Here, the minus sign transforms the calculation in the look-direction frame into the flow-frame.

### Temperature Tensor:

$$T_{xx} \equiv \left( \frac{2 \times 10^{-5}}{m^2 (n k_B T_{1eV})} (E_0 E_{1eV})^{\frac{5}{2}} \int_0^1 dU \frac{U^{\frac{3}{2}}}{(1-U)^2} \int_0^\pi d\theta \sin^3 \theta \int_0^{2\pi} d\varphi \cos^2 \varphi f(U, \theta, \varphi) \right) - \frac{10^{10} m}{k_B T_{1eV}} V_x^2 \quad (8)$$

$$T_{yy} \equiv \left( \frac{2 \times 10^{-5}}{m^2 (n k_B T_{1eV})} (E_0 E_{1eV})^{\frac{5}{2}} \int_0^1 dU \frac{U^{\frac{3}{2}}}{(1-U)^2} \int_0^\pi d\theta \sin^3 \theta \int_0^{2\pi} d\varphi \sin^2 \varphi f(U, \theta, \varphi) \right) - \frac{10^{10} m}{k_B T_{1eV}} V_y^2 \quad (9)$$

$$T_{zz} \equiv \left( \frac{2 \times 10^{-5}}{m^2 (n k_B T_{1eV})} (E_0 E_{1eV})^{\frac{5}{2}} \int_0^1 dU \frac{U^{\frac{3}{2}}}{(1-U)^{\frac{7}{2}}} \int_0^\pi d\theta \sin \theta \cos^2 \theta \int_0^{2\pi} d\varphi f(U, \theta, \varphi) \right) - \frac{10^{10} m}{k_B T_{1eV}} V_z^2 \quad (10)$$

$$T_{xy} \equiv \left( \frac{2 \times 10^{-5}}{m^2 (n k_B T_{1eV})} (E_0 E_{1eV})^{\frac{5}{2}} \int_0^1 dU \frac{U^{\frac{3}{2}}}{(1-U)^{\frac{7}{2}}} \int_0^\pi d\theta \sin^3 \theta \int_0^{2\pi} d\varphi \sin \varphi \cos \varphi f(U, \theta, \varphi) \right) - \frac{10^{10} m}{k_B T_{1eV}} V_x V_y \quad (11)$$

$$T_{xz} \equiv \left( \frac{2 \times 10^{-5}}{m^2 (n k_B T_{1eV})} (E_0 E_{1eV})^{\frac{5}{2}} \int_0^1 dU \frac{U^{\frac{3}{2}}}{(1-U)^{\frac{7}{2}}} \int_0^\pi d\theta \sin^2 \theta \cos \theta \int_0^{2\pi} d\varphi \cos \varphi f(U, \theta, \varphi) \right) - \frac{10^{10} m}{k_B T_{1eV}} V_x V_z \quad (12)$$

$$T_{yz} \equiv \left( \frac{2 \times 10^{-5}}{m^2 (n k_B T_{1eV})} (E_0 E_{1eV})^{\frac{5}{2}} \int_0^1 dU \frac{U^{\frac{3}{2}}}{(1-U)^{\frac{7}{2}}} \int_0^\pi d\theta \sin^2 \theta \cos \theta \int_0^{2\pi} d\varphi \sin \varphi f(U, \theta, \varphi) \right) - \frac{10^{10} m}{k_B T_{1eV}} V_y V_z \quad (13)$$

The temperature tensor is defined to be symmetric such that  $T_{ij} = T_{ji}$ .

#### Pressure Tensor:

$$P_{ij} \equiv 10^8 (n k_B T_{1eV}) T_{ij} \quad (14)$$

As with the temperature tensor, the pressure tensor is defined to be symmetric such that  $P_{ij} = P_{ji}$ .

#### Heat Flux Vector:

$$q_x \equiv \left( -\frac{2}{m^2} (E_0 E_{1eV})^3 \int_0^1 dU \frac{U^2}{(1-U)^4} \int_0^\pi d\theta \sin^2 \theta \int_0^{2\pi} d\varphi \cos \varphi f(U, \theta, \varphi) \right) - 10^{-3} (P_{xx} V_x + P_{xy} V_y + P_{xz} V_z) - 10^5 V_x \left( \frac{10^{-8} (P_{xx} + P_{yy} + P_{zz}) + 10^{10} n m (V_x^2 + V_y^2 + V_z^2)}{2} \right) \quad (15)$$

$$q_y \equiv \left( -\frac{2}{m^2} (E_0 E_{1eV})^3 \int_0^1 dU \frac{U^2}{(1-U)^4} \int_0^\pi d\theta \sin^2 \theta \int_0^{2\pi} d\varphi \sin \varphi f(U, \theta, \varphi) \right) - 10^{-3} (P_{xy} V_x + P_{yy} V_y + P_{yz} V_z) - 10^5 V_y \left( \frac{10^{-8} (P_{xx} + P_{yy} + P_{zz}) + 10^{10} n m (V_x^2 + V_y^2 + V_z^2)}{2} \right) \quad (16)$$

$$q_z \equiv \left( -\frac{2}{m^2} (E_0 E_{1eV})^3 \int_0^1 dU \frac{U^2}{(1-U)^4} \int_0^\pi d\theta \sin \theta \cos \theta \int_0^{2\pi} d\varphi f(U, \theta, \varphi) \right) - 10^{-3} (P_{xz} V_x + P_{yz} V_y + P_{zz} V_z) - 10^5 V_z \left( \frac{10^{-8} (P_{xx} + P_{yy} + P_{zz}) + 10^{10} n m (V_x^2 + V_y^2 + V_z^2)}{2} \right) \quad (17)$$

As with the bulk velocity, the minus sign in front of the integral denotes the transformation from the look-direction frame into the flow frame.

#### Magnetic Field Direction Calculation:

The magnetic field unit vector (**b**) is obtained by averaging each component of the magnetic field in DBCS coordinates over the relevant FPI measurement interval and calculating the direction. The particular magnetic field file used is found in the Level-2 FPI moms CDF meta data as global attribute 'Magnetic\_field\_filenames.' This unit vector is used for calculation of parallel and perpendicular temperatures and well as pitch-angle spectrograms.

Temperatures parallel to and perpendicular to the magnetic field direction (unit vector  $\mathbf{b}$ ) are calculated from the temperature tensor using:

$$T_{\parallel} \equiv \mathbf{b}^T \bar{\mathbf{T}} \mathbf{b} \quad (18)$$

$$T_{\perp} \equiv \frac{(tr\bar{\mathbf{T}} - T_{\parallel})}{2} \quad (19)$$

Note that because the average value is used, if the  $\mathbf{b}$  varies significantly over the record time, there may be corresponding errors in the reported  $T_{\parallel}$  and  $T_{\perp}$  moments.

### Energy-Angle Spectrograms:

In addition to plasma moments, FPI provides a set of energy-angle spectrograms in its Level-2 moments CDFs. Similar to distribution functions, Level-2 spectrograms provided in FPI CDFs do not include any corrections for instrument photoelectrons or spacecraft potential.

To obtain spectrograms, first sampled energies ( $E$  in eV) are converted to velocities ( $v$  in cm/s) using,

$$v = \sqrt{\frac{2EE_{1eV}}{m}} \quad (20)$$

Phase space density ( $f$  in  $s^3/cm^6$ ) is converted to differential energy flux ( $dJ/dE$  in  $cm^{-2} s^{-1} eV/eV sr^{-1}$ ) as,

$$\frac{dJ(E)}{dE} = \frac{v^4}{2} \frac{\sum_i f(E, \theta_i, \varphi_i) \sin \theta_i}{\sum_i \sin \theta_i} \quad (21)$$

Here, subscripts  $i$  represent the set of angular bins at a given energy that meet a specified criteria for a desired data product. The contribution of each bin is weighted by its solid angle in spherical coordinates (i.e.,  $\sin \theta$ ). The angular bins used here correspond to those distribution function CDFs, i.e., are in look-direction rather than flow-direction coordinates.

Table 4-11 describes the criteria used to form each **average** (not summed) spectrogram.  $\hat{\mathbf{v}}$  and  $\hat{\mathbf{b}}$  describe the units vectors of look-direction and magnetic field direction (DBCS), respectively.

Data Product	Description	Relevant Angular Bins
energyspectr_omni	Omni-directional electron/ion energy spectrum	All
energyspectr_px	Electron/Ion energy spectrum "near" +X in DBCS	$\theta_i$ between $45^\circ$ and $135^\circ$ $\varphi_i$ between $135^\circ$ and $225^\circ$
energyspectr_mx	Electron/Ion energy spectrum "near" -X in DBCS	$\theta_i$ between $45^\circ$ and $135^\circ$ $\varphi_i$ between $315^\circ$ and $45^\circ$
energyspectr_py	Electron/Ion energy spectrum "near" +Y in DBCS	$\theta_i$ between $45^\circ$ and $135^\circ$ $\varphi_i$ between $225^\circ$ and $315^\circ$
energyspectr_my	Electron/Ion energy spectrum "near" -Y in DBCS	$\theta_i$ between $45^\circ$ and $135^\circ$ $\varphi_i$ between $45^\circ$ and $135^\circ$
energyspectr_pz	Electron/Ion energy spectrum "near" +Z in DBCS	$\theta_i$ between $135^\circ$ and $180^\circ$ All $\varphi_i$
energyspectr_mz	Electron/Ion energy spectrum "near" -Z in DBCS	$\theta_i$ between $0^\circ$ and $45^\circ$ All $\varphi_i$
pitchangdist_lowen (DES only)	Electron pitch-angle distribution for "low" energies	Energy indices 0 to 10 $\cos^{-1}(-\hat{\mathbf{v}} \cdot \hat{\mathbf{b}})$ in $5^\circ$ bins
pitchangdist_miden (DES only)	Electron pitch-angle distribution for "mid" energies	Energy indices 11 to 20 $\cos^{-1}(-\hat{\mathbf{v}} \cdot \hat{\mathbf{b}})$ in $5^\circ$ bins

pitchangdist_highen (DES only)	Electron pitch-angle distribution for "high" energies	Energy indices 21 to 31 $\cos^{-1}(-\hat{v} \cdot \hat{b})$ in 5° bins
energyspectr_par (DES only)	Electron energy parallel to the magnetic field direction	$\cos^{-1}(-\hat{v} \cdot \hat{b}) \leq 30^\circ$
energyspectr_anti (DES only)	Electron energy anti-parallel to the magnetic field direction	$\cos^{-1}(-\hat{v} \cdot \hat{b}) \geq 150^\circ$
energyspectr_perp (DES only)	Electron energy perpendicular to the magnetic field direction	$60^\circ < \cos^{-1}(-\hat{v} \cdot \hat{b}) < 120^\circ$

**Table 4-11 Pitchangdist Spectrograms**

For the pitchangdist\_\* spectrograms, the energies whose differential energy fluxes are averaged together can be obtained through examination of the ‘energy’ variable for the record of interest.

Spectrograms that use magnetic pitch-angle in their calculation are provided for DES only, because the electron flow frame is approximately equal to the spacecraft observation frame. In cases where the electron flow velocity approaches the sound speed, these spectrograms may be less meaningful. Ion pitch-angle distributions require a shift by the ion bulk velocity in order to be scientifically meaningful.

#### Partial Moments:

Partial moment CDF files contain 32-independent values for each plasma moment. Here, each value represents the numerical integration of the distribution function (methods described above) with a varying low energy bound.

The record-varying field *energy* contains a mapping of which index corresponds to which energy. The same index can be used for all elements. For example, if the 10<sup>th</sup> element of the energy array (e.g., *energy[9]*) in a given record were equal to 100 eV, then the 10<sup>th</sup> element of each corresponding moment would correspond to integrals where measurements below 100 eV were ignored (e.g., *numberdensity\_part[9]*, *temppara\_part[9]*, *bulkv\_part\_gse[9,0]*).

Note that low-energy extrapolation is disabled for all partial moments, leading to some differences between a partial moment starting at ~10eV and nominal Level-2 DES moments. Use of partial moments is most effective in the magnetotail when there is no significant cold electron or ion population.

#### Statistical Errors:

Statistical uncertainties are provided for number density, bulk velocity, temperature tensor, pressure tensor, and heat flux vector quantities in DBCS coordinates following *Gershman et al.* [2015]. These uncertainties are intended to serve as the equivalent of the standard deviation obtained from repeated Monte Carlo resampling of the dist fields in the distribution functions according to the disterr fields. For computational efficiency, Riemann sums rather than trapezoidal integration are used, and no additional boundary points or extrapolation methods are implemented.

Paschmann, G., A. N. Fazakerley, and S. J. Schwartz (1998), Moments of plasma velocity distributions, in *Analysis Methods for Multi-Spacecraft Data*, pp. 125–158, ISSI SA Publications Division, Noordwijk, Netherlands.



Torbert, R. B., Burch, J. L., Phan, T. D., Hesse, M., Argall, M., Shuster, R. J., et al. (2018). Electron-scale dynamics of the diffusion region during symmetric magnetic reconnection in space. *Science*. <https://doi.org/10.1126/science.aat2998>

More information about statistical errors can be found in the publication:

Gershman, D. J., Dorelli, J. C., F.-Viñas, A., and Pollock, C. J. (2015), The calculation of moment uncertainties from velocity distribution functions with random errors, *J. Geophys. Res. Space Physics*, 120, 6633– 6645, doi:10.1002/2014JA020775.

#### 4.6.6 Calculation of L3 DES/DIS Pseudo Moments

FPI produces a selection of pseudo-moments, at the full burst resolution, based on the onboard trigger quantities (*See MMS/FPI-BDEP*). The dynamic range of the environment is preserved by tuning the limited range of the system to an appropriate interval using a scaling system. These simplified data undergo a robust, neural network based correction process on the ground leading to physically meaningful quantities that are accurate to within several percent of the raw high resolution science data. Because these simplified onboard data integrals are significantly smaller in data volume, all of them can be downlinked leading to a dramatic increase in available scientific data from the mission.

The available pseudo-moments include:

Electrons: Density, Pressure, Temperature, Mag Parallel Flux  
Ions: Density, XY (Spin Plane) Flux, Z (Spin Axis) Flux

A full description of the design of FPI and its pre-flight and ground calibration results can be found in the publication:

Barrie, A. C., et al, Physically Accurate Large Dynamic Range Pseudo Moments for the MMS Fast Plasma Investigation (2018), <https://doi.org/10.1029/2018EA000407>.

### 4.7 FPI APPENDIXES

#### 4.7.1 Appendix A- Voltages Over Time / Voltage Operations

The following tables represent the MMS voltage operations over time from mission launch in 2015, as demonstrated through the V14 Setting, to the current V43 Setting, as of September 30, 2022.

**MMS 1**

Unit	V14 Setting	V18 (124)	V20 (170)	V21 (210)	V23 (239)	V24 (267)	V25 (301)	V26 (335)
FM002H0	-2350	-50	-50	0	0	0	-25	0
FM002H1	-2400	-50	0	0	0	0	0	0
FM005H0	-2350	0	0	0	0	0	0	0
FM005H1	-2350	0	0	0	0	0	0	0
FM006H0	-2400	-50	0	0	0	0	0	0
FM006H1	-2350	-75	0	0	0	0	-25	0
FM013H0	-2300	-50	-25	0	0	0	0	0

FM013H1	-2250	-50	0	0	-25	0	0	0
FM207H0	2100	50	0	50	100	0	75	0
FM207H1	2040	50	0	25	100	25	50	0
FM209H0	2100	50	0	25	100	25	75	0
FM209H1	2070	25	0	50	75	25	75	25
FM211H0	2130	25	0	25	75	25	75	0
FM211H1	2010	50	0	50	75	25	50	0
FM212H0	2010	25	0	50	100	0	75	0
FM212H1	1980	25	0	50	75	0	100	0

**Table 4-12 MMS 1 Voltage Operations (Settings V14 – V26)**

Unit	V27 (373)	V28 (511)	V29 (652)	V30 (697)	V31 (743)	V32 (768)	V33 (801)	V34 (819)
FM002H0	0	0	0	-50	-75	75	0	-25
FM002H1	-25	0	0	-25	-75	25	0	0
FM005H0	0	0	0	-25	-75	25	0	0
FM005H1	0	0	0	-25	-75	25	0	0
FM006H0	0	0	0	-25	-75	50	0	-25
FM006H1	0	0	0	0	-75	0	0	0
FM013H0	0	0	0	-25	-25	25	0	-25
FM013H1	0	0	0	-25	-75	25	0	0
FM207H0	0	25	0	25	25	-25	0	0
FM207H1	0	25	0	25	50	-25	0	25
FM209H0	25	0	0	50	75	-50	0	0
FM209H1	25	0	25	50	50	-50	0	25
FM211H0	0	50	0	25	25	-25	0	25
FM211H1	0	50	0	25	25	-25	0	25
FM212H0	0	25	0	25	25	-25	0	0
FM212H1	0	25	0	25	50	-25	0	0

**Table 4-13 MMS 1 Voltage Operations (Settings V27 – V34)**

Unit	V35 (851)	V37 (931)	V38 (1003)	V39 (1055)	V41 (1177)	V43 (1269)	V43 Setting
FM002H0	-25	-25	-25	0	0	0	-2625
FM002H1	0	-25	-25	0	0	0	-2600
FM005H0	-25	0	-25	0	0	0	-2475
FM005H1	0	-25	-25	0	0	0	-2475
FM006H0	0	-25	-25	0	0	0	-2575
FM006H1	0	0	-25	0	0	0	-2550

FM013H0	0	-50	-25	0	0	0	-2500
FM013H1	0	0	-25	0	0	0	-2425
FM207H0	50	25	25	25	25	50	2625
FM207H1	50	50	25	25	50	50	2640
FM209H0	50	50	25	25	50	50	2725
FM209H1	50	50	25	25	50	50	2720
FM211H0	25	50	25	25	50	50	2680
FM211H1	25	50	25	25	50	50	2585
FM212H0	50	50	25	25	50	50	2560
FM212H1	50	50	25	25	50	50	2555

**Table 4-14 MMS 1 Voltage Operations (Settings V35 – V43)**

**MMS 2**

<b>Unit</b>	<b>V14 Setting</b>	<b>V18 (124)</b>	<b>V20 (170)</b>	<b>V21 (210)</b>	<b>V23 (239)</b>	<b>V24 (267)</b>	<b>V25 (301)</b>	<b>V26 (335)</b>
FM001H0	-2436	0	0	50	0	0	0	0
FM001H1	-2388	0	0	50	0	0	0	0
FM009H0	-2350	-100	-25	0	0	0	0	0
FM009H1	-2300	-25	-25	0	0	0	0	0
FM012H0	-2200	-50	0	0	0	0	0	0
FM012H1	-2300	-125	-50	0	0	0	0	0
FM014H0	-2275	-25	0	0	0	0	-25	0
FM014H1	-2250	0	0	0	0	0	0	0
FM201H0	2130	0	0	25	75	25	100	25
FM201H1	2100	-30	0	50	100	25	100	25
FM202H0	2100	0	0	50	100	0	100	25
FM202H1	2070	50	0	50	125	25	100	25
FM203H0	2130	0	0	25	75	25	75	25
FM203H1	2070	-50	0	50	125	25	75	25
FM204H0	2010	0	0	25	100	25	100	0
FM204H1	2100	50	0	50	100	25	75	25

**Table 4-15 MMS 2 Voltage Operations (Settings V14 – V26)**

<b>Unit</b>	<b>V27 (373)</b>	<b>V28 (511)</b>	<b>V29 (652)</b>	<b>V30 (697)</b>	<b>V31 (743)</b>	<b>V32 (768)</b>	<b>V33 (801)</b>	<b>V34 (819)</b>
FM001H0	0	0	0	0	-75	0	0	0
FM001H1	0	0	0	0	-75	0	0	0
FM009H0	0	0	0	0	-75	0	0	0

FM009H1	0	0	0	-25	-100	25	0	0
FM012H0	0	0	0	-25	-75	25	0	-25
FM012H1	0	0	0	-50	-50	50	0	0
FM014H0	0	0	0	0	-75	0	0	0
FM014H1	0	0	0	-25	-75	25	0	-25
FM201H0	0	50	0	50	75	-50	0	25
FM201H1	0	25	0	25	75	-25	0	0
FM202H0	25	25	25	50	100	-50	0	0
FM202H1	0	25	25	50	75	-50	0	0
FM203H0	0	25	0	25	50	-25	0	25
FM203H1	25	50	25	50	100	-50	0	0
FM204H0	25	0	0	50	75	-50	0	0
FM204H1	0	50	0	75	100	-75	0	0

**Table 4-16 MMS 2 Voltage Operations (Settings V27 – V34)**

Unit	V35 (851)	V37 (931)	V38 (1003)	V39 (1055)	V41 (1177)	V43 (1269)	V43 Setting
FM001H0	0	0	-25	0	0	0	-2486
FM001H1	0	-25	-25	0	0	0	-2463
FM009H0	0	-25	-25	0	0	0	-2600
FM009H1	0	0	0	0	0	0	-2450
FM012H0	0	-25	-25	0	0	0	-2400
FM012H1	-25	-50	0	0	0	0	-2600
FM014H0	0	-25	-25	0	0	0	-2450
FM014H1	0	-25	-25	0	0	0	-2400
FM201H0	50	50	25	25	50	50	2780
FM201H1	50	25	25	25	25	50	2670
FM202H0	50	50	25	25	50	50	2800
FM202H1	50	50	25	25	50	50	2820
FM203H0	50	50	25	25	50	50	2705
FM203H1	50	50	25	0	50	50	2745
FM204H0	50	50	25	25	50	50	2610
FM204H1	50	50	25	25	50	50	2825

**Table 4-17 MMS 2 Voltage Operations (Settings V35 – V43)**

**MMS 3**

Unit	V14 Setting	V18 (124)	V20 (170)	V21 (210)	V23 (239)	V24 (267)	V25 (301)	V26 (335)

FM007H0	-2350	0	0	25	0	0	0	0
FM007H1	-2350	0	0	50	0	0	0	0
FM008H0	-2250	-50	0	0	0	0	0	0
FM008H1	-2350	-125	-25	0	0	0	0	0
FM015H0	-2200	-50	0	0	0	0	0	0
FM015H1	-2325	-25	0	0	0	0	-25	0
FM016H0	-2275	0	-25	0	0	0	-25	0
FM016H1	-2350	-100	0	0	0	0	-25	0
FM206H0	2160	0	0	50	100	0	100	0
FM206H1	2130	0	0	25	75	25	75	0
FM213H0	2100	0	0	50	100	0	75	0
FM213H1	2190	0	0	50	100	0	75	25
FM214H0	2100	0	0	50	100	0	100	0
FM214H1	2130	0	-25	50	75	0	75	25
FM216H0	2130	25	0	25	100	25	75	25
FM216H1	2070	0	0	50	100	25	75	25

**Table 4-18 MMS 3 Voltage Operations (Settings V14 – V26)**

<b>Unit</b>	<b>V27 (373)</b>	<b>V28 (511)</b>	<b>V29 (652)</b>	<b>V30 (697)</b>	<b>V31 (743)</b>	<b>V32 (768)</b>	<b>V33 (801)</b>	<b>V34 (819)</b>
FM007H0	0	0	0	-25	-75	25	0	0
FM007H1	0	0	0	0	-75	0	0	0
FM008H0	0	0	0	-25	-75	25	0	0
FM008H1	0	0	0	0	-50	0	0	0
FM015H0	0	0	0	-50	-75	50	0	-25
FM015H1	0	0	0	-25	-50	25	0	0
FM016H0	0	0	0	-25	-75	25	0	0
FM016H1	0	0	0	-25	-75	25	0	0
FM206H0	25	0	0	25	25	-25	0	0
FM206H1	0	50	0	25	25	-25	0	25
FM213H0	0	75	0	25	50	-25	0	25
FM213H1	0	25	0	25	50	-25	0	0
FM214H0	0	50	0	25	50	-25	0	0
FM214H1	0	25	25	25	50	-25	0	0
FM216H0	25	0	0	25	75	-25	0	0
FM216H1	0	25	0	50	50	-50	0	25

**Table 4-19 MMS 3 Voltage Operations (Settings V27 – V34)**

Unit	V35 (851)	V37 (931)	V38 (1003)	V39 (1055)	V41 (1177)	V43 (1269)	V43 Setting
FM007H0	0	-25	-25	0	0	0	-2450
FM007H1	0	0	-25	0	0	0	-2400
FM008H0	0	-50	-25	0	0	0	-2450
FM008H1	-25	-25	-25	0	0	0	-2625
FM015H0	0	0	-50	0	0	0	-2400
FM015H1	0	-25	-25	0	0	0	-2475
FM016H0	0	-25	-25	0	0	0	-2450
FM016H1	0	-25	-25	0	0	0	-2600
FM206H0	25	50	25	25	50	50	2685
FM206H1	25	50	25	25	50	50	2655
FM213H0	25	50	25	25	25	50	2675
FM213H1	50	50	25	25	50	50	2765
FM214H0	50	50	25	0	50	50	2675
FM214H1	50	25	25	0	50	25	2605
FM216H0	50	50	25	25	25	50	2730
FM216H1	50	50	25	25	50	50	2695

**Table 4-20 MMS 3 Voltage Operations (Settings V35 – V43)**

**MMS 4**

Unit	V14 Setting	V18 (124)	V20 (170)	V21 (210)	V23 (239)	V24 (267)	V25 (301)	V26 (335)
FM003H0	-2300	-50	0	25	0	0	0	0
FM003H1	-2300	0	0	25	0	0	0	0
FM004H0	-2350	-75	-50	0	-50	0	0	0
FM004H1	-2400	-100	-50	0	0	0	-25	0
FM010H0	-2250	0	0	0	0	0	0	0
FM010H1	-2250	-25	-25	0	-25	0	0	0
FM011H0	-2350	-75	0	0	0	0	-25	0
FM011H1	-2275	-25	0	0	0	0	0	0
FM205H0	2100	25	0	50	75	50	75	0
FM205H1	1950	50	0	50	125	0	75	25
FM208H0	2100	50	0	25	75	25	75	25
FM208H1	2040	50	0	50	75	25	100	0
FM210H0	2100	25	0	50	125	0	100	0
FM210H1	2100	50	0	25	75	25	50	0
FM215H0	2160	25	0	50	100	0	75	0
FM215H1	2040	25	0	25	50	25	50	0

**Table 4-21 MMS 4 Voltage Operations (Settings V14 – V26)**

Unit	V27 (373)	V28 (511)	V29 (652)	V30 (697)	V31 (743)	V32 (768)	V33 (801)	V34 (819)
FM003H0	0	0	0	-25	-75	25	0	0
FM003H1	0	0	0	0	-75	0	0	-25
FM004H0	0	0	0	-25	-75	25	0	0
FM004H1	0	0	0	0	-75	25	0	-25
FM010H0	0	0	0	-25	-75	50	0	-50
FM010H1	0	0	0	-25	-75	25	0	0
FM011H0	0	0	0	-25	-75	25	0	0
FM011H1	0	0	0	0	-50	0	0	0
FM205H0	25	25	0	25	75	-25	0	0
FM205H1	0	25	25	25	75	-25	0	0
FM208H0	0	25	0	50	50	-50	0	25
FM208H1	0	25	0	50	50	-50	0	25
FM210H0	0	50	0	50	75	-50	0	0
FM210H1	25	25	0	50	50	-50	0	25
FM215H0	25	25	0	50	50	-50	0	25
FM215H1	-25	75	0	0	25	0	0	25

**Table 4-22 MMS 4 Voltage Operations (Settings V27 – V34)**

Unit	V35 (851)	V37 (931)	V38 (1003)	V39 (1055)	V41 (1177)	V43 (1269)	V43 Setting
FM003H0	0	-25	-25	0	0	0	-2450
FM003H1	0	-25	-25	0	0	0	-2425
FM004H0	0	-25	-25	0	0	0	-2650
FM004H1	0	-25	-25	0	0	0	-2700
FM010H0	0	-25	-25	0	0	0	-2400
FM010H1	0	-25	-25	0	0	0	-2450
FM011H0	0	-25	-25	0	0	0	-2575
FM011H1	0	-25	-25	0	0	0	-2400
FM205H0	50	50	25	25	50	50	2750
FM205H1	50	25	25	25	50	25	2600
FM208H0	50	50	25	25	50	50	2725
FM208H1	50	50	0	25	50	25	2640
FM210H0	50	0	0	0	0	0	Unit Off
FM210H1	50	0	0	0	0	0	Unit Off
FM215H0	25	0	0	0	0	0	Unit Off

FM215H1	25	0	0	0	0	0	Unit Off
---------	----	---	---	---	---	---	----------

**Table 4-23 MMS 4 Voltage Operations (Settings V35 – V43)**

#### 4.7.2 Appendix B- Stepping Tables Over Time

The following is a list of energy stepping tables used by FPI for science operations by mission phase, date, and table designation. The start date in each row indicates when a change was made to stepping tables. A given table version would be utilized for all operations following a change and before the next change.

Start Date	Mission Phase	Table Designator	Notes
9/1/2015	1A	v04	Utilized through to Phase 1B
9/26/2016	1B	v05 & v06	Both tables identical for science purposes.
5/7/2017	2B	v07 & v08	Tables are identical for science, except for minor changes for MMS3 DIS0 only in v08.
11/14/2017	3B	v08 & v09	First use of 3 SROIs per orbit. Tables identical except for max energy range changes for DIS.

**Table 4-24 List of Energy Stepping Tables Used by FPI for Science Operations by Mission Phase, Date, and Table Designation**

The tables below correspond to the four rows listed above and contain details for DES and DIS stepper tables that include energy step and center energy for each step.

	Start Date: 9/1/2015 Table Designator: v04		Start Date: 9/26/2016 Table Designator: v05&06	
Species:	DES (electrons)	DIS (ions)	DES (electrons)	DIS (ions)
Step #	Center Energy (eV)	Center Energy (eV)	Center Energy (eV)	Center Energy (eV)
1	6.5	2.2	6.0	1.7
2	8.5	3.9	7.9	3.4
3	11.2	7.1	10.3	6.7
4	14.6	10.9	13.6	10.9
5	19.1	14.5	17.8	14.5
6	25.1	19.2	23.4	19.1
7	32.8	25.4	30.7	25.3
8	43.0	33.6	40.3	33.4
9	56.2	44.5	52.8	44.2
10	73.6	58.9	69.4	58.5
11	96.3	78.0	91.0	77.4
12	126.1	103.2	119.5	102.4
13	165.1	136.7	156.8	135.4
14	216.1	181.0	205.8	179.1
15	282.9	239.6	270.1	236.9
16	370.3	317.3	354.6	313.3
17	484.7	420.1	465.4	414.4
18	634.5	556.2	610.8	548.1
19	830.6	736.4	801.7	725.0
20	1087.3	975.1	1052.2	959.0
21	1423.3	1291.0	1381.0	1268.4
22	1863.2	1709.4	1812.6	1677.8
23	2438.9	2263.3	2379.1	2219.2
24	3192.6	2996.6	3122.6	2935.3



25	4179.2	3967.6	4098.4	3882.5
26	5470.7	5253.2	5379.2	5135.4
27	7161.3	6955.5	7060.2	6792.6
28	9374.3	9209.2	9266.6	8984.5
29	12271.1	12193.3	12162.6	11883.7
30	16063.2	16144.3	15963.5	15718.6
31	21027.1	21375.6	20952.2	20790.9
32	27525.0	28301.9	27500.0	27500.0

**Table 4-25 Phase 1A & Phase 1B DES & DIS Stepper Table**

	<b>Start Date: 5/7/2017</b>	
	<b>Table Designator: v07&amp;08</b>	
<b>Species:</b>	<b>DES (electrons)</b>	<b>DIS (ions)</b>
<b>Step #</b>	<b>Center Energy (eV)</b>	<b>Center Energy (eV)</b>
1	6.5	2.2
2	8.5	3.9
3	11.2	7.1
4	14.6	10.9
5	19.1	14.5
6	25.1	19.2
7	32.8	25.4
8	43.0	33.6
9	56.2	44.5
10	73.6	58.9
11	96.3	78.0
12	126.1	103.2
13	165.1	136.7
14	216.1	181.0
15	282.9	239.6
16	370.3	317.3
17	484.7	420.1
18	634.5	556.2
19	830.6	736.5
20	1087.3	975.1
21	1423.3	1291.0
22	1863.2	1709.4
23	2438.9	2263.3
24	3192.6	2996.6
25	4179.2	3967.6
26	5470.7	5253.2
27	7161.3	6955.5
28	9374.3	9209.2
29	12271.1	12193.3
30	16063.2	16144.3
31	21027.1	21375.6
32	27525.0	28301.9

**Table 4-26 Phase 2B DES & DIS Stepper Table**

	<b>Start Date: 11/14/2017</b>
	<b>Table Designator: v08&amp;09</b>

<b>EEPROM/ Table ID</b>	<b>EEPROM1 Tail</b>		<b>EEPROM2 Sheath</b>		<b>EEPROM4 Solar Wind</b>	
<b>Species:</b>	<b>DES (electrons)</b>	<b>DIS (ions)</b>	<b>DES (electrons)</b>	<b>DIS (ions)</b>	<b>DES (electrons)</b>	<b>DIS (ions)</b>
<b>Step #</b>	<b>Center Energy (eV)</b>	<b>Center Energy (eV)</b>	<b>Center Energy (eV)</b>	<b>Center Energy (eV)</b>	<b>Center Energy (eV)</b>	<b>Center Energy (eV)</b>
1	6.5	2.2	6.5	2.16	4.4	210.0
2	8.5	3.9	8.5	3.91	5.2	236.8
3	11.2	7.1	11.2	7.07	6.2	267.0
4	14.6	10.9	14.6	10.93	7.3	301.1
5	19.1	14.5	19.1	14.24	8.7	339.6
6	25.1	19.2	25.1	18.54	10.3	382.9
7	32.8	25.4	32.8	24.14	12.2	431.8
8	43.0	33.6	43.0	31.44	14.5	486.9
9	56.2	44.5	56.2	40.94	17.1	549.0
10	73.6	58.9	73.6	53.32	20.3	619.1
11	96.3	78.0	96.3	69.44	24.1	698.1
12	126.1	103.2	126.1	90.43	28.6	787.2
13	165.1	136.7	165.1	117.77	33.9	887.7
14	216.1	181.0	216.1	153.36	40.2	1001.0
15	282.9	239.6	282.9	199.72	47.7	1128.8
16	370.3	317.3	370.3	260.10	56.6	1272.9
17	484.7	420.1	484.7	338.72	67.1	1435.3
18	634.5	556.2	634.5	441.11	79.6	1618.6
19	830.6	736.5	830.6	574.45	94.4	1825.1
20	1087.3	975.1	1087.3	748.10	112.0	2058.1
21	1423.3	1291.0	1423.3	974.23	132.8	2320.8
22	1863.2	1709.4	1863.2	1268.72	157.5	2617.0
23	2438.9	2263.3	2438.9	1652.24	186.9	2951.1
24	3192.6	2996.6	3192.6	2151.68	221.6	3327.8
25	4179.2	3967.6	4179.2	2802.10	262.9	3752.5
26	5470.7	5253.2	5470.7	3649.12	311.8	4231.5
27	7161.3	6955.5	7161.3	4752.19	369.8	4771.6
28	9374.3	9209.2	9374.3	6188.69	438.6	5380.7
29	12271.1	12193.3	12271.1	8059.43	520.2	6067.5
30	16063.2	16144.3	16063.2	10495.65	617.0	6841.9
31	21027.1	21375.6	21027.1	13668.31	731.8	7715.2
32	27525.0	28301.9	27525.0	17800.00	868.0	8700.0

**Table 4-27 Phase 3B DES & DIS Stepper Table**

#### 4.7.3 Appendix C- Energy Profiles by Mission Phase

FPI science data collection energy configurations are dependent on mission phase. Energy steps used in a particular data file are provided in the *energy* variable. Energy profiles used since the start of the mission are listed in the following table.

<b>Mission Phase</b>	<b>Orbit Range</b>	<b>FPI Energy Profile</b>	<b>Comments</b>
Commissioning	1-172	P1	Not consistently operational
Phase 1A	173-362	P1	
Phase 1X	363-516, 531-551	N/A	Not operational

	517-534	Various	Burst Bulk Flow testing
Phase 1B	552-565	N/A	Not operational
	566-693	P2	
Phase 2A	694-696	N/A	Not operational
	697-702	P2	
	703-747	N/A	Not operational
Phase 2B	748-791	P2	
Phase 3A	792-817	P2	
Phase 3B	818-843	P2, SW	
	844-859	P3, SW	
Phase 3C	860-873	P3, SW	
	874-885	P3	
Phase 3D	886-918	P2	
	919-930	P3	
Phase 4A	931-952	P3	
Phase 4B	953-996	P3, SW	
Phase 4C	997-1010	P3, SW	
	1011-1016	P3	
	1017	P2	
Phase 4D	1018-1044	P2	
Phase 5A	1045-1048	P2	
	1049-1058	P3	
	1059	P3, SW	
Phase 5B	1060-1102	P3, SW	
Phase 5C	1103-1108	P3, SW	
	1109-1118	P3	
	1119-1120	P2	
Phase 5D	1121-1150	P2	
Phase 6A	1151-1160	P2	
	1161-1162	P3	
	1163-1164	P3, SW	
Phase 6B	1165-1208	P3, SW	
Phase 6C	1209-1216	P3, SW	
	1217-1222	P3	
	1223-1224	P2	
Phase 6D	1225-1254	P2	
Phase 7A	1255-1266	P2	
	1267-1271	P3	
	1272-1278	P3, SW	
Phase 7B	1279-1312	P3, SW	
Phase 7C	1313-1318	P3, SW	
	1319-1324	P2	
Phase 7D	1324-1356	P2	

**Table 4-28 FPI Energy Profiles Since Mission Start**

The following table lists the energy collection profiles that FPI has employed since launch. Note that the profile of MMS3 DIS was modified to prevent the taking of measurements above 11 keV starting with orbit 748, as discussed above.

Profile	DES	DIS
P1	10 eV - 30 keV in 32 energy steps and 4 deflection states yielding 11.25 deg angular bins	10 eV - 30 keV in 32 energy steps and 4 deflection states yielding 11.25 deg angular

	in elevation and azimuth dimensions; energy is interleaved across 2 parities	bins in elevation and azimuth dimensions; energy is interleaved across 2 parities
P2	6 eV - 30 keV in 32 energy steps and 4 deflection states yielding 11.25 deg angular bins in elevation and azimuth dimensions. Energy is identical across 2 parities	2 eV - 30 keV in 32 energy steps and 4 deflection states yielding 11.25 deg angular bins in elevation and azimuth dimensions. Energy is identical across 2 parities
P3	Identical to P2	2 eV - 18 keV in 32 energy steps and 4 deflection states yielding 11.25 deg angular bins in elevation and azimuth dimensions. Energy is identical across 2 parities
SW (solar wind)	4 eV - 940 eV in 32 energy steps and 4 deflection states yielding 11.25 deg angular bins in elevation and azimuth dimensions. Energy is identical across 2 parities	197 eV - 9222 eV in 32 energy steps and 4 effective deflection states yielding 11.25 deg effective angular bins in elevation and azimuth dimensions. Energy is identical across 2 parities. Deflection states are interleaved across 2 parities, but, due to convolution with spacecraft spin, do not provide increased angular resolution

**Table 4-29 FPI Energy Collection Profiles**

#### 4.7.4 Appendix D- FPI References

The following is a list of applicable references and publications.

Section	Document Number	Title	Revision/Date
	<a href="https://doi.org/10.1029/2021JA029149">https://doi.org/10.1029/2021JA029149</a>	Barrie, A. C., Schiff, C., Gershman, D. J., Giles, B. L., & Rand, D. (2021). Calibrating electrostatic deflection of charged particle sensors using ambient plasma measurements. <i>Journal of Geophysical Research: Space Physics</i> , 126, e2021JA029149.	
	<a href="https://doi.org/10.1002/2016JA022645">https://doi.org/10.1002/2016JA022645</a>	Barrie, A. C., S. E. Smith, J. C. Dorelli, D. J. Gershman, P. Yeh, C. Schiff, and L. A. Avanov (2017), Performance of a space-based wavelet compressor for plasma count data on the MMS Fast Plasma Investigation, <i>J. Geophys. Res. Space Physics</i> , 122, 765–779.	
	<a href="https://doi.org/10.1029/2018EA000407">https://doi.org/10.1029/2018EA000407</a>	Barrie, A. C., et al. "Physically Accurate Large Dynamic Range Pseudo Moments for the MMS Fast Plasma Investigation." <i>Earth and Space Science</i> 5.9 (2018): 503-515.	
	<a href="https://doi.org/10.1063/1.5119344">https://doi.org/10.1063/1.5119344</a>	Barrie, A. C., et al. "Characterizing spacecraft potential effects on measured particle trajectories." <i>Physics of Plasmas</i> 26.10 (2019): 103504.	
	<a href="https://doi.org/10.1029/2019JA027181">https://doi.org/10.1029/2019JA027181</a>	da Silva, D., Barrie, A., Gershman, D., Elkington, S., Dorelli, J., Giles, B., & Paterson, W. (2020). Neural network repair of Lossy compression Artifacts in the September 2015 to March 2016 duration of the MMS/FPI data set. <i>Journal of Geophysical Research: Space Physics</i> , 125, e2019JA027181.	

	<p><a href="https://doi.org/10.1002/2017JA024518">https://doi.org/10.1002/2017JA024518</a></p>	<p>Gershman, D. J., Avakov, L. A., Boardsen, S. A., Dorelli, J. C., Gliese, U., Barrie, A. C., ... Pollock, C. J. (2017). Spacecraft and instrument photoelectrons measured by the dual electron spectrometers on MMS. <i>Journal of Geophysical Research: Space Physics</i>, 122, 11,548–11,558.</p>	
	<p><a href="https://doi.org/10.1029/2019JA026980">https://doi.org/10.1029/2019JA026980</a></p>	<p>Gershman, D. J., Dorelli, J. C., Avakov, L. A., Gliese, U., Barrie, A., Schiff, C., et al. (2019). Systematic uncertainties in plasma parameters reported by the fast plasma investigation on NASA's magnetospheric multiscale mission. <i>Journal of Geophysical Research: Space Physics</i>, 124, 10345– 10359.</p>	
	<p><a href="https://doi.org/10.1007/s11214-016-0245-4">https://doi.org/10.1007/s11214-016-0245-4</a></p>	<p>Pollock, C., Moore, T., Jacques, A., Burch, J., Gliese, U., Saito, Y., ... &amp; Zeuch, M. (2016). Fast plasma investigation for magnetospheric multiscale. <i>Space Science Reviews</i>, 199(1), 331-406.</p>	
	<p><a href="https://doi.org/10.1002/2017GL076260">https://doi.org/10.1002/2017GL076260</a></p>	<p>Rager, A. C., Dorelli, J. C., Gershman, D. J., Uritsky, V., Avakov, L. A., Torbert, R. B., ... Saito, Y. (2018). Electron crescent distributions as a manifestation of diamagnetic drift in an electron-scale current sheet: Magnetospheric Multiscale observations using new 7.5 ms Fast Plasma Investigation moments. <i>Geophysical Research Letters</i>, 45, 578–584.</p>	
	<p><a href="https://doi.org/10.1029/2021JA029784">https://doi.org/10.1029/2021JA029784</a></p>	<p>Roberts, O. W., Nakamura, R., Coffey, V. N., Gershman, D. J., Volwerk, M., Varsani, A., et al. (2021). A study of the solar wind ion and electron measurements from the magnetospheric multiscale mission's fast plasma investigation. <i>Journal of Geophysical Research: Space Physics</i>, 126, e2021JA029784.</p>	
	<p><a href="https://doi.org/10.1029/2019GL083549">https://doi.org/10.1029/2019GL083549</a></p>	<p>Shuster, J. R., D. J. Gershman, L. Chen, S. Wang, N. Bessho, J. C. Dorelli, D. E. Silva, B. L. Giles, W. R. Paterson, R. E. Denton, S. J. Schwartz, C. Norgren, F. D. Wilder, P. A. Cassak, M. Swisdak, V. Uritsky, C. Schiff, A. C. Rager, S. Smith, L. A. Avakov, and A. F. Viñas (2019), MMS Measurements of the Vlasov Equation: Probing the Electron Pressure Divergence Within Thin Current Sheets, <i>Geophysical Research Letters</i>, 46(14), 7862-7872, <a href="https://agupubs.onlinelibrary.wiley.com/doi/full/10.1029/2019GL083549">https://agupubs.onlinelibrary.wiley.com/doi/full/10.1029/2019GL083549</a></p>	
	<p><a href="https://doi.org/10.1038/s41567-021-01280-6">https://doi.org/10.1038/s41567-021-01280-6</a></p>	<p>Shuster, J. R., D. J. Gershman, J. C. Dorelli, B. L. Giles, S. Wang, N. Bessho, L.-J. Chen, P. Cassak, S. Schwartz, R. Denton, V. Uritsky, W. R. Paterson, C. Schiff, A. Vinas, J. Ng, L. A. Avakov, D. da Silva, and R. Torbert (2021), Structures in the terms of the Vlasov equation observed at Earth's magnetopause, <i>Nature Physics</i>, <a href="https://www.nature.com/articles/s41567-021-01280-6">https://www.nature.com/articles/s41567-021-01280-6</a></p>	

	<a href="https://doi.org/10.1126/science.aat2998">https://doi.org/10.1126/science.aat2998</a>	Torbert, R. B., Burch, J. L., Phan, T. D., Hesse, M., Argall, M., Shuster, R. J., et al. (2018). Electron-scale dynamics of the diffusion region during symmetric magnetic reconnection in space. <i>Science</i> .	
--	---	--	--

**Table 4-30 FPI Applicable Documents**

## 5.0 HOT PLASMA COMPOSITION ANALYZER (HPCA)

### 5.1 HPCA OVERVIEW

The Hot Plasma Composition Analyzer (HPCA) investigation supports the Magnetospheric Multiscale mission (MMS) by determining the ways in which key marker species found in the solar wind and Earth's magnetosphere ( $H^+$ ,  $He^{++}$ ,  $He^+$  and  $O^+$ ) contribute to reconnection phenomena. The instrument is a time-of-flight (TOF) mass spectrometer designed to measure the velocity distributions of the four ion species ( $H^+$ ,  $He^{++}$ ,  $He^+$  and  $O^+$ ) known to be important in the reconnection process. The measurement technique is based on a combination of electrostatic energy-angle analysis with time-of-flight velocity analysis. The result is an accurate determination of the velocity distributions of the individual ion species. The HPCA instrument incorporates three new technologies. The first extends counting rate dynamic range by employing a novel radio frequency mass filter that allows minor species such as  $He^{++}$  and  $O^+$  to be measured accurately in the presence of intense proton fluxes found in the dayside magnetopause. The second ensures that TOF processing rates are high enough to overlap with the low end of the RF dynamic range, while the third enhances ion mass resolution.

A full description of the design of HPCA, its ground calibration setup and results, and its operational concept can be found in the publication:

Young, D.T., Burch, J.L., Gomez, R.G. et al, **Hot Plasma Composition Analyzer for the Magnetospheric Multiscale Mission**, Space Sci Rev 199, 407–470 (2016).  
<https://doi.org/10.1007/s11214-014-0119-6>

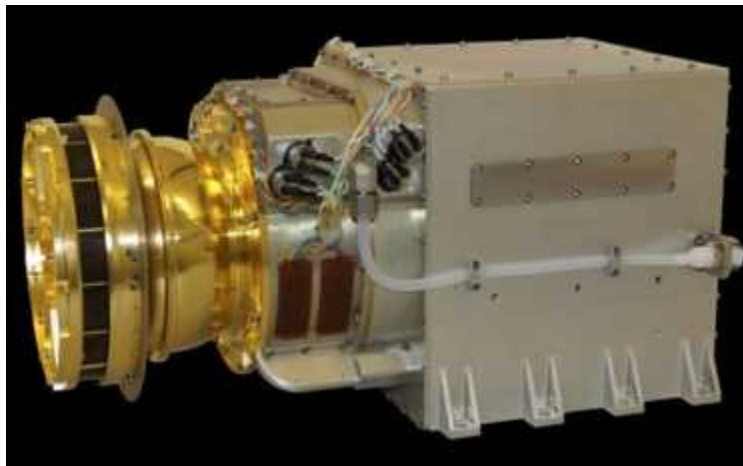


**Figure 5-1 Completed HPCA Flight Model 1**

For the purpose of the CMAD, a limited description is included here in order to provide the discussion for algorithm development.

#### 5.1.1 Status of the HPCA Instruments

One HPCA instrument is mounted on each MMS spacecraft. All the HPCA instruments are functioning nominally. Over the course of the mission there have been several anomalies that have affected the production of data, and have resulted in the instrument being rebooted to clear the error. Additionally, the instruments have been rebooted after uploading new parameter tables to make changes to the instrument

configuration. These changes should be transparent to the user of the L2 files, as these configuration changes have been accounted for within the data processing pipeline.

The HPCA ground system processes all available downlinked Fast Survey and burst data, including partial segments and those that were not downloaded for all MMS observations. However, there may still be time periods when there are incomplete records, missing data, zeroes in the data, or data that is not optimal for science.

- HPCA data with non-optimal voltage settings (degraded or harder to use science). Note that the voltage setting can be found in the Moments CDF file (see section 5.6.9), while nominal voltage settings are noted in Table 5-12.
  - Maneuvers: HPCA is placed into Maneuver mode which reduces the voltages.
  - On-Orbit Gain Tests: Voltages vary over a 45 minute time period and are scheduled roughly every 6 months.
  - Radiation Belt (RB) Mode: The MCP supply is raised to keep from oversaturating the microchannel plates. Nominally this occurs when the L-shell is 5 or less. This setting has changed over the course of the mission. HPCA also operated in RB mode between science regions of interest for a while.
  - Times when the instrument has been powered on, but the ATS command sequence has not placed the instrument into a science mode.
  - Parameter Loads: HPCA occasionally loads a new set of configuration parameters to the instrument, which requires a power-down, table load, and reboot cycle.
- No HPCA data is available
  - Spacecraft anomalies: No HPCA data is collected when an observatory is in emergency safe mode.
  - Scheduled downtime: HPCA does not collect data during the yearly long shadow periods.
  - Time periods where no magnetic field data is available.

## **5.2 HPCA MEASUREMENT STANDARDS, VOLUME, TIMING, AND COORDINATES**

### **5.2.1 Accuracy of HPCA Time Tags in L2 Data**

The time variable in all HPCA data products mark the beginning of the data collection interval. TOF measurements over 512 bins are taken at 64 different energy steps every 11.25 degrees of spacecraft rotation. Note that the 360-degree FOV is divided into 16 polar segments that correspond to the 16 simultaneously acquired histograms that are reported by the TOF hardware for each acquisition period.

- The 11.25 degrees of spacecraft rotation are the azimuth (AZ) steps
- The 64 voltage steps in each 11.25 degrees are the Energy (E/Q) steps
- The same Power Supply/RF Frequency profile is repeated for each 11.25 degree set (azimuth)
- There are 1,024 TOF data sets created every 10-second half-spin of the spacecraft (full sky view), calculated as  $(16 \text{ AZ}) * (64 \text{ Energy}) = 1024 \text{ TOF data sets}$

## **5.3 RELATIVE TELEMETRY ALLOCATIONS AND DATA VOLUME**

During the nominal mission, HPCA was assigned allocation rates for slow and fast survey, as well as burst. Due to the fact that we run with both lossy and lossless compression, the size of our data can vary, based on how well the data compresses. After analyzing the rates during early mission, HPCA was able to back off on the decimation of some data products to allow for less decimated data to be downlinked.



Mode	% of Time Operated	% of HPCA Data Transmitted	Daily Allocation Rate	Daily Allocation
Slow Survey	~50%	7.4%	0.8 kbit/s	~34 Mbit
Fast Survey	~50%	51.3%	5.6 kbit/s	~236 Mbit
Fast Survey (Burst)	1.25%	41.3%	180 kbit/s	~190 Mbit
TOTAL	100%	100%	N/A	~460 Mbit

Table 5-1 HPCA Nominal Modes and Volume

### 5.3.1 Basic Instrument Information for Algorithm Development

MMS-HPCA measures the energy and composition of magnetospheric plasmas with an electrostatic energy analyzer (ESA) which is optically coupled to a carbon-foil based time-of-flight (TOF) section. The following sections address the operational principles of both ion-optical components.

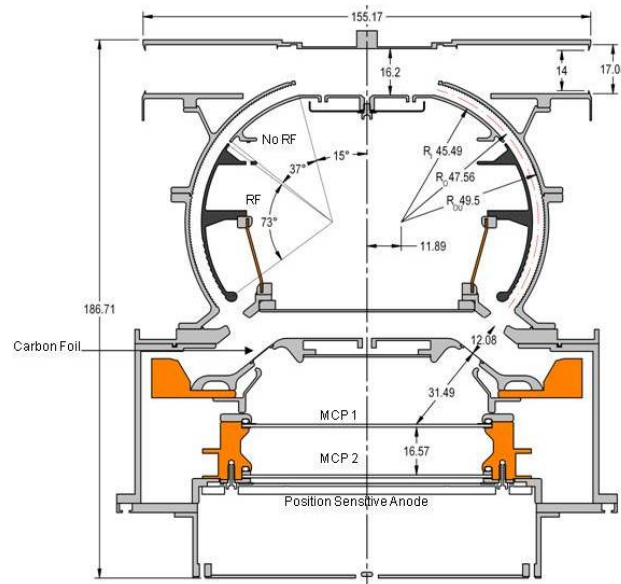


Figure 5-2 HPCA Dimensions

#### 5.3.1.1 ESA

HPCA scans plasmas in the energy range 1 eV - 40 keV using an ESA with inner and outer conducting electrode radii of  $R_1 = 45.5$  mm and  $R_2 = 49.5$  mm. These conducting electrodes are more commonly called ESA plates. The ESA bending angle of  $\gamma = 125.0^\circ$  insures that UV photons from the sun do not have a direct path to the particle sensitive microchannel plates (MCPs), which can cause excessive background during data acquisition. ESAs deflect the paths of charged particles in a specified energy range set by the plate spacing ( $\Delta R = R_2 - R_1$ ), the average plate radius,  $R_0 = (R_2 + R_1)/2$ , and the voltage

difference between the plates,  $\Delta V = V_2 - V_1$ ; where  $V_{1/2}$  is the voltage applied to the inner/outer plate. The analyzer geometry determines the energy and angular resolutions as well as the ESA's analyzer constant,  $k$ ; a constant of proportionality between the ESA plate voltage difference and central energy of the acceptance passband. This energy is set according to (5-1):

$$E = k\Delta V \quad (5-1)$$

The analyzer constants of all four HPCA flight models were determined from calibration results at eight energies; 98 eV, 312 eV, 512 eV, 995 eV, 3159 eV, 10059 eV, 19525 eV, and 32040 eV. Their  $k$ 's are shown in the next table.

HPCA Flight Model	Analyzer Constant - $k$ [eV/V]	Uncertainty (+/-) [eV/V]
1	5.42	0.01
2	5.42	0.01
3	5.39	0.04
4	5.39	0.02

**Table 5-2 HPCA Flight Model Analyzer Constants**

During operation, voltage is applied to the inner ESA plate of HPCA; the outer plate is held at spacecraft ground, so  $\Delta V$  is just the voltage on the inner plate;  $\Delta V = V_1$ .

### 5.3.1.2 TOF

Particles that are permitted through the ESA plates, exit and are post-accelerated by a 15 kV potential on their way to one of sixteen thin carbon foils placed at the entrance to the TOF section. Ion impacts cause secondary electron emission from both foil surfaces. In the vast majority of interactions, ions assume a neutral charge state through charge exchange with the foil. Electrons emitted from the bottom surface facing the TOF section are accelerated, and focused with steering electrodes to MCP1 (see Figure 5-2), where their signals are amplified by over 6 orders of magnitude. These amplified signals then impact one of the sixteen elevation-start ( $\beta$ ) pads shown in Figure 5-3.

Electron transit times within the TOF region are short ( $< 5.0$  ns). By comparison, the transit time for a proton at 45 keV (60 keV with the 15 kV post acceleration), the highest energy scanned by HPCA, is  $> 9.0$  ns. Because of this time difference, electron signals at the pads are used to signal the start of a time-of-flight measurement (TOF).

Ion signals impact MCP1 above the concentric array of sixteen anode rings (Figure 5-3). The rings are used to correct for the change in the particle flight path due to angular scattering within the foil. The ion signals are the stop signals for a TOF measurement. The ion time of flight (TOF) in this region has the analytical form (5-1):

$$TOF = \frac{d}{\sqrt{\frac{2E}{m}}} \quad (5-1)$$

where  $d$  is the length of the nominal flight path (3.15 cm),  $E$  the ion energy in eV, and  $m$  the ion mass-to-charge ratios provided in Table 5-3. HPCA measures ion TOF from 0 ns to 256 ns in 0.5 ns resolution (512 TOF channels).

Ion Species	Mass-to-Charge Ratio (M/q) [AMU/e]	Mass-to-Charge Ratio [eV/c <sup>2</sup> e]
H <sup>+</sup>	1	0.939494061e9
He <sup>++</sup> (alpha particle)	2	1.87898812e9
He <sup>+</sup>	4	3.75797624e9
O <sup>++</sup> (Doubly Charged Oxygen)	8	7.51595249e9
O <sup>+</sup>	16	15.031905e9

**Table 5-3 HPCA Species Mass-to-Charge Ratios**

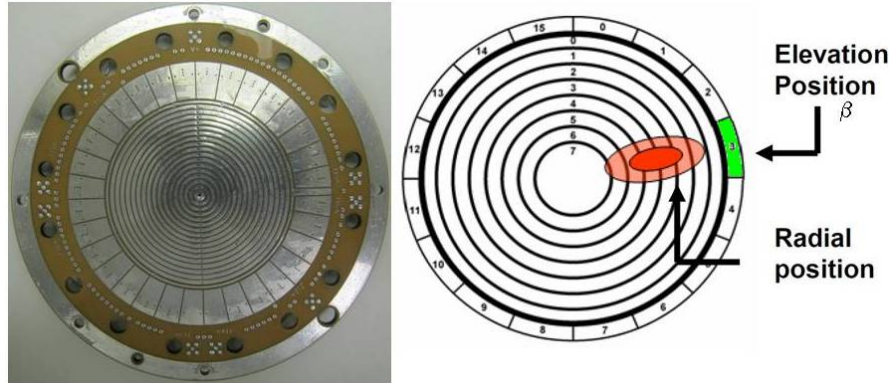


**Figure 5-3 HPCA Position Sensitive Anode [At left, the anode with 16 elevation-start pads and 16 concentric stop rings. At right, the operation of the anode with respect to elevation detection, and flight distance correction]**

HPCA's dual delay line, and the uncertainty in the energy loss from foil straggling makes an analytical fit with (5-1) very difficult. Instead, energy dependent TOF measurements made during calibration are used to assign channels of the TOF spectrum to specific ions as shown in Figure 5-4.

Also shown in Figure 5-4, ions of a given mass (e.g. H<sup>+</sup>, 1 AMU) will populate a specific range of TOF channels, at a given post foil energy. The measured responses at eight energies are used to interpolate, and extrapolate the responses at other energies. Note that O<sup>2+</sup> bins are not shown in Figure 5-4. This is because getting these counts requires special treatment of the background ion count product. This treatment will be discussed shortly. In addition to energy and composition, the HPCA's construction allows surveys of the plasma phase space with high resolution in solid angle. These resolutions will be discussed in later sections; but first we will discuss the technique used to get O<sup>2+</sup> counts from the background ion count product.

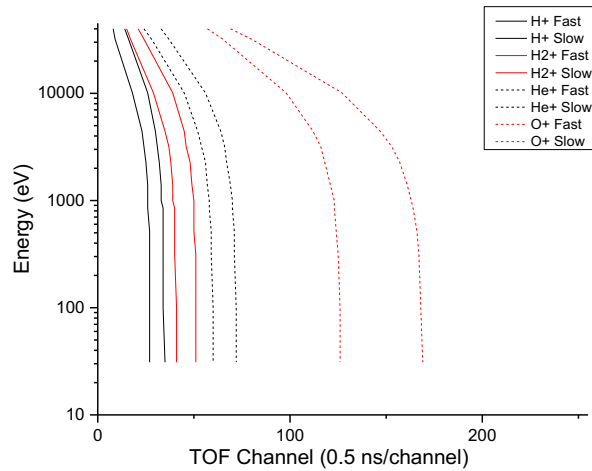


**Figure 5-4 HPCA TOF Channel Assignment from Calibration**

### 5.3.1.3 Determining Doubly Charged Oxygen Counts

The basic HPCA data product is an array of counts for 5 ion species, at 63 energies, for each elevation anode (16). Sixteen basic products, also called azimuths, are acquired every 10 seconds; half a spacecraft spin period nominally has 16 azimuths. The five ion species are protons ( $H^+$ ), alpha particles ( $He^{2+}$ ), helium ions ( $He^+$ ), singly charged Oxygen ( $O^+$ ), and background counts. The background counts are acquired in the TOF bin range between the slowest helium, and fastest singly charged oxygen ion at each energy (see Figure 5-4). These bin ranges contain ranges where the TOFs of doubly charged oxygen ions ( $O^{2+}$ ) can be counted as well. To get these counts out of the background counts requires manipulation of the background product.

To start, we perform the following operation on the background ion counts:

$$\left[ \frac{\text{noise}}{\text{bin}} \right]_{\beta} = \frac{\sum_{E=0}^{63} N_{E,\beta, \text{Background}}}{\sum_{E=0}^{63} [N(\text{bins})_{\text{background}}]_E} \quad (5-2)$$

which is based on the following assumptions:

1. The background is independent of energy
2. Background can be influenced by the gain of individual detector pixels
3. Ion species that can populate the background bins are in low concentration in most plasmas
4. HPCA, with its double coincidence detection scheme, greatly reduces spurious noise

In (5-2) the variable  $[N(\text{bins})_{\text{background}}]$  is the number of bins, at respective energies, over which the background counts are accumulated. Note that the sum is carried out over energy only, which addresses assumptions 1 and 2 in the list.  $[\text{Noise}/\text{Bin}]$  is then a 16 element array. Once computed, it is used to determine the corrected ion flux.

The ion flux at energy  $E$  in counts  $\text{cm}^{-2} \text{sr}^{-1} \text{eV}^{-1}$  is determined from:

$$J_{E,\beta,s} = \frac{C_{E,\beta,s}}{G(E) \left(\frac{E}{q}\right)_s} \quad (5-3)$$

Where  $G(E)$  is the energy specific geometric factor of the instrument at  $E$ . However, before computing  $J_{E,\beta,s}$  the corrected ion counts must be calculated by subtracting the  $[\text{noise}/\text{bin}]_\beta$  value as shown:

$$C_{E,\beta,s} = \left( N_{E,\beta,s} - N(\text{bins})_{s,E} \times \left[ \frac{\text{noise}}{\text{bin}} \right]_\beta \right) / \Delta\tau \quad (5-4)$$

Where  $N(\text{bins})_s$  is the number of bins, at energy  $E$ , for which ion species  $s$  counts are accumulated. The doubly charged oxygen product comes from this when the background counter is operated upon as shown here:

$$C_{E,\beta,O^{++}} = \left( N_{E,\beta,\text{background}} - N(\text{bins})_{\text{background},E} \times \left[ \frac{\text{noise}}{\text{bin}} \right]_\beta \right) / \Delta\tau \quad (5-5)$$

Then the  $O^{++}$  flux is computed from:

$$J_{E,\beta,O^{++}} = \frac{C_{E,\beta,O^{++}}}{G(E) \left(\frac{E}{q}\right)_s} \quad (5-6)$$

### 5.3.2 Coordinates / Phase Space Scanning Dimensions

HPCA bins the phase-space of a plasma under observation into one dimension of energy, two of angles, and five ion masses as shown in the following table. Also included in the table are the HPCA parameters which control the dimensions, the dimensional symbols, the indices of these parameters and their ranges.

Dimension	Mediating Parameter	Symbol	Index	Index Values
Energy	ESA Voltage	$E$	$i$	0-62 (63 is flyback)
Elevation	Start Anode	$\beta$	$j$	0-15
Azimuth	Spin-Energy Sweep	$\alpha$	$k$	0-15
Ion Species	Time-of-Flight Binning	$m$	$s$	0-4 : 0 = $H^+$ ; 1 = $He^{2+}$ ; 2 = $He^+$ ; 3 = $O^+$ , 4 = background

**Table 5-4 HPCA Parameters Controlling Dimensions, Symbols, and Indices**

Each of these dimensions, and how they are sampled, are included below.

#### 5.3.2.1 ESA Voltages – Energy

During normal operation, the energy range (1 eV - 40 keV) is scanned by using a table of logarithmically spaced ESA voltages. Regardless of the instrument sampling mode (slow survey, fast survey, or burst - these modes will be discussed shortly), HPCA scans this energy range in 625 ms, including ramp and sample times. The sample time at each energy is 8.950 ms. There are 63 energy sample steps in the HPCA table; the 64th is a flyback step which sets the inner plate voltage to spacecraft ground, making  $\Delta V = 0$  V.

The energy at each step is determined using (5-1). The voltages are set according to the voltage sweep tables supplied to each instrument.

### 5.3.2.2 Start Anodes – Elevation

At each voltage step,  $V_i$ , HPCA captures 16 individual TOF measurements; one for each elevation anode. Because of the clocking of the microchannel plates and the bias angle of their channels, there is signal gain variation between adjacent anodes which requires specific corrections. This effect is plainly evident in an elevation scan about the instrument aperture (shown in Figure 5-5).

In addition, as shown in Figure 5-2, HPCA's top-hat ESA configuration means that ions are accepted across the instrument's symmetry plane and their signals are registered on the anode that sits opposite the location of ion entry in the instrument aperture. The anode, and flight model specific, gain corrections are included in Figure 5-5.

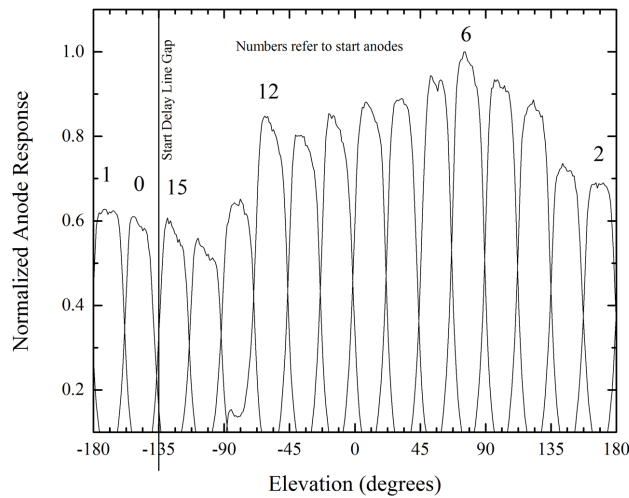


**Figure 5-5 HPCA Flight Model 4 (FM4 on MMS3) Elevation and Anode Gain Response**

Anode	FM1	FM2	FM3 (MMS4)	FM4 (MMS3)
0	1.69	1.96	1.58	1.63
1	1.30	1.58	1.35	1.47
2	1.39	1.52	1.42	1.42
3	1.30	1.36	1.30	1.31
4	1.20	1.16	1.23	1.11
5	1.09	1.21	1.07	1.04
6	1.05	1.14	1.00	1.00
7	1.02	1.00	1.09	1.09
8	1.04	1.02	1.05	1.14
9	1.00	1.04	1.06	1.06
10	1.06	1.09	1.13	1.13
11	1.10	1.12	1.07	1.16
12	1.07	1.14	1.04	1.05
13	1.29	1.23	1.28	1.33

14	1.65	1.41	1.38	1.65
15	1.70	1.67	1.64	1.68

**Table 5-5 Anode Specific Gain Correction Factors for HPCA Flight Models 1-4**

The elevation anode locations (yellow numbers on pads) and their look directions (black numbers within outer dotted circle in the figure) are shown in Figure 5-5.

The nominal centers of ion arrival directions for the instrument mounted on the spacecraft, are supplied in Table 5-6. The top-hat ESA configuration allows eight anodes to view one azimuthal direction, while the other eight view azimuthal space that is angularly displaced by 180°. The centers of the 16 anodes trace out circles of constant elevation as the spacecraft spins. As shown in Figure 5-6 and as indicated in Table 5-6, the anodes sample elevation space in its entirety;  $0^\circ \leq \beta \leq 180^\circ$ .

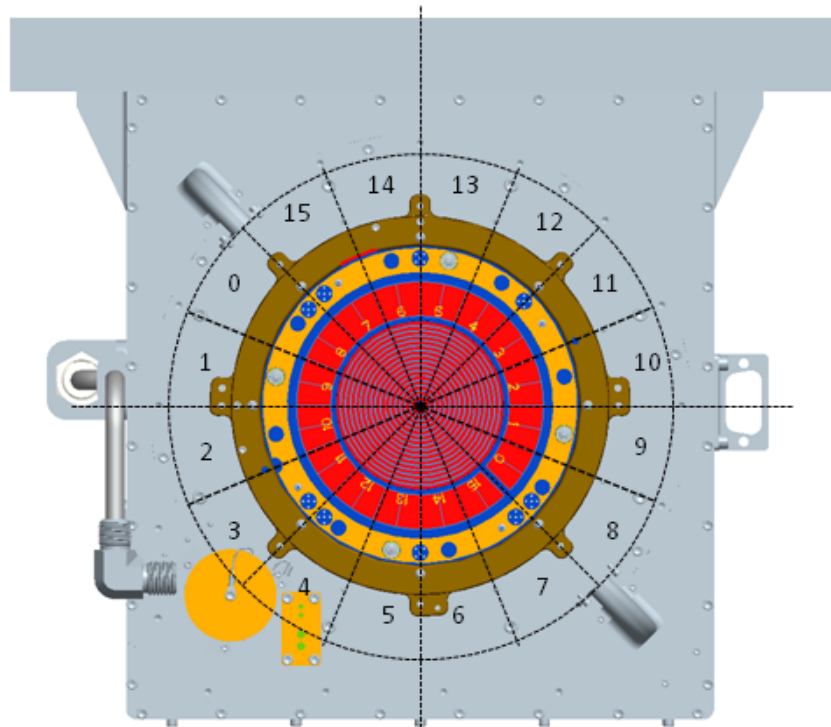


**Figure 5-6 HPCA Start Anode Arrangement and Field-of-View (FOV) Sectors for Instrument Mounted on MMS Spacecraft**

Anode	Centroid $\beta$ View ( $^\circ$ ) - Elevation
0	123.75
1	101.25
2	78.75
3	56.25
4	33.75
5	11.25
6	11.25
7	33.75
8	56.25

9	78.75
10	101.25
11	123.75
12	146.25
13	168.75
14	168.75
15	146.25

**Table 5-6 HPCA Start Nominal Anode Look Directions**

The FWHM field of view (FOV) is averaged over 16 anodes and 63 energies. This value, which is unique to each flight model, is provided in Table 5-7 along with the measured uncertainty in this parameter. The values in Table 5-6 and Table 5-7 are important for determining the moments of the plasma distribution function,  $f(\mathbf{v})$ . Computing these moments is a subject of later sections.

Flight Model	$\Delta\beta$ FWHM [°]	$\Delta\beta$ FWHM-Error [°]
1	24.0	0.7
2	24.8	0.7
3	24.1	0.7
4	23.8	0.7

**Table 5-7 HPCA Anode-Elevation Response**

In addition to gain, a correction for sky coverage is required in the calculations. Each HPCA anode covers approximately  $24^\circ$  or 0.419 radians (Table 5-7) in elevation. Anode centers are separated by  $22.5^\circ$  as shown in Table 5-6 (or 1.07 steradians). Per full energy sweep at a spin rate of 3 Hz,  $11.25^\circ$  of azimuthal angle space is covered. However, as shown in Figure 5-7, there is an excess of  $7^\circ$  (0.122 radians) in this field-of-view. Thus each anode sees 0.133 steradians of solid angle space at this spin rate. This gives an overestimation in particle flux for a given phase-space parcel, which leads to errors in  $f(\mathbf{v})$  and moment calculations. The following table (Table 5-8) provides the correction factors to prevent this error.

Anode	Solid Angle Space Correction
0	2.09
1	1.78
2	1.78
3	2.09
4	3.13
5	8.93
6	8.93
7	3.13
8	2.09
9	1.78
10	1.78
11	2.09
12	3.13
13	8.93
14	8.93
15	3.13

**Table 5-8 HPCA Solid Angle Space Correction Factors**



The next section addresses how the azimuth components of the plasma distribution are acquired.

### 5.3.2.3 Spacecraft Rotation – Azimuth

MMS has a nominal a spin period of 20 seconds. HPCA has a  $90^\circ$  azimuthal offset, relative to the DSS sun pulse detector, for elevation anodes 14, 15, 0, 1, 2, 3, 4, and 5, and  $270^\circ$  for the remaining anodes. Because of HPCA's elevation FOV and top-hat construction it sees  $4\pi$  steradians (full sky view) in half a spacecraft spin. In 10 seconds, HPCA will sweep the entire energy range of 1eV - 40 keV 16 times. While the uniform sample time at each energy step was already discussed in section 5.3.2.1, the dwell times were not. These time steps are not uniform, and increase with increasing voltage magnitude. Because of these steps the azimuthal look directions vary between adjacent steps. HPCA also has an inherent FWHM azimuthal resolution of  $7.0^\circ$ . This is plotted in Figure 5-6.

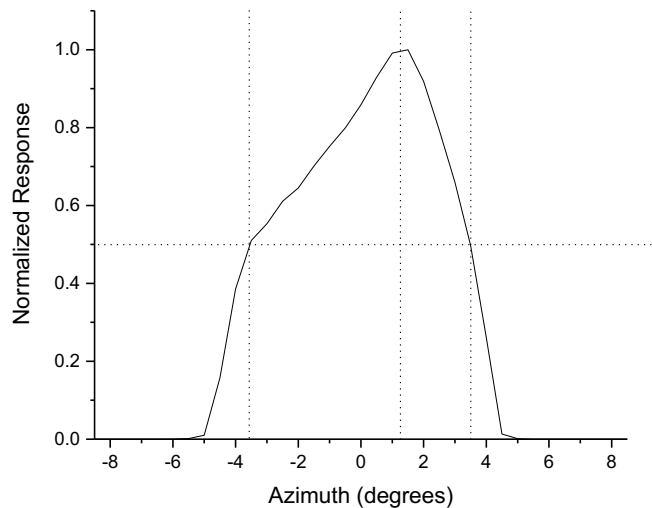


**Figure 5-7 HPCA Azimuth ( $\alpha$ ) Response**

The horizontal line in Figure 5-7 indicates the half-maximum response. The vertical lines, from left to right are the negative half-maximum limit, the center response, and the positive half-maximum limit. As seen here, HPCAs FWHM response is for all intents symmetric. However, the center response is offset by  $+1^\circ$ .

This angular response is swept through  $11.25^\circ$  in one energy sweep. In the graphs shown below (Figure 5-8), the sequence of energies and  $\alpha$  angles are shown as a function time, assuming at HPCA starts at Sweep Time = 0 on the x-axis. The first  $\alpha$ -look direction is  $0.275^\circ$  at an energy of 1.34 eV ( $V_{i=0} = -0.2477$  V), and the last acquisition at  $V_{i=62} = 6936$  V (37454.4 eV) occurs when the  $\alpha$ -look is  $10.940^\circ$ . At the end of the sweep 625 ms later  $\alpha = 11.25^\circ$ , and  $V_{i=63} = 0$  V.

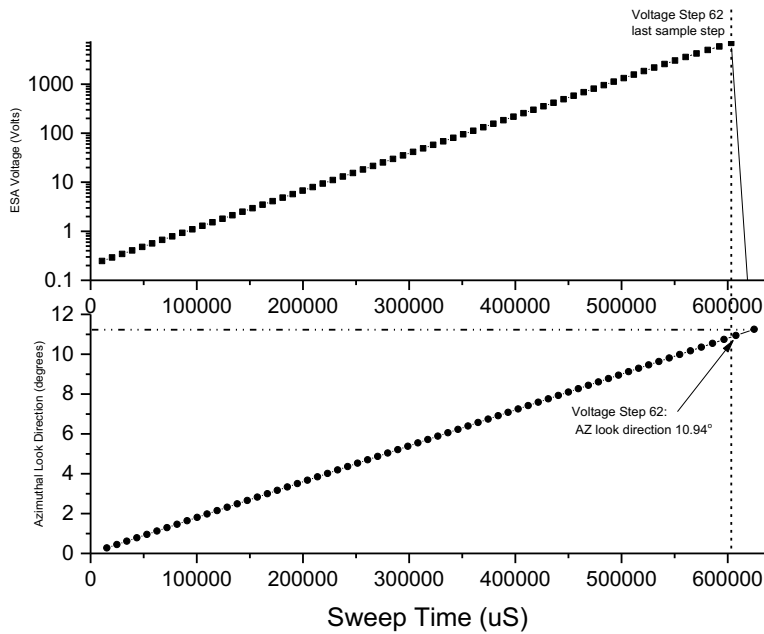


**Figure 5-8 HPCA Energy Sweeping and Azimuth Look Direction**

The  $\alpha$ -look directions, calculated at the center of each energy acquisition step, are in Table 5-9.

Energy Step	$\alpha$ -look (°) Anodes 14, 15, 0-5	$\alpha$ -look (°) Anodes 6-13
0	0	180
1	0.17	180.17
2	0.341	180.341
3	0.511	180.511
4	0.681	180.681
5	0.851	180.851
6	1.021	181.021
7	1.191	181.191
8	1.361	181.361
9	1.531	181.531
10	1.701	181.701
11	1.871	181.871
12	2.042	182.042
13	2.212	182.212
14	2.382	182.382
15	2.552	182.552
16	2.722	182.722
17	2.892	182.892
18	3.062	183.062

19	3.232	183.232
20	3.402	183.402
21	3.572	183.572
22	3.743	183.743
23	3.913	183.913
24	4.083	184.083
25	4.253	184.253
26	4.423	184.423
27	4.593	184.593
28	4.763	184.763
29	4.933	184.933
30	5.103	185.103
31	5.273	185.273
32	5.444	185.444
33	5.614	185.614
34	5.784	185.784
35	5.954	185.954
36	6.124	186.124
37	6.294	186.294
38	6.464	186.464
39	6.634	186.634
40	6.804	186.804
41	6.974	186.974
42	7.145	187.145
43	7.315	187.315
44	7.485	187.485
45	7.655	187.655
46	7.825	187.825
47	7.995	187.995
48	8.165	188.165
49	8.335	188.335
50	8.505	188.505
51	8.675	188.675
52	8.846	188.846
53	9.016	189.016
54	9.187	189.187
55	9.36	189.36
56	9.535	189.535
57	9.713	189.713
58	9.894	189.894
59	10.079	190.079

60	10.269	190.269
61	10.464	190.464
62	10.666	190.666
63	10.975	190.975

**Table 5-9 HPCA Azimuthal Arrival Directions in 1 Energy Sweep**

**Note: The values in this table are provided for diagnostic purposes. Whether they will be used to compute moments is still under consideration.**

The values shown in Table 5-9 were calculated using a spacecraft spin period of 20 seconds. If this is not the case then the general expression for the HPCA azimuthal look direction is:

$$\alpha_{HPCA} = \frac{121^\circ \pi}{180^\circ} + \frac{2\pi}{\tau_{sc}} \left( \Delta t + \frac{\tau_{acq}}{2} + k \times \tau_{acq} \right) \quad (5-7)$$

where in (5-7)  $\tau_{sc}$  is the spacecraft spin period, or the time between two sequential sun pulses.  $\Delta t$  is the time that has passed since the most recent sun pulse.  $\tau_{acq}$  is the acquisition time for a full energy sweep (0.625 s). Recall that (5-7) applies to elevation anodes 14, 15, and 0-5; for anodes 6-13 add  $\pi$  radians, up to a maximum of  $2\pi$ .

### 5.3.3 Geometric Factor

The convolved differential field-of-views (FOVs) in energy and solid angle space for a single HPCA elevation pixel is called its geometric factor; denoted G. G depends on energy (i) and on a pixel dependent gain factor (already discussed in Table 5-5). In this case G becomes  $G_{i,j}$  and it is expressed as (5-8).

$$G_{i,j} = A_{eff}(E_i, \beta_j, \alpha_k) \left\langle \frac{\Delta E}{E} \Delta \alpha \right\rangle \Delta \beta \quad (5-8)$$

where  $A_{eff}$  is an area external to the instrument which corresponds to the  $j^{\text{th}}$  start pixel's flux sensitivity; this also includes detector efficiencies. Also included are the integrated energy-azimuth response,  $\langle \Delta E/E \Delta \alpha \rangle$ , which is a differential quantity that is unique to the instrument and is energy independent.  $\Delta \beta$  is the FWHM elevation response of the HPCA flight model given in Table 5-7. We will first discuss  $A_{eff}$ .

#### 5.3.3.1 Effective Area

The  $A_{eff}$  of an elevation anode, as shown in (5-9), is a sensitive external area,  $A_0$ , divided by the gain factor of the respective anode,  $g_j$  (Table 5-5).

$$A_{eff} = \frac{A_0(E_i)}{g_j} \quad (5-9)$$

The anode with the largest response is assigned a  $g_j$  value of 1.  $A_0$  is computed with the calibration data from this anode. The  $A_0$  values of all four FMs, which are energy dependent, are provided in Table 5-10.

Voltage Step (i)	$A_0$ FM 1 (cm <sup>2</sup> )	$A_0$ FM 2 (cm <sup>2</sup> )	$A_0$ FM 3 (cm <sup>2</sup> ) (on mms4)	$A_0$ FM 4 (cm <sup>2</sup> ) (on mms3)
0	0.025	0.021	0.023	0.024
1	0.025	0.021	0.023	0.024

2	0.026	0.022	0.024	0.025
3	0.026	0.022	0.024	0.025
4	0.026	0.022	0.024	0.025
5	0.027	0.023	0.025	0.026
6	0.027	0.023	0.025	0.026
7	0.028	0.024	0.025	0.027
8	0.028	0.024	0.025	0.027
9	0.029	0.024	0.026	0.028
10	0.029	0.024	0.026	0.028
11	0.03	0.025	0.027	0.029
12	0.03	0.025	0.027	0.029
13	0.031	0.026	0.028	0.029
14	0.031	0.026	0.028	0.029
15	0.032	0.027	0.029	0.030
16	0.032	0.027	0.029	0.030
17	0.033	0.028	0.030	0.031
18	0.033	0.028	0.030	0.031
19	0.034	0.029	0.031	0.032
20	0.035	0.029	0.032	0.033
21	0.035	0.029	0.032	0.033
22	0.036	0.030	0.033	0.034
23	0.036	0.030	0.033	0.034
24	0.037	0.031	0.034	0.035
25	0.037	0.031	0.034	0.035
26	0.038	0.032	0.035	0.036
27	0.039	0.033	0.035	0.037
28	0.039	0.033	0.035	0.037
29	0.04	0.034	0.036	0.038
30	0.041	0.035	0.037	0.039
31	0.041	0.035	0.037	0.039
32	0.042	0.035	0.038	0.040
33	0.043	0.036	0.039	0.041
34	0.043	0.036	0.039	0.041
35	0.044	0.037	0.040	0.042
36	0.045	0.038	0.041	0.043
37	0.046	0.039	0.042	0.044
38	0.046	0.039	0.042	0.044
39	0.047	0.040	0.043	0.045
40	0.048	0.040	0.044	0.046
41	0.049	0.041	0.045	0.047
42	0.05	0.042	0.046	0.048
43	0.05	0.042	0.046	0.048
44	0.051	0.043	0.046	0.048
45	0.052	0.044	0.047	0.049
46	0.053	0.045	0.048	0.050
47	0.054	0.045	0.049	0.051
48	0.055	0.046	0.050	0.052
49	0.056	0.047	0.051	0.053
50	0.057	0.048	0.052	0.054
51	0.058	0.049	0.053	0.055
52	0.059	0.050	0.054	0.056
53	0.06	0.051	0.055	0.057
54	0.06	0.051	0.055	0.057

55	0.062	0.052	0.056	0.059
56	0.063	0.053	0.057	0.060
57	0.064	0.054	0.058	0.061
58	0.068	0.057	0.062	0.065
59	0.066	0.056	0.060	0.063
60	0.063	0.053	0.057	0.060
61	0.061	0.051	0.056	0.058
62	0.057	0.048	0.052	0.054
63	0	0.000	0.000	0.000

**Table 5-10  $A_0$ 's (updated per discussion in section 5.4.1)**

With the values of  $A_0$  and anode specific gain  $g_j$  discussed, we now turn to the integrated response,  $\langle \Delta E/E \Delta \alpha \rangle$ .

### 5.3.3.2 Integrated Energy-Azimuth Response, $\langle \Delta E/E \Delta \alpha \rangle$

The integrated response describes the instantaneous phase space view of HPCA, when it is tuned to center passband energy  $E_i$ , as described in (5-1) and in section 5.3.4.1. This response is a consequence of the ESA geometry; it is unique, and independent of energy. The values for FMs 1-4 are provided in Table 5-11.

Flight Model	$\langle \Delta E/E \Delta \alpha \rangle$ [eV/eV rads]
FM1	9.68E-03
FM2	8.27E-03
FM3 (on mms4)	7.63E-03
FM4 (on mms3)	7.46E-03

**Table 5-11  $\langle \Delta E/E \Delta \alpha \rangle$  for HPCA FMs 1-4**

These values are determined from the average instrument responses at all eight calibration energies.

### 5.3.3.3 Geometric Factor for HPCA

With the values included in the tables, the expression for geometric factor is now (5-10):

$$G_{i,j} = \frac{A_0(E_i)}{g_j} \langle \frac{\Delta E}{E} \Delta \alpha \rangle \Delta \beta \frac{\pi}{180^\circ} \quad (5-10)$$

where the appropriate values have now been inserted for  $A_0$ ,  $g_j$  and  $\Delta \beta$ . The  $\pi/180^\circ$  conversion is necessary because  $\Delta \beta$  is provided in degrees in Table 5-7. With these values, it is now possible to compute particle flux, the velocity distribution function,  $f(\mathbf{v})$ , and other data products. These will be covered in the later section 5.6.

## 5.4 HPCA CALIBRATION AND VALIDATION

### 5.4.1 Pre-Flight / On-Ground Calibration

The HPCA instruments were calibration on the ground, prior to delivery. As noted earlier in section 5.3.2 and in Table 5-4, the analyzer constants of all four HPCA flight models were determined from calibration results. Additionally, the  $A_0$  values were also acquired via calibration.

In August 2015, discrepancies in moment calculations (particularly number density) were discovered. These discrepancies were traced to errors in beam current measurement during calibration. Once this was realized, the research team began inspecting magnetosheath data at the highest resolution (fast survey) to determine the inter-instrument correction factors, assuming MMS1-HPCA is accurate. The distance between the spacecraft was negligible over the time space for this data, so the flux seen by each instrument is essentially the same. The data for each instrument was averaged over the time interval into count arrays of 64 energies by 16 elevation anodes. The expression for flux (5-12) was used, with G expanded into the form shown in (5-10). With equal fluxes, and the other values accounted for, the correction values were found by solving  $A_{0(FMk)} = C_k A_{0(FM1)}$ , where  $k = 2, 3, \text{ or } 4$ . The table determined from this analysis is reported in Table 5-10.

#### 5.4.2 In-Flight Calibration

HPCA performs in-flight MCP “calibrations” on a half-yearly basis. The goal of the MCP gain test is to look for degradation of signal in the counting statistics, and to determine if voltages need to be adjusted to increase the signal.

After analysis of the data on the ground, the science team decides whether it is necessary to increase the MCP value on the flight unit in order to maintain optimal counting per sensor in Table 5-12.

Spacecraft	Launch (2015)	Aug 8, 2017	Dec 6, 2017	Aug 17, 2021
MMS1	-800V	-850V	-850V	-900V
MMS2	-800V	-850V	-850V	-850V
MMS3	-700V	-800V	-800V	-800V
MMS4	-650V	-750V	-800V	-800V

**Table 5-12 Microchannel Plate (MCP) Voltage Settings**

#### 5.4.3 Compression Pipeline and Lossy Compression

Science processing on board consists of three distinct parts. Part 1 is the high-speed pipeline which controls the TOF data collection, reads the raw data from the TOF board into the FPGA, performs primary data decimation in the FPGA, reads the partially decimated data into the Sparc memory, and performs the secondary decimation in FSW. Part 2 consists of a sequence of operations performed on each data product as the product becomes available, rather than a pipeline, and generates each science data message sent to CIDP. The rate at which this data is processed is determined by the decimation factors. At the highest rate, Part 2 processing may occur more frequently than once per azimuth. Once a set of decimated data is available to the software, the Part 1 pipeline is directed to a second data buffer in the Sparc memory, and the first memory is processed (Part 2 processing). This processing consists of performing lossy compression and recomposing the data for subsequent operations. Part 3 is lossless compression, which ends with the data ready for inclusion in the CCSDS packet. The CCSDS packet is then composed (including adding header information such as the size [which is variable as a result of the lossless compression] and the checksum). The completed packet is handed back to the FPGA for transmission to the CIDP.

#### 5.4.4 Validation

HPCA validates by internal science use, and use by the external community. In addition, cross-comparison with other MMS instruments have also been done. Discrepancies found generate an internal review and assessment. This has led to several adjustments being made to processing, effective area, and RF correction factors. Additionally, any anomalies during the processing of the data (found by operations

personnel or by the science community), have led to reprocessing of the entire data set to correct the errors. The current version of data is v4.2.

## 5.5 MEASUREMENT ALGORITHM DESCRIPTIONS

### 5.5.1 Theoretical Basis

The information contained in this section can also be found in the HPCA instrument paper, though an effort has been made to summarize. The sections for the detailed discussion will be noted.

In order to meet science requirements the HPCA must be capable of determining the following parameters under all conditions and in all regions where reconnection occurs:

1. Ion energy from 10 eV to 30 keV with a resolution of 20%
2. Ion arrival directions over  $4\pi$  sr resolved into  $\sim 20^\circ \times 20^\circ$  pixels
3. Ion energy flux from  $\sim 10^4$  to  $\sim 3 \times 10^9$  keV/cm sr keV
4. Ion velocity distributions resolved into  $H^+$ ,  $He^{++}$ ,  $He^+$  and  $O^+$
5. Complete this suite of measurements within 10 s (1/2 spacecraft spin period)

[HPCA instrument paper; section 2 and 3]

From the above list of measurement requirements, corresponding performance requirements determined the detailed design of the instrument. The four ion species of interest have mass/charge ( $M_i/q$ ) ratios of  $i = 1, 2, 4$  and  $16$  which requires relatively low mass resolution  $M/\Delta M = 4$  for separation. Because the HPCA is a time-of-flight instrument we need TOF resolution  $T/\Delta T = 2M/\Delta M = 8$ . The table below summarizes the HPCA performance requirements.

Parameter	Variable	Required Value
Sensitivity	Energy-dependent geometric factor	$3 \times 10^{-3}$ cm <sup>2</sup> sr keV/keV (total)
	Maximum potential counting rate	20 MHz
Mass/charge	Range	1 to 16 amu/e
	Resolution ( $M/\Delta M$ )	4 at FWHM
Energy/charge	Range	10 eV to 40 keV
	Resolution ( $\Delta E/E$ )	$\leq 0.2$ FWHM
	Energy range scan rate	64 log-spaced samples per 0.625 s
Angle	Field-of-regard	$11.25^\circ \times 360^\circ$
	Field-of-view resolution	$11.25^\circ$ azimuth x $22.5^\circ$ elevation FWHM
	Number of pixels over $4\pi$ sr	32 azimuth x 16 elevations
Dynamic range	Maximum detectable energy flux	$\sim 3 \times 10^9$ keV/cm <sup>2</sup> sr s keV of $H^+$
	Minimum detectable energy flux	$\sim 3 \times 10^4$ keV/cm <sup>2</sup> sr s keV of $H^+$
	Dynamim range	$\geq 10^5$
Timing	3-D velocity distribution	$\frac{1}{2}$ spacecraft spin (10 s)
	2-D energy-elevation scan	625 ms
	Single sample all elevations	8.95 ms

**Table 5-13 HPCA Performance Requirements**

The instrument paper (section 4) discusses how some of the choices were made. The CMAD discussion in sections 5.3 and 5.4 walks through a high level instrument overview and how to apply the parameters that were chosen. For the in-depth details regarding the instrument design, including details regarding the Electrostatic Analyzer' (ESA) ion optics and electronics, see the instrument paper (section 6.1). For in-depth details about the Time of Flight Analyzer's (TOF) ion optics as well as the measurement and position coding, see section 6.2 of the instrument paper.



In section 6.4 of the instrument paper, the dynamic range choices are discussed in detail. The section addresses the problems that intense proton fluxes can produce high counting rates that could cause saturation which would swamp the signal, as well as a potential that the TOF electronics would not be able to keep up. These two problems are addressed in depth in this section, and how we chose to use the RF (radio frequency) system to reduce proton fluxes. Discussion in section 5.6.5 below show how corrections for RF are applied as needed.

### 5.5.2 Error Analysis and Known Features

One of the known features of the data is in regards to the volume of counts in the survey data vs the burst data. The lossy compression scheme was designed to throw away the least significant bit. The assumption was that single counts were just noise. Whereas this might normally be a good assumption, the problem is that HPCA was designed and built as a triple coincident system, such that single counts are truly counts, and not just noise. This problem was discovered in late 2018, when comparing burst data with survey data. Because of the higher levels of decimation in survey mode, the “single” counts were being added with other single counts and as such, they were making it through the lossy compression. In the case of the burst data, those same counts were removed, as if they were noise.

Testing was performed in late 2018, and an updated lossy table was loaded to the instruments on April 16, 2019. Unfortunately, the updated lossy compression table requires reloading after the instrument is powered off, which happened on August 17, 2019. This mistake was not caught until April 2021. The lossy compression table was loaded to all instruments on May 24, 2021. Additionally, all power-cycling procedures were updated to include the new lossy compression table. Lossy compression that does not remove single counts will be active from May 24, 2021 forward.

## 5.6 DATA PRODUCTION ALGORITHM DESCRIPTIONS

### 5.6.1 Level 0 - Counts

The counts acquired in a single energy sweep gives 63 values of the single acquisition product. At each  $(E, \beta, \alpha)$  combination, the count rate of ion species  $s$  is (5-11):

$$C_{i,j,k,s} = \frac{N_s(E_i, \beta_j, \alpha_k)}{\Delta\tau} \quad (5-11)$$

where  $N_s$  is the number of ions counted at energy  $i$ , on anode  $j$ , in azimuth  $k$ , in the acquisition period  $\Delta\tau$ . This data product requires no processing; it is a raw count measurement.

### 5.6.2 Level 1a - Flux

The next data product to compute is the ion flux of species  $s$ . This is the first derived data product. The raw counts are converted to flux in units of  $(e \text{ eV}^{-1} \text{ sr cm}^{-2} \text{ s}^{-1})$ . The conversion from count rate to flux is (5-12):

$$J_{i,j,k,s} = \frac{C_{i,j,k,s}}{G_j(E_i) \left(\frac{E_i}{q}\right)_s} \quad (5-12)$$

In this equation, the term in the numerator  $(E_i/q)_s$  is the mass-to-charge ratio for the ion species  $s$ : For singly charged ion species ( $\text{H}^+$ ,  $\text{He}^+$ ,  $\text{O}^+$ ), this is equal to  $(E_i/e)_s$  where  $e$  is the elementary charge ( $e=1.602 \times 10^{-19}$  coulombs); it is  $(E_i/2e)_s$  for doubly charged ions ( $\text{He}^{2+}$ ,  $\text{O}^{2+}$ ).

### 5.6.3 Level 1b - $f_s(v)$

The next data product to determine is the velocity distribution function of the ion species  $s$ . This product depends on the acquisition mode of the instrument which determines data decimation and timing. There are three HPCA survey modes: slow survey, fast survey, and burst. The nominal decimations and timing are shown in Table 5-14.

Mode	$\alpha$	$\beta$	Energies E	Full Sampling Period	$f(v)$ dimensions
Slow Survey	8	8	16	3.5 Spins (70 seconds)	5 species x $16\alpha$ x $16\beta$ x 64E
Fast Survey	8	8	16	1/2 Spin (10 seconds)	5 species x $16\alpha$ x $16\beta$ x 64E
Burst	16	16	64	1/2 Spin (10 Seconds)	5 species x $16\alpha$ x $16\beta$ x 64E

**Table 5-14 Nominal Decimations and Timing**

As shown in Table 5-14, the only acquisition mode that has data in full resolution is Burst mode. Slow and Fast Survey modes have the same decimation, but are sampled at different cadences. However, moment calculations will always be carried out with an array having the burst dimensions. Because of this computing the velocity distribution function is not straightforward and it requires some discussion. In fast and slow survey the 4 steps are co-added in energy, which means that the value is the sum of 4 smaller steps. To get this to a proper count rate this value should be divided by 4 times the acquisition time,  $\Delta\tau$ . For decimation in elevation the new values for each are divided by two, since they are summed over two elevation bins. This process is shown in Figure 5-9.

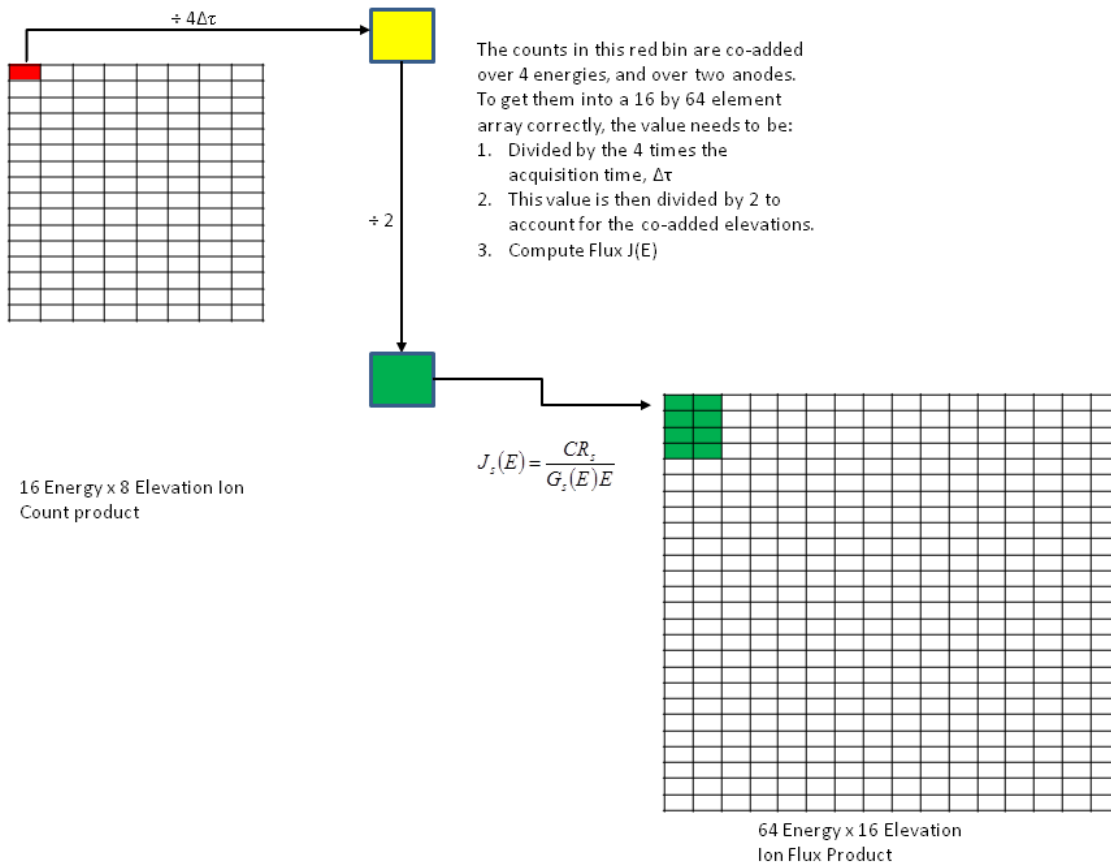


**Figure 5-9 Correcting Counts for Decimation Before Converting to Flux**

Up to this point, the flux is corrected for energy, and elevation decimations. It still needs to be corrected for the decimation in azimuth. This calculation only affects  $f_s(\nu)$ . Slow and fast survey azimuths are co-added, resulting in 8 azimuths per full sky view. Each of the 8 flux measurements need to be divided by 2 and made into 16 flux measurements. Once done,  $f_s(\nu)$  can be determined as shown in (5-13):

$$f_{i,j,k,s} = \frac{J_{i,j,k,s}}{2E_i} m_s^2 \quad (5-13)$$

where  $f_{i,j,k}$  is the velocity distribution function for each ion species  $s$ , in  $\text{cm}^{-6} \text{s}^3$ . The value  $m_s$  is actually the mass of the ion species  $s$  in AMU multiplied by  $1.0453453 \times 10^{-12} \text{ eV s}^2 / \text{AMU cm}^2$ . The methods used to compute the moments from this distribution will be discussed in the following sections.

#### 5.6.4 Plasma Distribution Moments

In the following sections computation of the distribution moments will be discussed.

### 5.6.4.1 Ion Number Density ( $n_s$ )

The number density of ion species  $s$  is determined by performing the following operation on the plasma distribution array  $f_{i,j,k,s}$ :

$$n_s = \sum_{k=0}^{15} \Delta\alpha \sum_{i=0}^{62} \frac{v_{i+1}^3 - v_i^3}{3} \sum_{j=0}^{15} 2 \sin(\bar{\beta}_j) \sin\left(\frac{\Delta\beta}{2}\right) f_{i,j,k,s} \quad (5-14)$$

where  $\Delta\alpha$  is the azimuthal angle coverage in an acquisition period ( $18.25^\circ = 0.318$  radians). The velocity values  $v_i, v_{i+1}$  are determined from the energy centroids, FWHM energy passbands of the instrument, and the mass of the respective ions,  $m_s$ .  $\Delta\beta$  is the measured average FWHM elevation response of the anodes,  $\Delta\beta = 22.44^\circ = 0.39$  radians.  $\beta_j$  is the look direction of the  $j^{\text{th}}$  anode from Table 5-6. The velocity bin size for each ion species  $s$ , at energy step  $i$  will be supplied in flight model specific spreadsheets.

With these simplifications, (5-14) can now be expressed in form (5-15):

$$n_s = 2\Delta\alpha \sin\left(\frac{\Delta\beta}{2}\right) \left[ \sum_{j=0 \dots 5,14,15} \frac{1}{\Lambda_j} \sin(\bar{\beta}_j) \sum_{k=0}^{15} \sum_{i=0}^{62} \frac{v_{i+1}^3 - v_i^3}{3} f_{i,(j=0 \dots 5,14,15),k,s} + \sum_{j=6 \dots 13} \frac{1}{\Lambda_j} \sin(\bar{\beta}_j) \sum_{k=0}^{15} \sum_{i=0}^{62} \frac{v_{i+1}^3 - v_i^3}{3} f_{i,(j=6 \dots 13),k,s} \right] \quad (5-15)$$

where  $n_s$  is in units of  $\text{cm}^{-3}$ . The  $j$  subscripts show that the sum is carried out over two parts  $j = 0-5,14,15$  and  $j = 6-13$ . This is because HPCA has two sets of anodes that view azimuth spaces that are displaced 180 degrees from each other, simultaneously. Also note the inclusion of the anode coverage correction factors,  $\Lambda_j$ , from Table 5-8 included in the  $j$  summation. These will be included in all moment calculations.

### 5.6.4.2 Ion Bulk Velocity ( $u_s$ )

The three components of the bulk velocity of ion species  $s$  are computed from the following:

$$u_{x,s} = \frac{2}{n_s} \sin\left(\frac{\Delta\alpha}{2}\right) \times \left[ \sum_{j=0 \dots 5,14,15} \frac{1}{\Lambda_j} \left[ \frac{1}{2} \Delta\beta - \frac{1}{2} \sin(\Delta\beta) \cos(2\bar{\beta}_j) \right] \sum_{k=0}^{15} \cos(\alpha_k) \sum_{i=0}^{62} \frac{v_{i+1}^4 - v_i^4}{4} f_{i,(j=0 \dots 5,14,15),k,s} + \sum_{j=6 \dots 13} \frac{1}{\Lambda_j} \left[ \frac{1}{2} \Delta\beta - \frac{1}{2} \sin(\Delta\beta) \cos(2\bar{\beta}_j) \right] \sum_{k=0}^{15} \cos(\alpha_k) \sum_{i=0}^{62} \frac{v_{i+1}^4 - v_i^4}{4} f_{i,(j=6 \dots 13),k,s} \right] \quad (5-16)$$

$$u_{y,s} = \frac{2}{n_s} \sin\left(\frac{\Delta\alpha}{2}\right) \times$$

$$\left[ \begin{array}{l} \sum_{j=0 \dots 5,14,15} \frac{1}{\Lambda_j} \left[ \frac{1}{2} \Delta\beta - \frac{1}{2} \sin(\Delta\beta) \cos(2\bar{\beta}_j) \right] \sum_{k=0}^{15} \sin(\alpha_k) \sum_{i=0}^{62} \frac{v_{i+1}^4 - v_i^4}{4} f_{i,(j=0 \dots 5,14,15),k,s} + \\ \sum_{j=6 \dots 13} \frac{1}{\Lambda_j} \left[ \frac{1}{2} \Delta\beta - \frac{1}{2} \sin(\Delta\beta) \cos(2\bar{\beta}_j) \right] \sum_{k=0}^{15} \sin(\alpha_k) \sum_{i=0}^{62} \frac{v_{i+1}^4 - v_i^4}{4} f_{i,(j=6 \dots 13),k,s} \end{array} \right]$$

$$u_{z,s} = \frac{1}{2n_s} \Delta\alpha \sin(\Delta\beta) \times \left[ \begin{array}{l} \sum_{j=0 \dots 5,14,15} \frac{1}{\Lambda_j} \sin(2\bar{\beta}_j) \sum_{k=0}^{15} \sum_{i=0}^{62} \frac{v_{i+1}^4 - v_i^4}{4} f_{i,(j=0 \dots 5,14,15),k,s} \\ + \sum_{j=6 \dots 13} \frac{1}{\Lambda_j} \sin(2\bar{\beta}_j) \sum_{k=0}^{15} \sum_{i=0}^{62} \frac{v_{i+1}^4 - v_i^4}{4} f_{i,(j=6 \dots 13),k,s} \end{array} \right]$$

The vector  $u_s$  is now expressed component wise as:

$$u_s = u_{x,s} \hat{i} + u_{y,s} \hat{j} + u_{z,s} \hat{k}$$

where  $\Delta\beta$ , and  $\Delta\alpha$  have already been discussed. These equations result in velocity components in units of  $\text{cm s}^{-1}$ . However, they need to be reported in units of  $\text{km s}^{-1}$ . To make this conversion multiply the components by the conversion factor  $1 \text{ km} / 10^5 \text{ cm}$ .

### 5.6.4.3 Scalar Ion Temperature

The scalar ion temperature is determined with the following formula:

$$T_s = \left[ \begin{array}{l} 2\Delta\alpha \frac{m_s}{3n_s} \sin\left(\frac{\Delta\beta}{2}\right) \sum_{j=0 \dots 5,14,15} \frac{1}{\Lambda_j} \sin(\bar{\beta}_j) \sum_{k=0}^{15} \sum_{i=0}^{62} \frac{v_{i+1}^5 - v_i^5}{5} f_{i,0 \dots 5,14,15,k,s} \\ + 2\Delta\alpha \frac{m_s}{3n_s} \sin\left(\frac{\Delta\beta}{2}\right) \sum_{j=6 \dots 13} \frac{1}{\Lambda_j} \sin(\bar{\beta}_j) \sum_{k=0}^{15} \sum_{i=0}^{62} \frac{v_{i+1}^5 - v_i^5}{5} f_{i,j=6 \dots 13,k,s} \end{array} \right] - \frac{u_s^2 m_s}{3} \quad (5-17)$$

where the value of  $m_s$  is given in the following table, in units of  $\text{eV s}^2/\text{cm}^2$ . At the end of the calculation, the species specific scalar temperature is reported in eV.

Ion Species	Mass-to-Charge Ratio (M/q) [AMU/e]	$m_s$ [eV s <sup>2</sup> /cm <sup>2</sup> ]
H <sup>+</sup>	1	1.04535E-12
He <sup>++</sup> (alpha particle)	2	4.18138E-12
He <sup>+</sup>	4	4.18138E-12
O <sup>++</sup> (Doubly Charged Oxygen)	8	1.67255E-11
O <sup>+</sup>	16	1.67255E-11

**Table 5-15  $m_s$  values for Temperature Calculation**

Note that the bulk velocity,  $u_s$ , is used in (5-17) is of form (5-18):

$$\|u_s\| = \sqrt{u_{x,s}^2 + u_{y,s}^2 + u_{z,s}^2} \quad (5-18)$$

#### 5.6.4.4 Ion Temperature Tensor

The ion temperature tensor is computed from the pressure tensor,  $P_{ij}$ . The nine components of the tensor are computed from:

First the diagonal terms:

$$P_{xx,s} = m_s \sum_{k=0}^{15} \alpha_{k+1} - \alpha_k + \sin(\alpha_{k+1}) - \sin(\alpha_k) \sum_{i=0}^{62} \frac{v_{i+1}^5 - v_i^5}{5} - 2u_s \frac{v_{i+1}^4 - v_i^4}{4} \\ + u_s^2 \frac{v_{i+1}^3 - v_i^3}{3} \sum_{j=0}^{15} \frac{1}{12} [\cos(3\beta_{j+1}) - \cos(3\beta_j) + 9(\cos(\beta_{j+1}) - \cos(\beta_j))] f_{i,j,k,s}$$

To remove confusion from the subscripts, we first take note that:

$$\alpha_{k+1} - \alpha_k = \Delta\alpha$$

which is the 18.25 degrees (based on a 20 second spin period) used in previous calculations.

We can also use:

$$\sin(\alpha_{k+1}) - \sin(\alpha_k) = 2 \cos\left(\frac{\alpha_{k+1} + \alpha_k}{2}\right) \sin\left(\frac{\alpha_{k+1} - \alpha_k}{2}\right) \quad (5-19)$$

Then:

$$\frac{\alpha_{k+1} + \alpha_k}{2} = \alpha_k$$

which is the midpoint of the azimuth FOV during a single energy sweep. With these substitutions  $P_{xx,s}$  becomes:

$$P_{xx,s} = m_s \sum_{k=0}^{15} \frac{\Delta\alpha}{2} + \frac{1}{2} \cos(\alpha_k) \sin(\Delta\alpha) \sum_{i=0}^{62} \frac{v_{i+1}^5 - v_i^5}{5} \\ + \sum_{j=0}^{15} \left[ \frac{3}{2} \sin(\beta_j) \sin\left(\frac{\Delta\beta}{2}\right) - \frac{1}{6} \sin(3\beta_j) \sin\left(3\frac{\Delta\beta}{2}\right) \right] f_{i,j,k,s} \\ - m_s n_s u_{x,s}^2$$

Which is difficult to work with because of the sum over  $k$ . This can be re-expressed as:

$$\begin{aligned}
p_{xx,s} = m_s \left[ \sum_{j=0 \dots 5,14,15}^{15} \frac{1}{\Lambda_j} \left[ \frac{3}{2} \sin(\beta_j) \sin\left(\frac{\Delta\beta}{2}\right) - \frac{1}{6} \sin(3\beta_j) \sin\left(3\frac{\Delta\beta}{2}\right) \right] \sum_{k=0}^{15} \frac{\Delta\alpha}{2} \right. \\
+ \frac{1}{2} \cos(2\alpha_k) \sin(\Delta\alpha) \sum_{i=0}^{62} \frac{v_{i+1}^5 - v_i^5}{5} f_{i,(j=0 \dots 5,14,15),k,s} \\
+ \sum_{j=6 \dots 13}^{15} \frac{1}{\Lambda_j} \left[ \frac{3}{2} \sin(\beta_j) \sin\left(\frac{\Delta\beta}{2}\right) \right. \\
\left. - \frac{1}{6} \sin(3\beta_j) \sin\left(3\frac{\Delta\beta}{2}\right) \right] \sum_{k=0}^{15} \frac{\Delta\alpha}{2} \\
\left. + \frac{1}{2} \cos(2\alpha_k) \sin(\Delta\alpha) \sum_{i=0}^{62} \frac{v_{i+1}^5 - v_i^5}{5} f_{i,(j=6 \dots 13),k,s} \right] - m_s n_s u_{x,s}^2
\end{aligned}$$

The remaining terms are much simpler to handle. Starting with  $P_{yy,s}$

$$\begin{aligned}
P_{yy,s} = m_s \left[ \sum_{j=0 \dots 5,14,15}^{15} \frac{1}{\Lambda_j} \left[ \frac{3}{2} \sin(\beta_j) \sin\left(\frac{\Delta\beta}{2}\right) - \frac{1}{6} \sin(3\beta_j) \sin\left(3\frac{\Delta\beta}{2}\right) \right] \sum_{k=0}^{15} \frac{\Delta\alpha}{2} \right. \\
- \frac{1}{2} \cos(2\alpha_k) \sin(\Delta\alpha) \sum_{i=0}^{62} \frac{v_{i+1}^5 - v_i^5}{5} f_{i,(j=0 \dots 5,14,15),k,s} \\
+ \sum_{j=6 \dots 13}^{15} \frac{1}{\Lambda_j} \left[ \frac{3}{2} \sin(\beta_j) \sin\left(\frac{\Delta\beta}{2}\right) - \frac{1}{6} \sin(3\beta_j) \sin\left(3\frac{\Delta\beta}{2}\right) \right] \sum_{k=0}^{15} \frac{\Delta\alpha}{2} \\
\left. - \frac{1}{2} \cos(2\alpha_k) \sin(\Delta\alpha) \sum_{i=0}^{62} \frac{v_{i+1}^5 - v_i^5}{5} f_{i,(j=6 \dots 13),k,s} \right] - m_s n_s u_{y,s}^2
\end{aligned}$$

$$\begin{aligned}
P_{zz,s} = m_s \Delta\alpha \left[ \sum_{j=0 \dots 5,14,15}^{15} \frac{1}{\Lambda_j} \left[ \frac{1}{6} \sin(3\beta_j) \sin\left(3\frac{\Delta\beta}{2}\right) \right. \right. \\
+ \left. \frac{1}{2} \sin(\beta_j) \sin\left(\frac{\Delta\beta}{2}\right) \right] \sum_{k=0}^{15} \sum_{i=0}^{62} \frac{v_{i+1}^5 - v_i^5}{5} f_{i,(j=0 \dots 5,14,15),k,s} \\
+ \sum_{j=6 \dots 13}^{15} \frac{1}{\Lambda_j} \left[ \frac{1}{6} \sin(3\beta_j) \sin\left(3\frac{\Delta\beta}{2}\right) \right. \\
\left. + \frac{1}{2} \sin(\beta_j) \sin\left(\frac{\Delta\beta}{2}\right) \right] \sum_{k=0}^{15} \sum_{i=0}^{62} \frac{v_{i+1}^5 - v_i^5}{5} f_{i,(j=6 \dots 13),k,s} \left. \right] - m_s n_s u_{z,s}^2
\end{aligned}$$

Now the off diagonal terms with some degeneracy:

$$\begin{aligned}
P_{xy,s} = m_s & \left[ \sum_{j=0 \dots 5,14,15}^{15} \frac{1}{\Lambda_j} \left[ \frac{3}{2} \sin(\beta_j) \sin\left(\frac{\Delta\beta}{2}\right) \right. \right. \\
& - \left. \frac{1}{6} \sin(3\beta_j) \sin\left(3\frac{\Delta\beta}{2}\right) \right] \sum_{k=0}^{15} \left[ \frac{1}{2} \sin(2\alpha_k) \sin(\Delta\alpha) \right] \sum_{i=0}^{62} \frac{v_{i+1}^5 - v_i^5}{5} f_{i,(j=0 \dots 5,14,15),k,s} \\
& + \sum_{j=6 \dots 13}^{15} \frac{1}{\Lambda_j} \left[ \frac{3}{2} \sin(\beta_j) \sin\left(\frac{\Delta\beta}{2}\right) \right. \\
& - \left. \frac{1}{6} \sin(3\beta_j) \sin\left(3\frac{\Delta\beta}{2}\right) \right] \sum_{k=0}^{15} \left[ \frac{1}{2} \sin(2\alpha_k) \sin(\Delta\alpha) \right] \sum_{i=0}^{62} \frac{v_{i+1}^5 - v_i^5}{5} f_{i,(j=6 \dots 13),k,s} \left. \right] \\
& - m_s n_s u_{x,s} u_{y,s}
\end{aligned}$$

$$P_{yx,s} = P_{xy,s}$$

$$\begin{aligned}
P_{xz,s} = m_s & \left[ \sum_{j=0 \dots 5,14,15}^{15} \frac{1}{\Lambda_j} \left[ \frac{1}{2} \cos(\beta_j) \sin\left(\frac{\Delta\beta}{2}\right) \right. \right. \\
& - \left. \frac{1}{6} \cos(3\beta_j) \sin\left(3\frac{\Delta\beta}{2}\right) \right] \sum_{k=0}^{15} \left[ 2 \cos(\alpha_k) \sin\left(\frac{\Delta\alpha}{2}\right) \right] \sum_{i=0}^{62} \frac{v_{i+1}^5 - v_i^5}{5} f_{i,(j=0 \dots 5,14,15),k,s} \\
& + \sum_{j=6 \dots 13}^{15} \frac{1}{\Lambda_j} \left[ \frac{1}{2} \cos(\beta_j) \sin\left(\frac{\Delta\beta}{2}\right) \right. \\
& - \left. \frac{1}{6} \cos(3\beta_j) \sin\left(3\frac{\Delta\beta}{2}\right) \right] \sum_{k=0}^{15} \left[ 2 \cos(\alpha_k) \sin\left(\frac{\Delta\alpha}{2}\right) \right] \sum_{i=0}^{62} \frac{v_{i+1}^5 - v_i^5}{5} f_{i,(j=6 \dots 13),k,s} \left. \right] \\
& - m_s n_s u_{x,s} u_{z,s}
\end{aligned}$$

$$P_{zx,s} = P_{xz,s}$$

$$\begin{aligned}
& P_{yz,s} \\
= m_s & \left[ \sum_{j=0 \dots 5,14,15}^{15} \frac{1}{\Lambda_j} \left[ \frac{1}{2} \cos(\beta_j) \sin\left(\frac{\Delta\beta}{2}\right) \right. \right. \\
& - \left. \frac{1}{6} \cos(3\beta_j) \sin\left(3\frac{\Delta\beta}{2}\right) \right] \sum_{k=0}^{15} \left[ 2 \sin(\alpha_k) \sin\left(\frac{\Delta\alpha}{2}\right) \right] \sum_{i=0}^{62} \frac{v_{i+1}^5 - v_i^5}{5} f_{i,(j=0 \dots 5,14,15),k,s} \\
& + \sum_{j=6 \dots 13}^{15} \frac{1}{\Lambda_j} \left[ \frac{1}{2} \cos(\beta_j) \sin\left(\frac{\Delta\beta}{2}\right) \right. \\
& - \left. \frac{1}{6} \cos(3\beta_j) \sin\left(3\frac{\Delta\beta}{2}\right) \right] \sum_{k=0}^{15} \left[ 2 \sin(\alpha_k) \sin\left(\frac{\Delta\alpha}{2}\right) \right] \sum_{i=0}^{62} \frac{v_{i+1}^5 - v_i^5}{5} f_{i,(j=6 \dots 13),k,s} \left. \right] \\
& - m_s n_s u_{y,s} u_{z,s}
\end{aligned}$$

$$P_{zy,s} = P_{yz,s}$$



With the Pressure Tensor expressed as:

$$P_s = \begin{bmatrix} P_{xx,s} & P_{yx,s} & P_{zx,s} \\ P_{xy,s} & P_{yy,s} & P_{zy,s} \\ P_{xz,s} & P_{yz,s} & P_{zz,s} \end{bmatrix}$$

where the units of pressure are eV/cm<sup>3</sup>; 1 eV/cm<sup>3</sup> = 1.602e-4 nanopascals.

To diagonalize the tensor we use the algorithm devised by Joachim Kopp [2008].  
When diagonalized, P has the form:

$$P'_s = \begin{bmatrix} P'_{xx,s} & 0 & 0 \\ 0 & P'_{yy,s} & 0 \\ 0 & 0 & P'_{zz,s} \end{bmatrix}$$

where ' indicates the component following diagonalization.

From the diagonalized form of the pressure tensor, we then determine  $T_s$  from:

$$T_s = \frac{P'_s}{n_s}$$

Where  $n_s$  is the number density of ion species  $s$  determined previously.

### 5.6.5 Data Products with RF

When computing flux with RF, multiply the counts for ion species  $s$  by the values specific to the energy step and ion species. This needs to be done for energy steps 36 - 49 (14 steps in all). Three RF tables are built: one which attenuates proton flux by 50%, one that attenuates 90%, and one more that decreases proton flux by a 99%. The computation for the flux is then:

$$J_{i,j,k,s} = \frac{C_{i,j,k,s} \varepsilon_i}{G_j(E_i) E_i} \quad (5-20)$$

where  $\varepsilon_i$  is the attenuation correction from one of the 3 tables. Calculations of  $f(v)$  and moments follow directly from these values.

### 5.6.6 Level 2 Data Products: In the Magnetic Field Reference Frame

HPCA data products and moments are computed in the spacecraft reference frame using the magnetic field data acquired with the magnetometer probes on each of the spacecraft. Scalar moments, such as the number density and scalar temperature require no transformation. The remainder of this section will focus on the values which do; bulk velocity, and the pressure/temperature tensor.

#### 5.6.6.1 Bulk Velocity in the Magnetic Field Frame

Transforming the bulk velocity into the magnetic field frame requires that we first determine a magnetic field unit vector:

$$\hat{\mathbf{b}} = \frac{\vec{B}}{\|B\|} = \frac{B_x \hat{i} + B_y \hat{j} + B_z \hat{k}}{\sqrt{B_x^2 + B_y^2 + B_z^2}} \quad (5-21)$$

Once  $\mathbf{b}$  is determined, the magnitude of the bulk velocity of species  $s$  in the direction of the magnetic field is:

$$V_{\parallel,s} = \vec{u}_s \cdot \hat{\mathbf{b}} = u_{x,s} b_x + u_{y,s} b_y + u_{z,s} b_z \quad (5-22)$$

and the velocity vector of the ion species, parallel to the magnetic field (v-parallel) is then:

$$\vec{V}_{\parallel,s} = V_{\parallel,s} \hat{\mathbf{b}} = V_{\parallel,s} b_x \hat{i} + V_{\parallel,s} b_y \hat{j} + V_{\parallel,s} b_z \hat{k} \quad (5-23)$$

Once found, we can then use the parallel velocity vector to find the velocity vector perpendicular to the magnetic field (v-perpendicular):

$$\vec{V}_{\perp,s} = \vec{u}_s - \vec{V}_{\parallel,s} = (u_{x,s} - V_{\parallel,x,s}) \hat{i} + (u_{y,s} - V_{\parallel,y,s}) \hat{j} + (u_{z,s} - V_{\parallel,z,s}) \hat{k} \quad (5-24)$$

### 5.6.6.2 F(v) in Field Aligned Coordinates

Expressing the velocity distribution function in the magnetic field frame involves a translation in velocity, and a rotation. For each bin  $f_{ijk}$  in the discretized distribution function (remember that 16 adjacent azimuths/full energy sweeps constitute a full-sky observation) there will be three vector components associated with that bin, that represent the velocity relative to a component system in which the magnetic field is directed in the positive  $z$  direction. The vector components in translated into the magnetic field frame (the primed coordinate system) are determined from the base system (unprimed system) with the following:

$$\begin{aligned} \vec{v}'_{ijk,s} &= \vec{v}_{ijk,s} - \vec{V}_{\perp,H^+} \\ &= (v_{x,ijk,s} - V_{\perp,x,H^+}) \hat{i} + (v_{y,ijk,s} - V_{\perp,y,H^+}) \hat{j} \\ &\quad + (v_{z,ijk,s} - V_{\perp,z,H^+}) \hat{k} \end{aligned} \quad (5-25)$$

where  $v_{x,ijk,s}$  is:

$$v_{x,ijk,s} = \sqrt{\frac{2E_i}{m_s}} \sin(\beta_j) \cos(\alpha_k) \quad (5-26)$$

$v_{y,ijk,s}$  is:

$$v_{y,ijk,s} = \sqrt{\frac{2E_i}{m_s}} \sin(\beta_j) \sin(\alpha_k) \quad (5-27)$$

and:

$$v_{z,ijk,s} = \sqrt{\frac{2E_i}{m_s}} \cos(\beta_j) \quad (5-28)$$

Each primed velocity value is computed on a bin-by-bin basis. The energies  $E_i$  are instrument specific and based on the voltage at each step with the analyzer constants from Table 5-2. The  $m_s$  values are found in Table 5-15. For instance,  $f_{000,H^+}$  will be accompanied by values of:

$$v'_{x,000,H^+} = \sqrt{\frac{2E_0}{m_s}} \sin(123.75^\circ) \cos(180^\circ) - (u_{x,H^+} - V_{\parallel x,H^+}) \quad (5-29)$$

$$v'_{y,000,H^+} = \sqrt{\frac{2E_0}{m_s}} \sin(123.75^\circ) \sin(180^\circ) - (u_{y,H^+} - V_{\parallel y,H^+}) \quad (5-30)$$

$$v'_{z,000,H^+} = \sqrt{\frac{2E_0}{m_s}} \cos(123.75^\circ) - (u_{z,H^+} - V_{\parallel z,H^+}) \quad (5-31)$$

and so on, until all 64 velocities, 16 elevation, and 16 azimuths are accounted for.

In addition to the velocity translation, the coordinate system must be rotated such that the magnetic field is in the direction of the +Z axis. The unit vectors of this coordinate system are:

$$\hat{X}_s = \frac{(\hat{b} \times \vec{u}_s) \times \hat{b}}{\|\vec{u}_s\|} = \frac{[-(b_x u_z - u_x b_z) b_z - (b_x u_y - u_x b_y) b_y] \hat{i} + [(b_y u_z - u_y b_z) b_z - (b_x u_y - u_x b_y) b_x] \hat{j} + [(b_y u_z - u_y b_z) b_y - (b_x u_z - u_x b_z) b_x] \hat{k}}{\|\vec{u}_s\|} \quad (5-32)$$

$$\hat{Y}_s = \frac{(\hat{b} \times \vec{u}_s)}{\|\vec{u}_s\|} = \frac{(b_y u_{z,s} - b_z u_{y,s}) \hat{i} - (b_x u_{z,s} - b_z u_{x,s}) \hat{j} + (b_x u_{y,s} - b_y u_{x,s}) \hat{k}}{\|\vec{u}_s\|} \quad (5-33)$$

$$\hat{Z}_s = \hat{b} = \frac{B_x \hat{i} + B_y \hat{j} + B_z \hat{k}}{\sqrt{B_x^2 + B_y^2 + B_z^2}} = b_x \hat{i} + b_y \hat{j} + b_z \hat{k} \quad (5-34)$$

With the vector so determined, rotation matrix is:

$$T = \begin{bmatrix} \frac{[-(b_x u_z - u_x b_z) b_z - (b_x u_y - u_x b_y) b_y]}{\|\vec{u}_s\|} & \frac{[(b_y u_z - u_y b_z) b_z - (b_x u_y - u_x b_y) b_x]}{\|\vec{u}_s\|} & \frac{[(b_y u_z - u_y b_z) b_z - (b_x u_y - u_x b_y) b_x]}{\|\vec{u}_s\|} \\ \frac{(b_y u_{z,s} - b_z u_{y,s})}{\|\vec{u}_s\|} & \frac{(b_x u_{z,s} - b_z u_{x,s})}{\|\vec{u}_s\|} & \frac{(b_x u_{y,s} - b_y u_{x,s})}{\|\vec{u}_s\|} / b_z \\ b_x & b_y & b_z \end{bmatrix} \quad (5-35)$$

And the matrix used to rotate the velocity components in the field aligned coordinate system is the transpose of this matrix

$$T^t = \begin{bmatrix} \frac{[-(b_x u_z - u_x b_z) b_z - (b_x u_y - u_x b_y) b_y]}{\|\vec{u}_s\|} & \frac{(b_y u_{z,s} - b_z u_{y,s})}{\|\vec{u}_s\|} & b_x \\ \frac{[(b_y u_z - u_y b_z) b_z - (b_x u_y - u_x b_y) b_x]}{\|\vec{u}_s\|} & \frac{(b_x u_{z,s} - b_z u_{x,s})}{\|\vec{u}_s\|} & b_y \\ \frac{[(b_y u_z - u_y b_z) b_y - (b_x u_z - u_x b_z) b_x]}{\|\vec{u}_s\|} & \frac{(b_x u_{y,s} - b_y u_{x,s})}{\|\vec{u}_s\|} & b_z \end{bmatrix} \quad (5-37)$$

With the operation:

$$\vec{v}'_s = T^t \vec{v}'_s \quad (5-38)$$

From the primed coordinates in equation 6.

### 5.6.7 HPCA Quality Flags

Quality flags are described at the top of each CDF files and is defined as follows:

Quality Flag Value	Meaning
0	Bad
1	Good
2	Good, RF on, Background on
3	Good, RF on, Background on
4	Good, RF on, Background on
5	Good, RF on, Background on
6	Good, non-sweeping data

**Table 5-16 HPCA Quality Flags Definition**

These quality flags are used throughout the different files and many of the different science fields have their own quality indicators based on this description.

### 5.6.8 File Structure L2 Ion CDF File

Most variables in the ion files are preceded by mmsX\_hPCA\_ (with X being 1, 2, 3 or 4 depending upon the spacecraft on which the instrument is located). Names have been shorted here to allow for more space. The exception to the preceded name is the Epoch\_ variables.

Variable	Units	Type	Dim	Description
Epoch	Ns	CDF_TT2000	1	Start time for the record
Epoch_MINUS	Ms	CDF_UINT2	1	Delta start time for the record from the central time
Epoch_PLUS	Ms	CDF_UINT2	1	Delta stop time for the record from the central time
polar_anode_number	n/a	CDF_UINT2	16	Polar Anode Index Value
azimuth_decimation_factor	n/a	CDF_UINT2	1	Azimuth decimation factor
polar_decimation_factor	n/a	CDF_UINT2	1	Polar Anode decimation factor
energy_decimation_factor	n/a	CDF_UINT2	1	Energy decimation factor
sweep_table_number	n/a	CDF_UINT1	1	Sweep Table index as defined in the HPCA science algorithm document
start_azimuth	n/a	CDF_UINT1	1	Start azimuth
science_mode	n/a	CDF_UINT1	1	Science mode value as defined in the HPCA science algorithm document
ion_energy	eV/q	CDF_REAL4	63	Electron voltage associated with the ion counts
hplus_flux	$1/(\text{cm}^2 \text{ s sr eV})$	CDF_REAL8	16 x 63	Hydrogen+ Flux for all elevation anodes across all energies
hplus_phase_space_density	$\text{cm}^{-6} \text{ s}^3$	CDF_REAL8	16 x 63	Hydrogen+ Phase Space Density for all Elevation Anodes across all energies
hplus_data_quality	n/a	CDF_UINT2	1	Per sweep status for H+, see Data_Quality_Key global attribute
heplus_flux	$1/(\text{cm}^2 \text{ s sr eV})$	CDF_REAL8	16 x 63	Helium+ Flux for all elevation anodes across all energies
heplus_phase_space_density	$\text{cm}^{-6} \text{ s}^3$	CDF_REAL8	16 x 63	Helium+ Phase Space Density for all Elevation Anodes across all energies
heplus_data_quality	n/a	CDF_UINT2	1	Per sweep status for He+, see Data_Quality_Key global attribute
heplusplus_flux	$1/(\text{cm}^2 \text{ s sr eV})$	CDF_REAL8	16 x 63	Helium++ Flux for all elevation anodes across all energies
heplusplus_phase_space_density	$\text{cm}^{-6} \text{ s}^3$	CDF_REAL8	16 x 63	Helium++ Phase Space Density for all Elevation Anodes across all energies

heplusplus_data_quality	n/a	CDF_UINT2	1	Per sweep status for He <sup>++</sup> , see Data_Quality_Key global attribute
oplus_flux	1/(cm <sup>2</sup> s sr eV)	CDF_REAL8	16 x 63	Oxygen+ Flux for all elevation anodes across all energies
oplus_phase_space_density	cm <sup>-6</sup> s <sup>3</sup>	CDF_REAL8	16 x 63	Oxygen+ Phase Space Density for all Elevation Anodes across all energies
oplus_data_quality	n/a	CDF_UINT2	1	Per sweep status for O <sup>+</sup> , see Data_Quality_Key global attribute
B_GSE_sweep_avg	nT	CDF_REAL4	4	Magnetic field vector in DMPA plus Btotal (8 or 16 S/s), Despun MPA-aligned cartesian coordinates (from afg_srvy_l2pre_dmpa)
B_GSM_sweep_avg	nT	CDF_REAL4	4	Magnetic field vector in GSM plus Btotal (8 or 16 S/s), Geocentric Solar Magnetospheric (GSM) cartesian coordinates (see aft_srvy_l2pre_gsm)
Epoch_Angles	ns	CDF_TT2000	1	Start time for the Azimuth Angles Associated with each 1/2 spin
Epoch_MINUS_Angles	ms	CDF_UINT4	1	Delta start time for the record from the central time
Epoch_PLUS_Angles	ms	CDF_UINT4	1	Delta stop time for the record from the central time
azimuth_angles_degrees	degree	CDF_REAL8	16 x 16	Azimuth Angles in degrees for each anode for each HPCA half-spin
azimuth_angles_per_ev_degrees	degree	CDF_REAL8	16x16x63	Azimuth Angles per eV in degrees for each anode for each HPCA half-spin
centroid_elevation_angle	degree	CDF_DOUBLE	16	Center Elevation Angles of each of the Anodes
azimuth_index	n/a	CDF_UINT2	16	Azimuth index value
energy_step_number	n/a	CDF_UINT2	63	Energy step index value

**Table 5-17 L2 Ion CDF File**

### 5.6.9 File Structure L2 Moments CDF File

Most variables in the moments files are preceded by mmsX\_hpca\_ (with X being 1, 2, 3 or 4 depending upon the spacecraft on which the instrument is located). Names have been shorted here to allow for more space.

Variable	Units	Type	Dim	Description
Epoch	ns	CDF_TT2000	1	Start time for the record
Epoch_MINUS	ms	CDF_UINT2	1	Delta start time for the record from the central time
Epoch_PLUS	ms	CDF_UINT2	1	Delta stop time for the record from the central time
spin_number	n/a	CDF_UINT4	1	Spin Number for each HPCA half-spin
ion_energy	eV/q	CDF_REAL4	63	Electron Voltage associated with the ion counts
sweep_table_number	n/a	CDF_UINT1	1	Sweep Table Index as defined in the HPCA Science Algorithm Document
science_mode	n/a	CDF_UINT1	1	Science Mode Value as defined in the HPCA Science Algorithm Document
hplus_number_density	cm <sup>-3</sup>	CDF_REAL8	1	Number Density Hydrogen+ for each HPCA half-spin
hplus_ion_bulk_velocity	km/s	CDF_REAL8	3	Ion Bulk Velocity Hydrogen+ for each HPCA half-spin (x, y, z)
hplus_scalar_temperature	eV	CDF_REAL8	1	Scalar Temperature Hydrogen+ for each HPCA half-spin
hplus_ion_pressure	nPa	CDF_REAL8	3 x 3	Ion Pressure Tensor Hydrogen+ for each HPCA half-spin (xx,yx,zx,xy,yy,zy,xz,yz,zz)
hplus_temperature_tensor	eV	CDF_REAL8	3 x 3	Ion Temp. Tensor Hydrogen+ for each HPCA half-spin (xx,yx,zx,xy,yy,zy,xz,yz,zz)
heplus_number_density	cm <sup>-3</sup>	CDF_REAL8	1	Number Density Helium+ for each HPCA half-spin
heplus_ion_bulk_velocity	km/s	CDF_REAL8	3	Ion Bulk Velocity Helium+ for each HPCA half-spin (x, y, z)
heplus_scalar_temperature	eV	CDF_REAL8	1	Scalar Temperature Helium+ for each HPCA half-spin
heplus_ion_pressure	nPa	CDF_REAL8	3 x 3	Ion Pressure Tensor Helium+ for each HPCA half-spin (xx,yx,zx,xy,yy,zy,xz,yz,zz)
heplus_temperature_tensor	eV	CDF_REAL8	3 x 3	Ion Temp. Tensor Helium+ for each HPCA half-spin (xx,yx,zx,xy,yy,zy,xz,yz,zz)
heplusplus_number_density	cm <sup>-3</sup>	CDF_REAL8	1	Number Density Helium++ for each HPCA half-spin
heplusplus_ion_bulk_velocity	km/s	CDF_REAL8	3	Ion Bulk Velocity Helium++ for each HPCA half-spin (x, y, z)
heplusplus_scalar_temperature	eV	CDF_REAL8	1	Scalar Temperature Helium++ for each HPCA half-spin
heplusplus_ion_pressure	nPa	CDF_REAL8	3 x 3	Ion Pressure Tensor Helium++ for each HPCA half-spin (xx,yx,zx,xy,yy,zy,xz,yz,zz)
heplusplus_temperature_tensor	eV	CDF_REAL8	3 x 3	Ion Temp. Tensor Helium++ for each HPCA half-spin (xx,yx,zx,xy,yy,zy,xz,yz,zz)

oplus_number_density	cm <sup>-3</sup>	CDF_REAL8	1	Number Density Oxygen+ for each HPCA half-spin
oplus_ion_bulk_velocity	km/s	CDF_REAL8	3	Ion Bulk Velocity Oxygen+ for each HPCA half-spin (x, y, z)
oplus_scalar_temperature	eV	CDF_REAL8	1	Scalar Temperature Oxygen+ for each HPCA half-spin
oplus_ion_pressure	nPa	CDF_REAL8	3 x 3	Ion Pressure Tensor Oxygen+ for each HPCA half-spin (xx,yx,zx,xy,yy,zy,xz,yz,zz)
oplus_temperature_tensor	eV	CDF_REAL8	3 x 3	Ion Temp. Tensor Oxygen+ for each HPCA half-spin (xx,yx,zx,xy,yy,zy,xz,yz,zz)
B_GSE_spin_avg	nT	CDF_REAL4	4	Magnetic field vector in DMPA plus Btotal (8 or 16 S/s) for each HPCA half-spin (x, y, z, total) [see afg_srvy_l2pre_dmpa]
B_GSM_spin_avg	nT	CDF_REAL4	4	Magnetic field vector in GSM plus Btotal (8 or 16 S/s) for each HPCA half-spin (x, y, z, total) [see afg_srvy_l2pre_gsm]
hplus_ion_bulk_velocity_GSM	km/s	CDF_REAL8	3	Bulk Velocity in GSM for H+ for each HPCA half-spin (x, y, z)
hplus_tperp	eV	CDF_REAL8	1	Tperp H+ for each HPCA half-spin
hplus_tparallel	eV	CDF_REAL8	1	Tparallel H+ for each HPCA half-spin
hplus_vperp	km/s	CDF_REAL8	4	Vperp vector plus Magnitude for H+ for each HPCA half-spin (x, y, z, total)
hplus_vparallel	km/s	CDF_REAL8	4	Vparallel vector plus Magnitude for H+ for each HPCA half-spin (x, y, z, total)
hplus_vperp_GSM	km/s	CDF_REAL8	4	Vperp vector plus Magnitude in GSM for H+ for each HPCA half-spin (x, y, z, total)
hplus_vparallel_GSM	km/s	CDF_REAL8	4	Vparallel vector plus Magnitude in GSM for H+ for each HPCA half-spin (x, y, z, total)
heplus_ion_bulk_velocity_GSM	km/s	CDF_REAL8	3	Bulk Velocity in GSM for He+ for each HPCA half-spin (x, y, z)
heplus_tperp	eV	CDF_REAL8	1	Tperp He+ for each HPCA half-spin
heplus_tparallel	eV	CDF_REAL8	1	Tparallel He+ for each HPCA half-spin
heplus_vperp	km/s	CDF_REAL8	4	Vperp vector plus Magnitude for He+ for each HPCA half-spin (x, y, z, total)
heplus_vparallel	km/s	CDF_REAL8	4	Vparallel vector plus Magnitude for He+ for each HPCA half-spin (x, y, z, total)
heplus_vperp_GSM	km/s	CDF_REAL8	4	Vperp vector plus Magnitude in GSM for He+ for each HPCA half-spin (x, y, z, total)
heplus_vparallel_GSM	km/s	CDF_REAL8	4	Vparallel vector plus Magnitude in GSM for He+ for each HPCA half-spin (x, y, z, total)
heplusplus_ion_bulk_velocity_GSM	km/s	CDF_REAL8	3	Bulk Velocity in GSM for He++ for each HPCA half-spin (x, y, z)
heplusplus_tperp	eV	CDF_REAL8	1	Tperp He++ for each HPCA half-spin
heplusplus_tparallel	eV	CDF_REAL8	1	Tparallel He++ for each HPCA half-spin



heplusplus_vperp	km/s	CDF_REAL8	4	Vperp vector plus Magnitude for He++ for each HPCA half-spin (x, y, z, total)
heplusplus_vparallel	km/s	CDF_REAL8	4	Vparallel vector plus Magnitude for He++ for each HPCA half-spin (x, y, z, total)
heplusplus_vperp_GSM	km/s	CDF_REAL8	4	Vperp vector plus Magnitude in GSM for He++ for each HPCA half-spin (x, y, z, total)
heplusplus_vparallel_GSM	km/s	CDF_REAL8	4	Vparallel vector plus Magnitude in GSM for He++ for each HPCA half-spin (x, y, z, total)
oplus_ion_bulk_velocity_GSM	km/s	CDF_REAL8	3	Bulk Velocity in GSM for O+ for each HPCA half-spin (x, y, z)
oplus_tperp	eV	CDF_REAL8	1	Tperp O+ for each HPCA half-spin
oplus_tparallel	eV	CDF_REAL8	1	Tparallel O+ for each HPCA half-spin
oplus_vperp	km/s	CDF_REAL8	4	Vperp vector plus Magnitude for O+ for each HPCA half-spin (x, y, z, total)
oplus_vparallel	km/s	CDF_REAL8	4	Vparallel vector plus Magnitude for O+ for each HPCA half-spin (x, y, z, total)
oplus_vperp_GSM	km/s	CDF_REAL8	4	Vperp vector plus Magnitude in GSM for O+ for each HPCA half-spin (x, y, z, total)
oplus_vparallel_GSM	km/s	CDF_REAL8	4	Vparallel vector plus Magnitude in GSM for O+ for each HPCA half-spin (x, y, z, total)
MCP_VMON_MIN_converted	V	CDF_DOUBLE	1	Minimum Microchannel plate (MCP) voltage
TOF_VMON_MIN_converted	V	CDF_DOUBLE	1	Minimum Time of Flight (TOF) voltage

**Table 5-18 L2 Moments CDF File**

### 5.6.10 File Structure L2 TOF Counts CDF File

Variable	Units	Type	Dim	Description
Epoch	ns	CDF_TT2000	1	Start time for the record
Epoch_MINUS	ms	CDF_UINT2	1	Delta start time for the record from the central time
Epoch_PLUS	ms	CDF_UINT2	1	Delta stop time for the record from the central time
tof_energy	eV/q	CDF_FLOAT	8	Electron Voltage associated with the tof counts
tof_energy_delta_minus	eV	CDF_FLOAT	8	Delta eV for the record from the central TOF voltage
tof_energy_delta_plus	eV	CDF_FLOAT	8	Delta eV for the record from the central TOF voltage
tof_bin_index	n/a	CDF_UINT1	128	TOF binning index
tof_counts	counts	CDF_UINT2	8 x 128	TOF Counts for all angles, across all energies

**Table 5-19 L2 TOF Counts CDF File**

**5.7 APPENDIX A- HCPA REFERENCES**

The following is a list of applicable references and publications.

<b>Section</b>	<b>Document Number</b>	<b>Title</b>	<b>Revision/Date</b>
All	10160.13-HPCA_CONOPS	Hot Plasma Composition Analyzer Concept of Operations for the MMS mission	2010
All	10160.13-MMS-HPCA_IUM-01	HPCA Instrument User Manual (IUM)	2013
5.6.4.4	<a href="https://doi.org/10.1142/S0129183108012303">https://doi.org/10.1142/S0129183108012303</a>	J. Kopp, “Efficient Numerical Diagonalization of Hermitian $3 \times 3$ Matricies,” <i>International Journal of Modern Physics C</i> , vol. 19, no. 03.	March 2008
All	10160.13-MMS-HPCA_SCI_ALG_UM	MMS HPCA Science Algorithms and User Manual	20160310
5	670-Proj-Plan-CMAD	MMS Project Calibration & Measurement Algorithms Document (CMAD)	2020
All	<a href="https://doi.org/10.1007/s11214-014-0119-6">https://doi.org/10.1007/s11214-014-0119-6</a>	Young, D., J. L. Burch, R. G. Gomez, A. De Los Santos, G. P. Miller, P. Wilson IV, N. Paschalidis, S. A. Fuselier, K. Pickens, E. Hertzberg, C. J. Pollock, J. Scherrer, P. B. Wood, E. T. Donald, D. Aaron, J. Furman, D. George, R. S. Gurnee, R. S. Hourani, A. Jacques, T. Johnson, T. Orr, K. S. Pan, S. Persyn, S. Pope, J. Roberts, M. R. Stokes, K. J. Trattner, J. M. Webster (2016), Hot Plasma Composition Analyzer for the Magnetospheric Multiscale Mission, <i>Space Science Reviews</i> , 199(1-4), 407-470.	2016

**Table 5-20 HCPA Applicable Documents**

## 6.0 ENERGETIC PARTICLE DETECTOR (EPD)

### 6.1 EPD OVERVIEW

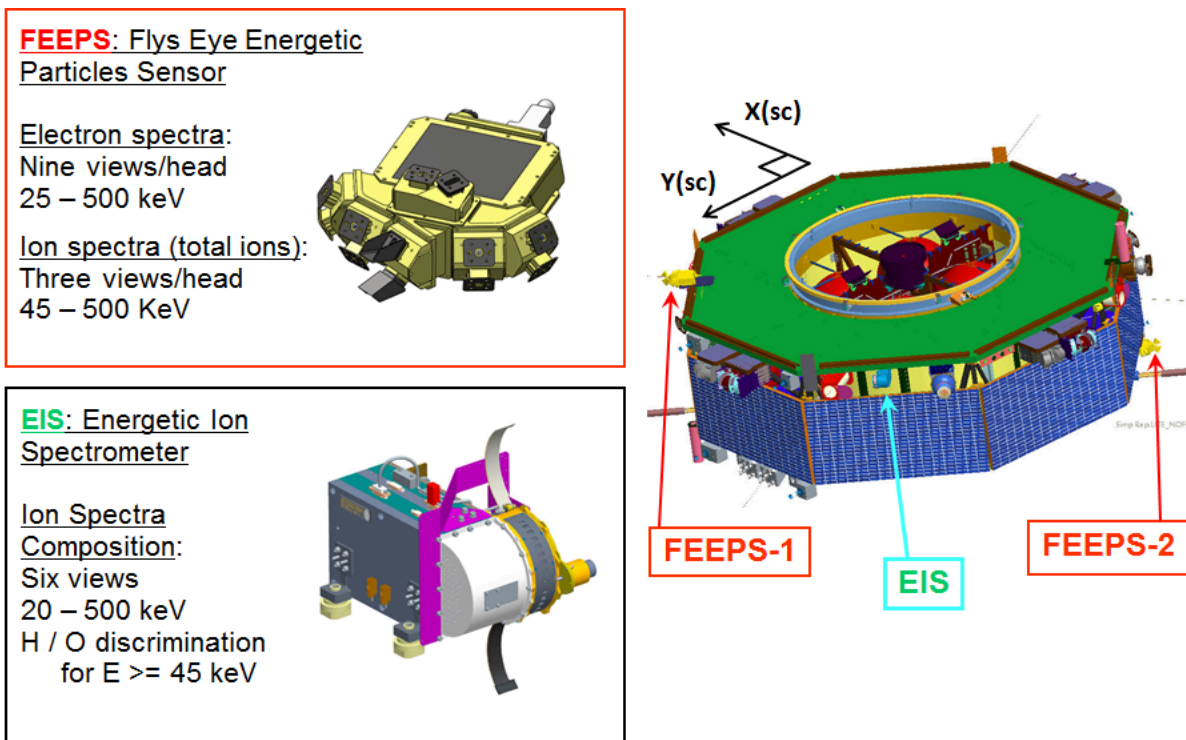


**Figure 6-1 Summary of the Capabilities and Spacecraft Mounting of the EPD Instruments: EIS and FEEPS. [Note that the energy ranges of measurements have varied somewhat over the course of the mission] (from Mauk et al., 2016)**

The science objectives and an overview of the Energetic Particle Detector (EPD) investigation are provided in Mauk et al. (2016). EPD comprises two different instrument types: the Energetic Ion Spectrometer (EIS; with a detailed description provided by Mauk et al., 2016) and the Fly’s Eye Energetic Particle Spectrometer (FEEPS; Blake et al., 2016). There are two FEEPS instruments and one EIS instrument on each spacecraft (Figure 6-1). They are intended to yield an instantaneous all-sky view for electrons (Figure 6-2) and fast all-sky sampling for ions. This set of sensors (two FEEPS instruments plus one EIS instrument) is identical on each of the four MMS spacecraft. To obtain true “allsky” electron sampling from the FEEPS sensors, it was necessary to mount one of the instruments on the instrument deck and the other onto the spacecraft subsystem deck (Figure 6-1). The two instruments are identical to each other, and they are designed such that when one of them is turned upside down with respect to the other, the fields of view complement each other (Figure 6-2). Also, the orientation of the ion sensors provides two fan-shaped fields of spaced  $120^\circ$  apart, with EIS providing the 3rd fan, resulting in EPD ion 3 sensors each located  $120^\circ$  apart (Figure 6-2).

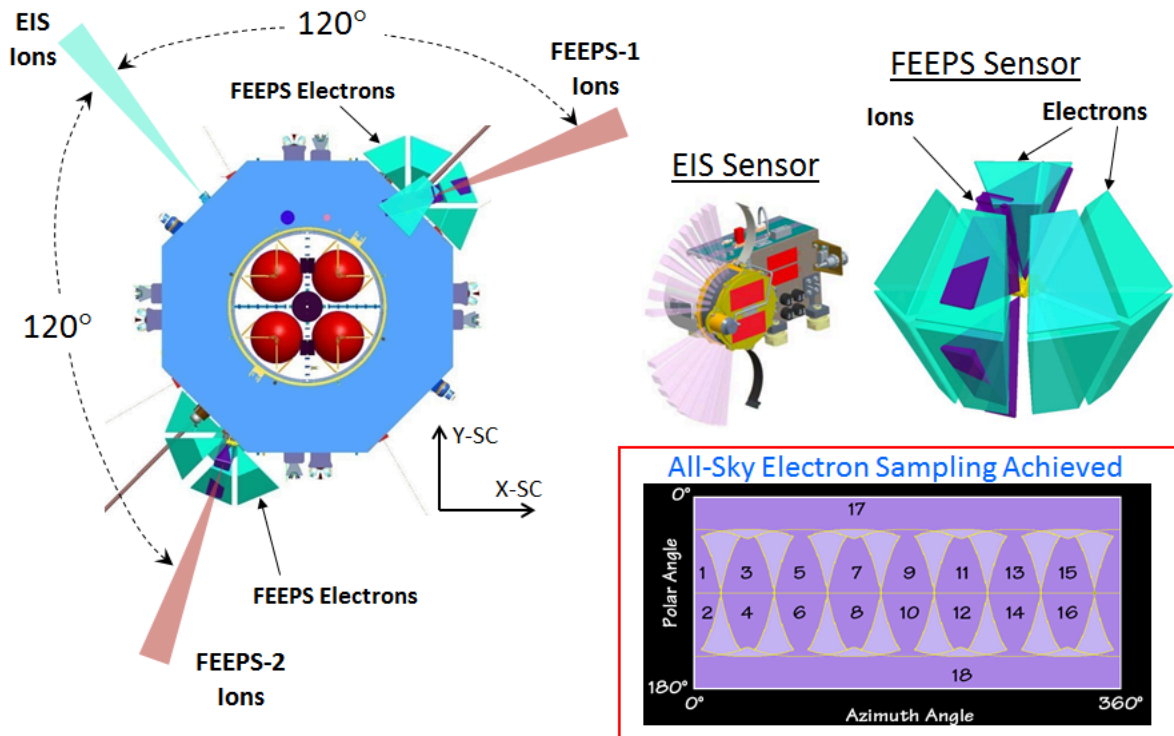


**Figure 6-2 The EPD fields-of-view are Configured to Provide Maximum Sky Coverage of Energetic Particles. [The two FEEPS sensors provide nearly simultaneous full-sky electron coverage, whereas the two FEEPS sensors complement the EIS fan-shaped FOV to provide ion coverage in approximately 1/3 of a spin.] (from Mauk et al. [2016])**

The Energetic Particle Detector suite of sensors supports the study of the fundamental physics of magnetic reconnection by:

1. Remotely sensing the positions and speeds of boundaries and other structures near reconnection sites using energetic ions.
2. Sensing the magnetic topology of near reconnection sites using energetic electrons.
3. Remotely sensing reconnection acceleration sites using both electrons and ions.
4. Determining the cause of energization of energetic electrons and ions by reconnection.

### 6.1.1 Energetic Ion Spectrometer (EIS)

Each EIS instrument (Figure 6-1) combines multi-directional viewing into a single compact sensor head using: 1) a time-of-flight (TOF) system that uses a microchannel plate (MCP) detector and thin foils that generate secondary electrons, to measure particle TOF and pulse height (PH); and 2) six solid-state detectors (SSDs) that measure particle energy (E). The MCP has start and stop anodes. Measuring the time difference between start and stop signals determines the particle's TOF. The anodes are divided into six angular segments; these provide a measure of the particle's direction of travel. EIS measures ion energy, directional, and compositional distributions using "Energy by Time-of-Flight" (ExTOF) for the higher-energy ions and "MCP-Pulse- Height by Time-of-Flight" (PHxTOF) for the lower-energy ions. EIS also measures electron energy and directional distributions using collimated SSD energy measurements (from designated "electron SSDs" that have 2  $\mu\text{m}$  of aluminum flashing deposited on them to keep out protons with energies less than about 250 keV).

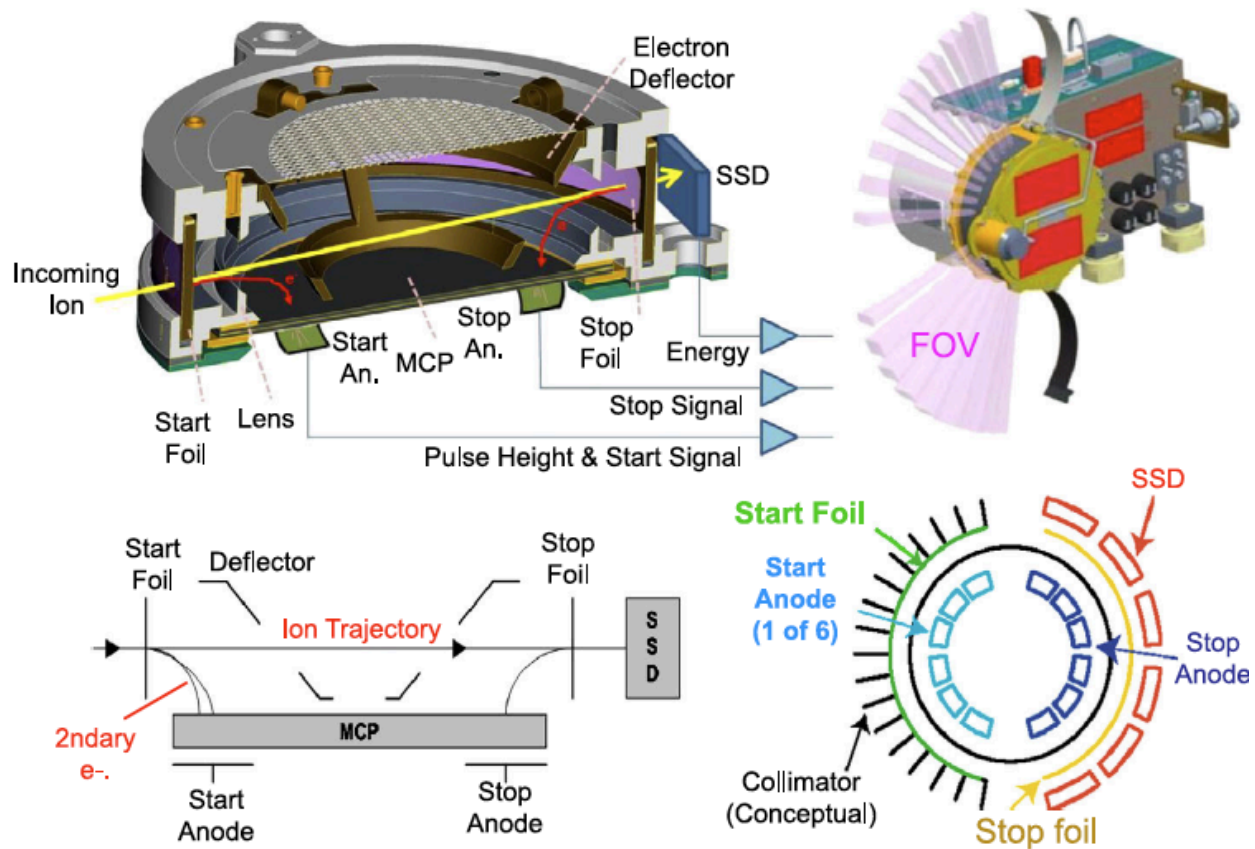


**Figure 6-3 Schematics Detailing How the EIS Sensor Works**

### 6.1.2 Fly’s Eye Energetic Particle Sensor (FEEPS)

The second EPD instrument, is the Fly’s Eye Energetic Particle Spectrometer (FEEPS). These sensors (Figure 6-2) measure:

- 1) the energy-angle distribution and composition of ions (20-500 keV, with a goal of 10-1000 keV) at a time resolution of <30 seconds;
- 2) the energy-angle distribution of total ions (45-500 keV, with a goal of 40-1000 keV) at a time resolution of <10 seconds; and
- 3) the coarse and fine energy-angle distribution of energetic electrons (25-500 keV, with a goal of 20-1000 keV) at time resolutions of <0.5 and <10 seconds, respectively.

FEEPS provides an instantaneous all-sky view of electrons (with coarse angular resolution), then turns coarse into more refined angular resolution by means of rotation. The two FEEPS ion “fans”, in conjunction with the one EIS ion fan, provide all-sky total-ion coverage every  $\frac{1}{3}$  of a spin. Each of the two FEEPS instruments on each spacecraft comprises 12 individual fields of view; 9 electron views (Figure 6-4a) and 3 ion views (Figure 6-4b). Eight of the nine electron views are grouped into pairs resulting in four “heads” comprising two “eyes” each. Each electron eye comprises a shaped pinhole, a 1.8-micron aluminum foil that blocks protons with energy >200, and a shaped, 1-mm SSD measures the energy of the incoming electron. The combination of the pinhole and of the SSD shapes yield a trapezoidal shape for the field of view for each eye (Figure 6-4a).

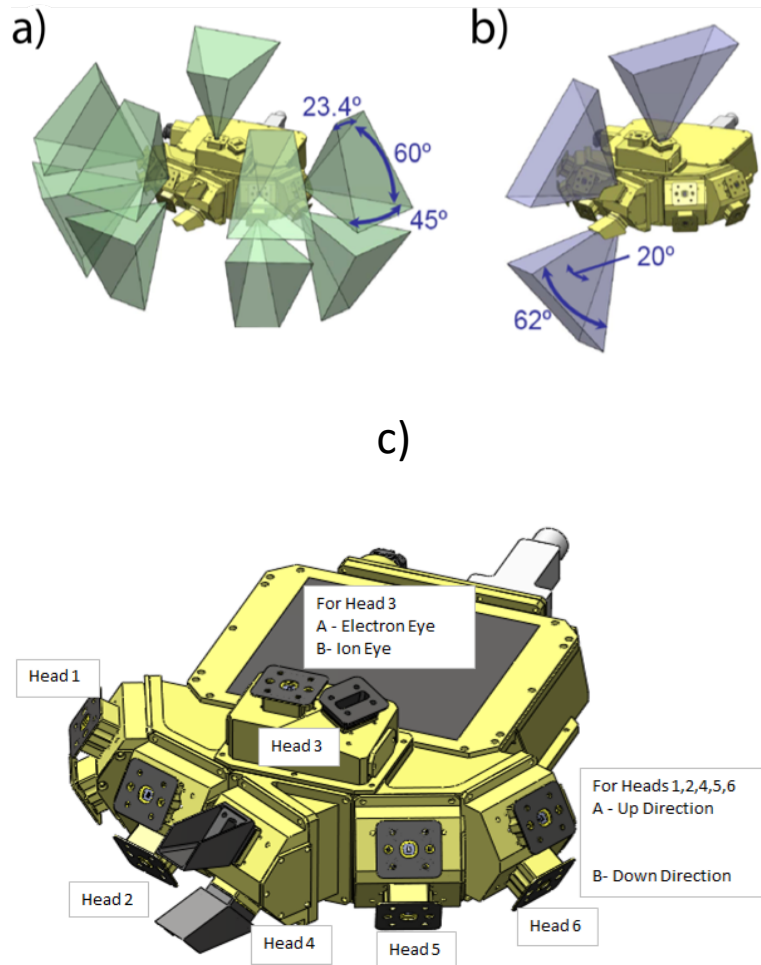


**Figure 6-4 The FOVs of the FEEPS (a) Electron and (b) Ion Sensors, or “Eyes”, while (c) Each Pair of Eyes is Combined into One of Twelve “Heads” on Each FEEPS Sensor (from Blake et al. [2016])**

Two of the ion sensors (i.e., “eyes”) on each FEEPS instrument are combined into a single “head” (Figure 6-4c). Each ion eye comprises a slot-shaped pinhole followed by a rectangular-shaped, 9-micron thick SSD which measures the energy of the ions. The response of these detectors to electrons is minimized by the thinness of the SSD’s; electrons tend to pass right through leaving a signal below the detection threshold, and ions are stopped, resulting in the detection of above-threshold energies. There will be residual electron contamination in the ion responses that needs to be managed. The two “equatorial” ion sensors each have a sunshade (Figure 6-4c) to keep the sun from illuminating the entrance slot (the ion sensors are very sensitive to the sun, whereas nominally, the electron sensors are not because of the thin foils placed over the telescope apertures). The slot shape of the pinhole and the rectangular shape of the SSD together yield a fan-like field-of-view of about 20° x 60° (Figure 6-4a-b).

A final set of electron and ion views is held by a 3<sup>rd</sup> type of head, the Electron-Ion Head (e.g., Head 3 in Figure 6-4c). This head contains one electron eye and one ion eye. Ideally, the field-of-view of the third ion head should be carefully aligned with the views of the other two ion heads to effectively yield a broad, 280° fan-shaped field of view. However, to keep the third ion sensor from viewing the axial electric field sensors, the third view had to be tilted somewhat away from the ideal configuration (Figure 6-4b).



### 6.1.3 Status of EPD Sensors

On MMS1, the solid-state detector (SSD) utilized in telescope T4 (for both ExTOF ion and electron data), is responding anomalously, and should not be used at this point in time. It acts like it is under-biased, but the true cause is unknown.

For the MMS1 spacecraft, the HV system experienced micro-discharge anomalies that caused the HV to be shut down by the onboard software on 30 January 2016, with some anomalous behavior seen for the first time on 21 January 2016, about 6 months after HV turn on. Because only 3 EIS units were required, the HV on EIS1 was disabled for the rest of the prime mission. Beginning on 18 April 2016, EIS1 was put into high-resolution electron mode with “electronenergy” burst data enabled. On 31 January 2018, HV (and ion species data) on MMS1 was re-enabled and no further anomalies have been reported to-date. EIS1 data prior to 21 January 2016 are assumed to be unaffected by these anomalies.

The efficiency of ion detection for making ExTOF and PHxTOF ion measurements evolves over time because of variations of the gain of the microchannel plate in each of the EIS units. To-date a nominal efficiency multiplier is utilized with the Level 2 data, but slow evolutions of those efficiencies have not been folded into the data processing. The multiplicative error is up to about  $\pm 30\%$ .

Many of the FEEPS eyes suffer from light contamination, likely due to direct sunlight and glint coming through foils that were damaged during launch. This and other issues have been substantially, though not completely, corrected via a series of CIDP updates implemented between October 2016 and August 2017.

The first energy channels (i.e., lowest energy channel, with index 0) from FEEPS ion and electron sensors have their threshold set very near to or within the noise threshold. These channels from most (but not all) eyes are often measuring noise and should not be used for scientific data analysis. See section 6.4.3 for additional details.

## 6.2 EPD MEASUREMENTS STANDARDS, VOLUME, AND TIMING

### 6.2.1 EIS Viewing

	TOF x PH				TOF x E and Ions				Electrons			
	Degrees	Unit-X	Unit-Y	Unit-Z	Degrees	Unit-X	Unit-Y	Unit-Z	Degrees	Unit-X	Unit-Y	Unit-Z
T0	72.18	0.306	-0.952	0.000	72.18	0.306	-0.952	0.000	61.12	0.483	-0.876	0.000
T1	45.56	0.700	-0.714	0.000	45.56	0.700	-0.714	0.000	34.5	0.824	-0.566	0.000
T2	20	0.940	-0.342	0.000	20	0.940	-0.342	0.000	9	0.988	-0.156	0.000
T3	-9	0.988	0.156	0.000	-9	0.988	0.156	0.000	-20	0.940	0.342	0.000
T4	-34.5	0.824	0.566	0.000	-34.5	0.824	0.566	0.000	-45.56	0.700	0.714	0.000
T5	-61.12	0.483	0.876	0.000	-61.12	0.483	0.876	0.000	-72.18	0.306	0.952	0.000

**Figure 6-5 The Unit Vectors of the Look Directions of the EIS Telescopes. [Care should be exercised when considering the telescopes highlighted in the differently-shaded rows as these look directions are substantially blocked.] (from Mauk et al. [2016])**

The quantitative centroids of the view directions for all six look directions, within the EIS coordinate system, for each of the EIS data products, are shown in Figure 6-5. The central directions of the center of each PHxTOF, ExTOF, Ion-SSD (the same as ExTOF), and Electron-SSD pixel are given as the angle from the X-axis within the XY-plane, with positive angles towards the -Y-axis (also toward the direction that has been designated the “T0” direction; we realize that it is unusual to have positive angles towards

the -Y-axis rather than the +Y-axis). To the right of each angle in Figure 6-5 is the unit vector of the view direction in the instrument coordinate system. Views T2 for electrons and T3 for ions have substantial obstruction from the shielding needed to keep the sun out (see Figure 10 in Mauk et al. [2016]). The off-color rows are the views that are substantially obstructed. Nonetheless these views corrected to the best of our ability and are represented in our data products. Care should be exercised for these particular views.

The transformation matrix that transforms a vector (e.g., a unit view direction such as those provided in Figure 6-5) into the MMS Spacecraft Frame is provided here.  $v_{sc} = T_{EIS} \cdot V_{EIS}$ , where  $V_{EIS}$  is the vector in the EIS frame of reference,  $T_{EIS}$  is the 3 x 3 transformation matrix, and  $v_{sc}$  is the vector in the spacecraft frame. For this expression:

$$T_{EIS} = \begin{pmatrix} \frac{-1}{\sqrt{2}} & 0 & \frac{1}{\sqrt{2}} \\ \frac{1}{\sqrt{2}} & 0 & \frac{1}{\sqrt{2}} \\ 0 & 1 & 0 \end{pmatrix}$$

*NOTE: The version of this transformation matrix reported in Mauk et al. (2016) is incorrect and this one should be used instead.*

ID#	Head	Orientation	Species	Azimuth	Elevation	Weighted Elevation	Unit-X	Unit-Y	Unit-Z
1	1	Up	Electons	-67.5	30	25	0.347	-0.837	0.423
2	1	Down	Electons	-67.5	-30	-25	0.347	-0.837	-0.423
3	2	Up	Electons	-22.5	30	25	0.837	-0.347	0.423
4	2	Down	Electons	-22.5	-30	-25	0.837	-0.347	-0.423
5	3	Top	Electons	0	90	95	-0.087	0.000	0.996
6	3	Top	Ions	60	78	78	0.104	0.180	0.978
7	4	Up	Ions	-30	41	41	0.654	-0.377	0.656
8	4	Down	Ions	-30	-41	-41	0.654	-0.377	-0.656
9	5	Up	Electons	22.5	30	25	0.837	0.347	0.423
10	5	Down	Electons	22.5	-30	-25	0.837	0.347	-0.423
11	6	Up	Electons	67.5	30	25	0.347	0.837	0.423
12	6	Down	Electons	67.5	-30	-25	0.347	0.837	-0.423

**Figure 6-6 The Look Direction Unit Vector (v) of Each FFEPS Eye in the FFEPS Coordinate System (FCS) (from Mauk et al. [2016])**

### 6.2.2 FFEPS Viewing

Figure 6-6 shows the unit vectors for each of the 12 FFEPS eyes in the FFEPS Coordinate System (FCS). The “elevation” angle is the angle made by unit vectors out of the XY-plane. The “weighted elevation” adjusts the elevation to account for the non-symmetric shape of the electron fields of view with respect to their centers. Note that the transformation of vectors ( $v$ ) from the FFEPS<sub>1</sub> (FFEPS-payload-deck or the “up” direction) or FFEPS-2 (FFEPS-bottom-deck) to the spacecraft coordinate system (BCS) is achieved using  $v_{FFEPS} = T_{1,2_{FFEPS_{1,2}}} \cdot v_{FFEPS}$ , where

$$T_{1_{FFEPS_1}} = \begin{pmatrix} \frac{1}{\sqrt{2}} & \frac{-1}{\sqrt{2}} & 0 \\ \frac{1}{\sqrt{2}} & \frac{1}{\sqrt{2}} & 0 \\ 0 & 0 & 1 \end{pmatrix} \quad \text{and} \quad T_{2_{FFEPS_2}} = \begin{pmatrix} \frac{-1}{\sqrt{2}} & \frac{-1}{\sqrt{2}} & 0 \\ \frac{-1}{\sqrt{2}} & \frac{1}{\sqrt{2}} & 0 \\ 0 & 0 & -1 \end{pmatrix}$$

These are rotation matrices which convert the FFEPS telescope look direction vectors ( $v_{FFEPS}$ ), from the FFEPS coordinate frame (FCS) to BCS. These vectors are defined looking out to space along the center



line for each telescope's field-of-view and are the same for both the top and bottom units.  $v_{FEEPS}$  in FCS is given in Figure 6-6 for each sensor.

### 6.2.3 EPD Ephemeris and Magnetic Field Information Requirements

Because EPD is spin-based and the spin phase relative to the Sun is known onboard, the EPD team will estimate the L1B transformation matrix between the SC coordinate system and GSE by assuming that the following is roughly true:  $SC_{z\_GSE} = (\sin 2.5^\circ, 0, \cos 2.5^\circ)$ . While this estimate suffices for Level 1b where ephemeris data is not available on the correct timescale, it **IS NOT SUFFICIENT** for Level 2. In the estimated transformation matrix, there is a  $\pm 30^\circ$  uncertainty in the angle that the  $SC_z$  axis makes with respect to the  $XZ_{GSE}$ -plane. This is due to the substantial variability in that angle which is allowed by mission standards.

The following are the data provided in FEEPS data products which are essential to data analysis:

- For Each Detector Look Direction (within each spin sector)
  1. Pitch Angle (using available magnetic field vector in SC coordinates)
  2. Unit Vector in GSE of Look Directions.

These data are included for convenience:

- One set for each spin sector
  3. BX, BY, BZ in SC coordinates\*
  4. SC position (X, Y, Z) in GSE\*
  5. SC latitude and longitude in GSM\*
  6. Moon position in GSE\*
  7. SC to GSE Transformation Matrix\* (9 numbers)
  8. GSE to GSM Transformation Matrix\* (9 numbers)
  9. Spin Rate\*

*\*These required parameters are provided for users in the L1b and L2 EIS or FEEPS data files.*

The possibility of earthshine contamination of the FEEPS ion detectors can be computed using the negative of the SC position in GSE (#4 above) and the detector look direction in SC coordinates. In addition, the possibility of sunshine contamination is derived using the detector look direction in GSE with respect to the  $X_{GSE}$ -axis. At Level 1B, earthshine estimations will have an uncertainty of  $\pm 30^\circ$ , while sunshine contamination will be fairly accurate because the primary uncertainty in the spacecraft orientation resides in the roll angle about the spacecraft-Sun line.

### 6.2.4 EIS File Versioning

To optimize scientific return, the instrument team may infrequently alter the onboard lookup tables (LUT), which define the spectral “channels” (see instrument description below) in a given EIS data product over the course of the mission. Each such change defines a new “LUT period” with each LUT period containing its own unique set of spectral channels. This means that over the course of the mission, a given data variable may change in structure (i.e., number or species specification of energy channels). To highlight and record these changes, the LUT period of a given spectral variable is indicated by a “\_P<n>\_” in the names of affected variables. Additionally, regular changes in the “Calibration Matrices” used for ground-based data processing, which do not require the introduction of a new LUT, such as adjusting high voltage states to address MCP gain levels or data optimization (i.e., changing decimation factors). These changes will affect the nature of the data within data files, but not the variable names.

Changes to both the onboard LUTs and ground-based “Cal Matrices” define specific data “regimes”, which are indicated using a unique EIS file versioning paradigm where the version indices “\*\_x.y.z.cdf” correspond to:

- x: the LUT period and associated “P<n>” in CDF variable names
- y: the specific iteration of the Cal Matrix used for data processing
- z: processing iteration of specific file
- 

Each “vX.Y” combination corresponds to a given data “regime”, summarized in Table 6-1 below.

Regime (New 2021)	Regime (Old)	Period Start	Period End	Changes
v1.0	v1.0	3/12/2015 (Launch)	2015-07-29/00:00:00	Initial LUT & processing state
v2.0	v2.0	2015-07-29/00:00:00	2015-08-29/00:00:00	Changes to extof & electronenergy channels
v2.1	v2.1	2015-08-29/00:00:00	2015-09-24/00:00:00	phxtof decimation changed
v3.0	v3.0	2015-09-24/00:00:00	2015-11-20/00:00:00	Changes to phxtof channelization
v3.1	v3.1	2015-11-20/00:00:00	2016-01-30/00:00:00	Changes to post-processing calibration factors
v3.2	v3.1	2016-01-30/00:00:00	2016-08-04/00:00:00	HV raised to improve MCP gain on MMS4
v3.3	v3.2	2016-08-04/00:00:00	2016-08-06/00:00:00	phxtof decimation changed
v3.4	v3.3	2016-08-06/00:00:00	2016-09-26/00:00:00	HV raised to improve MCP gain on MMS3
v4.0	v4.0	2016-09-26/00:00:00	2016-11-01/00:00:00	Changes to extof, phxtof, & electronenergy channels
v4.1	v4.1	2016-11-01/00:00:00	2017-04-30/00:00:00	Changes to post-processing calibration factors
v4.2	v4.1	2017-04-30/00:00:00	2017-11-17/00:00:00	Changes to post-processing calibration factors
v4.3	v4.2	2017-11-17/00:00:00	2018-04-30/00:00:00	Changes to phxtof and extof efficiencies/spectra, etc.
v4.4	v4.2	2018-04-30/00:00:00	2018-11-30/00:00:00	Changes to post-processing calibration factors
v4.5	v4.2	2018-11-30/00:00:00	2019-05-01/00:00:00	Changes to post-processing calibration factors
v4.6	v4.2	2019-05-01/00:00:00	2019-12-05/00:00:00	Changes to post-processing calibration factors

V5.0	V5.0	2019-12-05/00:00:00	Present	Changes to electronenergy channels on MMS4
------	------	---------------------	---------	--

**Table 6-1 Summary of the EIS Versioning Scheme**

### 6.3 EPD CALIBRATION AND VALIDATION

#### 6.3.1 EIS Pre-Flight / On-Ground Calibration

A full description of the design of EIS and its pre-flight and ground calibration results can be found in the following publication:

Mauk B.H. et al, **The Energetic Particle Detector (EPD) Investigation and the Energetic Ion Spectrometer (EIS) for the Magnetospheric Multiscale (MMS) Mission**, Space Sci Rev 199, 471-514 (2016). <https://doi.org/10.1007/s11214-014-0055-5>

As explained in Mauk et al. (2016), the full range of parameters (azimuth angle, elevation angle, particle input position, energy, species) **could** not be exercised within calibration facilities. Instead, a combination of theory, empirical expressions, and spot validation were used to construction the calibration matrix. Initial estimates of the particle energies throughout the sensor, scattering efficiencies, and detection efficiencies was developed with a Mathematica routine that utilized various available empirical relationships (energy losses in materials, scattering characterizations, efficiency of secondary electron generation, solid-state-detector pulse-height-defect, etc., etc.). That routine created numerous 6-order polynomials for the functional relationships between the various parameters. Those polynomials were then tweaked according to beams calibration runs, cross-checks with similar instruments that had gone through cross-calibration activities (RBSPICE on Van Allen Probes), and then, flight cross-calibration on MMS as described in the section 6.3.2.

Understanding of the EIS instrument response is based on a coordinated array of approaches, specifically: (i) bench testing of channel gains and other characteristics based on calibrated pulse inputs, (ii) calibrations using particle accelerator beams, (iii) calibrations using radiation sources, (iv) simulations of particle interactions with matter using such tools as GEANT4, and (v) geometric calculations. Two particle accelerators were used for calibrating EIS: (1) the APL ion particle accelerator that generates narrow ion beams of H, He, O (N often used as proxy), Ar, and other ions species from energies as low as about 12 keV up to 170 keV; and (2) the GSFC Van de Graff, accelerator that generates electron and ion species beams from ~100 keV to > 1MeV. Two different radiation sources were used: a Ba133 source and a degraded Am241 radiation source (the source is degraded by placing a thin mylar foil between the source and the sensor, which yields a very broad spectrum of alpha particle energies). To perform the calibrations, sources were procured in a configuration to completely fill the instrument field-of-view and thus calibrate all six (6) look directions simultaneously.

Details of the EIS calibration matrices are provided in section 6.4.4. The EIS calibration matrix carries parameters that correct for different responses of the six different telescopes within each unit. Flat-fielding has been carried out by examining the relative responses of the six different telescopes in each EIS unit to environments that are roughly isotropic.

#### 6.3.2 EIS In-Flight Calibration

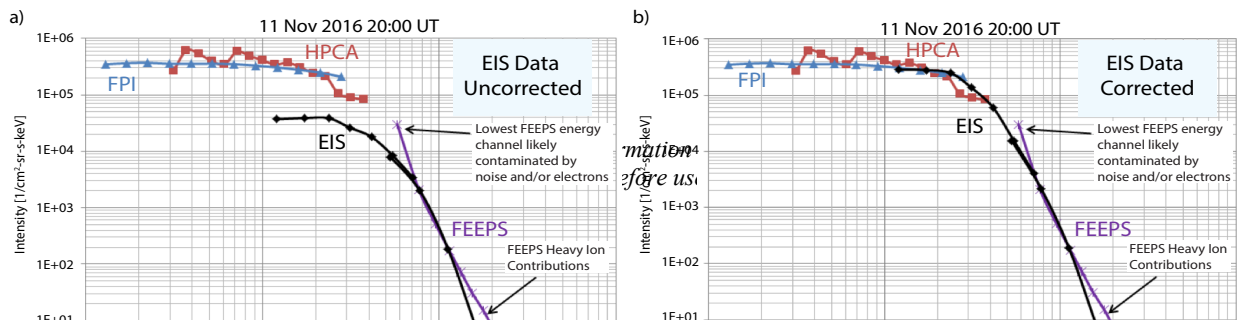


**Figure 6-7 Example of the Comparison of Omni-directional Proton Spectra from the EIS, FEEPS, HPCA, and FPI/DIS Sensors on MMS 3 (a) before and (b) after the EIS Data was Corrected [L2 data was used for all sensors except HPCA (L1b), which did not have L2 data available at the time that the cross-calibration efforts were made]**

Considerable efforts were made in Spring/Summer 2017 regarding the cross-calibration of ion (specifically proton) measurements amongst the MMS instruments: EIS, FEEPS, FPI/DIS, and HPCA. The basic gain state of the EIS sensor for measuring protons, which is variable because of changing microchannel plate efficiencies, is established by comparing the EIS and FEEPS ion measurements at ~80 keV. That energy is low enough to where we have become confident that protons dominate over heavy ions, and it is high enough to avoid energy-dependent efficiency problems that occur at lower energies. Additional cross-calibration efforts revealed that the EIS PHxTOF data, which bridges the energy gap between the upper energy limits of FPI/DIS (30 keV) and HPCA (40 keV) and the lower energy limit of the ExTOF (~50 keV) and FEEPS (~60 keV) data, was underestimating the flux by approximately a factor of 5. Based on the strong agreement between the plasma sensors (FPI/DIS and HPCA) and the high confidence in the relatively “pure” ion measurement by FEEPS (due to their very thin SSDs), the decision was made to adjust the EIS PHxTOF data by applying an energy-dependent numerical correction of the form:

$$E_{\text{PHxTOF}} = \frac{1}{\frac{1}{2} \left[ 1 + \alpha_{\text{PH}} \left( \tanh\left(\frac{E - \beta_{\text{PH}}}{\gamma_{\text{PH}}}\right) + 1 \right) \right]}$$

where  $E$  is energy and  $\alpha_{\text{PH}}$ ,  $\beta_{\text{PH}}$ ,  $\gamma_{\text{PH}}$  are coefficients equal to 0.3, 45, and 1, respectively.

Figure 6-7 shows an example comparing the proton spectra from the various instruments (a) before and (b) after the EIS data was corrected. Minor adjustments were also made to the lowest energy EIS ExTOF data to correct for foil efficiencies. This correction is of the form:

$$E_{\text{ExTOF}} = \frac{1}{\frac{1}{2} \left[ 1 + \alpha_{\text{E}} \left( 1 - \tanh\left(\frac{E - \beta_{\text{E}}}{\gamma_{\text{E}}}\right) + 1 \right) \right]}$$

where  $E$  is energy and  $\alpha_{\text{E}}$ ,  $\beta_{\text{E}}$ ,  $\gamma_{\text{E}}$  are coefficients equal to 0.3, 45, and 1, respectively.

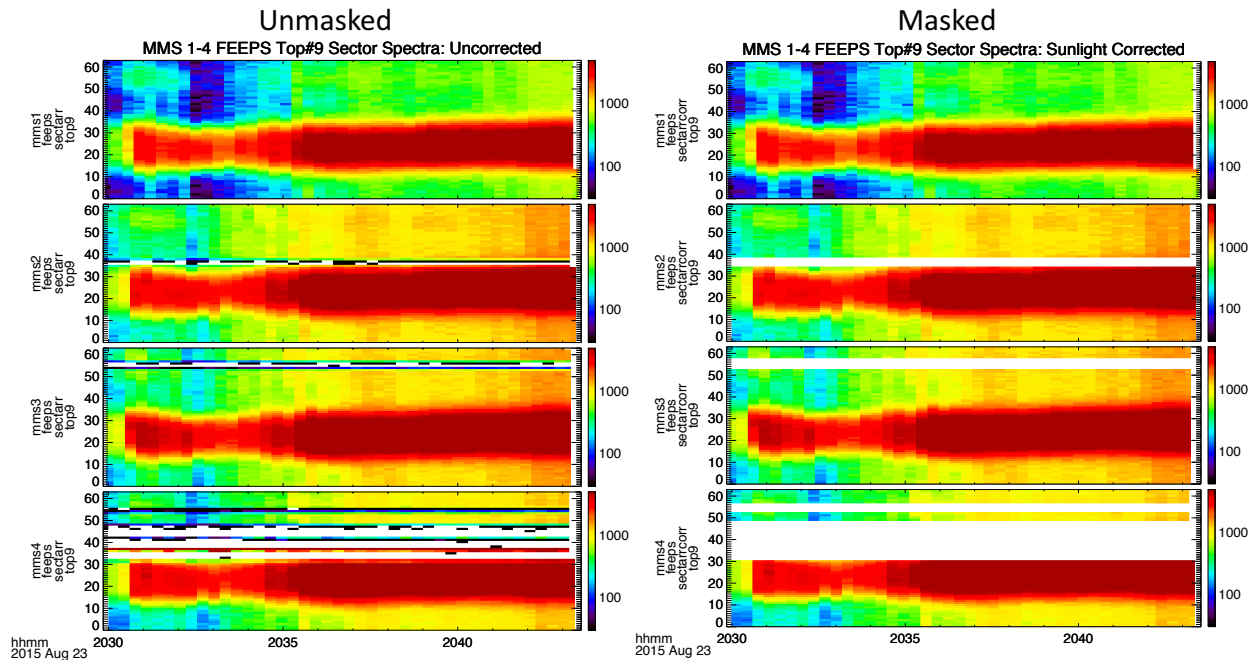


**Figure 6-8 An Example of the Effects of Sunlight Contamination in the FEEPS Burst Data [This data shows intensity for time versus spin sector for each spacecraft (MMS1-4 from top to bottom) for 23 August 2015. The white and black splotted horizontal lines permeating the MMS2-4 data on the left shows the effect of sunlight contamination on certain sectors. The panels on the right show the same data with the affected sectors appropriately masked]**

Cross calibration has also taken place for electrons between EIS and FEEPS. Pre-launch characterization for EIS has been found to be adequate (see [section 6.3.3](#)). Efficiencies for EIS electrons were obtained from cross-calibration activities that took place with EIS’s sister instrument, RBSPICE, on the Van Allen Probes mission.

Further details and results of the EIS in-flight calibration can be found in the publication:

Cohen, I. J., et al., **Dominance of high-energy (>150 keV) heavy ion intensities in Earth’s middle to outer magnetosphere**, J. Geophys. Res. Space Physics (2017)  
<https://doi.org/10.1002/2017JA024351>

### 6.3.3 FEEPS Pre-Flight / On-Ground Calibration

Pre-flight calibration is covered in the FEEPS instrument paper (Blake, et al., 2016). As summarized in [section 6.1.3](#), many of the FEEPS eyes suffer from light contamination, likely due to sunlight and glint coming through foils (on electron eyes) that were perforated during launch. An example of the light contamination is shown in Figure 6-8, which plots FEEPS burst data from electron eye #9 of the bottom deck. The Y-axis is the spin sector, the X-axis is time, and intensities are plotted in color. The horizontal lines containing discontinuities contained in the second through fourth plots in the left column show sectors affected by sunlight contamination, whereas the top left plot for MMS1, lacking these rows, indicates an uncontaminated sensor. The plots in the right column, marked “Masked”, show how those sunlight contaminated sectors can be effectively removed.

Using such FEEPS burst data sector maps, one can identify the affected sectors during any period of the mission on all eyes of the FEEPS instruments. For example, Figure 6-9 shows the sector masks that were produced after a survey of contamination conducted during August-September 2015. These masks flag all sectors that were affected by contamination during the period examined. These plots show the contaminated sectors (X-axis) from each eye (Y-axis) for each of the spacecraft during this period. Yellow blocks identify affected eyes/sectors, while blue blocks are good, unaffected eyes/sectors.

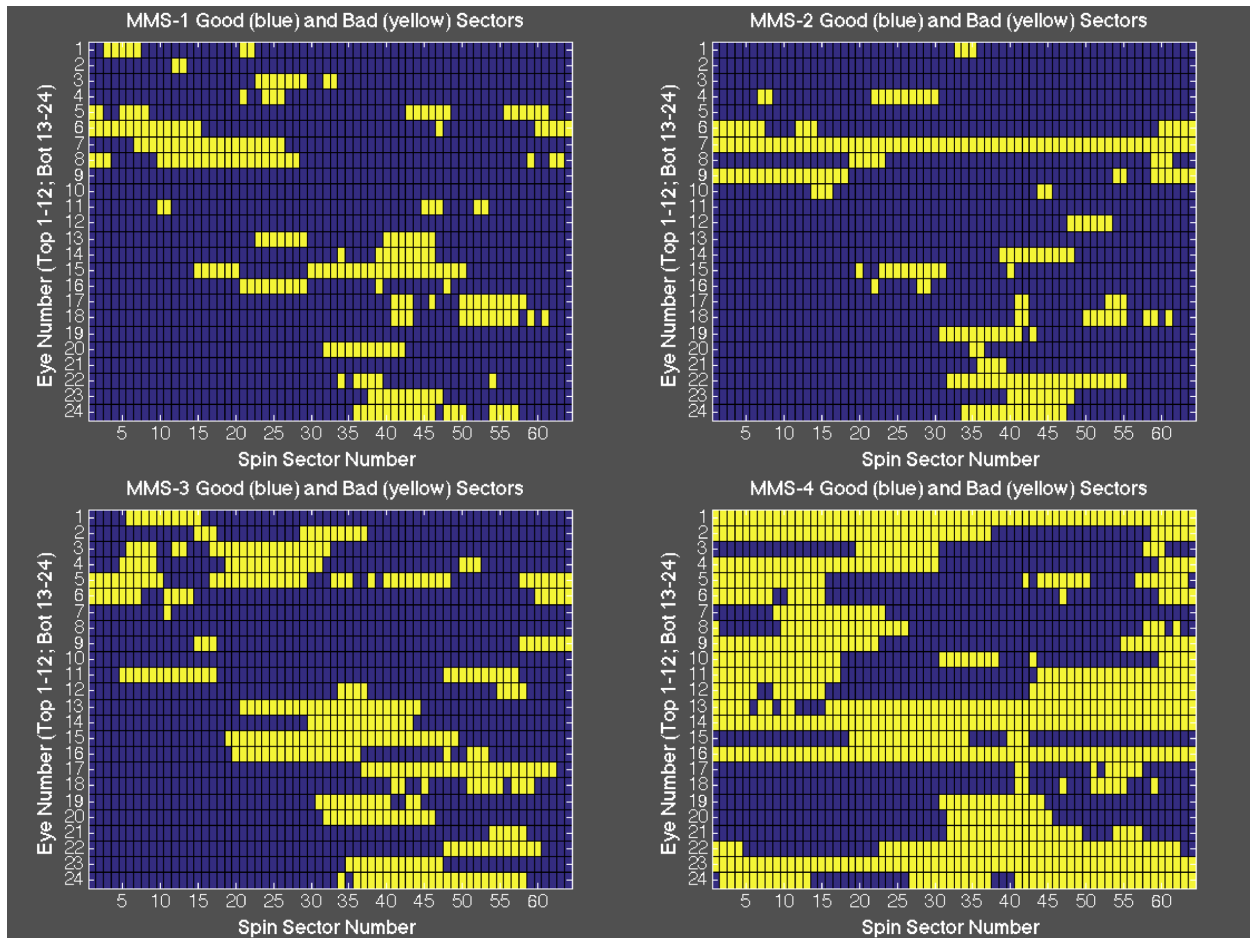


**Figure 6-9 Mapping of those Sectors from Each Eye Affected (yellow) and Unaffected (blue) by Sunlight Contamination on Each Spacecraft during August-September 2015**

### 6.3.3.1 FEEPS Lowest-Energy Channels

As previously mentioned, the first energy channels (i.e., lowest energy channel, with index 0) from FEEPS ion and electron instruments have their threshold set very near to or within the noise threshold. These channels from most (but not all) eyes are thus measuring noise and should not be used for scientific data analysis. Additionally, on several of the FEEPS eyes, the second and/or third energy channels require threshold adjustment as of 04 April 2016. An example of the effects from this are shown in the energy distributions in Figure 6-10. Here, energy distributions (in count rates) from a relatively isotropic angular distribution with high-count-rates from 02 August 2015 are shown from each of the electron eyes on MMS1. Different colors show the different eyes, as labeled, with eyes from the top deck instrument (e.g., T10) shown with stars and those from the bottom deck instrument (e.g., B10) shown with diamonds.

These distributions show how the first few channels on several eyes are counting lower than the other eyes. These affected eyes should not be included for science analysis.

### 6.3.3.2 FEEPS Flat Field

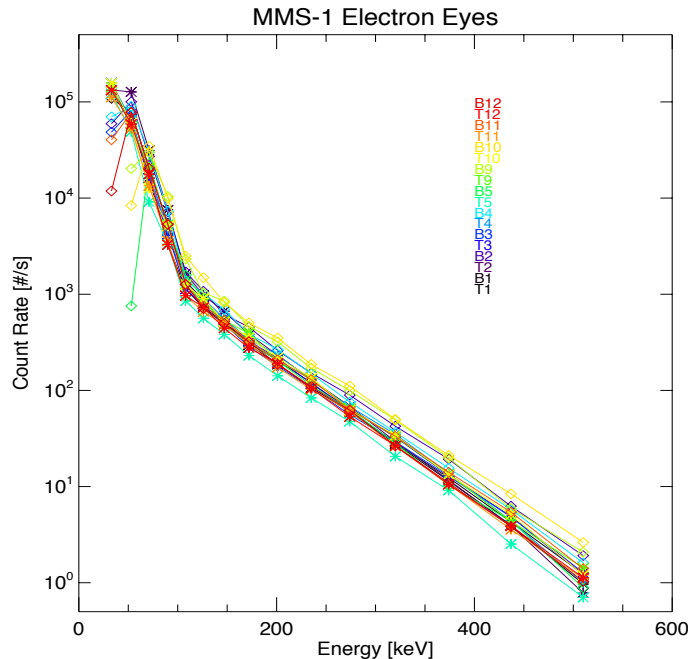


**Figure 6-10 Energy Spectra of the 24 Individual FEEPS Eyes (3 ion and 9 electrons per sensor, top and bottom) on MMS1 [The reduced count rates observed in the lowest energy channel for multiple eyes is contributed to thresholds set near or at the sensor’s noise threshold]**

A flat-fielding effort has been made to ensure that FEEPS data from all of the FEEPS telescopes are consistent. For the electron data, the correction involves a linear shift in the energy channels. For these, a constant energy is added or subtracted to each eye’s energy channels’ limits. That method was deemed necessary due to the nature of the disagreement from eye to eye, which showed a stronger disagreement at lower energies. Also, the effectiveness of this correction was clear during injection events, in which energy dispersed enhancements of electrons were observed by the spacecraft. To determine these energy offset corrections, we examined a number of periods (>10) during 2016 that exhibited steady local plasma conditions and high FEEPS count rates. During these periods, we compared the 1-spin averaged omnidirectional distributions from all of the eyes on each spacecraft and calculated the correction offsets that brought each closest to the mean distribution from all eyes. That method assumes that the correction factors are all spread around the true distribution, which is confirmed by comparisons to the EIS average distributions from the same times. The same method was applied for the ion eyes, though (interestingly) the corrections for the ion eyes were best when applied using a gain (i.e., multiplicative) factor. These correction factors have been organized into tables containing adjustments for each FEEPS channel and eye over all instruments and spacecraft.

### 6.3.4 FEEPS In-Flight Calibration

Figure 6-11 presents an example of the effect of the light contamination in survey data. From top to bottom it shows: electron omnidirectional averaged energy spectra from survey data, ion omnidirectional

averaged energy spectra from fast survey data, and the spin sector number from a period 02 August 2015. Note that the spin-tone signatures in the electron and ion data are the result of sunlight contamination in the survey data product. This is masked onboard via masking tables loaded onto the spacecraft periodically since August 2016. Figure 6-3 records the onboard masking tables used to-date to mask sunlight-contaminated raw spin sectors in the onboard production of FEEPS fast and slow survey data. For data products prior to these changes, please refer to the data quality flags when using any FEEPS survey data for science. Sunlight contamination is removable from burst data products using masks identified from sector masks as described previously in section 6.3.3.

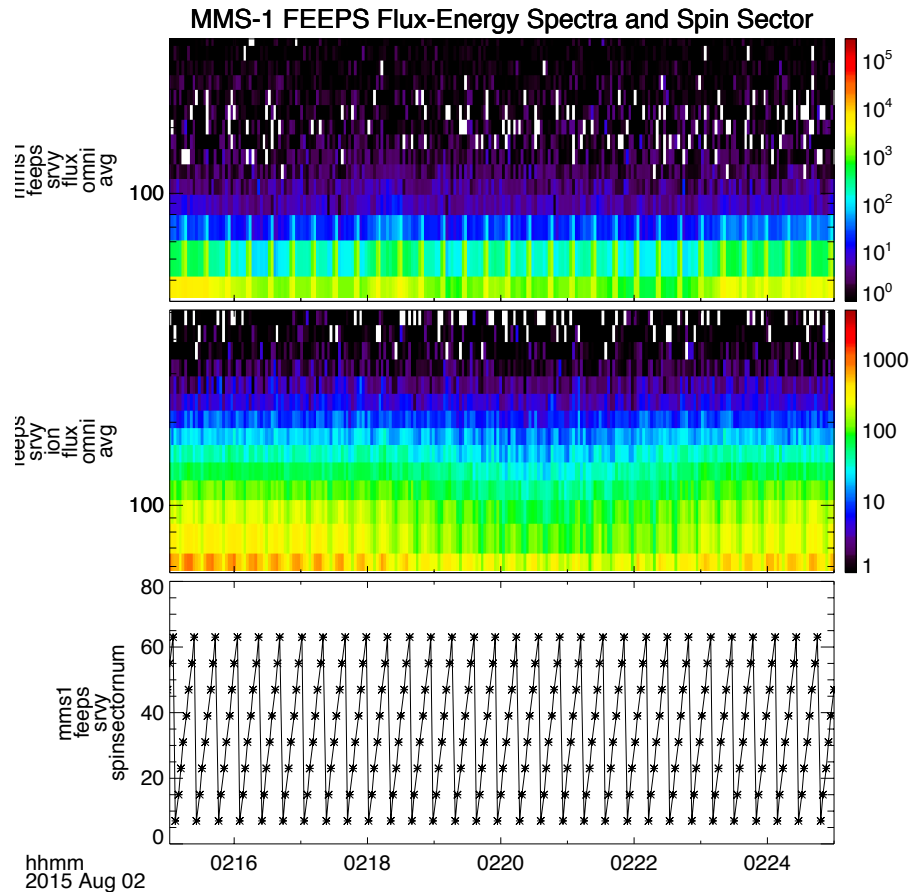


**Figure 6-11 Example of the Effect of Sunlight Contamination on FEEPS Survey Data [Omni-directionally-averaged energy spectra for electrons and ions are shown in the top and middle panels, respectively. The bottom panel shows the spin sector]**



Upload/Change	MMS1 Execution	MMS2 Execution	MMS3 Execution	MMS4 Execution
1 <sup>st</sup> onboard table <sup>1</sup>	2016-08-05/20:05:00	2016-08-05/21:17:40	2016-08-06/02:04:13	2016-08-06/03:46:46
Fix to 1 <sup>st</sup> onboard table <sup>2</sup>	2016-09-14/16:15:00	2016-09-14/17:30:00	2016-09-14/18:44:51	2016-09-14/19:59:46
Fix to 1 <sup>st</sup> onboard table <sup>3</sup>	2017-02-16/19:30:05	2017-02-14/23:29:54	2017-02-17/14:20:14	2017-02-17/15:50:07
2 <sup>nd</sup> onboard table (top)	2017-08-16/19:40:06	2017-08-16/21:45:38	2017-08-16/23:41:07	2017-08-17/13:34:12
2 <sup>nd</sup> onboard table (bottom)	2017-08-16/19:44:03	2017-08-16/21:48:55	2017-08-16/23:44:24	2017-08-17/13:31:15
3 <sup>rd</sup> onboard table	2018-01-24/01:43:31	2018-01-24/22:08:27	2018-01-18/16:11:39	2018-01-18/17:54:34
<sup>1</sup> incorrectly applied masking table for top units to the count observations on both top and bottom units, failed to mask live-time correction (LTC), & applied the masking tables to all burst count observations; <sup>2</sup> removed masking of survey & burst count observations in the bottom units - no changes to top units; <sup>3</sup> implemented correct unit specific onboard masking to survey counts and LTC along with removing masking of burst count observations;				

**Table 6-2 History of Sunlight Contaminating Masking Tables Implemented to-date Onboard MMS Spacecraft**

### 6.3.5 Data Processing Pipeline

Figure 6-12 shows the plan for processing the EPD (FEEPS and EIS) data. Algorithms for generating Levels 1a and 1b data are generated by the EPD Team at LASP (FEEPS) and APL (EIS), and are transferred to the MMS SOC at LASP for execution. Level 2 data for FEEPS and EIS are generated by the EPD Team at LASP (with certification by Aerospace) and APL, respectively. The Level 2 products are then delivered to the MMS SOC. Figure 6-12 shows details of the processing, including highlighting the need for the availability of magnetic field data and ephemeris data at various stages of the production. Figure 6-13 shows additional details of the more complex FEEPS data production chain.

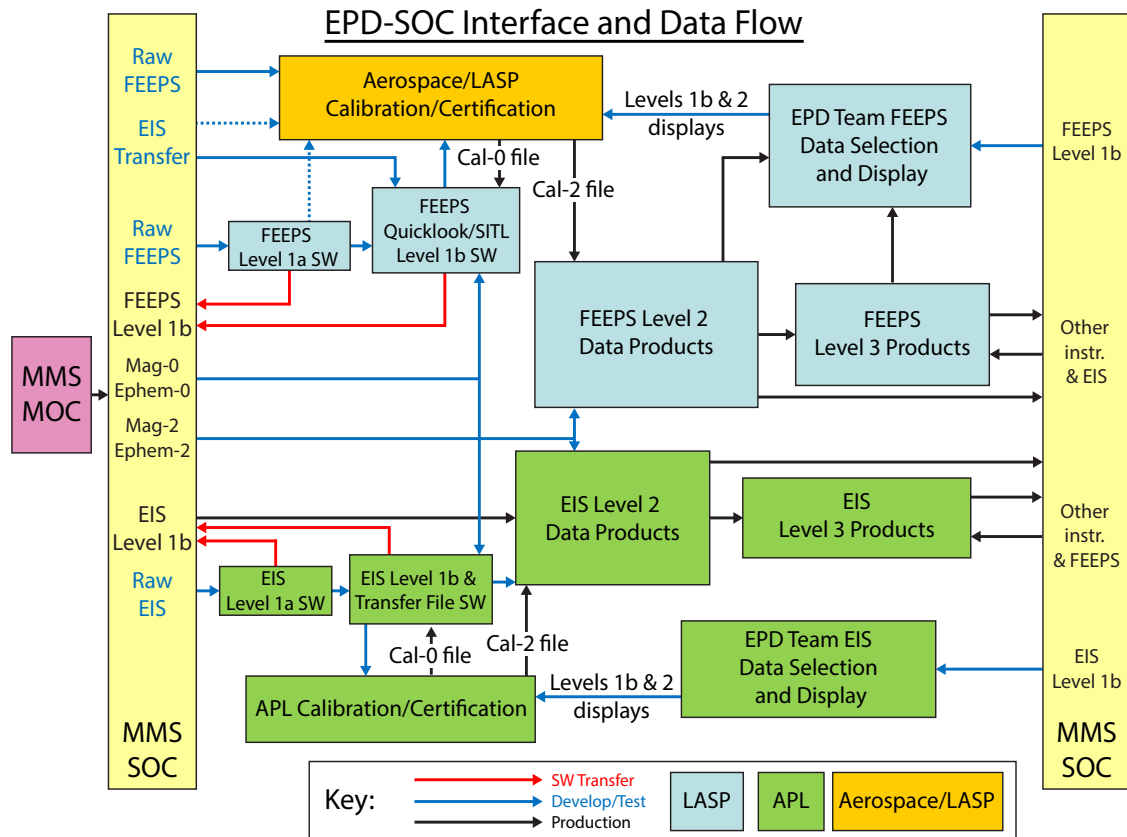


**Figure 6-12 Details of the EPD-SOC Interface and Data Flow [Levels 1a and 1b are generated by the MMS SOC at LASP, while Level 2 and higher products are generated by the EPD team at LASP (FEEPS) and APL (EIS)]**

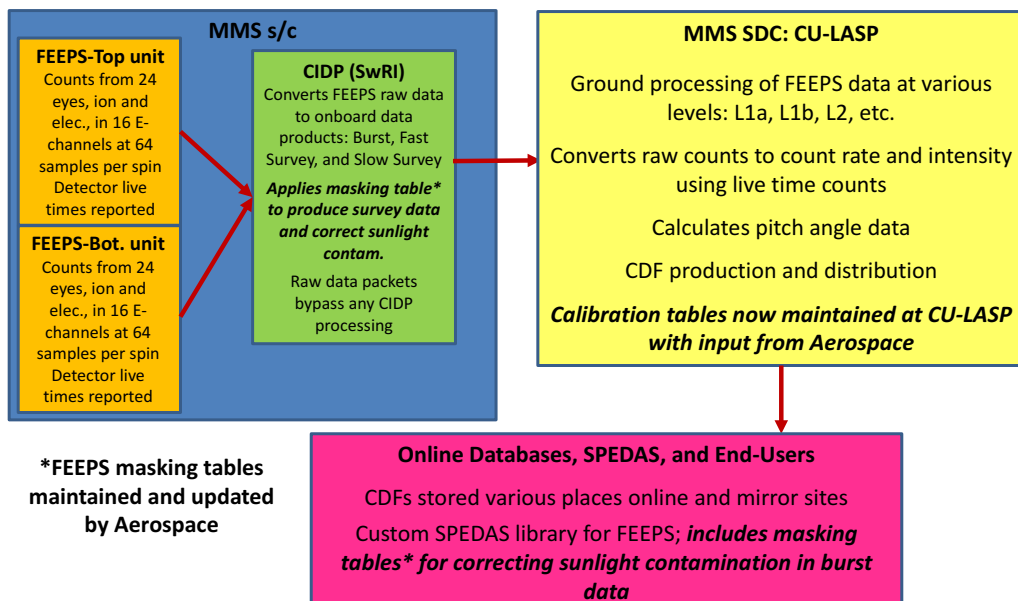


**Figure 6-13 The Four Institutions Involved in Producing the Final FEEPS Data Set [SwRI (responsible for the CIDP onboard each spacecraft), LASP (responsible for calibration tables, data processing, and the POC), Aerospace (responsible for data calibration factors and updates), and APL (responsible for validation and management)]**

### 6.3.6 Validation

Over the mission lifespan, data validation has been conducted by the EPD Investigation Team, broader MMS Science Working Team, and the general user community. Prior to launch, validation was conducted through a rigorous suite of testing and verification processes summarized in Mauk et al. (2016). Since launch, validation has continued via regular ongoing reviews of the data as well as corrections to the instruments as needed as the data continues to progress. As detailed in section 6.3.2, cross-comparison with other MMS instruments has been conducted. Resulting discrepancies generated an internal review and assessment that led to several adjustments being made to efficiencies and other parameters included in the EIS calibration matrices. Additionally, any anomalies during the processing of the data (found by operations personnel or by the science community), have led to reprocessing of the entire data set to correct the errors. The EPD team confirms that any missing science data correlates with expected routine or anomalous outages.

## 6.4 EPD ALGORITHM DESCRIPTIONS

### 6.4.1 Conversion from Counts/sec to Flux (L1->L2)

The data that comes down from both EIS and FEEPS is mostly in the form of counts per accumulation period (i.e., spin sector) per sensor. A “sensor” is a small portion of measurement parameter space, where the parameters correspond to “look direction” (in 2 dimensions), energy, and “species” (i.e., electrons or ions; where ions are protons, helium ions, or oxygen ions). The prime challenge for ground processing is to turn each of these data values from a “counts per accumulation” ( $C/A$ ) to intensity [ $1/(\text{cm}^2\text{-s-sr-keV})$ ] for the particular parameter state represented by the sensor. The algorithm for doing so is documented here.

- 1) Because a SSD response (output rate for a given channel) tends to be roughly linear when rates are low, but non-linear when rates are high, for high rates one must be prepared to perform a “dead-time correction” to reconstruct the true input rates. That correction is performed using a “live-time ( $LT$ ) counter” (for FEEPS) or a “dead-time counter” (for EIS). Depending on how this number is generated, there is a conversion procedure to convert it into a “fractional live-time” (e.g.,  $FLT = \text{accumulation time} / LT$ ). For EIS there are other factors that go into the dead-time correction (e. g., processor speed) and the full algorithm is documented elsewhere.
- 2) Convert  $C/A$  to *counts per second* ( $C/S \equiv R$ ) using:

$$R = \frac{C/A}{TA \times FLT},$$

where  $TA$  is the channel accumulation period and  $FLT$  is the aforementioned live-time correction.

- 3) If judged to be needed, subtract off a background, generally caused by cosmic rays:

$$RC = R - CR_{BG}.$$

To-date, this correction remains unapplied in EPD data. This background is apparent in instances of low counting statistics. Note that CR\_BG is energy-dependent with a peak corresponding to a minimum ionizing energy near 300 keV for FEEPS and 160 keV for EIS (with its thinner detectors).

- 4) Convert  $R$  to *Intensity* ( $I$ ) as such:

$$I = \frac{R}{(E_2 - E_1) \times eG},$$

where  $eG$  is the efficiency ( $e$ ) times the geometric factor ( $G$ ) and  $E_1$  and  $E_2$  are the lower and upper energy bounds of the channel, respectively. *Note that  $eG$ ,  $E_1$ , and  $E_2$  are “calibration factors” that are provided in the “Calibration Matrix” spreadsheet (see Appendix A) to the processing software. There is one complete set of numbers for each of the hundreds of channels.*

More about these factors is provided in [section 5.1](#).

- 5) When plotting the data or using it for calculations, the intensity is often identified with a central energy, often estimated as the geometric mean ( $E_{gm} = \sqrt{E_1 \times E_2}$ ), an estimate that would be exact if the spectral index ( $g$ ) were equal to 2 in the expression  $I + C \times E^{-g}$ , where  $C$  is a constant and  $E$  is energy.

The result of all of this processing can be notionally thought of as filling one or more spreadsheets with the column headings for each look direction like:

- Spacecraft
- Instrument
- Direction ( $\theta, \phi$ )
- Pitch Angle
- Energy ( $E_1, E_2, E_{gm}$ )
- Counts per Accumulation ( $C/A$ )
- Counts per Second ( $C/S$ )
- Intensity ( $I$ )
- Species

The pitch angle (PA) is the angle of the look direction with respect to the magnetic field ( $PA = \cos^{-1}[\vec{d} \times \vec{b}]$ ), where  $\vec{d}$  is minus the unit view direction vector in spacecraft coordinates (i.e., the look direction in GSE coordinates) and  $\vec{b}$  is the unit magnetic field vector in spacecraft coordinates (BCS). This angle is needed immediately because ordering the particle data by the magnetic field is central to understanding the data.

The generation of low and high-level data products from this notional spreadsheet is all about organizing the data in different ways (e.g., choose one look direction – or average all look directions - and one species generate an energy spectrum, etc.).

#### 6.4.2 FEEPS Conversion from Counts to Flux (L1->L2)

**Level 1b:** FEEPS L2 data is organized into CDF formatted data files. The variables in these files correspond to data derived from the counts variable contained in L1A, primarily count rate and intensity, as well as variables containing magnetic field pitch angle data, ephemeris data and data quality indicators. The intensity value is calculated using the following components:

**Live Time (LT):**

$$LT = C * LTC,$$

where  $C = 8E-6$  and  $LTC$  is the Live Time Counts.

**Count Rate (CtRt):**

$$CtRt = Ct / LT - CRBG = Ct / (C*LTC) - CRBG,$$

where  $Ct$  is the counts and  $CRBG$  is the cosmic ray background, which is currently defined in the FEEPS calibration file as a constant ( $CRBG = 0.0$ ).

**Intensity (I):**

$$I = CtRt / ((E2-E1)*Eff*GF)$$

where  $E1$  and  $E2$  are the energy step bounds,  $Eff$  is the efficiency, and  $GF$  is the geometric factor defined in the FEEPS calibration file.

**Percent Uncertainty ( $\% \sigma$ ):**

$$\% \sigma = 100\% * \sqrt{Ct},$$

where the one standard deviation measurement uncertainty of the counts is defined by the standard Poisson counting error  $\sigma_Q = \sqrt{Ct}$

There are four types of FEEPS L1b data:

1. L2 electron burst
2. L2 ion burst
3. L2 electron survey
4. L2 ion survey

These types are represented in the data file names. Note that the top/bottom field of the L1A file names have been moved into the files as a component of the variable names:

- mms1\_feeps\_brst\_11b\_electron\_20211019023633\_v6.1.1.cdf
- mms1\_feeps\_srvy\_11b\_ion\_20211019000000\_v6.1.1.cdf

### 6.4.3 FEEPS Data Quality Flags

MMS FEEPS data quality indicators allow the scientific community access to the most comprehensive FEEPS data set without being overwhelmed by detailed characteristics of the instrument health. A simple system of quality indicators is advantageous for encouraging the correct usage of the MMS FEEPS data by scientists within and outside the MMS team. The system of data quality indicators is identical for Burst and Survey data products, although some quality indicators will be unique to Survey data and unused for Burst data. A quality indicator is assigned to each time step for each FEEPS eye (i.e., telescope).

The FEEPS data quality indicators combine knowledge of contamination features in the FEEPS observations and onboard operations. FEEPS Team members have used the high resolution FEEPS observations (burst mode) to identify sun contamination features which are dependent on the spacecraft spin, i.e., dependency on spin sector. Onboard spin sector masking has been implemented before the summation of high-resolution observations into low resolution Survey sectors to avoid the irreversible contamination of Survey data. Furthermore, the FEEPS instrument is routinely operated in an instrument calibration mode which is unsuitable for scientific research. In summary, the quality indicators are a product of the comparison between sun contamination tables, onboard masking tables, and onboard calibration times.

The highest-resolution FEEPS observations are recorded in burst mode at a rate of 64 samples per spin, which are referred to as spin sectors. In survey mode, the FEEPS observations are recorded at an eighth of

the burst-mode resolution by summing the 64 spin sectors into 8 survey sectors per spin onboard the spacecraft. Removing sunlight contamination from the survey data requires masking contaminated spin sectors onboard before summing into survey sectors and transmitting to Earth. A spin sector mask table can be updated on each of the MMS spacecraft to avoid contamination in future survey mode observations and since the burst data contains the highest available angular resolution, onboard burst masking is not necessary.

The time-dependent contamination tables and onboard masking tables share a similar structure where both tables for a single spacecraft consist of a 64×24 table, with the 64 rows representing the 64 spin sectors in a spin and each column representing a FEEPS eye/sensor (top 1 – 12 and bottom 1 – 12). In a contamination table, each individual entry consists of a “0” or “1”, representing “clean” or “contaminated”. In an onboard masking table, each individual entry consists of 4 digits where each digit indicates if each of the following values have been masked (=1) or not masked (=0): survey counts, survey LTC, burst counts, burst LTC. The onboard calibration time periods are marked with the binary L1a variable “...calstate”. The corresponding time dependent contamination table and onboard masking table is included in the FEEPS data products for transparency in the assignment of the quality indicators. The more advanced user does have the option to pick and choose whether to accept these quality indicators, although, this more advanced option is highly discouraged without the guidance of a FEEPS team member.

An overview of the quality indicators can be found below and is followed by a detailed description of each quality indicator assignment. While the following description uses a color scheme to indicate data quality, similar to a traffic light, the quality indicators are reported as integers in the data products.

These are the data quality flags are included in Level 2 data products.

For BURST- and RAW-mode data, there are three possible quality indicators:

- Green (Quality Indicator = 0): No contaminated or masked spin sectors (best data quality);
- Red (Quality Indicator = 3): Contaminated spin sector is associated with BURST and RAW data (this data is not recommended for scientific use);
- Grey (Quality Indicator = 4): FEEPS calibration data (this data is generated by the instrument itself and is not recommended for scientific use);

For SURVEY-mode data, there are five possible quality indicators:

- Green (Quality Indicator = 0): No contaminated or masked spin sectors (best data quality);
- Yellow (Quality Indicator = 1): Among the spin sectors used to create a SURVEY aggregate spin sector, onboard masking is successfully applied to a minimum of 1 and a maximum of 7 spin sectors and there is no contamination in any of the individual spin sectors . Note that since this indicator applies only when onboard masking is applied, some sectors are not observed.
- Orange (Quality Indicator = 2): There is contamination of between 0 and 50% of the not-masked sectors. Warning: this data contains contamination;
- Red (Quality Indicator = 3): Same as orange except that there is contamination of 50% or more of the not-masked sectors. IN ADDITION, this indicator applies to the case where onboard masking is applied to all 8 spin sectors in the aggregate sector.
- Grey (Quality Indicator = 4): FEEPS calibration data (this data is generated by the instrument itself and is not recommended for scientific use);

Burst-mode observations only use the “Green”, “Red”, and Grey” quality indicators. If a burst spin sector is contaminated and/or masked in any way (counts or LTC), the spin sector is recorded with the “Red” quality indicator (1) and is not recommended for scientific use. Without contamination and masking, a burst spin sector is recorded with the “Green” quality indicator (0), representing the best available data. The “Grey” quality indicator will be described later in this document. Using the contamination table and onboard masking table to assign a quality indicator is described in “pseudo code” below. Remember, the onboard masking table entry contains four digits, with the third and fourth digit recording the burst count masking and LTC masking.

```
IF (Contamination EQ 1) OR (Onboard[3] EQ 1) OR (Onboard[4] EQ 1) THEN Quality = 1
```

All five quality indicators (“Green”, “Yellow”, “Orange”, “Red”, “Grey”) can be assigned to the survey observations. In survey mode, eight spin sectors are accumulated onboard into a single survey sector and thus, onboard masking is used to remove contamination, although, not always successfully. If a survey sector does not contain any contaminated or masked spin sectors, then the survey sector is recorded with the “Green” quality indicator (0) and represents the best available data. If a survey sector does not contain any contamination and includes a total of 1 to 7 masked spin sectors, then the survey sector is recorded with the “Yellow” quality indicator (2). The “Yellow” quality indicator shows the user that not all spin sectors have been observed within the survey sector and thus the data will not represent the full angular coverage of the survey sector. Both “Green” and “Yellow” quality indicators do not contain any contamination and are encouraged for scientific use.

Since the onboard masking began in August 2016 and the contamination identification has evolved over time, not all contamination has been masked onboard before summing into survey sectors. The “Orange” quality indicator (3) is recorded when a survey sector contains less than 50% contaminated spin sectors. The user should exercise caution when using “Orange” quality data and is encouraged to contact FEEPS team members for guidance when publishing scientific results. Lastly, data recorded with the “Red” quality indicator (1) is not recommended for scientific use. The “Red” quality indicator applies to any survey sector which contains more than 50%. The “Grey” quality indicator will be described later in this document.

As a reminder, an onboard masking table entry contains four digits, with the first and second digit recording the survey count masking and LTC masking. The onboard masking must include counts and LTC to be considered completely masked and a partially masked spin sector is considered the same as a contaminated spin sector. Partially masked spin sectors are primarily a concern during the initial implementation of onboard masking between July 2016 and February 2017. Assigning a quality indicator to a survey sector requires examining the contamination and masking status of each of the eight summed spin sectors and comparing the total masked and contaminated spin sectors with the above quality indicator criteria. Again, “pseudo code” for the survey quality indicator is below.

```
Clean = 0 ;Initialize clean spin sector counter at 0
Bad = 0 ;Initialize bad spin sector counter at 0
Masked = 0 ;Initialize masked spin sector counter at 0
FOR spinSect = 1, 8 DO BEGIN
    Onboard = the 4-digit Onboard masking table entry for current spin sector
    Contamination = the sun contamination table entry for the current spin sector
    IF (Onboard[1] NE Onboard[2]) THEN BEGIN
        Bad = Bad + 1 ; Increment bad counter bc current spin sector is not completely masked
        STOP
    ENDIF ELSE IF (Contamination EQ 1 ) AND ( Onboard[1] EQ 0 ) THEN BEGIN
```

```
Bad = Bad + 1 ; Increment bad counter bc current contaminated spin sector isn't masked
STOP
ENDIF ELSE IF (Onboard[1] EQ 1 ) THEN BEGIN
Masked = Masked + 1 ; Increment masked counter
STOP
ENDIF ELSE Clean = Clean + 1 ; Increment clean counter
ENDFOR
IF (Clean EQ 8 ) THEN BEGIN
Quality = 0 ; All 8 spin sectors are clean, assign "Green" quality indicator
ENDIF ELSE IF (Masked EQ 8 ) THEN BEGIN
Quality = 1 ; All 8 spin sectors are masked, assign "Red" quality indicator
ENDIF ELSE IF ( (Bad EQ 0) & (Masked > 0) ) THEN BEGIN
Quality = 2 ; Masked sectors total between 1 and 7, assign "Yellow" quality indicator
ENDIF ELSE IF (Bad/(Bad+Clean) < 0.5 ) THEN BEGIN
Quality = 3 ; Less than 50% spin sectors are bad, assign "Orange" quality indicator
ENDIF ELSE Quality = 1 ; 50% or greater spin sectors are bad, assign "Red" quality indicator
```

The final input into the assignment of data quality indicators is the timing of onboard calibration testing. The time intervals when the FEEPS instrument is in the onboard calibration mode are marked with the binary L1a variable "...calstate" and the data is not suitable for scientific research. If a burst or survey sector contains calibration testing data, the sector is assigned the "Grey" quality indicator (4).

```
IF (calstate EQ 1 ) THEN Quality = 4
```

These data quality indicators allow for quick sorting of the FEEPS data for scientific use, although the more advanced user does have the option to pick and choose whether to accept these quality indicators. This more advanced option is highly discouraged, but is provided to show transparency in the assignment of the quality indicators. The FEEPS data sets contain variables for the sun contamination tables, onboard masking tables, and calibration mode, such that the data quality indicators can be reproduced by others.

#### 6.4.4 EIS Calibration Matrix Overview

The response of the EIS sensors is complicated, and our understanding is based on a coordinated array of approaches, specifically:

- i) bench testing of channel gains and other characteristics based on calibrated pulse inputs;
- ii) calibrations using particle accelerator beams;
- iii) calibrations using radiation sources;
- iv) simulations of particle interactions with matter using such tools as GEANT4; and
- v) geometric calculations.

All of this information can be captured within an Excel Spreadsheet, with one sheet per sensor head. This spreadsheet captures various functional relationships with polynomial fits up to the 6<sup>th</sup> order. We will be referencing various portions of such a spreadsheet and will often do so by specifying the cell that is in the upper left hand corner of the referenced region of the spreadsheet. All the information described below, plus an additional hard-wired geometric factor and flat field function for the six electron and six ion telescopes (look directions) per sensor (not shown), is sufficient to determine the efficiency of detection of particles within an EIS sensor.

An example of such a calibration matrix is shown in Figure 6-14 and specifically captures:



- 1) Rows 5-12: The coefficients of the 6th-order polynomial fit expressing the SSD-measured energy in keV as a function of the internal sensor SSD data numbers (E-DN) for the six large
- 2) electron (columns B-G) and six large ion (columns I-N) SSD pixels.
- 3) Rows 20-26: The coefficients of the 6th-order polynomial fit expressing the SSD-measured
- 4) energy in keV as a function of the internal sensor SSD data numbers (E-DN) for the six small
- 5) electron (columns A-G) and six small ion (columns H-N) SSD pixels.
- 6) Cells B31-37: The coefficients of the 6th-order polynomial fit expressing the ion TOF in nanoseconds (ns) as a function of the internal TOF data number (TOF-DN).
- 7) Cells D35-H41: The coefficients of the 6th-order polynomial fit expressing the TOF in ns (TOF[ns]) as a function of the ion energy in keV coming into the sensor for different species (H, He, and O), taking into account the amount of materials in the form of foils that the ion must pass through to get the time-of-flight section.
- 8) Cells J35-N41: The inverse of the cells in 4) for each species, i.e. the coefficients of the 6<sup>th</sup>-order polynomial fit expressing the ion energy coming into the sensor in keV as a function of the TOF(ns) in ns.
- 9) Cells B45-F52: The coefficients of the 6<sup>th</sup>-order polynomial fit expressing the SSD deposited energy in keV as a function of the measured energy in keV, taking into account the pulse height defect associated with SSD measurements.
- 10) Cells I45-M52: The coefficients of the 6<sup>th</sup>-order polynomial fit expressing the energy input to the sensor in keV as a function of the energy deposited within the sensitive volume of the SSD, accounting for all of the materials that an ion must pass through before getting to the sensitive area of the SSD, including the SSD dead-layer.
- 11) Cells B57-J63: The coefficients of the 6<sup>th</sup>-order polynomial fit expressing the scattering efficiency of the sensor (efficiency between 0 and 1) as a function of the incoming energy in keV for different particle species (e-, H, He, O, and S), taking into account the scattering within the collimator foil and the start foil and considering two possible software constraints on the valid time-of-flight (designated “P-1 sec” and “P-3 sec”). For electrons, this information includes scattering within the 2  $\mu\text{m}$  of Al flashing that is deposited on the front surface of the SSD to keep out energetic protons.
- 12) Cells L61-O66: The coefficients of the 6th-order polynomial fit expressing the  $dE/dX$  (electronic) in  $\text{keV}/\mu\text{m}$  as a function of the ion TOF in ns, based on the laboratory-validated finding that the efficiency of emission of secondary electrons from the start and stop foils scales according to the  $dE/dX$  (electronic) within the emitting surfaces of the foil. Cells L58-O59 provide the laboratory-determined number of secondary electrons emitted for a “standard candle” of  $\sim 4.5$  MeV alpha particles from a slightly degraded Am241 radiation source (with  $dE/dX$  of approximately  $160 \text{ keV}/\mu\text{m}$  within carbon).

In Figure 6-14, the information described above is used to determine the energy and efficiency characteristics for the various channels comprising the EIS onboard data products (the channels shown are notional, not comprehensive). Four different kinds of channels are defined: 1) electron energy channels (rows 74-77); 2) ion energy channels (derived strictly from SSD measurements; rows 81-84); 3) TOFxE channels (rows 88-98); and 4) TOFxPH channels (rows 102-108). The user of this spreadsheet fills out the information in Columns A through H (which includes the data numbers for the range of energy or TOF, depending on the channel type), and the spreadsheet automatically calculates all of the other columns, including incoming energy ranges (“Ein1”, “Ein2”) and various contributions to the detection efficiency. The final intensity of a channel is derived by normalizing the channel count-rate by a geometric factor (not shown), a flat-fielding function (now shown), and by the “Eff-2” shown in the right-most column of each row. This energy assigned to each channel is the geometric mean of the energy range, called “mean Ein” in column O.

A	B	C	D	E	F	G	H	I	J	K	L	M	N	O	P	Q
1	Note: All Energies are in keV															
2																
3	Linear-Linear: SSD Measured-Energy = P6(SSD Energy-Channel)															
4	Large Pixel Electrons								Large Pixel Ions							
5		Sec 0	Sec 1	Sec 2	Sec 3	Sec 4	Sec 5		Sec 0	Sec 1	Sec 2	Sec 3	Sec 4	Sec 5		
6	a0	-4.22E+00	-4.22E+00	-4.22E+00	-4.22E+00	-4.22E+00	-4.22E+00	a0	-4.2741	-4.2741	-4.2741	-4.2741	-4.2741	-4.2741		
7	a1	9.85E-01	9.85E-01	9.85E-01	9.85E-01	9.85E-01	9.85E-01	a1	9.73E-01	9.73E-01	9.73E-01	9.73E-01	9.73E-01	9.73E-01		
8	a2	-8.48E-04	-8.48E-04	-8.48E-04	-8.48E-04	-8.48E-04	-8.48E-04	a2	-8.53E-04	-8.53E-04	-8.53E-04	-8.53E-04	-8.53E-04	-8.53E-04		
9	a3	1.00E-06	1.00E-06	1.00E-06	1.00E-06	1.00E-06	1.00E-06	a3	1.07E-06	1.07E-06	1.07E-06	1.07E-06	1.07E-06	1.07E-06		
10	a4	-5.89E-10	-5.89E-10	-5.89E-10	-5.89E-10	-5.89E-10	-5.89E-10	a4	-7.02E-10	-7.02E-10	-7.02E-10	-7.02E-10	-7.02E-10	-7.02E-10		
11	a5	1.62E-13	1.62E-13	1.62E-13	1.62E-13	1.62E-13	1.62E-13	a5	2.35E-13	2.35E-13	2.35E-13	2.35E-13	2.35E-13	2.35E-13		
12	a6	-1.56E-17	-1.56E-17	-1.56E-17	-1.56E-17	-1.56E-17	-1.56E-17	a6	-3.14E-17	-3.14E-17	-3.14E-17	-3.14E-17	-3.14E-17	-3.14E-17		
13								Transition	1707	1707	1707	1707	1707	1707		
14								a0	-50205.45	-50205.45	-50205.45	-50205.45	-50205.45	-50205.45		
15								a1	29.41155	29.41155	29.41155	29.41155	29.41155	29.41155		
16								a2	0	0	0	0	0	0		
17																
18	Small Pixel Electrons								Small Pixel Ions							
19		Sec 0	Sec 1	Sec 2	Sec 3	Sec 4	Sec 5		Sec 0	Sec 1	Sec 2	Sec 3	Sec 4	Sec 5		
20	a0	-4.22E+00	-4.22E+00	-4.22E+00	-4.22E+00	-4.22E+00	-4.22E+00	a0	-4.2741	-4.2741	-4.2741	-4.2741	-4.2741	-4.2741		
21	a1	9.85E-01	9.85E-01	9.85E-01	9.85E-01	9.85E-01	9.85E-01	a1	9.73E-01	9.73E-01	9.73E-01	9.73E-01	9.73E-01	9.73E-01		
22	a2	-8.48E-04	-8.48E-04	-8.48E-04	-8.48E-04	-8.48E-04	-8.48E-04	a2	-8.53E-04	-8.53E-04	-8.53E-04	-8.53E-04	-8.53E-04	-8.53E-04		
23	a3	1.00E-06	1.00E-06	1.00E-06	1.00E-06	1.00E-06	1.00E-06	a3	1.07E-06	1.07E-06	1.07E-06	1.07E-06	1.07E-06	1.07E-06		
24	a4	-5.89E-10	-5.89E-10	-5.89E-10	-5.89E-10	-5.89E-10	-5.89E-10	a4	-7.02E-10	-7.02E-10	-7.02E-10	-7.02E-10	-7.02E-10	-7.02E-10		
25	a5	1.62E-13	1.62E-13	1.62E-13	1.62E-13	1.62E-13	1.62E-13	a5	2.35E-13	2.35E-13	2.35E-13	2.35E-13	2.35E-13	2.35E-13		
26	a6	-1.56E-17	-1.56E-17	-1.56E-17	-1.56E-17	-1.56E-17	-1.56E-17	a6	-3.14E-17	-3.14E-17	-3.14E-17	-3.14E-17	-3.14E-17	-3.14E-17		
27								Transition	1707	1707	1707	1707	1707	1707		
28	Time of Flight: Linear-Linear								Time of Flight							
29	TOF(ns) = P6[TOF-channel]								TOF(ns) = P6[TOF-channel]							
30								a0	-50205.45	-50205.45	-50205.45	-50205.45	-50205.45	-50205.45		
31	a0	0						a1	29.41155	29.41155	29.41155	29.41155	29.41155	29.41155		
32	a1	0.25						a2	0	0	0	0	0	0		
33	a2	0														
34	a3	0														
35	a4	0														
36	a5	0														
37	a6	0														
38																
39																
40																
41																
42																
43	Pulse-Height Defect								Given SSD energy. What are the input energies coming into the sensor							
44	Log10(SSD Deposited-Energy) = P6[Log10(SSD Measured-Energy)]								Log10(Input Energy) = P6[Log10(SSD Deposited Energy)]							
45		e	H	He	O	S			e	H	He	O	S			
46	a0	0	0.11867	0.307255	0.529719	0.550292		a0	1.05307	1.25705	1.54463	1.2593	1.26368			
47	a1	1	0.896368	0.776169	0.920533	0.958583		a1	0.14046	0.171718	-0.34265	2.27329	2.42085			
48	a2	0	0.02439	0.035927	-0.080915	-0.030018		a2	-0.373825	0.087186	0.579905	-2.62401	-2.82329			
49	a3	0	0.000589	0.005311	-0.025027	-0.049949		a3	0.647852	-0.004526	-0.187744	1.49633	1.63798			
50	a4	0	-0.000518	-0.001249	0.032986	0.028446		a4	-0.274551	0.027604	0.043237	-0.404066	-0.458966			
51	a5	0	0	0	-0.008163	-0.00513		a5	0.049721	-0.009543	-0.005471	0.053539	0.063008			
52	a6	0	0	0	0.000636	0.000314		a6	-0.003351	0.000892	0.000268	-0.002806	-0.003447			
53																
54	Scatter Efficiency								For Foil Efficiencies							
55	Log10(Efficiency) = P6[Log10(incoming Energy)]								Log10(dE/dX (keV/mic)) = P6[Log10(E in TOF chamber)]							
56		e 3-Sec	p 1-Sec	p 3-Sec	He 1-Sec	He 3-Sec	O 1-Sec	O 3-Sec	S 1-Sec	S 3-Sec						
57	a0	-21.897	-23.1498	-17.0693	-35.4583	-24.5146	-60.122	-30.9256	4.80265	2.77665						
58	a1	46.2624	49.6625	35.5823	69.4742	45.9133	87.6626	34.7874	-50.9711	-39.7241						
59	a2	-39.7908	-43.3106	-30.1752	-55.6854	-35.0682	-49.4277	-10.1167	66.6342	53.1123						
60	a3	17.8517	19.6744	13.3435	23.3922	13.9965	13.1316	-2.23677	-36.4353	-29.3104						
61	a4	-4.41111	-4.91613	-3.24984	-5.43708	-3.08225	-1.48922	1.84537	10.0107	8.10283						
62	a5	0.569924	0.641564	0.413957	0.663662	0.355483	0.011999	-0.369034	-1.37094	-1.11556						
63	a6	-0.030119	-0.034211	-0.021576	-0.033269	-0.016793	0.007043	0.02497	0.074683	0.061086						
64																
65																
66																

Figure 6-14 Example of Coefficients of up to the 6<sup>th</sup>-Order Used to Define the Functional Relationship of Multiple Parameters in the EIS Calibration Matrix

### 6.4.5 Known Features in the Dataset (Data Caveats)

#### 6.4.5.1 EIS

- a) Telescopes (T3-ion, T2-electron) affected by sun shield: Ion telescope T3 and electron telescope T2 are substantially blocked by the instrument's sun shield. Although these telescopes obtain valid data and are supplied in the EIS data products, care should be exercised in using these telescopes if anomalies are seen.

- b) EIS1 telescope (T4) SSD anomaly: On MMS1, the solid-state detector (SSD) utilized in telescope T4 (for both ExTOF ion and electron data), is responding anomalously and should not be used at this point in time. It acts like it is under-biased, but the true cause is unknown.
- c) EIS1 HV micro-discharges anomalies: For the MMS1 spacecraft, the HV system experienced micro-discharge anomalies that caused the HV to be shut down by the onboard software on 30 January 2016, with some anomalous behavior seen for the first time on 21 January 2016, about 6 months after HV turn on. Because only 3 EIS units were required, the HV on EIS1 was disabled for the rest of the prime mission. EIS1 data prior to 21 January 2016 are assumed to be unaffected by these anomalies.
  - i. Beginning on 18 April 2016, EIS1 was put into high-resolution electron mode with “electronenergy” burst data enabled.
  - ii. HV (and ion species data) on MMS1 was re-enabled beginning on 31 January 2018. No further issues have been recorded to-date.
- d) HV turnoff in inner magnetosphere: From launch through 8 August 2016, the high voltage (ion data) on all EIS units was turned off inside a radial distance of 7  $R_E$ . The disabling of the HV system does not affect the collection of electron data.
  - i. Beginning on 8 August 2016, this turn on/off point was reduced to 6  $R_E$  on MMS2; the change to 6  $R_E$  was implemented on all spacecraft beginning on 22 March 2017.
  - ii. On 1 March 2018, the HV on/off flight rule was changed from 6  $R_E$  to  $L=6$ .
  - iii. On 12 March 2019, the HV on/off flight rule was changed from  $L=6$  to  $L=5$  for MMS4; after analysis revealed little degradation this was applied to MMS1-3 on 4 June 2019.
- e) HV turnoffs during long eclipse seasons and campaigns: At the following times, certain or all EIS units had the HV disabled or were entirely powered off – affecting data availability.
  - i. 12-30 June 2016 – Long-eclipse season
  - ii. 6-15 March 2019 – Turbulence campaign
  - iii. 17-31 August 2019 – Long-eclipse season
  - iv. 8-19 August 2020 – Long-eclipse season
- f) EIS electron data availability: Because of data volume limitations, and because the FEEPS sensors are the primary energetic electrons sensors, electrons are only measured on certain EIS units at any given time; which units are used for electrons was switched approximately every 14 orbits (~14 days) during MMS Phases 1, and was changed to every 3 orbits (~15 days) before the beginning of Phase 2b. Prior to the EIS1 HV anomaly detailed in item c), electrons were measured either on EIS1/3 or EIS 2/4. The units that are not generating electron data are instead generating what is called “event” data for diagnosing instrument performance.
  - i. After the EIS1 high-resolution electron mode was enabled, the swapping was disabled for EIS1, but remains in effect for EIS2-4.
  - ii. Beginning on 15 March 2017, this swapping was changed to every 5 orbits (~15 days). Burst electron data is obtained only from EIS1 and only following the reconfiguration of EIS1 into a high-resolution electron sensor.
  - iii. EIS electron data collection beyond 6  $R_E$  was discontinued for MMS2-4 on 14 November 2017; electron data ceased on MMS1 with the re-enabling of the HV on 31 January 2018 (see item c.ii above).
  - iv. EIS electron data was re-enabled on MMS4 only on 5 December 2019 with new energy channels covering from ~300 keV to >1.8 MeV
- g) Cosmic ray background in electron data: Penetrating cosmic rays generate a low-level band of contamination in the electron spectra (at about 1 count/s) centered between 150-200 keV. This contamination has not been subtracted from the foreground.
- h) Helium charge-state: Despite being labeled as “alpha” in the ExTOF files, the charge state of the helium (and oxygen) ions is unmeasured.
  - i. New vX.Y.100+ files of L2 EIS data, produced and made publicly available in Summer 2021 changed the names of these “alpha” variables to “helium” to more accurately represent their content. These

corrections were not applied to L1a/b data files and older data files that include the original “alpha” variable names should not be used.

- i) PHxTOF species determination: While in principle the low energy PHxTOF data products are able to discriminate between proton and oxygen, this discrimination works only when the heavy and light ion intensities are similar. Given the reality of the relative intensities, there is no automated procedure that can cleanly separate the light and heavy ion intensities for the PHxTOF lower energies, and the PHxTOF oxygen measurements are deemed unreliable and should be used with great caution. As such, several PHxTOF oxygen channels were reallocated to allow for better proton energy resolution beginning on 26 September 2016.
- j) Solar proton contamination in electron measurements: Because of the technique used by EIS to measure electrons, a simple SSD with 2  $\mu\text{m}$  of aluminum flashing on top, there will be periods of time (for solar proton events in particular) when the electron measurements are contaminated with  $>250$  keV protons.
- k) Cross-calibration efforts: During the first half of 2017, a considerable effort went into cross calibrating the EIS, FPI, HPCA, and FEEPS-ion sensors in their overlap regions. Based on this effort, the calibration matrices for EIS were substantially modified. As of this writing the new calibration matrices have been applied to all data following 1 November 2016. It is our intention to apply the calibration matrices on earlier data over time. The major change is in the efficiencies of protons at energies less than 50 keV, yielding intensities near 30 keV that are a factor of 5 higher than originally estimated.
  - i. The results of these cross-calibration efforts were implemented in the reprocessing of the complete L2 EIS dataset (new vX.Y.100+ files) that were made publicly available in Summer 2021. These corrections were not applied to L1a/b data files.
- l) Flat-fielding: An initial flat-fielding attempt has been made to adjust the EIS intensities. This initial attempt is known to be imperfect and is expected to be improved over time.
- m) Efficiency effects on flux determinations: The efficiency of ion detection for making ExTOF and PHxTOF ion measurements evolves over time because of variations of the gain of the microchannel plate in each of the EIS units. To-date a nominal efficiency multiplier is utilized with the Level 2 data, but slow evolutions of those efficiencies have not been folded into the data processing. The multiplicative error is up to about  $\pm 30\%$ .
- n) EIS file versioning: The full reprocessing of the L2 EIS dataset in Summer 2021 (new vX.Y.100+ files) updated the file versioning reported in Figure 6-2.

#### 6.4.5.2 FEEPS

- a) Sunlight contamination in survey data: Many of the FEEPS eyes suffer from light contamination, likely due to direct sunlight and glint coming through foils that were damaged during launch. This light contamination is identifiable in spectra specific to an individual spin sector and, therefore, correctable in burst mode data. For survey data products, prior to the CIDP changes implemented in October 2016, this contamination has an uncorrectable effect on some of the FEEPS eyes. Since the survey data products are produced by aggregating burst resolution data onboard each spacecraft for some eyes, the sunlight-contaminated sectors are unfortunately being combined with good sectors to produce the lower resolution corrupted survey sectors. This and other issues have been corrected via a series of CIDP updates implemented between October 2016 and August 2017. However, the fix is not perfect; some sunlight contamination still manages to make its way into the data product and should always be considered first when contamination associated with rotation are clear in the “spin tones” of the data products. For all data before and after these changes, please be aware of this contamination source and account for it in your studies. With burst data, please ensure that the affected eyes/sectors have been removed for analysis, and with survey data, be aware of the presence of this contamination in the data and proceed with caution for any scientific studies with that portion of the dataset. Badly

affected telescopes can also be removed from studies using survey data. More details, including examples of the sunlight contamination and examples of maps of the affected eyes and sectors from each spacecraft are provided in [section 6.3.2](#). NOTE: these effects change over time. Quality flags are provided in Level 2 data products to aid in the cautious use of survey data products. The MMS-specific IDL-based SPEDAS routines for FEEPS have been implemented with a hardwired filtering for eliminating the bad eyes and sectors.

- b) Sunlight contamination in burst data: For data between October 2016 and August 2017, some burst data were also adversely affected; please refer to [section 6.3.2](#) and contact members of the EPD team for guidance on any data analyses using data during this period.
- c) Spin tone: Despite flat fielding efforts (see [section 6.3.2.1](#)), the spin tone is still often visible in FEEPS electron data binned by pitch angle or gyro-phase. This is because the flat fielding changes the energy channel bounds for each FEEPS eye and sunlight contamination removes sectors from some telescopes in each spin. In effect, different telescopes are measuring slightly different energies. In a future version of the Level 2 data product, the data will be interpolated onto a common energy grid, which should mostly remove the spin-tone due to flat fielding. Currently, these inconsistencies can have a noticeable effect when combined with exponentially decaying energy spectra. In addition, the maximum or minimum values in the spin distribution might be missed if they fall in a contaminated sector.
- d) FEEPS unit timing: Prior to the October 2016 Central Instrument Data Processor (CIDP) changes, the FEEPS top and bottom units used independent times for the initial (i.e., 0<sup>th</sup>) sector of each spin. This misalignment is being accounted for in the data products, and the onboard correction was implemented on each spacecraft with the CIDP changes in October 2016. The CIDP changes will ensure that both top and bottom instruments trigger simultaneously on the sun-pulse signal on each spacecraft and that no alignment on the ground will be necessary. Prior to this date, the science data will contain a default fill value indicating NAN for any sectors that were affected by the misalignment. This effect is mostly superficial, but is documented here for completeness.
- e) Energy thresholds for lowest energy channels: The first energy channels (i.e., those with the smallest indices) from FEEPS ion and electron sensors have their threshold set very near to or within the noise threshold. These channels from most (but not all) eyes are often measuring noise and should not be used for scientific data analysis. When included in the omni-directional product, these eyes result in a discrepancy at the lowest energy channel(s). On several of the FEEPS eyes, the second energy channels also require threshold adjustment as of 04 April 2016. The effect of this is clear when comparing energy spectra from independent eyes during periods with high count rates and isotropic angular distributions. The affected eyes/energy-channels will show large (factor of 5 or more) decreases or increases in the count rates compared to the other eyes. An example of this is shown in Figure 6-10. The affected channels should **not** be included for any scientific analysis.
- f) Integral channels: The last energy channels (i.e., those with the highest energy level, with index 15) for FEEPS ion and electron instruments are effectively integral channels, combining counts from all energies greater than those in index 14. Thus, these data are an independent and different dataset from the other channels and should not be included in combined spectra or energy distributions with the other channels.
- g) Solar Energetic Particle (SEP) contamination in electron channels: it is expected that there will be some response in the electron sensors to SEPs, however, as of 04 April 2016), the electron measurements seem to be relatively unaffected by these events.
- h) Ion measurement contamination by electrons: the ion measurements are largely unaffected by energetic electron contamination. This is due to the ultra-thin detectors used in the FEEPS ion eyes, which are less than 15  $\mu\text{m}$  thick.
- i) Radiation belts: As of 3 April 2020, the FEEPS data agree well with Van Allen Probes in Earth's outer radiation belt, however, some contamination of the electron data may be present due to enhanced background levels during times of very hard radiation belt spectra (i.e., high intensities of

>1 MeV electrons). Caution should be taken when using these data in the radiation belts, but they do provide a reasonably accurate measure of outer radiation belt electrons. If the opportunity arises in the future there will be an effort to monitor the >500 keV fluxes at GEO (using GOES13, 14, 15, 16 and 17) for cases of hard spectra and then use the results to generate a baseline hardness at which the contamination starts to rise. As of writing, it has been too magnetically quiet to obtain that data.

- j) X-ray response: Based on tests conducted during solar X-ray flares on 04 and 09 November 2015, the FEEPS ion and electron instruments have no significant response to solar X-rays.
- k) Cross-calibration efforts: Preliminary cross-calibration has been conducted between FEEPS with EIS and FPI. Those results show good agreement between the instruments; however, no formal cross-calibration factors have been applied to the dataset, so use caution when combining these data products. Combined distributions are expected to be officially produced as a Level 3 data product.
- l) Quality indicators: Level 2 data products contain a data quality indicator which is described in section 6.4.2.
- m) Cosmic ray background in electron data: Penetrating cosmic rays generate a low-level band of contamination in the electron spectra (at about 1 count/s) centered on about ~300-350 keV. This contamination has not been subtracted from the foreground.

---

## 6.5 DATA PRODUCTS

### 6.5.1 Data Products Overview

Three levels of data product available for scientific or engineering use referred to as L1A, L1B, and L2. The first level, L1A, contains sensor counts represented as numerical values (as opposed to telemetry bytes in level 0), L1B contains synthesized data such as pitch angles and intensity. L2 data contains refinements to pitch angle and ephemeris data and is the data level intended for use in scientific analysis. The dataset consists of a collection of timestamped files which are formatted in accordance with the International Solar-Terrestrial Physics/Space Physics Data Facility (ISTP/SPDF) standard Common Data Format (CDF).

**Level 1b:** The CDF variables in these files correspond to data derived from the counts variable contained in L1A (count rate and intensity) as well as variables containing magnetic field pitch angle data, ephemeris data and data quality indicators. The algorithm for calculating intensity is provided in section 6.4.1.

There are four types of FEEPS L1b data:

1. L1B electron burst
2. L1B ion burst
3. L1B electron survey
4. L1B ion survey

These types are represented in the data file names.

- mms1\_feeps\_brst\_l1b\_electron\_20211019023633\_v6.1.1.cdf
- mms1\_feeps\_srvy\_l1b\_ion\_20211019000000\_v6.1.1.cdf

**Level 1b:** These are observatory level data products; for each spacecraft, there would be one set from FEEPS (the two instruments combined) and one set from EIS. At the “Record” level there is time (UTC), a quality flag, (bad sector flag, but no quality flag in FEEPS L1b) an accumulation time for each channel,

a spin sector, perhaps a spin number, and magnetic field and ephemeris data. At the detector or look direction level there is pitch angle, GSE look direction (Solar Angle + Elevation), live-time (not in FEEPS L1b) or dead-time, and the E1 of the lowest energy channel. At the channel level, there are 4-position “vectors”, specifically: {EGM, counts-per-accumulation, counts-per-second, rough-intensity}, where EGM is the geometric mean of  $E_1$  and  $E_2$  [ $\sqrt{E_1 \times E_2}$ ], the energy bounds of the energy channel. The deviations of  $E_1$  and  $E_2$  for each channel from EGM are also reported. Here the “rough-intensity” is results from the conversion of “counts-per-second” to “intensity” using only approximate, uncertified calibration matrices, as are the energies,  $E$  (and  $E^*$ ). No live-time or dead-time correction is applied to the counts, the counts/second, or the rough intensity. As with the Level 1a product, for each record the UTC time (or equivalent) must be recorded and a standard for whether that time is the beginning or the middle of an accumulation time. Quicklook data displays and any needed SITL data products are generated at this level. Note that there are no EIS and FEEPS data that are joined together at this point in time. The Level 1b data products are listed here, with FEEPS in black and EIS in green (note that “top” and “bottom” FEEPS sensors are now combined):

01. L1b-FEEPS-Electron-Burst
02. L1b-FEEPS-Electron-Survey
03. L1b-FEEPS-Ion-Burst
04. L1b-FEEPS-Ion-Survey
05. L1b-EIS-PhxTOF-Ion-Burst
06. L1b-EIS-ExTOF-Ion-Burst
07. L1b-EIS-PhxTOF-Ion-Survey
08. L1b-EIS-ExTOF-Ion-Survey
09. L1b-EIS-Electron-Energy-Survey (diagnostic)\*
10. L1b-EIS-Electron-Energy-Burst (diagnostic)\*\*
11. L1b-EIS-Ion-Energy-Burst (diagnostic)
12. L1b-EIS-Ion-Energy-Survey (diagnostic)

\*EIS Electron Energy Survey is only available on select spacecraft at any given time.

\*\*EIS Electron Energy Burst became a standard data product for EIS1 in April 2016.

NOTE: EIS Level 1b data is used for Quicklook Plotting and Scientist-in-the-Loop (SITL) considerations.

**Level 2:** These data are identical in format and content as the Level 1b dataset. The difference is: 1) live-time or dead-time corrections are applied to the counts per second as reported in this product, and before the generation of intensity. 2) “rough-intensity” values are replaced with “refined-intensity”, 3) rough values of E1 and E2 are replaced with refined values, 4) preliminary magnetic field is replaced with updated magnetic field, 5) predict ephemeris is replaced with updated ephemeris, and 6) the record-level quality flag is updated. The list of Level 2 data products is nearly identical to the Level 1b products. Note that only Level 2 products 1-8 are generally available to the scientific community, with 9 and 10 selectively available. Again, products from FEEPS are in black and those from EIS are in blue:

01. L2-FEEPS-Electron-Burst
  02. L2-FEEPS-Electron-Survey
  03. L2-FEEPS-Ion-Burst
  04. L2-FEEPS-Ion-Survey
  05. L2-EIS-PhxTOF-Ion-Burst
  06. L2-EIS-ExTOF-Ion-Burst
  07. L2-EIS-PhxTOF-Ion-Survey
  08. L2-EIS-ExTOF-Ion-Survey
- There are several types of EIS L2 data products
05. L2-EIS-PhxTOF-Ion-Burst

06. L2-EIS-ExTOF-Ion-Burst
07. L2-EIS-PhxTOF-Ion-Survey
08. L2-EIS-ExTOF-Ion-Survey
09. L2-EIS-Electron-Energy-Survey (diagnostic)\*
10. L2-EIS-Electron-Energy-Burst (diagnostic)\*\*
11. L2-EIS-Ion-Energy-Burst (diagnostic)
12. L2-EIS-Ion-Energy-Survey (diagnostic)

These types are represented in data file names such as:

- mms1\_epd-eis\_brst\_l2\_extof\_20210822071603\_v5.0.4.cdf

**Level 3:** Refer to section 6.5.7, “Level 3 EPD Data Products” for a detailed description of higher-level data products.

### 6.5.2 File Structure L2 FEEPS Electron

The variables contained within the FEEPS Level 2 Products generated within the MMS Science Data Center (SDC), are outlined in Table 6-3 and Table 6-4 below. All of these FEEPS variables begin with,

$$\langle \text{prefix} \rangle = \text{mms}\langle \# \rangle \_ \text{epd\_feeps\_}\langle \text{DATA\_RATE} \rangle \_ \text{l2\_}$$

where  $\langle \# \rangle$  is the spacecraft number and  $\langle \text{DATA\_RATE} \rangle$  is the telemetry mode (srvy, brst, or raw).  $\langle \text{SIDE} \rangle$  will be “top” or “bottom” to indicate which FEEPS unit the data correspond to. The  $\langle \# \rangle$  portion found in several variables represents the sensor identifier number.

Data Parameter	Description	Units
Epoch	UTC timestamp at sector center	TT2000
$\langle \text{prefix} \rangle \_ \text{electron\_spinsectnum}$	Spin sector in which the spacecraft was oriented during data acquisition	-----
$\langle \text{prefix} \rangle \_ \text{electron\_energy}$	Centroid of differential energy channels associated with each of 16 FEEPS channels	keV
$\langle \text{prefix} \rangle \_ \text{electron\_energy\_lower\_bound}$	Lower bound of differential energy channels associated with each of 16 FEEPS channels	keV
$\langle \text{prefix} \rangle \_ \text{electron\_energy\_upper\_bound}$	Upper bound of differential energy channels associated with each of 16 FEEPS channels	keV
$\langle \text{prefix} \rangle \_ \langle \text{SIDE} \rangle \_ \text{electron\_count\_rate\_sensorid\_}\langle \# \rangle$	Count rate	counts/s
$\langle \text{prefix} \rangle \_ \langle \text{SIDE} \rangle \_ \text{electron\_intensity\_sensorid\_}\langle \# \rangle$	Unidirectional differential flux per spin sector	1/(cm <sup>2</sup> -s-sr-keV)
$\langle \text{prefix} \rangle \_ \langle \text{SIDE} \rangle \_ \text{electron\_sector\_mask\_sensorid\_}\langle \# \rangle$	Array of bad sector flags for a packet	-----
$\langle \text{prefix} \rangle \_ \text{electron\_spin}$	The number of spacecraft rotations	Seconds
$\langle \text{prefix} \rangle \_ \text{electron\_spin\_duration}$	Period of the spin	-----
$\langle \text{prefix} \rangle \_ \text{electron\_integration\_sectors}$	Integration sectors	-----
$\langle \text{prefix} \rangle \_ \text{electron\_bfield}$	Magnetic field vector	nT
$\langle \text{prefix} \rangle \_ \text{electron\_pitch\_angle}$	Pitch angle with respect to local magnetic field	Degrees



<i>&lt;prefix&gt;_electron_scpos_ec_gse</i>	Spacecraft position in Earth-centered geocentric solar ecliptic coordinates	Km
<i>&lt;prefix&gt;_electron_scz_vec_gse</i>	Spacecraft Unit Vector Z-Axis in Earth-centered Geophysical Coordinates	-----
<i>&lt;prefix&gt;_electron_scy_vec_gse</i>	Spacecraft Unit Vector Y-Axis in Earth-centered Geophysical Coordinates	-----
<i>&lt;prefix&gt;_electron_scx_vec_gse</i>	Spacecraft Unit Vector X-Axis in Earth-centered Geophysical Coordinates	-----
<i>&lt;prefix&gt;_electron_moon_pos_gse</i>	Position of the moon in Earth-centered Geophysical Coordinates	Km
<i>&lt;prefix&gt;_electron_radius</i>	Radial distance in Earth radii	R <sub>E</sub> (Earth radii)
<i>&lt;prefix&gt;_electron_lat_gse</i>	Latitude in Earth-centered Geophysical Coordinates	Degrees
<i>&lt;prefix&gt;_electron_lon_gse</i>	Longitude in Earth-centered Geophysical Coordinates	Degrees
<i>&lt;prefix&gt;_electron_l_shell</i>	Dipole L shell in Earth radii determined using Solar Magnetospheric latitude	R <sub>E</sub> (Earth radii)
<i>&lt;prefix&gt;_electron_lat_gsm</i>	Latitude in Solar Magnetospheric Coordinates	Degrees
<i>&lt;prefix&gt;_electron_lon_gsm</i>	Longitude in Solar Magnetospheric Coordinates	Degrees

**Table 6-3 List of the Burst Variable Included in the FEEPS Electron Data Product**

<b>Data Parameter</b>	<b>Description</b>	<b>Units</b>
<i>epoch</i>	UTC timestamp at sector center	TT2000
<i>&lt;prefix&gt;_electron_spinsectnum</i>	spin sector in which the spacecraft was oriented during data acquisition	-----
<i>&lt;prefix&gt;_electron_energy</i>	Centroid of differential energy channels associated with each of 16 FEEPS channels	keV
<i>&lt;prefix&gt;_electron_energy_lower_bound</i>	Lower bound of differential energy channels associated with each of 16 FEEPS channels	keV
<i>&lt;prefix&gt;_electron_energy_upper_bound</i>	Upper bound of differential energy channels associated with each of 16 FEEPS channels	keV
<i>&lt;prefix&gt;_&lt;SIDE&gt;_electron_count_rate_sensorid_&lt;#&gt;</i>	Count rate	counts/s
<i>&lt;prefix&gt;_&lt;SIDE&gt;_electron_intensity_sensorid_&lt;#&gt;</i>	Unidirectional differential flux per spin sector	1/(cm <sup>2</sup> -s-sr-keV)
<i>&lt;prefix&gt;_&lt;SIDE&gt;_electron_sector_mask_sensorid_&lt;#&gt;</i>	array of bad sector flags for a packet	-----
<i>&lt;prefix&gt;_electron_spin</i>	The number of spacecraft rotations	-----
<i>&lt;prefix&gt;_electron_spin_duration</i>	period of the spin	Seconds
<i>&lt;prefix&gt;_electron_integration_sectors</i>	integration sectors	-----
<i>&lt;prefix&gt;_electron_bfield</i>	magnetic field vector	nT
<i>&lt;prefix&gt;_electron_pitch_angle</i>	Pitch angle wrt local magnetic field	Degrees
<i>&lt;prefix&gt;_electron_scpos_ec_gse</i>	Spacecraft position in Earth-centered geocentric solar ecliptic coordinates	Km

<prefix>_electron_scz_vec_gse	Spacecraft Unit Vector Z-Axis in Earth-centered Geophysical Coordinates	----
<prefix>_electron_scy_vec_gse	Spacecraft Unit Vector Y-Axis in Earth-centered Geophysical Coordinates	----
<prefix>_electron_scx_vec_gse	Spacecraft Unit Vector X-Axis in Earth-centered Geophysical Coordinates	----
<prefix>_electron_moon_pos_gse	the position of the moon in Earth-centered Geophysical Coordinates	Km
<prefix>_electron_radius	radial distance in Earth radii	R <sub>E</sub> (Earth radii)
<prefix>_electron_lat_gse	latitude in Earth-centered Geophysical Coordinates	Degrees
<prefix>_electron_lon_gse	longitude in Earth-centered Geophysical Coordinates	Degrees
<prefix>_electron_l_shell	Dipole L shell in Earth radii determined using Solar Magnetospheric latitude	R <sub>E</sub> (Earth radii)
<prefix>_electron_lat_gsm	latitude in Solar Magnetospheric Coordinates	Degrees
<prefix>_electron_lon_gsm	longitude in Solar Magnetospheric Coordinates	Degrees

**Table 6-4 List of the Survey Variable Included in the FEEPS Electron Data Product**

### 6.5.3 File Structure L2 FEEPS Ion

The variables contained within the FEEPS Level 2 Products generated within the MMS Science Data Center (SDC), are outlined in Table 6-5 and Table 6-6 below. All of these FEEPS variables begin with,

$$\langle \text{prefix} \rangle = \text{mms}\langle \# \rangle\_epd\_feeps\_ \langle \text{DATA\_RATE} \rangle\_l2\_ ,$$

where <#> is the spacecraft number and <DATA\_RATE> is the telemetry mode (srvy, brst, or raw). <SIDE> will be “top” or “bottom” to indicate which FEEPS unit the data correspond to. The <#> portion found in several variables represents the sensor identifier number.

Data Parameter	Description	Units
<i>Epoch</i>	UTC timestamp at sector center	TT2000
<prefix>_ion_spinsectnum	Spin sector in which the spacecraft was oriented during data acquisition	----
<prefix>_ion_energy	Centroid of differential energy channels associated with each of 16 FEEPS channels	keV
<prefix>_ion_energy_lower_bound	Lower bound of differential energy channels associated with each of 16 FEEPS channels	keV
<prefix>_ion_energy_upper_bound	Upper bound of differential energy channels associated with each of 16 FEEPS channels	keV
<prefix>_<SIDE>_ion_count_rate_sensorid_<#>	Count rate	counts/s
<prefix>_<SIDE>_ion_intensity_sensorid_<#>	Unidirectional differential flux per spin sector	1/(cm <sup>2</sup> -s-sr-keV)
<prefix>_<SIDE>_ion_sector_mask_sensorid_<#>	Array of bad sector flags for a packet	----
<prefix>_ion_spin	The number of spacecraft rotations	----

<i>&lt;prefix&gt;_ion_spin_duration</i>	Period of the spin	Seconds
<i>&lt;prefix&gt;_ion_integration_sectors</i>	Integration sectors	-----
<i>&lt;prefix&gt;_ion_bfield</i>	Magnetic field vector	nT
<i>&lt;prefix&gt;_ion_pitch_angle</i>	Pitch angle with respect to local magnetic field	Degrees
<i>&lt;prefix&gt;_ion_scpos_ec_gse</i>	Spacecraft position in Earth-centered geocentric solar ecliptic coordinates	Km
<i>&lt;prefix&gt;_ion_scz_vec_gse</i>	Spacecraft Unit Vector Z-Axis in Earth-centered Geophysical Coordinates	-----
<i>&lt;prefix&gt;_ion_scy_vec_gse</i>	Spacecraft Unit Vector Y-Axis in Earth-centered Geophysical Coordinates	-----
<i>&lt;prefix&gt;_ion_scx_vec_gse</i>	Spacecraft Unit Vector X-Axis in Earth-centered Geophysical Coordinates	-----
<i>&lt;prefix&gt;_ion_moon_pos_gse</i>	Position of the moon in Earth-centered Geophysical Coordinates	Km
<i>&lt;prefix&gt;_ion_radius</i>	Radial distance in Earth radii	R <sub>E</sub> (Earth radii)
<i>&lt;prefix&gt;_ion_lat_gse</i>	Latitude in Earth-centered Geophysical Coordinates	Degrees
<i>&lt;prefix&gt;_ion_lon_gse</i>	Longitude in Earth-centered Geophysical Coordinates	Degrees
<i>&lt;prefix&gt;_ion_l_shell</i>	Dipole L shell in Earth radii determined using Solar Magnetospheric latitude	R <sub>E</sub> (Earth radii)
<i>&lt;prefix&gt;_ion_lat_gsm</i>	Latitude in Solar Magnetospheric Coordinates	Degrees
<i>&lt;prefix&gt;_ion_lon_gsm</i>	Longitude in Solar Magnetospheric Coordinates	Degrees

**Table 6-5 List of the Burst Variables Included in the FEEPS Ion Data Product**

<b>Data Parameter</b>	<b>Description</b>	<b>Units</b>
<i>Epoch</i>	UTC timestamp at sector center	TT2000
<i>&lt;prefix&gt;_ion_spinsectnum</i>	Spin sector in which the spacecraft was oriented during data acquisition	-----
<i>&lt;prefix&gt;_ion_energy</i>	Centroid of differential energy channels associated with each of 16 FEEPS channels	keV
<i>&lt;prefix&gt;_ion_energy_lower_bound</i>	Lower bound of differential energy channels associated with each of 16 FEEPS channels	keV
<i>&lt;prefix&gt;_ion_energy_upper_bound</i>	Upper bound of differential energy channels associated with each of 16 FEEPS channels	keV
<i>&lt;prefix&gt;_&lt;side&gt;_ion_count_rate_sensorid_&lt;#&gt;</i>	Count rate	counts/s
<i>&lt;prefix&gt;_&lt;side&gt;_ion_intensity_sensorid_&lt;#&gt;</i>	Unidirectional differential flux per spin sector	1/(cm <sup>2</sup> -s-sr-keV)
<i>&lt;prefix&gt;_&lt;side&gt;_ion_sector_mask_sensorid_&lt;#&gt;</i>	Array of bad sector flags for a packet	-----
<i>&lt;prefix&gt;_ion_spin</i>	The number of spacecraft rotations	-----
<i>&lt;prefix&gt;_ion_spin_duration</i>	Period of the spin	seconds
<i>&lt;prefix&gt;_ion_integration_sectors</i>	Integration sectors	-----

<prefix>_ion_bfield	Magnetic field vector	nT
<prefix>_ion_pitch_angle	Pitch angle with respect to local magnetic field	Degrees
<prefix>_ion_scpos_ec_gse	Spacecraft position in Earth-centered geocentric solar ecliptic coordinates	Km
<prefix>_ion_scz_vec_gse	Spacecraft Unit Vector Z-Axis in Earth-centered Geophysical Coordinates	-----
<prefix>_ion_scy_vec_gse	Spacecraft Unit Vector Y-Axis in Earth-centered Geophysical Coordinates	-----
<prefix>_ion_scx_vec_gse	Spacecraft Unit Vector X-Axis in Earth-centered Geophysical Coordinates	-----
<prefix>_ion_moon_pos_gse	Position of the moon in Earth-centered Geophysical Coordinates	Km
<prefix>_ion_radius	Radial distance in Earth radii	R <sub>E</sub> (Earth radii)
<prefix>_ion_lat_gse	Latitude in Earth-centered Geophysical Coordinates	degrees
<prefix>_ion_lon_gse	Longitude in Earth-centered Geophysical Coordinates	degrees
<prefix>_ion_l_shell	Dipole L shell in Earth radii determined using Solar Magnetospheric latitude	R <sub>E</sub> (Earth radii)
<prefix>_ion_lat_gsm	Latitude in Solar Magnetospheric Coordinates	Degrees
<prefix>_ion_lon_gsm	Longitude in Solar Magnetospheric Coordinates	degrees

**Table 6-6 List of the Survey Variables Included in the FEPS Ion Data Product**

#### 6.5.4 File Structure EIS Electronenergy

These data are identical in format and content as the Level 1b dataset. The difference is: 1) live-time or dead-time corrections are applied to the counts per second as reported in this product, and before the generation of intensity. 2) “rough-intensity” values are replaced with “refined-intensity”, 3) rough values of E1 and E2 are replaced with refined values, 4) preliminary magnetic field is replaced with updated magnetic field, 5) predict ephemeris is replaced with updated ephemeris, and 6) the record-level quality flag is updated. The list of Level 2 data products is nearly identical to the Level 1b products. Note that only Level 2 products 1-8 are generally available to the scientific community, with 9 and 10 selectively.

#### 6.5.5 File Structure L2 EIS ExTOF and PHxTOF

Level 1B (L1B) files are exactly the same format as Level 2 (L2) files, they have merely been produced with less reliable data including some or all of the following: predicted ephemeris an attitude information (as opposed to definitive information), lower-level FGM data, preliminary calibration tables.

The files are International Solar-Terrestrial Physics/Space Physics Data Facility (ISTP/SPDF) standard Common Data Format (CDF) files. There are three L2 files, one for each data type.

1. electronenergy: (note that electron data may be contaminated with (>250 keV protons).
2. extof: High-energy (ExTOF) ion spectra organized by particle species.
3. phxtof: Low-energy (PHxTOF) ion spectra organized by particle species.

All the principal variables in each file have the same “time axis” (DEPEND\_0 attribute), so the file can be thought of as a simple rectangular “table” with each time value of the Epoch variable defining a “row”

and each non-constant CDF variable as a “column”. The Epoch is the midpoint of the accumulation interval. Time\_Minus and Time\_Plus (DELTA\_PLUS and DELTA\_MINUS attributes) give the start and stop edges of the time bin as specified by the ISTP CDF standard.

There is one spectral variable for each “species”: electron, proton, alpha, oxygen, or “dump” (where “dump” captures every event that was not classified as one of the defined species). Each spectral variable has a DEPEND\_1 attribute that points to a (constant) variable which gives the centers of the energy bins and that variable, in turn, has DELTA\_PLUS and DELTA\_MINUS attributes that point to variables giving the bin edges (as described in the ISTP CDF standard). Each spectrum is given in three data units (or using three “calibrations”):

1. counts: The raw number of counts collected during the current accumulation interval (see discussion of the “Timing and Geometry Block” below). This value is uncorrected in any way and may be used to calculate the relative uncertainty of all three “calibrations” using standard Poisson statistics.
2. cps: The count rate [counts/s] in each energy bin. This quantity may be corrected for instrument saturation effects (this procedure is still in development).
3. flux: The calibrated differential intensity [1/cm<sup>2</sup>-sr-s-keV] of charged particles in each energy bin.

There are 6 spectral variables for each calibration (numbered 0-5) corresponding to the 6 look directions (or “telescopes”) of the instrument.

The variables in each spectral file can be grouped into four conceptual “blocks”:

1. Timing and Geometry: Describes the time period over which the measurement was taken and low-level attitude and instrument configuration data needed to calibrate the raw counting rates in these files.
2. Spectral: One CDF variable for each species and calibration.
3. Ephemeris, Attitude, and Pitch Angle: Spacecraft position, look direction, pitch angle, and magnetic field.
4. Basic Rates: Raw total counting rates in various instrument subsystems. These give a quick overview of the measured environment and state of the instrument.

Apart from the Epoch variables, which follow the general ISTP standard, the EIS variables all begin with a “prefix” following the standard MMS naming scheme:

`<eis_prefix> = mms<#>_epd_eis_<DATA_RATE>_<LEVEL>_<DATA_TYPE>_`,  
indicated in the variables below by “\*”.

- 1) The Timing and Geometry block consists of the following variables:
  - *epoch*, *time minus*, *time plus* – Standard CDF time specifications for the measurement window.
  - *\*starttai*, *\*midtai*, *\*endtai* – The beginning, middle, and end of the measurement window in International Atomic Time (TAI) expressed as seconds since 1958 (standard MMS spacecraft time).
  - *\*spin* – A 16-bit spin counter (0-65535). This is retained in L2 data for instrument team use in file validation.
  - *\*sector* – The first sector (0-31) of the measurement that may include multiple sectors. A full revolution of the spacecraft is divided into 32 evenly spaced sectors. Several sectors are combined for measurements in most data products so that only 8 or 16 measurements, for example, are made in a revolution. Data products may be collected only every nth spin. This is

retained in L2 data primarily for instrument team use in validation, but it may prove useful to other investigators as a simple way of performing rough attitude filtering or grouping.

- *\*quality* – bit flags indicating reliability of the data, these values are still under development.
- 2) The Spectral block variables are named with the form:  
***\*<SPECIES> P<LUT PERIOD> <DATA UNITS> T<#>***
- 3) The Ephemeris, Attitude, and Pitch Angle block consists of the following variables:
- *\*pitch\_angle\_t<#>* - The angle between the particle flow vector and the magnetic field for each of the 6 “telescopes”. The particle flow vector is the negative of the telescope look direction.
  - *\*look\_t<#>* – The look direction of the telescope in the standard GSE coordinate frame.
  - *\*b* – The magnetic field used to derive the pitch angle.
  - *\*position\_gse* – The spacecraft position with respect to the Earth in the GSE frame
  - *\*position\_gsm* – The spacecraft position with respect to the Earth in the GSM frame
  - *\*moon\_gse* – The spacecraft position with respect to the Moon in the GSE frame
  - *\*sc\_to\_gse* – Transformation matrix for rotating a vector from the spacecraft frame (BCS) to the GSE frame [entries are by row: row1 = row1, row2 = 4-6, row3 = 7-9]
  - *\*gse\_to\_gsm* – Transformation matrix for rotating a vector from the GSE frame to the GSM frame [entries are by row: row1 = row1, row2 = 4-6, row3 = 7-9]
  - *\*r* – Spacecraft distance from Earth in kilometers
  - *\*l* – Spacecraft position L-shell for a dipole magnetic field
  - *\*gse\_lat*, *\*gse\_lon*, *\*gsm\_lat*, *\*gsm\_lon*, *\*sm\_lat*, *\*sm\_lon* – Spacecraft position latitude and longitude in GSE, GSM, or SM frame.
  - *\*orbit\_num* – MMS mission orbit number
- 4) The Basic Rates block consists of the following variables:
- For all data types:***
- *\*ssd<#>* – Number of pulses detected on the solid-state energy detector for telescope number 0-5
  - *\*vep* – Valid Events Processed – Number of events actually processed by the flight software
- For electron data:***
- *\*vee* – Valid Energy Events – Total number of events in all SSD (Energy) detectors.
- For ion data types:***
- *\*start0anode*, *\*stop0anode* – Number of pulses on the end of the Start or Stop anode nearest to look direction 0
  - *\*pulseheight* – Number of events above TOF pulse height threshold
  - *\*vtofxee* – Number of valid ExTOF events counted.
  - *\*vtofpxhe* – Number of valid PHxTOF events counted.

As of Summer 2021 (see §0.h.i), the EIS data variables listed in Exhibits 19-24 all include the following <eis\_prefix> = mms<#>\_epd\_eis\_<DATA\_RATE>\_l2, where <#> is the spacecraft number and <DATA\_RATE> is the sampling mode (“srvy” or “brst”).

### 6.5.6 File Structure L2 EIS PHxTOF

<u>Data Parameter</u>	<u>Description</u>	<u>Units</u>
Time_Minus	<support data> Delta from measurement window start to midpoint	s
Time_Plus	<support data> Delta from midpoint to measurement window end	s
<eis_prefix>_phxtof_duration	<support data> Total exposure time for accumulation	s
<eis_prefix>_phxtof_deadtime	<support data> Instrument deadtime	s

<eis_prefix>_phxtof_largepixel	<support data> Instrument large pixel in use (yes/no)	-----
<eis_prefix>_phxtof_starttai	<support data> Begin measurement window, TAI since 1958	s
<eis_prefix>_phxtof_midtai	<support data> Nominal measurement time, TAI since 1958	s
<eis_prefix>_phxtof_endtai	<support data> End measurement window, TAI since 1958	s
<eis_prefix>_phxtof_spin	<support data> Spacecraft spin number	-----
<eis_prefix>_phxtof_sector	<support data> Spacecraft spin sector	-----
<eis_prefix>_phxtof_quality	<support data> Quality word	-----
<eis_prefix>_phxtof_proton_P<X>_counts_t<#>	Individual telescope (look direction) proton counts for each energy channel	counts
<eis_prefix>_phxtof_proton_P<X>_cps_t<#>	Individual telescope (look direction) proton counts per second for each energy channel	1/s
<eis_prefix>_phxtof_proton_P<X>_flux_t<#>	Individual telescope (look direction) proton intensity (flux) for each energy channel	1/(cm <sup>2</sup> -s-sr-keV)
<eis_prefix>_phxtof_oxygen_P<X>_counts_t<#>	Individual telescope (look direction) oxygen (charge state unmeasured) counts for each energy channel	counts
<eis_prefix>_phxtof_oxygen_P<X>_cps_t<#>	Individual telescope (look direction) oxygen (charge state unmeasured) counts per second for each energy channel	1/s
<eis_prefix>_phxtof_oxygen_P<X>_flux_t<#>	Individual telescope (look direction) oxygen (charge state unmeasured) intensity (flux) for each energy channel	1/(cm <sup>2</sup> -s-sr-keV)
<eis_prefix>_phxtof_dump_counts_t<#>	Individual telescope (look direction) ion counts dump bin for each energy channel	counts
<eis_prefix>_phxtof_dump_cps_t<#>	Individual telescope (look direction) ion counts per second dump bin for each energy channel	1/s
<eis_prefix>_phxtof_dump_flux_t<#>	Individual telescope (look direction) ion intensity (flux) dump bin for each energy channel	-----
<eis_prefix>_phxtof_pitch_angle_t<#>	Pitch angle for individual telescope (look direction)	degrees
<eis_prefix>_phxtof_look_t<#>	Look direction vector in GSE for individual telescope	-----
<eis_prefix>_phxtof_b	Magnetic field in BCS coordinates	nT
<eis_prefix>_phxtof_position_gse	Spacecraft position vector in GSE	km
<eis_prefix>_phxtof_position_gsm	Spacecraft position vector in GSM	km
<eis_prefix>_phxtof_moon_gse	Spacecraft-to-moon vector in GSE	km
<eis_prefix>_phxtof_sc_to_gse	Transformation matrix from SC to GSE coordinates	-----
<eis_prefix>_phxtof_gse_to_gsm	Transformation matrix from GSE to GSM coordinates	-----
<eis_prefix>_phxtof_r	Magnitude of radial distance	km
<eis_prefix>_phxtof_l	L-shell value (dipole approximation)	-----
<eis_prefix>_phxtof_gse_lat	Latitude in GSE frame	degrees

<eis_prefix>_phxtof_gse_lon	Longitude in GSE frame	degrees
<eis_prefix>_phxtof_gsm_lat	Latitude in GSM frame	degrees
<eis_prefix>_phxtof_gsm_lon	Longitude in GSM frame	degrees
<eis_prefix>_phxtof_sm_lat	Latitude in SM frame	degrees
<eis_prefix>_phxtof_sm_lon	Longitude in SM frame	degrees
<eis_prefix>_phxtof_orbit_num	Orbit number	degrees
<eis_prefix>_phxtof_ssd<#>	Raw count rate from individual SSD	1/s
<eis_prefix>_phxtof_vep	Number of electron events processed and binned by onboard processor per second	1/s
<eis_prefix>_phxtof_start0anode	Count rate from all start anode regions	1/s
<eis_prefix>_phxtof_stop0anode	Count rate from all stop anode regions	1/s
<eis_prefix>_phxtof_pulseheight	Count rate from all start anode regions that satisfy a minimum MCP pulse height	1/s
<eis_prefix>_phxtof_vtofxee	Number of valid energy by time-of-flight (ExTOF) events per second	1/s
<eis_prefix>_phxtof_vtofxphe	Number of valid pulse height by time-of-flight (PHxTOF) events per second	1/s

**Table 6-7 List of the Variables Included in the L2 EIS phxtof Burst Data Product**

<b>Data Parameter</b>	<b>Description</b>	<b>Units</b>
Time_Minus	<support data> Delta from measurement window start to midpoint	s
Time_Plus	<support data> Delta from midpoint to measurement window end	s
<eis_prefix>_phxtof_duration	<support data> Total exposure time for accumulation	s
<eis_prefix>_phxtof_deadtime	<support data> Instrument deadtime	s
<eis_prefix>_phxtof_largepixel	<support data> Instrument large pixel in use (yes/no)	-----
<eis_prefix>_phxtof_starttai	<support data> Begin measurement window, TAI since 1958	s
<eis_prefix>_phxtof_midtai	<support data> Nominal measurement time, TAI since 1958	s
<eis_prefix>_phxtof_endtai	<support data> End measurement window, TAI since 1958	s
<eis_prefix>_phxtof_spin	<support data> Spacecraft spin number	-----
<eis_prefix>_phxtof_sector	<support data> Spacecraft spin sector	-----
<eis_prefix>_phxtof_quality	<support data> Quality word	-----
<eis_prefix>_phxtof_proton_P<X>_counts_t<#>	Individual telescope (look direction) proton counts for each energy channel	counts
<eis_prefix>_phxtof_proton_P<X>_cps_t<#>	Individual telescope (look direction) proton counts per second for each energy channel	1/s
<eis_prefix>_phxtof_proton_P<X>_flux_t<#>	Individual telescope (look direction) proton intensity (flux) for each energy channel	1/(cm <sup>2</sup> -s-sr-keV)



<eis_prefix>_phxtof_oxygen_P<X>_counts_t<#>	Individual telescope (look direction) oxygen (charge state unmeasured) counts for each energy channel	counts
<eis_prefix>_phxtof_oxygen_P<X>_cps_t<#>	Individual telescope (look direction) oxygen (charge state unmeasured) counts per second for each energy channel	1/s
<eis_prefix>_phxtof_oxygen_P<X>_flux_t<#>	Individual telescope (look direction) oxygen (charge state unmeasured) intensity (flux) for each energy channel	1/(cm <sup>2</sup> -s-sr-keV)
<eis_prefix>_phxtof_dump_counts_t<#>	Individual telescope (look direction) ion counts dump bin for each energy channel	counts
<eis_prefix>_phxtof_dump_cps_t<#>	Individual telescope (look direction) ion counts per second dump bin for each energy channel	1/s
<eis_prefix>_phxtof_dump_flux_t<#>	Individual telescope (look direction) ion intensity (flux) dump bin for each energy channel	-----
<eis_prefix>_phxtof_pitch_angle_t<#>	Pitch angle for individual telescope (look direction)	degrees
<eis_prefix>_phxtof_look_t<#>	Look direction vector in GSE for individual telescope	-----
<eis_prefix>_phxtof_b	Magnetic field in BCS coordinates	nT
<eis_prefix>_phxtof_position_gse	Spacecraft position vector in GSE	km
<eis_prefix>_phxtof_position_gsm	Spacecraft position vector in GSM	km
<eis_prefix>_phxtof_moon_gse	Spacecraft-to-moon vector in GSE	km
<eis_prefix>_phxtof_sc_to_gse	Transformation matrix from SC to GSE coordinates	-----
<eis_prefix>_phxtof_gse_to_gsm	Transformation matrix from GSE to GSM coordinates	-----
<eis_prefix>_phxtof_r	Magnitude of radial distance	km
<eis_prefix>_phxtof_l	L-shell value (dipole approximation)	-----
<eis_prefix>_phxtof_gse_lat	Latitude in GSE frame	degrees
<eis_prefix>_phxtof_gse_lon	Longitude in GSE frame	degrees
<eis_prefix>_phxtof_gsm_lat	Latitude in GSM frame	degrees
<eis_prefix>_phxtof_gsm_lon	Longitude in GSM frame	degrees
<eis_prefix>_phxtof_sm_lat	Latitude in SM frame	degrees
<eis_prefix>_phxtof_sm_lon	Longitude in SM frame	degrees
<eis_prefix>_phxtof_orbit_num	Orbit number	degrees
<eis_prefix>_phxtof_ssd<#>	Raw count rate from individual SSD	1/s
<eis_prefix>_phxtof_vep	Number of electron events processed and binned by onboard processor per second	1/s
<eis_prefix>_phxtof_start0anode	Count rate from all start anode regions	1/s
<eis_prefix>_phxtof_stop0anode	Count rate from all stop anode regions	1/s
<eis_prefix>_phxtof_pulseheight	Count rate from all start anode regions that satisfy a minimum MCP pulse height	1/s

<eis_prefix>_phxtof_vtofxee	Number of valid energy by time-of-flight (ExTOF) events per second	1/s
<eis_prefix>_phxtof_vtofxphe	Number of valid pulse height by time-of-flight (PHxTOF) events per second	1/s

**Table 6-8 List of the Variables Included in the EIS phxtof Survey Data Product**

**6.5.7 Level 3 EPD Products**

The variables contained within the EPD Level-3 products available from the MMS Science Data Center (SDC), are outlined in Exhibits 37-38 below. All of these variables begin with either,

$$\begin{aligned} \langle \text{feeps\_l3\_prefix} \rangle &= \text{mms}\langle \# \rangle\_ \text{epd\_feeps\_}\langle \text{DATA\_RATE} \rangle\_ \text{l3\_OR} \\ \langle \text{eis\_l3\_prefix} \rangle &= \text{mms}\langle \# \rangle\_ \text{epd\_eis\_}\langle \text{DATA\_RATE} \rangle\_ \text{l3\_} \end{aligned}$$

where <#> is the spacecraft number and <DATA\_RATE> is the telemetry mode (“srvy” or “brst”).

The data files from each MMS spacecraft will include the variables below from both that spacecraft as well as combined across all available spacecraft (“mmsx”).

<b>Data Parameter</b>	<b>Description</b>	<b>Units</b>
<feeps_prefix>_electron_intensity_omni	Omni-directional (averaged over all eyes/sensors) intensity (flux) from FEEPS	1/(cm <sup>2</sup> -s-sr-keV)
<feeps_prefix>_electron_intensity_omni_###-###keV_pad	3-sample smoothed omni-directional pitch angle distribution for specified FEEPS energy channel(s)	1/(cm <sup>2</sup> -s-sr-keV)
<feeps_prefix>_electron_intensity_omni_integral_gt###kev_pad	3-sample smoothed omni-directional pitch angle distribution for all FEEPS energies above specified value	1/(cm <sup>2</sup> -s-sr-keV)
<feeps_prefix>_electron_SCincluded	Binary indicator of which S/C FEEPS data are included in the MMS-X products	----
<eis_prefix>_electron_flux_omni	Omni-directional (averaged over all telescopes) intensity (flux) from EIS	1/(cm <sup>2</sup> -s-sr-keV)
<eis_prefix>_electron_flux_omni_###-###keV_pad	Omni-directional pitch angle distribution for specified EIS energy channel(s)	1/(cm <sup>2</sup> -s-sr-keV)
<eis_prefix>_electron_SCincluded	Binary indicator of which S/C EIS data are included in the MMS-X products	----

**Table 6-9 List of the Variables in the L3 EPD Electron Survey and Burst Data Products [the only differences in the variables is the <DATA\_RATE> in the prefix]**

<b>Data Parameter</b>	<b>Description</b>	<b>Units</b>
<feeps_prefix>_ion_intensity_omni	Omni-directional (averaged over all eyes/sensors) intensity (flux) from FEEPS	1/(cm <sup>2</sup> -s-sr-keV)

<feeps_prefix>_ion_intensity_omni_###-###keV_pad	3-sample smoothed omni-directional pitch angle distribution for energy channel(s) specified by range from FEEPS	1/(cm <sup>2</sup> -s-sr-keV)
<feeps_prefix>_ion_intensity_omni_integral_gt###kev_pad	3-sample smoothed omni-directional pitch angle distribution for all energies above specified value from FEEPS	1/(cm <sup>2</sup> -s-sr-keV)
<feeps_prefix>_ion_SCincluded	Binary indicator of which S/C FEEPS data are included in the MMS-X products	-----
<eis_prefix>_extof_proton_flux_omni	Omni-directional (averaged over all telescopes) intensity (flux) from EIS	1/(cm <sup>2</sup> -s-sr-keV)
<eis_prefix>_extof_helium_flux_omni	Omni-directional (averaged over all telescopes) intensity (flux) from EIS	1/(cm <sup>2</sup> -s-sr-keV)
<eis_prefix>_extof_oxygen_flux_omni	Omni-directional (averaged over all telescopes) intensity (flux) from EIS	1/(cm <sup>2</sup> -s-sr-keV)
<eis_prefix>_extof_###-###keV_proton_flux_omni_pad	Omni-directional pitch angle distribution for energy channel(s) specified by range from EIS	1/(cm <sup>2</sup> -s-sr-keV)
<eis_prefix>_extof_###-###keV_helium_flux_omni_pad		
<eis_prefix>_extof_###-###keV_oxygen_flux_omni_pad		
<eis_prefix>_phxtof_proton_flux_omni	Omni-directional (averaged over all telescopes) intensity (flux) from EIS	1/(cm <sup>2</sup> -s-sr-keV)
<eis_prefix>_phxtof_###-###keV_proton_flux_omni_pad	Omni-directional pitch angle distribution for energy channel(s) specified by range from EIS	1/(cm <sup>2</sup> -s-sr-keV)
<eis_prefix>_combined_proton_flux_omni	Omni-directional (averaged over all telescopes) intensity (flux) from EIS	1/(cm <sup>2</sup> -s-sr-keV)
<eis_prefix>_combined_###-###keV_proton_flux_omni_pad	Omni-directional pitch angle distribution for energy channel(s) specified by range from EIS	1/(cm <sup>2</sup> -s-sr-keV)
<eis_prefix>_ion_SCincluded	Binary indicator of which S/C EIS data are included in the MMS-X products	-----

**Table 6-10 List of the Variables Included in the L3 EPD Ion Survey Data Product**

<b>Data Parameter</b>	<b>Description</b>	<b>Units</b>
<feeps_prefix>_ion_intensity_omni	Omni-directional (averaged over all eyes/sensors) intensity (flux) from FEEPS	1/(cm <sup>2</sup> -s-sr-keV)
<feeps_prefix>_ion_intensity_omni_###-###keV_pad	3-sample smoothed omni-directional pitch angle distribution for energy channel(s) specified by range from FEEPS	1/(cm <sup>2</sup> -s-sr-keV)

<feeps_prefix>_ion_intensity_omni_integral_gt###keV_pad	3-sample smoothed omni-directional pitch angle distribution for all energies above specified value from FEEPS	1/(cm2-s-sr-keV)
<feeps_prefix>_ion_SCincluded	Binary indicator of which S/C FEEPS data are included in the MMS-X products	----
<eis_prefix>_extof_proton_flux_omni	Omni-directional (averaged over all telescopes) proton energy-by-TOF intensity (flux) from EIS	1/(cm2-s-sr-keV)
<eis_prefix>_extof_helium_flux_omni	Omni-directional (averaged over all telescopes) helium energy-by-TOF intensity (flux) from EIS	1/(cm2-s-sr-keV)
<eis_prefix>_extof_oxygen_flux_omni	Omni-directional (averaged over all telescopes) oxygen energy-by-TOF intensity (flux) from EIS	1/(cm2-s-sr-keV)
<eis_prefix>_extof ###-###keV_proton_flux_omni_pad	Omni-directional proton energy-by-TOF pitch angle distribution for energy channel(s) specified by range from EIS	1/(cm2-s-sr-keV)
<eis_prefix>_extof ###-###keV_helium_flux_omni_pad	Omni-directional helium energy-by-TOF pitch angle distribution for energy channel(s) specified by range from EIS	
<eis_prefix>_extof ###-###keV_oxygen_flux_omni_pad	Omni-directional oxygen energy-by-TOF pitch angle distribution for energy channel(s) specified by range from EIS	
<eis_prefix>_phxtof_proton_flux_omni	Omni-directional (averaged over all telescopes) proton pulse height-by-TOF intensity (flux) from EIS	1/(cm2-s-sr-keV)
<eis_prefix>_phxtof ###-###keV_proton_flux_omni_pad	Omni-directional proton pulse height-by-TOF pitch angle distribution for energy channel(s) specified by range from EIS	1/(cm2-s-sr-keV)
<eis_prefix>_combined_proton_flux_omni	Omni-directional (averaged over all telescopes) proton combined pulse height-by-TOF and energy-by-TOF intensity (flux) from EIS	1/(cm2-s-sr-keV)
<eis_prefix>_combined ###-###keV_proton_flux_omni_pad	Omni-directional proton combined pulse height-by-TOF and energy-by-TOF pitch angle distribution for energy channel(s) specified by range from EIS	1/(cm2-s-sr-keV)
<eis_prefix>_ion_SCincluded	Binary indicator of which S/C EIS data are included in the MMS-X products	----
mms<#>_epd_brst_fast_ion_flux_omni	Omni-directional total ion intensity (flux) combined from EIS (protons only) and FEEPS	1/(cm2-s-sr-keV)
mms<#>_epd_brst_fast_ion ###-###keV_pad	Omni-directional total ion pitch angle distribution for energy channel(s) specified by range combined from EIS (protons only) and FEEPS	1/(cm2-s-sr-keV)

**Table 6-11 List of the Variables in the L3 EPD Ion Burst Data Product**

## 6.6 APPENDIX A- EIS REFERENCES

The following documents and drawings in effect on the day this specification was signed **shall** apply to the extent specified herein. In the event of conflict between this document and any referenced document, the document with latest publication date will govern.

The following is a list of applicable references and publications.

Section	Document Number	Title	Revision/Date
	<a href="https://doi.org/10.1002/2017JA024351">https://doi.org/10.1002/2017JA024351</a>	Cohen, I. J., Mitchell, D. G., Kistler, L. M., Mauk, B. H., Anderson, B. J., Westlake, J. H., Ohtani, S., Hamilton, D. C., Turner, D. L., Blake, J. B., Fennell, J. F., Jaynes, A. N., Leonard, T. W., Gerrard, A. J., Lanzerotti, L. J., Allen, R. C., Burch, J. L. (2017), Dominance of high-energy (>150 keV) heavy ion intensities in Earth's middle to outer magnetosphere, J. Geophys. Res. SpacePhysics, 122, 9282–9293.	
tbd	461-XXX-XXXX-0###	EPD Data Products Guide	Rev / date
	<a href="https://doi.org/10.1007/s11214-014-0055-5">https://doi.org/10.1007/s11214-014-0055-5</a>	Mauk, B., J. B. Blake, D. N. Baker, J. H. Clemmons, G. D. Reeves, H. E. Spence, S. E. Jaskulek, C. E. Schlemm, L. E. Brown, S. A. Cooper, J. V. Craft, J. F. Fennell, R. S. Gurnee, C. M. Hammock, J. R. Hayes, P. A. Hill, G. C. Ho, J. C. Hutcheson, A. D. Jacques, S. Kerem, D. G. Mitchell, K. S. Nelson, N. P. Paschalidis, E. Rossano, M. R. Stokes, J. H. Westlake (2016a), The Energetic Particle Detector (EPD) Investigation and the Energetic Ion Spectrometer (EIS) for the Magnetospheric Multiscale (MMS) Mission, Space Science Reviews, 199(1-4), 471-514.	

**Table 6-12 EIS Applicable Documents**

**6.7 APPENDIX A- FEEPS REFERENCES**

Section	Document Number	Title	Revision/Date
---------	-----------------	-------	---------------

	<a href="https://doi.org/10.1007/s11214-015-0163-x">https://doi.org/10.1007/s11214-015-0163-x</a>	Blake, J., B. H. Mauk, D. N. Baker, P. Carranza, J. H. Clemmons, J. Craft, W. R. Crain Jr., A. Crew, Y. Dotan, J. F. Fennell, R. H. Friedel, L. M. Friesen, F. Fuentes, R. Galvan, C. Ibscher, A. Jaynes, N. Katz, M. Lalic, A. Y. Lin, D. M. Mabry, T. Nguyen, C. Pancratz, M. Redding, G. D. Reeves, S. Smith, H. E. Spence, J. Westlake (2016), The Fly's Eye Energetic Particle Spectrometer (FEEPS) Sensors for the Magnetospheric Multiscale (MMS) Mission, Space Science Reviews, 199(1-4), 309-329.	
tbd	461-XXX-XXXX-0###	EPD Data Products Guide	Rev / date
		EDP Item Name	3.0 / date
	<a href="https://doi.org/10.1007/s11214-014-0055-5">https://doi.org/10.1007/s11214-014-0055-5</a>	Mauk, B., J. B. Blake, D. N. Baker, J. H. Clemmons, G. D. Reeves, H. E. Spence, S. E. Jaskulek, C. E. Schlemm, L. E. Brown, S. A. Cooper, J. V. Craft, J. F. Fennell, R. S. Gurnee, C. M. Hammock, J. R. Hayes, P. A. Hill, G. C. Ho, J. C. Hutcheson, A. D. Jacques, S. Kerem, D. G. Mitchell, K. S. Nelson, N. P. Paschalidis, E. Rossano, M. R. Stokes, J. H. Westlake (2016a), The Energetic Particle Detector (EPD) Investigation and the Energetic Ion Spectrometer (EIS) for the Magnetospheric Multiscale (MMS) Mission, Space Science Reviews, 199(1-4), 471-514.	

**Table 6-13 FEEPS Applicable Documents**

## 7.0 FIELDS

### 7.1 OVERVIEW

The FIELDS instrument suite consists of the Flux Gate Magnetometer (FGM), Search Coil Magnetometer (SCM), Electron Drift Instrument (EDI) and Electric Double Probes (EDP). Command and data handling for all FIELDS instrument are controlled by the FIELDS Command and Data Processing Unit (CDPU), ensuring that the precise time timing between measurements necessary for instrument operations and science data analysis are precisely measured and controlled. This section describes details of the FIELDS timing which are common to each of the FIELDS instruments. During the FIELDS Integration and Timing Test performed on each flight model, all analog and digital timing delays were measured and understood. This information is applied to all FIELDS telemetry processed from Level 0 to Level 1A on computers at the Science Data Center at LASP. Further processing is then performed at FIELDS member institutions, as described in section 8.0 (FGM), section 9.0 (SCM), section 10.0 (EDI) and section 11.0 (EDP).

### 7.2 FIELDS TIMING

The FIELDS CDPU receives a TAI time code and a Pulse Per Second (PPS) tone from the CIDP. The FIELDS CDPU latches the TAI time code and sets the coarse time to this whole second value at the arrival of the Time at the Tone Signal (PPS). The FIELDS CDPU has a free running clock that is used to define the fine time between the PPS tones. FIELDS data packets times are assigned with a combination of TAI (whole second) and FIELDS (fractional second) values.

The TAI and FIELDS clocks rates are different. A clock rate scaling factor (CRSF) between the TAI PPS and FIELDS clock is needed to accurately assign times to the data samples within each data packet. The clock rate scaling factor is approximated using the most frequent, routinely produced FIELDS packet is APID 0x105 packet, which is generated every 4 FIELDS clock seconds, as follows:

Let T1 be the time tag of an APID 0x105 packet. T1 consists of C1 (the latched TAI whole second) and F1 (the fractional second from the FIELDS clock). The actual TAI time corresponding to the T1 time tag can be calculated as

$$T1[TAI] = C1 + f * F1$$

where f is the CRSF between the TAI and FIELDS clocks.

Let T2 be the time tag of the subsequent packet consisting of C2 and F2 portions. The TAI time corresponding to the T2 time tag is

$$T2[TAI] = C2 + f * F2$$

These consecutive packets are 4 FIELDS seconds apart, or  $4 \times f$  in terms of the TAI clock. Subtracting the TAI times associated with these two packets we get:

$$4f = C2 - C1 + f * (F2 - F1)$$

Solving for the CRSF produces

$$f = (C2 - C1) / (4 - (F2 - F1)) \text{ or } \Delta C / (4 - \Delta F)$$

The CDPU retrieval of the CIDP time code could be delayed by up to 35 microseconds due to the encoding of the PPS, Sun Crossing, and Delphi pulses by the CIDP on a single interface (CIDP\_FIELDS\_ICD). Also the oscillator frequency on the FIELDS CDPU clock is temperature dependent which can cause the rate to vary by 35 ppm over the temperature range. The rate scaling factor calculation above provides a first order correction for both of these artifacts. The scaling factor applied in FIELDS CDF files is averaged over 10 minutes.

Aside from temperature variation, FIELDS sample spacing should be constant. Therefore, the sample spacing is defined as the last packet time minus the first packet time in an interval divided by the number of samples. Sample times are adjusted by known digital timing delays, as confirmed in the FIELDS FIT test, are used to determine sample time:

$$\text{sample\_time}[i] = \text{reference\_time} + \text{sample}[i] * \text{sample\_interval} - \text{delay}$$

Reference\_time is the time tag of the first packet of an interval without mode change or data gap. If there is a gap in packet sequence count, reference time becomes the time tag of the first packet after the sequence count gap for subsequent samples.

### 7.3 APPENDIX A- FIELDS REFERENCES

Section	Document Number	Title	Revision/Date
	UNH-MMS-CDPUFSWUM-01	FIELDS CDPU Flight Software <u>User Manual</u>	Rev-1.0 / 24 October 2011
	<a href="https://lasp.colorado.edu/mms/sdc/public/datasets/fields/FIELDS_MMS_Data_Products_v0.1.pdf">https://lasp.colorado.edu/mms/sdc/public/datasets/fields/FIELDS_MMS_Data_Products_v0.1.pdf</a>	FIELDS MMS Data Products Guide	0.1
	<a href="https://doi.org/10.1007/s11214-014-0109-8">https://doi.org/10.1007/s11214-014-0109-8</a>	Torbert, R.B., Russell, C.T., Magnes, W. et al. (2016). The FIELDS Instrument Suite on MMS: Scientific Objectives, Measurements, and Data Products. Space Sci Rev 199, 105–135.	

**Table 7-1 FIELDS Applicable Documents**



## 8.0 FLUX GATE MAGNETOMETER (FGM)

### 8.1 FGM OVERVIEW

The Flux Gate Magnetometer (FGM) measures magnetic field components on three orthogonal axes, by periodically saturating the ferromagnetic ring cores which in turn induce currents in the sense wires that are modulated by the strength of the ambient field. The MMS Flux Gate Magnetometer instrument on each observatory consists of an Analog Fluxgate Magnetometer (AFG) and a Digital Fluxgate Magnetometer (DFG), mounted on the end of two five-meter booms on either side of each observatory. Both AFG and DFG contain the same sensor design (c.f. Figure 8-1), but different electronics units. Electronic units for DFG are provided by the Space Research Institute of the Austrian Academy of Sciences (IWF), and for AFG are provided by the University of California, Los Angeles (UCLA). The instruments form a synchronized, redundant, cross- and inter-spacecraft calibrated pair of magnetometers on each observatory. The details of the instrument design are described in Russell et al. [2016].

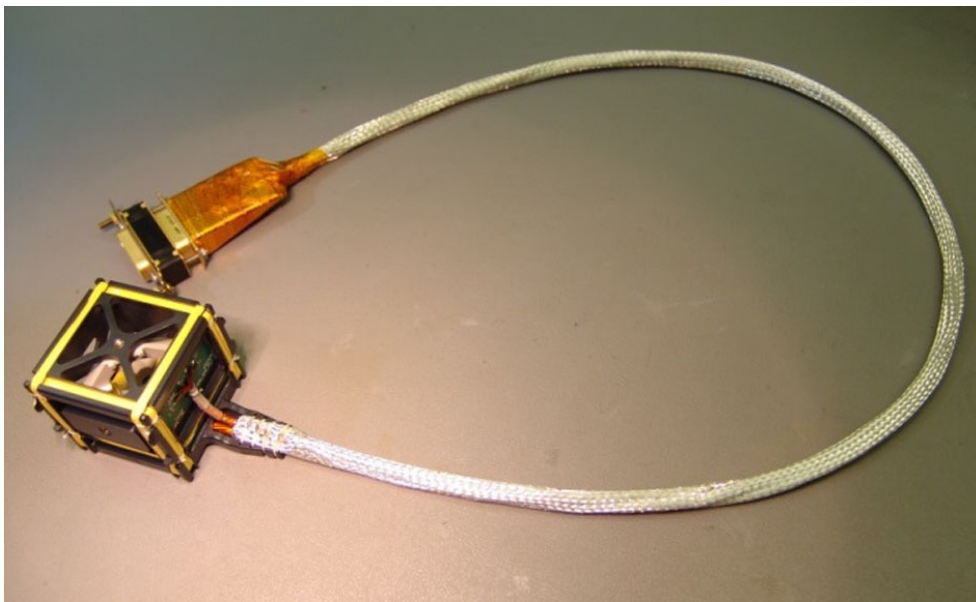


**Figure 8-1 Photograph of the Fluxgate Sensor with Pigtail Harness**

AFG and DFG represent a redundant system of magnetometers which enable cross-calibration to archive better data accuracy. AFG and DFG measure magnetic fields in two dynamic ranges, low-field and high field, as shown in Table 8-1.

	<b>Low Range</b>	<b>High Range</b>
AFG	+/- 510 nT	+/- 8200 nT
DFG	+/-650 nT	+/- 10500 nT

**Table 8-1 AFG and DFG Dynamic Ranges**

The ranges are commanded by the FIELDS Central Data Processing Unit (CDPU) using an algorithm with hysteresis based on the data from the magnetometer controllers.

- AFG: range change occurs at 450 nT for increasing field and at 400 nT for decreasing field. Two consecutive spins must meet this criterion.

- DFG: range change occurs at 550 nT for increasing field and at 500 nT for decreasing field. Four consecutive spins must meet this criterion.

Both AFG and DFG operate continuously, outputting data at 128 S/s for storage by the spacecraft in a burst memory buffer for later downlink. Meanwhile, FIELDS CDPUs decimate this data for continuous survey downlink, but also provides the 128 S/s data in real time to the EDI instrument to enable electron beam steering. DFG employs digital filters to produce the 128 S/s data, which have an inherent real-time delay. In order to ensure meeting the time latency requirements for EDI, DFG was designed to produce data in one of two digital filter length modes: DEC 32, which sacrifices noise performance to achieve shorter delay; and DEC 64, which employs a longer filter length to optimize noise performance.

For AFG, the noise level in high range is  $\sim 10$  pT/ Hz at 1 Hz, and the noise level in low range is  $\sim 5$  pT/ Hz at 1 Hz.

For DFG, the noise level in high range is  $\sim 100$  pT/ Hz at 1 Hz, and the noise level in low range is  $\sim 8$  pT/ Hz at 1 Hz (DEC 32 mode) or  $\sim 5$  pT/ Hz at 1 Hz (DEC 64 mode).

### 8.1.1 Status of FGM Magnetometers

All FGM units continue to operate nominally as of 2021-08-30.

#### Burst Mode Operations

At the beginning of the science phase, DEC 32 and DEC 64 modes were used on alternate orbits, to ensure that there were no adverse effects on EDI performance when using the DEC 64 mode, which is preferable for science. In March 2016, it was determined that DEC 64 was adequate for EDI operations, and that DFG should remain permanently in that mode. The history of these experimental operations is as follows:

2015-08-31	to 2015-12-13	Alternate orbits in DEC 32/DEC 64
2015-12-13	to 2016-01-18 15:00	Continuously in DEC 64
2016-01-18 15:00	to 2016-03-10 07:00	Alternate orbits in DEC 32/DEC 64
2016-03-10 07:00	to present	Continuously in DEC 64

Note that during periods when alternating from one orbit to the next, MMS4 operates on a schedule opposite to MMS1-3: i.e. MMS4 operates in DEC 32 mode on orbits when the others are in DEC 64, and vice versa.

#### Survey Mode Operations

In early 2020, the slow survey rate is increased, so that data is gathered continuously at 16 S/s. This mode of operation was first run experimentally on orbits 1059-1061 (2019/11/20-2019/11/27), and then implemented permanently as of orbit 1073 (2020/01/08). This is implemented by re-enabling fast survey mode immediately after the transition to Slow survey mode after each ROI. While this process generally works smoothly, there are occasional short ( $\sim 10$  second) gaps in fast survey data at the end of the ROI. [see section 8.5.2 for survey mode data processing and section 8.4.4 for a known issue with data overlap removal in v5 data products after this change in operations].

#### Level 2 Data Operations

The Level 2 FGM data product selects the best data suited for general science from AFG and DFG data to produce a single data product.

Currently, this is accomplished by using AFG for all FGM survey data, and DFG is used for all FGM burst data because of DFG's linear phase response.

Data Availability

FGM operates continuously for the full mission, except for times during extended eclipse when all MMS science instruments are powered off.

There have been occasional, brief instrument resets.

Anomalies and gaps in FGM data production are listed in Table 8-2.

<b>Date</b>	<b>Anomaly</b>	<b>Observatory Affected</b>
2015/12/11-12 Orbit 275	FIELDS reboot 23:15:00 - 00:35:00	MMS4
2015/12/12 Orbit 275	FIELDS reboot 00:50:00 - 01:50:00	MMS1
2015/12/12 Orbit 275	FIELDS reboot 02:05:00 - 03:05:00	MMS2
2015/12/12 Orbit 275	FIELDS reboot 03:20:00 - 04:20:00	MMS3
2016/7/12 Orbit 489	FIELDS reboot 21:16:00 - 22:07:00	MMS1
2016/7/19-20 Orbit 496-497	FIELDS reboot 19:41:00 - 05:24:00	MMS4
2016/7/22 Orbit 500	FIELDS reboot 18:23:00 - 19:11:00	MMS2
2016/7/22 Orbit 500	FIELDS reboot 19:56:30 - 22:44:00	MMS3
2017/01/01-04	MMS3 Timing anomaly caused undue errors in attitude/ephemeris. No L2 data available	MMS3
2017/06/08-09 Orbit 761	CDIP anomaly 03:46:16 - 16:20:00	MMS4
2017/06/30 - 2017/07/04 Orbit 769-770	CIDP reset 2017/06/30 03:38:22 - 2017/07/04 03:10:00	MMS4
2018-01-26 14:48:41 - 2018-01-27 19:48:16	0.26 s Navigation Timing anomaly: a slow drift then a reset, resulting in a slight error in spacecraft position.	MMS3
2019/01/13 - 2019/01/15 Orbit 969	S/C Processor Reset Anomaly 2019/01/13 16:35:37 - 2019/01/15 21:12:00	MMS4
2019/06/04 - 2019/06/06 Orbit 1011	S/C Processor Reset Anomaly 2019/06/04 09:16:55 2019/06/06 04:40:00	MMS3
2019/08/17 - 2019/08/28 Orbit 1032-1035	Extended eclipse: Instrument Suite Power Down	all MMS observatories and instruments
2020/04/16 - 2020/04/20	DFG latch-up: no L2 burst data	MMS2

Orbit 1101-1102	2020/04/16 19:21:20 – 2020/04/20 22:20:00	
2020/08/17 – 2020/08/28 Orbit 1132-1135	Extended eclipse: Instrument Suite Power Down	all MMS observatories and instruments
2021/08/01 – 2021/08/13 Orbit 1236-1239	Extended eclipse: Instrument Suite Power Down	all MMS observatories and instruments
2022/07/25 to 2022-08-09 1338-1342	Extended eclipse: Instrument Suite Power Down	all MMS observatories and instruments

**Table 8-2 FGM Data Anomalies**

## 8.2 FGM MEASUREMENT STANDARDS, VOLUME, AND TIMING

### 8.2.1 FGM Requirements

The requirement for the FIELDS Investigation is to measure the 3 axis DC Magnetic Field Vector to an accuracy of 0.1nT. This is achieved by FGM through cross-calibration with EDI. On its own, the FGM shall measure the 3 axis DC magnetic field vector in low range to an accuracy of better than or equal to 0.5 nT, with an accuracy goal of 0.1 nT in low range. The requirement for sensitivity is 0.01 nT/ $\sqrt{\text{Hz}}$ . The Level 2 data products should be available to the public within 30 days of downlink of the telemetry.

FGM is required to provide preliminary (L2pre) data products for use in the production of EDI, E-field, and particles Level 2 data products. The L2pre AFG and DFG data products provide the magnetic field vector with an accuracy of 1 degree and field magnitude with 1 % accuracy. In small fields where the magnetic field is less than 50 nT, the goal is to achieve 0.5 nT accuracy.

The requirements on the MMS observatory that affect the magnetometer measurement include:

- 1) at the location of AFG/DFG sensors, the spacecraft magnetic field shall be stable to +/-0.1nT over 4000 seconds.
- 2) the magnetometer boom stability shall be  $\pm 0.1^\circ$  about each axis during science operations, exclusive of disturbances caused by entry into/exit from umbra,
- 3) the observatory shall provide sufficient attitude sensor data to enable the ground to calculate spin axis orientation of the observatory relative to ecliptic normal to within  $\pm 0.1^\circ$  (3 sigma) both in sunlight and eclipse, and
- 4) the observatory shall provide sufficient attitude sensor data to enable the ground to calculate spin phase of the observatory to within  $\pm 0.1^\circ$  (3 sigma).

### 8.2.2 FGM Coordinate Systems

L2 data is provided in 4 coordinate systems:

- GSE – Geocentric Solar Ecliptic
- GSM – Geocentric Solar Magnetospheric
- BCS – The MMS Body Coordinate System
- DMPA – Despun Major Principal Axis, a spacecraft-specific approximation of the GSE coordinate system. Its X-axis is in the spin plane and nominally points towards the Sun, and the Z-axis is aligned with the Major Principal Axis (MPA), which is typically inclined 3-4° towards the Sun from the ecliptic normal.

Refer to section 3.2 for a general description of MMS coordinate systems and transformation methods. Figure 8-2 shows the relationship of the FGM instrument coordinates relative to spacecraft BCS coordinates.

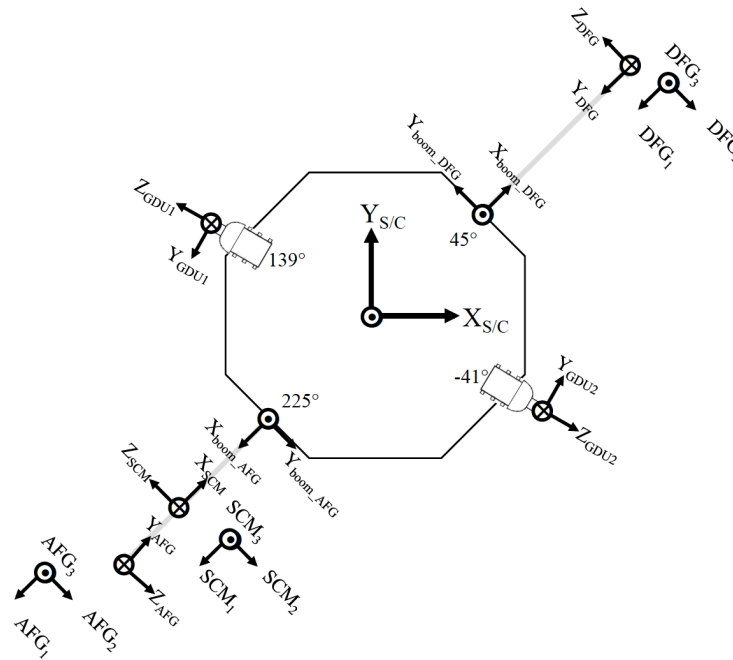


**Figure 8-2 The Relationship of AFG and DFG Instrument Coordinates Relative to the MMS S/C (or BCS) Coordinates and Other Magnetic Instrument Coordinates**

### 8.2.3 Accuracy of FGM Time Tags in L2 Data

The time tags of AFG and DFG on the same observatory are obtained from the same synchronous time base defined by the FIELDS independent clock. The FIELDS data packets times are assigned with a combination of TAI at whole second and FIELDS values at fractional second, in the following steps:

- 1) FIELDS CDPU receives a TAI time code and a Pulse Per Second (PPS) tone from the CIDP;
  - 2) FIELDS CDPU latches the TAI time code and sets the coarse time to this whole second value at the arrival of the time at the PPS tone signal;
  - 3) FIELDS CDPU has a free running clock that is used to define the fine time between the PPS tones.
- See section 7.0 FIELDS for more details.

In all FGM data products, time tags are center times for the sampling intervals. One time tag is provided for each 3-axis vector measurement. The effective sample times for AFG and DFG are not simultaneous. Timing accuracy relative to other FIELDS instruments is <0.1 millisecond for the spin axis component of each vector.

For DFG, the 3 vector components are sampled simultaneously to better than 100 micro-second, and the frequency response of all channels is identical, as the filters are implemented digitally. The frequency response for DEC 32 and DEC 64 modes are shown in Figure 8-3 and Figure 8-4, respectively. A DEC64/DEC32 flag is available as the `mms?_dfg_pfmnode` (where '?' matches the observatory number, 1, 2, 3, or 4) data quantity in L1A data, but this is not passed on to the L2 data files, as of v5. The planned upcoming v6 L2 FGM data files will include these flags.

For AFG, the 3 channels on each unit are simultaneous to better than 1 millisecond. Differences are due to difference in the frequency response of each channel, as shown in Figure 8-5. The frequency response of each unit, as well as each of the two redundant ADCs have similar, but not identical frequency response, which is well characterized by the Fields Integrated Timing (FIT) tests. The frequency response of the AFG analog filter is comparable to DFG DEC 64 mode. The time tags in the L2 data files are adjusted to correspond to the timing of the Instrument X-axis, which is nominally aligned with the spacecraft spin axis (denoted Z in the MMS coordinate systems). No signal processing is applied to correct the relative the delays between the spin plane channels and the spin axis channel, as this would alter the frequency response of the spin plane components. Further details of FGM timing and frequency response are discussed in Torbert [2014].

Frequency response of both AFG and DFG dominated by a recursive filter implemented in the FIELDS CDPU that is applied to all FGM data, regardless of instrument source (AFG or DFG), instrument mode (low range/high range), or instrument-dependent filtering (DEC32/DEC64 for DFG, ADCA/ADCB for AFG). Timing corrections appropriate to each instrument and each mode of operation are fully characterized by the FIT tests. Each AFG/DFG L0 telemetry data packet contains housekeeping data indicating the instrument mode. UNH L1A processing software applies timing corrections accordingly for each mode.

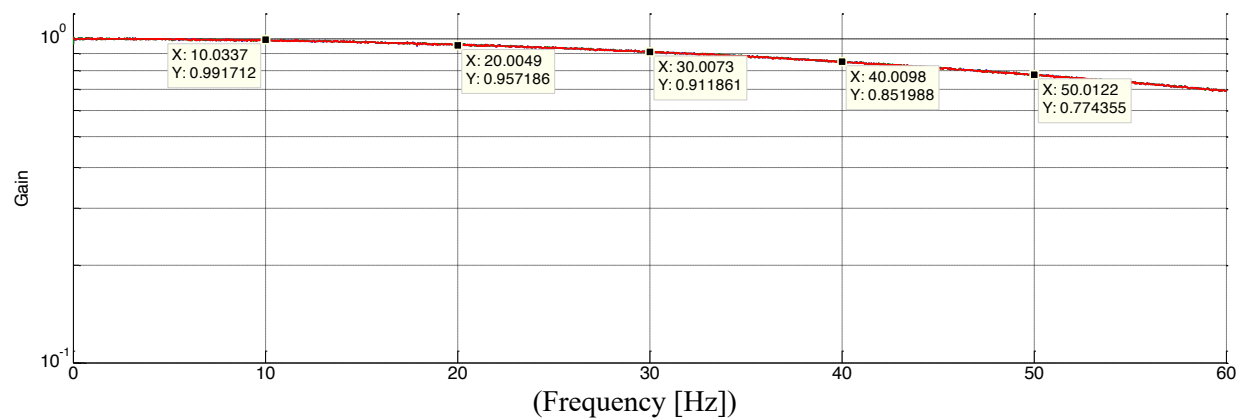


**Figure 8-3 Frequency Response for DEC 32 Mode of DFG in Low Range**

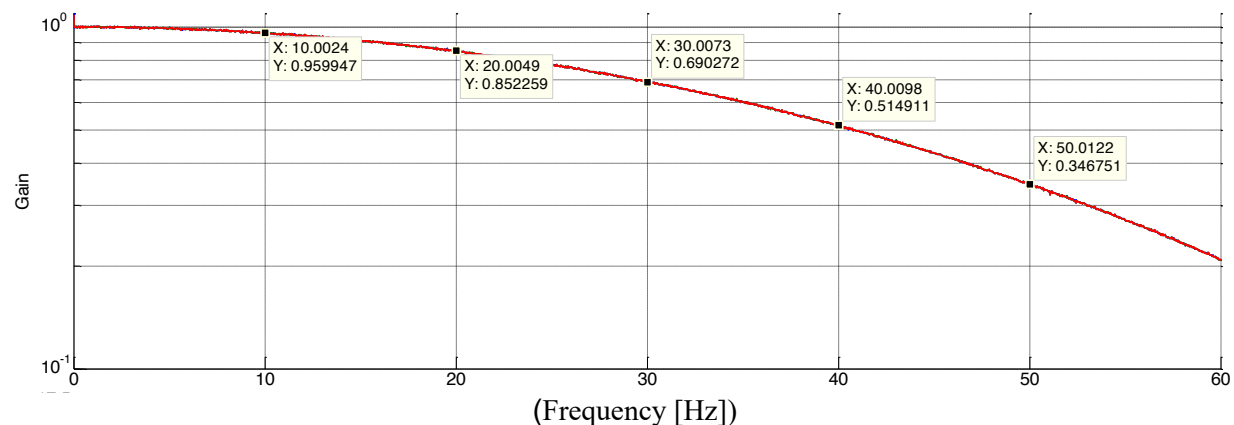


**Figure 8-4 Frequency Response for DEC 64 Mode of DFG in Low Range**

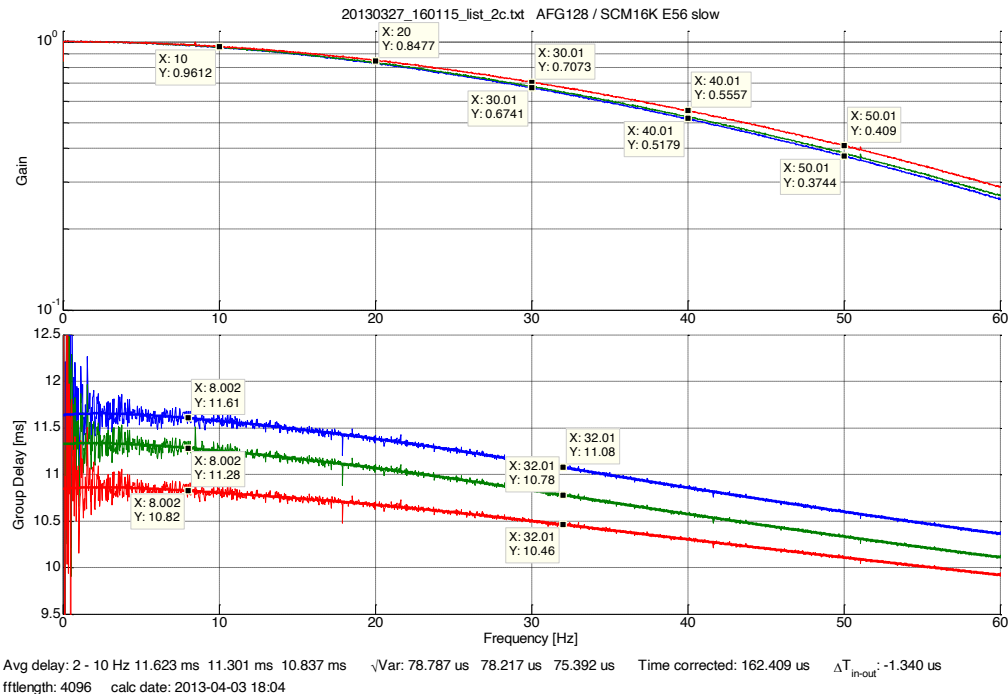


**Figure 8-5 AFG FM4 128 S/s Frequency Response for X (Blue), Y (Green), and Z (Red) Instrument Axes**

Each FGM unit provides data to the FIELDS CDPU at a fixed rate of 128 samples/sec. These data are stored in burst memory for downlink by command. In addition, the FIELDS CDPU reduces the sample rate to implement fast and slow survey modes for continuous transmission to the ground. Data rates are shown in Table 8-3.

Mode	Sample Rate
Burst	128/sec
Fast Survey	16/sec
Slow Survey	8/sec

**Table 8-3 FGM Data Rate Modes**

The sampling on different observatories is not synchronized. For calculations using multi-spacecraft data, such as curlometer, the users are recommended to first interpolate the data to the same time stamp.

#### 8.2.4 Data Volume

	Survey		Burst
	SLOW	FAST	
Raw data rate (bit/sec)	60	120	960
Orbit averaged rate (bit/sec)	90* (currently 120)		11.4**

**Table 8-4 Raw and Orbit-Averaged Telemetry Downlink Rates for AFG and DFG [\*Assuming 50% Duty Cycle for ROI Per Orbit (Current ROI duty cycle is less; however, Fast Survey currently runs at 100% duty cycle). \*\*Assuming 17 Minutes of Burst Downlink/day]**

Telemetry is compressed by a factor of 2, and is uncompressed and converted to floating point values in L1A data processing. Data volume for L2 is higher, as it is provided in multiple coordinate systems.

Average data volume per daily L2 survey file: 68 MB

Data volume per L2 burst file:

For first 6 months of science phase, average burst file size was about 1 MB, with an average of 27 burst files per day.

### 8.3 MAGNETOMETER MEASUREMENT ALGORITHM AND UNCERTAINTY ESTIMATION

#### 8.3.1 Measurement Algorithm

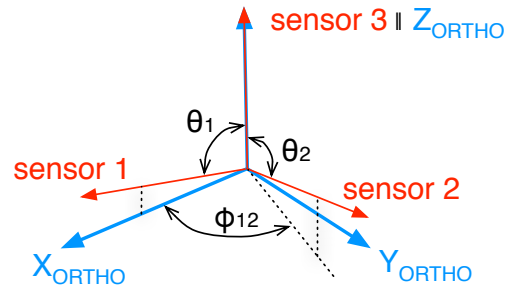
Three components of the magnetic field are measured in the spinning spacecraft frame and are converted into a true vector measurement that can be transformed into geophysical coordinates with the aid of spacecraft attitude measurements. The magnetometer measurements from the three sensor axes need to be corrected by the offsets and gains for each axis, and then by a series of angular corrections illustrated in Figure 8-6. The three sensor axes (marked as  $\mathbf{e}_1$ ,  $\mathbf{e}_2$ , and  $\mathbf{e}_3$ ) are not exactly orthogonal, thus the first step is to convert the sensor coordinates into an orthogonalized sensor system, with  $\theta_1$  being the angle between  $Z_{\text{Ortho}}$  and  $\mathbf{e}_1$ ,  $\theta_2$  being the angle between  $\mathbf{e}_2$  and  $\mathbf{e}_3$ , and  $\phi_{12}$  being the angle between  $X_{\text{Ortho}}$  and the projection of  $\mathbf{e}_2$  in the  $X\text{-}Y_{\text{Ortho}}$  plane. A differential gain factor  $g_{\text{SP}}$  accounts for the difference in gain between the measurements along the  $\mathbf{e}_1$  and  $\mathbf{e}_2$  vectors. Step 2 is to align  $\mathbf{z}_{\text{Ortho}}$  to the Spin Axis (SA) frame – more properly called the major principal axis (MPA) frame – with  $s_x$  and  $s_y$  being the projections of  $\mathbf{z}_{\text{Ortho}}$  along  $\mathbf{x}_{\text{SA}}$  and  $\mathbf{y}_{\text{SA}}$ , and  $\theta$  being the angle between  $\mathbf{z}_{\text{SA}}$  and  $\mathbf{z}_{\text{Ortho}}$ . In step 3, the absolute determination of the azimuth, denoted  $\phi_{\text{abs}}$ , of  $\mathbf{x}_{\text{SA}}$  relative to the nominal radial direction of the AFG boom in the spin plane yields the rotation to a boom direction principal axis frame, denoted Orthogonalized Magnetometer Boom (OMB). The gain factors  $g_{\text{SA\_abs}}$  and  $g_{\text{SP\_abs}}$  are applied to the spin axis and spin data, respectively. In step 4, the measurements are transformed into the spinning MMS spacecraft major principal axis (SMPA) frame, by rotating by  $-225^\circ$  with respect to the spin axis. Note that the SMPA frame is a close approximation to the BCS frame.\* The  $\mathbf{B}_{\text{SMPA}}$  data is despun to the  $\mathbf{B}_{\text{DMPA}}$  frame (which is a close approximation to GSE coordinates) using spin phase data provided by the Flight Dynamics and Orbital Analysis (FDOA) branch of GSFC. Finally, the  $\mathbf{B}_{\text{DMPA}}$  data are transformed into GSE and GSM geophysical coordinates under the assumption that the MPA is aligned with the angular momentum vector provided by the definitive attitude data products.

Full details of this process are discussed in Anderson et al. [2022].

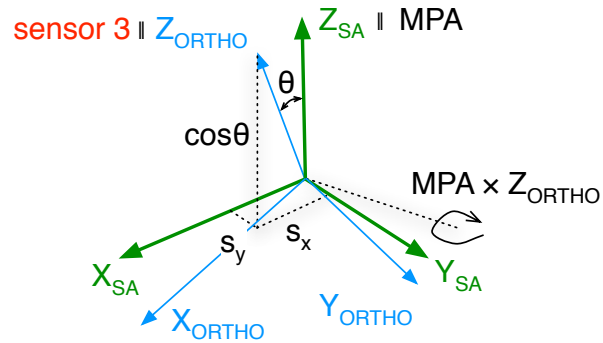
---

\* SMPA differs from BCS only by a  $\lesssim 1^\circ$  misalignment of the MPA from the BCS Z-axis. The MPA vector in BCS coordinates is used to transform  $\mathbf{B}_{\text{SMPA}}$  to the  $\mathbf{B}_{\text{BCS}}$  data product that is provided in the L2 data files. The most up-to-date measurement of the MPA vector relative to the BCS is found in the INERTIA TENSOR CALIBRATION REPORT (INERTIACAL) generated by the FDOA after each spacecraft maneuver.

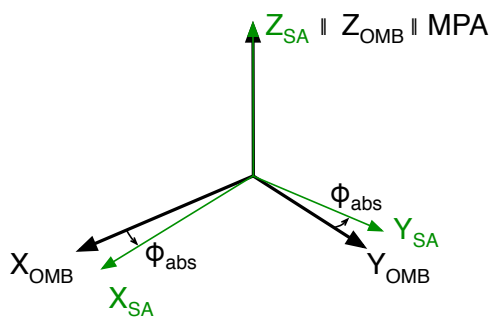




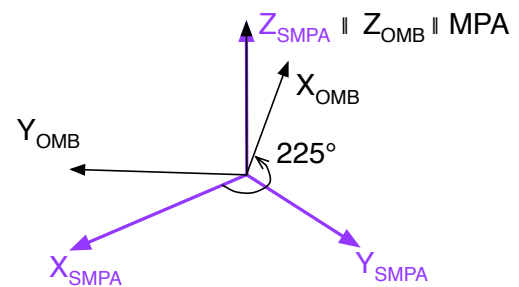
Step 1.  
Orthogonalized (ORTHO)  
sensor system



Step 2.  
Spin-aligned (SA) sensor system



Step 3.  
Orthogonalized Magnetometer  
Boom (OMB) system



Step 4.  
Spinning MPA (SMPA)  
coordinates

**Figure 8-6 Diagram of the Coordinates and Axes Used in the Calibration Process**

In the above figure, angles and parameters derived for the calibrations are also shown. Top left panel shows the coordinate system 1-2-3 described by the unit vectors  $\hat{e}_1$ ,  $\hat{e}_2$ , and  $\hat{e}_3$ , (cf. Figure 2.1-1 and 2.1-2 of Anderson et al. [2021]). Top right panel shows the spin aligned sensor system,  $X_{SA}$ ,  $Y_{SA}$ ,  $Z_{SA}$ , and the angle between  $\hat{e}_3$  and the spin axis (defined as  $Z_{SA}$ ) together with the projections of  $\hat{e}_3$  in the  $X_{SA}$  and  $Y_{SA}$  directions. Left bottom panel shows the orthogonal magnetometer boom (OMB) system and its relationship to the SA system consisting of a rotation of  $\phi_{abs}$  about the spin axis,  $Z_{SA}$ . The lower right panel shows the definition of the SMPA frame, which is closely aligned with the Body Coordinate System (BCS) of the MMS spacecraft. Rotation from OMB to SMPA consists of a rotation about the spin axis from boom coordinates into spacecraft coordinates

### 8.3.2 Net Uncertainty Estimation

The sources of uncertainty in the FGM measurements come from the uncertainties in the sensor offsets, gains, and angular parameters. A complete discussion of uncertainty estimation and mathematical equations can be found in Anderson et al. [2023].

The uncertainty due to gains comes from the  $g_{abs}$  uncertainty times the background field. The pre-flight gain calibrations are accurate to 0.01% or better [Russell et al., 2016]. Refinements in the gain are typically smaller than this, so while important for resolving offsets, the gains are not major contributors to

the total uncertainty [Plaschke et al., 2019]. In flight, the absolute gain calibrations exhibit apparently random variability between spacecraft of about 0.01%. In the ROI, the magnetic field is  $\sim 100$  nT so the uncertainty due to gains is on the order of  $\sim 10$  pT.

The uncertainty due to orientation is also proportional to the background field. The star camera accuracy is  $0.01^\circ$  or better [Tooley et al., 2016] and corrections to the axes orthogonality and sensor orientation relative to pre-flight calibration are typically less than  $0.05^\circ$  their variability, indicative of errors between spacecraft, is less than  $0.01^\circ$ . Hence, in the ROI where the magnetic field is  $\sim 100$  nT, the angular error in the vector orientation is of order  $0.01^\circ$  ( $10^{-4}$  radians), so the orientation error is of order 10 pT.

As discussed in detail in section 4 of Anderson et al. [2023], the offsets typically vary by 0.1 to 0.3 nT over an orbit, but variations of up to 1 nT do occur during eclipse epochs when the sensor temperature varies substantially. These variations are determined to somewhat better than  $\sim 100$  pT. Note the offset error dominates the contributions of the net relative calibration uncertainty and the primary focus of minimizing errors in the inter-spacecraft calibration is on the offsets. Efforts to optimize the gain and orientation calibrations are motivated because of their effects on the offset estimation rather than for their direct influence on the uncertainties.

## 8.4 FGM CALIBRATION AND VALIDATION

Ground and in-flight calibrations determine the twelve calibration parameters defined in section 8.3.1, which include the six angular parameters defined in Figure 8-6, the offsets on each sensor axes ( $o_1$ ,  $o_2$  and  $o_3$ ), the relative and absolute gains in spin plane ( $g_{SA\_abs}$ ,  $g_{SP}$ ) and the absolute gain along spin axis ( $g_{SP\_abs}$ ).

The methods of pre-flight calibration are discussed in Russell et al. [2016]. The application of these pre-flight calibrations to the data, and the methods of in-flight calibration are discussed in Anderson et al. [2023].

### 8.4.1 Pre-Flight Calibration / On-Ground Calibration

To assure intra-sensor timing knowledge, an extensive suite of calibrations was conducted as part of the FIELDS Interference and Timing (FIT) campaign [Torbert et al., 2014]. The phase and gain curves versus frequency, and the relative timing delay as compared to other FIELDS instruments were measured with 10 microsecond accuracy for each of the of the AFG and DFG sensor channels. These calibration data show that both the AFG and DFG have the capability to measure the DC and low frequency component of the vector magnetic field over the full range of each magnetometer with a timing accuracy of better than 0.1 ms. Timing corrections were determined for each flight unit, for each data rate (Burst, Fast/Slow Survey), digital filter length (for DFG only) and magnetic field range (High/Low). These timing calibrations are applied in L1A data, as described in section 8.5.2.

An extensive magnetic cleanliness program for the MMS satellite system was supervised and validated by the magnetometer team, as described in Russell et al. [2016]. Pre-flight measurements of spacecraft-generated magnetic fields at the sensor locations were compared with in-flight observations of the instrument offsets [Anderson et al., 2023].

As described in Russell et al. [2016], extensive calibration and cross-calibration of the magnetometers was undertaken by Technical University Braunschweig, Germany, at the magnetic coil facility MAGNETSRODE, as well as at the  $\mu$ -metal chamber at UCLA. Gain (sensitivity) versus sensor temperature and electronic temperature, non-linearity of the gain, as well as alignment as a function of

sensor temperature is determined. These measurements are determined for high range and low range on each unit, as cross-talk characteristics may differ between ranges.

#### 8.4.2 In-Flight Calibration

The FGM in-flight calibration methods are described in Russell et al. [2016]. Details of implementation have changed, as described or referenced in this document. Anderson et al. [2023] provides a consolidated presentation of the current in-flight calibration process.

In-flight calibrations adjust the 12 parameters of gain, offset and alignment summarized in Table 8-5. These parameters are determined after the pre-flight characterization of gain (as a function of sensor and electronics temperature) and non-linearity (section 8.4.1) have been applied. The 12 calibration parameters must be determined for each field range. On a spin-stabilized spacecraft, 8 of these calibration parameters can be determined independently in 4 pairs:  $o_1, o_2$ ;  $s_x, s_y$ ;  $\theta_1, \theta_2$  and  $\varphi_{12}, g_{SP}$  [Plaschke, Auster et al., 2019]. Bromund et al. [2015] describes how this process is adapted to MMS FGM and performed independently on each magnetic field range. The spin axis offset,  $o_3$ , is determined in low range by the EDI method [Plaschke, Nakamura et al., 2014] or Solar Wind Alfvén method [Plaschke, 2019]. This offset can be extrapolated to high range, while low range spin axis gain can be extrapolated from high range, where it is determined by comparison with the Earth magnetic field T02 model, along with the absolute spin phase alignment. The in-flight calibration effort is coordinated among three institutions: Goddard Space Flight Center (GSFC), IWF, and UCLA. On a weekly basis, the full magnetometer team (FGM, SCM, EDI) reviews the combined calibration product in a magnetometer conference (or “MagCon”) led by UCLA [Bromund et al., 2015].

#### Orthogonalization and Spin Plane Offsets

As discussed in section 8.3.2, the primary sources of error are the instrument offsets, and these parameters have the largest variability. The spin plane offsets can be evaluated accurately on 15-minute time windows generally for > 50% of each orbit, while the spin axis offsets can be evaluated accurately on an orbit-by-orbit basis. Figure 8-7 gives a sense of the relative magnitude of short- and long-term trends on the offsets in the low range.

		Calibration Parameters	Parameter Names and Time Window		Physical Methods Used	Owner
			Low field range	High Field Range		
CALIBRATION PROCESS	"ORTHOGONALIZATION"	spin plane offsets	$\theta_1, \theta_2$ ~15 min	$\theta_1, \theta_2$ ~2 hour	Minimize spectral power at $\omega_{spin}$ in the spin plane.	GSFC
		spin plane gain differential and non-orthogonality	$g_{SP}, \varphi_{12}$ ~1 day	$g_{SP}, \varphi_{12}$ ~2 hour	Minimize spectral power at $2\omega_{spin}$ in the spin plane.	
		orthogonality of spin plane sensors relative to spin axis sensor	$\theta_1, \theta_2$ >7days	$\theta_1, \theta_2$ ~2 hour	Minimize linear regression factor between spin-plane sensor offset (determined by sine fit to each spin) and the spin-axis field.	
		sensor alignment relative to spin axis	$s_x, s_y$ ~1 day	$s_x, s_y$ ~2 hour	Minimize spectral power at $\omega_{spin}$ on the spin axis.	
	EDI	spin axis offset	$\theta_3$ ~1 day		Electron time of flight method: Electron Drift Instrument (EDI) provides $ B $ Solar Wind method: optimize $\theta_3$ to minimize $ B_{measured} $	IWF
	EARTH FIELD	high range: absolute gains, absolute phase		$g_{SP\_abs}, g_{SA\_abs}, \varphi_{abs}$ 1 month	Fit to Data to Earth Field Model using weighted linear regression.	UCLA
	RANGE JOINING and INTERSPACECRAFT	spin axis: low range gain, high range offset	$g_{SA\_abs}$ ~1 month	$\theta_3$ ~1 month	Propagate high range gains to low range, cross-calibrating AFG, DFG, 4 observatories. Propagate low range offset to high range.	
low range spin plane: absolute gain, absolute phase		$g_{SP\_abs}, \varphi_{abs}$ ~1 month		Match gain and phase of low range data to high range data, cross-calibrating AFG, DFG, and the 4 observatories while AFG is in high range and DFG is in low range.		

**Table 8-5 In-flight Calibration Methods Listed in the Order of Evaluation [The calibration quantities determined by each method in each gain range are listed, together with the approximate time window required to calculate updates in the calibration files. The calibration effort is divided between three institutions, with each institution taking ownership of a subset of the calibration methods, as shown]**

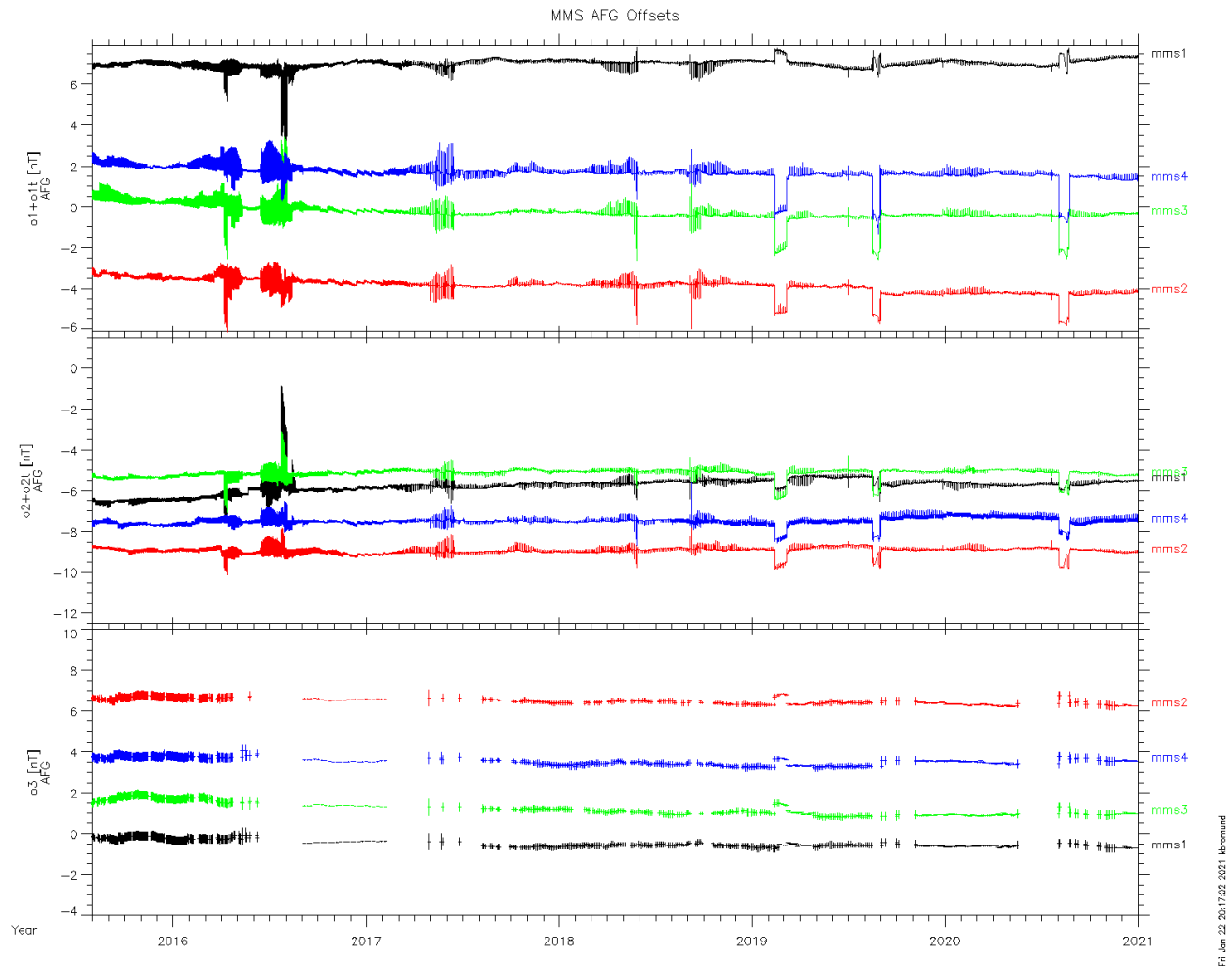


**Figure 8-7 Mission Trend of AFG Offsets [DFG shows similar short-term variations and trends. Spin axis offsets ( $o_1+o_{1t}$  and  $o_2+o_{2t}$ ) show measured (and corrected) short-term offset changes. Error on spin plane offset measurements are  $<0.05$  nT. Error bars are shown on spin axis data to estimate probable level of orbit-scale variations. Note that large changes in spin axis offsets during maneuvers are not always reflected in the  $o_3$  measurements due to insufficient data]**

As will be documented in Anderson et al. [2023], the quality of the calibration process has improved over the course of the mission primarily because of improved dynamic models for the variations in the offset parameters  $o_1$ ,  $o_2$  in low range, as well as the dynamic models of the alignment angles  $\theta_1$ ,  $\theta_2$ . Each of these refinements are cumulative and can be summarized as follows.

- 1) The dynamic model for  $o_1$ ,  $o_2$  is a constant value that is updated once each orbit at perigee, and the dynamic model for  $\theta_1$ ,  $\theta_2$  is a constant value that is updated once each week. Updates for each interval are based solely on data available during each interval.
- 2) The model for  $o_1$ ,  $o_2$  has an additional component that is a function of sensor temperature that is determined empirically in-flight. This accounting for variations as large as 0.5 nT in low range (excluding the larger variations during eclipse), as described in Bromund, et al. [2016].

- 3) The model for  $o_1, o_2$  has an additional component that is a linear function of electronics temperature (consistent with pre-flight calibrations), accounting for errors as large as 0.2 nT, often during the ROI.
- 4) The constant component of  $o_1, o_2$  may be updated at times of maneuvers, in addition to each perigee update.
- 5) Dynamic changes in the  $\theta_1, \theta_2$  parameters are derived from measured sensor temperature using second order polynomial functions, whose linear and quadratic factors were determined from pre-flight alignment calibrations. Empirical constants added to the polynomial fits and are updated only as necessary to account for variations with time scale  $> 1$  month, as observed in mission trends. This eliminates reliance on data within each 7-day evaluation window, which by late 2016 were found to exhibit bias  $> 0.02$  deg. for periods  $> 1$  month, causing errors  $> 0.2$  nT in  $\sim 400$  nT fields.
- 6) The constant component of  $o_1, o_2$  may be updated at arbitrary times within an orbit, as required to fit observed dynamic changes on time scales ranging from 1 minute to  $\sim 1$  day, with magnitudes ranging from 0.05 nT to  $\sim 0.3$  nT. Such changes become more common later in the mission, but also existed earlier and were not systematically corrected.
- 7) The model for  $o_1, o_2$  has two additional components that depend on the thermal loading from the Sun and Earth, respectively, on the spin-axis oriented faces of the sensor, as described in Bromund, et al. [2021].
  - a. Thermal loading on the sunward-tilted face is related to the sun angle (the angle of the spin axis direction,  $\hat{\mathbf{L}}$ , relative to the spacecraft-sun direction,  $\hat{\mathbf{r}}_S$ ). The sun angle drifts seasonally with the orbit and is adjusted by  $\sim 1$  deg. on routine maneuvers to maintain the nominal  $\sim 3^\circ$  sun angle. In addition, spin axis tilt maneuvers increase the sun angle to  $\sim 15^\circ$  during sun tilt maneuvers for extended eclipses (2019 and later). This contributes a component to the offset that is proportional to  $\hat{\mathbf{r}}_S \cdot \hat{\mathbf{L}}$ . The constants of proportionality are determined empirically.
  - b. Thermal loading from Outgoing Longwave Radiation (OLR) from the Earth onto the sensor face that is normal or anti-normal to the spin axis (i.e. the ‘top’ or ‘bottom’ of the sensor, respectively). This contributes a component to the offset that is proportional to  $(\hat{\mathbf{r}}_E \cdot \hat{\mathbf{L}})/r_E^2$  i.e. it is a function of the angle of the spin axis of the spacecraft relative to the direction towards the Earth,  $\hat{\mathbf{r}}_E$ , and the inverse square of the distance from the Earth,  $r_E$ . Constants of proportionality are determined empirically for the separate cases of OLR incident on the top or bottom of the sensor.

### Spin Axis Offset Calibration

When the EDI instrument operates in Field-mode, the spin axis offset can be determined from the EDI time-of-flight (TOF) method. The TOF is measured from emitting and receiving of time-coded sequences of electron beams perpendicular to the ambient magnetic field, which provides independent measurements of the magnetic field modulus [Plaschke, Nakamura et al., 2014]. When the spacecraft trajectory is in the solar wind, the spin axis offset can also be determined from the Alfvén technique, as described in Plaschke [2019]. The Alfvén technique uses the intervals when the solar wind perturbations are predominately transverse to the magnetic field (i.e. Alfvénic disturbances), so the spin axis offset can be estimated by minimizing the variability of the field magnitude (i.e. compressional power). The offsets estimated from the TOF method started to become less reliable in Feb 2019, so a combination of TOF method and Alfvén method has been implemented. During intervals when neither method is available (e.g. in the tail season), the relative offsets are adjusted to minimize AFG-DFG and inter-spacecraft differences, and absolute offsets are corrected only after a reliable calibration results from either the EDI or Solar Wind method.

### Calibration for Absolute Accuracy and Inter-Calibration

The Earth field comparison / range joining process that is described in Russell, et al. [2016] process was updated in the second year of the science operations to improve the inter-calibration of the 4 observatories, and the current process is described as follows.

### Earth Field Model Comparison for High Range Data

The measurement near perigee are used to inter-calibrate the magnetometers to the same external field, using the Tsyganenko T02 model with IGRF2015 Earth main field model. The spin axial component and spin component need to be greater than 2000 nT to perform the comparison because earth field model being more accurate in the high field region. And both components need to be less than 8000 nT to avoid the influence of instrument saturation (c.f. Table 8-1). For each instrument, the high range  $g_{SP\_abs}$ ,  $g_{SA\_abs}$ ,  $\phi_{abs}$  are obtained for each orbit and then averaged over a four-week window to minimize the influence of orbit-to-orbit variations, but keeping the long-term variations. Because all instruments deviate from the reference model by very similar amounts, while the relative difference between each instruments are over an order of magnitude less than the averaged difference between all instruments and the model, the magnetometer team decided to only correct the relative difference between instruments and attribute the averaged difference between all eight instruments and the model to the error in the model rather than the error in the instruments.

### Range Joining and Inter-Spacecraft Calibration

In the region where the AFG and DFG magnetometers change from low range to high range the median of the four AFG magnetometers and the four DFG magnetometers are cross-calibrated. In the inbound orbits the AFG magnetometers switch from low range to high range first, and the high range median AFG data are adjusted to match the low range median DFG data by specifying a delta for the median high range AFG offset. The median DFG high range data are then adjusted to match the high range median AFG data. Finally, these changes are propagated back to low range to adjust the median gains and offsets for low range. The individual magnetometers are then adjusted to match the new medians. As a result, for the spin axis data new high range offsets and low range gains and offsets are determined. These methods are performed in GSE coordinates, in order enable inter-spacecraft calibration. The spin plane data are monitored as part of the process, with the primary effect being a misalignment in terms of relative pointing between the different instruments, but this is generally below the 0.1% level, not significant for portions of the orbit where MMS is acquiring fast mode data, and thus the spin plane calibration parameters are not routinely adjusted.

### **8.4.3 Science Data Assessment (Validation)**

There are plasma environments encountered by MMS providing natural conditions suitable to test the accuracy of the calibrated data. The magnetotail lobe has low plasma density and nearly uniform magnetic field, thus the differences in the measurements between MMS spacecraft are dominated by uncertainty in the calibrated data. Another region for testing is in the quiet solar wind, when the field magnitude is low, less than about 5 nT, any residual errors in the calibrated data are more readily identified owing to the small natural magnetic field and its variations.

Figure 8-8 shows an example of an MMS magnetotail pass, and the vertical dashed lines and arrow indicate the northern magnetotail lobe encounter lasting roughly four hours on 14 July 2019. Panel (g) and (h) shows the current density (derived from  $\nabla \times \mathbf{B}$ ), and  $\nabla \cdot \mathbf{B}$ , and panel (i) shows the magnetic field error estimates,  $\varepsilon B_J$  and  $\varepsilon B_{Div}$ , calculated as the product of spacecraft separation  $s$  and the deduced current

density or the divergence of  $\mathbf{B}$ . The  $\varepsilon B_{\text{Div}}$  are unambiguously error estimates, but the  $\varepsilon B_J$  are dominated by real currents except in the lobe. Thus in the lobe, the  $\varepsilon B_J$  are considered as an error upper limit since the current density should be very small, but is not identically zero. In this example,  $\varepsilon B_J$  is generally below 60 pT and  $\varepsilon B_{\text{Div}}$  is no larger than 30 pT, which indicate the accuracies being better than the 100 pT objective.

Within this figure below, panel (a) shows FGM1 magnetic field data in GSE coordinates from MMS1 and panel (b) shows the field magnitude. Panels c through e are show data from HPCA on MMS1 showing the proton flux versus energy (c), proton density (d), and proton temperature (e). Panel (f) shows the tetrahedron quality factor in black (left axis) and the average MMS separation in red (right axis). Panel (g) shows the current density,  $\mathbf{J}$ , derived from  $\nabla \times \mathbf{B}$ , and panel (h) shows  $\nabla \cdot \mathbf{B}$  both calculated using finite difference derivatives from all four MMS observatories. Bottom panel (i) shows estimates of the magnetic field error estimates,  $\varepsilon B_J$  and  $\varepsilon B_{\text{Div}}$ .

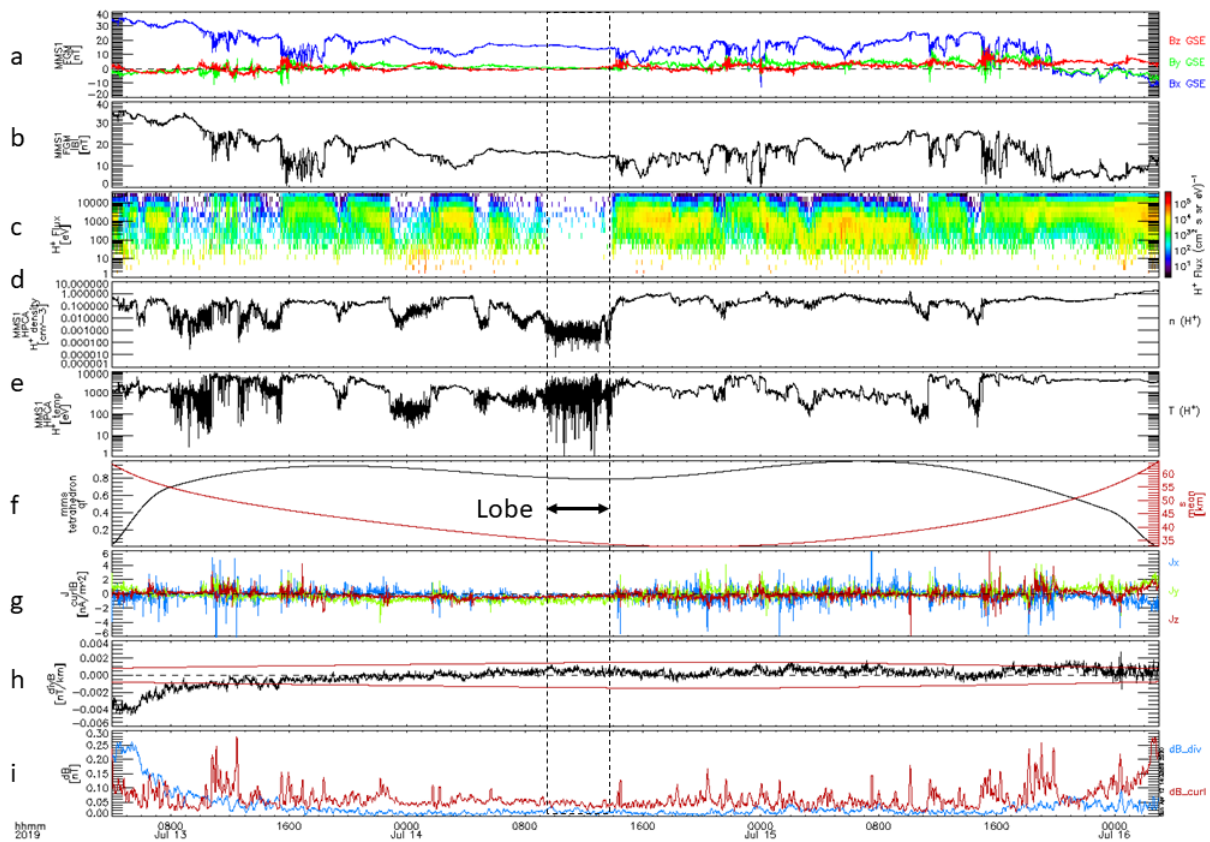


**Figure 8-8 Overview of MMS Magnetotail Pass on 13 to 16 July 2019**

Similar analysis is performed for the solar wind interval on May 1 to 3, 2019. During close spacecraft separation of 15 to 25 km,  $\varepsilon B_J$  and  $\varepsilon B_{\text{Div}}$ , are in the range of 0.1 to 0.2 nT throughout the solar wind interval on 1 and 2 May, indicating that the gradient scale lengths in the solar wind may be sufficiently short to introduce errors in the finite difference gradient calculations. Thus, the curl and divergence error estimates in the solar wind are not useful measures of the data uncertainty. Instead, we use pairwise differences between MMS spacecraft to identify systematic errors. Figure 8-9 shows pairwise differences in the magnetic field for the interval from 08:50 to 09:00 UT on 2 May 2019, which has a steady and weak solar wind magnetic field. The X-GSE and Y-GSE differences have small baseline shifts and a dominant spin tone signal with amplitudes anywhere from below 20 pT to above 50 pT, but below 100



pT. This indicates that errors in the calibrated data in the spin plane, nearly coincident with the GSE X-Y plane, are below 100 pT. The Z-GSE differences indicate consistent offsets between observatories between 0.1 and 0.2 nT for the 1-3 and 3-4 pairs, approaching 0.1 nT for the 1-2, 2-3, and 2-4 pairs, and well below 0.1 nT only for the 1-4 pair. The results for this solar wind interval indicate that on some occasions the calibration process does not achieve the goal of 0.1 nT accuracy.

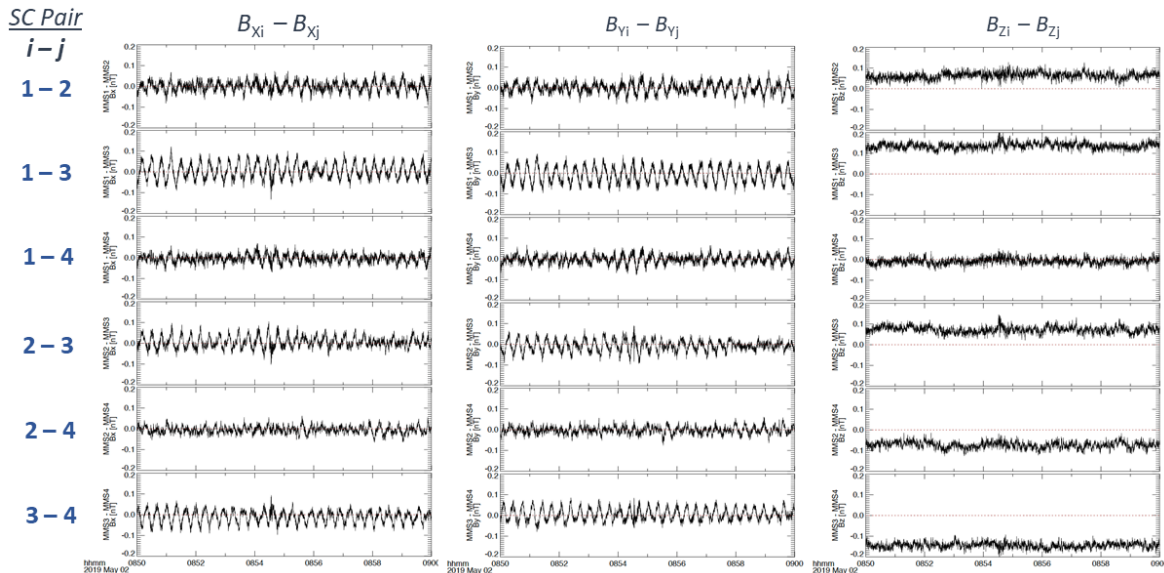


**Figure 8-9 Expanded View of the Pairwise Differences in the Magnetic Field for the 08:50 to 09:00 UT Interval on 2 May 2019 Showing Differences in the Magnetic Field for All Three Magnetic Field Components in GSE Coordinates**

In general, the FGM L2 data accuracy should meet the 100pT requirement, but there could be intervals having higher data errors. More examples of uncertainty analysis and statistical estimates can be found in section 6 of Anderson et al. [2023]. The next section will discuss the possible causes that limit measurement accuracy.

#### 8.4.4 Known Issues

The known issues with data accuracy fall into the following categories:

##### Issues requiring improvements to the data processing software that is run at the MMS SDC

The version of the data processing algorithm is recorded in the X-version of the L2 files (c.f. section 8.5.3.4). The version release notes are listed in Table 8-6. The improvements that affect science data are primarily the implementation of new data flags, data overlap issues, and improvements to attitude data processing.

- Data overlap issues after the implementation of continuous 16 S/s survey mode operations (c.f. section 8.1.1) are corrected in v6, but can be corrected by users of v5 data files by inspecting the `mms?_fgm_mode_srvy_l2` housekeeping value (c.f. Table 8-10), and removing all data points where `mms?_fgm_mode_srvy_l2` is less than 15 S/s.

- Data discontinuities at L2 survey data file boundaries (00:00 UTC). These are due using the average L-vector for 24-hour time period in each data file. As the L-vector typically changes by  $\sim 0.05^\circ$  with each perigee pass, jumps of  $\sim 0.1$  nT can be introduced into data within the ROI. This issue is fixed in v5.
- A 7-minute wobble with amplitude  $\sim 0.05^\circ$  in the effective spin axis, attributed to oscillation of the SDP wire booms after maneuvers. The oscillation decays with a time scale on the order of  $\sim 10$  hours, when it can result in errors of  $\sim 0.1$  nT in the measured difference of the magnetic field between separate spacecraft, which can result in errors in current density as calculated by curlometer techniques. This issue is also fixed in v5.
- An 18-second nutation in the spacecraft spin axis, which decays over a period of hours after a maneuver. And has a similar effect as the 7-minute wobble. This is not currently planned to be corrected, but can be anticipated after perigee and times of maneuver.

X-Version	Notes	First Epoch Available as of 2021-11-20	Last Epoch When Used for Production
4	<ul style="list-style-type: none"> <li>• First version used for public release of L2.</li> <li>• Renamed variables to conform with new MMS variable name guidelines (obs_instr_paramName[_coordSys]_mode_level) <ul style="list-style-type: none"> <li>○ Mag field parameters include ‘b’ for paramName.</li> <li>○ Use ‘r’ instead of ‘pos’ for S/C position paramName.</li> <li>○ Eliminated ‘rate’, replaced with ‘bdeltahalf’. Added ‘rdeltahalf’.</li> <li>○ 11a_mode is now just ‘mode’</li> </ul> </li> <li>• Variable names are not backwards compatible with v3 data files available to MMS instrument teams during commissioning!</li> </ul>	2015-09-01	2017-05-05
5	<ul style="list-style-type: none"> <li>• Y-version number comes from cal file entries.</li> <li>• Ensures there are 2 ephemeris points before/after data to enable proper spline.</li> <li>• Fix to depend_0 of rdeltahalf: fixes bug when reading position data.</li> <li>• L-vector for DMPA2GSE transformation is smoothed with a gaussian filter, instead of using a single average value for the day. This short-term filter avoids introducing artificial jumps at 00:00 UTC and removes 7-minute ‘wobble’ after maneuvers in the GSE and GSM results.</li> <li>• Fixes error with DEFATT file selection found when choosing the daily DEFATT files to be used in Phase 2.</li> <li>• Fixed bug where reference Etemp was used for high range gain. Now uses measured Etemp.</li> </ul>	2016-09-01	TBD
6	<ul style="list-style-type: none"> <li>• Able to read flag files that are delivered to the SDC together with updated calibration files. New flags implemented by v6 are: MNVR, SHAD, NOISE, OFFST, O3WARN and STWARN.</li> <li>• Add DFG PFMODE flag as support data to indicate DEC 32 mode</li> </ul>	TBD	

	<ul style="list-style-type: none"> <li>• Fix data overlap issues (simultaneous 8 S/s and 16 S/s data) at ‘fast/slow’ survey mode changes.</li> <li>• Use CDF_REAL8 (double precision) CDF data type for ephemeris data, instead of CDF_REAL4 (single precision float).</li> <li>• Apply temperature dependent gain when converting offsets specified as nT into pseudo-nT before applying calibrations.</li> </ul>		
--	--	--	--

**Table 8-6 Data File X-Version Release Notes [See FGM Version Release Notes at the SDC web site Datasets section for latest updates ([https://lasp.colorado.edu/mms/sdc/public/datasets/fields/fgm\\_vrn.txt](https://lasp.colorado.edu/mms/sdc/public/datasets/fields/fgm_vrn.txt))]**

Issues corrected by improvements to the calibration algorithms:

Calibration methods that help to achieve the FGM accuracy goal of 0.100 nT are incorporated into L2 production as soon as practical. However, reprocessing and validating previous data requires additional effort, and thus these issues may still be present in data versions currently available for earlier epochs. The Y-version number of the L2 files may be used to determine if these processes have been applied to the data in any given file. For a full discussion of the FGM versioning conventions, see section 8.5.3.4. The primary improvements to the calibration process are discussed in section 8.4.2. Table 8-7 lists each of the significant improvements, the Y-version and Epoch when they were first incorporated into L2 processing and the Epoch when they are first available in re-processed data.

<b>Modification to Calibration Process</b>	<b>Y-version first available in L2</b>	<b>Epoch when routinely introduced; (first epoch of data re-processed with this method, if applicable, as of 2022-10-20)</b>
New data selection criteria avoid periods of rapid temperature change when evaluating $\theta$ angles	31 or earlier	2016-05-05 ~00:30
Remove spintone related to changes in Sensor Temperature during each orbit.	43	2016-07-01 18:07:46
Current method for Earth Field Comparison first applied	53	2016-09-01
Remove spintone due to changes in offset baseline when necessary, particularly at maneuvers. (v10)	61	2016-11-18 01:52:28 (2016-09-01)
Manual changes allowed to update the values of $s_x$ and $s_y$ immediately after a maneuver (rather than on the next orbit after the maneuver). Reduces spin tone on the Z-axis on some orbits with maneuvers.	77	2017-03-14
Use mission averages of alignment angles (Theta1, Theta2), replacing weekly evaluations. This can improve the evaluation of the temperature dependence of the offsets, potentially reducing spin tone within the ROI by ~0.05-0.10 nT	86	2017-05-21 16:47:49 (2016-09-01)
Remove spintone related to changes in Electronics Temperature in MMS1 Survey data (AFG).	86	2017-05-21 16:47:49 (2016-09-01)
Range Joining: Spin Axis Gains: evaluated on the interval 2016-08-31 11:05 to 2017-02-10 16:07; Weekly updates of low range spin axis offsets throughout that same interval.	87	2017-06-14 (2016-09-01)

Remove spintone related to changes in Electronics Temperature in Survey data (AFG) for all spacecraft.	138	2018-05-16 11:04:27
Remove spintone due to magnetic offset baseline shifts at arbitrary times, as identified in AFG-DFG differences. This method identifies baseline shifts as small as 0.05 nT, with timing accuracy <60s. even when obscured by variations in the ambient field.	141	2018-05-28 15:38:00
0.14 nT ‘Glitches’ began to occur randomly in MMS4 Survey (AFG) data as of 2017-09-22. Spin tone amplitude will be enhanced by 0.14 nT for an average of 45 minutes. Glitches recur at random after an average of 10 hours. Durations follow a power law distribution. Glitches that persist longer than 30 seconds are corrected by an automated process.	151	2018-07-31 12:33:06
Solar Wind method used for spin axis offsets, when possible.	181	2019-02-27
Range Joining update of low range spin axis gain, evaluated on interval 2018/11/15T12:58 to 2019/04/23T16:07	188	2019-05-19
Account for offset variations due to Thermal Loading from Earth IR. Reduces spin tone in high fields by ~0.05-0.20 nT and improves evaluation of temperature dependence of the offsets, potentially reducing spin tone within the ROI by 0.05 – 0.1 nT.	304	2021-07-06 19:40:34

**Table 8-7 Lists the Y-Version and Epoch of L2 Data at which Improvements to the Calibration or Calibration Process were Introduced to the Calibration File, as well as the Earliest Epoch Reprocessed with these Improvements**

Issues that cannot be corrected, but are flagged in L2 data:

Flagged data are not removed from the data files, as they may still be valid and usable for some applications. However, flagged data should not be loaded by L2 data access routines (e.g. mms\_load\_fgm in SPEDAS) by default. The flags parameter should always be examined to determine whether missing data can be loaded by overriding this default behavior.\*

Flagged data issues fall into 3 categories:

- Issues that are flagged in all available L2 data.
- Issues that are tracked and recorded by the FGM team, to be flagged in the v6 data files planned for release in the near future.
- Issues that may persist for an indeterminate amount of time after the flagged intervals. These issues are primarily related to recovery from eclipse or maneuvers.

Currently flagged categories are listed and described in Table 8-8 and the L2 flag format may be found in Table 8-12 in section 8.5.3.6.

---

\* Note that the data quality flag should always be loaded by default, to raise visibility. Unfortunately, the flags parameter is classified as CDF ‘support data’ in v5 or earlier L2 files, and thus this parameter is not loaded by default by many CDF reader utilities. This will be corrected in v6 data files.

Description of Issue	Method of Flagging	Flag Name (data version availability)
Saturation: The magnetic field exceeds the dynamic range of the instrument. In the early phases of the mission, saturation occurs in high field range at every perigee pass. Low field range saturation is not an issue, due to range change operations implemented automatically by the FIELDS CDPU For each sensor axis.	Data are automatically flagged by the L2 processing software when the raw value of the data contained in the L1A data are equal to the maximum or minimum integer value that can be expressed in the 24-bit ADC output, corresponding approximately to the values expressed in nT in Table 8.1.	B1SAT, B2SAT, B3SAT, (v3+)
Range Change data spikes. Times changes of dynamic range are not precisely flagged in raw data. Data are corrected to the extent possible, but some spikes may remain. Also, any ringing due to anti-alias filtering of the sudden change cannot be corrected.	Data intervals at the times range changes are automatically flag	RANGE (v3+)
Data spikes of ~0.1-0.2 nT that remain after correcting for sudden changes in the offset on one of the spin plane sensors.	Identified by examining differences between AFG and DFG on each spin axis sensor.	OFFST (v6+)
Periods of rapid ~0.1 nT or larger offset shifting. Appears as excess noise in the data. See example in Figure 8-10.	Identified primarily by examining the difference between the fields measured by AFG and DFG, which can be attributed to a specific instrument by comparisons of spectrograms.	NOISE (v6+)
Noise due to thruster solenoid during maneuvers. Data spikes repeating with a 10-second period.	Flagged according to the mission timeline provided by the FDOA.	MNVR (v6+)
Nutation with 18-sec period, decaying with a time constant on the order of 1 hour. Seen as a spin tone in the spin plane.	May be inferred by the presence of the MNVR flag in earlier data	MNVR (v6+)
Excess spin tone due to increased variability of offsets during eclipse.	In v6, shadow periods are automatically identified by the rapid decrease in temperature.	SHAD (v6+)
Spin tone as large as ~0.2 nT on the Z-axis (~ecliptic normal). This is due to the fact that alignment of Sensor 3 with respect to the spin axis is sensitive to temperature. The calibration process does not account for these angular changes, which primarily only affect data in fields larger than typical in the ROI.	In v6, shadow periods are automatically identified by the rapid decrease in temperature. Thus, the initial portion of this issue will be flagged. In all data versions, the sensor temperature parameter STEMP (c.f. Table 8-10) so the user may identify periods of rapidly decreasing temperature.	SHAD (v6+)
Offset on the spin axis significantly larger than 0.10 nT.	Inferred by AFG-DFG and inter-spacecraft comparison, in absence of good EDI or Solar Wind data.	O3WARN (v6+)

Spin tone significantly larger than 0.1 nT may be present: amplitude of spin tone is too variable to be corrected with existing methods.	Inferred by comparison of AFG-DFG, or from observed spin tone.	SPWARN (v6+)
--	--	--------------

**Table 8-8 Known Issues Flagged in FGM Data**

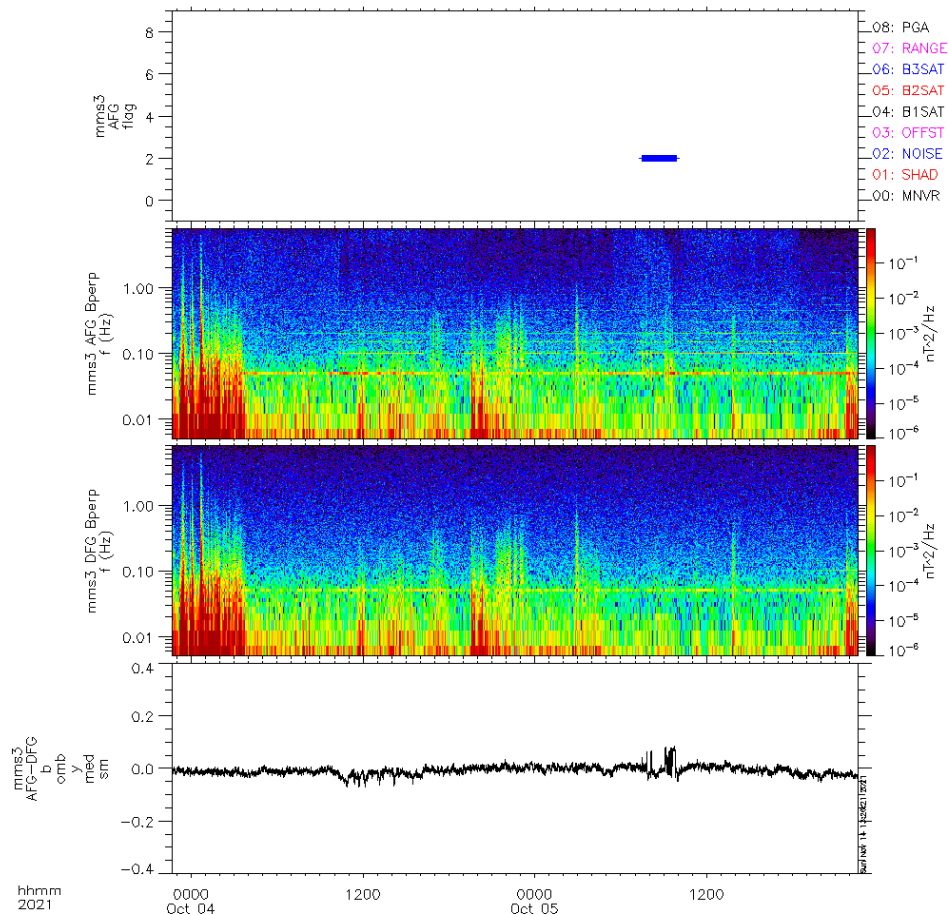


**Figure 8-10 Example of an Interval that will be Flagged as NOISE**

Regarding the above figure, an interval that will be flagged as NOISE is indicated by the horizontal line on the top panel corresponding to the interval of rapid  $\sim 0.1$  nT changes in the offset identifiable when examining the difference between the fields measured by AFG and DFG (bottom panel). The second and third panels show the time variation of power spectral density for AFG and DFG, respectively, clearly revealing excess noise only on AFG during that time period. At the same time, there are unusually prominent higher harmonics of the spin tone, as well as distinct periods where broadband noise exceeds the typical AFG noise level of  $5 \text{ nT}/\sqrt{\text{Hz}}$  @ 1Hz by less than a factor of 2, and thus is not flagged. The NOISE flag is set in L2 Survey data (taken from AFG), but not in L2 Burst (taken from DFG).

## 8.5 FGM DATA PRODUCTION ALGORITHM DESCRIPTIONS

### 8.5.1 Description of Data Products

FGM Level 2 science products use the best available calibration applied that is available 26 days after receipt. However, revised L2 products will be released if significantly better calibrations become available later in the mission. The rather involved calibration procedure is described in Anderson et al. [2023]. The Level 2 files do not contain the abbreviations “AFG” or “DFG”, instead “FGM” is being used. The data files are processed with final ephemeris, attitude and spin phase information. L2 data are available from 2015, Sep. 01 onwards. Data prior to this date gathered during the MMS commissioning phase were available to the MMS team as preliminary L2 (L2pre) data files.

The FGM data product combines the DFG and AFG data into a single data product, choosing the best data suited for general science. The L2 FGM survey data is taken from the AFG due to consistent low noise (low and high range), but because of the linear phase response (constant group delay) of the DFG, L2 FGM burst data is taken from the DFG.

In addition to the magnetic field measurements, the files contain ephemeris information provided at the intrinsic FDOA product resolution (30 sec). Cubic spline interpolation may be used to interpolate the ephemeris data to the times of the magnetic field measurements for the purpose of deriving spacecraft separation vectors. Enough ephemeris data will be included to allow for proper interpolation of the ephemeris vectors to each magnetic field vector contained within the file. L2 burst and L2 survey data files will always contain at least two ephemeris data points before the start of the data and two ephemeris data points after the end of the data. For example, even if the duration of a burst is only a few seconds, the data file will contain at least 4 ephemeris data points (2 minutes of ephemeris) to allow for a proper cubic spline fit. This may lead to data overlap when concatenating consecutive bursts, but as each burst is downloaded and processed separately, in order for the ephemeris data to always be useful, each burst file must be treated as if there will be no consecutive bursts. [Note: as of 2015/4/18, only one ephemeris vector is guaranteed before and after the magnetometer data. In the worst case, there may be only 2 or 3 ephemeris data points in a short burst file.]

### 8.5.2 Data Production Algorithms

The algorithms for data production are as follows:

#### Level 1A (L1A):

- Decompress Level 0 telemetry (c.f. FIELDS CDPU Flight Software User’s Manual)
- Apply a single FIELDS time tag to each vector measurement
- Correct FIELDS time to TAI (c.f. section 7.0 FIELDS)
- Correct for delay of Mag measurement relative to FIELDS time determined from FIT testing
- Convert 24-bit counts are converted floating point pseudo-nT values, by dividing by the following scale factors:
  - AFG low range: -16000
  - AFG high range: 1000
  - DFG low range: 13000
  - DFG high range: 800
- Re-arrange instrument X,Y,Z axes to Sensor 1,2,3 axes. [c.f. Torbert et al. [2014] figure 13]

#### Level 2 (L2):

The Level 2 process accepts Level 1A as an input, and applies processes in the following sequence:

1. Combine Fast and Slow survey data, removing data overlap:
  - Slow and Fast survey data are separate data products produced by the CDPU, with an intentional overlap between modes to avoid data gaps.
  - The separate Level 1A data products are combined into a single Level 2 survey data product, where each sample is tagged with its source sampling rate.
2. Correct known glitches from pre-flight testing (range change glitches)
3. Post-process housekeeping sensor and electronics temperature data (smoothing filters, glitch removal)
4. Apply pre-flight calibrations for gain (including temperature dependence) and non-linearity
5. Apply In-flight calibration – adjustments to gain, alignment, and offset
6. Flag (but not remove) artifacts identified during in-flight calibration
7. Apply post-processing to definitive attitude (smoothing and interpolation) and ephemeris (Hermite spline interpolation from intrinsic (> 30 sec) resolution)
8. Rotate each vector into spacecraft and geophysical coordinates

Details of these processes are provided in Russell et al. [2016], updated as appropriate by Anderson et al. [2023].

Note that the preliminary L2 data that supports L2 data processing for other instruments are produced with these identical algorithms. The only difference is that the preliminary calibrations have not been updated by comparison with the earth's magnetic field to make (generally minor) adjustments to the instrument gain, and the magnetic offsets on the spin axis have not been updated with either the EDI or Solar Wind method.

### 8.5.3 L2 File Structure

FGM L2 data files that follow the MMS CDF data format guidelines for variable names and metadata content. Separate files are produced for each spacecraft, MMS1, MMS2, MMS3 and MMS4. In the filenames and variable names listed in this section, replace '#' with 1,2,3, or 4 to correspond to MMS1, MMS2, MMS3 or MMS4, respectively. Separate files are available Survey data and Burst data. The content of Burst and Survey files are the same, however, the parameter names differ in each file. This section lists the parameter names for Survey data files, for burst files, replace '\_srvy' with '\_brst' in Table 8-9 through Table 8-11.

All L2 data files specify the instrument name as 'fgm'. Note that the L2pre data described in section 8.5.1 is available in the same format as L2 data, except that both AFG and DFG data available in burst as well as survey mode, and the filenames and parameter names differ in that they indicate "afg" or "dfg" rather than "fgm". Note that L2pre data files that were available to the MMS team during the commissioning phase used the v3 data format for parameter names, which is not compatible with the v4 format described in this document.

#### Notes Regarding Preliminary L2 Commissioning data:

L2pre AFG and DFG files that were available to the MMS team for the commissioning phase used the v3 data format, which is not compatible with the v4 format described in this document, because the variable names are slightly different. These commissioning data were last re-processed on 2015-12-17 using Y-version 11 calibrations.

For significant portions of the commissioning phase, survey data was acquired at 128 samples/second. These survey data are available in L2pre srvy mode files in a decimated format, with a data rate of 16 S/s.



The full resolution 128 S/s data are available only in special ‘iwfl2pre’ CDF files that do not follow the standard filename and variable name conventions. These iwfl2pre files provide data in GSE and GSM coordinates and were processed using the same calibrations as the v3 l2pre commissioning files. They are available in the SDC hierarchy as mode ‘f128’, and level ‘iwfl2pre’.

### 8.5.3.1 Survey File Conventions

The survey data files combine Slow Survey and Fast Survey data into a single data product. The `mms?_fgm_mode_srvy_l2` parameter identifies the whether a given data point was collected in slow survey or fast survey mode, by specifying the precise data rate of the L1A FAST or SLOW survey file from which it was obtained. This floating point parameter will be nearly, but not precisely, equal to 8.0 or 16.0 S/s for SLOW and FAST survey, respectively.

Survey files start at with the first complete packet following the even 00:00:00.000 UTC day boundary, so the file names can be uniquely specified by the Year, Month and Day (yyyyMMdd) of the file start time.

### 8.5.3.2 Burst File Conventions

Burst data are measured inside the region of interest at specific times and are downlinked with 128 samples per second.

There is one burst file for each burst segment, as defined by the MMS burst memory management. It may be necessary to concatenate multiple burst files to obtain all data for continuous burst intervals that span multiple segments. There is generally more than one burst file per day, so the name of the burst file specifies the start time of the burst, rounded down to the nearest second: yyyyMMddHHmmss.

### 8.5.3.3 File Name Conventions

File names specify the observatory (Replace ‘#’ with 1, 2, 3, or 4 for MMS1, MMS2, MMS3, or MMS4, respectively), instrument (always fgm for FGM), data mode (srvy for Survey, brst for burst, data level, yyyy for year, MM for Month, dd for day, and version numbers X, Y, Z, as described below in section 8.5.3.4.

Survey Files: `mms?_fgm_srvy_l2_YYYYMMdd_vX.Y.Z.cdf`

Burst Files: `mms?_fgm_brst_l2_YYYYMMddHHmmss_vX.Y.Z.cdf`

### 8.5.3.4 Version Numbering Conventions

Version numbers are specified as vX.Y.Z, following the general MMS guidelines for file versioning. The descriptions of each version level, as specifically interpreted for FGM, are as follows:

- X is the interface number. Increments in X represent a significant change to the format of the file has been made. E.g. new parameters added, or parameters re-named. X also increments upon significant change in the algorithm of the processing software.
- Y is the quality number. This number represents a change in the quality of the data in the file, which would require re-processing of previously processed data. FGM has a slightly non-standard usage of the Y quality number:

- The Y version number of the calibration increments with each weekly Magnetometer Conference, at which a new calibration file is released. Usually, the only change to the calibration is that the tables are extended to include later epochs. However, a new calibration version Y may also revise previous epochs. These revisions are listed in Table 8-7.
- Thus, for FGM, a change in Y version from file to the next does not necessarily indicate a better calibration method was used to data released for previous epochs with a lower Y version. This behavior differs between data files with X-version 4 and X-version 5 or higher:
  - X-version 4: Reprocessed data files for a given epoch will have a higher Y-version, even though the calibration for the epoch of the data file has not changed, if the only change to the calibration file was to extend the calibration to later epochs.
  - X-version 5 or higher: The Y-version of a data files corresponds to the sequence number of the Magnetometer Conference at which the calibration for the epochs contained within the data file was last revised. However, it is possible that the revised calibration methods that result in an increment of the Y-version may not result in a significantly improved calibration for all epochs.
- Y does not reset to 0 when X increments.
- Z is the revision number. Z is set to 0 the first time a given file is processed, and is incremented each time the file is re-processed for any reason. Z is reset to 0 after X or Y is incremented.

### 8.5.3.5 L2 File Content

The content of Burst and Survey files are the same. For the Burst parameter names and labels, replace ‘\_srvy’ with ‘\_brst’ in Table 8-9 through Table 8-11.

The parameters in each CDF file are summarized in Table 8-9, Table 8-10, and Table 8-11. Table 8-9 lists the names of the magnetic field data parameters. Table 8-10 lists the magnetic field housekeeping parameters that are designated as VAR\_TYPE = ‘support\_data’.

The content of Burst and Survey files are the same. For the Burst parameter names and labels, replace ‘\_srvy’ with ‘\_brst’ in Table 8-9, Table 8-10, and Table 8-11.

Name	Type	Dimension	Labels [description]	Unit
Epoch	CDF_TIME_TT2000	0:[]	TT2000	Nanoseconds, epoch terrestrial time J2000
mms?_fgm_b_gse_srvy_l2	CDF_REAL4	1:[4]	Bx GSE, By GSE, Bz GSE, Bt	nT
mms?_fgm_b_gsm_srvy_l2	CDF_REAL4	1:[4]	Bx GSM, By GSM, Bz GSM, Bt	nT
mms?_fgm_b_dmpa_srvy_l2	CDF_REAL4	1:[4]	Bx DMPA, By DMPA, Bz DMPA, Bt	nT
mms?_fgm_b_bcs_srvy_l2	CDF_REAL4	1:[4]	Bx BCS, By BCS, Bz BCS, Bt	nT
mms?_fgm_flag_srvy_l2 *	CDF_UINT4	0:[]	mms?_fgm_flag_srvy_l2 *	0=good. See Table 8-12 for bit definitions

**Table 8-9 L2 Magnetic Field Time Series Data Parameters [All parameters have VAR\_TYPE = 'data'. For burst files, replace '\_srvy' with '\_brst' in the parameter names and labels]. \* indicates VAR\_TYPE was 'support\_data' prior to v6.**

Name	Type	Dimension	Labels [description]	Unit
mms?_fgm_hirange_srvy_l2	CDF_UINT1	0:[]	mms?_fgm_hirange_srvy_l2 [high/low magnetic field range]	1=high range, 0=low range
mms?_fgm_stemp_srvy_l2	CDF_FLOAT	0:[]	mms?_fgm_stemp_srvy_l2 [sensor temperature]	C
mms?_fgm_etemp_srvy_l2	CDF_FLOAT	0:[]	mms?_fgm_etemp_srvy_l2 [electronics temperature]	C
mms?_fgm_pfmode_srvy_l2 **	CDF_UINT1	0:[]	mms?_fgm_pfmode_srvy_l2 [DEC mode]	1 = DEC 32 0 = DEC 64
mms?_fgm_mode_srvy_l2	CDF_FLOAT	0:[]	mms?_fgm_mode_srvy_l2 [data rate, accounting for clock drift. Unambiguously identifies the source data mode of a given record, regardless of the output time sequence delta-t.]	Samples/s

**Table 8-10 L2 Housekeeping Data Parameters Associated Record-for-Record with the Magnetic Field Data. All parameters are VAR\_TYPE='support\_data'. For burst files, replace ‘\_srvy’ with ‘\_brst’ in the parameter names and labels. \*\* indicates parameters not available prior to v6.**

Name	Type	Dimension	Labels	Unit
Epoch_state	CDF_TIME_TT2000	0:[]	TT2000 [time tags for ephemeris data]	Nanoseconds, epoch terrestrial time J2000
mms?_fgm_r_gse_srvy_l2	CDF_REAL8 ***	1:[4]	X GSE, Y GSE, Z GSE, R	Km
mms?_fgm_r_gsm_srvy_l2	CDF_REAL8 ***	1:[4]	X GSM, Y GSM, Z GSM, R	Km
mms?_fgm_rdeltahalf_srvy_l2 *	CDF_FLOAT	0:[]	mms?_fgm_rdeltahalf_srvy_l2 [1/2 delta-t for ephemeris data]	s

**Table 8-11 L2 CDF File Ancillary Ephemeris Parameters have VAR\_TYPE = 'data', except \* indicates VAR\_TYPE= 'support\_data'. \*\*\* indicates data type was CDF\_REAL4 prior to v6) [For burst files, replace ‘\_srvy’ with ‘\_brst’ in the parameter names and labels]**

### 8.5.3.6 Data Flag Definitions

Table 8-12 summarizes the flags that may be applied to the data, identifying the associated bit flags within the 32-bit mms?\_fgm\_flag\_srvy\_l2 data quantity. New X-version may implement new flags, so the table also shows the X-version in which each flag is first introduced. Flagged issues are discussed in detail in section 8.4.4.

MNEMONIC	Bit	Meaning	Example Figure	X-Version First implemented
MNVR	00	Maneuver	TBD	6
SHAD	01	Shadow	TBD	6
NOISE	02	Noise (rapid offset shifting).	TBD	6
OFFST	03	Abrupt Offset shift	TBD	6
B1SAT	04	B1 saturated	TBD	2
B2SAT	05	B2 saturated	TBD	2
B3SAT	06	B3 saturated	TBD	2
RANGE	07	Range-change glitch	TBD	2
O3WARN	08	Offset on axis 3 (Spin Axis)	TBD	6
STWARN	09	Spin Tone warning	TBD	6

**Table 8-12 List of Types of Flags that may be Applied to the Data [identifying the associated bit flags within the 32-bit word stored in the mms#\_fgm\_flag\_srvy\_l2 parameter, and the X-version of the data file when the flag is first available. A bit value of 1 indicates that a given flag is set, so that an overall flag word value of 0 indicates good data]**

Flags can be displayed in SPEDAS (Angelopoulos et al., 2019) using the ‘bitplot’ tplot option, e.g.:

```
labels = strsplit("MNEM MNVR SHAD NOISE OFFST B1SAT B2SAT B3SAT RANGE O3WARN STWARN")
options, " mms?_fgm_flag_srvy_l2", tplot_routine='bitplot', psyms=1, colors = 'lrbm', labels=labels, yrange=[-1,N_ELEMENTS(labels)]
```

### 8.5.3.7 Error Estimation Metadata in CDF Files

No specific CDF metadata are provided to give quantitative estimates of the error of each record. Each CDF file contains the global TEXT attribute that provides a description of the data set, including the current overall error estimate. Data points that may not meet these criteria are flagged, as discussed in section 8.4.4. The format of the flags is defined above in section 8.5.3.6.

## 8.6 APPENDIX A- FGM REFERENCES

Section	Document Number	Title	Revision/Date
	TBD	Anderson, B. J. et al. (in preparation to be submitted 2023), In-Flight Calibration and Performance of the Magnetospheric Multiscale Fluxgate Magnetometers, <i>Space Sci. Rev.</i>	
	<a href="https://doi.org/10.1007/s11214-018-0576-4">https://doi.org/10.1007/s11214-018-0576-4</a>	Angelopoulos, V., Cruce, P., Drozdov, A. <i>et al.</i> (2019) The Space Physics Environment Data Analysis System (SPEDAS). <i>Space Sci Rev</i> 215, 9.	

	<a href="https://ntrs.nasa.gov/api/citations/20170003856">ntrs.nasa.gov/api/citations/20170003856</a>	Bromund, K. R., H. K. Leinweber, F. Plaschke et al., In-Flight Calibration Processes for the MMS Fluxgate Magnetometers, Abstract SM51A-2555 presented at 2015 Fall Meeting, AGU, 14-18 Dec.	
	<a href="https://ntrs.nasa.gov/api/citations/20160014711">ntrs.nasa.gov/api/citations/20160014711</a>	Bromund, K. R., F. Plaschke, R. J. Strangeway, B. J. Anderson, B. G. Huang, et al. (2016) In-Flight Calibration Methods for Temperature-Dependent Offsets in the MMS Fluxgate Magnetometers, Abstract SM21A-2455 presented at 2016 Fall Meeting, AGU, 12-16 Dec.	
	<a href="https://agu2021fallmeeting.agu.ipostersessions.com/Default.aspx?s=8F-AB-99-DF-DF-34-6B-3C-29-4D-04-F6-AC-C1-C3-7D">agu2021fallmeeting-agu.ipostersessions.com/Default.aspx?s=8F-AB-99-DF-DF-34-6B-3C-29-4D-04-F6-AC-C1-C3-7D</a>	Bromund, K. R., B. G. Huang, B. J. Anderson, et al. (2021), Crucial Role of Thermal Gradients in MMS Fluxgate In-Flight Calibration, Poster SH35D-2103 presented at 2021 Fall Meeting, AGU, 13-17 Dec	
	UNH-MMS-CDPUFSWUM-01	FIELDS CDPU Flight Software User's Manual	Rev-1.0 / 24 October 2011
	<a href="https://lasp.colorado.edu/mms/sdc/public/datasets/fields/FIELDS_MMS_Data_Products_v0.1.pdf">lasp.colorado.edu/mms/sdc/public/datasets/fields/FIELDS_MMS_Data_Products_v0.1.pdf</a>	FIELDS MMS Data Products Guide	1.0 / April 20, 2016
	<a href="https://lasp.colorado.edu/mms/sdc/public/datasets/fields/FGM_DataProductsGuide2016Apr20.pdf">lasp.colorado.edu/mms/sdc/public/datasets/fields/FGM_DataProductsGuide2016Apr20.pdf</a> (superseded by this document)	Leinweber, H. K. et al., The MMS Fluxgate Magnetometers Science Data Products Guide	
	461-SYS-SPEC-0115	MMS Alignment and Coordinate System Document	Rev C/ July 22, 2014

	<p><a href="https://doi.org/10.1088/0957-0233/25/10/105008">https://doi.org/10.1088/0957-0233/25/10/105008</a></p>	<p>Plaschke, F., Nakamura, R., Leinweber, H. K., Chutter, M., Vaith, H., Baumjohann, W., Steller, M., and Magnes, W. (2014) Fluxgate magnetometer spin axis offset calibration using the electron drift instrument, Meas. Sci. Technol., 25, 105008.</p>	
	<p><a href="https://doi.org/10.5194/gi-8-63-2019">https://doi.org/10.5194/gi-8-63-2019</a></p>	<p>Plaschke, F., H. U. Auster, et al. (2019) Advanced calibration of magnetometers on spin-stabilized spacecraft based on parameter decoupling, Geosci. Instrum. Method. Data Syst., 8, 63–76.</p>	
	<p><a href="https://doi.org/10.5194/gi-8-285-2019">https://doi.org/10.5194/gi-8-285-2019</a></p>	<p>Plaschke, F. (2019) How many solar wind data are sufficient for accurate fluxgate magnetometer offset determinations?, Geosci. Instrum. Method. Data Syst., 8, 285–291.</p>	
	<p><a href="https://doi.org/10.1007/s11214-014-0057-3">https://doi.org/10.1007/s11214-014-0057-3</a></p>	<p>Russell, C., B. J. Anderson, W. Baumjohann, K. R. Bromund, D. Dearborn, D. Fischer, G. Le, H. K. Leinweber, D. Leneman, W. Magnes, J. D. Means, M. B. Moldwin, R. Nakamura, D. Pierce, F. Plaschke, K. M. Rowe, J. A. Slavin, R. J. Strangeway, R. Torbert, C. Hagen, I. Jernej, A. Valavanoglou, I. Richter (2016), The Magnetospheric Multiscale Magnetometers, Space Science Reviews, 199(1-4), 189-256.</p>	
	<p><a href="https://doi.org/10.1007/s11214-015-0220-5">https://doi.org/10.1007/s11214-015-0220-5</a></p>	<p>Tooley, C., R. Black, B. Robertson, J. Stone, S. Pope, and G. Davis (2016), The Magnetospheric Multiscale Constellation, Space Science Reviews, 199(1-4), 23-76.</p>	

	<a href="https://doi.org/10.1007/s11214-014-0109-8">https://doi.org/10.1007/s11214-014-0109-8</a>	Torbert, R.B., Russell, C.T., Magnes, W. et al. (2016). The FIELDS Instrument Suite on MMS: Scientific Objectives, Measurements, and Data Products. Space Sci Rev 199, 105–135.	
--	---	---	--

**Table 8-13 FGM Applicable Documents**



## 9.0 SEARCH COIL MAGNETOMETER (SCM)

### 9.1 SCM OVERVIEW

The tri-axial search-coil magnetometer (SCM) with its associated preamplifier provides the three-dimensional measurement of the magnetic field fluctuations. The analog magnetic waveforms measured by the SCM are digitized and processed inside the digital signal processor (DSP) together with the electric field data provided by the spin-plane double probe (SDP) and the axial double probe (ADP). Both magnetic and electric field data are collected and stored by the central instrument data processor (CIDP) via the Fields central electronics box (CEB). Magnetic waveforms and spectra are available at different time resolution depending on the selected mode. Finally, the SCM calibration is checked at least once per orbit thanks to the onboard calibration signal provided by DSP and the SCM sensor temperature is measured by a thermistance (housekeeping data). A full description of the design of SCM, its ground calibration results, its in-flight calibration sequence, its operational concept, and an overview of its data products can be found in the publication:

Le Contel, O. et al, **The search-coil magnetometer for MMS**, *Space Sci Rev* **199**, 257–282 (2016). <https://doi.org/10.1007/s11214-014-0096-9>

Updated information can be found in the SCM data product guide.

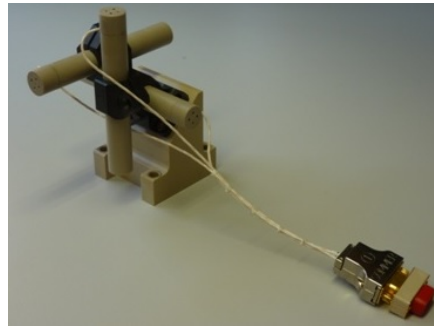


**Figure 9-1 SCM Sensor**



**Figure 9-2 SCM Pre-Amplifier**

## 9.2 AC MAGNETIC FIELD WAVEFORMS (ACB)

### 9.2.1 Overview

The SCM waveform is sampled at 32 samples per second (S/s) in the survey mode<sup>1</sup>, 8192 S/s in the burst mode and finally 16384 S/s in the high-speed burst mode.

#### 9.2.1.1 Heritage

Similar SCM have been previously flown by LPP (or formerly) on many earth-orbiting (GEOS-2, Cluster/STAFF, THEMIS/SCM) and interplanetary (Galileo, Cassini) missions. Multi-chip vertical technology has been already used for SCM preamplifier on THEMIS probes. MMS like search-coil have been also provided by LPP to equip the future Magnetospheric Mercury orbiter of the ESA/JAXA BepiColombo mission.

Search Coil Magnetometer	Cluster II (ESA)	THEMIS (NASA)	MMS (NASA)
SCM Instrument	STAFF-SC(LPP*)	SCM(LPP*)	SCM(LPP)
SCM Onboard Spectra	STAFF-SA (LESIA)	DSP(LASP)	DSP (LASP)
Language	WF: Fortran Spectra: IDL	IDL	IDL
WF Calibration method	Continuous Fourier domain	Continuous Time domain	Continuous Time domain

**Table 9-1 Heritage of SCM Waveform Samples and Onboard Spectra**

\* CETP became LPP on Jan. 1st, 2009

#### 9.2.1.2 Product Description

Operation Modes	Data Type	# Comp.	Frequency Range	APID/HEX	Sample Rate S/s
Slow survey (SS)	Waveform	3		16e	32

1SCM waveforms are sampled at the same sample rate (32 S/s) for both slow and fast survey modes and stored in the same survey CDF file.

Relative Allocation: 50% (1% of downlinked data)	LFB (DSP) spectra	2	0.2 Hz-6kHz (64 bins)	171	0.06 (1 sp/16 s)
Fast survey (FS) RA: 50 % (25% of downlinked data)	Waveform	3		16e	32
	LFB (DSP) spectra	3	0.2 Hz-6kHz (64 bins)	171	0.25 (1 sp/ 4s)
Burst (B) RA: 50% but only 1-2% downlinked (74% of data)	Waveform	3		2a8/2c2	1024/8192
	LFB (DSP) spectra	3	0.2 Hz-6kHz (64 bins)	2b0	10

**Table 9-2 Product Descriptions**

**9.2.2 Theoretical Description**

Responsibility	Usual Convention	MMS/SCM Convention	Usual Files Content	MMS/SCM Wave Form Products
Mission Level NASA	Raw data		Telemetry packets	
Mission level NASA+SDC	Level 0	L0	De-commuted data	Binary files TM counts
Instrument suite level FIELDS/UNH	Level 1	L1A	Decompressed and time tagged data	CDF files TM counts (LONG64) Time tagged (TT2000) SCM123 instrument spinning frame
Instrument team level SCM/LPP	Level 2	L1B	Calibrated data	CDF files nT (FLOAT) <input type="checkbox"/> <b>Converting counts to V to nT is a tricky process!</b> High-pass filtered SCM123 instrument spinning frame (~OMB)
SCM/LPP		L2		CDF files

				nT High-pass filtered GSE frame
<b>Instruments and/or science teams level</b>	Level 3	L2+	Value added data: Use of a model and/or external data (e.g. merged products, automated noise removal, polarization parameters, etc.)	Work in progress: Merged FGM(LF)/SCM(HF) data  Interference cleanup (?)

**Table 9-3 Theoretic Descriptions**

**Decompression:**

- Takes care of data loss due to compression (need of a status flag/fillvalue)
- Also takes care of saturation (status flag/fillvalue)

**Timing:**

- Packet time, clock derivation, delay is taken care of at the Fields consortium level

**Waveform: from Counts to Volts**

- ADC conversion  $\pm 2.5V$  on 16bits with an input DSP gain of 0.403 to fit the  $\pm 6.25V$  output to DSP:
- [Optional] Centering of Waveform (removing DC):

**Waveform: from Volts to nT**

performed continuously in time domain by convolution  
 $in(t) = out(t) * c(t)$  where  $c(t) = FT^{-1}[1/h(f)]$  is called kernel  
(nk is the size of the kernel) and h(f) is the transfer function or frequency response of the antenna, Bessel low-pass filter and digital filter.

- a large nk gives better calibration, but is time consuming
- Get kernel suitable for use by shifting by nk/2, applying Hanning window.
- Note: IDL control function assumes that the center of the kernel is at index nk/2, so no delay is introduced.

Edge behavior determined by /edge\_zero, /edge\_wrap, or /edge\_truncate.  
For MMS L1B, we added and use /edge\_mirror. With no /edge keyword, set all data within nk/2 samples of the edge to zero.

**Kernel Size**

Lower limit depends on the frequency resolution we want.

Criteria :  $\Delta f/f < 1$  at  $F_{\min}$  where  $\Delta f/f = f_s / (nk * f)$   $\square nk_{\min} > f_s / f_{\min}$

Higher limit depends on the computing time and the loss of the first half and last half of the convolution window we can afford.

Our choice for L2 production:

Mode	Name	$f_s = \text{sample rate}$ (S/s)	$f_{\min(L1B)}$ (Hz)	$f_{\min(L2)}$ (Hz)	$f_{\max} = f_{\text{Nyquist}}$ (Hz)	nk
<b>Slow Survey &amp; Fast Survey</b>	scsrvy	32	0.03	0.5	16	2048
<b>Burst (Nightside)</b>	scb	8192	0.5	1	4096	32768
<b>High Burst</b>	schb	16384	16	32	8192	2048

**Table 9-4 Parameters Used by the SCM Calibration Program for Each Sampling Mode**

**Antenna Frequency Response**

Search Coil Magnetometer response or transfer function (TF) is frequency dependent!

$\square$  Need to apply a different gain and phase correction for each considered frequency

**Filters Frequency Response**

Digital filter

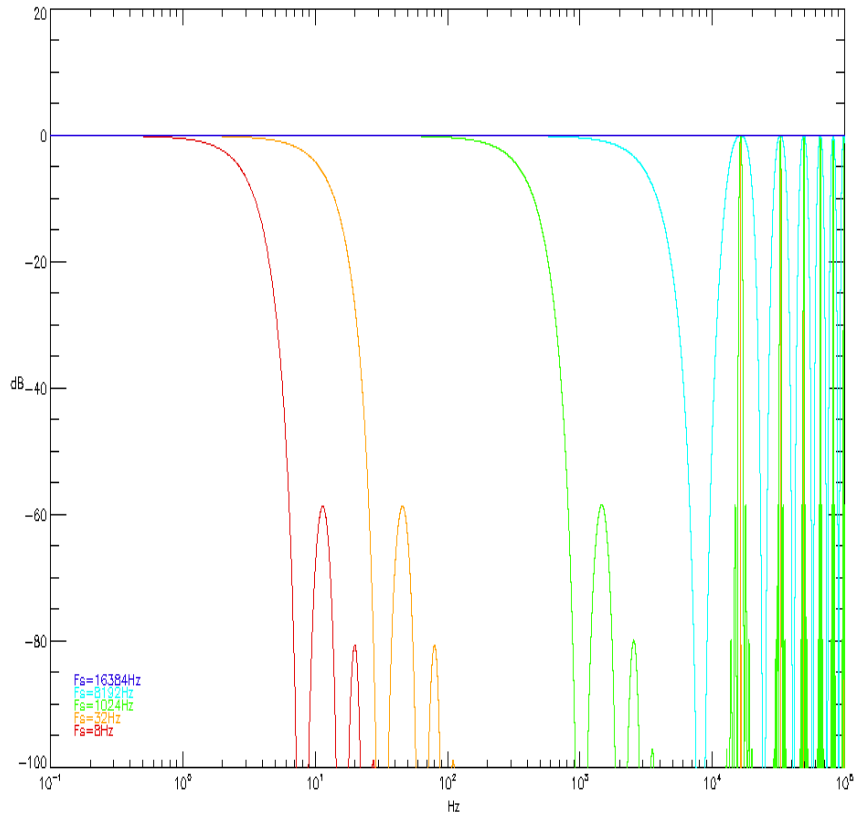


**Figure 9-3 Frequency Response of Digital Filters**

5-pole low pass Bessel ( -3dB at 6.5kHz)

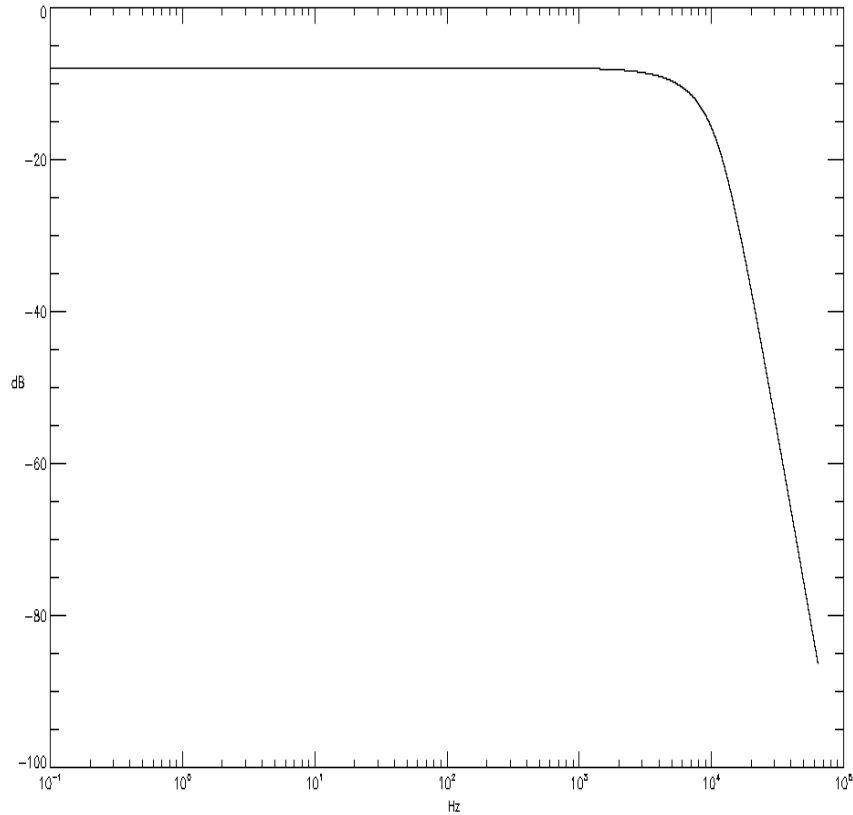


**Figure 9-4 Frequency Response of 5-Pole Low Pass Bessel Filter**

Their responses are taken into account:

$$h(f) = \text{Antenna\_resp}(f) \times \text{DFB}(f) \times \text{Bessel\_filter\_resp}(f) \quad (+\text{filter between } F_{\min} \text{ and } F_{\max})$$

### Waveform Calibration Algorithm

- Instrument and filter responses:

$$\begin{aligned} \text{kernel}_{\text{complex}}(i_f) &= h_{\text{ant}}(i_f) \times h_{\text{DFB}}(i_f) \times h_{\text{HP\_Bessel}}(i_f) \\ \text{with } f(i_f) &= i_f * df, \quad i_f = 0 \dots nk \text{ and } df = f_{\text{Nyquist}} / nk \end{aligned}$$

- Filter  $f < f_{\min}$ :  $\text{kernel}_{\text{complex}}(i_f < i_{f\min}) = 0$
- Filter  $f > f_{\max}$ :  $\text{kernel}_{\text{complex}}(i_f > i_{f\max}) = 0$
- Obtain kernel:  $\text{kernel}_{\text{real}}(i_t) = \text{Real}(\text{FT}^{-1}[\text{kernel}_{\text{complex}}(i_f)])$  (Check that Imaginary part is 0)
- Zero time of the kernel is at index  $i_t = 0$ , shift that to index  $nk/2$  to get a kernel suitable for linear convolution and to allow application of the window
- Hanning windowing (As this is a continuous calibration, the window must be applied to kernel, rather than to the waveform):  $\text{kernel}(i_t) = \text{kernel}_{\text{real}}(i_t) \times \text{Hanning}(nk)$  (Other possibilities, coscub, trapez, etc.)
- Normalize kernel:  $\text{kernel}(i_t) = \text{kernel}(i_t) / nk$
- Convolve signal with kernel:  $\text{in}(t) = \text{out}_{+\text{edge\_mirror}}(t) * \text{kernel}((i_t))$  (Don't forget to shift back  $-nk/2$ )

- Remove average from signal.

### Contiguous Burst Segments Calibration Algorithm

- L1a CDF files are reprocessed for contiguous burst periods (with precise time tag recalculations)
- Six contiguous L1a CDF files in a single run and the four inner segments are kept to produce L1b and L2 CDF files having the same time tag for CDF name as others instruments. The same operation is then repeated with a shift by four segments for the next six segments
- Note that because all burst periods are not downlinked at the same time, but depending on their Figure of Merit attributed by the SITL selection, this processing is run again one month after the downlink of the last isolated burst segment. It allows to check if a new contiguous burst period has been downlinked and if a longer merged burst period can be produced.

### CDF versioning

SCM cdf files use a versioning defined as follows: x.y.z.cdf where

- x means an important change of the calibration program or cdf content
- y means an improvement of the data quality (e. g., change of the calibration file)
- z a minor bug correction or reprocessing

SCM version history can be found here:

<https://lasp.colorado.edu/galaxy/pages/viewpage.action?spaceKey=mms&title=SCM+Release+Notes> (restricted access to MMS team members)

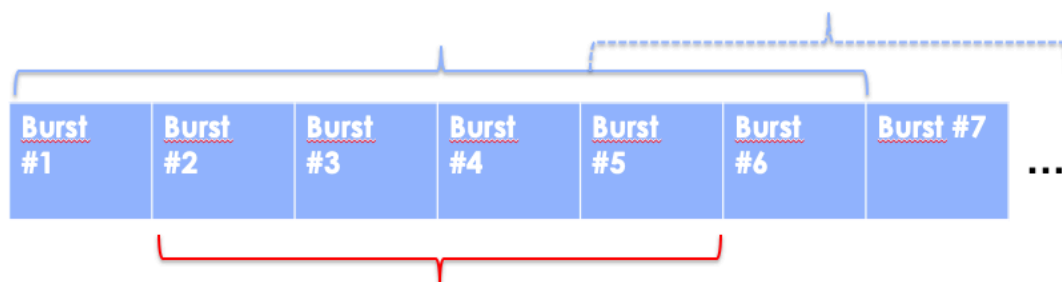
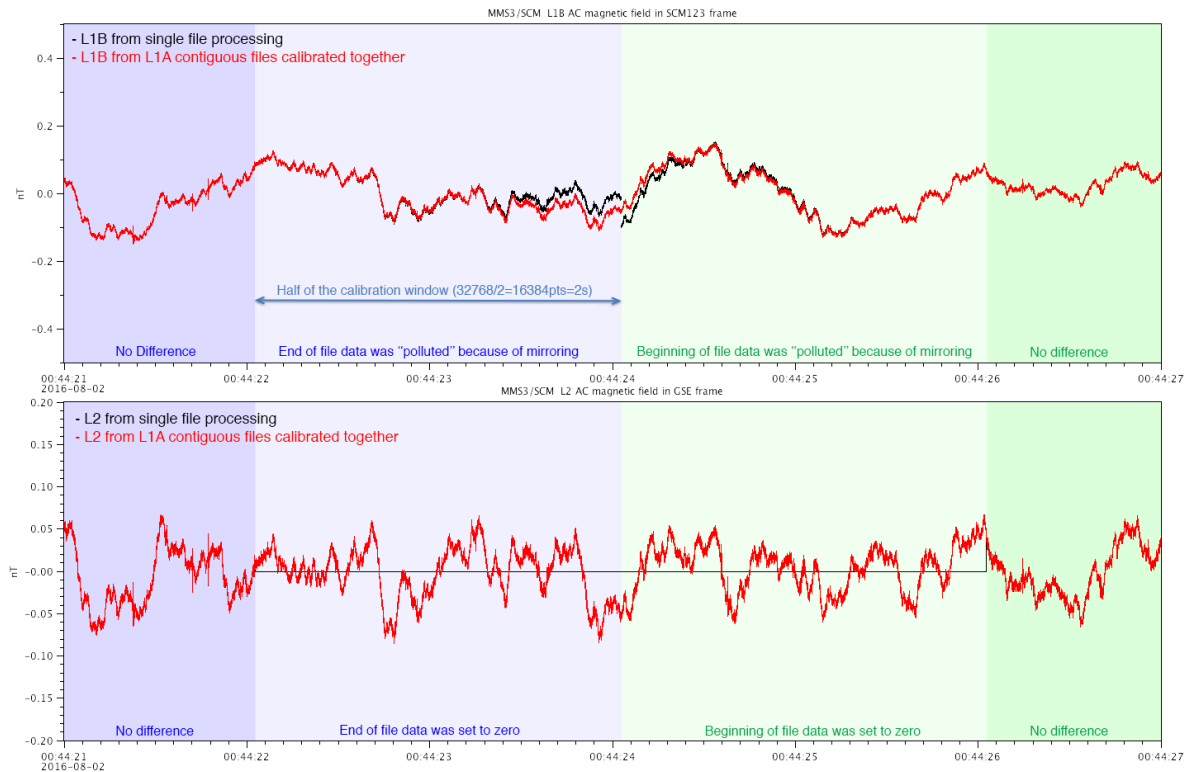


Figure 9-5 Contiguous Segments Management





**Figure 9-6 Comparison Between Non-Contiguous (Black) and Contiguous (Red) Processing**

### Spin Tone Removal:

Spin tone (DC magnetic field signature on spinning components X and Y) was removed for Cluster/STAFF (and THEMIS/SCM) for higher computation precision during the calibration process. Not hard to do with strong Earth DC magnetic field and 4 or 5s spin period. However, fitting MMS 20s spin period is tricky as ‘constant’ magnetic field may vary a lot during these 20s. Anyway, spin tone removal is not needed anymore as ‘double precision’ (64bits floats) allows to keep the spin tone in the X and Y components without losing precision.

Data is also high-pass filtered. Only few spin-tone remains at very strong DC magnetic fields (perigee). Notice that MMS/SCM never saturated even at high DC field.

De-spin is done when moving from SCM123(OMB) to GSE using the FDOA attitude and ephemeris files.

## 9.2.3 Calibration and Validation

### 9.2.3.1 Calibration

The initial SCM calibration consists of measuring the frequency response of transfer function (gain and phase) of the three antennas mounted onboard each spacecraft. This measurement is carried out on the ground in a facility with a very high cleanliness electromagnetic environment. The stability of each transfer function is monitored along the mission life thanks to an in-flight calibration sequence performed at least once per orbit.

### 9.2.3.1.1 Pre-Flight / On-Ground Calibration

#### Antenna complex frequency response obtained from gain and phase measurements on-ground in Chambon-la-Forêt:

SCM standalone transfer functions have been measured at the National Magnetic observatory of Chambon-la-forêt without their thermal blanket and using 2m diameter Helmholtz coils facility at ambient temperature.

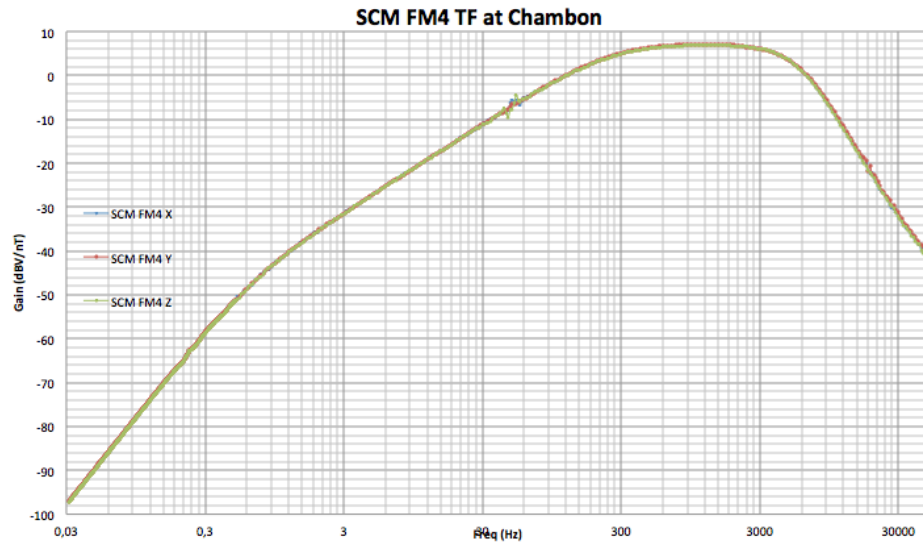


Figure 9-7 SCM FM4 TF at Chambon

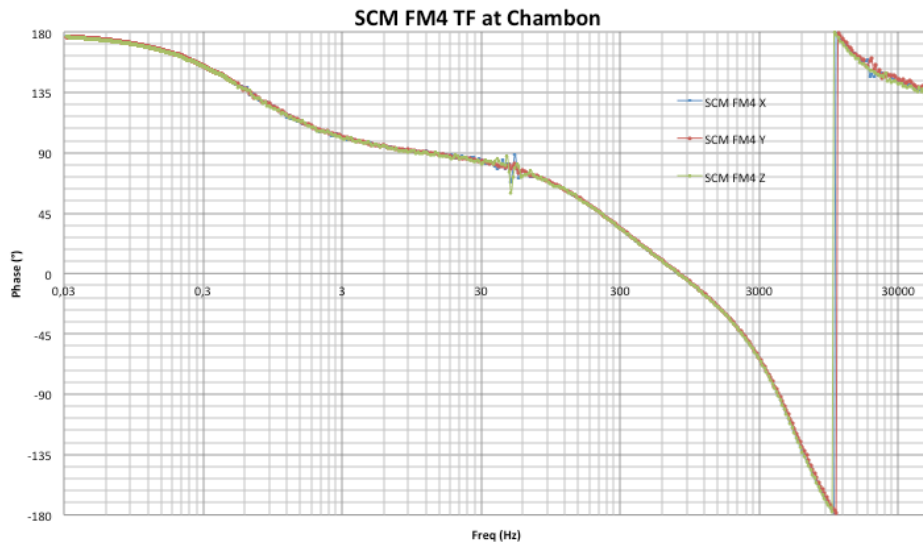


Figure 9-8 SCM FM4 TF at Chambon

### 9.2.3.1.2 In-Flight Calibration

The SCM calibration is executed at least once per orbit. The calibration signal sweep is broken into 4 segments with increasing sample frequencies and the whole calibration sequence lasts less than 90 sec. The frequency of the calibration signal doubles every 4 cycles from 0.125 Hz to 4096 Hz. Each segment will consist of four different frequencies as shown in the table.

<b>Duration (Seconds)</b>	64	4	.3125	.078125
<b>Cal Signal Frequencies (Hz)</b>	.125 .25 .5 1	2 4 8 16	32 64 128 256	512 1024 2048 4096
<b>Sampling Rate (Samples/Second)</b>	16	256	4096	16384

**Table 9-5 Description of the SCM Calibration Sequence**

SCM transfer function verification loop

1. estimates the output amplitude for each frequency (using 4 cycles)
2. computes the 16 ratios (from 0.125 to 4096 Hz) between input and output signals and detect possible phase delay
3. compares gain and phase with the previous calibration transfer function values (first files being transfer functions measured at laboratory)
4. updates, if needed the SCM, transfer function by generating a new SCM transfer function with corrected gain and phase for the corresponding frequency.

### 9.2.3.2 Confidence in Measurements

The gain (resp. phase) differences at 1 kHz between different antennas of the same tri-axis are less than 0.1 dBV/nT (resp. 1.5°) and between antennas of different tri-axis are less than 0.3 dBV/nT (resp. 1.5°). Also, it has been checked that the gain (resp. phase) differences with and without a thermal blanket are no larger than 0.1 dBV/nT in gain (resp. 1°).

### 9.2.3.3 Comparison of Other Measurements

- Cross-calibrations (DFG, AFG) based on spin modulation @20s, 2 components in the spin plane.
- Cross-calibrations (DFG, AFG) based on common frequency range (0.1-4Hz: slow survey, 0.1-8Hz: fast survey, burst 0.1-32 Hz), 3 components.

From in-flight AFG/DFG and SCM comparisons, SCM gains have been found to be lower than DFG/AFG gains by about 14%. This gain correction have been applied to all antennas onboard all satellites and all SCM L2 CDF have been reprocessed. .

- Tests of synchronization with electric field waveform (SDP-ADP).

### 9.2.3.4 Quality Control and Diagnostics

1) A quality factor is given for each data point. This is a string of 3 characters where each letter refers to one SCM physical antenna in the SCM123 order (see Figure 9-1):

- 'G' : good data. Only these data points can be used for scientific analysis

- 'Z': data that are affected (L1B) or set to zero (L2) by convolution boundary effect,
- 'S' : saturated data (equal to VALIDMIN or VALIDMAX)
- 'X' : out of range data (<VALIDMIN or > VALIDMAX)
- 'B' : fillvalue/bad data (Not a Number : NaN)

In-flight calibration sequences described above are analyzed routinely (every orbit) to check that the transfer function of each antenna (4x12) remains unchanged. Plots and statistics are produced and available on line for consultation at <http://mms.lpp.upmc.fr/?page=calibration>.

SCM spectra averaged over the time period corresponding to the mode (survey, burst) and dynamic spectra are produced routinely and available for consultation at <http://mms.lpp.upmc.fr/?page=quicklook>. They allow to detect possible anomalous behavior of antennas. Data validation is based on these two diagnostics in addition to inspection of individual periods and further investigations as required. AC Magnetic Field Power Spectral Density (BPSD).

### 9.3 AC MAGNETIC FIELD POWER SPECTRAL DENSITY (BPSD)

#### 9.3.1 Overview

Onboard Fourier spectra computed by DSP are available from 0.2 Hz to 6 kHz with a time resolution of 16 s in Slow Survey, 2 s in Fast Survey.

##### 9.3.1.1 Heritage

Similar SCM have been previously flown by LPP (or formerly CETP) on many earth-orbiting (GEOS-2, Cluster/STAFF, THEMIS/SCM) and interplanetary (Galileo, Cassini) missions. Multi-chip vertical technology has been already used for SCM preamplifier on THEMIS probes. MMS like search-coil have been also provided by LPP to equip the future Magnetospheric Mercury orbiter of the ESA/JAXA BepiColombo mission.

In particular, the analog magnetic waveforms measured by the SCM are digitized and processed inside the digital signal processor (DSP) developed by LASP (Ergun et al., 2016) based on the THEMIS heritage (Cully et al., 2008).

Cully, C.M., Ergun, R.E., Stevens, K. *et al.* The THEMIS Digital Fields Board. *Space Sci Rev* **141**, 343–355 (2008). <https://doi.org/10.1007/s11214-008-9417-1>

#### 9.3.2 Product Description

Power spectral density of Magnetic field fluctuations ( $\text{nT}^2/\text{Hz}$ ) computed by onboard FFTs by the Digital Signal Processor (DSP) from SCM waveforms during slow survey modes between 0 and 8192 Hz. Their nominal time resolution is 16 s for slow survey and 2 s for fast survey, and nominal number of frequency channels is 56 with logarithmic frequency scale.

This product is computed in space from individual components that are not synchronized to the 1 second pulse. Therefore, the timing between channels can be inaccurate by a fraction of a second. The samples times are interval start times taken from the x component.

- SCM1 (spin plane component, -x SCM sensor) component magnetic power spectral density.
- SCM2 (spin plane component, -z SCM sensor) component magnetic power spectral density.
- SCM3 (spin axis component, -y SCM sensor) component magnetic power spectral density.
- Omni-directional magnetic power spectral density: square root of the sum of the squares of **3 components**.

### 9.3.3 Theoretical Description

$$nT^2/Hz=(SdC)(G_{ADC})^2(G_{DSP})^2(BWC)(HWC)(SCDRC)DSPFRC)(SCMFRC)$$

where

SdC = Spectra Data deCompressed (Spec counts<sup>2</sup>)

G<sub>ADC</sub> = ADC Gain (Volts per count in the ADC) = (2.5V ADC / 32767counts)

G<sub>DSP</sub> = DSP(EWO) Gain (Volts at DSP input / Volts at ADC) = (1./0.403V DSP Input) / (V ADC)

BWC = Bandwidth correction = (1) / (8Hz)

HWC = Hanning window correction= (1) / (0.375)

SCDRC = Spectral Compression Dynamic Range Correction = (1 Waveform Counts<sup>2</sup>) / (16 Spec Counts<sup>2</sup>)

DSPFRC = DSP Frequency Response Correction = 5-pole low pass Bessel, -3dB at 6.5 f(Hz)

No digital filter correction because sampling frequency is not downscaled (16kS/s).

SCMFRC = SCM Frequency Response Correction = SCM TF f(Hz)

### 9.3.4 Calibration and Validation

In addition of the transfer function checking and corrections that we perform for SCM Waveforms (see 9.2.3), the power spectral density obtain from the waveforms and the one coming from DSP are also compared to validate their value.

9.4 APPENDIX A- SCM REFERENCES

Section	Document Number	Title	Revision/Date
	<a href="https://doi.org/10.1007/s11214-008-9417-1">https://doi.org/10.1007/s11214-008-9417-1</a>	Cully, C.M., Ergun, R.E., Stevens, K. et al. (2008). The THEMIS Digital Fields Board. Space Sci Rev 141, 343–355.	
	<a href="https://doi.org/10.1007/s11214-014-0115-x">https://doi.org/10.1007/s11214-014-0115-x</a>	Ergun, R. E., et al., (2016). The Axial Double Probe and Fields Signal Processing for the MMS Mission. Space Sci Rev 199, 167–188.	
	<a href="https://doi.org/10.1007/s11214-008-9371-y">https://doi.org/10.1007/s11214-008-9371-y</a>	Le Contel, O., Roux, A., Robert, P. et al. (2008). First Results of the THEMIS Search Coil Magnetometers . Space Sci Rev 141, 509–534.	
	<a href="https://doi.org/10.1007/s11214-014-0096-9">https://doi.org/10.1007/s11214-014-0096-9</a>	Le Contel, O., Leroy, P., Roux, A. et al. (2016). The Search-Coil Magnetometer for MMS. Space Sci Rev 199, 257–282.	
	<b>Science_Data_Products_Guide_vol2_SCM_v11_20160301.pdf</b>	MMS-SMART Science Data Products Guide: SCM	
	<a href="https://doi.org/10.1007/s11214-014-0109-8">https://doi.org/10.1007/s11214-014-0109-8</a>	Torbert, R.B., Russell, C.T., Magnes, W. et	

		al. (2016). The FIELDS Instrument Suite on MMS: Scientific Objectives, Measurements, and Data Products. Space Sci Rev 199, 105–135.	
--	--	---	--

**Table 9-6 SCM Applicable Documents**

## 10.0 ELECTRON DRIFT INSTRUMENT (EDI)

### 10.1 EDI OVERVIEW

The Electron Drift Instrument on MMS measures the displacement of a weak beam of test electrons that, when emitted in certain directions in the plane perpendicular to the magnetic field, return to the spacecraft after one or more gyrations. This displacement (drift step) is related to the electric field. Two Gun-Detector Units (GDU) are mounted on opposite sides of each spacecraft and face opposite hemispheres. They are controlled via a DPU board (EDI Controller) inside the FIELDS Central Electronics Box (CEB). Two measurement techniques are used that are run in parallel and complement each other: for small drift steps, the displacement is obtained from triangulation of beam directions; for larger drift steps the difference in times-of-flight of beams that are injected in nearly anti-parallel directions is used to calculate the drift step. The time-of-flight measurements also provide the magnetic field strength, thereby enabling the determination of the offsets in the spin axis component of the AFG and DFG flux gate magnetometers. A by-product of this operating mode (Electric Field Mode) are ambient electrons at pitch angle 90 degrees within the energy window of the detectors. These are transmitted in telemetry whenever no return beam has been detected within a fixed time interval. Due to the data quality categories used on-board these are referred to as “Quality Zero” data. In a second operating mode (Ambient Mode) the EDI detectors can be used to sample ambient electrons at pitch angles 0, 90 and 180 degrees at high time resolution.

A full description of the design of EDI, its ground calibration and its operational modes can be found in the publication:

Torbert, R.B., et al, **The Electron Drift Instrument for MMS**, Space Sci Rev 199, 283–305 (2016). <https://doi.org/10.1007/s11214-015-0182-7>

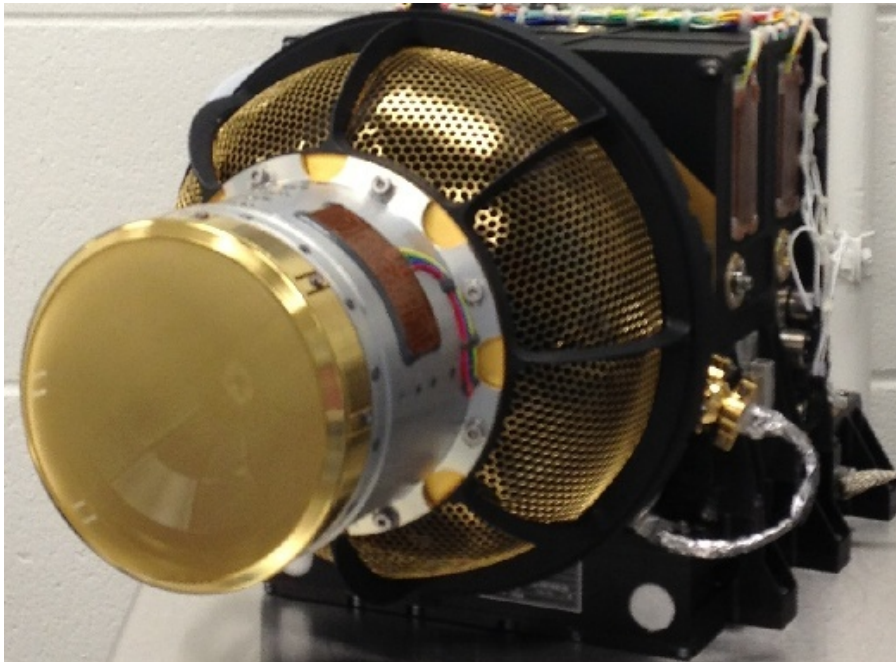


**Figure 10-1 EDI Gun-Detector Unit**



### 10.1.1 Status of EDI

Several of the opto-couplers in the high voltage amplifiers in the Gun and Gun-Detector Electronics (GDE) continue to experience trends, limiting the life of the instrument and impacting available operational choices. This was known already during integration and testing on the ground. Continual trending analysis throughout the mission aided in making operational decisions that ensured the extension of the opto-coupler life cycle. In addition, a few failures occurred due to HV discharges, and in one case the filament of the electron beam generation system in the Gun reached its end of life. Table 10-1 provides a summary of the opto-coupler trending situation and the component failures and their impact on operations, ordered by observatory.

<b>Date</b>	<b>Observatory / Unit / Hardware Element</b>	<b>Event / Failure / Trending</b>	<b>Impacted Mode</b>	<b>Operational Change</b>
Jan 2022	MMS1 / GDU1 / Gun Deflector1	Optocoupler Deterioration	EFIELD: Loss of beam return in azimuthal section for large deflections from symmetry axis	None; Safe Mode entry prevented by increasing out-of-limits persistence
Nov 2016	MMS2 / GDU2 / Gun Anode Amplifier	HV discharge	EFIELD: GDU2 no longer usable	Continued with single-gun EFIELD mode
Feb 2022	MMS2 / GDU1 / Gun Filament	End of life	EFIELD: GDU1 no longer usable	EFIELD: GDU1 no longer usable
Jun 2022	MMS2 / GDU1 / Optics Lower Injector	Optocoupler Deterioration	AMBIENT: future loss of geometric factor for large polar look directions	Minimize continuing deterioration by avoiding perpendicular and alternating pitch angle sampling
May 2017	MMS3 / GDU1 / Gun Cathode	Optocoupler Deterioration	EFIELD: GDU1 no longer usable	Continued with single-gun EFIELD mode
Sep 2019	MMS3 / GDU2 / Gun Deflection System	Sudden deterioration after HV discharge	EFIELD: Beam pointing accuracy degradation	Stopped L2 EFIELD production; continued L1A production for Flux Gate spin axis offset calibration using EDI time-of-flight measurements
Jan 2020	MMS3 / GDU2 / Gun Deflector5	Optocoupler Deterioration	EFIELD: Loss of beam return in azimuthal section for large deflection from symmetry axis	None; Safe Mode entry prevented by increasing out-of-limits persistence

May 2021	MMS3 / GDU2 / Optics Upper Injector	Optocoupler Deterioration	AMBIENT: loss of geometric factor for poleward look directions (in field aligned and alternating pitch angle modes)	Restrict sampling to perpendicular pitch angles (least amount of stress on optocoupler)
Jan 2022	MMS3 / GDU1 / Optics Upper Deflector	Optocoupler Deterioration	EFIELD: potential loss of geometric factor and ability to detect signal return for poleward look directions	None; Safe Mode entry prevented by increasing out-of-limits persistence
Apr 2020	MMS4 / GDU2 / Optics Upper Deflector	Optocoupler Deterioration	EFIELD: potential loss of geometric factor and ability to detect signal return for poleward look directions	None; Safe Mode entry prevented by increasing out-of-limits persistence
Sep 2022	MMS4 / GDU1 / Optics Upper Injector	Optocoupler Deterioration	EFIELD: potential loss of geometric factor and ability to detect signal return for poleward look directions	Decision pending

**Table 10-1 Summary of EDI Instrument Degradation and Operational Impact**

### 10.1.2 Mode Scheduling

In the first years of the mission science operations were restricted to altitudes above 4 Re. Later in the mission this limit was reduced to 3Re in order to help with EDP calibration in the inner magnetosphere. EFIELD operations were typically scheduled on the outbound and inbound side for several hours (typically 5 hours), except in mission phase 1X where operations were reduced to conserve opto-coupler life, and phase 2A where no EFIELD operations were scheduled for the same reason.

In the remaining part of the orbit, Ambient Mode was used. Originally one sampling mode, field aligned or alternating between field aligned and perpendicular electrons, was used per orbit. Starting with phase 3B this was changed to switching between three sampling modes, where the first sampling intervals ended at the end of SROI1 and the third interval started at the beginning of SROI3. The detector energy was 500eV initially, but was later reduced to 250eV due to deteriorating opto-couplers. Table 10-2 summarizes the Ambient Mode Operations over the mission.

OBS	Mission Phase	From	To	Sampling Mode	L2 Data Product		
					Field Aligned	Perpendicular	Alternating
1	1A	2015-09-01	2016-01-06	FA	amb		
234	1A	2015-09-01	2016-01-04	FA	amb		
1	1A, 1X	2016-01-14	2016-06-12	FA	amb-pm2		
234	1A, 1X	2016-01-04	2016-06-12	FA	amb-pm2		

1234	1X	2016-07-29	2016-09-12	ALT			amb-alt-cc
134	1B	2016-09-12	2016-10-13	ALT			amb-alt-oc
2	1B	2016-09-12	2016-10-07	ALT			amb-alt-oc
2	1B	2016-10-09	2016-10-09	ALT			amb-alt-cc
2	1B	2016-10-10	2016-10-13	ALT			amb-alt-oc
1234	1B, 2A	2016-10-14	2017-05-05	FA	amb-pm2		
1234	2B	2017-05-05	2017-05-24	ALT			amb-alt-oob
1234	2B, 3A	2017-06-18	2017-11-14	FA	amb-pm2		
1234	3B, 3C	2017-11-14	2018-05-10	FA / ALT / FA	amb-pm2		amb-alt-oob
1234	3C, 3D, 4A	2018-05-10	2019-02-12	FA	amb-pm2		
1234	4B	2019-02-12	2019-03-05	FA / ALT / FA	amb-pm2		amb-alt-oob
1234	4B-D, 5A	2019-03-05	2019-10-31	FA / ALT / 90	amb-pm2	amb-perp-ob	amb-alt-oob
1234	5A-C	2019-10-31	2020-05-11	FA / ALT / 90	amb-pm2	amb-perp-ob	amb-alt-oob
123	5C	2020-05-11	2020-06-23	FA / ALT / 90	amb-pm2	amb-perp-ob	amb-alt-oob
1	5D, 6A	2020-06-23	2020-11-02	FA / ALT / 90	amb-pm2	amb-perp-ob	amb-alt-oob
123	6A	2020-11-02	2020-11-24	FA / ALT / 90	amb-pm2	amb-perp-ob	amb-alt-oob
123	6B	2020-11-24	2020-12-08	FA / 90 / 90	amb-pm2	amb-perp-ob	
123	6B, 6C	2020-12-08	2021-05-04	FA / Safe / 90	amb-pm2	amb-perp-ob	
1	6C-D, 7A-D	2021-05-04	current	90 / FA / 90	amb-pm2	amb-perp-ob	
3	6C-D, 7A-D	2021-05-04	current	90 / 90 / 90		amb-perp-ob	
2	7D	2022-06-16	current	Safe / Safe / FA	amb-pm2		

**Table 10-2 Ambient Mode Sampling Options Summary**

## 10.2 EDI DATA VOLUME AND TIMING

### 10.2.1 Electric Field Mode Time Tags

Raw (level 0) EDI electric field mode data are organized in data structures that contain electron beam firing directions and measured times-of-flight of detected return beams, along with a quality indicator,

timing information and other measurement settings such as the time-of-flight correlator code clock dividers that are needed for the ground analysis, as well as some auxiliary information. The raw data structures have the same size and content in burst and survey telemetry, although they are organized differently in the level 0 telemetry.

The time tags assigned to L2 data are not the centers of the 5 second analysis time intervals, but are calculated as the average of the times of all detected return beams that contributed to the result. For that reason the EDI L2 electric field data are not spaced regularly in time. Moreover, there are times when no adequate data are found in a given 5 second interval, resulting in data gaps.

The E-Field telemetry bit rates and volume are shown in Table 10-3.

### 10.2.2 Ambient Electron Mode Time Tags

Ambient Electron Mode data are sampled on a regular basis at a rate of 1024 samples per second for burst data and 32 samples per second for survey data. The sampling for burst data is contiguous. That is, there is no gap between the accumulation windows of subsequent samples. In survey the accumulation windows cover only 50% of the time between two subsequent samples.

Given the regular sampling, the raw telemetry contains only the packet coarse and fine time in each packet and the time tags for each sample are constructed on the ground during the processing of the L1A data. The time tags identify the centers of the accumulation windows. The onboard timing is controlled by the  $2^{23}$  Hz (8,338 MHz) FIELDS Master clock. The frequency error of this clock (of the order of 10 ppm) is corrected for on the ground when constructing the sample time tags. The residual error on the time tags is 50us.

### 10.2.3 EDI Data Volume

Table 10-3 shows the Survey and Burst data volumes for EDI in E-Field and Ambient Mode.

Telemetry Mode	EDI Mode	Size (bytes)	Cadence (seconds)	Bit Rate (bits per second)
Survey	E-Field	794	4	1588
Survey	Ambient	786	4	1572
Burst	E-Field	5216	1	41728
Burst	Ambient	8746	1	69968

**Table 10-3 EDI Data Volume in Survey and Burst for E-Field and Ambient Mode**

## 10.3 EDI CALIBRATION AND VALIDATION

### 10.3.1 Pre-Flight / On-Ground Calibration

For successful operation of electric field mode precise knowledge and control of the electron beam firing direction of the gun is mandatory, requiring a dedicated ground calibration to determine the deviation of the actual deflection characteristics from a modeled behavior individually for each gun.

The EDI detector on the other hand has a fairly wide field of view in order to be able to accommodate the aberration of the return beam direction with respect to the firing direction which can be up to several degrees depending on electric and magnetic field conditions. In addition, the uniformity requirements on the detector over the azimuth angle (translating into sensor anodes) of its look direction are not too stringent since the variation of the signal is dominated by the variability of the electric and magnetic

fields as well as statistical effects in the correlator that is used for electron beam modulation, return beam detection and time-of-flight measurement. For that reason, a detector characterization on the ground was deemed sufficient.

A more elaborate characterization of the detector for the purpose of Ambient Mode data processing was performed in orbit.

A description of the design of EDI and a summary of its pre-flight and ground calibration results can be found in the publication:

Torbert, R.B., et al, **The Electron Drift Instrument for MMS**, Space Sci Rev 199, 283–305 (2016). <https://doi.org/10.1007/s11214-015-0182-7>

### 10.3.1.1 Electron Guns

The main purpose of the gun calibration was the determination of two gun deflection voltages (called XD and YD) as a function of polar and azimuth angles of the beam firing direction on a fine angular grid. Due to the deflection characteristics two grid sizes were used, two degrees for polar angles below 70 degrees, and one degree between 70 and 96 degrees. The azimuthal grid size was one degree. In addition to the beam pointing calibration, values of the gun focus voltage and wehnelt voltage were determined, and beam profiles were recorded for a subset of the beam pointing directions. While the wehnelt voltage is fixed for a given energy and is tuned to achieve maximum output beam current, the focus voltage impacts the beam profile and is dependent on the beam pointing directions, although a coarser grid than for the beam pointing was sufficient. These calibrations were performed for two energies, 1 keV and 500eV, and for two guns also for 250 eV. Since the reference voltages for the gun are generated in the Gun-Detector electronics (GDE) a particular gun calibration is always valid for the pair of Gun and GDE that were used together in the calibration.

The calibrations were carried out at the Space Research Institute (Institut für Weltraumforschung) in Graz, Austria, using a dedicated vacuum chamber. Stepper motors were used to orient the gun with respect to a position sensitive detector. An iterative approach was used to determine the XD and YD deflection voltages that pointed the beam's center (as defined by peak emission) on the detector. The requirement for beam pointing accuracy is 1 degree, with a goal of a residual error below 0.1 degrees for the deviation of the calculated location of the beam current peak on the detector from the reference point.

Figure 10-2 shows the residual angular error at 500eV energy as a polar color map for Gun SN 4 in GDU SN 9 which is installed as GDU2 on MMS4 500eV energy. Figure 10-3 shows the residual error at 1 keV for the same Gun. Except for isolated small regions near the center (symmetry axis) the goal of 0.1 degrees residual error is met for both energies.

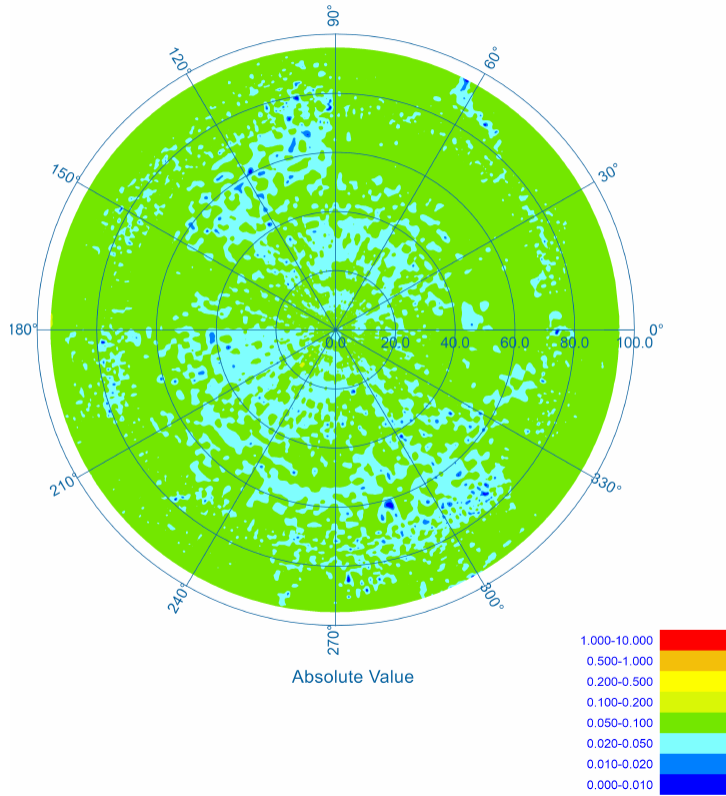


**Figure 10-2 Gun SN 4 Residual Beam Pointing Error at 500 eV**

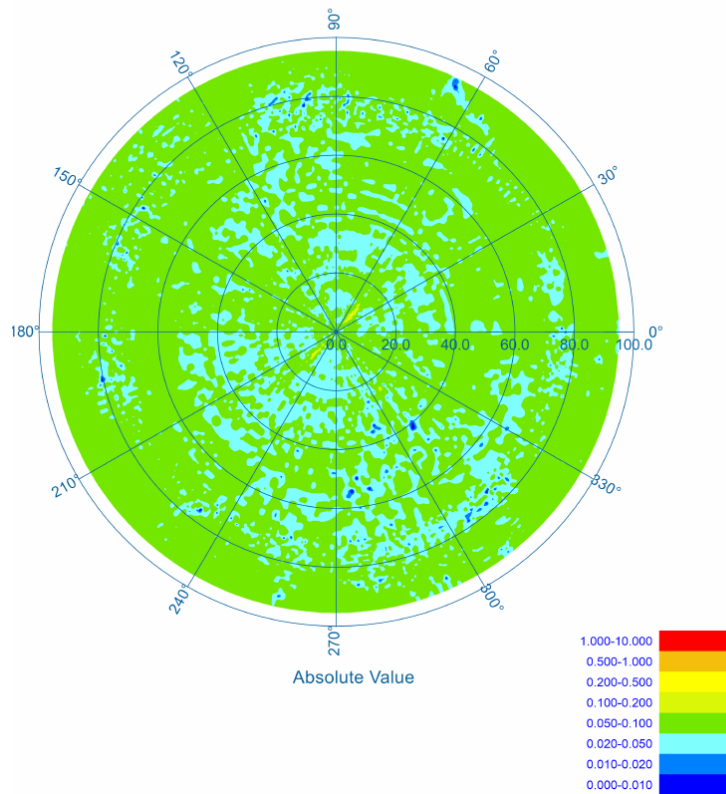


**Figure 10-3 Gun SN 4 Residual Beam Pointing Error at 1 keV**

### 10.3.1.2 Detectors

#### 10.3.1.2.1 Sensor Tests

The sensor subunit of each GDU with its micro-channel plates (MCP), HV supply, custom pre-amplifiers and subsequent processing electronics went through a standalone testing sequence that was tightly interwoven with the sensor assembly. The test steps consisted of preamplifier threshold trimming, pre-amplifier delay variation measurement, a thermal test and electrical tests prior to and after board coating and a final vacuum test where MCP gain uniformity as well as aliveness of the signal path for each of the 32 azimuthal channels were demonstrated by rotating the sensor slowly by 360 degrees around its symmetry axis while illuminating the MCP input face with a fine pencil electron beam, and the MCP operating voltage was determined

The subsequent figures are from Sensor SN 8 which is integrated in GDU SN9 on MMS4.

Figure 10-4 shows the measured preamplifier signal delay variation as a function of input pulse height. The test was performed using test pulses and only for only two of the 32 amplifiers, channels 7 and 27. Channel 27 is special in that there is a calibration spoke near its anode which leads to increased capacitance for this channel, resulting in a slightly larger signal delay through the pre-amplifier. The minimum delay (for large input pulse height) was approximately 20 ns. The largest delay at 1.2 x

threshold was 60 ns for channel 27, leading to a variation of 40 ns which is well below the 60 ns specified in the sensor requirements.

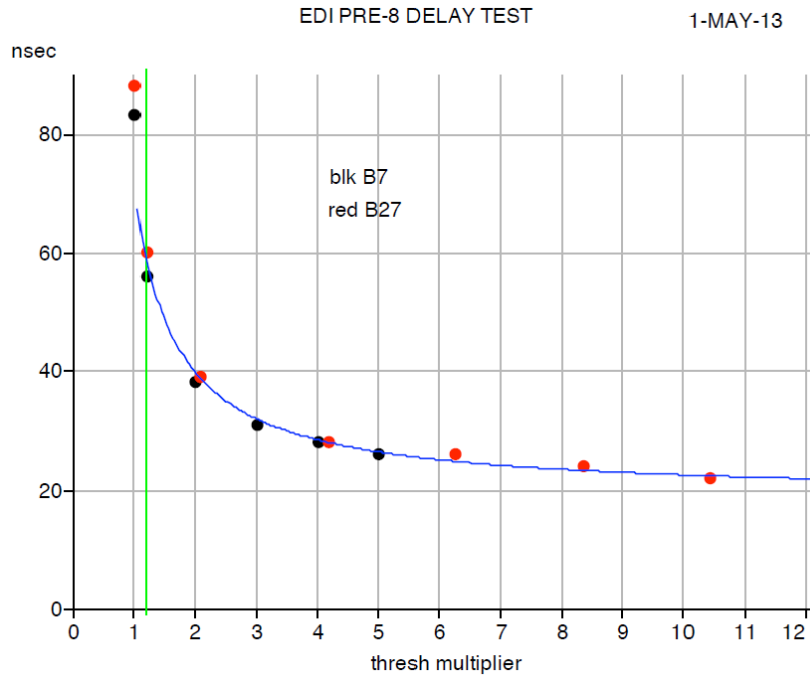


**Figure 10-4 EDI Sensor SN8 Preamplifier Delay Measurements**

Figure 10-5 shows the result of the roll test of Sensor SN8. Due to the fine electron beam used and the fine grained azimuthal steps of the 360 degree roll the gaps between anodes were resolved, as indicated by the periodic dips of the count rate. The worst-case change in count rate over all channels was approximately 10%, well below the required 25%, for the operational MCP high voltage of 2400 volts.

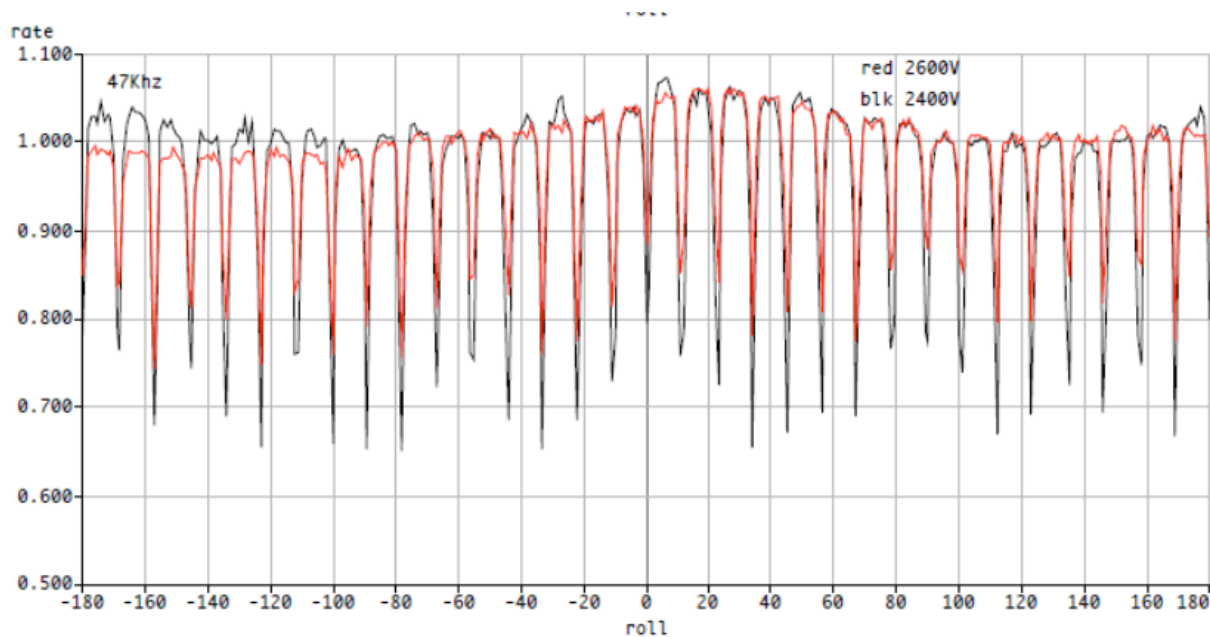


**Figure 10-5 EDI Sensor SN8 Roll Test Results at 2400V and 2600V**



### 10.3.1.2.2 Optics Modeling

The large number of electrodes in the electrostatic optics of the detector section of the EDI GDUs results in a large parameter space for the operation of the detector. The commercial “Lorentz” software suite was used to perform extensive simulations of the optics in order to determine appropriate sets of voltages to achieve the desired response to the incoming electron beam. Driving factors were finding suitable tradeoffs between signal-to-noise ratio and angular acceptance window width.

The Lorentz software provided both the electric field solution as well as the calculation of electron trajectories taking the physical structure of the optics into account. For any given look direction thousands of trajectories were calculated and the positions of those which would hit the micro-channel plates were recorded. The input trajectories were varied over input angle and location so that all possible successful trajectories over the full range of angles and source locations were bounded by the simulation. With the simulation results maps of input angle versus Sensor anode number were built for a given look direction.

Figure 10-6 shows a comparison of between simulated and measured response for three optics look directions (polar angle) of 30, 60 and 90 degrees. There is good agreement regarding the shape and extent of the response. The agreement provided verification that the simulation is accurate and could be used with confidence for developing lookup tables for the electrode voltages of the optics.

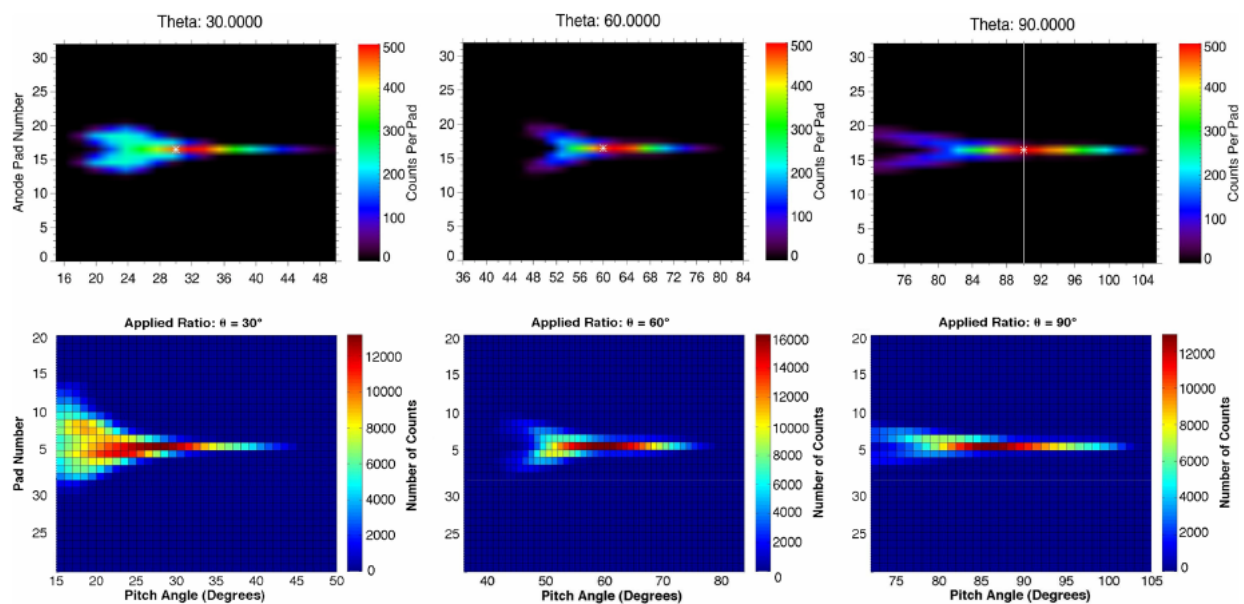


**Figure 10-6 Comparison of Simulated Response (top row) and Measured Response (bottom row) of the EDI Optics for Three Look Directions [The vertical axis shows the anode pad number of the counts received by that pad and the horizontal axis shows the angular range relative to the symmetry axis of the GDU]**

### 10.3.1.2.3 Detector Characterization

Characterizations of the detectors were performed on all flight GDUs during component level testing. The electron source for these characterizations was a broad beam generated using a UV backlit thin plate with chrome coating. The plate was biased negatively at the desired voltage (energy) and photoelectrons emanating from the plate were accelerated towards a grid at ground potential between the plate and the GDU. The GDU was mounted on a manipulation table that allowed the rotation of the GDU 360 degrees

around its symmetry axis and pitching the GDU towards/away from the beam so that incident angles between 0 and 110 degrees relative to the symmetry axis could be achieved. Figure 10-7 illustrates the test setup.

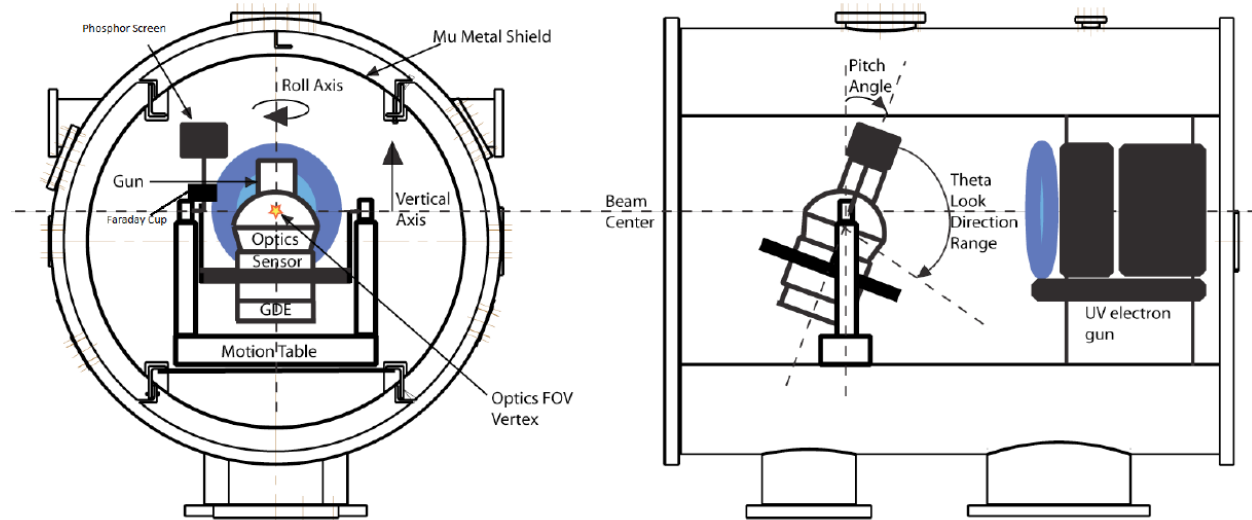
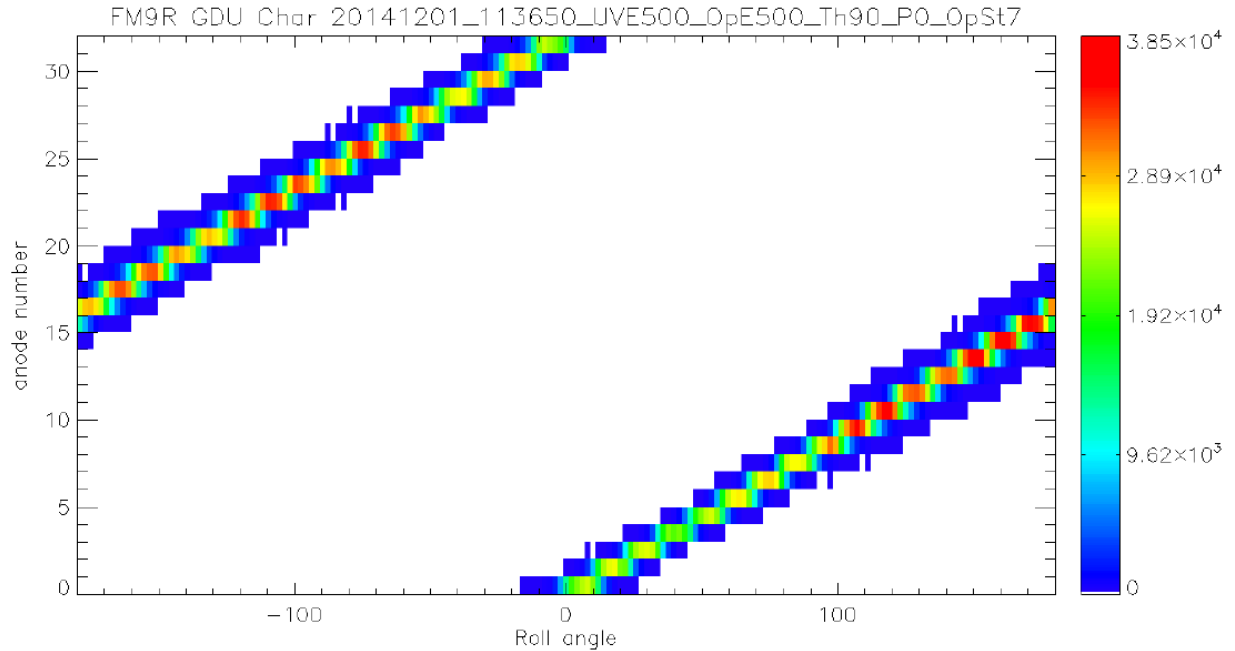


**Figure 10-7 EDI GDU Detector Characterization Test Setup**

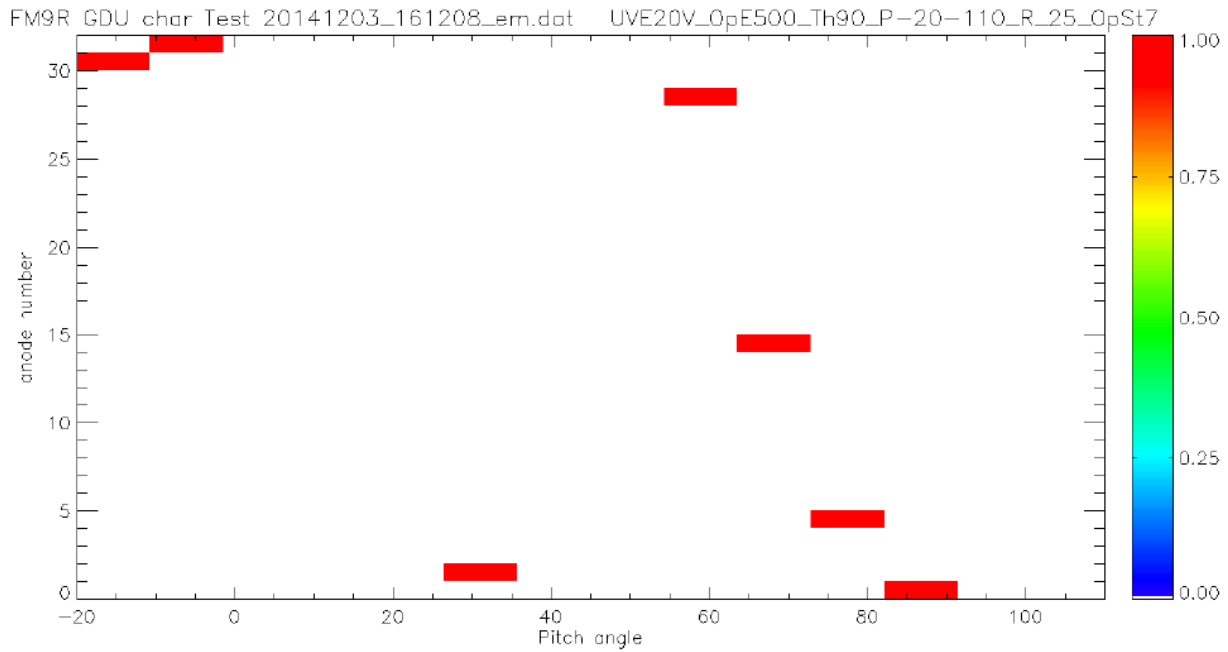
The characterization performed consisted of roll tests around the symmetry axis for selected combinations of optics look-angles and associated pitch angles. These tests demonstrated the desired degree of uniformity of the integrated detector system and established the dependency of the effective beam area on polar angle for monodirectional and monoenergetic beams. Another set of tests was run to demonstrate and characterize the polar acceptance. In these tests the GDU was pitched for a number of look directions, from 0 to 110 degrees at fixed roll angle and fixed optics look direction (that is, fixed optics electrode voltages). In addition to these tests, adequate rejection of UV light was demonstrated. All tests were performed at 500 eV and 1 keV beam energy and included variations of the beam energy by 10% relative to the energy setting of the detector.

Figure 10-8 illustrates the result of a roll test at 500eV energy for pitch angle zero and a optics look direction of 90 degrees. This combination of instrument pitch angle and optics look angle results in the beam entering the optics along the center of polar acceptance window for the configured look direction. The beam is focused onto a narrow azimuthal range and the variation in count rates for roll angles that map the peak response to a single anode is well below the desired goal of 50%.

Figure 10-9 shows the result of a UV sensitivity test that demonstrates excellent UV rejection. The optics energy was 500 eV and the look angle was 90 degrees. At most one count was seen in any pitch angle / sensor anode bin within in the accumulation time window of 125 ms.



**Figure 10-8 GDU SN9 Roll Test at 500 eV for Pitch Angle 0 (GDU Symmetry Axis Vertically, Perpendicular to the Beam) and Optics Look Direction 90 Degrees**



**Figure 10-9 GDU SN9 UV Sensitivity Test at 500 eV [Counts per 125 ms as a function of pitch angle and anode number for a fixed roll angle of 25 degrees and an optics look direction of 90 degrees]**

## 10.3.2 In-Flight Calibration

### 10.3.2.1 Electric Field Mode

For Electric Field Mode the crucial calibration is that of beam firing direction vs deflection voltages, as it impacts both the ability to fire the beam accurately in the plane perpendicular to B and the ability to perform triangulation in the ground analysis. On the engineering model GDU it was demonstrated that the calibration remains valid after subjection the gun to a vibration test. In-orbit calibration of the gun was therefore not needed. The rate of return beams seen by each GDU during the commissioning phase was considered adequate to perform successful ground analysis. Also, in-orbit calibration would have required excessive amounts of run time in a diagnostic version of electric field mode where small voltage offsets are added on top of the calibrated values to determine if this results in a better rate of beam return detections. As several of the EDI high voltage opto-couplers were known to be limiting the useful life of the instrument it was decided not to pursue this diagnostic mode.

### 10.3.2.2 Ambient Electron Mode

Ambient Mode calibration consists of three steps: flat-fielding the detector response, relative adjustment between the two GDUs on each observatory and conversion to fluxes.

For the purpose of determining the instrument correction function that flat-fields the detectors' response as a function of look direction, a special diagnostic "Detector Characterization" has been run at the beginning of the outbound operations (4Re) every other orbit between September 2016 and April 2017, and then once every 7 orbits until November 2020. Each detector characterization steps the optics look direction from 0 (along the symmetry axis) to 101 degrees. Near the pole more fine grained stepping is used as the instrument's response function exhibits a higher change per degree in that region. For each look direction setting a special Sensor test mode is run. This mode samples counts from all 32 anodes in eight steps of four contiguous and simultaneously sampled anodes and sends the counts down in a special telemetry packet. The sampling time is set slightly below 125 ms so that a complete sampling of all 32 anodes is completed in slightly under one second. The mode is run repeatedly for each optics look angle setting. The total duration of one complete detector characterization is approximately 12 minutes. In the analysis the obtained data are filtered to eliminate effects of natural time variation and pitch angle dependency of fluxes. The result of a detector characterization is a map of anode-to-anode variations in count rates that are due to the instrument's response. Results from several detector characterizations have been combined to get a good average and remove uncertainties from residuals in undesired effects (e.g. pitch angle dependency of fluxes). Figure 10-10 shows the derived azimuthal correction factors for GDU1 (SN 3) on MMS1 from the seven executions of the detector characterization that have been merged to arrive at a single averaged azimuthal correction map.

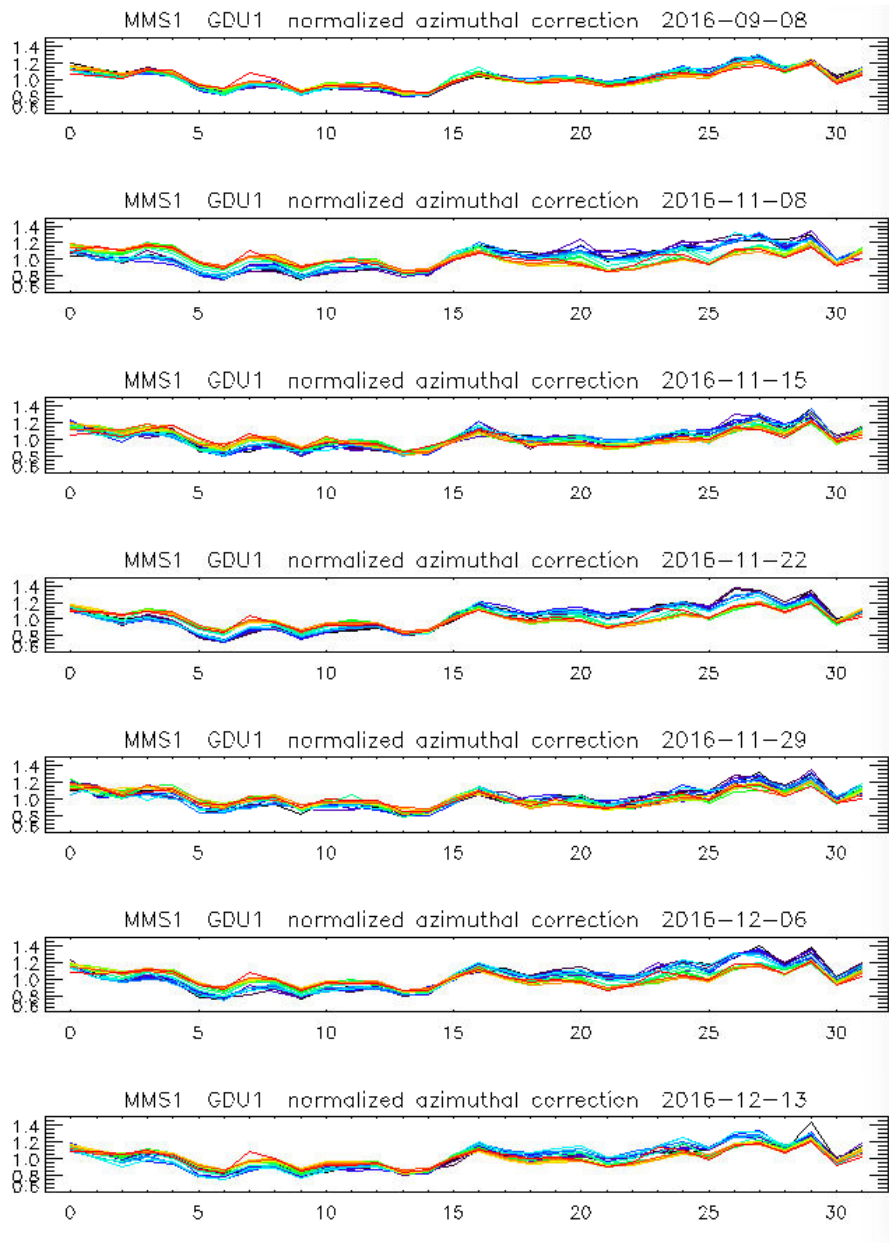


**Figure 10-10 Azimuthal Correction Factors for MMS1 GDU1 (SN3) for the Seven Detector Characterizations that were Used to Arrive at an Average Azimuthal Correction Map [The colors in each panel separate data from different optics looks angles]**

The second part of the flat-fielding concerns the polar correction (dependency on optics look direction). This correction has been initially derived from short time intervals of Ambient Mode data during the commissioning phase. Improvements to the map have been made by using the data from the above detector characterizations as well as comparisons with L2 DES fluxes. Figure 10-11 shows the resulting polar flat-fielding function which is generic and is applied to all GDUs.

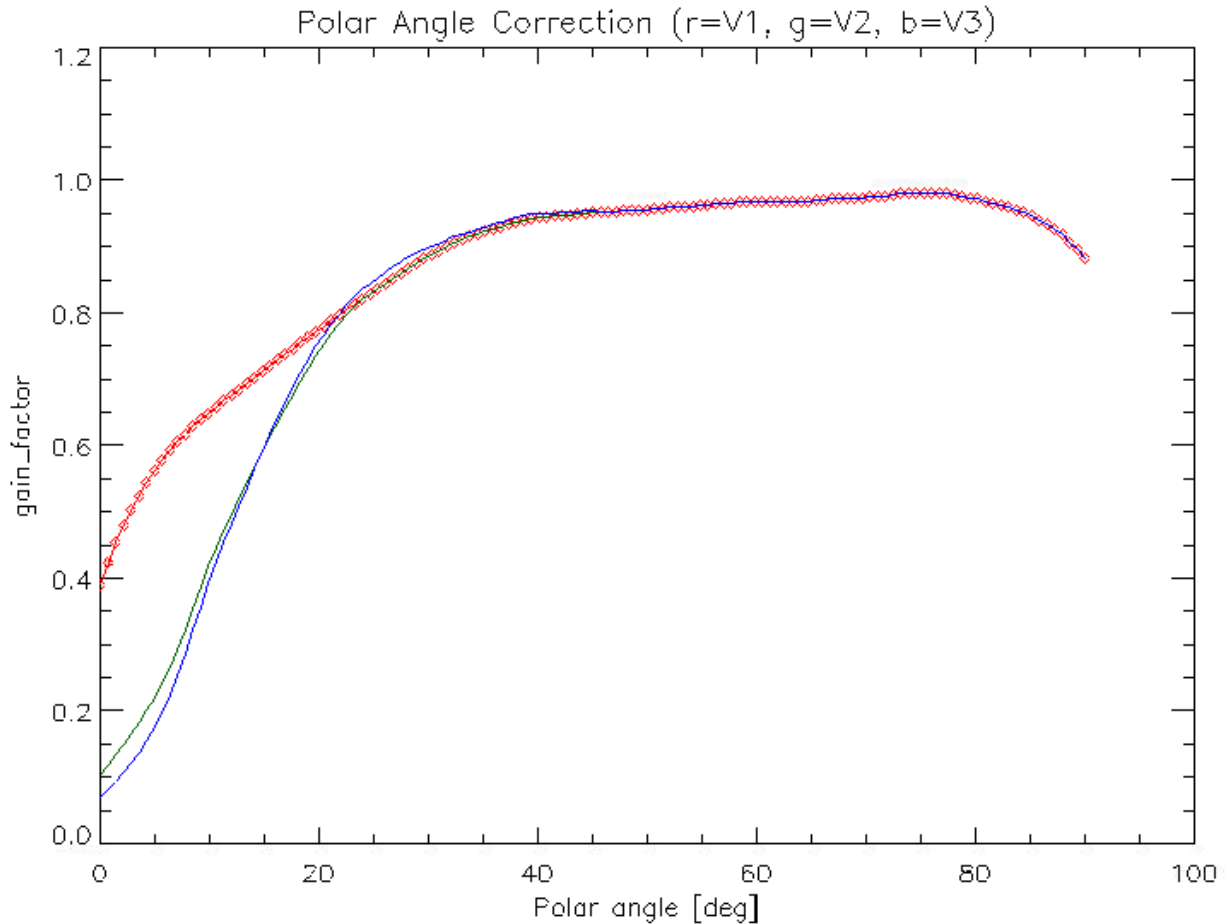


**Figure 10-11 Polar Correction for EDI Ambient Mode Data [The red trace shows the original version (V1) derived from EDI burst data during a quiet interval during the commissioning phase. The green trace is the improved correction derived from in-flight detector characterization data. The blue trace (V3) is a slight correction for small polar angle values derived by comparing EDI data with L2 DES fluxes]**

Relative counts levels of the two GDUs are determined from daily Ambient Mode data separately for field-aligned and perpendicular samples and by removing data from times of high variability of the count rates.

The absolute calibration factors for the conversion to fluxes are determined from comparison with FPI DES L2 data.

### 10.3.3 Validation

EDI Electric field data are validated by their usage in the cross-calibration of the EDP electric field data. They serve as a baseline to establish and remove offsets in the EDP data.

EDI Ambient Mode data are validated by their cross-calibration with DES fluxes using DES energy bins closest to the EDI Detector energy setting.

## 10.4 EDI ELECTRIC FIELD MEASUREMENT ALGORITHM DESCRIPTIONS

### 10.4.1 Theoretical Basis

The basic concept of determining the displacement (“drift step”) of a test beam of electrons after one or more gyrations in the ambient magnetic field from triangulation of firing directions and from time-of-flight differences is described in section 3 of

Torbert, R.B., et al, **The Electron Drift Instrument for MMS**, Space Sci Rev 199, 283–305 (2016). <https://doi.org/10.1007/s11214-015-0182-7>

To find the beam directions that will hit the detector, EDI sweeps each beam in the plane perpendicular to B at a fixed angular rate of 0.22°/ms until a signal has been acquired by the detector. Once signal has been acquired, the beams are swept back and forth to stay on target. Beam detection is not determined from the changes in the count-rates directly, but from the square of the beam counts divided by the background counts from ambient electrons, i.e., from the square of the instantaneous signal-to-noise-ratio, SNR<sup>2</sup>. This quantity is computed from data provided by the correlator in the Gun-Detector Electronics that also generates the coding pattern imposed on the outgoing beams. If the squared signal-to-noise ratio exceeds a threshold, this is taken as evidence that the beam is returning to the detector. The thresholds for SNR<sup>2</sup> are chosen dependent on background fluxes. They represent a compromise between getting false hits (induced by strong variations in background electron fluxes) and missing true beam hits. The basic software loop that controls EDI operations is executed every 2 ms. As the times when the beams hit their detectors are neither synchronized with the telemetry nor equidistant, EDI data have no fixed time-resolution. Data are reported in telemetry slots. In Survey, using the standard packing mode 0, there are eight telemetry slots per second and GDU. The last beam detected during the previous slot will be reported in the current slot. If no beam has been detected the data quality will be set to zero. In Burst telemetry there are 128 slots per second and GDU. The data in each slot consists of information regarding the beam firing directions (stored in the form of analytic gun deflection voltages), times-of-flight (if successfully measured), quality indicators, time stamps of the beam hits, and some auxiliary correlator-related information.

### 10.4.2 Error Analysis and Known Features in the Dataset

Triangulation errors are determined from the radial and azimuthal extent of the 95% confidence level iso-contour of the 2-dimensional cost function, and are propagated from the 2-dimensional drift step in the gyro-plane to the 3-dimensional drift velocity and electric field vectors in the target coordinate systems.

Time-of-flight method errors on the drift step magnitude are computed using the student’s t-test which measures the significance of a difference of means. The errors are reported at the 95% confidence level. The azimuthal error is determined from the spread of the firing directions. Propagation of the errors to the 3-dimensional drift velocity and electric field vectors is done in the same way as for the triangulation analysis.

### 10.4.3 EDI Quality Flags

There are no quality flags in the L2 E-Field data products. For data derived from triangulation analysis the reduced  $\chi^2$  value is available in the L2 data set in case filtering of the data is desired.

## 10.5 EDI AMBIENT ELECTRON MEASUREMENT ALGORITHM DESCRIPTIONS

### 10.5.1 Theoretical Basis

EDI Ambient Electron Mode has the capability to sample at either 90 degrees pitch angle or at 0/180 degrees (field aligned), or to alternate between 90 degrees and field aligned with selectable dwell times. The choices for energy are 250eV, 500eV and 1keV. The two EDI Gun-Detector Units are mounted on opposite sides of the spacecraft and their detectors are facing opposite hemispheres. At any given time their look directions are set to look strictly into opposite directions. So, when sampling field aligned data, while one detector is looking along **B** the other is looking anti-parallel to **B** (corresponding to pitch angles of 180 and 0 degrees, respectively). The detectors switch roles approximately every half spin of the spacecraft as the tip of the magnetic field vector spins outside the field of view of one detector and into the field of view of the other detector.

The look direction of the detector is defined by a polar angle with respect to the symmetry axis of the detector, and an azimuth angle. The polar angle is set by applying the correct voltages to the electrodes in the upper section of the EDI optics. The azimuth angle impacts the selection of four contiguous (out of 32) anodes of the sensor. There is a variety of configuration options regarding the detailed anode selection with regard to the nominal pitch angle. To make the choice apparent to the L2 end user in an easy way, the chosen option together with the sampled pitch angles impacts the name of the L2 data product. This is outlined in detail in the following subsections.

#### 10.5.1.1 Ambient Mode Raw Telemetry

##### 10.5.1.1.1 Survey Telemetry

Survey telemetry reports a single channel per GDU. Sampled data are from non-contiguous time intervals. There are 32 samples per second, so samples are spaced by 31.25 ms. Each sample is accumulated over half of the sample spacing, or 15.625 ms. The associated time tags identify the center of each sampling interval.

The single channel per GDU can be either a combination (sum) of two adjacent anodes, or a data from one anode. This is controlled independently for field aligned and perpendicular sampling. The details are given in a table further below.

Look directions are reported at the same rate as the count rate channels. The azimuth angle reported in L1A telemetry (`mmsX_edi_amb_phi`) can be turned into the respective anode numbers for GDU1 and GDU2 for the purpose of applying a relative calibration, as outlined in a table further below. Note, however, that as a function of spacecraft rotation and magnetic field orientation, the anode used for the sampling may have actually changed during the sampling interval.

##### 10.5.1.1.2 Burst Telemetry

Burst telemetry reports four channels (numbered 1 through 4) per GDU from four contiguous anodes with one ms time resolution (1024 samples per second), using continuous sampling. The counts in the reported channels are compressed in the L0 data, using a lossy compression (errors in the reconstruction of the uncompressed counts are below one sigma). The L1A data stores the de-compressed counts data.

Look directions are reported at one eighth of the count channels rate (one set of look directions every 7.8125 ms). For the determination of anode numbers the azimuth of the look direction (`mmsX_edi_amb_phi`) must be expanded to match the time resolution of the counts channels. A cross-



reference between reported azimuth and the anode number for each counts channel as a function of the mode configuration is given in a table further below.

#### 10.5.1.1.3 Flip Flags

The flight software maintains the detector look directions in its basic processing cycle every 2ms such that the polar angle of the optics and the sensor anode numbers best match the selected pitch angles in accordance with the mode configuration options. Owing to spacecraft rotation and directional magnetic field variation, the direction to be maintained can slide out of the field of view of the detector. This happens typically every half spin, and the two detectors swap their roles. As this occurs when the polar angle reaches 90 degrees (“horizon”), this kind of swap impacts only the azimuth angle (and thus the sensor anode selection), while the polar angle remains close to 90 degrees for each detector.

When Ambient Mode is configured to alternate between field aligned and perpendicular sampling, there is, in addition, a rapid switch of look directions each time the dwell time for the current pitch angle expires. This change in look direction impacts the polar angle and thus causes a slew of high voltages on some of the electrodes in the upper section of the optics. The response time of the HV amplifiers is of the order of 2 ms. Each time this kind of switch takes place, there is therefore a transitional period during which the sampled counts represent neither perpendicular nor field aligned data.

Both the horizon flips and the field aligned/perpendicular flips are indicated via flip flags (L1A variable `mmsX_edi_flip`) in L1A telemetry. The flip flags should be used to eliminate transitional burst data in alternating mode. Details are given further below.

The dwell times in alternating modes are restricted to values that ensure that the look direction switches between field aligned and perpendicular sampling fall into the non-data taking periods of the non-contiguous sampling of the survey data.

#### 10.5.1.1.4 Anode Selection / Placemat

Two options exist for the selection of sensor anodes. They are referred to as *centered* and *one-sided* placement. These options can be selected separately for field aligned and perpendicular data. In the case of centered placement, the number of the four contiguous anodes are chosen such that their combined center (the gap between the inner two anodes) is the best match for the current pitch angle. In the case of one-sided placement, the anode numbers are chosen such that the center of the lowest numbered of the four anodes is the best match for the current pitch angle.

For one-sided perpendicular sampling there is an additional option that impacts only the burst telemetry channels 2, 3, and 4:

- either place the other three anodes (burst channels 2,3,4) such that they sample towards lower pitch angles in both GDUs
- or let the anodes in GDU1 sample towards lower pitch angles (90° and lower) and the anodes in GDU2 sample towards higher pitch angles (90° and higher)

#### 10.5.1.2 L1A Variable Relation to L2 Data Product Names

This section describes the L1A variables that impact the L2 data product names.

**`mmsX_edi_amb_pitchmode`** -- This L1A variable indicates which pitch angles have been sampled.

- 0: Field aligned sampling only (pitch angles 0°/180°)
- 1 or 3: Alternating between field aligned (pitch angles 0°/180°) and perpendicular (pitch angle 90°) sampling. In this case the L1A variable “mmsN\_edi\_amb\_dwell” indicates the amount of time spent sampling data in between switches between field aligned and perpendicular directions. The number is given in units of 1/512 seconds.
- 2: Perpendicular sampling only (pitch angle 90° only)

**mmsX\_edi\_amb\_pacmo** -- This L1A variable impacts, for field aligned sampling:

- the anode selection (centered vs one-sided)
- the number of anodes that are summed in the channel reported in survey telemetry:
  - two anodes for centered
  - one anode in the case of one-sided anode placement

**mmsX\_edi\_amb\_perp\_onesided** -- This L1A variable impacts, for perpendicular sampling:

- the anode selection (centered vs one-sided)
- the number of anodes that are summed in the channel reported in survey telemetry:
  - two anodes for centered
  - one anode in the case of one-sided anode placement

**mmsX\_edi\_amb\_perp\_bidirectional** -- This L1A variable impacts only burst data for perpendicular sampling. It indicates whether both GDUs sample pitch angle 90° and lower (“mono-directional”), or whether GDU1 and GDU2, respectively, sample pitch angle 90° and lower / higher (“bidirectional”).

Table 10-4 summarizes how the discussed L1A variables are related to the L2 data product names.

L2 Data Product Name	L1A Variable mmsX_edi_amb_...				Sampled Pitch Angles
	...pitchmode	...pacmo	...perp_onesided	...perp_bidirectional	
amb	0	1	N/A	N/A	0 / 180
amb-pm2	0	2	N/A	N/A	0 / 180
amb-alt-oc	1 o 3	2	0	N/A	0 / 180 and 90
amb-alt-cc	1 or 3	1	0	N/A	0 / 180 and 90
amb-alt-oom	1 or 3	2	1	0	0 / 180 and 90
amb-alt-oob	1 or 3	2	1	1	0 / 180 and 90
amb-perp-ob	2	2	1	1	90

**Table 10-4 EDI Ambient Mode L2 Data Product Names**

Table 10-5 below summarizes the anode placement and pitch angle 90° sampling direction for each L2 data product.

L2 Data Product Name	Anode Placement for PA 0°/180°	Anode Placement for PA 90°	Pitch angle 90° sampling direction
----------------------	--------------------------------	----------------------------	------------------------------------

amb	centered	N/A	N/A
amb-pm2	one-sided	N/A	N/A
amb-alt-oc	one-sided	centered	N/A
amb-alt-cc	centered	centered	N/A
amb-alt-oom	one-sided	one-sided	mono-directional
amb-alt-oob	one-sided	one-sided	bi-directional
amb-perp-ob	N/A	one-sided	bi-directional

**Table 10-5 Sensor Anode Placement for EDI L2 Ambient Mode Data Products**

### 10.5.1.3 Anode Placement Details

For the purpose of identifying the anodes used for each survey and burst data channel, it is best to turn the L1A azimuth angle  $mmsX\_edi\_amb\_phi$  into a reference anode number  $N$  that serves as a basis for identifying the per-channel anode numbers dependent on the mode configuration details:

$$N = \text{round}(mmsX\_edi\_amb\_phi / 11.25)$$

The table below shows how the per-channel anode numbers can be derived from the reference anode number  $N$  for each L2 data product. The per-channel anode numbers can be used as indices into the 2D relative calibration tables for each GDU.

L2 Data Product	Pitch Angle	Anode Placement	Survey		Burst								
			GDU1	GDU2	GDU1				GDU2				
					ch1	ch2	ch3	ch4	ch1	ch2	ch3	ch4	
amb	0/180												
amb-alt-cc	0/180/90	centered	$N - 1, N$	$15 - N, 16 - N$	$N - 2$	$N - 1$	$N$	$N + 1$	$14 - N$	$15 - N$	$16 - N$	$17 - N$	
amb-alt-oc	90												
amb-pm2	0/180												
amb-alt-oc	0/180	one-sided	$N$	$15 - N$	$N$	$N + 1$	$N + 2$	$N + 3$	$15 - N$	$16 - N$	$17 - N$	$18 - N$	
amb-alt-oom	0/180/90												
amb-alt-oob	0/180/90	one-sided	$N$	$15 - N$	$N$	$N + 1$	$N + 2$	$N + 3$	$15 - N$	$14 - N$	$13 - N$	$12 - N$	
amb-perp-ob	90	one-sided	$N$	$15 - N$	$N$	$N + 1$	$N + 2$	$N + 3$	$15 - N$	$14 - N$	$13 - N$	$12 - N$	

**Table 10-6 Sensor Anode Numbers per Channel for Each EDI L2 Ambient Mode Data Product**

### 10.5.1.4 Calculation of Azimuth Angles for Data Channels

For the calculation of particle trajectories in the L2 data, the per-channel anode numbers from the above table need to be turned into azimuth angles. Table 10-7 provides the necessary formulas. Note that GDU2 angles are given in GDU2 coordinates.

$N$  = reference anode number, derived from L1A telemetry variable  $mmsX\_edi\_amb\_phi$   
 $A$  = per-channel anode number, as given in Table 10-7

Telemetry	Anode Placement	GDU1	GDU2
Burst	any	$\phi = (A + 0.5) * 11.25^\circ$	$\phi = (A + 0.5) * 11.25^\circ$

Survey	centered	$\phi = N * 11.25^\circ$	$\phi = (16 - N) * 11.25^\circ$
Survey	one-sided	$\phi = (N + 0.5) * 11.25^\circ$	$\phi = (15.5 - N) * 11.25^\circ$

**Table 10-7 Relation of Sensor Anode Numbers to Azimuth Angles of EDI Detector Look Direction**

### 10.5.1.5 Flip Flag Summary

Table 10-8 summarizes how flip flags are handled, depending on L2 data product and telemetry.

L2 Data Product Name	Survey	Burst
amb	ignored	ignored
amb-pm2	ignored	ignored
amb-alt-oc	ignored	insert fill data for the pair of flagged data points (fluxes) and the data point immediately following
amb-alt-cc	ignored	insert fill data for the pair of flagged data points (fluxes) and the data point immediately following
amb-alt-oom	ignored	insert fill data for the pair of flagged data points (fluxes) and the data point immediately following
amb-alt-oob	ignored	insert fill data for the pair of flagged data points (fluxes) and the data point immediately following
amb-perp-ob	ignored	ignore

**Table 10-8 EDI Ambient Mode Flip Flag Handling**

## 10.5.2 Error Analysis and Known features in the Dataset

The error analysis of the EDI ambient electron data takes into account the statistical variation of the raw counts, properly propagated through the sensor deadtime correction as well as uncertainties from the three calibration steps.

### 10.5.2.1 Dead Time Correction

The dead time correction is given by

$$C = R \cdot t_A / (t_A - R \cdot t_D)$$

with the following abbreviations:

$C$	dead time corrected counts
$R$	raw counts
$t_A$	the accumulation time (1/1024 sec for burst, 1/64 sec for survey)
$t_D$	the sensor dead time (200ns)

The error propagation from raw to dead time corrected counts is

$$err_C = err_R \cdot [t_A / (t_A - R \cdot t_D)]^2$$

where the one-sigma error  $\sqrt{R}$  is used for  $err_R$ .

### 10.5.2.2 Calculation of Ambient Electron Flux Errors

The calculation of absolute fluxes is given by the formula

$$F = C \cdot R \cdot A$$

where

- $F$  is the absolute flux
- $C$  is the dead time corrected counts
- $R$  is the relative calibration (a function of detector look angles)
- $A$  is the absolute calibration factor

The error in the absolute flux is calculated according to

$$err_F = F \cdot \text{SQRT} [ (err_C / C)^2 + (err_R / R)^2 + (err_A / A)^2 ]$$

The error  $err_C$  for the dead time corrected counts is given in section 3.4.1. The second term  $err_R/R$  is ignored at the moment, as the information on the relative calibration is still being improved, especially for small polar look angles where the relative calibration  $R$  factor is largest. For the third term  $err_A/A$ , we assume a factor of 0.2 (20% error), based on the general level of agreement in comparisons between DES burst Quicklook data and EDI ambient burst data.

### 10.5.3 EDI Quality Flags

Currently there are no quality flags in the L2 Ambient Electron data sets. It is planned to add a flip flag that indicates times during which the detectors were in a transitional state due to rapid changes of look directions.

## 10.6 EDI DATA PRODUCTION ALGORITHM DESCRIPTIONS

The following Level 2 EDI data products are being generated.

**Electric Field Data** -- This is the primary data product generated from data collected in electric field mode. The science data generated are drift velocity and electric field data in various coordinate systems. They are derived from triangulation and/or time-of-flight analysis. Where both methods are applicable, their results will be combined using a weighting approach based on their relative errors.

**Quality-Zero Data** -- These data are a by-product generated from data collected in electric field mode. Whenever no return beam is found in a particular time slot by the flight software, the data to be reported will be flagged with the lowest quality level (quality zero). The ground processing generates a separate data product from these counts data.

**Ambient Electron Data** -- The raw counts data collected in ambient mode are going through a three step calibration for conversion to fluxes. The first step performs a dead time correction of the raw counts and applies a flat-fielding calibration that removes the instrument response dependency on look direction (optics polar angle and sensor anode pad number). The second step brings the flat-fielded counts from the GDUs to the same level. The third step is a multiplication with a factor to convert from relative, dead time corrected counts to fluxes.

### 10.6.1 E-Field Data Processing

Generation of L2 Electric Field Mode data is a three step process as illustrated in Figure 10-12. In the first step L1A files are generated from L0 raw telemetry. Aside from extraction of data this involves a conversion of the analytic voltages that represent the gun firing direction in the L0 data to the azimuth and polar angles of a spherical coordinate system that has its Z axis along the GDU symmetry axis pointing outward in the spacecraft spin plane and the X axis along the negative spacecraft body Z axis. In addition, since the return beam hits are asynchronous in nature to any onboard clock, separate time tags in TT2000 format are calculated for every individual beam based on the timing information in the L0 files. Raw times-of-flight in digital units are converted to micro-seconds.

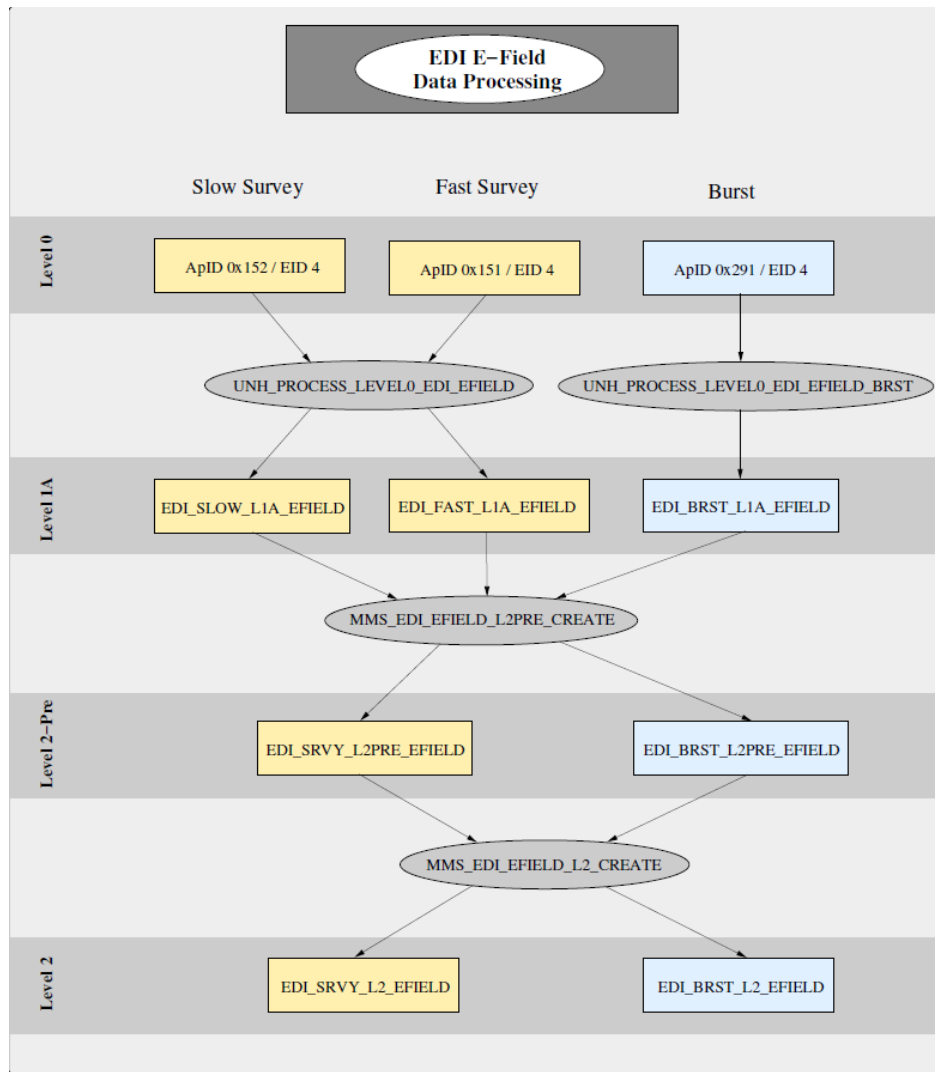


**Figure 10-12 EDI Electric Field Mode Data Processing Flow**

In the second step the L1A data are processed to level L2-Pre. Data are preselected by quality and are sent through a process that attempts to determine the number of gyrations for each beam based on its time-of-flight and the gyro time derived from DFG L2Pre magnetic field data. The resulting data set is analyzed with both the triangulation and time of flight method as outlined further below. For the purpose of the analysis the data are grouped into five-second time intervals. For each analysis interval an average magnetic field vector is calculated for the definition of a gyro plane, that is, the plane perpendicular to the

magnetic field. Beam firing directions are then represented as clock angles in that plane with respect to a reference direction which is chosen to be closest to the line towards the sun.

#### 10.6.1.1 Triangulation Analysis

The triangulation analysis procedure determines the drift step by searching for the target-point that minimizes an appropriate ‘cost-function’. The cost-function is constructed, for each grid-point in the plane, by adding up the (squared) angle-deviations of all beams in a chosen time interval from the direction to that grid-point. Each beam contribution to the cost-function is normalized by the (squared) error in the firing directions, which is a function of beam pointing direction and varies between  $1^\circ$  and  $4^\circ$ , using an analytic model for the beam profile as a function of the polar angle of the gun firing direction. The grid-point with the smallest value of the cost-function is taken as the target. If a beam has been identified as a multi-runner of order  $N$  by the preceding runner order analysis, it is associated with a grid-point at  $N$  times the radial distance. When identification of the order from the runner order analysis is ambiguous, the respective beams are treated as single-runners. This assumption works well in most cases, as, compared the EDI implementation on ESA’s Cluster project, the design of the correlator and the choice of code frequencies makes the occurrence of multi-runners much less likely. To speed up the search, the procedure uses a coarse grid to identify a restricted range in which the final search is performed with a much finer grid. The electron trajectories are approximated by circles whose radius is based on the magnetic field strength.

The analysis fails if the drift step and/or the magnetic field significantly vary within the chosen time interval (5 seconds). Such cases can be identified by the variance in the magnetic field, by the quality of the fit (as measured by its reduced  $\chi^2$ ), and by the errors in the computed drift step.

Using the DFG L2pre magnetic field data, the drift steps can be converted to drift velocities and electric field data.

Errors are determined from the radial and azimuthal extent of the 95% confidence level iso-contour of the 2-dimensional cost function and are propagated from the 2-dimensional drift step in the gyro-plane to the 3-dimensional drift velocity and electric field vectors in the target coordinate systems.

In addition to the drift step, drift velocity and electric field vectors and their respective errors, various processing parameters such as the number of beams involved in the analysis and the reduced  $\chi^2$  are stored in the resulting L2pre data files for the purpose of reducing the L2pre data set to L2 data as described in section 3.2.3.

#### 10.6.1.2 Time-of-Flight Analysis

Deduction of the drift step (and the drift velocity) from analysis of the difference in the times-of-flight of the two beams is, in principle, straightforward. If the drift step is large enough such that the firing directions become nearly parallel, the beams in the analysis interval can be grouped into two nearly oppositely directed sets. The set with the larger times-of-flight then must contain the beams directed towards the target, the other set those directed away from the target. This assignment settles the drift direction, and the drift magnitude is then computed from the magnitude of the difference in the times-of-flight.

This simple scheme would require stable conditions (i.e., non-varying gyro time and times-of-flight) over the analysis interval. Since this is not always the case, especially in the magnetosheath, the analysis makes use of the gyro time determined from the DFG L2pre data and interpolated to the times of the EDI

beam hits. The differences between the measured times-of-flight and the interpolated gyro times are calculated separately for the two sets of beams. For each set the average difference from the gyro time is calculated and the two averages are then combined. This way any fixed magnitude offset in the gyro-time that might result from a residual error in the magnetic field calibration will cancel out. The set with the larger average identifies the direction towards the target. Multiplication of half the time-of-flight difference (the combination of the two averages as described above) with the electron velocity yields the drift step magnitude.

Calculation of drift velocities and electric fields is done in the same fashion as for the triangulation analysis.

The error on the drift step magnitude is computed using the student's t-test which measures the significance of a difference of means. The error is reported at the 95% confidence level. The azimuthal error is determined from the spread of the firing directions. Propagation of the errors to the 3-dimensional drift velocity and electric field vectors is done in the same way as for the triangulation analysis.

### 10.6.1.3 Filtering of L2 Pre Data

In the final step the L2Pre data are filtered using various quantities stored in the L2pre files. For triangulation, the filter criteria are:

- (1) Reduced  $\chi^2$  below 10000
- (2) At least three beams in the analysis interval
- (3) Beam spread is greater than 15 degrees
- (4) Drift step magnitude is less than 3 times the triangulation baseline
- (5) Product of triangulation baseline [m], number of beams and B magnitude [nT] is greater than 5000
- (6) Electric Field error is less than 1 mV/m
- (7) Electric Field error is larger than 0.1 mV/m
- (8) The relative error of the electric field magnitude less than 1 (100%)

Filter (5) was not present originally. It was added in October 2016 to remove bad data in variable fields.

For the time-of-flight analysis the filter criteria are:

- (1) Drift step magnitude greater than 1 meter
- (2) Electric field error less than 1 mV/m
- (3) Relative error of electric field magnitude less than 1 (100%)

### 10.6.1.4 File Structure L2 EFIELD Data

For the L2 electric field data product, survey and burst files contain the same quantities with only the telemetry identifier (<tlm>) being different (<tlm> = srvy or <tlm> = brst).

Filenames:

mms<N>\_edi\_srvy\_l2\_efield\_<yyyymmdd>\_v<x.y.z>.cdf  
mms<N>\_edi\_brst\_l2\_efield\_<yyyymmddhhmmss>\_v<x.y.z>.cdf

**Important note:** The drift velocities and electric field quantities in the L2 EDI electric field data files are not corrected for spacecraft velocities. They are given in the moving spacecraft frame of reference. That is, “gse” and “gsm” in the variable names refer only to coordinate systems, not frames of reference.



Name	Description	Type	Units
mms<N>_edi_vdrift_dsl_<tlm>_l2	Drift velocity vector in DSL coordinates	FLOAT	km/s
mms<N>_edi_vdrift_gse_<tlm>_l2	Drift velocity vector in GSE coordinates	FLOAT	km/s
mms<N>_edi_vdrift_gsm_<tlm>_l2	Drift velocity vector in GSM coordinates	FLOAT	km/s
mms<N>_edi_e_dsl_<tlm>_l2	Electric field vector in DSL coordinates	FLOAT	mV/m
mms<N>_edi_e_gse_<tlm>_l2	Electric field vector in GSE coordinates	FLOAT	mV/m
mms<N>_edi_e_gsm_<tlm>_l2	Electric field vector in GSM coordinates	FLOAT	mV/m
mms<N>_edi_tri_weight_<tlm>_l2	Weight of triangulation method when merging results from triangulation and time-of-flight analyses	INT2	percent
<b>Support Data</b>			
Epoch	Time tags	TT2000	ns
mms<N>_edi_t_delta_minus_<tlm>_l2	Time between start of analysis interval and time tag	FLOAT	ns
mms<N>_edi_t_delta_plus_<tlm>_l2	Time between time tag and end of analysis interval	FLOAT	ns
mms<N>_edi_tri_rchisq_<tlm>_l2	Reduced Chi-Squared from triangulation analysis	FLOAT	none
mms<N>_edi_v_dsl_delta_minus_<tlm>_l2	Drift velocity negative error	FLOAT	km/s
mms<N>_edi_v_dsl_delta_plus_<tlm>_l2	Drift velocity positive error	FLOAT	km/s
mms<N>_edi_v_gse_delta_minus_<tlm>_l2	Drift velocity negative error	FLOAT	km/s
mms<N>_edi_v_gse_delta_plus_<tlm>_l2	Drift velocity positive error	FLOAT	km/s
mms<N>_edi_v_gsm_delta_minus_<tlm>_l2	Drift velocity negative error	FLOAT	km/s
mms<N>_edi_v_gsm_delta_plus_<tlm>_l2	Drift velocity positive error	FLOAT	km/s
mms<N>_edi_e_dsl_delta_minus_<tlm>_l2	E-field negative error	FLOAT	mV/m
mms<N>_edi_e_dsl_delta_plus_<tlm>_l2	E-field positive error	FLOAT	mV/m
mms<N>_edi_e_gse_delta_minus_<tlm>_l2	E-field negative error	FLOAT	mV/m
mms<N>_edi_e_gse_delta_plus_<tlm>_l2	E-field positive error	FLOAT	mV/m
mms<N>_edi_e_gsm_delta_minus_<tlm>_l2	E-field negative error	FLOAT	mV/m
mms<N>_edi_e_gsm_delta_plus_<tlm>_l2	E-field positive error	FLOAT	mV/m

**Table 10-9 L2 E-FIELD Data**

### 10.6.2 Quality-Zero Data

The lowest quality level in the raw (and in the L1A) electric field data (quality zero) signals that no return beam was detected during a given time slot. Counts accumulated in these time slot are considered a proxy for the ambient electron flux at the energy of the detector. In regions with high variability of the magnetic/electric fields, very low magnetic fields, or high ambient electron fluxes at the energy of the detector, EDI will have difficulty identifying the return beams (if there are any). Consequently, in those regions there will be a higher rate of quality-zero data. Care must be taken in general when interpreting these data. First, they are uncalibrated raw counts. Second, even though they did not pass the detection

threshold for the squared signal-to-noise ratio, some of the counts samples can represent a mix of beam and background electrons. The data can be useful as boundary markers, or for detecting anisotropies in the 90 degree pitch angle data.

The processing extracts the counts data (one ms accumulation time base) and the gun firing directions. From the latter the associated detector look directions are deduced and the particle motion directions are calculated. Particle motion directions are specified in the form of azimuth and polar angle in the respective coordinate system (GSE, GSM) using the following convention:

- Polar angle =  $\text{acos}( z / \text{magnitude} )$
- Azimuth angle =  $\text{atan}( y / x )$

Since the counts are unmodified raw counts, no error is specified as it is straightforward for the user to calculate the one-sigma error (square root of the counts). The uncertainty in the particle motion direction is given as a single constant angular error number that is derived from the characteristic FWHM of the optics' polar acceptance and the half width of the sensor's azimuthal field of view.

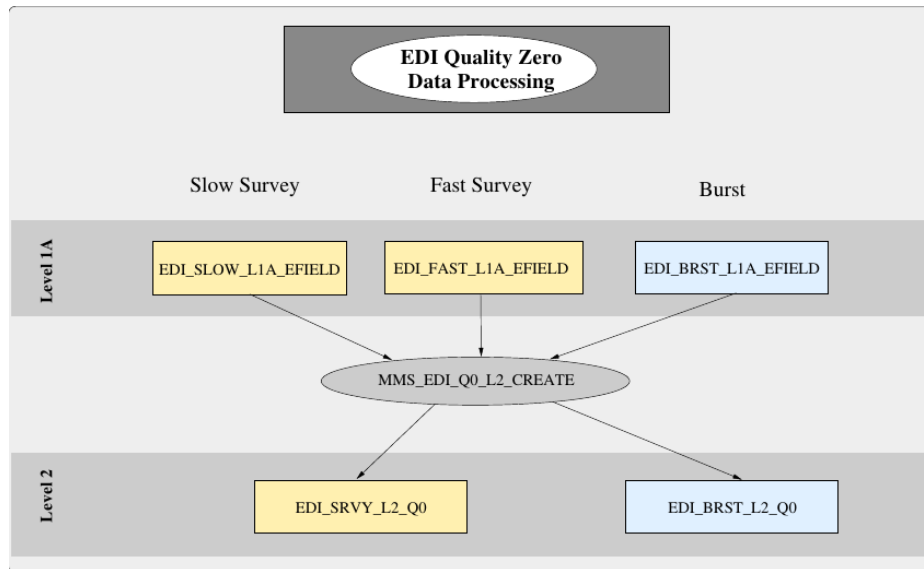


Figure 10-13 EDI Quality-Zero Data Processing

### 10.6.2.1 File Structure L2 Quality-Zero Data

For the L2 quality zero data product, survey and burst files contain the same quantities with only the telemetry identifier being different (<tlm> = srvy or <tlm> = brst)

File Names:

mms<N>\_edi\_srvy\_q0\_l2\_<yyyymmdd>\_v<x.y.z>.cdf  
mms<N>\_edi\_brst\_q0\_l2\_<yyyymmddhhmmss>\_v<x.y.z>.cdf

Name	Description	Type	Units
mms<N>_edi_counts_gdu1_<tlm>_l2	Raw counts measured by the detector in GDU1; accumulation time is 1/1024 seconds	UINT2	counts

mms<N>_edi_counts_gdu2_<tlm>_l2	Raw counts measured by the detector in GDU2; accumulation time is 1/1024 seconds	UINT2	counts
mms<N>_edi_traj_gse_gdu1_<tlm>_l2	Direction of particle motion for GDU1 electrons in GSE	FLOAT	degrees
mms<N>_edi_traj_gse_gdu2_<tlm>_l2	Direction of particle motion for GDU2 electrons in GSE	FLOAT	degrees
mms<N>_edi_traj_gsm_gdu1_<tlm>_l2	Direction of particle motion for GDU1 electrons in GSM	FLOAT	degrees
mms<N>_edi_traj_gsm_gdu2_<tlm>_l2	Direction of particle motion for GDU2 electrons in GSM	FLOAT	degrees
<b>Support Data</b>			
epoch_gdu1	Time tags for GDU1 counts, trajectories and detector energy	TT2000	ns
epoch_gdu2	Time tags for GDU2 counts, trajectories and detector energy	TT2000	ns
epoch_timetag	Time tags for optics state variable	TT2000	ns
mms<N>_edi_optics_state_<tlm>_l2	Optics State	UINT2	none
mms<N>_edi_energy_gdu1_<tlm>_l2	GDU1 detector energy	UINT2	eV
mms<N>_edi_energy_gdu2_<tlm>_l2	GDU2 detector energy	UINT2	eV

**Table 10-10 L2 Quality-Zero Data**

### 10.6.3 Ambient Mode Data

Ambient Mode data processing of Level 2 data and Quicklook (QL) data is illustrated in Figure 10-14. The initial common step is the generation of L1A data from the raw L0 data. In this step data are extracted, time tags in TT2000 format are added to each record, and for burst data the compressed counts data are decompressed.

For the QuickLook Data, the counts data are corrected for dead time effects, the instrument response function that removes the geometric factor dependency on the look direction is applied (flat-fielding) and the counts from the GDUs are brought to the same level (relative calibration).

For the L2 ambient data, the absolute calibration factor is applied in addition, and an error for the resulting fluxes is calculated that takes into account various error terms as outlined in section 10.5.2.2. Particle motion directions are calculated and given in GSE and DBCS coordinates. As in the case of the quality zero data the uncertainty in these directions is specified as a single angle.

The order of steps for the calculation of fluxes in the ambient data processing is:

1. Dead time correction – for survey data where the telemetry channels contain the summed counts of two adjacent anodes (data products amb, amb-alt-cc and the perpendicular data of amb-alt-oc)

the assumption is made that both anodes contribute evenly. The raw counts must be divided by two, then the deadtime correction is performed, and the result is then multiplied by a factor of 2

2. Relative calibration (flat-fielding)
3. Application of Inter-GDU adjustment factor
4. Conversion to fluxes – the absolute calibration factors stored in the L2 calibration files are for burst data. That is, they are valid for accumulation times of 1 ms and single anodes. For survey data the following adjustments are made:
  - a. One-sided anode placement (single anode): division of the absolute calibration factor by 16 to account for the longer accumulation time of survey data, This applies to data products amb-pm2, amb-alt-oom, amb-alt-oob, amb-perp-ob and the field aligned data in amb-alt-oc
  - b. Centered anode placement: division of the absolute calibration factor by 32 to account for the longer accumulation time of survey data and the fact that data from two anodes have been combined. This applies to data products amb, amb-alt-cc and the perpendicular data of amb-alt-oc

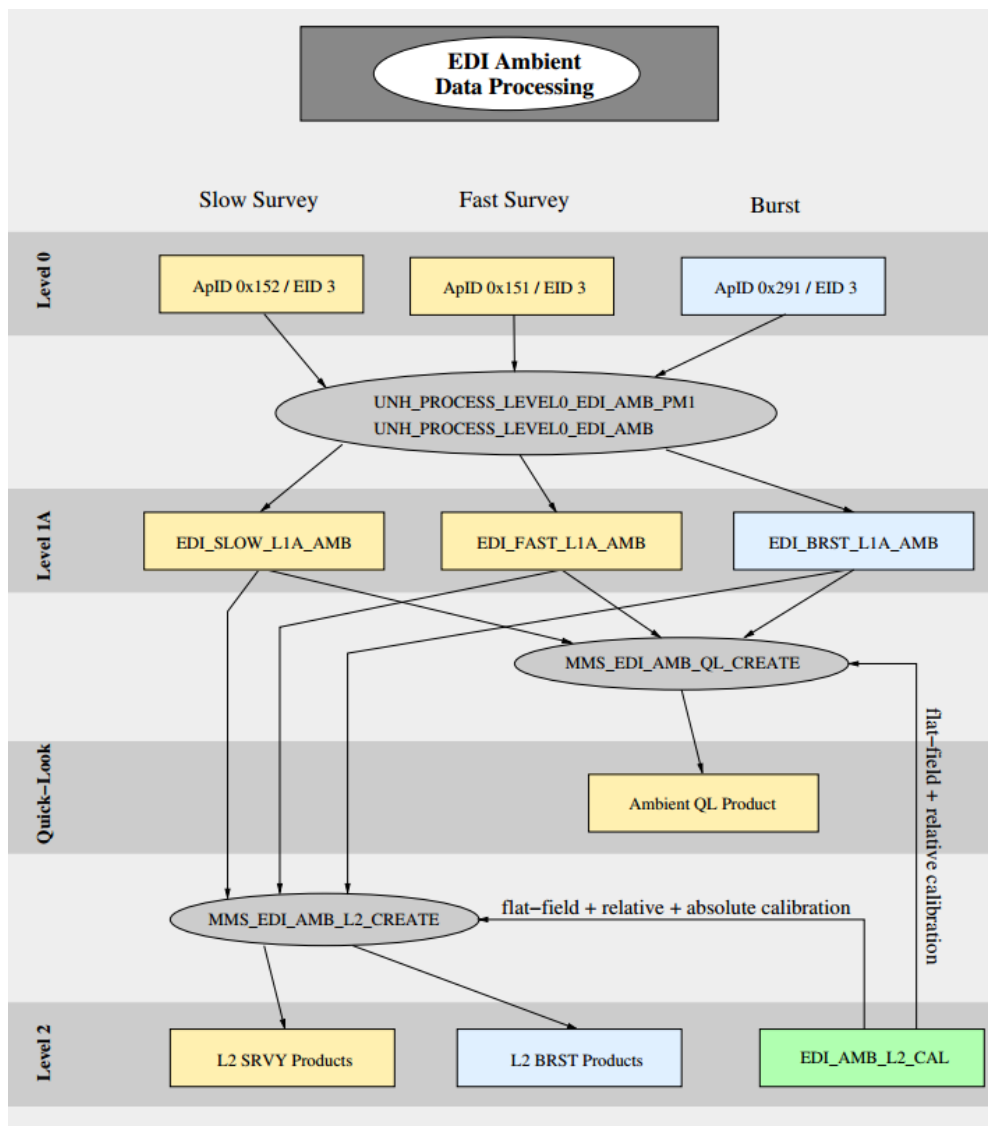


**Figure 10-14 EDI Ambient Mode Data Processing Flow**

### 10.6.3.1 File Structure L2 AMBIENT Field Aligned Mode Data

#### 10.6.3.1.1 Survey

File Names:

mms<N>\_edi\_srvy\_l2\_amb\_<yyyymmdd>\_v<x.y.z>.cdf  
mms<N>\_edi\_srvy\_l2\_amb-pm2\_<yyyymmdd>\_v<x.y.z>.cdf

Name	Description	Type	Units
mms<N>_edi_flux1_0_srvy_l2	Electron flux along pitch angle 0	FLOAT	$\text{cm}^{-2} \text{s}^{-1} \text{sr}^{-1}$
mms<N>_edi_flux1_180_srvy_l2	Electron flux along pitch angle 180	FLOAT	$\text{cm}^{-2} \text{s}^{-1} \text{sr}^{-1}$
mms<N>_edi_traj1_dbcs_0_srvy_l2	Direction of particle motion for pitch angle 0 electrons in DBCS, given as in spherical coordinates. First component: azimuth (in DBCS xy plane), second component: polar angle (with respect to DBCS z)	FLOAT	degrees
mms<N>_edi_traj1_dbcs_180_srvy_l2	Direction of particle motion for pitch angle 180 electrons in DBCS	FLOAT	degrees
mms<N>_edi_traj1_gse_0_srvy_l2	Direction of particle motion for pitch angle 0 electrons in GSE	FLOAT	degrees
mms<N>_edi_traj1_gse_180_srvy_l2	Direction of particle motion for pitch angle 180 electrons in GSE	FLOAT	Degrees
<b>Support data</b>			
Epoch	Time tags for fluxes, trajectories, GDU numbers, flux errors and flip indicator	TT_2000	ns
epoch_timetag	Time tags for optics state and GDU energies	TT_2000	ns
mms<N>_edi_flip_0_180_srvy_l2	Indicator for rapid detector look direction changes	UINT1	none
mms<N>_edi_optics_state_srvy_l2	EDI detector optics state	UINT1	none
mms<N>_edi_energy_gdu1_srvy_l2	EDI GDU1 energy	UINT2	eV
mms<N>_edi_energy_gdu2_srvy_l2	EDI GDU2 energy	UINT2	eV
mms<N>_edi_gdu_0_srvy_l2	GDU number for pitch angle 0 data	UINT1	none
mms<N>_edi_gdu_180_srvy_l2	GDU number for pitch angle 180 data	UINT1	none
mms<N>_edi_flux1_0_delta_srvy_l2	Error for pitch angle 0 flux	FLOAT	$\text{cm}^{-2} \text{s}^{-1} \text{sr}^{-1}$

mms<N>_edi_flux1_180_delta_srvy_l2	Error for pitch angle 180 flux	FLOAT	cm <sup>-2</sup> s <sup>-1</sup> sr <sup>-1</sup>
------------------------------------	--------------------------------	-------	---

**Table 10-11 L2 Ambient Field Aligned Mode Survey Data**

**10.6.3.1.2 Burst**

File Names:

mms<N>\_edi\_brst\_l2\_amb\_<yyyymmddhhmmss>\_v<x.y.z>.cdf  
mms<N>\_edi\_brst\_l2\_amb-pm2\_<yyyymmddhhmmss>\_v<x.y.z>.cdf

Name	Description	Type	Units
mms<N>_edi_flux1_0_brst_l2 mms<N>_edi_flux2_0_brst_l2 mms<N>_edi_flux3_0_brst_l2 mms<N>_edi_flux4_0_brst_l2	Electron flux in four separate directional channels close to pitch angle 0	FLOAT	cm <sup>-2</sup> s <sup>-1</sup> sr <sup>-1</sup>
mms<N>_edi_flux1_180_brst_l2 mms<N>_edi_flux2_180_brst_l2 mms<N>_edi_flux3_180_brst_l2 mms<N>_edi_flux4_180_brst_l2	Electron flux in four separate directional channels close to pitch angle 180	FLOAT	cm <sup>-2</sup> s <sup>-1</sup> sr <sup>-1</sup>
mms<N>_edi_traj1_dbcs_0_brst_l2 mms<N>_edi_traj2_dbcs_0_brst_l2 mms<N>_edi_traj3_dbcs_0_brst_l2 mms<N>_edi_traj4_dbcs_0_brst_l2	Particle motion directions for the four channels close to pitch angle 0 in DBCS	FLOAT	degrees
mms<N>_edi_traj1_dbcs_180_brst_l2 mms<N>_edi_traj2_dbcs_180_brst_l2 mms<N>_edi_traj3_dbcs_180_brst_l2 mms<N>_edi_traj4_dbcs_180_brst_l2	Particle motion directions for the four channels close to pitch angle 180 in DBCS	FLOAT	degrees
mms<N>_edi_traj1_gse_0_brst_l2 mms<N>_edi_traj2_gse_0_brst_l2 mms<N>_edi_traj3_gse_0_brst_l2 mms<N>_edi_traj4_gse_0_brst_l2	Particle motion directions for the four channels close to pitch angle 0 in GSE	FLOAT	degrees
mms<N>_edi_traj1_gse_180_brst_l2 mms<N>_edi_traj2_gse_180_brst_l2 mms<N>_edi_traj3_gse_180_brst_l2 mms<N>_edi_traj4_gse_180_brst_l2	Particle motion directions for the four channels close to pitch angle 180 in GSE	FLOAT	degrees
<b>Support data</b>			
Epoch	Time tags for fluxes, trajectories, GDU numbers, flux errors and flip indicator	TT_2000	ns
epoch_timetag	Time tags for optics state and GDU energies	TT_2000	ns
mms<N>_edi_flip_0_180_brst_l2	Indicator for rapid detector look direction changes	UINT1	none
mms<N>_edi_optics_state_brst_l2	EDI detector optics state	UINT1	none
mms<N>_edi_energy_gdu1_brst_l2	EDI GDU1 energy	UINT2	eV
mms<N>_edi_energy_gdu2_brst_l2	EDI GDU2 energy	UINT2	eV
mms<N>_edi_gdu_0_brst_l2	GDU number for pitch angle 0 data	UINT1	none

mms<N>_edi_gdu_180_brst_l2	GDU number for pitch angle 180 data	UINT1	none
mms<N>_edi_flux1_0_delta_brst_l2 mms<N>_edi_flux2_0_delta_brst_l2 mms<N>_edi_flux3_0_delta_brst_l2 mms<N>_edi_flux4_0_delta_brst_l2	Errors for pitch angle 0 flux channels	FLOAT	cm <sup>-2</sup> s <sup>-1</sup> sr <sup>-1</sup>
mms<N>_edi_flux1_180_delta_brst_l2 mms<N>_edi_flux2_180_delta_brst_l2 mms<N>_edi_flux3_180_delta_brst_l2 mms<N>_edi_flux4_180_delta_brst_l2	Errors for pitch angle 180 flux channels	FLOAT	cm <sup>-2</sup> s <sup>-1</sup> sr <sup>-1</sup>

**Table 10-12 L2 Ambient Field Aligned Burst Data**

### 10.6.3.2 File Structure L2 AMBIENT Alternating Pitch Angle Mode Data

#### 10.6.3.2.1 Survey

File Names:

mms<N>\_edi\_srvy\_l2\_amb-alt-cc\_<yyyymmdd>\_v<x.y.z>.cdf  
mms<N>\_edi\_srvy\_l2\_amb-alt-oc\_<yyyymmdd>\_v<x.y.z>.cdf  
mms<N>\_edi\_srvy\_l2\_amb-alt-oob\_<yyyymmdd>\_v<x.y.z>.cdf

Name	Description	Type	Units
mms<N>_edi_flux1_0_srvy_l2	Electron flux along pitch angle 0	FLOAT	cm <sup>-2</sup> s <sup>-1</sup> sr <sup>-1</sup>
mms<N>_edi_flux1_90_gdu1_srvy_l2	Electron flux for pitch angle 90, measured by GDU1	FLOAT	cm <sup>-2</sup> s <sup>-1</sup> sr <sup>-1</sup>
mms<N>_edi_flux1_90_gdu2_srvy_l2	Electron flux for pitch angle 90, measured by GDU2	FLOAT	cm <sup>-2</sup> s <sup>-1</sup> sr <sup>-1</sup>
mms<N>_edi_flux1_180_srvy_l2	Electron flux along pitch angle 180	FLOAT	cm <sup>-2</sup> s <sup>-1</sup> sr <sup>-1</sup>
mms<N>_edi_traj1_dbcs_0_srvy_l2	Direction of particle motion for pitch angle 0 electrons in DBCS, given as in spherical coordinates. First component: azimuth (in DBCS xy plane), second component: polar angle (with respect to DBCS z)	FLOAT	degrees
mms<N>_edi_traj1_dbcs_90_gdu1_srvy_l2	Direction of GDU1 particle motion for pitch angle 90 electrons in DBCS	FLOAT	degrees
mms<N>_edi_traj1_dbcs_90_gdu2_srvy_l2	Direction of GDU2 particle motion for pitch angle 90 electrons in DBCS	FLOAT	degrees

mms<N>_edi_traj1_dbcs_180_srvy_l2	Direction of particle motion for pitch angle 180 electrons in DBCS	FLOAT	degrees
mms<N>_edi_traj1_gse_0_srvy_l2	Direction of particle motion for pitch angle 0 electrons in GSE	FLOAT	degrees
mms<N>_edi_traj1_gse_90_gdu1_srvy_l2	Direction of GDU1 particle motion for pitch angle 90 electrons in GSE	FLOAT	degrees
mms<N>_edi_traj1_gse_90_gdu2_srvy_l2	Direction of GDU2 particle motion for pitch angle 90 electrons in GSE	FLOAT	degrees
mms<N>_edi_traj1_gse_180_srvy_l2	Direction of particle motion for pitch angle 180 electrons in GSE	FLOAT	degrees
<b>Support Data</b>			
Epoch_0_180	Time tags for pitch angle 0 and 180 fluxes, associated trajectories, GDU numbers, flux errors and flip indicators	TT_2000	ns
Epoch_90	Time tags for GDU1 and GDU2 pitch angle 90 fluxes, associated trajectories, flux errors and flip indicators	TT_2000	ns
epoch_timetag	Time tags for optics state, GDU energies and dwell time	TT_2000	ns
mms<N>_edi_flip_0_180_srvy_l2	Indicator for rapid detector look direction changes	UINT1	none
mms<N>_edi_flip_90_srvy_l2	Indicator for rapid detector look direction changes	UINT1	none
mms<N>_edi_optics_state_srvy_l2	EDI detector optics state	UINT1	none
mms<N>_edi_dwell_srvy_l2	Dwell time setting for sampling field aligned and perpendicular pitch angle data	FLOAT	s
mms<N>_edi_energy_gdu1_srvy_l2	EDI GDU1 energy	UINT2	eV
mms<N>_edi_energy_gdu2_srvy_l2	EDI GDU2 energy	UINT2	eV
mms<N>_edi_gdu_0_srvy_l2	GDU number for pitch angle 0 data	UINT1	none
mms<N>_edi_gdu_180_srvy_l2	GDU number for pitch angle 180 data	UINT1	none
mms<N>_edi_flux1_0_delta_srvy_l2	Error for pitch angle 0 flux	FLOAT	$\text{cm}^{-2} \text{s}^{-1} \text{sr}^{-1}$
mms<N>_edi_flux1_90_delta_gdu1_srvy_l2	Error for GDU1 pitch angle 90 flux	FLOAT	$\text{cm}^{-2} \text{s}^{-1} \text{sr}^{-1}$



mms<N>_edi_flux1_90_delta_gdu2_srvy_l2	Error for GDU2 pitch angle 90 flux	FLOAT	cm <sup>-2</sup> s <sup>-1</sup> sr <sup>-1</sup>
mms<N>_edi_flux1_180_delta_srvy_l2	Error for pitch angle 180 flux	FLOAT	cm <sup>-2</sup> s <sup>-1</sup> sr <sup>-1</sup>

**Table 10-13 L2 Ambient Alternating Pitch Angle Mode Survey Data**

**10.6.3.2.2 Burst**

File Names:

mms<N>\_edi\_brst\_l2\_amb-alt-cc\_<yyyymmddhhmmss>\_v<x.y.z>.cdf  
mms<N>\_edi\_brst\_l2\_amb-alt-oc\_<yyyymmddhhmmss>\_v<x.y.z>.cdf  
mms<N>\_edi\_brst\_l2\_amb-alt-oob\_<yyyymmddhhmmss>\_v<x.y.z>.cdf

Name	Description	Type	Units
mms<N>_edi_flux1_0_brst_l2 mms<N>_edi_flux2_0_brst_l2 mms<N>_edi_flux3_0_brst_l2 mms<N>_edi_flux4_0_brst_l2	Electron flux in four separate directional channels close to pitch angle 0	FLOAT	cm <sup>-2</sup> s <sup>-1</sup> sr <sup>-1</sup>
mms<N>_edi_flux1_90_gdu1_brst_l2 mms<N>_edi_flux2_90_gdu1_brst_l2 mms<N>_edi_flux3_90_gdu1_brst_l2 mms<N>_edi_flux4_90_gdu1_brst_l2	Electron flux in four separate directional channels close to pitch angle 90, measured by GDU1	FLOAT	cm <sup>-2</sup> s <sup>-1</sup> sr <sup>-1</sup>
mms<N>_edi_flux1_90_gdu2_brst_l2 mms<N>_edi_flux2_90_gdu2_brst_l2 mms<N>_edi_flux3_90_gdu2_brst_l2 mms<N>_edi_flux4_90_gdu2_brst_l2	Electron flux in four separate directional channels close to pitch angle 90, measured by GDU2	FLOAT	cm <sup>-2</sup> s <sup>-1</sup> sr <sup>-1</sup>
mms<N>_edi_flux1_180_brst_l2 mms<N>_edi_flux2_180_brst_l2 mms<N>_edi_flux3_180_brst_l2 mms<N>_edi_flux4_180_brst_l2	Electron flux in four separate directional channels close to pitch angle 180	FLOAT	cm <sup>-2</sup> s <sup>-1</sup> sr <sup>-1</sup>
mms<N>_edi_traj1_dbcs_0_brst_l2 mms<N>_edi_traj2_dbcs_0_brst_l2 mms<N>_edi_traj3_dbcs_0_brst_l2 mms<N>_edi_traj4_dbcs_0_brst_l2	Particle motion directions for the four channels close to pitch angle 0 in DBCS	FLOAT	degrees
mms<N>_edi_traj1_dbcs_90_gdu1_brst_l2 mms<N>_edi_traj2_dbcs_90_gdu1_brst_l2 mms<N>_edi_traj3_dbcs_90_gdu1_brst_l2 mms<N>_edi_traj4_dbcs_90_gdu1_brst_l2	Particle motion directions for the four channels close to pitch angle 90 in DBCS, measured by GDU1	FLOAT	degrees
mms<N>_edi_traj1_dbcs_90_gdu2_brst_l2 mms<N>_edi_traj2_dbcs_90_gdu2_brst_l2 mms<N>_edi_traj3_dbcs_90_gdu2_brst_l2 mms<N>_edi_traj4_dbcs_90_gdu2_brst_l2	Particle motion directions for the four channels close to pitch angle 90 in DBCS, measured by GDU2	FLOAT	degrees
mms<N>_edi_traj1_dbcs_180_brst_l2 mms<N>_edi_traj2_dbcs_180_brst_l2 mms<N>_edi_traj3_dbcs_180_brst_l2 mms<N>_edi_traj4_dbcs_180_brst_l2	Particle motion directions for the four channels close to pitch angle 180 in DBCS	FLOAT	degrees

mms<N>_edi_traj1_gse_0_brst_l2 mms<N>_edi_traj2_gse_0_brst_l2 mms<N>_edi_traj3_gse_0_brst_l2 mms<N>_edi_traj4_gse_0_brst_l2	Particle motion directions for the four channels close to pitch angle 0 in GSE	FLOAT	degrees
mms<N>_edi_traj1_gse_90_gdu1_brst_l2 mms<N>_edi_traj2_gse_90_gdu1_brst_l2 mms<N>_edi_traj3_gse_90_gdu1_brst_l2 mms<N>_edi_traj4_gse_90_gdu1_brst_l2	Particle motion directions for the four channels close to pitch angle 90 in GSE, measured by GDU1	FLOAT	degrees
mms<N>_edi_traj1_gse_90_gdu2_brst_l2 mms<N>_edi_traj2_gse_90_gdu2_brst_l2 mms<N>_edi_traj3_gse_90_gdu2_brst_l2 mms<N>_edi_traj4_gse_90_gdu2_brst_l2	Particle motion directions for the four channels close to pitch angle 90 in GSE, measured by GDU2	FLOAT	degrees
mms<N>_edi_traj1_gse_180_brst_l2 mms<N>_edi_traj2_gse_180_brst_l2 mms<N>_edi_traj3_gse_180_brst_l2 mms<N>_edi_traj4_gse_180_brst_l2	Particle motion directions for the four channels close to pitch angle 180 in GSE	FLOAT	degrees
<b>Support Data</b>			
Epoch_0_180	Time tags for pitch angle 0 and 180 fluxes, associated trajectories, GDU numbers, flux errors and flip indicators	TT_2000	ns
Epoch_90	Time tags for GDU1 and GDU2 pitch angle 90 fluxes, associated trajectories, flux errors and flip indicators	TT_2000	ns
epoch_timetag	Time tags for optics state, GDU energies and dwell time	TT_2000	ns
mms<N>_edi_flip_0_180_brst_l2	Indicator for rapid detector look direction changes	UINT1	none
mms<N>_edi_flip_90_brst_l2	Indicator for rapid detector look direction changes	UINT1	none
mms<N>_edi_optics_state_brst_l2	EDI detector optics state	UINT1	none
mms<N>_edi_dwell_brst_l2	Dwell time setting for sampling field aligned and perpendicular pitch angle data	FLOAT	s
mms<N>_edi_energy_gdu1_brst_l2	EDI GDU1 energy	UINT2	eV
mms<N>_edi_energy_gdu2_brst_l2	EDI GDU2 energy	UINT2	eV
mms<N>_edi_gdu_0_brst_l2	GDU number for pitch angle 0 data	UINT1	none
mms<N>_edi_gdu_180_brst_l2	GDU number for pitch angle 180 data	UINT1	none
mms<N>_edi_flux1_0_delta_brst_l2 mms<N>_edi_flux2_0_delta_brst_l2 mms<N>_edi_flux3_0_delta_brst_l2 mms<N>_edi_flux4_0_delta_brst_l2	Errors for pitch angle 0 flux channels	FLOAT	cm <sup>-2</sup> s <sup>-1</sup> sr <sup>-1</sup>

mms<N>_edi_flux1_90_delta_gdu1_brst_l2 mms<N>_edi_flux2_90_delta_gdu1_brst_l2 mms<N>_edi_flux3_90_delta_gdu1_brst_l2 mms<N>_edi_flux4_90_delta_gdu1_brst_l2	Errors for GDU1 pitch angle 90 flux channels	FLOAT	cm <sup>-2</sup> s <sup>-1</sup> sr <sup>-1</sup>
mms<N>_edi_flux1_90_delta_gdu2_brst_l2 mms<N>_edi_flux2_90_delta_gdu2_brst_l2 mms<N>_edi_flux3_90_delta_gdu2_brst_l2 mms<N>_edi_flux4_90_delta_gdu2_brst_l2	Errors for GDU2 pitch angle 90 flux channels	FLOAT	cm <sup>-2</sup> s <sup>-1</sup> sr <sup>-1</sup>
mms<N>_edi_flux1_180_delta_brst_l2 mms<N>_edi_flux2_180_delta_brst_l2 mms<N>_edi_flux3_180_delta_brst_l2 mms<N>_edi_flux4_180_delta_brst_l2	Errors for pitch angle 180 flux channels	FLOAT	cm <sup>-2</sup> s <sup>-1</sup> sr <sup>-1</sup>

**Table 10-14 L2 Ambient Alternating Pitch Angle Mode Burst Data**

### 10.6.3.3 File Structure L2 AMBIENT Perpendicular Mode Data

#### 10.6.3.3.1 Survey

File Names:

mms<N>\_edi\_srvy\_l2\_amb-perp-ob\_<yyyymmdd>\_v<x.y.z>.cdf

Name	Description	Type	Units
mms<N>_edi_flux1_90_gdu1_srvy_l2	Electron flux for pitch angle 90, measured by GDU1	FLOAT	cm <sup>-2</sup> s <sup>-1</sup> sr <sup>-1</sup>
mms<N>_edi_flux1_90_gdu2_srvy_l2	Electron flux for pitch angle 90, measured by GDU2	FLOAT	cm <sup>-2</sup> s <sup>-1</sup> sr <sup>-1</sup>
mms<N>_edi_traj1_dbcs_90_gdu1_srvy_l2	Direction of GDU1 particle motion for pitch angle 90 electrons in DBCS	FLOAT	degrees
mms<N>_edi_traj1_dbcs_90_gdu2_srvy_l2	Direction of GDU2 particle motion for pitch angle 90 electrons in DBCS	FLOAT	degrees
mms<N>_edi_traj1_gse_90_gdu1_srvy_l2	Direction of GDU1 particle motion for pitch angle 90 electrons in GSE	FLOAT	degrees
mms<N>_edi_traj1_gse_90_gdu2_srvy_l2	Direction of GDU2 particle motion for pitch angle 90 electrons in GSE	FLOAT	degrees
<b>Support Data</b>			
Epoch	Time tags for fluxes, associated trajectories and flux errors	TT_2000	ns
epoch_timetag	Time tags for optics state and GDU energies	TT_2000	ns
mms<N>_edi_optics_state_srvy_l2	EDI detector optics state	UINT1	none
mms<N>_edi_energy_gdu1_srvy_l2	EDI GDU1 energy	UINT2	eV

mms<N>_edi_energy_gdu2_srvy_l2	EDI GDU2 energy	UINT2	eV
mms<N>_edi_flux1_90_delta_gdu1_srvy_l2	Error for GDU1 pitch angle 90 flux	FLOAT	cm <sup>-2</sup> s <sup>-1</sup> sr <sup>-1</sup>
mms<N>_edi_flux1_90_delta_gdu2_srvy_l2	Error for GDU2 pitch angle 90 flux	FLOAT	cm <sup>-2</sup> s <sup>-1</sup> sr <sup>-1</sup>

**Table 10-15 L2 Ambient Perpendicular Mode Survey Data**

### 10.6.3.3.2 Burst

File Names:

mms<N>\_edi\_brst\_l2\_amb-perp-ob\_<yyyymmddhhmmss>\_v<x.y.z>.cdf

Name	Description	Type	Units
mms<N>_edi_flux1_90_gdu1_brst_l2 mms<N>_edi_flux2_90_gdu1_brst_l2 mms<N>_edi_flux3_90_gdu1_brst_l2 mms<N>_edi_flux4_90_gdu1_brst_l2	Electron flux in four separate directional channels close to pitch angle 90, measured by GDU1	FLOAT	cm <sup>-2</sup> s <sup>-1</sup> sr <sup>-1</sup>
mms<N>_edi_flux1_90_gdu2_brst_l2 mms<N>_edi_flux2_90_gdu2_brst_l2 mms<N>_edi_flux3_90_gdu2_brst_l2 mms<N>_edi_flux4_90_gdu2_brst_l2	Electron flux in four separate directional channels close to pitch angle 90, measured by GDU2	FLOAT	cm <sup>-2</sup> s <sup>-1</sup> sr <sup>-1</sup>
mms<N>_edi_traj1_dbcs_90_gdu1_brst_l2 mms<N>_edi_traj2_dbcs_90_gdu1_brst_l2 mms<N>_edi_traj3_dbcs_90_gdu1_brst_l2 mms<N>_edi_traj4_dbcs_90_gdu1_brst_l2	Particle motion directions for the four channels close to pitch angle 90 in DBCS, measured by GDU1	FLOAT	degrees
mms<N>_edi_traj1_dbcs_90_gdu2_brst_l2 mms<N>_edi_traj2_dbcs_90_gdu2_brst_l2 mms<N>_edi_traj3_dbcs_90_gdu2_brst_l2 mms<N>_edi_traj4_dbcs_90_gdu2_brst_l2	Particle motion directions for the four channels close to pitch angle 90 in DBCS, measured by GDU2	FLOAT	degrees
mms<N>_edi_traj1_gse_90_gdu1_brst_l2 mms<N>_edi_traj2_gse_90_gdu1_brst_l2 mms<N>_edi_traj3_gse_90_gdu1_brst_l2 mms<N>_edi_traj4_gse_90_gdu1_brst_l2	Particle motion directions for the four channels close to pitch angle 90 in GSE, measured by GDU1	FLOAT	degrees
mms<N>_edi_traj1_gse_90_gdu2_brst_l2 mms<N>_edi_traj2_gse_90_gdu2_brst_l2 mms<N>_edi_traj3_gse_90_gdu2_brst_l2 mms<N>_edi_traj4_gse_90_gdu2_brst_l2	Particle motion directions for the four channels close to pitch angle 90 in GSE, measured by GDU2	FLOAT	degrees
<b>Support data</b>			
Epoch	Time tags for fluxes, associated trajectories and flux errors	TT_2000	ns
epoch_timetag	Time tags for optics state and GDU energies	TT_2000	ns
mms<N>_edi_optics_state_brst_l2	EDI detector optics state	UINT1	none
mms<N>_edi_energy_gdu1_brst_l2	EDI GDU1 energy	UINT2	eV
mms<N>_edi_energy_gdu2_brst_l2	EDI GDU2 energy	UINT2	eV
mms<N>_edi_flux1_90_delta_gdu1_brst_l2 mms<N>_edi_flux2_90_delta_gdu1_brst_l2	Errors for GDU1 pitch angle 90 flux channels	FLOAT	cm <sup>-2</sup> s <sup>-1</sup> sr <sup>-1</sup>

G-254

mms<N>_edi_flux3_90_delta_gdu1_brst_l2 mms<N>_edi_flux4_90_delta_gdu1_brst_l2			
mms<N>_edi_flux1_90_delta_gdu2_brst_l2 mms<N>_edi_flux2_90_delta_gdu2_brst_l2 mms<N>_edi_flux3_90_delta_gdu2_brst_l2 mms<N>_edi_flux4_90_delta_gdu2_brst_l2	Errors for GDU2 pitch angle 90 flux channels	FLOAT	$\text{cm}^{-2} \text{s}^{-1} \text{sr}^{-1}$

**Table 10-16 L2 Ambient Perpendicular Mode Burst Data**

### 10.7 APPENDIX A- EDI REFERENCES

The following documents and drawings in effect on the day this specification was signed **shall** apply to the extent specified herein. In the event of conflict between this document and any referenced document, the document with latest publication date will govern.

The following is a list of applicable references and publications.

Section	Document Number	Title	Revision/Date
	<a href="https://doi.org/10.1007/s11214-016-0238-3">https://doi.org/10.1007/s11214-016-0238-3</a>	Torbert, R.B., Vaith, H., Granoff, M. et al. (2016). Erratum to: The Electron Drift Instrument for MMS. Space Sci Rev 199, 307–308.	
	<a href="https://doi.org/10.1007/s11214-015-0182-7">https://doi.org/10.1007/s11214-015-0182-7</a>	Torbert, R.B., Vaith, H., Granoff, M. et al. (2016). The Electron Drift Instrument for MMS. Space Sci Rev 199, 283–305.	
	<a href="https://doi.org/10.1007/s11214-014-0109-8">https://doi.org/10.1007/s11214-014-0109-8</a>	Torbert, R.B., Russell, C.T., Magnes, W. et al. (2016). The FIELDS Instrument Suite on MMS: Scientific Objectives, Measurements, and Data Products. Space Sci Rev 199, 105–135.	

**Table 10-17 EDI Applicable Documents**

## 11.0 ELECTRIC DOUBLE PROBES (EDP)

### 11.1 EDP OVERVIEW

The Spin-plane Double Probe (SDP) and the Axial Double Probe (ADP) instruments are part of the FIELDS instrument suite of the MMS. The combination of SDP and ADP is referred to as the Electric field Double Probe (EDP) instrument. EDP measures the 3-D electric field with an accuracy of 0.5mV/m over the frequency range from DC to 100kHz. SDP consists of 4 biased spherical probes extended on 60m long wire booms 90 degrees apart in the spin plane, giving a 120m baseline for each of the two spin-plane electric field components. ADP consists of 2 biased cylindrical probes extended on 12m long stiff booms along the spacecraft axis, giving a 29.2m baseline for the axial electric field component. SDP and ADP should measure the spin-plane electric field with accuracy 0.5 mV/m and the axial electric field with accuracy of 1 mV/m. Double-probe electric field experiments have been flown on a number of spacecraft including Cluster. The EFW instrument on Cluster has been operating since 2000. MMS data analysis will leverage the work done for Cluster.

The detector of the SDP instrument consists of four orthogonal spherical sensors deployed from 60m cables in the spin plane of the spacecraft, four mechanical deployment units, each containing 3 boom electronic boards (BEBs). The detector of ADP consists of two cylindrical sensors deployed on 12m long stiff booms along the spacecraft axis, each containing 2 BEBs. The analog to digital conversion of the signals is done by the DSP (Digital Signal Processor) located in the FIELDS CEB (Central Electronic Box). The potential drop between two opposing spherical or cylindrical sensors is measured to provide an electric field measurement. The average value of SDP probe to spacecraft potential provides information on the spacecraft potential. The instrument can also perform current sweeps to provide the current-voltage curve and, thus, the electron temperature and density. The potentials of each spherical and cylindrical sensor and nearby conductors are controlled in order to minimize errors associated with photoemission from the spheres and impact of plasma electrons and ions on the spheres. For more details on SDP, ADP and DSP refer to the instrument descriptions in Lindqvist et al., (2016) and Ergun et al., (2016). The SDP has four probes configured in two orthogonal probe pairs in the spin plane on each spacecraft and ADP has two probes approximately along the spacecraft spin axis as shown in Figure 11-1. The angle between the probe pair 12 and  $X_{SC}$  is approximately 30 degrees.

The instrument sends a negative bias current to the probes. The total of the plasma and photoelectron currents must then equal the bias current, so the probe potential adjusts to the operating point shown in Figure 11-2 (assuming a bias current of 140 nA). This has the advantage of putting the instrument on the steep part of the curve (i.e. the low resistance part), even in low density environments. Small fluctuations in the currents (whether caused by actual changes in the plasma or simply stray currents) then do not significantly affect the probe voltage. The probe pairs remain stably grounded (with a small offset) to their local plasma environment. Stray currents and plasma density fluctuations do not show up as an electric potential drop between the probes.

The optimal value of the bias current is determined to large extent by the photoelectron current, which in turn depends on the solar UV flux as well as on the photo-emissive properties of the probe surfaces. Therefore, the bias current needs to be adjusted over the course of the mission to account for changing solar UV flux and probe surface characteristics.

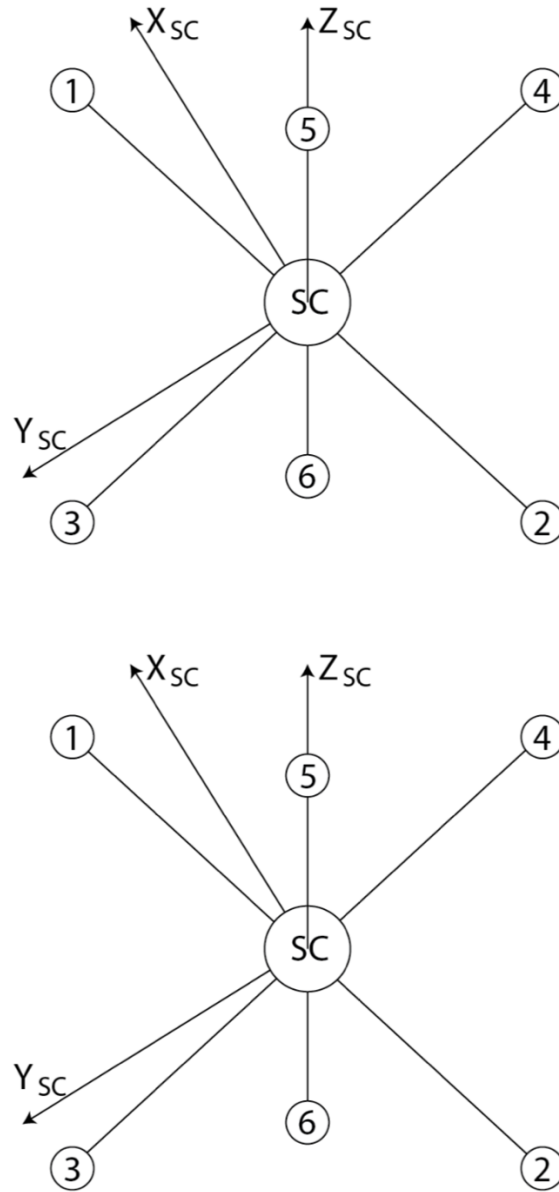


**Figure 11-1 Schematic of SDP and ADP Probes**

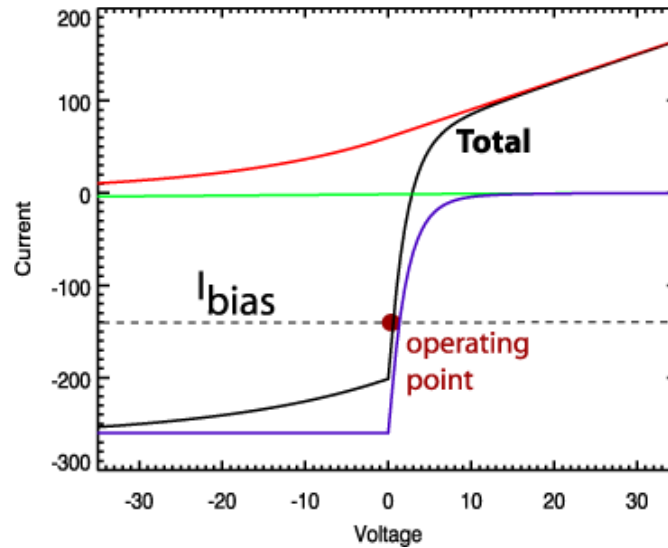


**Figure 11-2 Idealized Current-Voltage Curve of a Biased Probe in a Low Density (1 cc) Plasma [The total current to the probe is sum of electron current (red), ion current (green) and photoelectron current (purple)]**

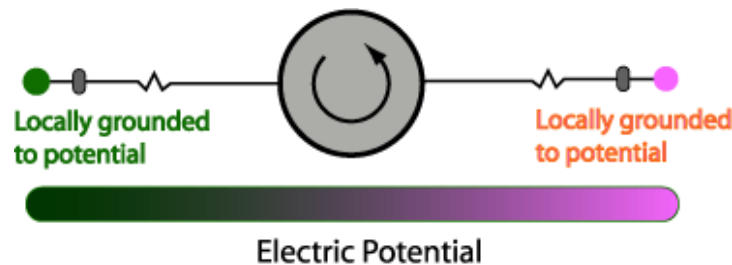


**Figure 11-3 Electric Field Mode (biased probes)**

Since the current biasing grounds each probe to the local plasma potential, the difference between the probe potentials divided by the length between the probes gives the electric field as shown in Figure 11-3. Normally, the full spin plane electric field is computed using the orthogonal signals P12 and P34 and axial electric field using P56 (see Figure 11-1). The average value of the probe to spacecraft potentials provides the spacecraft potential.

### 11.1.1 Status of EDP Probes

Probe 2 on MMS2 and Probe 4 on MMS4 are out of commission and they are no longer being used for electric field measurements. In each case, a micro-meteoroid severed a wire in the thick cable (between spacecraft and pre-amplifier). Probe 2 on MMS3 was recently hit by a micro-meteoroid and this probe is also out of commission.

Probe 4 on MMS4 can be used for AC High Frequency Electric field measurements, but has zero bias current, so it is not useable for DC measurements. The Pre-amplifier on MMS2, Probe 2, has no supply voltage on one side, so it cannot be used. MMS2, MMS3 and MMS4 are producing AC and DC fields



using 3 Spin-plane probes and the two unaffected axial probes. All probes on MMS1 are healthy and functioning.

Full 3D electric field measurements continue within specifications for all spacecraft. In June 2016, a micrometeoroid severed a single bias wire of MMS4 Probe 4 (SDP4) adversely affecting the frequency range DC-~600 Hz. For this range, the FIELDS team successfully reconfigured the electric field instrument and implemented a post-processing routine using the 3 healthy probes to determine the E-field components in the spin plane. Using comparison data from before June 2016, Figure 11-4 shows that the resulting uncertainty remains less than the 0.5 mV/m mission success requirement with only a modest increase in the noise floor. A second micrometeoroid impact occurred in Sept 2018 to Probe2 (SDP2) on MMS2 which severed its 12V power. A flight software mod in early Oct 2018 reconfigured signals from the three remaining SDP probes to continue MMS2 spacecraft potential calculations, several burst trigger quantities, and the 1% duty cycled AC E-field, keeping MMS2 within specifications. More recently, on May 8, 2022, a micrometeoroid impacted MMS3 on probe 2, resulting in loss of function of that probe. Once again, the remaining 3 probes were configured so that full L1 performance continues. Thus, all four spacecraft are still returning the full science performance requirement.

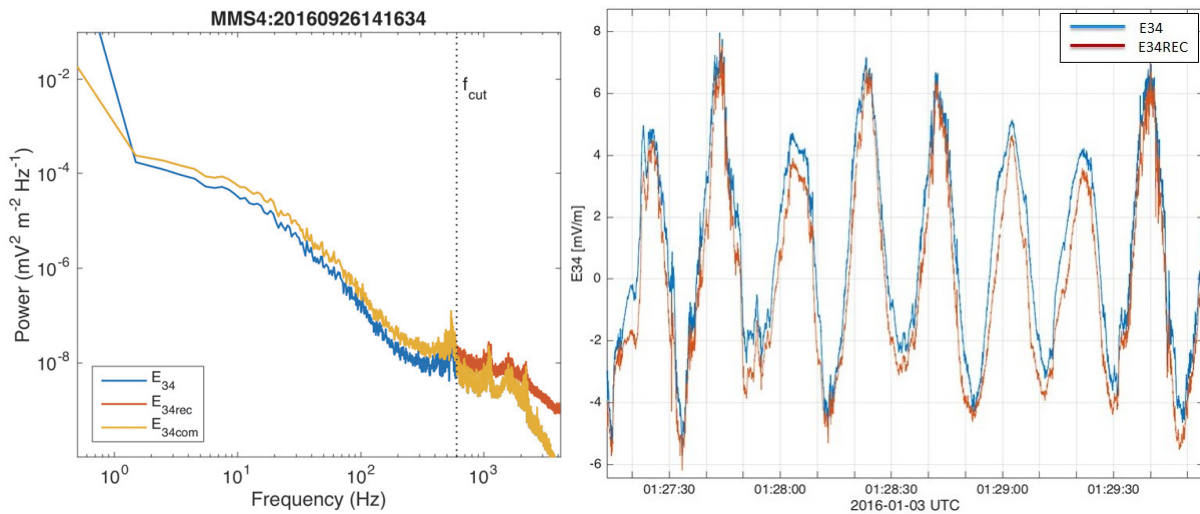


**Figure 11-4 Comparison of (Left) Measured (Blue) and Reconstructed (Orange) Wave Forms Using Data Taken Prior to the Anomaly and (Right) Post-Anomaly Noise Levels of the Measured (Blue), Reconstructed (Orange), and Combined (Yellow) Products Along the SDP3-4 Axis**

## 11.2 EDP MEASUREMENTS AND TIMING

The basic EDP sample rates are 8 samples/second in slow survey, 32 samples/seconds-1 in fast survey, and 8192 samples/seconds-1 in burst mode. During the tail season (phase 1X), 21 April - 26 July 2016, the burst mode sample rate was increased to 16384 samples/second.s-1. During the dusk season (phase 1X-1B), 5 August - 13 October 2016, the slow survey sample rate was increased to 32 samples/second.s-1.

The sampling of the DC raw data signals (individual probe potentials and probe potential differences) are done by a single analog to digital converter (ADC) running at  $218 = 262144$  s-1. This means that the data are not sampled simultaneously, but in the following order, with a delta time of 2-18 s or about  $3.815 \mu\text{s}$  between each sample:

The data in the EDP CDF files have been time tagged to the sampling of V1, neglecting the time difference between the sampling of the different channels. For slow and fast survey data, with a time

resolution of 31.25 ms, the sample time delay of up to 34  $\mu\text{s}$  can be neglected. For detailed high time resolution studies using burst data, with a time resolution of 122  $\mu\text{s}$ , the sample time delay of up to 34  $\mu\text{s}$  may be significant. Users wishing to do, e.g., cross spectral analysis of burst data, are advised to correct the timing themselves, using the individual probe data in the Level 2 Spacecraft potential file (brst\_l2\_scpot).

Sequence Number	Signal Sample	Delay with respect to first sample [ $\mu\text{s}$ ]
0	V1	0
1	V2(*)	3.815
2	V3	7.629
3	V4(*)	11.444
4	V5	15.259
5	V6(*)	19.073
6	-	22.888
7	E12	26.703
8	E34	30.518
9	E56	34.332

**Table 11-1 Sampling Sequence and Delays of EDP DC Raw Data**

### 11.2.1 Pre-Flight / On-Ground Calibration

A description of the design of EDP and its pre-flight and ground calibration can be found in these publications. The combination of the spin plane probes and axial probes provides a 3D electric field on each spacecraft which is necessary for the science goals of the MMS mission. The details of the probe configurations and operations are explained in the EDP overview section 11.1.1 and these publications.

Ergun, R. E., et al. **The Axial Double Probe and Fields Signal Processing for the MMS Mission**. Space Sci Rev 199, (2016). <https://doi.org/10.1007/s11214-014-0115-x>

Lindqvist, P.-A., et al. **The Spin-Plane Double Probe Electric Field Instrument for MMS**. Space Sci Rev 199, (2016). <https://doi.org/10.1007/s11214-014-0116-9>

### 11.3 EDP CALIBRATION AND VALIDATION

There is no on-board processing performed on SDP/ADP data which will be included in the science products. Ground processing includes decommutation and calibration into physical units of raw data. Further scientific processing includes spin fitting of probe-probe difference signals, determination of offsets in the raw data, determination of DC offsets in the despun data (sunward and duskward offsets), amplitude correction, and despinning the full resolution data. The Axial Double Probe (ADP) instrument measures the DC to  $\sim 100\text{kHz}$  electric field along the spin axis of the MMS spacecraft, completing the vector electric field when combined with the SDP. We produce 2 levels of data L2pre DCE and L2. In

order to create L2pre electric field data, first we remove sweeps and maneuver time intervals where the measurements have been impacted by spacecraft thrusters. Then we remove the spacecraft spin tone from ADP and SDP and using E.B=0 iteration, we correct the ADP component and store it as L2pre DCE data. In L2pre DCE files, we restore SDP components to L2pre DCE2D. Figure 11-6 shows the algorithm for generating the L2pre data.

## 11.4 EDP ALGORITHM DESCRIPTIONS

### 11.4.1 Theoretical Basics

This section gives descriptions of the processing and calibration of SDP, ADP and EPSD raw data to obtain the final electric field data. The EDP raw probe potential data is saved in L1b level. There are six probes on each spacecraft that calculate the potential (V1 to V6). The potential data goes through the following steps as explained in this section to calculate the 3 dimensional electric field (2 components in spinning plane and one component in axial direction).

### 11.4.2 SDP Algorithm

As the first stage of calibration it is necessary to perform initial cleaning of the data at which we remove intervals with: bad data due to issues with electronics, probe saturations due to low plasma density in the magnetospheric lobes (when ASPOC is not operating), and saturations due to non-optimal bias current settings occurring in dense plasmas such as magnetosheath. If the spacecraft is in the solar wind we apply a correction for the wakes usually present in the raw data. All the possible problems with the data are recorded in the bitmask supplied with the data.

**Spin fits.** After initial cleaning of the data a spin fitting procedure is performed; the output of this procedure provides basic parameters, which are used later in the calibration procedure. In the presence of a constant ambient electric field, the raw data signal (probe potential difference) is a sine wave where the amplitude and phase give the electric field magnitude and direction. A least-squares fit to the raw data of the form

$$y = A + B \cos(\omega t) + C \sin(\omega t) + D \cos(2\omega t) + E \sin(2\omega t) + \dots$$

is done on 20 seconds of data once every 5 seconds (the spacecraft spin period is about 20 seconds). The fit is done individually on E12 and E34 to obtain a set of terms for each of the raw data signals.

The standard deviation of the raw data from the fitted sine wave can be used as indication of high frequency variations in the data. Higher order terms, D, E, ..., may be used for diagnostics of data quality: normally the higher order terms are much smaller than B and C, and the opposite situation would indicate problems with the measurements.

**Offsets.** The sine and cosine terms, B and C after correction for DSL offsets provide the 5-sec resolution electric field in DSL:

$$E_{x5s} = \alpha B - \Delta E_x$$

$$E_{y5s} = \alpha C - \Delta E_y$$

where  $\alpha$  is the amplitude correction factor due to the ambient electric field is “short-circuited” by the presence of the spacecraft and wire booms, and  $\Delta E_x$  and  $\Delta E_y$  are the *DSL offsets*, which are determined from cross-calibration with EDI and particle instruments, as well as from the inter-spacecraft calibration.

As the spin fitting procedure would typically yield different values for the electric field from the two different probe pairs, it is useful to introduce additional offset which describes the difference between the two measurements,  $\Delta p_{12p34}$ , which we call the *Delta offset*:

$$\Delta_x p12p34 = E_{x5s}(E12) - E_{x5s}(E34)$$

$$\Delta_y p12p34 = E_{y5s}(E12) - E_{y5s}(E34)$$

The delta offset is expected to vary relatively slowly, on a typical time-scale of several months and is therefore determined from statistical comparison of electric fields from the two probe pairs.

The despun full resolution electric field is obtained as follows:

$$E_x = \text{Re}[\epsilon12] - \Delta_x p12p34 + \text{Re}[\epsilon34]$$

$$E_y = \text{Im}[\epsilon12] - \Delta_y p12p34 + \text{Im}[\epsilon34]$$

where  $\epsilon12 = (E12 - \Delta_{\text{raw } 12})e^{i\phi12}$ ,  $\epsilon34 = (E34 - \Delta_{\text{raw } 34})e^{i\phi34}$ , and  $\phi12 = \phi34 + \pi/2$  is the spin phase of probe 1 with respect to the sun; *Raw data DC offset*,  $\Delta_{\text{raw}} = \langle A \rangle$ , is based on parameter  $A$  of the fit on first equation. Ideally, the DC level of the raw data should be zero, however small differences between the probe surfaces and in the electronics create a DC offset in the raw data. If not corrected, it shows up as a signal at the spin frequency in the despun electric field. The 5s resolution values of  $A$  are smoothed using 5 adjacent points according to the formula

$$\langle A \rangle = 0.1 * A_{i-2} + 0.25 * A_{i-1} + 0.3 * A_i + 0.25 * A_{i+1} + 0.1 * A_{i+2} \quad (8)$$

after which  $\langle A \rangle$  is resampled to the full time resolution of the data using linear interpolation.

It may be noted that asymmetries due to the direction to the sun have the dominant contribution to the offsets, so that the following inequalities are typically satisfied:

$$\Delta E_x \gg \Delta E_y$$

$$\Delta_x p12p34 \gg \Delta_y p12p34$$

This SDP calibration process will provide the L2pre DCE2D data products.

### 11.4.3 ADP Algorithm

The L2 pre DCE2D data is used as input to generate L2 pre DCE data and L2 data. In this stage of calibration, we use data from FPI, FGM and EDI instruments. IF fast FPI and survey E-field EDI data are available, they will be used for calibrations purposes. The L2 calibration code detects the solar wind, magnetosheath, magnetopause, magnetotail and inner magnetosphere regions to set the gain values based on plasma parameters in each environment. If the spacecraft is in solar wind, FPI data is not used for calibration.

**Offsets.** In order to remove offsets from the data, we use four baselines when the necessary data are available:

- A.  $E + V_i \times B$  median-smoothed to 60 s.
- B.  $E + V_e \times B$  median smoothed to 10s.
- C. EDI E-Field mode averaged to 10 s.
- D.  $E \cdot B$  averaged to 20 s only in magnetotail.

The  $E \cdot B$  baseline is only used in magnetotail regions.  $V_i$  and  $V_e$  are ion and electron velocities respectively provided by FPI instrument. All the available baselines are merged together to remove the

offset from L2 data. Figure 11-5 and Figure 11-6 show the algorithm for the L2 pre and L2 DCE data. The L2pre data can be reconstructed using L2 calibration processing data following this procedure:

$$\begin{aligned} \text{EL2pre.Y}(*,0) &= (\text{EL2.Y}(*,0) + \text{Residue.Y}(*,0)) / 1.06 \\ \text{EL2pre.Y}(*,1) &= (\text{EL2.Y}(*,1) + \text{Residue.Y}(*,1)) / 1.06 \\ \text{EL2pre.Y}(*,2) &= (\text{EL2.Y}(*,2) + \text{Residue.Y}(*,2)) / 1.12 - \text{ResidueL2pre.Y}(*,2) \end{aligned}$$

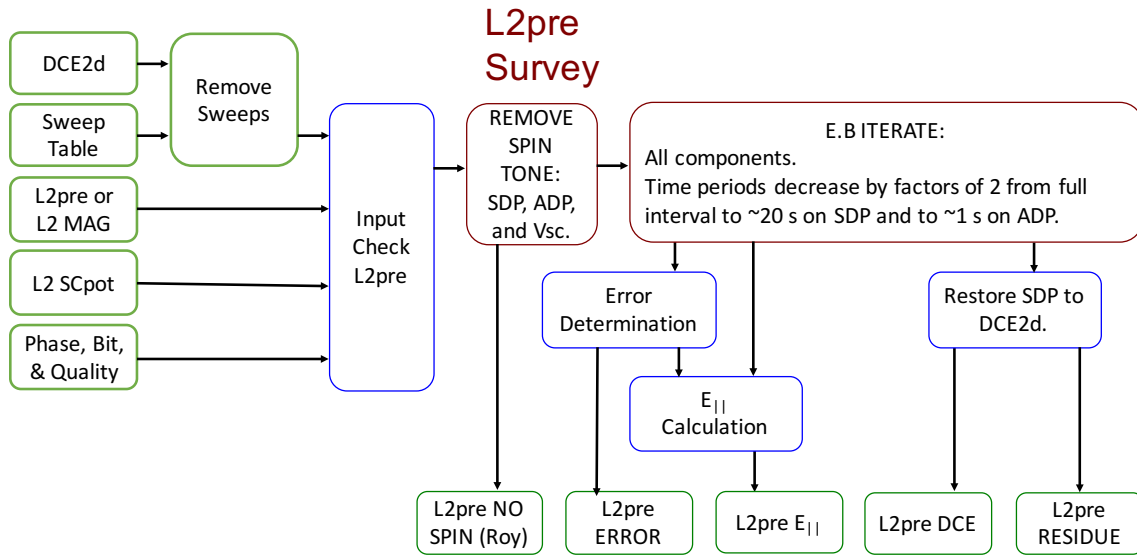


**Figure 11-5 L2Pre Calibration Algorithm**

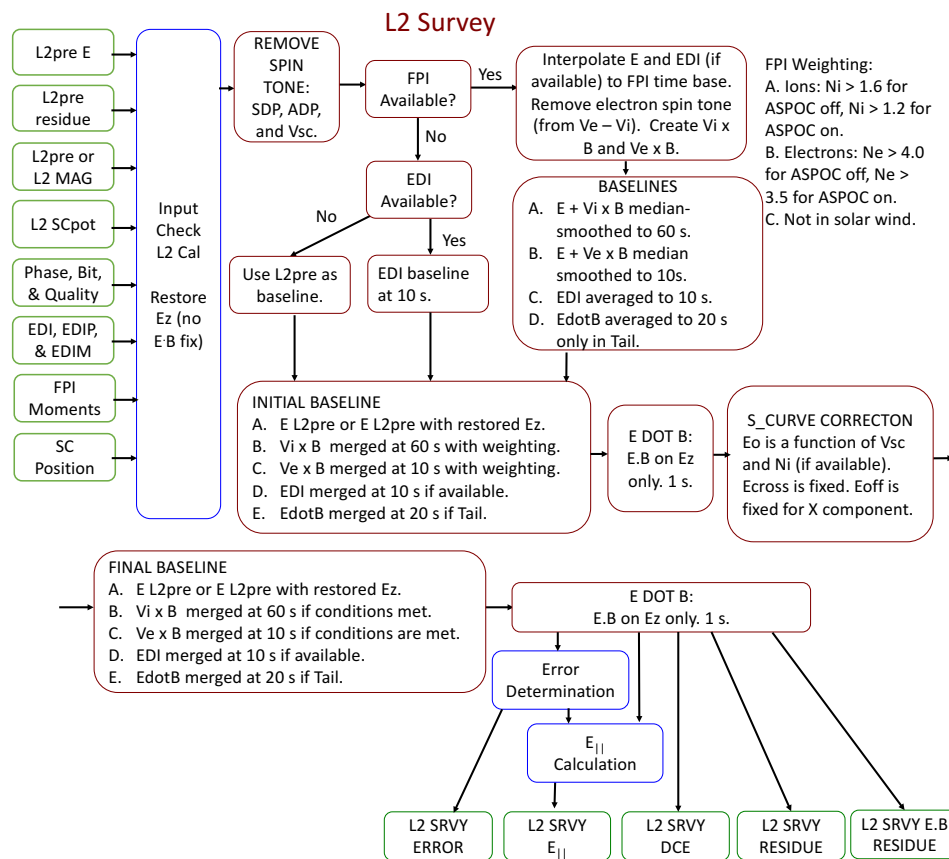


**Figure 11-6 L2 Calibration Algorithm**

### 11.4.4 EPSD Algorithm

The analog electric waveforms measured by EDP are digitalized and processed inside the digital signal processor (DSP) developed by Laboratory of Atmospheric and Space Physics (Ergun et al., 2016). This process provides the raw data for Electric field power spectral density (EPSD). The calibration code gets the processed on board data and applies corrections to hanning window and compressions performed in DSP. We also correct for DSP and Pre-amplifier gains.

The Solitary Wave Detector (SWD) is a data product created by the FIELDS Digital Signal Processor (DSP) board. The intent of the SWD is to make an approximate count of the number of kinetic electric field solitary structures (e.g. phase space holes or double layers) observed per unit time within a set of amplitude ranges. The SWD operates on 65,536 Sample/s waveform data from any of the three antenna differential pair AC-coupled signals (E12 AC, E34 AC, E56 AC). Nominally, and for most of the mission on most spacecraft, the SWD operates on E12 AC data. A window width (32, 64, 128 or 256 points) is specified, as are five threshold amplitude values. These threshold values define the upper and lower bounds on four amplitude bins. For each window, the SWD algorithm calculates a pseudo-rms value and a peak value of the input differential electric field waveform data. The pseudo-rms is calculated as follows: (i) the average of the data in each window is subtracted, (ii) the average-subtracted data within the window are summed, (ii) the summed value is divided by the number of points within the window. The ratio is then calculated of the peak amplitude (maximum absolute value of the average-subtracted data within the window) to the pseudo-rms. If this ratio exceeds 4, the algorithm adds one count to one

SWD amplitude bin. This bin is determined by the peak amplitude value and the used-defined bounds on the four amplitude bins.

The SWD is always active when FIELDS DSP is in Fast Survey, and it returns counts in each of the four defined amplitude bins at a reporting period of  $0.5 * (N + 1)$  seconds, where N can be set from 0 to 63. Internal to the SWD, counts are recorded as a 12-bit number. This number is compressed to eight bits using a lossy pseudo-log compression scheme (3 exponent, 5 mantissa bits) before being returned to the ground.

The SWD data product is successful at identifying regions where the peak/rms value of AC-coupled electric fields is often large (e.g. Hansel et al. 2021, <https://doi.org/10.1029/2021JA029389>).

## 11.5 DATA PRODUCTS

The EDP instrument runs in several modes: **Fast** survey (normally run in the scientific Region of Interest, ROI), **Slow** survey (normally used outside the ROI), and **Burst** (for selected intervals within the ROI). The EDP data products can be broadly divided in **Level 1** (raw data) and **Level 2** (science data). The following table lists the possible combinations and their corresponding folder names in the hierarchical mms data file structure:

Level	Mode			
	Fast	Slow	Burst	Survey
Level 1	L1b	L1b	L1b	L1b
Level 2	L2a, L2pre, L2	L2a, L2pre, L2	L2pre, L2	L2

**Table 11-2 EDP Operating Modes and Data Levels**

As seen, there is a collective name Survey, which encompasses both Fast and Slow survey. The designations l2a and l2pre are used for intermediate and preliminary Level 2 data. For each of the entries in the table above, there are a number of possible available data types:

Mode_Level	Data_type	Access	Description
Level 1 (raw data)			
{fast,slow,brst}_11b	dce	EDP internal	Raw electric field, Individual probe potentials
brst_11b	ace	EDP internal	(Only during commissioning)
brst_11b	hmfe	EDP internal	Raw electric field, $65536 \text{ s}^{-1}$ , 10% duty cycle (adjustable)
srvy_11b	ace	EDP internal	AC electric field, $131072 \text{ s}^{-1}$ , 0.1% duty cycle (16ms/16s)
srvy_11b	dce	EDP internal	Raw electric field, Individual probe potentials (Do not use)

srvy_11b	sweeps	EDP internal	Current-voltage sweeps
Level 2			
{fast,slow}_l2a	dce2d	EDP internal	Raw electric field, Spin fit results and offsets
{fast,slow,brst}_l2pre	dce2d	EDP internal	Despun electric field in DSL, Ez calculated using E.B=0
{fast,slow,brst}_l2pre	dce	EDP internal	Despun electric field in DSL after preliminary calibration
{fast,slow,brst}_l2	dce	Public	Despun electric field in DSL and GSE
brst_l2	hmfe	Public	Despun electric field in DSL, 65536 s <sup>-1</sup> , 10% duty cycle
srvy_l2	hfesp	Public	Electric Field spectra 592 - 65536 Hz
{fast,slow,brst}_l2	scpot	Public	Spacecraft potential, Individual probe potentials
fast_l2	epsd	Public	Power spectral density by DSP
fast_l2	swd	Public	Impulsive Electric Field Structure Counts

**Table 11-3 EDP Data Types and Descriptions**

In the table above, the third column indicates whether the data are intended for internal or public use.

All data are stored in CDF files according to the MMS-wide data standards. For EDP data, the file naming convention is:

<observatory>\_edp\_<mode>\_<level>\_<datatype>\_<datetime>\_<version>.cdf where

<observatory> = {mms1, mms2, mms3, mms4}

<mode> = {fast, slow, brst, srvy}

<level> = {11b, l2a, l2pre, l2, ql, sitl}

<datatype> = {dce, ace, hmfe, hfesp, sweeps, dce2d, scpot} <datetime> = {yyyymmdd, yyyymmddhhmmss}

<datatype> = {dce, ace, hmfe, hfesp, sweeps, dce2d, scpot}

<datetime> = {yyyymmdd, yyyymmddhhmmss}

<version> = vx.y.z

where x, y, and z are the major version, minor version, and revision.

The major version changes when updates to production software have been made to change file format and/or contents. The minor version changes with new calibrations and/or correction of errors which do not affect the file format. The revision is incremented each time a file is re-generated using the same software, e.g., due to more data becoming available.



### 11.5.1 L2 Data Products

**L2\_dce: Final 3D DC E-field in DSL and GSE coordinates.** Both spin plane and spin axis E-field have been processed through elaborate calibration procedures involving comparisons with FPI and EDI data to obtain the best possible scientific data quality. The E-field data are given in both DSL and GSE coordinates.

**L2\_hmfe: EDP despun AC electric field data in DSL.** It contains AC-coupled vector E-field burst data. Data are not sampled continuously, but using a duty cycle.

**L2\_hfesp: EDP E12 electric field spectra.** It contains power spectra of the E12 probe-probe potential difference. Data are not sampled continuously, but using a duty cycle.

**L2\_scpot: Spacecraft potential.** The spacecraft potential is calculated by averaging the four SDP probe-to-spacecraft potentials and correcting for the probe-plasma potential and the short-circuiting effect of the 60 m long booms. The product also contains the probe-spacecraft potential for all 6 EDP probes.

### 11.5.2 Bitmasks and Quality Flags

Many of the data products include a quality indicator and a bitmask indicating specific issues with the data. The quality indicator is a value between 0 and 3, with the meaning given in Table 11-4.

Quality indicator	Meaning
0	Very bad data or no data available
1	Bad data, use with caution
2	OK data, use with some caution
3	Good data

**Table 11-4 EDP Quality Indicator**

The EDP bitmask is a 16-bit unsigned integer where each bit indicates a specific issue with the data, as listed in Table 11-5.

Bit position	Hex value	Decimal value	Meaning if bit is set (1)	Quality index
0	0x0001	1	Probe(-s) are disabled	0
1	0x0002	2	Probe(-s) have bad bias setting	1
2	0x0004	4	Probe(-s) are saturated	0
3	0x0008	8	Probe(-s) are saturated due to low density	1
4	0x0010	16	Probe(-s) are sweeping bias current	1
5	0x0020	32	SDP Probe(-s) are in shadow from ADP Booms	1

6	0x0040	64	ASPOC is emitting non-zero current	2
7	0x0080	128	-	-
8	0x0100	256	Asymmetric probe configuration (e.g MMS4 after 2016-06-12)	2
9	0x0200	512	Maneuver is ongoing	1

**Table 11-5 EDP Bitmask Values and Corresponding Quality Indicator**

### 11.5.3 Level 1 Data Products

**L1b\_dce: EDP raw data (for internal use by the EDP team).** It contains the 3 probe-probe potential differences, used to calculate the vector electric field (E12, E34 and E56), and 3 of the individual probe-spacecraft potentials (V1, V3 and V5).

**L1b\_hmfe: EDP raw AC electric field data (for internal use by the EDP team).** It contains AC-coupled burst data from the 3 probe-probe potential differences. Data are not sampled continuously, but using a duty cycle.

**L1b\_ace: EDP raw AC E12 data (for internal use by the EDP team).** It contains AC-coupled data from the E12 probe-probe potential difference. Data are not sampled continuously, but using a duty cycle. Spectra are produced on ground.

**L1b\_sweeps: EDP current-voltage sweeps (for internal use by the EDP team).** It contains current-voltage sweeps done on the probes for diagnostic purposes, normally at the start and at the end of each ROI.

### 11.5.4 Level 2 Data Products

**L2a\_dce2d: An intermediate E-field product (for internal use by the EDP team).** It contains the electric field in the spinning frame, together with the computed spin fit coefficients, spin phase and various offsets. The L2a fast files are used as input to both the L2pre fast processing and the L2pre burst processing, ensuring consistency between the fast and burst data.

**L2pre\_dce2d: Preliminary 2D DC E-field in DSL coordinates (for internal use by the EDP team).** The spin plane E-field (E<sub>xy</sub>) is computed from the SDP probes (E12 and E34), corrected for various offsets. The spin axis E-field (E<sub>z</sub>) is obtained using the condition  $\mathbf{E} \cdot \mathbf{B} = 0$  when the magnetic field elevation above the spin plane is more than 10 degrees.

**L2pre\_dce: Preliminary 3D DC E-field in DSL coordinates (for internal use by the EDP team).** The spin plane E-field (E<sub>xy</sub>) is unchanged from the preliminary 2D DC E-field, and the spin axis E-field (E<sub>z</sub>) is computed from the ADP probes (E56).

**L2\_epsd: Electric field power spectral density.** It contains the electric field waveforms measured by DSP.

All level 2 data products are listed below.

<b>Brief description:</b> Despun electric field in DSL	
<b>File name:</b> mms{1,2,3,4} edp {fast,slow,brst} l2pre dce2d <datetime> v<x.y.z>.cdf	
Variable name	Description
mms# edp dce dsl {fast,slow,brst} l2pre	Ex, Ey, Ez: Electric field in DSL using E.B=0
mms# edp adp {fast,slow,brst} l2pre	Ez in DSL from ADP E56
mms# edp phase {fast,slow,brst} l2pre	Spacecraft spin phase
mms# edp adc offset {fast,slow,brst} l2pre	Removed ADC offsets
mms# edp delta offset {fast,slow,brst} l2pre	Removed delta offsets
mms# edp bitmask {fast,slow,brst} l2pre	Status bitmask
mms# edp quality {fast,slow,brst} l2pre	Quality flag

**Table 11-6 Despun Electric Field in DSL**

<b>Brief description:</b> Despun electric field in DSL after preliminary calibration	
<b>File name:</b> mms{1,2,3,4} edp {fast,slow,brst} l2pre dce <datetime> v<x.y.z>.cdf	
Variable name	Description
mms# edp dce dsl {fast,slow,brst} l2pre	Ex, Ey, Ez: Electric field in DSL
mms# edp dce par epar {fast,slow,brst} l2pre	Eerr, Epar: Parallel E field and its error
mms# edp dce dsl res {fast,slow,brst} l2pre	Ex, Ey, Ez: Electric field residue
mms# edp dce err {fast,slow} l2pre	Ex, Ey, Ez: Electric field error
mms# edp adc offset {fast,slow,brst} l2pre	Removed ADC offsets
mms# edp delta offset {fast,slow,brst} l2pre	Removed delta offsets
mms# edp bitmask {fast,slow,brst} l2pre	Status bitmask
mms# edp quality {fast,slow,brst} l2pre	Quality flag

**Table 11-7 Despun Electric Field in DSL After Preliminary Calibration**

<b>Brief description:</b> Despun electric field in DSL and GSE	
<b>File name:</b> mms{1,2,3,4} edp {fast,slow,brst} l2 dce <datetime> v<x.y.z>.cdf	
Variable name	Description
mms# edp dce gse {fast,slow,brst} l2	Ex, Ey, Ez: Electric field in GSE
mms# edp dce dsl {fast,slow,brst} l2	Ex, Ey, Ez: Electric field in DSL
mms# edp dce par epar {fast,slow,brst} l2	Eerr, Epar: Parallel E field and its error
mms# edp dce dsl res {fast,slow} l2	Ex, Ey, Ez: Electric field residue
mms# edp dce err {fast,slow} l2	Ex, Ey, Ez: Electric field error
mms# edp bitmask {fast,slow,brst} l2	Status bitmask
mms# edp quality {fast,slow,brst} l2	Quality flag
mms# dsp epsd x	Power spectral density of Ex by DSP
mms# dsp epsd y	Power spectral density of Ey by DSP
mms# dsp epsd z	Power spectral density of Ez by DSP
mms# dsp epsd omni	Omni-directional power spectral density
mms(1 or 4) dsp swd E12 Counts	Counts of waveform data on E12
mms(2 or 3) dsp swd E34 Counts	Counts of waveform data on E34 (Probe 2 disabled)

**Table 11-8 Despun Electric Field in DSL and GSE**

**11.6 APPENDIX A- EDP REFERENCES**

The following documents and drawings in effect on the day this specification was signed **shall** apply to the extent specified herein. In the event of conflict between this document and any referenced document, the document with latest publication date will govern.

The following is a list of applicable references and publications.

<b>Section</b>	<b>Document Number</b>	<b>Title</b>	<b>Revision/Date</b>
tbd	461-XXX-XXXX-0###	EDP Item Name	Rev / date
tbd	461-XXX-XXXX-0###	EDP Item Name	Rev / date
	<a href="https://doi.org/10.1007/s11214-014-0115-x">https://doi.org/10.1007/s11214-014-0115-x</a>	Ergun, R.E., Tucker, S., Westfall, J. et al. (2016). The Axial Double Probe and Fields Signal Processing for the MMS Mission. Space Sci Rev 199, 167–188.	
	<a href="https://doi.org/10.1007/s11214-014-0116-9">https://doi.org/10.1007/s11214-014-0116-9</a>	Lindqvist, P.-A., Olsson, G., Torbert, R.B., et al. (2016). The Spin-Plane Double Probe Electric Field Instrument for MMS. Space Sci Rev 199, 137-165.	

**Table 11-9 EDP Applicable Documents**

## 12.0 FLUXGATE-SEARCHCOIL-MERGED MAGNETIC FIELD (FSM)

### 12.1 FSM OVERVIEW

The Fluxgate-Searchcoil Merged (FSM) data product for the Magnetospheric Multiscale (MMS) mission is created by merging data from the fluxgate (FGM) and searchcoil (SCM) magnetometers into a single level-3 data product. The merging method involves pre-flight timing and noise floor analysis determining the in-flight noise floor as well as. The resulting data product has the DC component of FGM, the sampling rate and Nyquist frequency of SCM, and a reduced noise floor within the transition band of the merging filter. Here, we describe the statistical inter-calibration process as well as the merging filter. A full description of the SCM-FGM cross-calibration methodology, the merging filter, and the applications of the dataset can be found in the following two publications:

Fischer, D., Magnes, et al. (2016). Optimized merging of search coil and fluxgate data for MMS. *Geoscientific Instrumentation, Methods and Data Systems*, 5(2), 521–530.  
<https://doi.org/10.5194/gi-5-521-2016>

Argall, M. R., Fischer, D., Le Contel, O., Mirioni, L, et al. (2018). The Fluxgate-Searchcoil Merged (FSM) Magnetic Field Data Product for MMS. *ArXiv E-Prints*.  
<https://arxiv.org/abs/1809.07388>

### 12.2 INPUT DATA

Input data for the FSM data product comes from the L1A FGM and L1B SCM datasets. The L2 datasets are not used because the merging process needs to occur before data from the different axes are mixed via coordinate system rotations. For FGM and SCM, the closest common coordinate system is Orthogonalized Magnetometer (OMB), which, for FGM, differs from the 123 sensor coordinate system by an orthogonalization transformation and is equivalent to the SCM 123 sensor coordinate system. Data in OMB coordinates is not available at in L2.

In addition, only burst data is merged. The fast and slow survey mode data products are not merged.

#### 12.2.1 FGM

Two fluxgate magnetometers are used to create the FGM dataset: the analog fluxgate (AFG) and digital fluxgate (DFG) magnetometers. The sensors differ by the addition of a tuning capacitor in AFG. The electronics, however, were designed based on different operating principles (Russell et al. 2014; Magnes et al. 2008), providing robust redundancy. Data from AFG is used for the survey dataset and DFG is used for the burst dataset. As a result, the burst FSM data also uses data from the DFG instrument.

DFG data is sampled at 8192 S/s and is decimated to the burst data rate of 128 S/s by two, named DEC32 and DEC64. In DEC32 mode, the sampling rate is reduced to 256 S/s via a 32-point average, then is decimated to 128Hz. This mode produces aliasing, but reduces the group delay so that the magnetic field can be passed faster to the Electron Drift Instrument (EDI) (Torbert et al. 2015) for beam emittance angle adjustments, reducing the amount of prediction required. In DEC64 mode, the sampling rate is reduced to 128 S/s directly via 64-point averaging. Each mode has unique effects on the measured signal and so are handled separately in the production of the FSM dataset.

The DFG data in OMB coordinates is processed to L2-quality via the same algorithms that process the publicly available L2 datasets. This folds in the results of in-flight calibration, which entails 1) spin tone removal to determine orthogonalization parameters, 2) range joining to remove jumps between low- and high-range, 3) cross-calibration with the Electron Drift Instrument (EDI) (Torbert et al. 2014) and/or

application of the Davis-Smith method (Leinweber, et al. 2008) to remove spin-axis offsets, 4) earth-field comparisons to determine absolute calibration factors, and 5) inter-spacecraft comparisons to remove relative differences. Additional details of the calibration and L2 processing can be found in (Russell et al. 2014).

From here onward, DFG and AFG data are referred to as FGM data, where FGM burst data implies the use of DFG and FGM survey data implies the use of AFG. Individual instrument names will be used only when specific instrument characteristics require it.

### 12.2.2 SCM

The SCM L1B data is already calibrated by the SCM instrument team. This involves 1) decompression, 2) data cleaning, 3) conversion from counts to Volts, 4) application of a transfer function to convert Volts to nano-Tesla (nT), and 5) application of a high-pass filter with cutoff at 0.5 Hz for burst data. A definitive description of the SCM L1B data product can be found in the SCM section of this CMAD.

## 12.3 MERGING METHODOLOGY

The Finite Impulse Response (FIR) filter designed to merge the FGM and SCM datasets uses knowledge of the noise floor of each instrument observed in-flight to determine the cross-over frequency at which the two datasets are merged. The FSM data product consists primarily of FGM data below the cross-over frequency and SCM data above the cross-over frequency. The cross-over frequency is where the noise floors of the two instruments intersect.

### 12.3.1 In-Flight Noise Floor

The FGM and SCM instrument noise floors are determined in-flight. Figure 12-1 outlines the procedure. The top row of panels show the power spectral density (PSD) of the x-component of the magnetic field measured by DFG and SCM for an entire burst data file on 2015-09-01. Here and in the figures that follow, DFG data is presented in the left column and SCM data in the right column. The second row shows the distribution of signal as a function of frequency. At each frequency, the PSD was separated into bins of size  $0.5 \text{ Log}(nT^2/\text{Hz})$  and accumulated over the duration of the burst file. In the last row, histograms from all burst files in September of 2015 were accumulated into a single distribution.

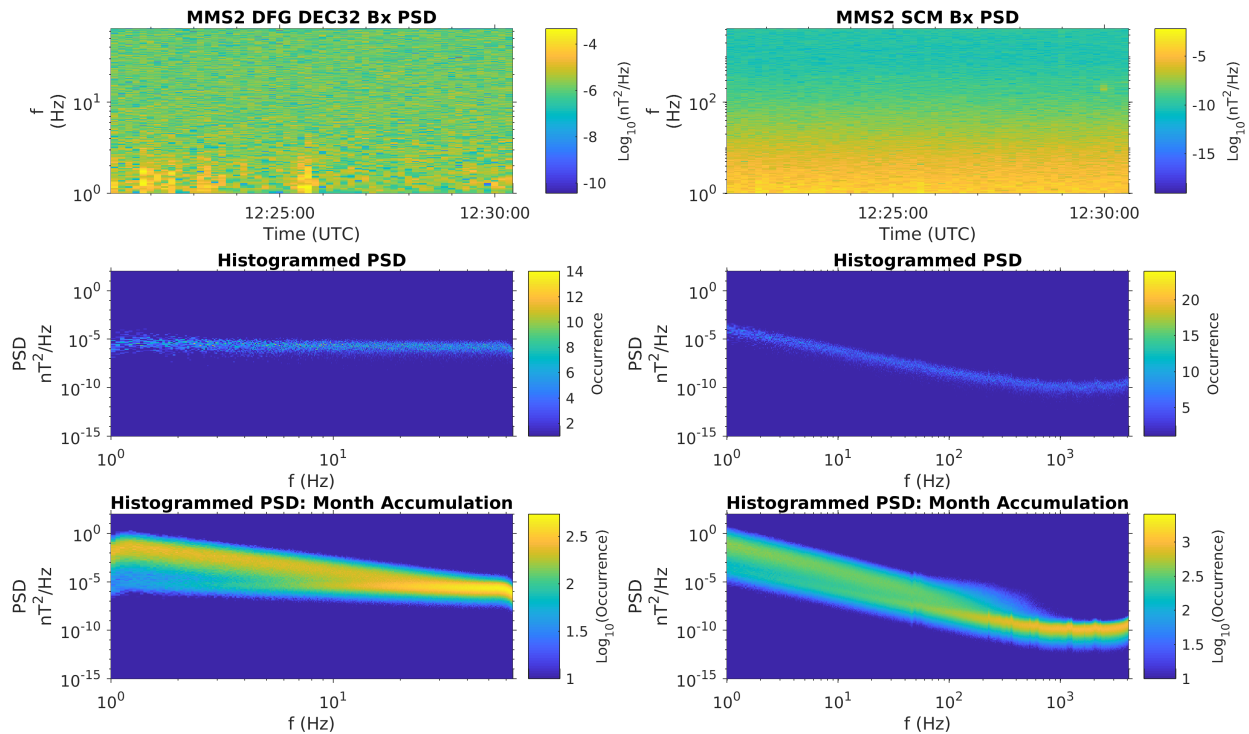


**Figure 12-1 Method for Determining the In-flight Noise Floors (top). The PSD of the Time Series Waveforms is Calculated for a Burst Interval (middle). The PSD is Histogrammed at Each Time Step (bottom). The Histograms are Accumulated Across All Burst Intervals.**

To compute the PSDs, FGM is first high-pass filtered with a cut-off frequency of  $f_c = 1\text{Hz}$  to mimic the SCM calibration process and to prevent leaking of DC signal to higher frequencies. Next, a sinc-function and Chebyshev window taper  $T = 20\text{ s}$  data intervals which are then Fast Fourier Transformed (FFT-ed) to the frequency domain to calculate PSD. Subsequent windows contain 50% overlap. A time interval of  $T = 20\text{ s}$  was chosen for both FGM and SCM for two reasons: 1) a frequency resolution of  $\Delta f = 1/T = f_s/N = 0.05\text{Hz}$  (where  $f_s$  is the sample rate and  $N$  is the number of samples per FFT) is high enough to decipher peaks in the statistical distributions, and 2) the frequency bins and their spacing are the same for DFG and SCM up to the Nyquist frequency  $f_N$  of DFG. This allows us to make gain and phase comparisons between the two instruments, as will be shown later.

The PSD histograms have a bimodal distribution that is better seen in Figure 12-2, which shows vertical cuts through each component at 2Hz. Overplotted as a blue vertical line is the mean value of the noise floor across each component. A peak at a PSD of  $\sim 10^{-6}\text{ nT}^2/\text{Hz}$  for FGM and  $\sim 10^{-5}\text{ nT}^2/\text{Hz}$  occurs slightly below the value of the ground-measured noise floor at 2Hz. This peak is the in-situ measured noise floor.

A second, larger distribution of occurs to the right of the first. Unlike the peaks associated with the noise floor, it is observed at the same PSD value of  $\sim 10^{-2}$  nT<sup>2</sup>/Hz for both FGM and SCM. Plots similar to were made for individual burst intervals containing significant wave activity and revealed peaks in the distribution coincident with this second peak (not shown). Thus, this second peak is associated with signal driven by physical phenomena.

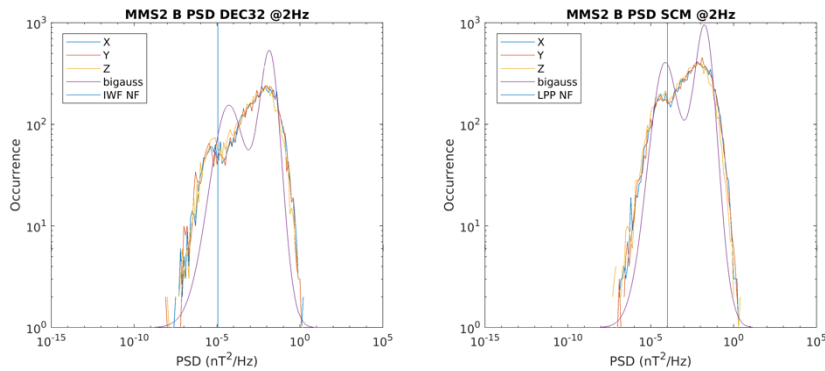


**Figure 12-2 Bimodal Distribution in PSD Identifies Noise Floor and Signal Peaks (A cut through the PSD histograms at 2 Hz reveals a bimodal distribution with the left peak associated with noise and the right peak associated with signal.)**

Such a procedure has been applied to all three components of the magnetic field (Figure 12-3). The peaks associated with the in-flight noise floor (green circles) and physical signal (magenta x's) were identified by eye at a select number of frequencies and fit with an exponential (solid lines of the same color). The noise floor determined on the ground for FGM and SCM is represented by the red dashed line in each panel. Note that the ground-measured noise floor overlaps with the noise floor observed in-flight.

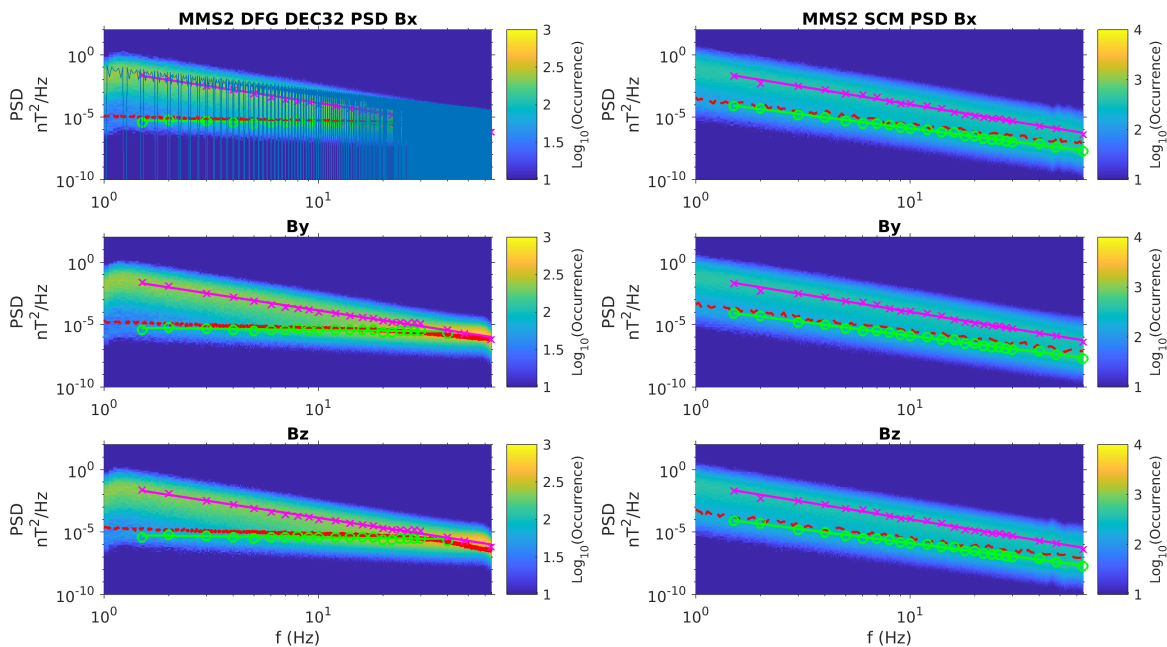


**Figure 12-3 In-flight Noise Floor Coincides with Ground-Measured Noise Floor (Histogrammed PSD for FGM (left) and SCM (right), x,y, and z-components (top, middle, bottom). Noise floors are overplotted in magenta. Hand-picked peaks in PSD are in green and magenta.)**



### 12.3.2 Cross-Over Frequency

Applying this methodology to all four spacecraft results in fits to the noise and signal distributions observed by each spacecraft. These are shown in Figure 12-4. The noise spectrum is distinct for each instrument, but the signal spectrum is the same to within the accuracy of the methodology, providing additional support for the classification.

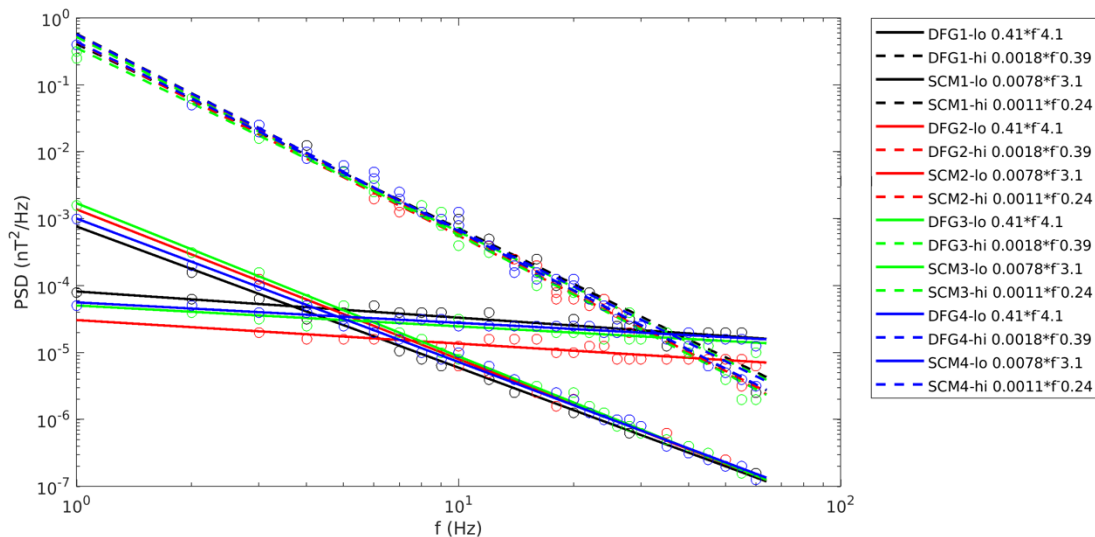


**Figure 12-4 Noise and Signal Distribution for FGM and SCM, Along with Their Functional Forms (“lo” (hi) represents the noise (signal) distribution fits.)**

The frequency at which the noise floor fits from FGM and SCM intersect one another (the “cross-over” frequency, 4-5 Hz) determines the cut-off frequency of the merging filter, described later.

### 12.3.3 Cross-Calibration

Signal gain and phase differences between FGM and SCM must be accounted for in the merging process. To calculate gain and phase delays, the noise and signal distributions must be separated. This is accomplished by selecting a frequency-dependent threshold value for PSD below which all values are considered noise and above which all values are considered signal. The threshold value is taken to be the maximum between components of the ground-measured noise floor at each frequency. This was chosen because the pre-flight noise floor is higher than the in-situ noise floor. By separating the signal from the noise distributions, we are able to compare DFG and SCM signals to determine long-term trends in gain and phase delays.

Gain for the signal distribution is shown in the left column of Figure 12-5. It is computed as  $G = |R^2|$ , where  $R = B(f)/\delta B(f)$  and  $B(f)$  and  $\delta B(f)$  are the FFTs of the magnetic field measured by FGM and SCM, respectively. The gain and phase delays are then histogrammed by the same procedures as for PSD described in section 12.3.1, with bin sizes for gain and frequency of 0.5 and 0.05Hz, respectively. Signal gain  $G_S = 1$  throughout the frequency range of FGM, which is a testament to the calibration and cross-calibration efforts undertaken by the magnetometer teams. The width of the distribution increases toward higher frequency, which is primarily caused by the lack of sufficiently strong signal and an inability to cleanly separate noise from signal at  $f > 20$  Hz.

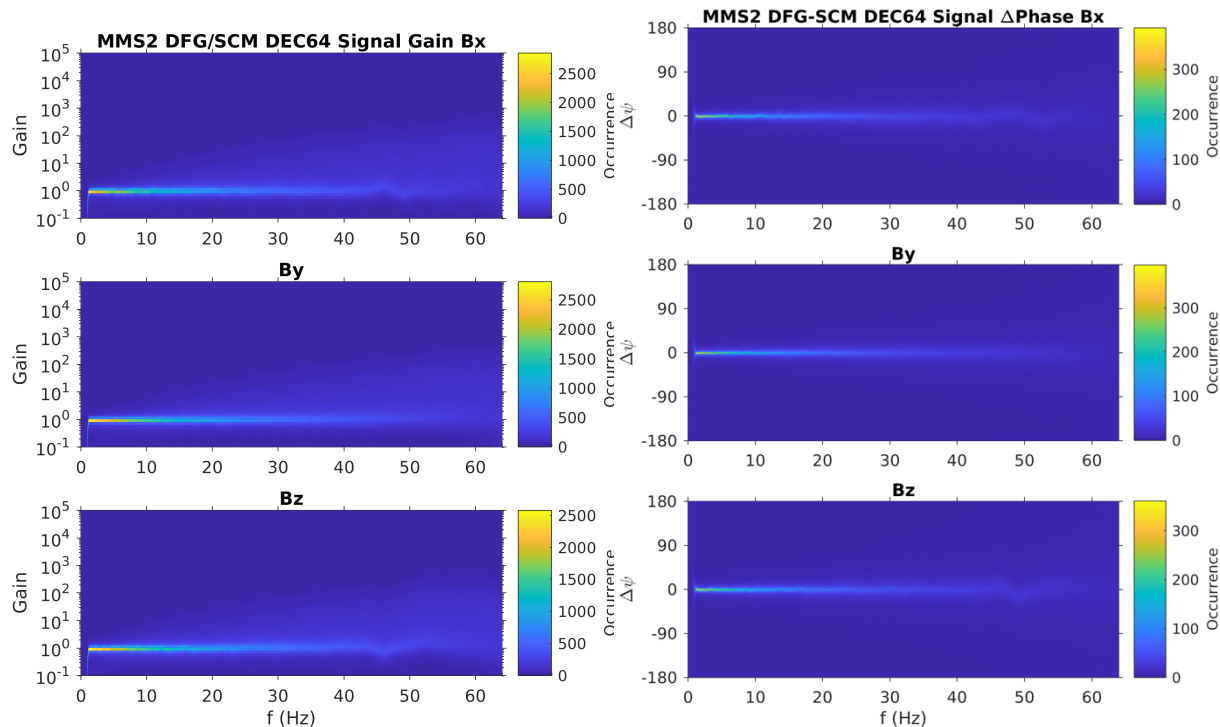


**Figure 12-5 Gain Ratio and Phase Differences Between DFG and SCM Used for Cross-Calibration Purposes (The gain ratio is unity and there is zero phase difference so there is no need for correction in the FSM algorithm.)**

Phase delay distributions are shown in the right half of Figure 12-5. Phase delay is computed as  $\Delta\varphi = \tan^{-1}(\Re(R)/\Im(R))$  then histogrammed in the same manner as PSD and gain. Distributions associated with signal are strongly peaked at  $\Delta\varphi = 0^\circ$ , indicating the high timing accuracy between the two instruments. Again, the distribution spreads as frequency approaches  $f_N$ .

In summary, cross-calibration reveals a signal gain of  $G_S = 1$  and a phase delay of  $\Delta\varphi = 0^\circ$ , indicating that no further corrections are required before merging the data.

### 12.3.4 FIR Filters

The FIR filter for FGM consists of three separate low-pass FIR filters with cutoff frequencies  $f_c$  of 4, 7, and 32 Hz. The two filters with  $f_{c1} = 4$  Hz and  $f_{c2} = 7$  Hz serve to provide an interval of 50% gain surrounding the cross-over frequency  $f_x$  of each instrument pair. Both are sinc functions truncated at 16385 points (2 s duration) and tapered with a Blackman window. The third FIR filter with  $f_{c3} = 32$  Hz acts as an anti-aliasing filter. It is a sinc function truncated at 2049 points (0.25 s duration) tapered with a Chebychev window. The total duration of the filter is 4.25 s.

An equivalent high-pass merging filter for SCM is constructed via spectral reversal of the low-pass FIR filter such that the sum of their gains is unity across all frequencies.

Figure 12-5 shows the impulse and frequency response of the low- and high-pass FIR filters. Cut-off frequencies of the three filters are depicted by green vertical lines in the frequencies response panels. Between the lower two cut-off frequencies, there is an interval of 50% gain for both filters, effectively averaging the two instruments together within the interval. The reason for this is that the noise distributions in Figure 12-2 and Figure 12-3 have a finite width, indicating that the cross-over frequency

is more of a cross-over frequency interval. This is apparent in individual spectra (shown later). Beyond 32 Hz, the antialiasing filter prevents signal above the FGM Nyquist frequency from folding back into the spectra.

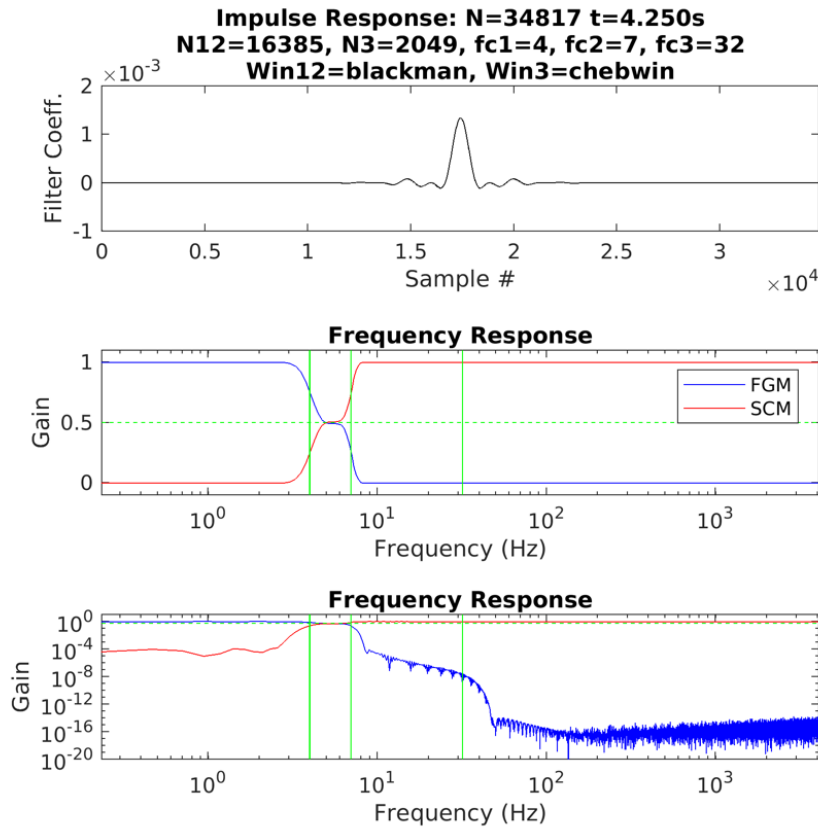


**Figure 12-6 FIR Filter that Merges the FGM and SCM Datasets (The impulse response (top) and frequency response (center, bottom ) of the FIR filter. Merging occurs between 3 and 6 Hz.)**

### 12.3.5 Improved Noise Floors

One benefit of the merging filter is that the resulting FSM dataset has a reduced noise floor within the bandpass of the merging filter when compared to the FGM and SCM noise floors individually. This is apparent when the merging filter is applied to the FGM and SCM noise spectra determined in Figure 12-2 and Figure 12-3. Figure 12-6 shows the results with the FGM noise and signal spectra shown in blue, the SCM noise and signal spectra shown in green, and the resulting FSM noise and signal spectra shown in red. The cut-off frequencies of the three merging filters are shown as vertical lines. Below  $f_{c1}$ , the FSM noise floor is that of FGM while above  $f_{c2}$  the FSM noise floor is that of SCM. Within the merging region, the resulting FSM noise floor is reduced compared to the FGM and SCM noise floors.

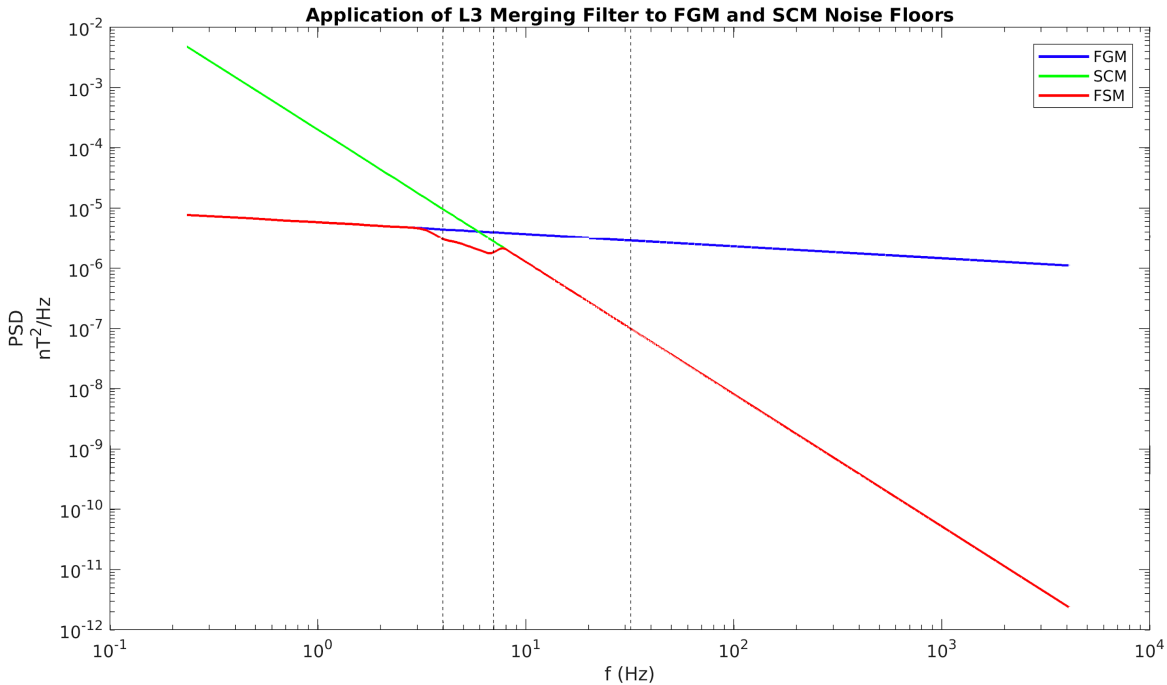


**Figure 12-7 Application of the Merging Filter Results in an Improved Noise Floor for the FSM Data Product (The merging filter is applied to the observed noise and signal spectra, resulting in a lower noise floor within the 4-7 Hz bandpass).**

### 12.3.6 Validation

To validate the merging filter, it is applied to FGM and SCM data during a quiet interval identified through spectrograms and histograms as in for events when the PSD distribution overlaps with the observed noise floor. The resulting spectra for FGM (solid blue), SCM (solid red), and FSM (solid black) are shown in Figure 12-8 for the x-, y-, and z-components. The respective ground-measured noise floor and the noise and signal distributions are plotted as dotted, dashed, and dot-dashed lines and the central frequency of the cross-over interval is represented by a vertical dashed line. The FSM spectra is invisible underneath the FGM and SCM spectra except near the cross-over frequency, where it is smaller in magnitude. Thus, the merging process successfully creates a new FSM data product that behaves like FGM at low frequencies, SCM at high frequencies, and has a lower noise floor in the merging interval.

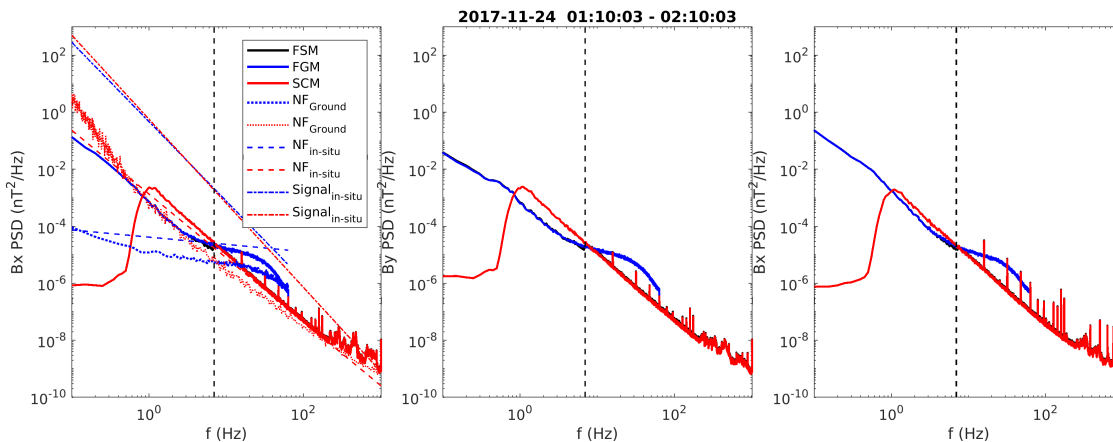


**Figure 12-8 FSM Data Shown as the Merger of FGM and SCM Data with Improved Noise Floor in the Merging Interval**

### 12.4 DATA PRODUCT ALGORITHM DESCRIPTIONS

An overview of the FSM algorithm is shown in Figure 12-9. Level 1A FGM data (upper-left green oval) in OMB coordinates is processed through the standard L2 data processing algorithm described in the FGM CMAD section. The data is then segregated by sampling rate, DEC32/DEC64, hi/lo-range, and other operating modes for individual analysis. To align the time tags with the SCM data, a 1 kHz compensation filter (Fischer, et al. 2016) is applied, the data is resampled to 8 kHz, and a fractional delay is applied. At this point, the FGM data is ready to be merged.

The L1B SCM data in OMB coordinates (lower-right green oval) is examined for mode (e.g. sampling rate) changes and data gaps produced by the low-pass filter (see the SCM CMAD section). It is then ready to be merged.

Next, the low-pass merging filter is applied to the FGM data, the high-pass merging filter is applied to the SCM data, and the resulting data is summed together to produce an FSM data product in OMB coordinates. Standard algorithms are then applied to transform the data into GSE and GSM coordinates.

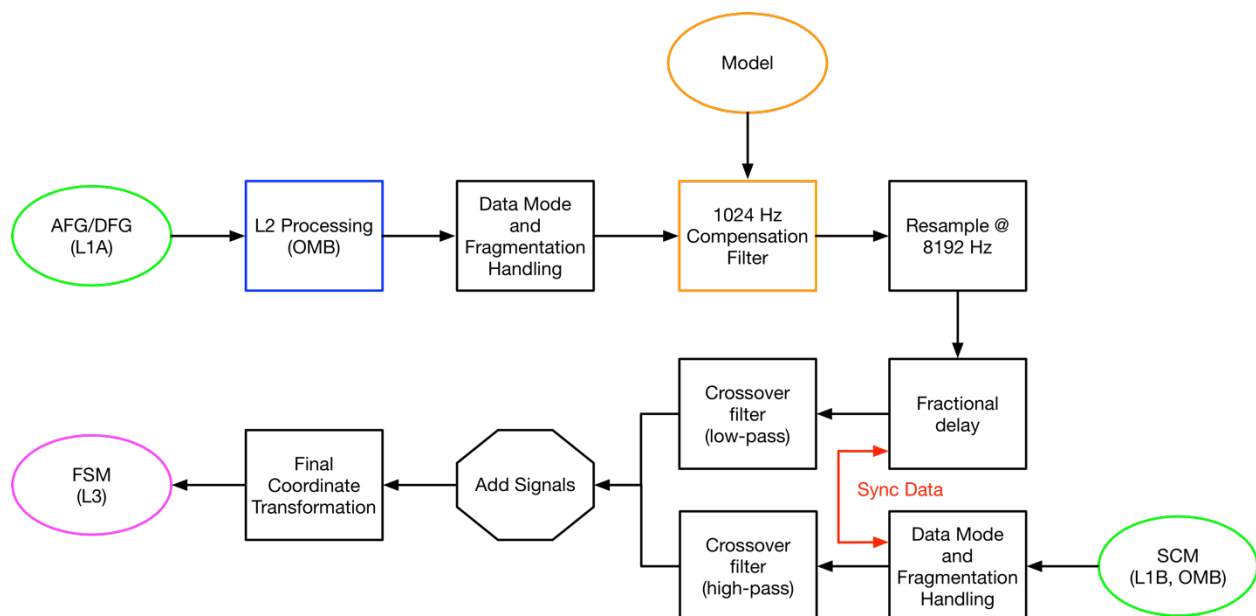


**Figure 12-9 Work Flow of the FSM Merging Process**

### 12.5 FILE STRUCTURE

#### 12.5.1 L3 FSM 8kHz

##### 12.5.1.1 Variables

Variable Name	Description
Epoch	Timestamps of the time series magnetic field data
[sc] fsm epoch delta brst l3	Sample interval of the time series magnetic field data
[sc] fsm b gse labls brst l3	Axis labels for the magnetic field data in GSE coordinates
Epoch state	Time stamps for the state variables

label r_gse	Axis labels for the spacecraft position in GSE coordinates
represent vec_tot	Components of the position variable
[sc] fsm b_gse brst l3	Vector magnetic field in GSE coordinates
[sc] fsm r_gse brst l3	Spacecraft position in GSE coordinates

**Table 12-1 FSM File Structure Variables**

### 12.5.1.2 File Versions

Version	Modifications
v1.0.0	First version
v1.1.0	Updated valid data range for B and DEPEND_0 for flags.

**Table 12-2 FSM File Versions**

## 12.6 APPENDIX A- FSM REFERENCES

The following documents and drawings in effect on the day this specification was signed **shall** apply to the extent specified herein. In the event of conflict between this document and any referenced document, the document with latest publication date will govern.

The following is a list of applicable references and publications.

Section	Document Number	Title	Revision/Date
	<a href="https://arxiv.org/abs/1809.07388">https://arxiv.org/abs/1809.07388</a> <a href="https://doi.org/10.48550/arXiv.1809.07388">https://doi.org/10.48550/arXiv.1809.07388</a>	Argall, M. R., et al., (2018). The Fluxgate-Searchcoil Merged (FSM) Magnetic Field Data Product for MMS. <i>ArXiv E-Prints</i> .	
	<a href="https://doi.org/10.5194/gi-5-521-2016">https://doi.org/10.5194/gi-5-521-2016</a>	Fischer, D., Magnes, et al. (2016). Optimized merging of search coil and fluxgate data for MMS. <i>Geoscientific Instrumentation, Methods and Data Systems</i> , 5(2), 521–530.	
	<a href="https://doi.org/10.1088/0957-0233/19/5/055104">https://doi.org/10.1088/0957-0233/19/5/055104</a>	Leinweber, H. K., Russell, C. T., Torkar, K., Zhang, T. L., & Angelopoulos, V. (2008). An advanced approach to finding magnetometer zero levels in the interplanetary magnetic field. <i>Measurement Science and Technology</i> , 19(5), 55104.	
		Magnes, W., Oberst, M., Valavanoglou, A., Hauer, H., Hagen, C., Jernej, I., et al. (2008). Highly integrated front-end electronics for spaceborne fluxgate sensors. <i>Measurement Science and Technology</i> , 19(11), 115801.	

	<a href="https://doi.org/10.1007/s11214-014-0057-3">https://doi.org/10.1007/s11214-014-0057-3</a>	Russell, C. T., Anderson, B. J., Baumjohann, W., Bromund, K. R., Dearborn, D., Fischer, D., et al. (2014). The Magnetospheric Multiscale Magnetometers. <i>Space Science Reviews</i> , 199(1), 189–256.	
	<a href="https://doi.org/10.1007/s11214-014-0109-8">https://doi.org/10.1007/s11214-014-0109-8</a>	Torbert, R. B., Russell, C. T., Magnes, W., Ergun, R. E., Lindqvist, P.-A., Le Contel, O., et al. (2016). The FIELDS Instrument Suite on MMS: Scientific Objectives, Measurements, and Data Products. <i>Space Science Reviews</i> , 199(1), 105–135.	
	<a href="https://doi.org/10.1007/s11214-015-0182-7">https://doi.org/10.1007/s11214-015-0182-7</a>	Torbert, R. B., Vaith, H., Granoff, M., Widholm, M., Gaidos, J. A., Briggs, B. H., et al. (2016). The Electron Drift Instrument for MMS. <i>Space Science Reviews</i> , 199(1), 283–305.	

**Table 12-3 FSM Applicable Documents**

### 13.0 APPENDIXES

List of abbreviations, acronyms, units, and measurements are gathered below. It is important to note that these charts are reflective of this document and may not be comprehensive of all of the possibilities and meanings for each term.

#### 13.1 ABBREVIATIONS AND ACRONYMS

Abbreviation / Acronym	Definition
ABM	Absolute Beam Monitor
AC	Alternating Current
ACB	AC Magnetic Field
ADCDES	Analog to Digital Converter Dual Electron Spectrometer
ADP	Axial Double Probe
ADPDIS	Axial Double Probes Dual Ion Spectrometer
AFG	Analog Flux Gate Magnetometer
APID	Application Process Identifier
APL	Applied Physics Laboratory
ASPOC	Active Spacecraft Potential Control Instrument
ATS	Absolute Time Sequence
AZ	Azimuth
BBF	Bursty Bulk Flow
BCS	Body Coordinate System
BDM	Burst Data Management
BEB	Boom Electronic Board
BEBFPI	Boom Electronic Board Fast Plasma Investigation
Bkgd	Background (in data quality the discussion is regarding correction for background counts)
BPS	Bits Per Second
BWC	Bandwidth Connection
CCSDS	Consultative Committee for Space Data Systems
CDF	Common Data Format
CDPU	Command and Data Processing Unit
CEB	Central Electronics Box
CETP	Centre d'étude des Environnements Terrestre et Planétaires
CIDP	Central Instrument Data Processor
CLN	Cleaning Active
CMAD	Calibration and Measurement Algorithms Document
COMP	Compensating Mode Option
CPOT	So-Called Feedback Mode
CRBG	Cosmic Ray Background
CRSF	Clock Rate Scaling Factor
Ct	Counts
CtRt	Count Rate
DBCS	De-spun Body Coordinate System
DC	Direct Current
DCC	DC Converter



DCE	3D DC E-field
DCE2D	2D DC E-field
DE	Development Ephemeris
DEF	Deflection
DES	Dual Electron Spectrometer
DFG	Digital Flux Gate Magnetometer
DIS	Dual Ion Spectrometer
DMPA	De-Spun Major Principal Axis
DPG	Data Products Guide
DPU	Data Processing Unit
DSCS	De-Spun Spin-Axis Coordinate System
DSL	Despun Spacecraft L-axis (coordinate system)
DSP	Digital Signal Processor
DSPFRC	DSP Frequency Response Range Correction
DWT	Discrete Wavelet Transform
DWT/BPE	Discrete Wavelet Transform and Bit Plane Encoder
ECEF	Earth-centered, Earth-fixed Coordinate System
ECI	Earth-Centered Inertial
EDI	Electron-Drift Instrument
EDP	Electric Double Probes
EIS	Energetic Ion Spectrometer
EPD	Energetic Particle Detector
EPSD	Electric field Power Spectral Density
E/Q	Energy Steps
ESA	Electrostatic Analyzer
EUV	Extreme Ultraviolet
FCS	FEEPS Coordinate System
FDOA	Flight Dynamics Operations Area
FEEPS	Fly's Eye Energetic Particle Spectrometer
FFT	Fast Fourier Transformed
FGM	Flux Gate Magnetometer
FIELDS	MMS Instrument Suite for the Measurement of Fields and Waves
FIR	Finite Impulse Response
FIT	FIELDS Integrated Timing/ FIELDS Interference and Timing
FK5	Fifth Fundamental Catalogue
FLT	Fractional Live Time
FM	Flight Model
FOV	Field of View
FPGA	Field Programmable Gate Arrays
FPI	Fast Plasma Investigation
FS	Fast Survey
FSM	Fluxgate-Searchcoil-merged Magnetic Field
FSW	Flight Software
FWHM	Full Width at Heigh Maximum

GDU	Gun-Detector Unit (two per Electron-Drift Instrument)
GEO	Geocentric Geographic
GEOS-2	Geostationary Scientific Satellite (European Space Agency)
GF	Geometric Factor
GSE	Geocentric Solar Ecliptic (coordinate system)
GSFC	Goddard Space Flight Center
GSL	Gnu Scientific Library
GSM	Geocentric Solar Magnetospheric
HEX	Hexadecimal
HOTS	Hot Standby Mode
HPCA	Hot Plasma Composition Analyzer
HV	High Voltage
HVPS	High Voltage Power Supplies
HWC	Hanning Window Correction
IAU	International Astronomical Union
ICRF	International Celestial Reference Frame
IDL	Interactive Data Language (coding language)
IDPU	Instrument Data Processing Units
IGRF	International Geomagnetic Reference Field
IION	Constant Ion Current Mode
IIR	Infinite Impulse Response
IMF	Interplanetary Magnetic Field
ION	Ion Data
IRAP	French Institut de Recherche en Astrophysique et Planetologie
IS	Instrument Suite
ISAS	Japanese Institute for Aeronautics and Astronautics
ISTP/SPDF	International Solar-Terrestrial Physics/Space Physics Data Facility
ITF	Instrument Team Facility
ITOT	Constant Total Current Mode
ITRF	International Terrestrial Reference Frame
IUM	Instrument User Manual
IWF	Space Research Institute of the Austrian Academy of Sciences
JAXA	Japan Aerospace Exploration Agency
JPL	Jet Propulsion Laboratory
L	Level
LASP	Laboratory for Atmospheric and Space Physics
LEEIF	Low Energy Electron and Ion Facility
LPP	Laboratoire de Physique des Plasmas
LT	Live Time
LTC	Live Time Correction
LUT	Onboard Lookup Tables
LVPC	Low Voltage Power Converters

MAGNETSRODE	Magnetic Coil Facility at the Technical University Braunschweig, Germany
MCP	Micro Channel Plate
MEC	Magnetic Ephemeris Coordinates
MLI	Multi-Layer Insulation
MMS	Magnetospheric Multiscale Mission
MOD	Mean of Date
MOM	Moments
MPA	Major Principle Axis
MSFC	Marshall Space Flight Center
NASA	National Aeronautics and Space Administration
NOE	No Emission (Startup Active)
OFF	Instrument Not Active
OLR	Outgoing Longwave Radiation
OMB	Orthogonalized Magnetometer Boom
PA	Pitch Angle
PDMP	Project Data Management Plan
PEF	Pseudo Earth Fixed
PH	Pulse Height
PPS	Pulse Per Second
PSD	Power Spectral Density
RB	Radiation Belt
RBSPICE	Radiation Belt Storm Probes Ion Composition Experiment
RF	Radio Frequency
ROI	Region of Interest
RPA	Retarding Potential Analyzer
RTS	Relative Time Sequence
SA	Spin Axis
S/C ; SC	Spacecraft Coordinate System; Signal Loss Crosstalk; Spacecraft
SCDRC	Spectral Compression Dynamic Range Correction
SCM	Search Coil Magnetometer
SCMFRC	SCM Frequency Response Correction
SdC	Spectra Data deCompressed
SDC	Science Data Center
SDP	Spin-Plan Double Probe Electric Field Instrument
SITL	Scientist In The Loop
SION	Fuel Save Mode Option
SLAV	Slave Mode
SLERP	Spherical Linear Interpolation
SM	Solar Magnetic Coordinates
SMPA	Spinning Major Principal Axis (MPA)-aligned Coordinates
SOC	Science Operations Center
SPEDAS	Space Physics Environment Data Analysis System
SPOT	Fuel Save Mode Option
SS	Slow Survey

SSD	Solid-state Detectors
SSL	Spinning Spacecraft, Angular Momentum Vector (L) Aligned
STAFF	Spatio-Temporal Analysis of Field Fluctuations experiment (ESA Cluster mission)
STDB	Standby Mode
STEMP	Sensor Temperature Parameter
STOT	Fuel Save Mode Option
STP	Solar Terrestrial Probe
STUP	Startup State
SwRI	Southwest Research Institute
TAI	International Atomic Time
TECH	Technical Mode
TEME	True Equator, Mean Equinox
TEST	Test and Commissioning Mode
TF	Search-coil Magnetometer Response
THEMIS	Time History of Events and Macroscale Interactions during Substorms (mission)
TOD	True of Date
TOF	Time of Flight
TOF-DN	Time of Flight Data Number
UCLA	University of California, Los Angeles
UNH	University of New Hampshire
UTC	Coordinated Universal Time / Universal Time Coordinated
UV	Ultraviolet
WF	Wave Form

### 13.2 UNITS AND MEASUREMENT

Abbreviation Unit / Measurement	Definition
b	Magnetic Field Unit Vector
B	Magnetic Field Strength
dB	Decibel
dBV/nT	Decibel Volts per NanoTesla
C/A	Counts per Accumulation
C/S	Counts per Second
deg	Degree
dxdv	Phase Space Volume Element
E	Particle Energy
$e$	Energy
e	Elementary Charge
Eff	Efficiency
EGM	Geometric Mean of the Energy Bounds of the Energy Channel
eV	Energy (electronvolt)
E <sub>xy</sub>	Spin Plane E-field
E <sub>z</sub>	Spin Axis E-field
F(v)	Plasma Distribution Function / Velocity Distribution Function
Hz	Frequency (Hertz)
$I$	Intensity
kbit/s	Kilobit/Second
keV	Energy (kiloelectronvolts)
kHz	Frequency (kilohertz)
km/s	Distance; kilometers/second; ExB Velocity
$m$	Ion Species Dimension Symbol; Time of Flight Binning Mediating Parameter; Ion Mass to Charge Ratios
Mbit	Megabit
Mbytes	Megabyte
ms	Time (milliseconds)
mV/m	Electric Field
nA	Current (nanoamps)
nT	Magnetic field strength (nanoteslas)
ns	Time (nanoseconds)
ohm	Electrical Resistance
P	Physical Values
ppm	Parts Per Million
R	Raw Values
R <sub>E</sub>	Earth Radii
S/s	Samples/Second
t	Time
TA	Channel Accumulation Period
VDEF	Voltage of the Deflector
VESA	Voltage of the Electrostatic Analyzer

$V_{e,x}$	Electron Velocity
$V_{i,x}$	Ion Velocity
$\Delta E_x$	DSL Offset
$\Delta E_y$	DSL Offset
$\nabla f_e$	Vector Spatial Gradient Term
$\alpha$	Amplitude Correction ; Azimuth Dimension ; Spin-energy Sweep Mediating Parameter
$\beta$	Elevation Dimension Symbol ; Start Anode Mediating Parameter
$\partial f_e / \partial t$	Temporal Derivatives
$\mu A$	Current (microamps)
$\mu s$	Time (microseconds)
$\omega t$	Angular Frequency times Time
$\theta$	Theta; Angle describing particle direction
$\varphi$	Angle describing particle direction
$\Phi$	Azimuth angle

### 13.3 LIST OF FIGURES

FIGURE 2-1 ASPOC INSTRUMENT PICTURE AND SPACECRAFT ACCOMMODATION .....	12
FIGURE 2-2 ASPOC RESULTS FROM THE EXTENDED DUAL-BEAM TEST ON MMS4 .....	15
FIGURE 2-3 ASPOC OPERATING MODES.....	17
FIGURE 3-1 RELATIONSHIP BETWEEN ASTROPHYSICAL AND MAGNETOSPHERIC COORDINATE SYSTEMS. (COORDINATE SYSTEMS AND TRANSFORMATIONS IN THE DASHED BOX ARE DESCRIBED IN DETAIL BY VALLADO [2007]. (ADAPTED FROM LANLGEOMAG DOCUMENTATION.)).....	36
FIGURE 4-1 THE 64 FPI SPECTROMETERS AND 4 IDPU .....	45
FIGURE 4-2 MEASUREMENTS OF THE ESA AND DEFLECTOR PLATES IN THE DxS .....	49
FIGURE 4-3 DISTRIBUTION OF DES IMAGE SIZES FOR THE FOUR OBSERVATORIES AFTER TWO DES WERE POWERED OFF .....	51
FIGURE 4-4 FPI IDPU STATE DIAGRAM OF MODES OF OPERATIONS.....	53
FIGURE 4-5 SAMPLE OPERATING POINT CALIBRATION PLOT (FOR ALL PIXELS AT CURRENT VOLTAGE (BLUE) AND AN INCREASE OF 50V (RED). VERTICAL BLACK LINES REPRESENT OPPORTUNITIES FOR A VOLTAGE INCREASE (MACRO LOADS).....	54
FIGURE 5-1 COMPLETED HPCA FLIGHT MODEL 1 .....	89
FIGURE 5-2 HPCA DIMENSIONS .....	91
FIGURE 5-3 HPCA POSITION SENSITIVE ANODE [AT LEFT, THE ANODE WITH 16 ELEVATION-START PADS AND 16 CONCENTRIC STOP RINGS. AT RIGHT, THE OPERATION OF THE ANODE WITH RESPECT TO ELEVATION DETECTION, AND FLIGHT DISTANCE CORRECTION].....	93
FIGURE 5-4 HPCA TOF CHANNEL ASSIGNMENT FROM CALIBRATION.....	94
FIGURE 5-5 HPCA FLIGHT MODEL 4 (FM4 ON MMS3) ELEVATION AND ANODE GAIN RESPONSE .....	96
FIGURE 5-6 HPCA START ANODE ARRANGEMENT AND FIELD-OF-VIEW (FOV) SECTORS FOR INSTRUMENT MOUNTED ON MMS SPACECRAFT .....	97
FIGURE 5-7 HPCA AZIMUTH (A) RESPONSE .....	99
FIGURE 5-8 HPCA ENERGY SWEEPING AND AZIMUTH LOOK DIRECTION .....	100
FIGURE 5-9 CORRECTING COUNTS FOR DECIMATION BEFORE CONVERTING TO FLUX .....	109
FIGURE 6-1 SUMMARY OF THE CAPABILITIES AND SPACECRAFT MOUNTING OF THE EPD INSTRUMENTS: EIS AND FEEPS. [NOTE THAT THE ENERGY RANGES OF MEASUREMENTS HAVE VARIED SOMEWHAT OVER THE COURSE OF THE MISSION] (FROM MAUK ET AL., 2016)	125
FIGURE 6-2 THE EPD FIELDS-OF-VIEW ARE CONFIGURED TO PROVIDE MAXIMUM SKY COVERAGE OF ENERGETIC PARTICLES. [THE TWO FEEPS SENSORS PROVIDE NEARLY SIMULTANEOUS FULL-SKY ELECTRON COVERAGE, WHEREAS THE TWO FEEPS SENSORS COMPLEMENT THE EIS FAN-SHAPED FOV TO PROVIDE ION COVERAGE IN APPROXIMATELY 1/3 OF A SPIN.] (FROM MAUK ET AL. [2016]) .....	126
FIGURE 6-3 SCHEMATICS DETAILING HOW THE EIS SENSOR WORKS .....	127
FIGURE 6-4 THE FOVS OF THE FEEPS (A) ELECTRON AND (B) ION SENSORS, OR “EYES”, WHILE (C) EACH PAIR OF EYES IS COMBINED INTO ONE OF TWELVE “HEADS” ON EACH FEEPS SENSOR (FROM BLAKE ET AL. [2016]).....	128
FIGURE 6-5 THE UNIT VECTORS OF THE LOOK DIRECTIONS OF THE EIS TELESCOPES. [CARE SHOULD BE EXERCISED WHEN CONSIDERING THE TELESCOPES HIGHLIGHTED IN THE DIFFERENTLY-SHADED ROWS AS THESE LOOK DIRECTIONS ARE SUBSTANTIALLY BLOCKED.] (FROM MAUK ET AL. [2016]) .....	129
FIGURE 6-6 THE LOOK DIRECTION UNIT VECTOR (v) OF EACH FEEPS EYE IN THE FEEPS COORDINATE SYSTEM (FCS) (FROM MAUK ET AL. [2016]) .....	130
FIGURE 6-7 EXAMPLE OF THE COMPARISON OF OMNI-DIRECTIONAL PROTON SPECTRA FROM THE EIS, FEEPS, HPCA, AND FPI/DIS SENSORS ON MMS 3 (A) BEFORE AND (B) AFTER THE EIS DATA WAS CORRECTED [L2 DATA WAS USED FOR ALL SENSORS EXCEPT HPCA (L1b), WHICH DID NOT HAVE L2 DATA AVAILABLE AT THE TIME THAT THE CROSS-CALIBRATION EFFORTS WERE MADE] .....	134
FIGURE 6-8 AN EXAMPLE OF THE EFFECTS OF SUNLIGHT CONTAMINATION IN THE FEEPS BURST DATA [THIS DATA SHOWS INTENSITY FOR TIME VERSUS SPIN SECTOR FOR EACH SPACECRAFT (MMS1-4 FROM TOP TO BOTTOM) FOR 23 AUGUST 2015. THE WHITE AND BLACK SPLOTCHED HORIZONTAL LINES PERMEATING THE MMS2-4 DATA ON THE LEFT SHOWS THE EFFECT OF SUNLIGHT CONTAMINATION ON CERTAIN SECTORS. THE PANELS ON THE RIGHT SHOW THE SAME DATA WITH THE AFFECTED SECTORS APPROPRIATELY MASKED] .....	135
FIGURE 6-9 MAPPING OF THOSE SECTORS FROM EACH EYE AFFECTED (YELLOW) AND UNAFFECTED (BLUE) BY SUNLIGHT CONTAMINATION ON EACH SPACECRAFT DURING AUGUST-SEPTEMBER 2015 .....	136
FIGURE 6-10 ENERGY SPECTRA OF THE 24 INDIVIDUAL FEEPS EYES (3 ION AND 9 ELECTRONS PER SENSOR, TOP AND BOTTOM) ON MMS1 [THE REDUCED COUNT RATES OBSERVED IN THE LOWEST ENERGY CHANNEL FOR MULTIPLE EYES IS CONTRIBUTED TO THRESHOLDS SET NEAR OR AT THE SENSOR’S NOISE THRESHOLD].....	137

FIGURE 6-11 EXAMPLE OF THE EFFECT OF SUNLIGHT CONTAMINATION ON FEEPS SURVEY DATA [OMNI-DIRECTIONALLY-AVERAGED ENERGY SPECTRA FOR ELECTRONS AND IONS ARE SHOWN IN THE TOP AND MIDDLE PANELS, RESPECTIVELY. THE BOTTOM PANEL SHOWS THE SPIN SECTOR] .....	138
FIGURE 6-12 DETAILS OF THE EPD-SOC INTERFACE AND DATA FLOW [LEVELS 1A AND 1B ARE GENERATED BY THE MMS SOC AT LASP, WHILE LEVEL 2 AND HIGHER PRODUCTS ARE GENERATED BY THE EPD TEAM AT LASP (FEEPS) AND APL (EIS)] .....	140
FIGURE 6-13 THE FOUR INSTITUTIONS INVOLVED IN PRODUCING THE FINAL FEEPS DATA SET [SWRI (RESPONSIBLE FOR THE CIDP ONBOARD EACH SPACECRAFT), LASP (RESPONSIBLE FOR CALIBRATION TABLES, DATA PROCESSING, AND THE POC), AEROSPACE (RESPONSIBLE FOR DATA CALIBRATION FACTORS AND UPDATES), AND APL (RESPONSIBLE FOR VALIDATION AND MANAGEMENT)] .....	141
FIGURE 6-14 EXAMPLE OF COEFFICIENTS OF UP TO THE 6 <sup>TH</sup> -ORDER USED TO DEFINE THE FUNCTIONAL RELATIONSHIP OF MULTIPLE PARAMETERS IN THE EIS CALIBRATION MATRIX .....	148
FIGURE 8-1 PHOTOGRAPH OF THE FLUXGATE SENSOR WITH PIGTAIL HARNESS .....	171
FIGURE 8-2 THE RELATIONSHIP OF AFG AND DFG INSTRUMENT COORDINATES RELATIVE TO THE MMS S/C (OR BCS) COORDINATES AND OTHER MAGNETIC INSTRUMENT COORDINATES .....	175
FIGURE 8-3 FREQUENCY RESPONSE FOR DEC 32 MODE OF DFG IN LOW RANGE .....	176
FIGURE 8-4 FREQUENCY RESPONSE FOR DEC 64 MODE OF DFG IN LOW RANGE .....	176
FIGURE 8-5 AFG FM4 128 S/S FREQUENCY RESPONSE FOR X (BLUE), Y (GREEN), AND Z (RED) INSTRUMENT AXES .....	177
FIGURE 8-6 DIAGRAM OF THE COORDINATES AND AXES USED IN THE CALIBRATION PROCESS .....	179
FIGURE 8-7 MISSION TREND OF AFG OFFSETS [DFG SHOWS SIMILAR SHORT-TERM VARIATIONS AND TRENDS. SPIN AXIS OFFSETS (O1+O1T AND O2+O2T) SHOW MEASURED (AND CORRECTED) SHORT-TERM OFFSET CHANGES. ERROR ON SPIN PLANE OFFSET MEASUREMENTS ARE <0.05 NT. ERROR BARS ARE SHOWN ON SPIN AXIS DATA TO ESTIMATE PROBABLE LEVEL OF ORBIT-SCALE VARIATIONS. NOTE THAT LARGE CHANGES IN SPIN AXIS OFFSETS DURING MANEUVERS ARE NOT ALWAYS REFLECTED IN THE O3 MEASUREMENTS DUE TO INSUFFICIENT DATA] .....	183
FIGURE 8-8 OVERVIEW OF MMS MAGNETOTAL PASS ON 13 TO 16 JULY 2019 .....	186
FIGURE 8-9 EXPANDED VIEW OF THE PAIRWISE DIFFERENCES IN THE MAGNETIC FIELD FOR THE 08:50 TO 09:00 UT INTERVAL ON 2 MAY 2019 SHOWING DIFFERENCES IN THE MAGNETIC FIELD FOR ALL THREE MAGNETIC FIELD COMPONENTS IN GSE COORDINATES .....	187
FIGURE 8-10 EXAMPLE OF AN INTERVAL THAT WILL BE FLAGGED AS NOISE .....	192
FIGURE 9-1 SCM SENSOR .....	203
FIGURE 9-2 SCM PRE-AMPLIFIER .....	203
FIGURE 9-3 FREQUENCY RESPONSE OF DIGITAL FILTERS .....	208
FIGURE 9-4 FREQUENCY RESPONSE OF 5-POLE LOW PASS BESSEL FILTER .....	209
FIGURE 9-5 CONTIGUOUS SEGMENTS MANAGEMENT .....	210
FIGURE 9-6 COMPARISON BETWEEN NON-CONTIGUOUS (BLACK) AND CONTIGUOUS (RED) PROCESSING .....	211
FIGURE 9-7 SCM FM4 TF AT CHAMBON .....	212
FIGURE 9-8 SCM FM4 TF AT CHAMBON .....	212
FIGURE 10-1 EDI GUN-DETECTOR UNIT .....	218
FIGURE 10-2 GUN SN 4 RESIDUAL BEAM POINTING ERROR AT 500 eV .....	224
FIGURE 10-3 GUN SN 4 RESIDUAL BEAM POINTING ERROR AT 1 keV .....	225
FIGURE 10-4 EDI SENSOR SN8 PREAMPLIFIER DELAY MEASUREMENTS .....	226
FIGURE 10-5 EDI SENSOR SN8 ROLL TEST RESULTS AT 2400V AND 2600V .....	226
FIGURE 10-6 COMPARISON OF SIMULATED RESPONSE (TOP ROW) AND MEASURED RESPONSE (BOTTOM ROW) OF THE EDI OPTICS FOR THREE LOOK DIRECTIONS [THE VERTICAL AXIS SHOWS THE ANODE PAD NUMBER OF THE COUNTS RECEIVED BY THAT PAD AND THE HORIZONTAL AXIS SHOWS THE ANGULAR RANGE RELATIVE TO THE SYMMETRY AXIS OF THE GDU] .....	227
FIGURE 10-7 EDI GDU DETECTOR CHARACTERIZATION TEST SETUP .....	228
FIGURE 10-8 GDU SN9 ROLL TEST AT 500 eV FOR PITCH ANGLE 0 (GDU SYMMETRY AXIS VERTICALLY, PERPENDICULAR TO THE BEAM) AND OPTICS LOOK DIRECTION 90 DEGREES .....	229
FIGURE 10-9 GDU SN9 UV SENSITIVITY TEST AT 500 eV [COUNTS PER 125 MS AS A FUNCTION OF PITCH ANGLE AND ANODE NUMBER FOR A FIXED ROLL ANGLE OF 25 DEGREES AND AN OPTICS LOOK DIRECTION OF 90 DEGREES] .....	229
FIGURE 10-10 AZIMUTHAL CORRECTION FACTORS FOR MMS1 GDU1 (SN3) FOR THE SEVEN DETECTOR CHARACTERIZATIONS THAT WERE USED TO ARRIVE AT AN AVERAGE AZIMUTHAL CORRECTION MAP [THE COLORS IN EACH PANEL SEPARATE DATA FROM DIFFERENT OPTICS LOOKS ANGLES] .....	231
FIGURE 10-11 POLAR CORRECTION FOR EDI AMBIENT MODE DATA [THE RED TRACE SHOWS THE ORIGINAL VERSION (V1) DERIVED FROM EDI BURST DATA DURING A QUIET INTERVAL DURING THE COMMISSIONING PHASE. THE GREEN TRACE IS THE IMPROVED CORRECTION	



DERIVED FROM IN-FLIGHT DETECTOR CHARACTERIZATION DATA. THE BLUE TRACE (V3) IS A SLIGHT CORRECTION FOR SMALL POLAR ANGLE VALUES DERIVED BY COMPARING EDI DATA WITH L2 DES FLUXES] .....232

FIGURE 10-12 EDI ELECTRIC FIELD MODE DATA PROCESSING FLOW .....240

FIGURE 10-13 EDI QUALITY-ZERO DATA PROCESSING .....244

FIGURE 10-14 EDI AMBIENT MODE DATA PROCESSING FLOW .....246

FIGURE 11-1 SCHEMATIC OF SDP AND ADP PROBES .....257

FIGURE 11-2 IDEALIZED CURRENT-VOLTAGE CURVE OF A BIASED PROBE IN A LOW DENSITY (1 CC) PLASMA [THE TOTAL CURRENT TO THE PROBE IS SUM OF ELECTRON CURRENT (RED), ION CURRENT (GREEN) AND PHOTOELECTRON CURRENT (PURPLE)] .....258

FIGURE 11-3 ELECTRIC FIELD MODE (BIASED PROBES).....258

FIGURE 11-4 COMPARISON OF (LEFT) MEASURED (BLUE) AND RECONSTRUCTED (ORANGE) WAVE FORMS USING DATA TAKEN PRIOR TO THE ANOMALY AND (RIGHT) POST-ANOMALY NOISE LEVELS OF THE MEASURED (BLUE), RECONSTRUCTED (ORANGE), AND COMBINED (YELLOW) PRODUCTS ALONG THE SDP3-4 AXIS .....259

FIGURE 11-5 L2Pre CALIBRATION ALGORITHM .....263

FIGURE 11-6 L2 CALIBRATION ALGORITHM.....264

FIGURE 12-1 METHOD FOR DETERMINING THE IN-FLIGHT NOISE FLOORS (TOP). THE PSD OF THE TIME SERIES WAVEFORMS IS CALCULATED FOR A BURST INTERVAL (MIDDLE). THE PSD IS HISTOGRAMMED AT EACH TIME STEP (BOTTOM). THE HISTOGRAMS ARE ACCUMULATED ACROSS ALL BURST INTERVALS. ....273

FIGURE 12-2 BIMODAL DISTRIBUTION IN PSD IDENTIFIES NOISE FLOOR AND SIGNAL PEAKS (A CUT THROUGH THE PSD HISTOGRAMS AT 2 HZ REVEALS A BIMODAL DISTRIBUTION WITH THE LEFT PEAK ASSOCIATED WITH NOISE AND THE RIGHT PEAK ASSOCIATED WITH SIGNAL.) .....274

FIGURE 12-3 IN-FLIGHT NOISE FLOOR COINCIDES WITH GROUND-MEASURED NOISE FLOOR (HISTOGRAMMED PSD FOR FGM (LEFT) AND SCM (RIGHT), X,Y, AND Z-COMPONENTS (TOP, MIDDLE, BOTTOM). NOISE FLOORS ARE OVERPLOTTED IN MAGENTA. HAND-PICKED PEAKS IN PSD ARE IN GREEN AND MAGENTA.) .....274

FIGURE 12-4 NOISE AND SIGNAL DISTRIBUTION FOR FGM AND SCM, ALONG WITH THEIR FUNCTIONAL FORMS (“LO” (HI) REPRESENTS THE NOISE (SIGNAL) DISTRIBUTION FITS.) .....275

FIGURE 12-5 GAIN RATIO AND PHASE DIFFERENCES BETWEEN DFG AND SCM USED FOR CROSS-CALIBRATION PURPOSES (THE GAIN RATIO IS UNITY AND THERE IS ZERO PHASE DIFFERENCE SO THERE IS NO NEED FOR CORRECTION IN THE FSM ALGORITHM.) .....276

FIGURE 12-6 FIR FILTER THAT MERGES THE FGM AND SCM DATASETS (THE IMPULSE RESPONSE (TOP) AND FREQUENCY RESPONSE (CENTER, BOTTOM ) OF THE FIR FILTER. MERGING OCCURS BETWEEN 3 AND 6 Hz.).....277

FIGURE 12-7 APPLICATION OF THE MERGING FILTER RESULTS IN AN IMPROVED NOISE FLOOR FOR THE FSM DATA PRODUCT (THE MERGING FILTER IS APPLIED TO THE OBSERVED NOISE AND SIGNAL SPECTRA, RESULTING IN A LOWER NOISE FLOOR WITHIN THE 4-7 Hz BANDPASS).....278

FIGURE 12-8 FSM DATA SHOWN AS THE MERGER OF FGM AND SCM DATA WITH IMPROVED NOISE FLOOR IN THE MERGING INTERVAL 279

FIGURE 12-9 WORK FLOW OF THE FSM MERGING PROCESS.....279

### 13.4 LIST OF TABLES

TABLE 1-1 CONTENTS: SECTIONS AND INSTRUMENTATION <sup>1</sup> .....	8
TABLE 1-2 INSTRUMENT STATUS TABLE .....	9
TABLE 1-3 MMS MISSION PHASES .....	10
TABLE 1-4 MMS PROJECT APPLICABLE DOCUMENTS .....	11
TABLE 2-1 STATUS OF ASPOC INSTRUMENTS TABLE .....	13
TABLE 2-2 ASPOC TELEMETRY ALLOCATION .....	14
TABLE 2-3 ASPOC CALIBRATION TABLE .....	19
TABLE 2-4 ASPOC DATA PRODUCT ISSUES AS OF 09/30/2022 .....	29
TABLE 2-5 ASPOC QUICKLOOK DATA PLOT .....	32
TABLE 2-6 ASPOC APPLICABLE DOCUMENTS .....	33
TABLE 3-1 ANCILLARY DATA .....	41
TABLE 3-2 ATTITUDE DATA .....	41
TABLE 3-3 COORDINATE TRANSFORMATION DATA .....	41
TABLE 3-4 POSITION AND VELOCITY DATA .....	42
TABLE 3-5 MAGNETIC FIELD MODE DEPENDENT QUANTITIES DATA .....	42
TABLE 3-6 MEC APPLICABLE DOCUMENTS .....	44
TABLE 4-1 FPI OFF-NOMINAL SPECTROMETER STATUS .....	46
TABLE 4-2 DATA USAGE SUMMARY CHECKLIST .....	48
TABLE 4-3 TELEMETRY USE RATES FOR FPI (KBIT/s) .....	50
TABLE 4-4 SPINTONE AMPLITUDES .....	63
TABLE 4-5 L2 3D DES/DIS SKYMAPS .....	65
TABLE 4-6 L2 DES DISTRIBUTION AUX .....	65
TABLE 4-7 L2 DES/DIS MOMENTS .....	67
TABLE 4-8 L2 DES/DIS MOMENTS AUX .....	69
TABLE 4-9 DEFINITION AND UNITS OF MMS/FPI PLASMA MOMENTS .....	70
TABLE 4-10 CONSTANTS USED IN THE CALCULATION IN MMS/FPI PLASMA MOMENTS .....	70
TABLE 4-11 PITCHANGDIST SPECTROGRAMS .....	74
TABLE 4-12 MMS 1 VOLTAGE OPERATIONS (SETTINGS V14 – V26) .....	76
TABLE 4-13 MMS 1 VOLTAGE OPERATIONS (SETTINGS V27 – V34) .....	76
TABLE 4-14 MMS 1 VOLTAGE OPERATIONS (SETTINGS V35 – V43) .....	77
TABLE 4-15 MMS 2 VOLTAGE OPERATIONS (SETTINGS V14 – V26) .....	77
TABLE 4-16 MMS 2 VOLTAGE OPERATIONS (SETTINGS V27 – V34) .....	78
TABLE 4-17 MMS 2 VOLTAGE OPERATIONS (SETTINGS V35 – V43) .....	78
TABLE 4-18 MMS 3 VOLTAGE OPERATIONS (SETTINGS V14 – V26) .....	79
TABLE 4-19 MMS 3 VOLTAGE OPERATIONS (SETTINGS V27 – V34) .....	79
TABLE 4-20 MMS 3 VOLTAGE OPERATIONS (SETTINGS V35 – V43) .....	80
TABLE 4-21 MMS 4 VOLTAGE OPERATIONS (SETTINGS V14 – V26) .....	81
TABLE 4-22 MMS 4 VOLTAGE OPERATIONS (SETTINGS V27 – V34) .....	81
TABLE 4-23 MMS 4 VOLTAGE OPERATIONS (SETTINGS V35 – V43) .....	82
TABLE 4-24 LIST OF ENERGY STEPPING TABLES USED BY FPI FOR SCIENCE OPERATIONS BY MISSION PHASE, DATE, AND TABLE DESIGNATION .....	82
TABLE 4-25 PHASE 1A & PHASE 1B DES & DIS STEPPER TABLE .....	83
TABLE 4-26 PHASE 2B DES & DIS STEPPER TABLE .....	83
TABLE 4-27 PHASE 3B DES & DIS STEPPER TABLE .....	84
TABLE 4-28 FPI ENERGY PROFILES SINCE MISSION START .....	85
TABLE 4-29 FPI ENERGY COLLECTION PROFILES .....	86
TABLE 4-30 FPI APPLICABLE DOCUMENTS .....	88
TABLE 5-1 HPCA NOMINAL MODES AND VOLUME .....	91
TABLE 5-2 HPCA FLIGHT MODEL ANALYZER CONSTANTS .....	92
TABLE 5-3 HPCA SPECIES MASS-TO-CHARGE RATIOS .....	93
TABLE 5-4 HPCA PARAMETERS CONTROLLING DIMENSIONS, SYMBOLS, AND INDICIES .....	95

TABLE 5-5 ANODE SPECIFIC GAIN CORRECTION FACTORS FOR HPCA FLIGHT MODELS 1-4.....	97
TABLE 5-6 HPCA START NOMINAL ANODE LOOK DIRECTIONS.....	98
TABLE 5-7 HPCA ANODE-ELEVATION RESPONSE .....	98
TABLE 5-8 HPCA SOLID ANGLE SPACE CORRECTION FACTORS.....	98
TABLE 5-9 HPCA AZIMUTHAL ARRIVAL DIRECTIONS IN 1 ENERGY SWEEP .....	102
TABLE 5-10 A <sub>0</sub> 's (UPDATED PER DISCUSSION IN SECTION 5.4.1).....	104
TABLE 5-11 <ΔE/E ΔA> FOR HPCA FMs 1-4 .....	104
TABLE 5-12 MICROCHANNEL PLATE (MCP) VOLTAGE SETTINGS .....	105
TABLE 5-13 HPCA PERFORMANCE REQUIREMENTS.....	106
TABLE 5-14 NOMINAL DECIMATIONS AND TIMING .....	108
TABLE 5-15 M <sub>s</sub> VALUES FOR TEMPERATURE CALCULATION.....	111
TABLE 5-16 HPCA QUALITY FLAGS DEFINITION.....	118
TABLE 5-17 L2 ION CDF FILE.....	120
TABLE 5-18 L2 MOMENTS CDF FILE .....	123
TABLE 5-19 L2 TOF COUNTS CDF FILE.....	123
TABLE 5-20 HPCA APPLICABLE DOCUMENTS.....	124
TABLE 6-1 SUMMARY OF THE EIS VERSIONING SCHEME .....	133
TABLE 6-2 HISTORY OF SUNLIGHT CONTAMINATING MASKING TABLES IMPLEMENTED TO-DATE ONBOARD MMS SPACECRAFT.....	139
TABLE 6-3 LIST OF THE BURST VARIABLE INCLUDED IN THE FEEPS ELECTRON DATA PRODUCT .....	155
TABLE 6-4 LIST OF THE SURVEY VARIABLE INCLUDED IN THE FEEPS ELECTRON DATA PRODUCT.....	156
TABLE 6-5 LIST OF THE BURST VARIABLES INCLUDED IN THE FEEPS ION DATA PRODUCT .....	157
TABLE 6-6 LIST OF THE SURVEY VARIABLES INCLUDED IN THE FEEPS ION DATA PRODUCT.....	158
TABLE 6-7 LIST OF THE VARIABLES INCLUDED IN THE L2 EIS PHXTOF BURST DATA PRODUCT.....	162
TABLE 6-8 LIST OF THE VARIABLES INCLUDED IN THE EIS PHXTOF SURVEY DATA PRODUCT .....	164
TABLE 6-9 LIST OF THE VARIABLES IN THE L3 EPD ELECTRON SURVEY AND BURST DATA PRODUCTS [THE ONLY DIFFERENCES IN THE VARIABLES IS THE <DATA_RATE> IN THE PREFIX] .....	164
TABLE 6-10 LIST OF THE VARIABLES INCLUDED IN THE L3 EPD ION SURVEY DATA PRODUCT.....	165
TABLE 6-11 LIST OF THE VARIABLES IN THE L3 EPD ION BURST DATA PRODUCT .....	166
TABLE 6-12 EIS APPLICABLE DOCUMENTS .....	167
TABLE 6-13 FEEPS APPLICABLE DOCUMENTS .....	168
TABLE 7-1 FIELDS APPLICABLE DOCUMENTS .....	170
TABLE 8-1 AFG AND DFG DYNAMIC RANGES.....	171
TABLE 8-2 FGM DATA ANOMALIES.....	174
TABLE 8-3 FGM DATA RATE MODES.....	177
TABLE 8-4 RAW AND ORBIT-AVERAGED TELEMETRY DOWNLINK RATES FOR AFG AND DFG [*ASSUMING 50% DUTY CYCLE FOR ROI PER ORBIT (CURRENT ROI DUTY CYCLE IS LESS; HOWEVER, FAST SURVEY CURRENTLY RUNS AT 100% DUTY CYCLE). **ASSUMING 17 MINUTES OF BURST DOWNLINK/DAY] .....	177
TABLE 8-5 IN-FLIGHT CALIBRATION METHODS LISTED IN THE ORDER OF EVALUATION [THE CALIBRATION QUANTITIES DETERMINED BY EACH METHOD IN EACH GAIN RANGE ARE LISTED, TOGETHER WITH THE APPROXIMATE TIME WINDOW REQUIRED TO CALCULATE UPDATES IN THE CALIBRATION FILES. THE CALIBRATION EFFORT IS DIVIDED BETWEEN THREE INSTITUTIONS, WITH EACH INSTITUTION TAKING OWNERSHIP OF A SUBSET OF THE CALIBRATION METHODS, AS SHOWN] .....	182
TABLE 8-6 DATA FILE X-VERSION RELEASE NOTES [SEE FGM VERSION RELEASE NOTES AT THE SDC WEB SITE DATASETS SECTION FOR LATEST UPDATES (HTTPS://LASP.COLORADO.EDU/MMS/SDC/PUBLIC/DATASETS/FIELDS/FGM_VRN.TXT)] .....	189
TABLE 8-7 LISTS THE Y-VERSION AND EPOCH OF L2 DATA AT WHICH IMPROVEMENTS TO THE CALIBRATION OR CALIBRATION PROCESS WERE INTRODUCED TO THE CALIBRATION FILE, AS WELL AS THE EARLIEST EPOCH REPROCESSED WITH THESE IMPROVEMENTS .....	190
TABLE 8-8 KNOWN ISSUES FLAGGED IN FGM DATA .....	192
TABLE 8-9 L2 MAGNETIC FIELD TIME SERIES DATA PARAMETERS [ALL PARAMETERS HAVE VAR_TYPE = 'DATA'. FOR BURST FILES, REPLACE ' _SRVY' WITH ' _BRST' IN THE PARAMETER NAMES AND LABELS]. * INDICATES VAR_TYPE WAS 'SUPPORT_DATA' PRIOR TO V6. ....	197
TABLE 8-10 L2 HOUSEKEEPING DATA PARAMETERS ASSOCIATED RECORD-FOR-RECORD WITH THE MAGNETIC FIELD DATA. ALL PARAMETERS ARE VAR_TYPE='SUPPORT_DATA'. FOR BURST FILES, REPLACE ' _SRVY' WITH ' _BRST' IN THE PARAMETER NAMES AND LABELS. ** INDICATES PARAMETERS NOT AVAILABLE PRIOR TO V6. ....	198

TABLE 8-11 L2 CDF FILE ANCILLARY EPHEMERIS PARAMETERS HAVE VAR\_TYPE = 'DATA', EXCEPT \* INDICATES VAR\_TYPE= 'SUPPORT\_DATA'. \*\*\* INDICATES DATA TYPE WAS CDF\_REAL4 PRIOR TO V6) [FOR BURST FILES, REPLACE '\_SRVY' WITH '\_BRST' IN THE PARAMETER NAMES AND LABELS] ..... 198

TABLE 8-12 LIST OF TYPES OF FLAGS THAT MAY BE APPLIED TO THE DATA [IDENTIFYING THE ASSOCIATED BIT FLAGS WITHIN THE 32-BIT WORD STORED IN THE MMS#\_FGM\_FLAG\_SRVY\_L2 PARAMETER, AND THE X-VERSION OF THE DATA FILE WHEN THE FLAG IS FIRST AVAILABLE. A BIT VALUE OF 1 INDICATES THAT A GIVEN FLAG IS SET, SO THAT AN OVERALL FLAG WORD VALUE OF 0 INDICATES GOOD DATA]..... 199

TABLE 8-13 FGM APPLICABLE DOCUMENTS ..... 202

TABLE 9-1 HERITAGE OF SCM WAVEFORM SAMPLES AND ONBOARD SPECTRA ..... 204

TABLE 9-2 PRODUCT DESCRIPTIONS ..... 205

TABLE 9-3 THEORETIC DESCRIPTIONS ..... 206

TABLE 9-4 PARAMETERS USED BY THE SCM CALIBRATION PROGRAM FOR EACH SAMPLING MODE..... 207

TABLE 9-5 DESCRIPTION OF THE SCM CALIBRATION SEQUENCE ..... 213

TABLE 9-6 SCM APPLICABLE DOCUMENTS..... 217

TABLE 10-1 SUMMARY OF EDI INSTRUMENT DEGRADATION AND OPERATIONAL IMPACT..... 220

TABLE 10-2 AMBIENT MODE SAMPLING OPTIONS SUMMARY ..... 221

TABLE 10-3 EDI DATA VOLUME IN SURVEY AND BURST FOR E-FIELD AND AMBIENT MODE ..... 222

TABLE 10-4 EDI AMBIENT MODE L2 DATA PRODUCT NAMES ..... 236

TABLE 10-5 SENSOR ANODE PLACEMENT FOR EDI L2 AMBIENT MODE DATA PRODUCTS ..... 237

TABLE 10-6 SENSOR ANODE NUMBERS PER CHANNEL FOR EACH EDI L2 AMBIENT MODE DATA PRODUCT ..... 237

TABLE 10-7 RELATION OF SENSOR ANODE NUMBERS TO AZIMUTH ANGLES OF EDI DETECTOR LOOK DIRECTION ..... 238

TABLE 10-8 EDI AMBIENT MODE FLIP FLAG HANDLING ..... 238

TABLE 10-9 L2 E-FIELD DATA ..... 243

TABLE 10-10 L2 QUALITY-ZERO DATA ..... 245

TABLE 10-11 L2 AMBIENT FIELD ALIGNED MODE SURVEY DATA..... 248

TABLE 10-12 L2 AMBIENT FIELD ALIGNED BURST DATA ..... 249

TABLE 10-13 L2 AMBIENT ALTERNATING PITCH ANGLE MODE SURVEY DATA ..... 251

TABLE 10-14 L2 AMBIENT ALTERNATING PITCH ANGLE MODE BURST DATA ..... 253

TABLE 10-15 L2 AMBIENT PERPENDICULAR MODE SURVEY DATA ..... 254

TABLE 10-16 L2 AMBIENT PERPENDICULAR MODE BURST DATA ..... 255

TABLE 10-17 EDI APPLICABLE DOCUMENTS..... 255

TABLE 11-1 SAMPLING SEQUENCE AND DELAYS OF EDP DC RAW DATA ..... 260

TABLE 11-2 EDP OPERATING MODES AND DATA LEVELS..... 265

TABLE 11-3 EDP DATA TYPES AND DESCRIPTIONS..... 266

TABLE 11-4 EDP QUALITY INDICATOR ..... 267

TABLE 11-5 EDP BITMASK VALUES AND CORRESPONDING QUALITY INDICATOR ..... 268

TABLE 11-6 DESPUN ELECTRIC FIELD IN DSL ..... 269

TABLE 11-7 DESPUN ELECTRIC FIELD IN DSL AFTER PRELIMINARY CALIBRATION..... 269

TABLE 11-8 DESPUN ELECTRIC FIELD IN DSL AND GSE..... 269

TABLE 11-9 EDP APPLICABLE DOCUMENTS ..... 270

TABLE 12-1 FSM FILE STRUCTURE VARIABLES ..... 280

TABLE 12-2 FSM FILE VERSIONS ..... 280

TABLE 12-3 FSM APPLICABLE DOCUMENTS ..... 281